SCUOLA INTERNAZIONALE SUPERIORE DI STUDI AVANZATI

DOCTORAL THESIS

Entanglement and correlations in one-dimensional quantum many-body systems

Author:
Paola RUGGIERO

Supervisor:
Prof. Pasquale CALABRESE

A thesis submitted in fulfillment of the requirements for the degree of Doctor of Philosophy

in the

Statistical Physics Group
SISSA

Alla tenacia e alla sensibilità,
meravigliosamente trasmessemi dalla mia famiglia.

Contents

List of Publications

1. **Paola Ruggiero**, Vincenzo Alba, Pasquale Calabrese,
Entanglement negativity in random spin chains,
Physical Review B 94, 035152 (2016).

2. **Paola Ruggiero**, Vincenzo Alba, Pasquale Calabrese,
Negativity spectrum of one-dimensional conformal field theories,
Physical Review B 94, 195121 (2016).

3. **Paola Ruggiero**, Pasquale Calabrese,
Relative Entanglement Entropies in 1+1-dimensional conformal field theories,
Journal of High Energy Physics (2017) 02, 039.

4. **Paola Ruggiero**, Erik Tonni, Pasquale Calabrese,
Entanglement entropy of two disjoint intervals and the recursion formula for conformal blocks,
Journal of Statistical Mechanics (2018) 113101.

5. Vincenzo Alba, Silvia N. Santalla, **Paola Ruggiero**, Javier Rodrigues-Laguna, Pasquale Calabrese,
Unusual area-law violation in random inhomogeneous systems,
Journal of Statistical Mechanics (2019) 023105.

6. Sara Murciano, **Paola Ruggiero**, Pasquale Calabrese,
Entanglement and relative entropies in excited stated of inhomogeneous systems via CFT,
Journal of Statistical Mechanics (2019) 034001.

7. **Paola Ruggiero** and Yannis Brun and Jérome Dubail,
Conformal field theory on top of a breathing one-dimensional gas of hard core bosons,
SciPost Physics 6, 051 (2019).

8. Jiaju Zhang, **Paola Ruggiero**, Pasquale Calabrese,
Subsystem Trace Distance in Quantum Field Theory,
Phys. Rev. Lett. 122, 141602 (2019).

9. Hassan Shapourian, **Paola Ruggiero**, Shinsei Ryu, Pasquale Calabrese,
Twisted and untwisted negativity spectrum of free fermions,
arXiv:1906.04211.

10. Riccarda Bonsignori, **Paola Ruggiero**, Pasquale Calabrese,
Symmetry resolved entanglement in free fermionic systems,
arXiv:1907.02084.

11. Jiaju Zhang, **Paola Ruggiero**, Pasquale Calabrese,
Subsystem trace distance in low-lying states of conformal field theories,
arXiv:1907.04332.

Chapter 1

Introduction

At the center of the debate on quantum mechanics since its foundations [1–3], entanglement is arguably not *one* but rather *the* distinguishing signature of the quantum world, "the one that enforces its entire departure from classical lines of thought" [1]. Einstein used to refer to it as "spooky action at a distance" [4], being at the origin of his criticisms to quantum theory. Due to entanglement, indeed, a local action on a quantum system can affect the state of all the rest of the system and this happens *instantaneously*, in sharp contrast with the classical paradigm according to which the propagation of correlations is strictly bounded by a maximum velocity [5].

If on one side the very nature of entanglement remains elusive, on the other a lot has been understood and today entanglement is one of the most studied topics in physics, at the center of many research lines. The interest in this quantum phenomenon comes in fact from different and apparently disconnected communities, ranging from the high-energy community (for instance, the quantum-gravity one) to the quantum information and the condensed matter community. The reason is that entanglement turns out to play a central role in many different problems in physics. To mention some, in quantum information theory entanglement is seen as a resource allowing to perform tasks which would be impossible in a classical world or at least very inefficient (it is the case of quantum cryptography [6], teleportation [7], quantum error correction codes [8], and quantum computation protocols [9]). Moreover, it is believed to be a crucial phenomenon in the black hole physics [10–12]: black holes, indeed, are known to carry an entropy, the so-called Bekenstein-Hawking entropy [13,14], and this is expected to be related and (at least partially) explained by means of the entanglement between the interior and the exterior degrees of freedom of the black hole itself. Entanglement plays an important role in statistical physics, particularly in the physics of phase transitions where it is often used as a tool to probe criticality: the entanglement behavior enables to distinguish if the system is in a gapped or gapless phase and is known to display universal features in critical systems [15–18]. Entanglement is also an important quantity to look at disordered systems where randomness gives rise to interesting phenomena as localization [19–21]: in these situations entanglement is a good indicator of such properties [22,23]. Moreover, entanglement is also useful to detect and characterize topological order [24,25], spin liquids [26,27], and in general new phases of matter for which a conventional order parameter does not exist and therefore do not admit a description in terms of the Ginzburg-Landau theory. Finally, it had a main role in the understanding and development of numerical algorithms, like the ones based on Matrix Product States (MPS) and Tensor Networks [28–32]: the efficiency of these algorithms is in fact quantified by the entanglement [33].

Remarkably, entanglement is not a quantity of merely theoretical interest. Recent important advances have made it possible to prepare, manipulate and measure atoms without loss of coherence, thus allowing to set up experiments in the context of many-body quantum systems, where the first entanglement measurements have already been performed [34–37].

At this point, it should be evident the need to quantify and characterize entanglement. This is a highly non-trivial problem to which a large literature is devoted. The main difficulty lies in the fact that there does not exist a 'tape' of entanglement so that there is not *a priori* a clear and unique way to quantify the amount of entanglement in a system. Therefore we need to define quantities that fulfill the right requirements to be in some sense (to be better specified in the following) 'good entanglement measures'. Starting with the quantum information community, a lot of work has been done in this direction and plenty of definitions of entanglement measures and, more generally speaking, entanglement related quantities are available today: we are going to discuss some of them in details.

If the problem of entanglement quantification and computation is hard already when dealing with simple few-body quantum systems, one can imagine how it gets more and more cumbersome when considering many-body quantum systems. From our point of view, these are the most interesting: many intriguing phenomena, indeed, such as phase transitions or symmetry breaking, take place when considering the thermodynamic limit (TDL), meaning the limit of infinitely many degrees of freedom (DOF). This thesis fits into this context, being devoted to the characterization of entanglement and correlations in several many-body systems. The focus is on low-dimensional systems, where powerful methods allowing for exact calculations are available. Particular emphasis is given to critical one-dimensional ($1d$) systems, whose universal features are described by two-dimensional ($2d$) conformal field theory (CFT). We will largely employ CFT methods, that, as we are going to see, can be extended to describe inhomogeneous and out of equilibrium systems as well. Nonetheless, also discrete lattice models are considered, with special reference to free models, allowing for very efficient numerical calculations and some fully analytical results. Finally, also the effect of disorder is considered in lattice models, where many entanglement properties can be derived via suitable renormalization group (RG) techniques.

In the remainder of the Introduction, we first introduce the main concepts and definitions, to gain some intuition about entanglement, what really is and in particular how to measure it. We then examine entanglement in greater detail in the context of many-body quantum systems, highlighting its properties and emphasizing the main results in the literature. The last two sections are devoted to reviewing theoretical and experimental tools available to characterize and detect entanglement.

1.1 The meaning of entanglement: an operational point of view

The usual setting is the one where two parties, usually denoted as Alice and Bob, share a bipartite quantum system, and can only access one of the two parts, denoted as A and B, that for the time being, we will assume to be complementary ($B = \bar{A}$). Such a situation is mathematically described as follows. The bipartition of the system induces a bipartition of the common Hilbert space as $\mathcal{H} = \mathcal{H}_A \otimes \mathcal{H}_B$. Vectors $|\psi\rangle \in \mathcal{H}$ represent states of the total system and the most general of such vectors can be written as

$$|\psi\rangle = \sum_i \lambda_i |\psi_A^{(i)}\rangle \otimes |\psi_B^{(i)}\rangle, \tag{1.1.1}$$

with $|\psi_{A/B}^{(i)}\rangle \in \mathcal{H}_{A/B}$. This is known as *Schmidt's decomposition* [38] (note that there is just a single sum in (1.1.1), even if $\mathcal{H}_A$ and $\mathcal{H}_B$ might have different dimensions) and the entanglement properties are fully encoded in the *Schmidt's coefficients*, $\{\lambda_i\}$. A special class of states are the factorized ones, meaning vectors of the form

$$|\psi\rangle = |\psi_A\rangle \otimes |\psi_B\rangle. \tag{1.1.2}$$

For vectors it is easy, in principle at least, to determine whether a state is entangled or not: as soon as the state is in a superposition as in (1.1.1) (with more than one $\lambda_i \neq 0$), the state is entangled. However not every state is expressed in this way: the elements $|\psi\rangle$ of $\mathcal{H}$ are just a subset of all possible states, called *pure* states. The most general ones, instead, are expressed in operatorial form through a density matrix ρ as

$$\rho = \sum_j c_j |\psi^{(j)}\rangle\langle\psi^{(j)}|, \tag{1.1.3}$$

with $|\psi^{(j)}\rangle \in \mathcal{H}$. These include *mixed* states where the Schmidt decomposition does not apply. Of course, pure states represent special cases of (1.1.3) (where all the coefficients $\{c_j\}$ but one are zero). In the language of density matrices, a product state $\rho = \rho_A \otimes \rho_B$ is similarly unentangled. However, a larger class of states, called *separable states* in the form

$$\rho = \sum_i p_i \rho_A^{(i)} \otimes \rho_B^{(i)}, \tag{1.1.4}$$

with $p_i \geq 0$ being classical probabilities, are only classically correlated and therefore do not contain any amount of entanglement. Hence, the fact that superposition implies entanglement in pure states does not simply generalize to mixed states. Instead, we define the most general entangled state as a non-separable state. Note that separability (and therefore entanglement) is not a property of the state alone, but the chosen bipartition as well.

1.1.1 LOCC, separable and PPT operations

By definition, a state is entangled if it is non-separable. However what 'entangled' really means is far from being intuitive and is actually better understood from an operational point of view: in particular, it is convenient to first identify a class of physical operations acting on the two subsystems that are expected not to create or increase the entanglement between them.

Among the possible operations, a special role is played by the so-called LOCC – *local operations* and *classical communication* [39, 40]. The very mathematical definition is hard and we will not enter in such details. To get some intuition, instead, we go back to Alice and Bob: using only LOCC, Alice is allowed, for example, to perform quantum operations on her part of the system, A, and then communicate classically the result to Bob, who in turn can decide to act on his share, conditioned on the information received. LOCC are crucially related to entanglement: separable states, indeed, are closed under LOCC operations whereas, all non-separable states cannot be reached by LOCC only starting from a given separable state. *Classical correlations*, then, are the ones that can be generated through LOCC, whereas the ones built-in the quantum state and not achievable in this way are the true *quantum correlations*.

It would seem natural at this point for all LOCC operations to be simply the 'separable' ones, meaning the ones that act separately on A and B (mathematically expressed as a tensor product into the two subsystems [41]). However, it has been proved [42] that this is not the case and LOCC are instead just a subset of the class of separable operations.

One can further consider more general classes of operations. An important definition is that of PPT – *positive partial transpose preserving* – operations [43, 44] based on the observation, also known as *Peres criterion* [45], that a necessary condition for a state to be separable is the positivity of its partial transpose (see Eq. (1.2.3) for a definition): in fact, while the density matrix itself is always positive definite, this is not in general ensured after partial transposition. Unfortunately, however, this is not a sufficient condition as well.

The main statement of the previous paragraphs is summarized in the following inclusions: LOCC $\subset$ separable $\subset$ PPT (both being strict bounds). Now, even if LOCC are the ones really connected to the concept of separability, separable and, in particular, PPT operations are much easier to define and deal with mathematically. Therefore, as we are going to discuss, they represent practically speaking very useful tools.

1.2 Quantifying entanglement: the axiomatic approach

Next, one would like to order the set of density matrices in terms of entanglement content. The question is whether it is possible to say uniquely that a given density matrix has more, equal or less entanglement compared to another one: in other words, we want to *quantify* entanglement.

Let us start with some observations. Since starting from a separable state, LOCC only allow to move into other separable states, entanglement cannot increase under LOCC manipulations [8,46–48]. Moreover, there exist *maximal entangled states*, namely states from which any other state can be obtained through LOCC only. Therefore one could think that LOCC is the right criterion giving such ordering. Unfortunately, this is not the case since LOCC provide instead only a partial ordering: it can be proved that there exist incomparable states [40]. That is why this operational approach to entanglement has been substituted by a *axiomatic* approach [47], according to which a given quantity is required to satisfy some given criteria or postulates to be an entanglement quantifier. On the other hand, we should emphasize that a common consensus about the postulates themselves does not exist yet. Below, instead, we limit ourselves to list

some of the most common requirements for a given map $E(\rho)$ from the space of density matrices ρ to real numbers to be a 'good entanglement measure' [49–51]:

- **Monotonicity under LOCC**, meaning that if $\Theta \in$ LOCC, then $E(\Theta(\rho)) \leq E(\rho)$: quantum local operations and classical communication can only decrease entanglement. It implies that $E(\rho)$ is constant on separable states and we can set such constant to zero. A function satisfying such property is said to be an *'entanglement monotone'*.
- **Convexity**, i.e., $E(\sum_i p_i\rho_i) \leq \sum_i p_i E(\rho_i)$. This means that entanglement cannot be created by *classically* mixing quantum states.
- **Additivity under tensor product**, i.e., $E(\otimes_i \rho_i) = \sum_i E(\rho_i)$. Entanglement indeed should not increase by just 'joining' quantum systems.

Monotonicity is considered the minimal requirement, but also convexity and additivity are usually demanded. Other properties can be required depending on the context and the problem at hand.

1.2.1 Entanglement measures for pure and mixed states

A key object entering the definition of most entanglement measures is the so-called *reduced density matrix* (RDM) of the subsystem A defined as $\rho_A \equiv \mathrm{Tr}_B\rho$, with ρ defining the state of the whole system. Of course equivalently one can consider the RDM associated with B, ρ_B.

As far as pure states are concerned (i.e., $\rho = |\psi\rangle\langle\psi|$, with $|\psi\rangle$ in (1.1.1)), the most popular measure of entanglement is the entropy of information within either subsystem, in the form of the von Neumann entropy or *entanglement entropy* (EE)

$$S(\rho_A) = -\mathrm{Tr}\,(\rho_A \log \rho_A) \tag{1.2.1}$$

It satisfies all the requirements to be considered a good measure (see above). Moreover, it satisfies two important inequalities [52, 53]

- Subadditivity, i.e., $S(\rho_{A\cup B}) \leq S(\rho_A) + S(\rho_B)$,
- Strong subadditivity, i.e., $S(\rho_{A\cup B}) + S(\rho_{A\cap B}) \leq S(\rho_A) + S(\rho_B)$,

where here A and B are not assumed to be complementary. Therefore, S basically solves the issue of the unicity of the measure already mentioned, at least for bipartite systems in a pure state, to the point that, usually, when using a different entanglement measure, one requires it to coincide with the entanglement entropy at least in some limit.

Other measures of entanglement are the so-called *Rényi entanglement entropies* (REEs) depending on the real parameter $n > 0$

$$S_n(\rho_A) = \frac{1}{1-n} \log \mathrm{Tr}\rho_A^n \tag{1.2.2}$$

from which the entanglement entropy is obtained in the limit $n \to 1$. The main drawback is that Rényi entropies do not satisfy subadditivity. Still, they remain very important quantities, in particular because of their relations with the *moments* $\mathrm{Tr}\rho_A^n$ of the RDM, that uniquely fix the spectrum of ρ_A, also known as *entanglement spectrum* [54].

Notice that $S(\rho_A) = S(\rho_B)$ and $S_n(\rho_A) = S_n(\rho_B)$, as immediately follows by employing the Schmidt's decomposition, Eq. (1.1.1).

Unfortunately, entanglement can be measured via entropies only if two conditions are satisfied. First of all the system (as a whole) has to be in a pure state. Moreover, entropies are good measures of entanglement only for bipartite systems. Since entanglement only measures genuine quantum correlations between two subsystems, any 'thermal' noise has to be factored out. But, as soon as the system becomes mixed, both quantum and classical effects contribute to the von Neumann and Rényi entropies and the actual amount

of quantum entanglement cannot be isolated. Also, one can easily realize that, among the properties seen before, convexity is not satisfied on general mixed states.

Even if many other measures are available in the literature, most of them are defined in terms of a variational calculus (typically involving a max or min over the Hilbert space in their definition) and therefore are not easily evaluated. Arguably, the only *computable* measure of entanglement for generic (mixed) states is the so-called *negativity*, defined in terms of the *partial transposed* (PT) *density matrix*. In the case of a bipartition of a mixed state, the PT is defined as the transposition with respect to one of the subsystems only. However, it is often useful to look at the total density matrix as arising from a larger system: when interested in the entanglement between two non-complementary subsystems A_1 and A_2 within a tripartite system ($A_1 \cup A_2 \cup B$), one can look at the PT of the RDM associated to the two subsystems of interest (e.g., A_1, A_2), after tracing out the rest (B). In practice, given the RDM $\rho_A = \sum_i \rho_{ijkl} \left|e^{(i)}_{A_1}, e^{(j)}_{A_2}\right\rangle \left\langle e^{(k)}_{A_1}, e^{(l)}_{A_2}\right|$ associated to $A = A_1 \cup A_2$, written in a local orthonormal basis $\{|e^{(k)}_{A_1}\rangle, |e^{(j)}_{A_2}\rangle\}$ of the two subsystems, the PT is obtained by exchanging the indices of subsystem A_2 (or A_1) as in

$$\rho_A^{T_2} = \sum_i \rho_{ijkl} \left|e^{(k)}_{A_1}, e^{(j)}_{A_2}\right\rangle \left\langle e^{(i)}_{A_1}, e^{(l)}_{A_2}\right| . \tag{1.2.3}$$

The negativity is then defined as

$$\mathcal{N}(\rho_A) = \frac{\left\|\rho_A^{T_2}\right\| - 1}{2}, \tag{1.2.4}$$

where $\|A\| = \mathrm{Tr}\sqrt{AA^\dagger}$ is the *trace distance* (see below). When A is Hermitian, the trace distance is simplified into the sum of the absolute value of the eigenvalues of A. Hence, the above quantities measure the *negativity* of the eigenvalues of ρ^{T_A} and can be seen as the quantitative version of Peres' criterion for separability. It can be shown that it is an entanglement monotone [55], it is convex but it is not additive. However one can consider its *logarithmic* version

$$\mathcal{E}(\rho_A) = \ln \left\|\rho_A^{T_2}\right\| , \tag{1.2.5}$$

which is additive by construction. Despite being not convex, its monotonicity under LOCC and actually under PPT operations as well was proven in [56]. Being based on the class of PPT operations, the vanishing of the logarithmic negativity is only a necessary but not a sufficient condition for a state to be separable. The other drawback is that it does not reduce to the entanglement entropy on pure states, but to Rényi with $n = 1/2$ instead.

A related interesting quantity is the spectrum of the PT density matrix, dubbed *negativity spectrum* [57], introduced as the analogue of the entanglement spectrum for generic mixed states. It can be obtained from the *moments* of the PT, $\mathrm{Tr}\left(\rho_A^{T_2}\right)^n$ and equally provides a useful entanglement-related tool (see Chapters 2 and 3).

Many other entanglement measures have been introduced and are largely used in different communities: *entanglement of formation* [7], *entanglement distillation* [43, 50], *entanglement cost* [8, 58], just to mention some. However here we chose to emphasize entropies and negativity because, as we are going to discuss further, these are the only measures we are able to deal with in extended quantum systems.

We conclude this brief discussion on entanglement measures with a final remark: one has to be aware that different measures can give different orderings between density matrices, and this can be regarded as evidence that a unique ordering according to entanglement does not exist.

1.2.2 More quantum information tools

Apart from the interest in entanglement in its own as a quantum phenomenon, in different communities entanglement measures have been borrowed from quantum information theory as powerful tools to characterize the state of the system and, more importantly, of subsystems. In fact, we have seen that, given an entanglement measure, it is possible to give an ordering in the space of RDMs associated with a given

subsystem. Further characterization of RDMs can be obtained by comparing them in several different ways. In particular, exploring other quantum information concepts may provide new insights when considering two different quantum states. In this direction, the problem of measuring the 'distance' between density matrices has also been intensively considered and several related quantities have been introduced to this aim and analyzed [9, 59].

In this respect, an interesting quantity to look at is the so-called *relative entropy* (ReE) [60–62] that for two given RDMs ρ_A and σ_A is defined as

$$S(\rho_A\|\sigma_A) = \mathrm{Tr}\,(\rho_A \log \rho_A) - \mathrm{Tr}\,(\rho_A \log \sigma_A)\,. \tag{1.2.6}$$

It can be interpreted as a measure of distinguishability of quantum states, but it is not a proper distance between ρ_A and σ_A in a mathematical sense. A measure of the difference between two RDMs should indeed be non-negative, symmetric in its inputs, equal to zero if and only if its two inputs are the same, and should obey the triangular inequality: in other words, it should be a *metric*. And this is not the case for the relative entropy, which is not symmetric and does not satisfy the triangular inequality either. Still, it is definitely a useful tool: besides being closely related to several entanglement measures [63, 64], it is also accessible in extended quantum systems, as we are going to discuss in Chapter 4.

An important family of proper metrics is instead given by

$$D_n(\rho_A, \sigma_A) = \frac{1}{2^{1/n}}\|\rho_A - \sigma_A\|_n, \tag{1.2.7}$$

which depends on the real parameter $n \geq 1$. These distances are known as *(Schatten) n-distances*, and are defined in terms of the (Schatten) n-norm [59] of a general matrix Λ, $\|\Lambda\|_n = \left(\sum_i \lambda_i^n\right)^{1/n}$, with λ_i being the absolute values of the non-vanishing eigenvalues of Λ (when Λ is hermitian). The limit $n \to 1$ of Eq. (1.2.7) gives the so-called *trace distance*, which, as we are going to see in Chapter 5, is on a special footing compared to the others.

1.3 Entanglement in quantum many body systems

In this Section, we give an overview of key properties and results of entanglement in many-body quantum systems, with particular focus on what is known in $1d$. However also a few important results valid in higher dimensions d will be mentioned along the way. Of course, we do not claim any completeness, considering the enormous amount of literature available. Instead, we choose from the beginning to restrict ourselves to stress a few important facts. For excellent reviews on the subject, suitable for different tastes and taking different points of view, depending on the authors' community of origin, we refer the reader to [65–68].

One of the most important results regarding the behavior of the EE in many-body systems goes under the name of *area law*. While *typical* states in the Hilbert space have an entropy that grows extensively with the system size (it is the case, for example, of maximally entangled states, excited eigenstates and ground states of hamiltonians with non-local interactions), the (subsystem) EE in the ground state of *gapped local* hamiltonians, is known to scale with the area of its boundary rather than with its volume [65–68]. In dimension d the scaling is of the form

$$S(\rho_A) \sim (\ell/\epsilon)^{d-1} \tag{1.3.1}$$

with ℓ denoting the typical length of the subsystem A and ϵ an *ultraviolet cut-off*. A similar behavior is found for the Rényi entropies. Note that in continuous models $\epsilon \to 0$, making the EE divergent. [We mention that one can consider suitable combinations of EE where such divergence gets canceled, as the so-called *mutual information* [9], which for two given subsystems A and B is defined as $\mathcal{I}_{A:B} \equiv S_A + S_B - S_{A\cup B}$ (where $S_X \equiv S(\rho_X)$). Unfortunately, it is well known that it provides only an upper bound to the entanglement between A and B.] For gapped many-body systems, there is a unanimous consensus that the area law is valid in arbitrary dimension [67], although a rigorous proof is only available for $1d$ systems [69]. This suggests that the ground state of local hamiltonians contains much less quantum correlation than what one might have expected, with enormous consequences for the simulability of quantum states using classical computers: for

instance, it underlies the extraordinary success of MPS methods, such as the Density Matrix Renormalization Group [30, 70–72] (DMRG), to effectively describe ground states of one-dimensional systems. As already mentioned, the efficiency of such algorithms strongly depends on the entanglement content: more specifically, the number of relevant parameters to have an approximate but faithful description of a quantum state grows with the amount of entanglement present within the state itself [33].

Nevertheless, there exist well known violations to the area law. It is in fact well known that the ground states of gapless free-fermionic hamiltonians exhibit logarithmic corrections to the area law [73–75], i.e., $S(\rho_A) = \mathcal{O}(\ell^{d-1} \ln \ell)$, in contrast with gapless bosonic systems [56], for which no corrections are present for $d \geq 2$. However, the most prominent examples of logarithmic area-law violations are critical one-dimensional models [15–18], and spin chains with a permutation symmetric ground state [76–79]. For critical systems, such corrections are particularly important: in this case, the low energy properties are captured by CFT and, besides signaling criticality, the logarithmic term turns out to be *universal*. Indeed it is proportional to the corresponding central charge, which does not depend on the microscopic details of the model but only on the universality class associated with a given fixed point of the renormalization group (RG) [80, 81]. Importantly, not only ground states but also the low-energy part of the spectrum of systems described by CFT shows sub-volume (logarithmic) scaling of the entanglement entropy. We also mention that such systems possess another universal (constant) source of entanglement, dubbed *boundary entropy* [82], related to the 'ground-state degeneracy', which depends on the universality class of the boundary conditions, and is in general non-integer. More details about the scaling of entanglement and more generally speaking CFT methods [83, 84] are given below in the Section 1.4.2. Also disorder and impurities can conspire with quantum fluctuations to induce non-trivial effects: as a remarkable example, relying on *strong disorder renormalization group* (SDRG) techniques [85] (see Section 1.4.4), a logarithmic violation of the area law has indeed been found for entanglement entropy in Ref. [86] in disordered spin chains. Furthermore, recently, more exotic examples of ground states violating the area law started to be discovered as well: for example, one can design specific spin chains whose ground state entanglement follows a volume law [87] or a square root growth with the subsystem size [88–91] (see Chapter 11 for an explicit example).

If the area law is to be physically interpreted as most of the quantum correlations being concentrated around the boundaries of the system, one would expect to observe it also when looking at different entanglement measures. And in fact, it was recently observed also for the logarithmic negativity in gapped one-dimensional systems [92, 93]. Analogously to the EE, logarithmic violations are present for the LN in critical [94] and disordered [95] spin chains (more details in Chapter 10).

We also mention that in higher dimensions further logarithmic contributions (subleading in this case) appear whenever the boundary is not smooth but contains corners instead: surprisingly such contributions also show some degrees of universality [68, 93].

In $2d$, another peculiar result concerning entanglement entropy is found for systems displaying topological order. In this case the area law reads $S(\rho_A) = \alpha\ell/\epsilon - \gamma$. While the coefficient in front of the area term is now cut-off dependent, the constant γ, dubbed *topological entropy* [24, 25], is a universal contribution. A similar topological term is present for the entanglement negativity as well [96, 97]. Hence, by computing the entanglement entropy (or negativity) and isolating the constant term in the size of the subsystem, we have a tool to detect topological order. Prototypical examples of this situation are the Kitaev model [98] and the two-dimensional electron gases in large magnetic fields in the fractional quantum Hall regime [99].

Deep insights on entanglement and its nature are provided by the celebrated *Ryu-Takayanagi* (RT) *formula* [100, 101]. Inspired to the Bekenstein-Hawking formula for the entropy of a black hole, today it is considered one of the most important results coming from the AdS/CFT correspondence, or gauge/gravity duality, proposed by Maldacena in [102] as a concrete realization of the holographic principle [103, 104]. The correspondence is between a gravity theory in the bulk of a $(d+1)$ space-time and a conformal field theory (without gravity) which lives on the boundary of that spacetime (i.e in d dimension). The RT formula, then, states that the entanglement of a region can be computed in the classical regime from the area of certain minimal surfaces, anchored to the entangling surface in the boundary and extending inside the bulk.

Quite recently, a connection between entanglement and the irreversibility of the RG between critical points has also been unveiled. Using Lorentz invariance and the strong subadditivity property of the entanglement entropy, an alternative proof of the well known c-theorem by Zamolodchikov [105] was found in

$(1+1)d$ [106, 107]. Soon after, entanglement (with special reference to entanglement and relative entropy) became a valuable tool in the attempt of extending the c-theorem to higher dimensions, historically considered a very hard problem (a conjecture for even dimensions is the one by Cardy [108], only recently proved in $4d$ in the form of the so-called a-theorem [109, 110]): holographic studies [111, 112] suggested that the c-function could be identified as the universal coefficient appearing in the entanglement entropy (importantly, also for *odd* dimensions, where Cardy's conjecture does not hold) and this turns out to be crucial to prove the F-theorem in $(2+1)d$ [113–115]. The so-called g-theorem, stating the decreasing under RG of the boundary entropy g, has been related to entanglement as well [116].

Another interesting aspect in the study of quantum correlations is their out-of-equilibrium dynamics, which is deeply intertwined with problems at the very foundation of statistical physics, like equilibration and thermalization [117–119]. In particular, the evolution of the entanglement entropy following a *quantum quench* [120] has been the focus of intense research: according to such protocol, the system is prepared in a given state which is not an eigenstate of the hamiltonian governing the dynamics and then let evolve. For a wide variety of global quenches, together with the powerful methods of CFT, which remarkably can be extended to deal with out of equilibrium situations [120–122], the so-called *quasiparticle picture* of Ref. [123] provides an understanding of the main qualitative features of the entanglement dynamics. The linear growth and saturation in time to an extensive value in the subsystem size, which can be observed numerically, is thus easily recovered. Recently, the quasiparticle picture complemented with the knowledge of the steady-state and its excitations was shown to lead to a complete prediction for the entanglement dynamics in *integrable models* (the ones possessing an extensive number of conserved charges) [124–126]. And this also allowed to understand the relation between entanglement evolution and how thermodynamics emerges in isolated systems. The quasiparticle picture may be extended to describe the entanglement spreading in mixed states as well: in particular, an exact prediction for the time evolution of the logarithmic negativity after a quench was given in [127]. As far as generic systems are concerned, then, entanglement is also expected to grow linearly (this expectation is mainly supported by numerical evidence [128–134]), but the quasiparticle picture does not apply and much less is known, especially from an analytical point of view. However, we mention a recent conjecture for the growth of entanglement entropy in generic (non-integrable) systems that has been put forward in Ref. [135], the so-called *minimal-cut picture*. The conjecture is derived under random unitary dynamics and is reminiscent of the RT formula, but the extent of its applicability is not clear yet. An interesting exception to the linear growth of entanglement is instead provided by *many body localized* (MBL) systems, where both interactions and disorder are usually present [20, 21, 136–138]. In the MBL phase, indeed, both entanglement growth [22, 23] and operator spreading [139–141] are associated with length scales that grow only logarithmically in time, due to localization. An even more severe exception is the bounded growth of entanglement seen in disordered non-interacting systems, a phenomenon known since a long time as *Anderson localization* [19].

We close by mentioning the essential role of the whole spectrum of the RDM, the *entanglement spectrum* [142], in the study of universal features of many-body systems in their different phases, and its analogue for mixed states, the *negativity spectrum* [57]. We will come back to this topic in Chapters 2 and 3 for an extensive discussion.

1.4 Theoretical approach to entanglement

All the results of the previous Section and many more have been achieved thanks to analytical and numerical techniques developed specifically to deal with entanglement measures and other quantum information tools in the context of many-body quantum systems. Below we review in some detail some of the most powerful techniques, focusing on the main ones used throughout the thesis.

1.4.1 Replica approach

One of the most successful strategies, widely used in many different contexts (from QFTs to disordered models and so on), is known as *replica approach* and was first introduced in this context by Holzhey *et*

al. [15] but then put on a more systematic basis by Calabrese and Cardy in [17].

To introduce the so-called *replica tricks*, we start from the EE. Sometimes we are not able to compute it from its very definition (1.2.1). It can happen that it is instead easier to compute the moments of the RDM, meaning the trace of its integer powers $\mathrm{Tr}\rho_A^n$. In this case, if we are able to analytically continue this function of the variable n from integer to complex values, then the EE is obtained through the limit

$$S(\rho_A) = -\lim_{n\to 1}\frac{\partial}{\partial n}\mathrm{Tr}\rho_A^n. \tag{1.4.1}$$

This is also known as *replica limit* and has been successfully applied to several systems.

A generalization of this replica trick (1.4.1) for the entanglement entropy has been then introduced in Refs. [143, 144] for the relative entropy, cf. Eq. (1.2.6). It relies on the generalized moments $\mathrm{Tr}\left(\rho_A^n\sigma_A^m\right)$, with ρ_A, σ_A being two RDMs and $n, m \in \mathbb{N}$, and reads

$$S(\rho_A\|\sigma_A) = -\lim_{n\to 1}\frac{\partial}{\partial n}\frac{\mathrm{Tr}\left(\rho_A\sigma_A^{n-1}\right)}{\mathrm{Tr}\rho_A^n}. \tag{1.4.2}$$

The replica trick associated with the negativity is instead a bit more involved. As a matter of fact, in this case, we need to realize that even and odd powers of the PT $\rho_A^{T_2}$, give rise to two different analytic continuations, as clear by writing them explicitly

$$\mathrm{Tr}\left(\rho_A^{T_2}\right)^{n_e} = \sum_{\lambda_i>0}|\lambda_i|^{n_e} + \sum_{\lambda_i<0}|\lambda_i|^{n_e}, \qquad \mathrm{Tr}\left(\rho_A^{T_2}\right)^{n_o} = \sum_{\lambda_i>0}|\lambda_i|^{n_o} - \sum_{\lambda_i<0}|\lambda_i|^{n_o} \tag{1.4.3}$$

with $n_e = 2m$ and $n_o = 2m+1$ ($m \in \mathbb{N}$). The right one, in order to reproduce the absolute value in the definition of logarithmic negativity (1.2.5), is associated with the *even* powers. Therefore we first need to consider their associated analytic continuation and at that point the negativity is given by the limit

$$\mathcal{E}(\rho_A) = \lim_{n_e\to 1}\ln\mathrm{Tr}\left(\rho_A^{T_2}\right)^{n_e} \tag{1.4.4}$$

This is the result of Calabrese, Cardy and Tonni in [94, 145].

Moreover, we recently introduced [146, 147] a replica trick similar in spirit to the one for the LN, allowing for the computation of the trace distance, as defined by the limit $n \to 1$ of (1.2.7). With n_e denoting again the sequence of the even powers, this is given by

$$D(\rho_A, \sigma_A) = \frac{1}{2}\lim_{n_e\to 1}\mathrm{Tr}(\rho_A - \sigma_A)^{n_e}. \tag{1.4.5}$$

Many more details together with explicit calculations are given in the following chapters.

Despite the huge success of this technique, it is however fair to stress that all the results based on some above-mentioned replica tricks ultimately require to perform an analytic continuation in the parameter n (or n_e) and this is a very technical step which remains a formidable task to be solved. We are going to discuss a viable way to (approximately) tackle this problem in the case of CFTs in Chapter 6.

1.4.2 QFT: Path integral approach, twist fields and the special case of $(1+1)d$ CFT

In the framework of QFT, computing the objects involved in the replica tricks turns out to be easy in the *path integral* formalism. For simplicity, we focus on one-dimensional systems, even if most of what follows can be generalized to arbitrary dimension. In path integral, a $1d$ quantum system can be formulated as a $(1+1)d$ classical system. The additional dimension corresponds to the imaginary time direction, τ. We parametrize the $2d$ geometry by a complex coordinate $w = x + i\tau$, where the domain of the spatial coordinate x can be

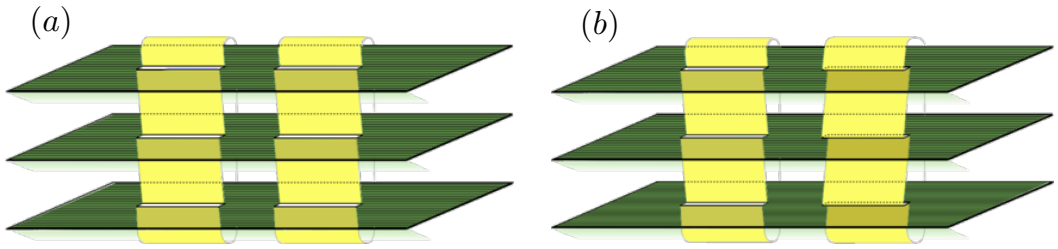

FIGURE 1.1: (a) Path integral representation of $\mathrm{Tr}\rho_A^n(\infty)$ (up to normalization, Z_1^n), giving a n-sheeted Riemann surface $\mathcal{R}_n$. (b) Path integral representation of $\mathrm{Tr}\left(\rho_A^{T_2}(\infty)\right)^n$: the geometry is different as compared with $\mathcal{R}_n$. As an example, $n=3$ and $A=[u1,v1]\cup[u2,v2]$ is shown. Reprinted from [94].

finite, semi-infinite or infinite. The ground-state density matrix then takes the form [17, 18]

$$\langle\phi|\rho(\infty)|\phi'\rangle = \frac{1}{Z}\int_{\varphi(-i\infty)=\phi}^{\varphi(i\infty)=\phi'}\mathcal{D}\varphi e^{-S(\varphi)}, \tag{1.4.6}$$

with the value of the field fixed at $w=\pm i\infty$ and $\{|\phi\rangle\}$ denoting the basis diagonalizing the field φ. $S(\varphi)$ is the euclidean action and Z the normalization to have $\mathrm{Tr}\rho(\infty)=1$. This is nothing but the $\beta\to\infty$ limit of the thermal density matrix, $\rho(\beta)$. Once identified a bipartition of the whole system, the RDM $\rho_A(\infty)$ associated to a generic subsystem A is obtained by closing $\rho_A(\infty)$ along $\bar{A}$ and leaving an open cut along A. Then $\mathrm{Tr}\rho_A^n(\infty)$ is given by n copies of $\rho_A(\infty)$ sewn cyclically along A. Following this procedure, we end up in a world-sheet which is a n-sheeted Riemann surface $\mathcal{R}_n$ (for a graphical representation see Fig. 1.1 (a)), and the moments of $\rho_A^n(\infty)$ are

$$\mathrm{Tr}\rho_A^n(\infty) = \frac{Z_n}{Z_1^n} \tag{1.4.7}$$

where Z_n is the path integral over the Riemann surface $\mathcal{R}_n$ and $Z_1\equiv Z$.

In $1d$, the problem of computing the partition function on $\mathcal{R}_n$ can be further simplified by introduced a special class of fields called *twist fields* [17, 18, 148]. The idea is to translate the problem of computing a partition function on a complicated worldsheet (the Riemann surface $\mathcal{R}_n$) of a theory with a simple target space (a single field φ) in the problem of computing a different partition function on a simpler worldsheet but in a theory with a more complicated target space $\{\varphi_1,\cdots,\varphi_n\}$ (note that n is exactly the number of sheets of $\mathcal{R}_n$).This is done through the insertion of some local fields in correspondence of the cut which 'implement' the initial geometry in terms of constraints among the φ_i's. In the end, we translate the initial problem in the computation of correlation functions of twist fields, but now on the complex plane. Specifically, for a subsystem A consisting of m disjoint intervals, $\mathrm{Tr}\rho_A^n(\infty)$ can be expressed (for integer n) as a $2m$-point correlation function of twist and antitwist fields, $\mathcal{T}$ and $\bar{\mathcal{T}}$. And this point of view easily generalizes to a state different from the ground state, whose moments $\mathrm{Tr}\rho_A^n$ are related to the same correlator but now evaluated in the state $\boldsymbol{\rho}_n=\otimes_{j=1}^n\rho_j$ of the corresponding n-fold theory, denoted as CFT^n, as shown in Figure 1.2 (left) for the special case $m=1$. In formulas, for a subsystem $A=\cup_{i=1}^m[u_i,v_i]$,

$$\mathrm{Tr}\rho_A^n = \langle\prod_{i=1}^m\mathcal{T}(u_i,u_i)\bar{\mathcal{T}}(v_i,v_i)\rangle_{\boldsymbol{\rho}_n}. \tag{1.4.8}$$

Twist fields can be defined as *local* operators in any $2d$ QFT and, indeed, have been successfully applied to massive [149–151], integrable [148, 152–154] field theories and much more. However, they turn out to be particularly useful when dealing with a CFT, where they are primary operators of CFT^n, with conformal weights [17, 148]

$$h_n=\bar{h}_n=\frac{c(n^2-1)}{24n}, \tag{1.4.9}$$

c being the central charge of the single copy CFT. For the ground state (vacuum) of the CFT, the moments

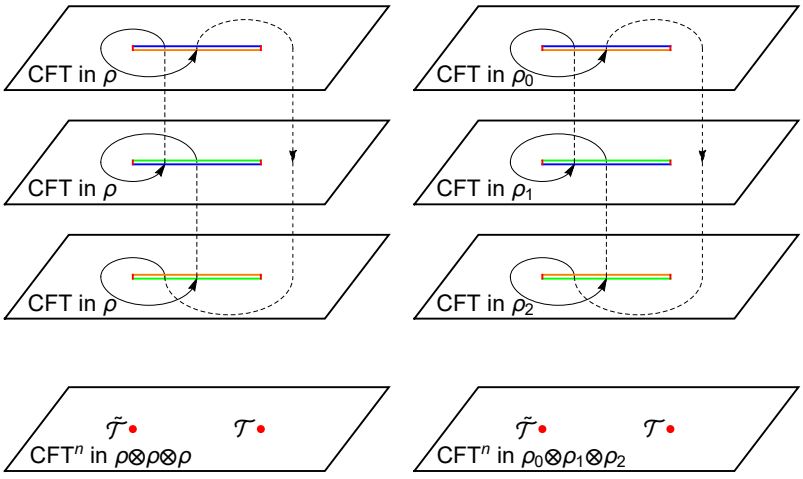

FIGURE 1.2: The replica trick to calculate $\mathrm{Tr}\rho_A^n$, Eq. (1.4.8), (left) and $\mathrm{Tr}(\rho_0\rho_1\cdots\rho_{n-1})$, Eq. (1.4.15), (right). Top: path integral in terms of Riemann surfaces. Bottom: equivalent representation in terms of the twist operators in CFT^n. We show the case $n=3$ as an example.

of the RDM, for A being a single interval in an infinite system, are fixed by global conformal invariance to be

$$\mathrm{Tr}\rho_A^n(\infty) = \langle \mathcal{T}(\ell,\ell)\bar{\mathcal{T}}(0,0)\rangle_{\rho_n} = c_n \left(\frac{\ell}{\epsilon}\right)^{-2(h_n+\bar{h}_n)}, \tag{1.4.10}$$

where c_n (with $c_1 = 1$) is the normalisation of the twist operators (related to the boundary conditions induced by the twist operators at the entangling surface [155–157]) and ϵ is the ultraviolet cutoff. And this lead to the celebrated result for the ground state EE

$$S(\rho_A(\infty)) = \frac{c}{3}\log\ell, \tag{1.4.11}$$

and REEs

$$S_n(\rho_A(\infty)) = \frac{c}{6}\frac{(n+1)}{n}\log\ell \tag{1.4.12}$$

(and similarly for finite systems, systems at finite temperature, and other situations: it is sufficient to replace ℓ with the relevant length in the considered regime, see e.g. [18]). Note that in Eqs. (1.4.11) and (1.4.12) above we omitted the explicit dependence on ϵ, that anyhow is there.

For disjoint intervals instead global invariance is not enough to fix the behavior of twist fields' correlation functions, but it may be exploited to rewrite Eq. (1.4.8) for generic m as

$$\mathrm{Tr}\rho_A^n(\infty) = c_n^m \left|\frac{\prod_{i<j}^m (u_j-u_i)(v_j-v_i)}{\prod_{i,j}^m (v_j-u_i)}\right|^{2\Delta_n} \mathcal{F}_{n,m}\left(x_1,\cdots,x_{2m-3}\right) \tag{1.4.13}$$

where $\Delta_n = h_n + \bar{h}_n$, and $\mathcal{F}_{n,m}$ is a model dependent *universal* (i.e., cutoff independent) function of the cross-ratios $\{x_k\}$ [83], encoding the full operator content of the model.

Coming back to generic states, also $\mathrm{Tr}\left(\rho_A^n\sigma_A^m\right)$ can be expressed in terms of correlation functions of twist fields, this time evaluated in the state $\otimes_{j=1}^n\rho_j\otimes_{k=1}^m\sigma_k$ in CFT^n. More details are given in Chapter 4. Moreover, as an anticipation to Chapter 5, we note that the quantity $\mathrm{Tr}(\rho_A-\sigma_A)^n$, entering the replica trick (1.4.5) of the trace distance, may be expanded as

$$\mathrm{Tr}(\rho_A-\sigma_A)^n = \sum_{\mathcal{S}}(-)^{|\mathcal{S}|}\mathrm{Tr}\left(\rho_{0_\mathcal{S}}\cdots\rho_{(n-1)_\mathcal{S}}\right), \tag{1.4.14}$$

where the summation $\mathcal{S}$ is over all the subsets of $\mathcal{S}_0 = \{0,\cdots,n-1\}$, $|\mathcal{S}|$ is the cardinality of $\mathcal{S}$ and

$\rho_{j_S} = \sigma_A$ if $j \in \mathcal{S}$ and ρ_A otherwise. Crucially, each term in the sum appearing in the r.h.s. of Eq. (1.4.14), may still be seen as a two-point function of twist fields (cfr., e.g., [158])

$$\mathrm{Tr}(\rho_{0_S} \cdots \rho_{(n-1)_S}) = \langle \mathcal{T}(\ell,\ell)\bar{\mathcal{T}}(0,0)\rangle_{\otimes_j \rho_{j_S}}. \tag{1.4.15}$$

These are indeed nothing but generalisations of (1.4.8) to the case where the replicas of the CFT are in different states. This is illustrated in Fig. 1.2 (right).

Finally, focusing on two more generic (not necessarily complementary) subsystems A_1 and A_2, also the problem of computing the moments of the PT, $\mathrm{Tr}\left(\rho_A^{T_2}\right)^n$, and therefore the LN, can be formulated in terms of correlation functions of twist fields: it is again a matter of geometry to realize that the partial transposition corresponds to the exchange of the position of twist and anti-twist fields in the correlation function. In formulas,

$$\mathrm{Tr}\left(\rho_A^{T_2}\right)^n = \langle \prod_{i=1}^{m_1} \mathcal{T}(u_i,u_i)\bar{\mathcal{T}}(v_i,v_i) \prod_{j=1}^{m_2} \bar{\mathcal{T}}(u_j,u_j)\mathcal{T}(v_j,v_j)\rangle_{\boldsymbol{\rho}_n} \tag{1.4.16}$$

when A_1 and A_2 are made by m_1 and m_2 intervals, respectively, in the state $\boldsymbol{\rho}_n$. For the simplest case $m_1 = m_2 = 1$, the corresponding geometry in the ground state is depicted in Figure 1.1 (b). Already in this simple case however, now we have to deal with a four-point correlation function, which, as mentioned, is fixed by conformal invariance only up to a model-dependent function of the cross-ratio. The only situation where an explicit result is known is that of adjacent intervals (i.e., $v_1 \to u_2$): in this case the calculation reduces to a three-point correlation function, which is instead completely determined in CFT and we recover the well known result [94, 145]

$$\mathcal{E}(\rho_A(\infty)) = \frac{c}{4}\log\left(\frac{\ell_1\ell_2}{\ell_1+\ell_2}\right) \tag{1.4.17}$$

for two intervals of length ℓ_1 and ℓ_2 embedded in an infinite system in the ground state. Also here the explicit dependence on the cutoff ϵ is hidden.

Note that the definition of twist fields is independent of the CFT being defined on flat space. Indeed many of the above results can be extended to CFTs in *curved spacetime*, which recently become a tool to deal with *inhomogeneous systems* [159]. Note that for such systems, which are the main subject of Part II of this thesis (Chapters 8 and 9), other viable analytical methods to compute entanglement (and quantum correlations in general) do not exist.

1.4.3 Free models: entanglement from correlation and overlap matrix

Sometimes just the structure of the density matrix is sufficient to compute the entanglement entropies, without knowing the full spectrum and, even worse, every matrix element. For the eigenstates of quadratic lattice Hamiltonians, this is, indeed, possible using Wick's theorem, as shown by Chung and Peschel [160–162]. Here we review the main steps of this result focusing on fermionic systems. However similar techniques are available for bosonic systems as well [163, 164].

The hamiltonian of a free fermion chain can be written in the form

$$\mathcal{H} = -\sum_{i,j} t_{ij} c_i^\dagger c_j. \tag{1.4.18}$$

with $c_i^\dagger$ (c_i) denoting the creation (annihilation) fermionic operators. Let us denote by $|K\rangle$ a generic eigenstate in which $K \equiv \{k\}$ stands for the set of occupied single-particle levels. By Wick theorem, it is easy to show that, for a given eigenstate, the RDM of a block of ℓ contiguous sites can be written as [16, 161, 162, 165]

$$\rho_A = \mathcal{K}\, e^{-H_A}, \tag{1.4.19}$$

where $\mathcal{K}$ is a normalization constant and H_A the *modular (or entanglement) Hamiltonian* that for Gaussian states takes the quadratic form

$$H_A = \sum_{ij} h_{ij} c_i^\dagger c_j \,. \tag{1.4.20}$$

This modular Hamiltonian is related to the *correlation matrix* C restricted to the block A, with elements $[C_A]_{nm} = \langle c_m^\dagger c_n \rangle_K$ ($n, m \in A$ and $\langle \cdots \rangle_K$ denotes the expectation value on the state $|K\rangle$), as [162]

$$H_A = \ln(C_A^{-1} - 1). \tag{1.4.21}$$

Denoting by $(1+\nu_m)/2$ the ℓ eigenvalues of C_A, the REEs can be expressed as

$$S_n(\rho_A) = \sum_{l=1}^{\ell} e_n(\nu_l)\,, \tag{1.4.22}$$

where

$$e_n(x) = \frac{1}{1-n} \ln\left[\left(\frac{1+x}{2}\right)^n + \left(\frac{1-x}{2}\right)^n\right] \tag{1.4.23}$$

and in the limit $n \to 1$

$$e_1(x) = \left(\frac{1+x}{2}\right) \ln\left(\frac{1+x}{2}\right) + \left(\frac{1-x}{2}\right) \ln\left(\frac{1-x}{2}\right). \tag{1.4.24}$$

The representation (1.4.22) is particularly convenient for numerical computations: the eigenvalues of C_A are determined by standard linear algebra methods and $S_n(\rho_A)$ is then computed using Eq. (1.4.22). This procedure reduces the problem of computing the RDM from an exponential to a linear problem in the system size.

We stress that the above construction refers to the block entanglement in the fermionic degrees of freedom. However, in the case of a single block, it can be extended to block entanglement in spin chains: in this case, the non-locality of the Jordan-Wigner transformation [166] does not change the eigenvalues of the RDM because it mixes only spins within the block. This ceases to be the case when two or more disjoint intervals are considered [167, 168] and other techniques need to be employed [169].

More generally speaking, when looking to the trace of products of RDMs in different eigenstates (it is the case for the quantities in the replica tricks of relative entropy (1.4.2) and trace distance (1.4.5)), they usually do not commute and so they cannot be simultaneously diagonalized in a common base. It is instead possible to use the composition properties of Gaussian density matrices, i.e. of the form (1.4.19). In order to make contact with Ref. [169], where the algebra of Gaussian RDMs was carefully analyzed, we work with the 2ℓ spatial Majorana modes defined as

$$\begin{cases} a_{2m-1} = c_m^\dagger + c_m, \\ a_{2m} = i(c_m^\dagger - c_m). \end{cases} \tag{1.4.25}$$

The Majorana correlation matrix Γ^K_{mn} is defined as

$$\Gamma^K_{mn} = \langle a_m a_n \rangle_K - \delta_{mn}, \tag{1.4.26}$$

and is trivially related to C_A defined above.

In Ref. [169], a *product rule* to express the product of Majorana RDMs (ρ_Γ's) in terms of operations on the respective correlation matrices (Γ's) has been derived. If we implicitly define the matrix operation $\Gamma \times \Gamma'$ by

$$\rho_\Gamma \rho_{\Gamma'} = \mathrm{Tr}\left[\rho_\Gamma \rho_{\Gamma'}\right]\ \rho_{\Gamma\times\Gamma'}, \tag{1.4.27}$$

the following identity holds

$$\Gamma \times \Gamma' = 1 - (1-\Gamma')\frac{1}{1+\Gamma\Gamma'}(1-\Gamma), \tag{1.4.28}$$

relating the correlation matrices of two RDMs to the one associated to their product. Then the trace of two fermionic operators can be computed as (singular cases and ambiguities are discussed in [169])

$$\{\Gamma,\Gamma'\} \equiv \mathrm{Tr}\,(\rho_\Gamma \rho_{\Gamma'}) = \prod_{\mu\in \mathrm{Spectrum}[\Gamma\Gamma']/2} \frac{1+\mu}{2}. \tag{1.4.29}$$

Finally, by associativity, one can extend (1.4.27) to more than two RDMs

$$\prod_{i=1}^{n} \rho_{\Gamma_i} = \{\Gamma_1,\cdots,\Gamma_n\}\rho_{\Gamma_1\times\cdots\times\Gamma_n}, \tag{1.4.30}$$

where

$$\{\Gamma_1,\cdots,\Gamma_n\} \equiv \mathrm{Tr}\,(\rho_{\Gamma_1}\cdots\rho_{\Gamma_n}) = \{\Gamma_1,\Gamma_2\}\{\Gamma_1\times\Gamma_2,\cdots\}. \tag{1.4.31}$$

Eq. (1.4.31) can be used to iteratively evaluate traces of products of fermionic RDMs.

Most of the results introduced above for lattice models can be easily generalized to models in the continuum through the *overlap matrix approach*. This technique has already been used for several applications in the context of the entanglement [75, 170–184].

For that, we consider a gas of N non-interacting spinless fermions. The many-body ground state is obtained by filling the N levels with lowest energies (and similarly for the excited states by filling the levels in a different way). The two-point correlation function then reads

$$C(x,y) \equiv \langle c^\dagger(x)c(y)\rangle = \sum_{k=1}^{N} \phi_k^*(x)\phi_k(y), \tag{1.4.32}$$

where $c(x)$ ($c^\dagger(x)$) is the fermionic annihilation (creation) operator and $\{\phi_k(x)\}$ are (normalised) eigenfunctions of the one-particle problem.

The reduced density matrix restricted to $A = [x_1, x_2]$ has still the Gaussian form

$$\rho_A \propto \exp - \int_{x_1}^{x_2} dy_1 dy_2 c^\dagger(y_1)\mathcal{H}(y_1,y_2)c(y_2), \tag{1.4.33}$$

where the entanglement Hamitonian $\mathcal{H}$ in terms of the reduced correlation matrix $C_A(x,y) = P_A C P_A$ (P_A is the projector on the interval A) is again as in (1.4.21): this is nothing but the continuum limit of what discussed for the fermionic lattice model.

The elements of the so-called *overlap matrix* $\mathbb{A}$ are defined as

$$\mathbb{A}_{nm} \equiv \int_{x_1}^{x_2} dz\, \phi_n^*(z)\phi_m(z). \tag{1.4.34}$$

According to this approach, the eigenvalues of the reduced correlation matrix (and hence REEs through (1.4.22)) are obtained from this $N \times N$ matrix, which has been shown to share its non-zero eigenvalues with $C_A(x,y)$ [170, 173, 185].

1.4.4 Entanglement in disordered models via SDRG

For disordered models, the SDRG –*strong disorder renormalization group* [85, 186] –, a tool not specifically devised for entanglement, turned out to be crucial instead to derive the scaling of different entanglement measures in the TDL.

We consider the random antiferromagnetic spin-$\frac{1}{2}$ XXZ chain, defined by the Hamiltonian

$$\mathcal{H} = \sum_{i=1} J_i (S_i^x S_{i+1}^x + S_i^y S_{i+1}^y + \Delta S_i^z S_{i+1}^z), \tag{1.4.35}$$

where $S_i^{x,y,z}$ are the spin components acting on site i, L is the length of the chain, Δ the anisotropy parameter, and $\{J_i\}$ are uncorrelated *positive* random variables, drawn from a distribution $P(J)$.

To elucidate the method, we focus the XXX chain ($\Delta = 1$). The main idea is to obtain a low-energy effective description of (1.4.35) by successively integrating out the strongest couplings, and renormalizing the remaining ones. Given an arbitrary coupling configuration $\{J_i\}$, one starts by identifying the strongest bond $J_M \equiv \max_i\{J_i\}$. The interaction between the two spins coupled by J_M (that we denote as $\vec{S}_l$ and $\vec{S}_r$) is given by the Hamiltonian $\mathcal{H}_0$ as

$$\mathcal{H}_0 = J_M \vec{S}_l \cdot \vec{S}_r. \tag{1.4.36}$$

The ground state of $\mathcal{H}_0$ is the singlet state $|s\rangle$

$$|s\rangle \equiv \frac{|\uparrow_l\downarrow_r\rangle - |\downarrow_l\uparrow_r\rangle}{\sqrt{2}}. \tag{1.4.37}$$

The interaction between $\vec{S}_l$ and $\vec{S}_r$, and their neighboring spins (here denoted as S'_l and S'_r, respectively) is described by the Hamiltonian $\mathcal{H}'$ as

$$\mathcal{H}' = J_l\ \vec{S}'_l \cdot \vec{S}_l + J_r\ \vec{S}_r \cdot \vec{S}'_r. \tag{1.4.38}$$

Since by definition $J_l, J_r < J_M$, one can treat $\mathcal{H}'$ as a perturbation. Within second-order perturbation theory, this leads to the effective Hamiltonian $\mathcal{H}^{eff}$ for $\vec{S}'_l, \vec{S}'_r$ as

$$\mathcal{H}^{eff} = \langle s|\mathcal{H}_0 + \mathcal{H}'|s\rangle + \sum_t \frac{|\langle s|\mathcal{H}'|t\rangle|^2}{E_s - E_t} \equiv E_0 + J'\ \vec{S}'_l \cdot \vec{S}'_r. \tag{1.4.39}$$

Here the sum is over the triplet states of two spins $|t\rangle = |\uparrow\uparrow\rangle, (|\uparrow\downarrow\rangle + |\downarrow\uparrow\rangle)/\sqrt{2}, |\downarrow\downarrow\rangle$. The corresponding energies are $E_t \equiv \langle t|\mathcal{H}_0|t\rangle = 1/4J_M$, whereas one has $E_s \equiv \langle s|\mathcal{H}_0|s\rangle = -3/4J_M$. In the last step in (1.4.39) we defined $E_0 = -3(4J_M + 3J_l^2 + 3J_r^2)/16$. The effective coupling J' between $\vec{S}'_l$ and $\vec{S}'_r$ reads

$$J' = \frac{J_l J_r}{2J_M}. \tag{1.4.40}$$

Note that (1.4.39) does not depend on $\vec{S}_l, \vec{S}_r$ anymore. Moreover, $\mathcal{H}^{eff}$ is still of the Heisenberg form (1.4.35) with the renormalized coupling J'. For a chain of length L, this process of decimating the spins connected by the strongest bond, renormalizing the remaining interactions, can be represented as

$$\Big(\cdots, J_l, J_M, J_r, \cdots\Big)_L \ \rightarrow\ \Big(\cdots, \frac{J_l J_r}{2J_M}, \cdots\Big)_{L-2}, \tag{1.4.41}$$

and it defines the so-called *Dasgupta-Ma rule* [187]. Crucially, since $J_l, J_r < J_M$, the repeated application of (1.4.41) reduces the energy scale of the model.

The low-energy properties of the model are asymptotically (i.e., after many iterations of (1.4.41)) described by the so-called *random-singlet phase* (RSP), illustrated in Fig. 1.3 (b). In the RSP, all the spins are paired (as stressed by the links in the Figure) in a random fashion. Paired spins form singlet. From (1.4.41) it is clear that longer-range singlets are generated at later steps of the SDRG.

The RSP can be quantitatively characterized through the asymptotic distribution of the couplings $\{J_i\}$. The iteration of the Dasgupta-Ma rule (1.4.41) leads to a flow for $P(J)$. It is convenient to introduce at the given SDRG step m the variables $\beta_i^{(m)}$ and $\Gamma^{(m)}$ as

$$\beta_i^{(m)} \equiv \ln \frac{J_M^{(m)}}{J_i^{(m)}}, \quad \Gamma^{(m)} \equiv \ln \frac{J_M^{(0)}}{J_M^{(m)}}. \tag{1.4.42}$$

Here, $J_M^{(m)}$ is the maximum coupling at the step m. The physical interpretation is that $\Gamma^{(m)}$ quantifies the

difference in energy scales between the initial step and step m, while the $\beta_i^{(m)}$ measures the broadness of the energy scales at a fixed step m. The equation describing the SDRG flow of $P(J)$ is given as [186]

$$\frac{dP}{d\Gamma} = \frac{\partial P(\beta)}{\partial \beta} P(0) \times \int_0^\infty d\beta_1 \int_0^\infty d\beta_2 \delta(\beta - \beta_1 - \beta_2) P(\beta_1) P(\beta_2). \tag{1.4.43}$$

It can be shown that (1.4.43) has a unique solution $P^*(\beta)$ given by

$$P^*(\beta) = \frac{1}{\Gamma} \exp\left(-\frac{\beta}{\Gamma}\right). \tag{1.4.44}$$

Here, $P^*(\beta)$ represents the fixed point of the SDRG flow. This fixed point is known as *infinite randomness fixed point* (IRFP) [186], to emphasize that the broadness of the distribution increases during the flow. This is reflected in $P^*(\beta)$ being flat, which corresponds to $P^*(J)$ being peaked at $J = 0$ [cf. (1.4.42)]. Note that this justifies the perturbative treatment [188] of $\mathcal{H}'$ in (1.4.39). Remarkably, (1.4.44) does not depend on the initial distribution which is a manifestation of its universality.

For different values of Δ a similar treatment holds. In particular we mention that for the XX chain [$\Delta = 0$ in (1.4.35)] the Dasgupta-Ma rule (1.4.41) gets modified as

$$\left(\cdots, J_l, J_M, J_r, \cdots\right)_L \rightarrow \left(\cdots, \frac{J_l J_r}{J_M}, \cdots\right)_{L-2}. \tag{1.4.45}$$

Consequently, the flow equation (1.4.43), and the fixed point distribution (1.4.44) remain the same as in the XXX case.

Now, crucially, for a given realization of the disorder, assuming that the chain is in a RSP, the entanglement in the ground state between two subsystems of the chain can be calculated analytically. Denoting by $n_{X:Y}$ the number of links between two given subsystems, X and Y, the EE between a subsystem A and its complement $\bar{A}$ reads

$$S(\rho_A) = n_{A:\bar{A}} \ln 2 \tag{1.4.46}$$

In a similar way, the LN between two generic (non complementary) subsystems A_1 and A_2 is

$$\mathcal{E}_{A_1:A_2} \equiv \mathcal{E}(\rho_A) = n_{A_1:A_2} \ln 2. \tag{1.4.47}$$

Such results do not come unexpected: the amount of entanglement in the RSP is clearly related in a simple fashion to the links connecting the subsystems of interest.

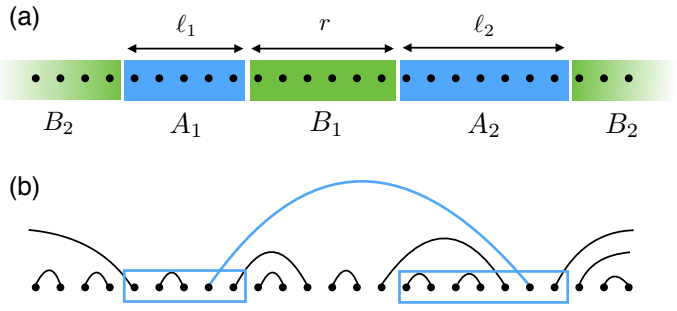

FIGURE 1.3: (a): Partition of an infinite spin chain corresponding to two disjoint intervals. The region of interest is $A_1 \cup A_2$. Two adjacent intervals correspond to $r = 0$. (b): Cartoon of the random singlet phase. The lines connect pairs of spins forming $SU(2)$ singlets. The amount of entanglement is proportional to the number of singlets $n_{A_1:A_2}$ shared between A_1 and A_2 (here $n_{A_1:A_2} = 1$).

Then, the average of this quantity over many realizations can then be computed using the SDRG and leads to the above mentioned logarithmic violation of the area law for the EE [86]

$$S(\rho_A) = \frac{\ln 2}{3} \ln \ell \tag{1.4.48}$$

and for the LN of adjacent and disjoint intervals [95]

$$\mathcal{E}_{A_1:A_2} = \frac{\ln 2}{6} \ln \left(\frac{\ell_1 \ell_2}{\ell_1 + \ell_2} \right), \qquad \mathcal{E}_{A_1:A_2} = -\frac{\ln 2}{6} \ln(1-x). \tag{1.4.49}$$

where the cross-ratio $x = \frac{\ell_1 \ell_2}{(\ell_1+r)(\ell_2+r)}$ is defined in terms of the length ℓ_1 and ℓ_2 of the two subsystems and their distance r, similar to the ones appearing in CFT. More details in the case of the LN are given in Chapter 10. The interplay of disorder and inhomogeneity, where SDRG plays a crucial role as well, is instead the subject of Chapter 11.

We close this Section by reminding that many other equally important tools are available and widely used in literature. Among them, we definitely need to mention AdS/CFT methods [189–191]. Other specific methods to deal with free theories (particularly QFTs) are reviewed in [192] (and will be partially recalled in Chapter 3). For free lattice models the so-called *(generalized) Fisher-Hartwig conjecture* [193,194] has been exploited as well [195–201] (see Chapter 7). Most of these techniques rely on the replica tricks reviewed above. Numerically, a lot has been understood thanks to classical [167, 202–206], quantum [27, 207–212] and variational [26] Monte Carlo techniques, also based on the replica approach. Finally, MPS and Tensor Network based algorithms (in higher dimensions as well) [30–32, 72, 213–215] allowed to numerically access the entanglement scaling in systems for which analytical tools do not exist yet.

1.5 Entanglement in experiments

Despite the fact that entanglement has emerged as an indispensable theoretical and numerical tool, it seemed impossible for a long time to device experiments able to detect and measure entanglement for many-body systems. The main difficulties were ascribed to its intrinsic non-locality and independence on any specific observable, which is also what makes entanglement an interesting feature to look at.

The very first proposals were limited to non-interacting systems [216–219], where special relations between the reduced density matrix of a subsystem and quantum noise (in terms of the full counting statistics) exist. Such relations, however, were shown to break down in the presence of interactions [220].

On the other hand, a very direct way to detect entanglement in a generic system is given by *quantum state tomography* [9], meaning the measurement of all density matrix elements, a method that allows accessing to multipartite entanglement as well. This method has been successfully applied to trapped ions [221, 222] and superconducting qubits [223] (noticeably up to 10 qubits [224]). Unfortunately, however, scaling this approach to systems with possibly hundreds or thousands of degrees of freedoms is clearly unfeasible: the number of measurements needed, indeed, increases exponentially with the number of qubits.

Generally speaking, it appears easier to look at the integer moments of the RDM, meaning the REEs (especially the Rényi $n = 2$), rather than the EE itself. This possibility relies again on the idea of replica trick: experimentally, one prepares n identical copies of a system and then let them interact in a specific way. Ultimately, one extracts the expectation value of the so-called *shift operator*, V_n, whose action is to cyclically permute the copies, $V_n|\psi_1\rangle \cdots |\psi_n\rangle = |\psi_n\rangle|\psi_1\rangle \cdots |\psi_{n-1}\rangle$. Such operator was first introduced in [225] and is directly related to the moments of a given density matrix ρ as

$$\mathrm{Tr}\rho^n = \mathrm{Tr}\left(V_n \rho^{\otimes n}\right). \tag{1.5.1}$$

In this way, the measurement of REEs is reduced to determining the expectation value of V_n in the n-copy state: this seems of great advantage compared to full quantum tomography. In particular, two different

approaches to implementing such measurement have been proposed in cold atom systems, which represent promising candidates to implement scalable entanglement measurements. The proposal by Cardy of Ref. [226], soon after followed by the one by Abanin and Demler in Ref. [227], is based on a quantum quench protocol, whereas the method presented in Refs. [228–230] relies on the quantum many-body equivalent of the Hong-Ou-Mandel (HOM) interference of two photons [231], often referred to as *beam-split*. In Ref. [228], in particular, it was first shown that a beam-splitter operation on two copies is sufficient to measure V_2. This was then generalized to V_n in [229] for bosonic and in [230] for fermionic systems. Remarkably, this second proposal has been later implemented in Greiner's group at Harvard [34] for the Bose-Hubbard model. The experiment observed the Mott insulator to superfluid transition from a direct measure of quantum purity, Rényi entanglement entropy, and mutual information in two identical copies of a 4-sites system of interacting delocalized particles (which cannot be detected by means of tomography). A subsequent experiment [35] was then able to show how thermalization occurs via entanglement by measuring the same quantities in 6-sites systems. Furthermore, a very similar experimental setup has been later proposed in [232] to probe the conformal Calabrese-Cardy scaling, which should be indeed possible with current experiments by taking into account (known) subleading corrections.

More recently protocols for measuring REEs which are not based on replicas (and do not rely on tomography either) have been put forward. It is the case of [233], mainly inspired by Ref. [234], where a scheme adaptable to generic atomic Hubbard and spin models has been presented for partitions in arbitrary spatial dimensions. The approach requires the preparation of only a single copy of the quantum system and is based on random measurements realized as random unitary operators applied to ρ_A. The idea of probing EE via randomized measurements has been further explored by Zoller and his group in Innsbruck in Ref. [36]. The experiment is carried out with a trapped-ion quantum simulator (both in the absence and presence of disorder) and is applicable to arbitrary quantum states of up to several tens of qubits (up to 10-qubit partitions of a 20-qubit string are reported).

We also mention the recent experiment by Lukin *et al.* [37]: they realized an MBL system in a disordered 8-sites Bose-Hubbard chain and characterize its entanglement properties through particle fluctuations and correlations. This experiment also showed the importance of understanding the "internal symmetry structure" of the entanglement, which is the topic analyzed (from a theoretical point of view) in Chapter 7 in terms of the so-called *symmetry-resolved* entanglement measures.

To conclude, even if many experiments have been already set up and the first entanglement measures are available, still, a significant gap remains between our ability to produce massively entangled states in controlled settings (up to a few thousands [235–241]), and our ability to characterize that entanglement quantitatively. In this respect, the main goal is definitely to achieve entanglement measures in larger systems. Finally, the experimental measure of entanglement in mixed states remains unexplored and represents another important challenge: in this direction, few proposals to access the LN can be found in Refs. [242–245].

1.6 Organization of the thesis & sketch of the results

This thesis encloses most of the work I have been doing during my Ph.D., in collaboration with colleagues at SISSA and many other researchers. It consists of three Parts and is organized as outlined below. Every Chapter contains a small abstract, a specific introduction, and its own final remarks together with possible developments so that here we give only a very brief overview and we also chose not to include an overall conclusion at the end.

Part I

The first part is about *replicas*, mostly within the context of QFT and more specifically $(1+1)d$ CFT. Nonetheless, some exact results for free lattice models are also considered.

- Chapter 2 deals with the negativity spectrum, as introduced above, whose distribution can be derived analytically for generic CFTs.

- In Chapter 3 considers the spectrum of two similar operators naturally associated with a generalized *fermionic* PT, where antiperiodic boundary conditions are taken into account. This time the analysis is restricted to free fermions where specific techniques can be employed.
- In Chapter 4 the replica trick for the relative entropy is considered and several numerical checks, together with new analytical results, for the free massless boson are provided.
- Chapter 5 introduces the replica trick for the trace distance in a generic QFT, with more explicit results in $2d$, especially for CFTs.
- In Chapter 6 the technical problem of the analytic continuation in the context of replica tricks is analyzed: in particular, a viable approach to approximate four-point correlation functions of twist fields in CFT is carefully described.
- Chapter 7 exploits the (generalized) Fisher-Hartwig conjecture to exactly evaluate the recently introduced symmetry-resolved EE and REEs in the $1d$ tight-binding model.

Part II

The second part deals with inhomogeneous and out-of-equilibrium systems: the CFT powerful methods are extended to deal with both those situations relying on CFT in curved spacetime.

- In Chapter 8 we computed entanglement and relative entropies for low-lying excited states in the inhomogeneous $1d$ Fermi gas whose homogeneous version is described by standard CFT.
- Chapter 9 for the first time we develop an extension of the method to out-of-equilibrium situations: the special case of the breathing Tonks-Girardeau gas is considered.

Part III

The last part is finally devoted to the interplay between entanglement and disorder.

- In Chapter 10 the scaling of the LN is derived for random spin models whose ground state is well approximated by a RSP, and several numerical checks are provided.
- In Chapter 11 a model displaying both disorder and inhomogeneities is considered as an example of unusual area-law violation. The phase diagram in the two associated parameters is analyzed.

Part I

ENTANGLEMENT & REPLICAS

Chapter 2

Negativity spectrum

The partial transpose $\rho_A^{T_2}$ of the RDM ρ_A is the key object to quantify the entanglement in mixed states, in particular through the presence of negative eigenvalues in its spectrum. Here we derive analytically the distribution of the eigenvalues of $\rho_A^{T_2}$, that we dub *negativity spectrum*, in the ground state of gapless one-dimensional systems described by a CFT, focusing on the case of two adjacent intervals. This is made possible through the replica approach, here used to represent the integer moments of $\rho_A^{T_2}$: they are in fact known to uniquely fix the distribution itself. This Chapter is based on Ref. [57].

2.1 Introduction

If a system is in a *mixed* state the entanglement entropy, Eq. (1.2.1), is not a good entanglement measure, as it is sensitive to both quantum and classical correlations. This happens for finite-temperature systems and if one is interested in the mutual entanglement between two non-complementary regions of a larger pure system. Given the tripartition of a system as $A_1 \cup A_2 \cup B$ (illustrated in Figure 2.1 (b)), with $A \equiv A_1 \cup A_2$ the region of interest, a computable measure of the entanglement between A_1 and A_2 is the *logarithmic negativity*, introduced in (1.2.5). Its scaling has been characterized analytically for the ground states of quantum critical models whose low energy physics is captured by a $2d$ CFT [94, 145, 246]. In particular, for disconnected intervals the logarithmic negativity encodes information about the full operator content of the CFT [94, 145], similar to the entanglement entropy [167, 169, 247–250]. Remarkably, for disjoint intervals the LN is scale invariant at generic quantum critical points [94, 145, 251–253]. Its scaling behavior is also known for finite temperature systems [254], in CFTs with large central charge [255], disordered spin chains [95], out of equilibrium models [256–259], some holographic [260, 261] and massive quantum field theories [150], topologically ordered phases [96, 97, 262], Kondo-like systems [263–265], and Chern-Simons theories [266, 267]. Some analytical results are available for free models [268], also in $d > 1$ dimensions [92, 93]. On the numerical side the negativity can be obtained in DMRG simulations [95, 246, 251].

Despite this intense theoretical effort, the properties of the eigenvalues of $\rho_A^{T_2}$ started to be studied only recently in Ref. [57] (however, Ref. [244] was in this direction already). In contrast, the study of the eigenvalues of the RDM (the so-called entanglement spectrum) proved to be an extremely powerful theoretical tool to analyze topological phases [54, 269–280], symmetry-broken phases [281–284], many-body localized phases [285–287], and to extract CFT data in models at quantum critical points or in gapless phases [142, 288]. For instance, in Ref. [142] it has been shown that for conformally invariant systems the entanglement spectrum distribution is described by a universal scaling function that depends only on the central charge of the underlying CFT. This distribution turned out to be a crucial quantity to understand the scaling (with the auxiliary tensor dimension) of matrix product states [33, 289, 290].

Here we report on the spectrum of $\rho_A^{T_2}$, dubbed *negativity spectrum*, for gapless one-dimensional models described by a CFT, based on the results of Ref. [57]. Specifically, we investigate, in the ground state of CFTs, the distribution $P(\lambda)$ of the negativity spectrum, which is defined as

$$P(\lambda) \equiv \sum_i \delta(\lambda - \lambda_i), \tag{2.1.1}$$

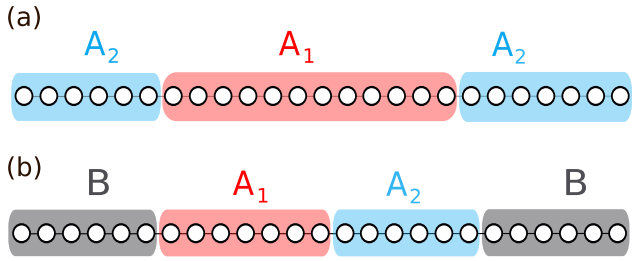

FIGURE 2.1: Partitions of the 1D pure systems considered in this Chapter. Periodic boundary conditions are always implied. (a) The bipartition into two intervals A_1 and $A_2 = \bar{A}_1$. (b) The tripartition of the chain into two adjacent intervals A_1 and A_2 with $A \equiv A_1 \cup A_2$ plus the remainder $B = \bar{A}$. In both (a) and (b) the partial transposition is performed with respect to the degrees of freedom in A_2.

with λ_i being the eigenvalues of $\rho_A^{T_2}$. Using the same techniques developed in Ref. [142] for the entanglement spectrum, we derive analytically $P(\lambda)$ for the case of two adjacent intervals as in Figures 2.1 (a) and (b). We show that the negativity spectrum is sensitive to whether the two intervals are in a pure (Figure 2.1 (a)) or in a mixed state (Figure 2.1 (b)). Moreover, the negativity spectrum distribution is universal and depends only on the central charge of the CFT via its largest eigenvalue. Its functional form (cf. Eqs. (2.2.20) and (2.2.36)) is reminiscent of that of the entanglement spectrum distribution. However, differently as compare to the entanglement spectrum, $P(\lambda)$ depends on the sign of λ and such dependence only disappears for the asymptotically small (in magnitude) eigenvalues, in both the pure and mixed case. Our results imply that the ratio between the total number of positive and negative eigenvalues goes to one in the limit of large intervals. We also investigate the scaling properties of the support of the negativity spectrum, a subject that has attracted some interest in the quantum information community where it has been shown [291, 292] that the eigenvalues of $\rho_A^{T_2}$ are in $[-1/2, 1]$. Here we focus on the smallest (negative) and the largest (positive) eigenvalues of $\rho_A^{T_2}$ (spectrum edges) and we show that for both the pure and mixed case, both the edges exhibit the same scaling behavior as a function of the intervals' length, which we characterize using CFT results. We show that in the limit of large subsystem the support of the negativity spectrum becomes symmetric, i.e. the smallest (negative) eigenvalue is minus the largest (positive) one. Interestingly, the negative edge exhibits strong scaling corrections. Finally, we provide accurate checks of our results in microscopic models using DMRG simulations, finding always excellent agreement.

This Chapter is organized as follows. In Section 2.2 we derive analytically $P(\lambda)$ using CFT results, for two adjacent intervals in a pure state in subsection 2.2.2, and in subsection 2.2.3 for the two intervals in a mixed state. These are compared with DMRG simulations for the critical transverse field Ising chain and the spin-1/2 isotropic Heisenberg chain (XXX chain) in Section 2.3, where also the scaling behavior of the support of the negativity spectrum is discussed. We also present exact numerical data for the harmonic chain. We conclude in Section 2.4.

2.2 Negativity spectrum: CFT results

In this Section we derive analytically the distribution of the eigenvalues of the PT RDM (negativity spectrum).

2.2.1 The moment problem

The negativity spectrum distribution $P(\lambda)$ defined in (2.1.1) can be reconstructed from the knowledge of its moments

$$R_n^{T_2} = \mathrm{Tr}(\rho_A^{T_2})^n, \tag{2.2.1}$$

as already done for the entanglement spectrum [142]. In terms of $P(\lambda)$, $R_n^{T_2}$ are given by

$$R_n^{T_2} \equiv \sum_i \lambda_i^n = \int d\lambda \lambda^n P(\lambda), \tag{2.2.2}$$

with λ_i being the eigenvalues of $\rho_A^{T_2}$. Introducing the Stieltjes transform of $\lambda P(\lambda)$

$$f(z) \equiv \frac{1}{\pi} \sum_{n=1}^{\infty} R_n^{T_2} z^{-n} = \frac{1}{\pi} \int d\lambda \frac{\lambda P(\lambda)}{z-\lambda}, \tag{2.2.3}$$

one has [293, 294]

$$\lambda P(\lambda) = \lim_{\epsilon \to 0} \mathrm{Im} f(\lambda - i\epsilon). \tag{2.2.4}$$

The distribution $P(\lambda)$ can be effectively reconstructed once the moments $R_n^{T_2}$ are analytically known, which is the case for models whose scaling limit is described by a CFT. The knowledge of the moments is indeed the starting point to obtain the logarithmic negativity via the replica trick [94, 145]

$$\mathcal{E} = \lim_{n_e \to 1} R_{n_e}^{T_2}, \quad \text{with} \quad n_e \text{ even}. \tag{2.2.5}$$

It is worth mentioning that, unlike the negativity, the moments $R_n^{T_2}$ can be worked out analytically in free-fermion models [183, 295–299] and numerically using classical [206] and quantum [207] Monte Carlo techniques. It is also possible in some cases to use numerical extrapolations to obtain the negativity from the replica limit of the moments [300].

We recall that this method based on the Stieltjes transform has been used in Ref. [142] to derive the distribution $P_S(\lambda)$ of the entanglement spectrum. The result reads [142]

$$P_S(\lambda) = \delta(\lambda_M - \lambda) + \frac{b\theta(\lambda_M - \lambda)}{\lambda \sqrt{b \ln(\lambda_M/\lambda)}} I_1(2\sqrt{b \ln(\lambda_M/\lambda)}). \tag{2.2.6}$$

where λ_M is the largest eigenvalue of ρ_A, $b \equiv -\ln \lambda_M$, and $I_k(z)$ denotes the modified Bessel functions of the first kind. From (2.2.6) the mean number of eigenvalues $n_S(\lambda)$ larger than λ, i.e., the tail distribution function, is obtained as [142]

$$n_S(\lambda) = \int_{\lambda}^{\lambda_M} d\lambda P_S(\lambda) = I_0(2\sqrt{b \ln(\lambda_M/\lambda)}). \tag{2.2.7}$$

The effectiveness of this distribution function to describe the entanglement spectrum of gapless 1D models has been tested in a few numerical examples [68, 78, 142, 301, 302], showing that apart from sizeable finite size corrections, Eq. (2.2.7) describes accurately the numerical data for the spectrum.

2.2.2 Two intervals in a pure state

We start considering the negativity spectrum for two intervals $A \equiv A_1 \cup A_2$ in a pure state as in Figure 2.1 (a). In this case, the moments of the PT, $R_n^{T_2}$, can be written in terms of the moments $R_n = \mathrm{Tr}\rho_{A_1}^n$ of the RDM of A_1 as [94, 145]

$$R_n^{T_2} = \begin{cases} \mathrm{Tr}\rho_{A_1}^{n_o}, & n_o \text{ odd}, \\ (\mathrm{Tr}\rho_{A_1}^{n_e/2})^2, & n_e \text{ even}. \end{cases} \tag{2.2.8}$$

Importantly, the result depends on the parity of n. This relation between R_n and $R_n^{T_2}$ signals that in the case of a bipartite pure state the negativity spectrum is not independent from the entanglement spectrum. Indeed, by using the Schmidt decomposition of an arbitrary bipartite pure state it is possible to relate all the eigenvalues of the PT $\lambda_{i,j}$ to the non-zero eigenvalues of the RDM ρ_{A_1} (or equivalently ρ_{A_2}). It is a simple linear algebra exercise to show the relation [94, 145, 292, 295]

$$\lambda_{i,j} = \begin{cases} \sqrt{\mu_i \mu_j} & i < j, \\ \mu_i & i = j, \\ -\sqrt{\mu_i \mu_j} & i > j. \end{cases} \tag{2.2.9}$$

The validity of the above relation between λ_{ij} and μ_j can be also inferred from the fact that the relations (2.2.8) force an infinite set of constraints on the eigenvalues: since (2.2.9) satisfy all of these constraints, it must be the only solution of the set of equations (2.2.8). Notice that the largest (positive) eigenvalue of $\rho_A^{T_2}$ coincides with the largest eigenvalue μ_1 of ρ_{A_1}, while the smallest (negative) eigenvalue of $\rho_A^{T_2}$ is given by $-\sqrt{\mu_1 \mu_2}$, where $\mu_{1,2}$ are the two largest eigenvalues of ρ_{A_1}.

Clearly the relations (2.2.9) are valid for an arbitrary pure state, but in the case of the ground state of a CFT, we can use them to derive the probability distribution $P(\lambda)$ of the $\lambda_{i,j}$ from that of μ_i, which, for a CFT, is given by $P_S(\mu)$ in (2.2.6). From (2.2.9), $P(\lambda)$ can be written as

$$P(\lambda) = \sum_{i,j} \delta(\lambda - \lambda_{i,j}) = \frac{\mathrm{sgn}(\lambda)}{2} P_S(|\lambda|) + \frac{1}{2} \int_0^\infty dx \int_0^\infty dy \, \delta(|\lambda| - \sqrt{xy}) P_S(x) P_S(y). \tag{2.2.10}$$

The $\mathrm{sgn}(\lambda)$ function in the first row in (2.2.10) is necessary in order to correctly take into account the $i = j$ term in (2.2.9). Plugging (2.2.6) into (2.2.10), the double integral can be explicitly performed (but it is a tedious calculation) and $P(\lambda)$ can be casted in a form which we will explicitly obtain from the moment problem (cf. (2.2.20) in the following).

Negativity spectrum from the moment problem

Although (2.2.10) provides already the final answer for the negativity spectrum for the bipartition of the ground state of a CFT, it is very instructive to recover the same result from the moment problem, especially to set up the calculation for the more important and difficult case of two adjacent intervals in a mixed state. The key ingredients are the moments of the partial transpose given in (2.2.8) in terms of the moments of ρ_{A_1}. These, for the ground states of models described by a CFT, in the case of one interval A_1 of length ℓ_1 embedded in an infinite system, are given by [17, 18]

$$\mathrm{Tr} \rho_{A_1}^n = c_n \ell_1^{-\frac{c}{6}(n - \frac{1}{n})}. \tag{2.2.11}$$

Here c is the central charge of the CFT and c_n is a non-universal constant. Plugging (2.2.11) in (2.2.8), we rewrite $R_n^{T_2}$ as

$$R_n^{T_2} = \begin{cases} c'_{n_o} e^{-b(n_o - \frac{1}{n_o})}, & n_o \text{ odd}, \\ c'_{n_e} e^{-b(n_e - \frac{4}{n_e})}, & n_e \text{ even}, \end{cases} \tag{2.2.12}$$

where the constants c'_n depend on the parity of n (from (2.2.8) and (2.2.11) one has $c'_{n_e} = c^2_{n_e/2}$ and $c'_{n_o} = c_{n_o}$, for n_e even and n_o odd, respectively). We have also defined

$$b \equiv -\ln \lambda_M = \frac{c}{6} \ln \ell_1 + \text{const.} \tag{2.2.13}$$

Here λ_M is the largest eigenvalue of $\rho_A^{T_2}$, isolated by taking the limit $n \to \infty$ in (2.2.12). This limit does not depend on the parity of n, making λ_M well defined. This is true not only for the leading logarithmic term in $\ln \ell_1$, but also for the additive constant, given that

$$\lim_{n_o \to \infty} \frac{\ln c'_{n_o}}{n_o} = \lim_{n \to \infty} \frac{\ln c_n}{n} = \lim_{n \to \infty} \frac{\ln c^2_{n/2}}{n} = \lim_{n_e \to \infty} \frac{\ln c'_{n_e}}{n_e}. \tag{2.2.14}$$

For a bipartition of the ground state of a CFT, the largest eigenvalue of $\rho_A^{T_2}$ coincides with the largest eigenvalue of ρ_{A_1}, in agreement with the general result (2.2.9).

At this point, we have all the ingredients to compute the Stieltjes transform just by plugging (2.2.12) into the definition of $f(z)$ in (2.2.3) and performing the sums over even and odd n separately, obtaining

$$f(z) = \frac{1}{\pi}\sum_{k=0}^{\infty}\frac{(4b)^k}{k!}\sum_{n=1}^{\infty}\frac{(e^{-b}/z)^{2n}}{(2n)^k} + \frac{1}{\pi}\sum_{k=0}^{\infty}\frac{b^k}{k!}\sum_{n=1}^{\infty}\frac{(e^{-b}/z)^{2n-1}}{(2n-1)^k}. \tag{2.2.15}$$

Here we ignored the presence of the non-universal constants c_n'. This relies on the assumptions that the c_n' do not change significantly upon varying n (more specifically, $\lim_{n\to\infty}\frac{1}{n}\ln c_n' < \infty$), as indicated by results in exactly solvable models [195] and numerical works [303]. The same assumption has been used in deriving the entanglement spectrum distribution in Ref. [142] (and the accuracy of the tail distribution function showed in numerical works [78, 301, 302] is a further confirmation of the plausibility of this assumption).

Remarkably, the two sums in (2.2.15) can be performed analytically, yielding

$$f(z) = \frac{1}{\pi}\sum_{k=0}^{\infty}\frac{(2b)^k}{k!}\mathrm{Li}_k((e^{-b}/z)^2) + \frac{1}{\pi}\frac{e^{-b}}{z}\sum_{k=0}^{\infty}\frac{(b/2)^k}{k!}\Phi((e^{-b}/z)^2), k, 1/2), \tag{2.2.16}$$

where $\mathrm{Li}_k(y)$ is the polylogarithm function and $\Phi(y,k,a)$ one of its generalization known as Lerch transcendent function. Using the relation

$$\frac{y}{2^k}\mathrm{Im}\Phi(y^2,k,1/2) = \frac{\mathrm{sgn}(y)}{2}\mathrm{Im}\left[\mathrm{Li}_k(|y|)\right], \tag{2.2.17}$$

the imaginary part of (2.2.16) reads

$$\mathrm{Im}f(z) = \frac{1}{\pi}\sum_{k=0}^{\infty}\frac{(2b)^k}{k!}\mathrm{Im}\,\mathrm{Li}_k((e^{-b}/z)^2) + \frac{1}{\pi}\frac{\mathrm{sgn}(e^{-b}/z)}{2}\sum_{k=0}^{\infty}\frac{b^k}{k!}\mathrm{Im}\,\mathrm{Li}_k(|e^{-b}/z|), \tag{2.2.18}$$

where $\mathrm{sgn}(y) \equiv y/|y|$ is the sign function. $\mathrm{Li}_k(y)$ is analytic in the complex plane, and it has a branch cut on the real axis for $y \geq 1$. Specifically, for $y > 1$ and $k \geq 1$ the discontinuity on the cut is $\lim_{\epsilon\to 0}\mathrm{Li}_k(y \pm i\epsilon) = \pm\pi(\ln y)^{k-1}/\Gamma(k)$, with $\Gamma(k)$ the Euler gamma function. This implies that

$$\lim_{\epsilon\to 0}\mathrm{Im}f(\lambda - i\epsilon) = \lambda_M\delta(\lambda_M - \lambda) + \frac{1}{2\ln(\lambda_M/|\lambda|)}\times\sum_{k=1}^{\infty}\frac{[b\ln(\lambda_M/|\lambda|)]^k}{k!\Gamma(k)}[1 + 4^k\mathrm{sgn}(\lambda)], \tag{2.2.19}$$

Note that the delta peak $\delta(\lambda_M - \lambda)$ originates from the $k = 0$ terms in (2.2.18). The sum over k in (2.2.19) can be performed explicitly and from (2.2.4), one obtains $P(\lambda)$ as

$$P(\lambda) = \delta(\lambda_M - \lambda) + \frac{b\theta(\lambda_M - |\lambda|)}{|\lambda|\xi}\left[\frac{\mathrm{sgn}(\lambda)}{2}I_1(2\xi) + I_1(4\xi)\right], \tag{2.2.20}$$

where, again, $I_k(z)$ denotes the modified Bessel function of the first kind, and we defined the scaling variable ξ as

$$\xi \equiv \sqrt{b\ln(\lambda_M/|\lambda|)}. \tag{2.2.21}$$

The distribution (2.2.20) is our final result for the negativity spectrum distribution of a bipartition of the ground state of a CFT. It is a tedious but elementary exercise to verify that (2.2.20) coincides with (2.2.10), as it should.

Some consistency checks

Before discussing the main properties and physical consequences of the negativity spectrum distribution (2.2.20), it is worth to provide some consistency checks of its correctness. A first check of (2.2.20) is the normalization condition $\int d\lambda\lambda P(\lambda) = 1$. Since the term $I_1(4\xi)$ in (2.2.20) is odd in the normalisation

integral, it gives a vanishing contribution, and so we have

$$\int d\lambda \lambda P(\lambda) = \lambda_M + \int_{-\lambda_M}^{\lambda_M} d\lambda \frac{b}{2\xi} I_1(2\xi) = 1. \tag{2.2.22}$$

A less trivial check of (2.2.20) is obtained by considering the scaling of the LN $\mathcal{E} = \ln \int d\lambda |\lambda| P(\lambda)$. First of all, let us notice that the negativity can be rewritten as

$$\mathcal{E} = \ln \lim_{n_e \to 1} \mathrm{Tr}\big(\rho_A^{T_2}\big)^{n_e} \simeq \frac{c}{2} \ln \ell_1 = -3 \ln \lambda_M. \tag{2.2.23}$$

By parity of the integral, the term $I_1(2\xi)$ in (2.2.20) does not contribute to $\mathcal{E}$. Using that $\int_{-\lambda_M}^{\lambda_M} d\lambda I_1(4\xi) b/\xi = \lambda_M^{-3} - \lambda_M$, one finds that (2.2.20) satisfies (2.2.23).

Properties of the negativity spectrum distribution

The negativity spectrum distribution (2.2.20) is reminiscent of the entanglement spectrum (2.2.6), but it is definitively different. First of all its support is $[-\lambda_M, \lambda_M]$. This could have been inferred also in two alternative and easier ways that did not require the knowledge of the full negativity spectrum distribution. First from the moments $R_n^{T_2}$, the smallest negative eigenvalue λ_m can be always obtained from the analytic continuations of the even and odd sequences. Indeed, one simply has

$$\lim_{n\to\infty} \frac{1}{n} \ln \mathrm{Tr}\Big[(\rho_A^{T_2})^{n_e=n} - (\rho_A^{T_2})^{n_o=n}\Big] = \lim_{n\to\infty} \frac{1}{n} \ln \Big(\sum |\lambda_i|^n - \sum \lambda_i^n \Big) = \lim_{n\to\infty} \frac{1}{n} \ln \Big(2 \sum_{\lambda_i<0} |\lambda_i|^n \Big) = \ln |\lambda_m| \,, \tag{2.2.24}$$

where we denoted with λ_i the eigenvalues of $\rho_A^{T_2}$. Plugging (2.2.12) in (2.2.24), one gets

$$\ln |\lambda_m| = -b = \ln \lambda_M. \tag{2.2.25}$$

The second method (which has even a more general validity) simply exploits the relations (2.2.9). From these we have, as already stated, that the smallest negative eigenvalue is given by $\lambda_m = -\sqrt{\mu_1 \mu_2}$ where $\mu_{1,2}$ are the two largest eigenvalues of the RDM. We have already seen that generically $\mu_1 = \lambda_M$. It is also known that for a CFT, the entanglement gap $\mu_1 - \mu_2$ closes (i.e. $\mu_1 - \mu_2 \to 0$) in the limit $\ell_1 \to \infty$ [142] (this result is based on earlier CFT results for the corner transfer matrix spectrum [304]). From this one concludes $\lambda_m = -\lambda_M$. However, this second derivation, also shows that the relation $\lambda_m = -\lambda_M$ should be handled with a lot of care when comparing with numerics. Indeed, it has been shown [142, 304] that the entanglement gap closes logarithmically upon increasing the interval length ℓ_1, i.e. $\mu_1 - \mu_2 \propto 1/\ln \ell_1$. Consequently, one has for any finite ℓ_1 that $|\lambda_m| < \lambda_M$ and $\lambda_M - |\lambda_m| \propto 1/\ln \ell_1$ for $\ell_1 \to \infty$. The fact that the gap closes only logarithmically with ℓ_1 means that in practice one would need extremely large intervals in order to see the equality between the largest and the smallest eigenvalues: this is practically impossible to observe in a numerical simulation.

A very important property of the negativity spectrum (2.2.20) is the presence of a delta peak in λ_M, in complete analogy with the standard entanglement spectrum (2.2.6). This means that there exists a single eigenvalue λ_M which provides a finite contribution to the negativity and to the other quantities obtainable from $P(\lambda)$ (as, e.g., the moments etc.). Notice that although the largest and the smallest eigenvalues are equal in the limit of very large interval, their contribution to the probability distribution function is very different, since at $\lambda = \lambda_M$ there is a delta function, which instead is absent at $\lambda = -\lambda_M$. This asymmetry has deep consequences on the various observables such as the number distribution function discussed in the following.

Apart from the delta peak, the negativity spectrum (2.2.20) has two other terms, one symmetric for $\lambda \to -\lambda$ and the other antisymmetric. Notice that $\xi \to 0$ corresponds to $\lambda \to \lambda_M$, while $\xi \to \infty$ to $\lambda \to 0$.

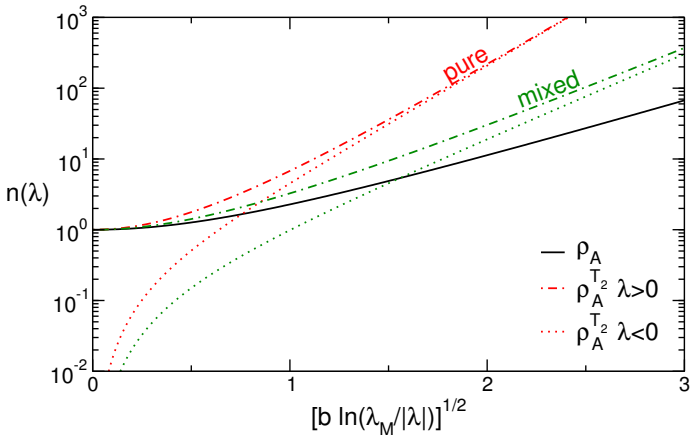

FIGURE 2.2: Negativity spectrum of two adjacent intervals: Survey of the CFT results for the number distribution function $n(\lambda)$ plotted versus the scaling variable $\xi \equiv [b \ln(\lambda_M/|\lambda|)]^{1/2}$, with $b \equiv -\ln \lambda_M$ and λ_M the largest (positive) eigenvalue of $\rho_A^{T_2}$. The continuous line shows for comparison the CFT result for the entanglement spectrum. The dash-dotted and dotted lines denote $n(\lambda)$ for $\lambda > 0$ and $\lambda < 0$, respectively. The different colors correspond to the case with the two intervals in a pure state and a mixed state.

Interestingly, in (2.2.20) the only dependence on the sign of λ is due to the term $I_1(2\xi)$. However, since $I_1(2\xi)/I_1(4\xi) \to 0$ for $\xi \to \infty$, the distribution of the small eigenvalues does not depend on their sign. This can be understood also from the general relation (2.2.9) in which the eigenvalues given by $\pm\sqrt{\mu_i \mu_j}$ are invariant under sign exchange and they are many more than the μ_i's, in the limit of large Hilbert spaces.

The number distribution function

A crucial observable that is easily obtainable from the negativity spectrum is the so-called tail distribution function introduced in (2.2.7) for the case of the entanglement spectrum, which in the following we refer to as *number distribution function*. We will consider a slightly different definition with respect to the (2.2.7), which consider separately the mean number of positive and negative eigenvalues, i.e.,

$$n(\lambda) \equiv \begin{cases} \int_{\lambda}^{\lambda_M} d\lambda P(\lambda) & \lambda > 0 \\ \int_{\lambda_m}^{\lambda} d\lambda P(\lambda) & \lambda < 0 \end{cases} \tag{2.2.26}$$

Performing the integral, the number distribution function can be written for every value of λ as

$$n(\lambda) = \frac{1}{2}\big[\mathrm{sgn}(\lambda) I_0(2\xi) + I_0(4\xi)\big]. \tag{2.2.27}$$

The interest in this function comes from the fact that it is a *super-universal* smooth function, as already known [142] for the entanglement spectrum (2.2.7). Equation (2.2.27) shows that, also for the negativity spectrum, $n(\lambda)$ is a function of the scaling variable ξ only, i.e., there are no free parameters, similarly to the entanglement spectrum (2.2.7). In this sense it is super-universal, meaning that it is the same for any CFT. Remarkably, the only CFT data appearing in (2.2.20) is the central charge, which enters via λ_M. However, when comparing with numerical data, λ_M can be fixed from numerics, and consequently there is no free/fitting parameter.

There are several interesting properties of the number distribution function worth to be mentioned. First of all, the limit for $|\lambda| \to \lambda_M$ (i.e. $\xi \to 0$) is very different whether one consider positive or negative λ. While for $\lambda > 0$, $n(\lambda) \to 1$ as $\lambda \to \lambda_M$, for $\lambda < 0$, $n(\lambda) \to 0$ as $\lambda \to -\lambda_M$. This is a straightforward consequence of the presence of the delta peak in $P(\lambda)$ (2.2.20) for $\lambda = \lambda_M$, but not for $\lambda = -\lambda_M$. In the opposite limit of small absolute value of the eigenvalues, $n(\lambda) \propto e^{4\xi}/(2\sqrt{2\pi\xi})$ for $\xi \to \infty$, independently of the sign of λ, signaling that the number of small eigenvalues does not depend on their sign. Finally, $n(\lambda)$

diverges for $\xi \to \infty$ reflecting that in the thermodynamic limit the number of eigenvalues of $\rho_A^{T_2}$ is infinite. Figure 2.2 reports a plot of the number distribution function versus ξ for both positive and negative λ. All the previously listed features should be apparent.

2.2.3 Two intervals in a mixed state

We now turn to discuss the case of two adjacent intervals in a mixed state as in Figure 2.1 (b). For two generic intervals A_1 and A_2, of length ℓ_1 and ℓ_2, respectively, the scaling of the moments $R_n^{T_2}$ is [94, 145]

$$R_n^{T_2} = c_n'' \begin{cases} (\ell_1\ell_2)^{-\frac{c}{6}(\frac{n_e}{2}-\frac{2}{n_e})}(\ell_1+\ell_2)^{-\frac{c}{6}(\frac{n_e}{2}+\frac{1}{n_e})}, \\ (\ell_1\ell_2(\ell_1+\ell_2))^{-\frac{c}{12}(n_o-\frac{1}{n_o})}, \end{cases} \tag{2.2.28}$$

where c is again the central charge and the non-universal constants c_n'' are analogous to c_n' in (2.2.12); they also depend on the parity of n, but, as before, are expected to depend on n in a very weak manner [94, 145] and so will be neglected in the following treatment. It is convenient to rewrite these moments as

$$R_n^{T_2} \simeq \begin{cases} \ell_1^{-\frac{c}{4}(n_e-\frac{2}{n_e})}\omega^{-\frac{c}{6}(\frac{n_e}{2}-\frac{2}{n_e})}(1+\omega)^{-\frac{c}{6}(\frac{n_e}{2}+\frac{1}{n_e})}, \\ \ell_1^{-\frac{c}{4}(n_o-\frac{1}{n_o})}[\omega(1+\omega)]^{-\frac{c}{12}(n_o-\frac{1}{n_o})}, \end{cases} \tag{2.2.29}$$

where $\omega \equiv \ell_2/\ell_1$ is the aspect ratio of the two intervals. Indeed, from (2.2.29) is clear that the largest eigenvalue of $\rho_A^{T_2}$ can be extracted by taking the limit $n \to \infty$ which yields the same results from both the even and odd sequences. This limit leads to

$$b \equiv -\ln\lambda_M = \frac{c}{12}\ln[\ell_1\ell_2(\ell_1+\ell_2)] + \text{cnst} = \frac{c}{4}\ln\ell_1 + \frac{c}{12}\ln\omega(1+\omega) + \text{cnst}. \tag{2.2.30}$$

We stress that the largest eigenvalue has a different dependence on the central charge compared to the pure case, since the prefactor of the logarithm is $c/4$ instead of $c/6$ in (2.2.13). Notice also that in this case the negativity is not simply a multiple of the logarithm of the largest eigenvalue as in the pure case (cf. (2.2.23)), but we have (ignoring additive constants)

$$\mathcal{E} = \ln \lim_{n_e\to 1} \mathrm{Tr}\big(\rho_A^{T_2}\big)^{n_e} \simeq \frac{c}{4}\ln\frac{\ell_1\ell_2}{\ell_1+\ell_2} = b + \frac{c}{6}\ln\frac{\omega}{(\omega+1)^2}. \tag{2.2.31}$$

At the leading order in ℓ_1, i.e. ignoring the geometry dependent factor ω, one has $\mathcal{E} \simeq -\ln\lambda_M$.

The derivation of $P(\lambda)$ from the moments (2.2.29) proceeds as for the pure case (see 2.2.2) by calculating the Stieltjes transform as sum over the moments (2.2.3), and taking the limit of its imaginary part as in (2.2.4). The sums entering in the Stieltjes transform are exactly the same as in the pure case, just with different factors. For this reason, we do not report the details of the entire calculation, since after the same algebra as in 2.2.2, we arrive to

$$P(\lambda) = \delta(\lambda_M-\lambda) + \frac{1}{2}\frac{\theta(\lambda_M-|\lambda|)}{|\lambda|}\Big[\frac{b}{\xi}I_1(2\xi)\mathrm{sgn}(\lambda) + \frac{\tilde b}{\tilde\xi}I_1(2\tilde\xi)\Big]. \tag{2.2.32}$$

Here we have introduced the scaling variable $\xi \equiv \sqrt{b\ln(\lambda_M/|\lambda|)}$ (which is the same as in (2.2.21), but λ_M is different) and also the auxiliary variable $\tilde\xi$ as

$$\tilde\xi \equiv \sqrt{\tilde b\ln(\lambda_M/|\lambda|)}, \quad \tilde b \equiv 2b + \frac{c}{6}\ln\frac{\omega}{(1+\omega)^2}. \tag{2.2.33}$$

From (2.2.32) we obtain the number distribution function

$$n(\lambda) = \frac{1}{2}\Big[I_0(2\xi)\mathrm{sgn}(\lambda) + I_0(2\tilde\xi)\Big]. \tag{2.2.34}$$

Interestingly, $n(\lambda)$ depends on both ξ and $\tilde{\xi}$. This also implies that it is not super-universal as for the pure case and for the entanglement spectrum. However, we will see soon that some major simplifications take place in the limit of large ℓ_1.

Some consistency checks

Before discussing the limit of large ℓ_1 and the main properties of the negativity spectrum distribution (2.2.32), it is worth to provide some consistency checks. As before, a first check of (2.2.32) is the normalization condition $\int d\lambda \lambda P(\lambda) = 1$. Since the term $I_1(2\tilde{\xi})$ in (2.2.20) is odd in the normalisation integral, it gives a vanishing contribution. The remaining integral is identical to (2.2.22) and provides $\int d\lambda \lambda P(\lambda) = 1$.

The second check is given by the scaling of the negativity $\mathcal{E} = \ln \int d\lambda |\lambda| P(\lambda)$. In this case, it is the term $I_1(2\xi)$ to give a vanishing contribution by parity. The remaining integral is straightforward and yields

$$\mathcal{E} = \ln \int d\lambda |\lambda| P(\lambda) = \tilde{b} - b = b + \frac{c}{6} \ln \frac{\omega}{(1+\omega)^2}, \tag{2.2.35}$$

which is the expected result in (2.2.31).

The support of the negativity spectrum is $[-\lambda_M, \lambda_M]$ exactly like in the pure case. The smallest negative eigenvalue λ_m can be also obtained by using (2.2.24) on the moments (2.2.29). This leads to $\lambda_m = -\lambda_M$ providing another consistency check for (2.2.32).

The limit of large ℓ_1 and the properties of the negativity spectrum

We have seen that in general both the probability distribution function $P(\lambda)$ and the resulting number distribution $n(\lambda)$ do not depend only on the scaling variable ξ, but also on $\tilde{\xi}$. However, in the limit $\ell_1 \to \infty$ many simplifications occur leading to super-universal results. First of all, for the largest eigenvalue we have $b = -\ln \lambda_M \to c/4 \ln \ell_1$ and also $\mathcal{E} \to b$, as clear from (2.2.30) and (2.2.31). Remarkably, this implies that the negativity spectrum distribution does not depend on the geometry of the tripartition at the leading order for large lengths of the intervals since from (2.2.33) one has $\tilde{\xi} \to \sqrt{2}\xi$. In this limit, the distribution $P(\lambda)$ simplifies to

$$P(\lambda) = \delta(\lambda_M - \lambda) + \frac{b\theta(\lambda_M - |\lambda|)}{2|\lambda|\xi} \Big[\mathrm{sgn}(\lambda) I_1(2\xi) + \sqrt{2} I_1(2\sqrt{2}\xi) \Big], \tag{2.2.36}$$

whereas $n(\lambda)$ is

$$n(\lambda) = \frac{1}{2} \big[\mathrm{sgn}(\lambda) I_0(2\xi) + I_0(2\sqrt{2}\xi) \big]. \tag{2.2.37}$$

In contrast with (2.2.34), in the limit $\ell_1 \gg 1$, $n(\lambda)$ is a function of the scaling variable ξ only and so it is super universal. Note that $P(\lambda)$ for the pure (cf. (2.2.20)) and mixed case (cf. (2.2.36)) have a similar structure, but are quantitatively different (the argument of the second Bessel function has a different multiplicative factor). Because of this similarity, the most important properties of the negativity spectrum resemble those of the pure case, that anyhow we repeat here for completeness.

As already said, the support of the negativity spectrum is $[-\lambda_M, \lambda_M]$. However, in analogy with the pure case, the largest and the smallest eigenvalue have a very asymmetrical role, because of the the presence of a delta peak in λ_M, but not at $\lambda_m = -\lambda_M$. This means that there exists a single eigenvalue λ_M which provides a finite contribution to the negativity and to the other quantities obtainable from $P(\lambda)$ (as e.g. the moments etc.). Oppositely, this is not the case for the smallest eigenvalue.

Moving to the number distribution function (2.2.37), the most striking feature is the consequence of the delta peak at λ_M in $P(\lambda)$. This is indeed the cause of the asymmetry that for $\lambda < 0$ one has $n(\lambda) \to 0$ in the limit $|\lambda| \to \lambda_M$, whereas one has $n(\lambda) \to 1$, for $\lambda > 0$. Instead the bulk of the negativity spectrum is symmetric. Indeed, for $\xi \to \infty$ (i.e. for small eigenvalues), one has $n(\lambda) \propto e^{2\sqrt{2}\xi} / (2^{5/4}\sqrt{\pi\xi})$, independently from the sign of λ. This is a slower divergence as compared with the pure case (see 2.2.2). Comparing (2.2.27) and (2.2.37), one has that in the bulk of the negativity spectrum, i.e., for small $|\lambda|$, the

scaling relation

$$n^{\rm pure}\Big(\frac{\xi}{\sqrt{2}}\Big) = n^{\rm mixed}(\xi), \tag{2.2.38}$$

holds.

Figure 2.2 summarizes all our results for $n(\lambda)$ for both pure and mixed states. It reports $n(\lambda)$ versus the scaling variable $\xi \equiv \sqrt{b\ln(\lambda_M/|\lambda|)}$. The dash-dotted and dotted lines correspond to $\lambda > 0$ and $\lambda < 0$, respectively. Different colors are used for the case of two intervals in a pure state (cf. (2.2.27)) and in a mixed state (cf. (2.2.37)). The full line shows $n(\lambda)$ for the eigenvalues of the RDM (entanglement spectrum). One has that for any λ, $n(\lambda)$ is always larger in the pure case. Moreover, for $|\lambda| \to 0$ (i.e. $\xi \to \infty$), $n(\lambda)$ exhibits the same behavior for negative and positive eigenvalues. Finally, since the asymptotic behavior of $n(\lambda)$ as $\xi \to \infty$ is independent of the sign of λ, the ratio between the total number of positive and negative eigenvalues of $\rho_A^{T_2}$ tends asymptotically to one in both cases.

2.2.4 Finite size negativity spectrum

All the results obtained so far in this Section are for finite intervals embedded in infinite one dimensional systems. However, one has often to deal with finite systems, especially in numerical simulations. Fortunately, all the previous CFT results are straightforwardly generalized to finite systems. Indeed, in a CFT, a finite system is obtained by conformally mapping the complex plane to a cylinder. The net effect of this mapping (for correlations of primary operators and hence for the moments on the RDM and of its partial transpose) is to replace all the lengths with the chord lengths $\ell \to L/\pi \sin(\pi\ell/L)$. For the two cases of interest here, this amounts to trivial and unimportant modifications because the probability distribution function $P(\lambda)$ and the number distribution function $n(\lambda)$ depend on the lengths only through the maximum eigenvalue. Hence, once we replace the maximum eigenvalue of $\rho_A^{T_2}$ with its finite volume counterpart equations such as (2.2.20), (2.2.27), (2.2.36), (2.2.37) still hold.

In order to be more specific, for the case of a finite periodic system of length L bipartite in two intervals of lengths ℓ_1 and $L-\ell_1$, the maximum eigenvalue of both ρ_{A_1} and $\rho_A^{T_2}$ is

$$-\ln\lambda_M = (c/6)\ln[L/\pi\sin(\pi\ell_1/L)] + \text{const.} \tag{2.2.39}$$

For the case of two adjacent intervals of length ℓ_1 and ℓ_2 such that $\ell_1+\ell_2 \neq L$, the largest eigenvalue of the $\rho_A^{T_2}$ is given by the CFT formula

$$-\ln\lambda_M = \frac{c}{12}\ln\Big[\Big(\frac{L}{\pi}\Big)^3 \sin\big(\frac{\pi\ell_1}{L}\big)\sin\big(\frac{\pi\ell_2}{L}\big)\sin\big(\frac{\pi(\ell_1+\ell_2)}{L}\big)\Big] + \text{const.} \tag{2.2.40}$$

However, in the following, when checking our results for the negativity spectrum with the super-universal CFT forms, we will simply fix λ_M from the numerical simulations and perform a parameter free comparison with (2.2.27) and (2.2.37).

2.3 Numerical results

In this Section we provide numerical evidence for the results obtained in Section 2.2. We focus on the ground state of the critical transverse field Ising chain, and on the spin-1/2 isotropic Heisenberg chain (XXX chain). We also consider the harmonic chain, for which the negativity spectrum can be calculated analytically. The Ising chain is defined by the Hamiltonian

$$\mathcal{H} \equiv -\frac{J}{2}\sum_{i=1}^{L} S_i^x S_{i+1}^x - h\sum_{i=1}^{L} S_i^z. \tag{2.3.1}$$

Here $S_i^{x,y,z} \equiv \sigma_i^{x,y,z}$, with σ_i^α the Pauli matrices, are spin-1/2 operators acting on site i, and L is the chain length. We use periodic boundary conditions, identifying sites 1 and $L+1$ of the chain. We consider the

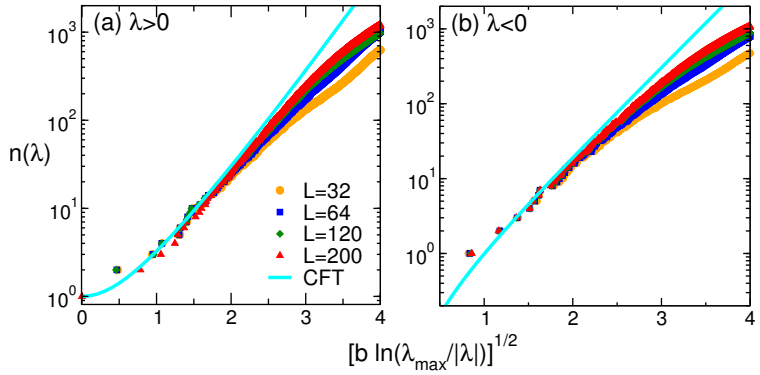

FIGURE 2.3: Negativity spectrum of two intervals in a pure state. DMRG results for the critical Ising chain (of sizes L) are compared with the CFT prediction for the tail distribution $n(\lambda)$ plotted as a function of $\xi \equiv [b \ln(\lambda_M/|\lambda|)]^{1/2}$ (cf. Eq. (2.2.21)). The subsystem size is always $\ell = L/2$. Panel (a) and (b) report $n(\lambda)$ for $\lambda > 0$ and $\lambda < 0$, respectively. In both panels the continuous line is the parameter-free CFT prediction.

critical point at $h = J$, where the low-energy behavior of the model is described by a free Majorana fermion, which is a $c = 1/2$ conformal field theory. The Heisenberg spin chain is instead defined by

$$\mathcal{H} \equiv J \sum_{i=1}^{L} (S_i^x S_{i+1}^x + S_i^y S_{i+1}^y + S_i^z S_{i+1}^z). \tag{2.3.2}$$

The XXX chain is critical, and its low-energy properties are described by the compactified free boson (Luttinger liquid), which is a $c = 1$ CFT. Again, we consider only periodic boundary conditions.

The Hamiltonian of the periodic harmonic chain is

$$\mathcal{H} \equiv \frac{1}{2} \sum_{j=1}^{L} \left[p_j^2 + \Omega q_j^2 + (q_{j+1} - q_j)^2 \right]. \tag{2.3.3}$$

Here p_j, q_j obey the standard bosonic commutation relations $[q_j, q_k] = [p_j, p_k] = 0$, $[q_j, p_k] = i\delta_{j,k}$, and $\Omega \in \mathbb{R}$ is a mass parameter. For $\Omega = 0$ the harmonic chain is critical, and in the scaling limit is described by a $c = 1$ free boson. Moreover, on the lattice, since (2.3.3) is quadratic, it can be solved exactly. The PT RDM has been calculated analytically in Ref. [268] (the technique introduced in Section 1.4.3 is always the starting point). Note that for $\Omega = 0$, (2.3.3) has a zero mode that leads to divergent expressions. For this reason, here we always consider the situation with $\Omega L \ll 1$, choosing $\Omega L = 10^{-6}$.

For Ising and Heisenberg spin chains, $\rho_A^{T_2}$ and the negativity spectrum are obtained using DMRG. Here we employ the method described in Ref. [95]. The method relies on the matrix product state (MPS) representation of the ground state of (2.3.1) and (2.3.2). The calculation of the negativity spectrum involves the diagonalization of a $\chi^2 \times \chi^2$ matrix, with χ the bond dimension of the MPS. The computational cost is therefore χ^6. In our simulations we use $\chi \lesssim 80$, which allows us to simulate system sizes up to $L \sim 200$ for the Ising chain, and up to $L \sim 100$ for the XXX chain.

Two intervals in a pure state

As we have discussed in Sec. 2.2.2 the negativity spectrum for a system in a pure state can be written as a function of the entanglement spectrum of one of the two subsystems. Consequently, testing the negativity spectrum of two complementary intervals A_1 and A_2 (Figure 2.1 (a)) in the ground state of a CFT is just a further confirmation of the range of validity of the CFT prediction for the entanglement spectrum (2.2.7). It is however instructive to have a look at it, exactly to control the range of validity and to test those effects that are not encoded in the CFT predictions such as corrections to the scaling and discreteness of the spectrum.

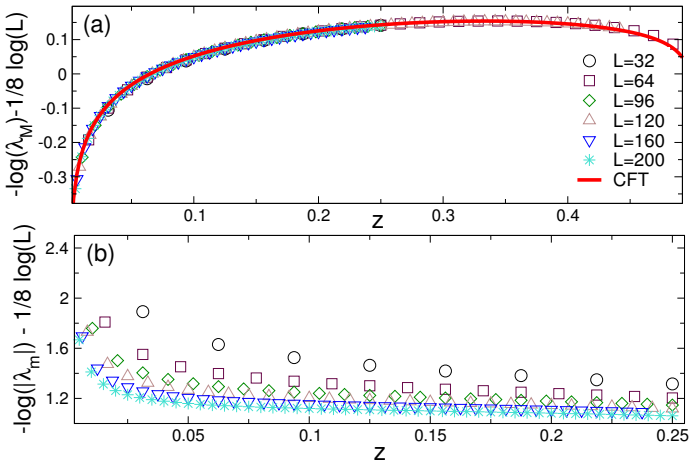

FIGURE 2.4: Largest and smallest negativity eigenvalues for two adjacent equal intervals of length ℓ in a mixed state for a critical Ising chain of length L as function of $z \equiv \ell/L$. Panel (a): The largest positive eigenvalue λ_M of $\rho_A^{T_2}$. The continuous line is the CFT prediction. Panel (b): The smallest (negative) eigenvalue λ_m of $\rho_A^{T_2}$.

Here we only provide results for the critical Ising chain considering systems of lengths $L = 64, 128, 256$ and a bipartition into two equal intervals of length $\ell_1 = \ell_2 = L/2$. We consider the tail distribution $n(\lambda)$ which is plotted in Figure 2.3 versus the scaling variable $\xi \equiv \sqrt{b \ln(\lambda_M/|\lambda|)}$. As we already stressed, $n(\lambda)$ depends (via ξ) only on λ_M. Since we used for λ_M the value obtained from the DMRG simulation, the CFT prediction for $n(\lambda)$ has no free parameters. Panels (a) and (b) in Figure 2.3 are for $\lambda > 0$ and $\lambda < 0$, respectively. The different symbols are the DMRG results for various system sizes, whereas the continuous line is the CFT prediction (2.2.27). The agreement between the CFT prediction and the numerical DMRG data is rather impressive taking into account that there are no fitting parameters. There are some small deviations for very small ξ (i.e. for the largest, in absolute value, eigenvalues) which are clearly due to the discreteness of the negativity spectrum. Then there is a quite large region with $1 \lesssim \xi \lesssim 2$ where the agreement is perfect for both positive and negative eigenvalues. For larger ξ (i.e. for very small eigenvalues) sizeable deviations appear. These do not come unexpected since they are a consequence of the finiteness of the Hilbert space for a block of spin of finite length. Consequently $n(\lambda)$ cannot grow indefinitely as in CFT. The same effect is well known and studied already for the entanglement spectrum [142, 301, 302]. However, upon increasing L the data exhibit a clear trend toward the CFT prediction, confiming that the observed discrepancy is due to scaling corrections and that it should disappear in the limit $\ell \to \infty$.

Two intervals in a mixed state: Support of the negativity spectrum

We now turn to discuss the negativity of two adjacent intervals A_1 and A_2 in a mixed state as in Figure 2.1 (b). Before discussing the full negativity spectrum, it is instructive to consider the scaling properties of its support. In particular, we focus on the scaling behavior of the largest (positive) eigenvalue λ_M and the smallest (negative) one λ_m. This allows us to control the range of validity of our result and to test those effects that are not encoded in the CFT prediction, such as scaling corrections. For simplicity, we restrict ourselves to the situation of two equal-length intervals.

Let us start by discussing the largest eigenvalue. An important consequence of (2.2.40) (with $\ell_1 = \ell_2 = \ell$) is that the combination $-\ln \lambda_M - c/4 \ln L$ is a function of $z = \ell/L$ only. For the critical Ising chain this is numerically demonstrated in Figure 2.4 (a) which reports $-\ln \lambda_M - 1/8 \ln L$ ($c = 1/2$ for the Ising chain) versus $0 \leq z \leq 1/2$. The different symbols are DMRG data for $L \leq 200$. The perfect data collapse for all system sizes provides a strong confirmation of (2.2.40). Moreover, the full line in the Figure is a fit to (2.2.40), with the additive constant as the only fitting parameter. The agreement with the data is excellent, providing conclusive evidence of the CFT scaling for the largest eigenvalue of $\rho_A^{T_2}$.

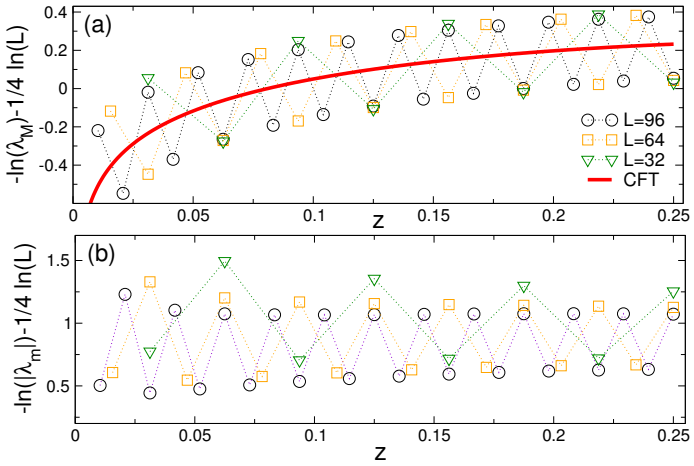

FIGURE 2.5: Largest and smallest negativity eigenvalues for two adjacent intervals in a mixed state: Same as in Figure 2.4 for the XXX chain. Note both in (a) and (b) the presence of oscillating scaling corrections.

As we have seen, the smallest negative eigenvalue of $\rho_A^{T_2}$ should scale like the largest positive one λ_M. For this reason, to illustrate the scaling behavior of λ_m, in Figure 2.4 (b) (for the Ising chain and the same tripartition as above) we report $\ln|\lambda_m| - 1/8 \ln L$ versus $z = \ell/L$. The data do not collapse on a single curve as seen for the largest eigenvalue in panel (a) and a quite weak dependence on z is observed. This in strikingly different for λ_M. Furthermore, it is clear that the data are not yet asymptotic, suggesting that strong corrections to the scaling are present for these values of L. This does not come unexpected, since we already discussed that strong logarithmic corrections to the scaling were expected for λ_m.

Similar results as in Figure 2.4 are observed for the XXX chain. The CFT scaling (2.2.40) with $c = 1$ is expected to hold for λ_M. Panel (a) in Figure 2.5 reports $-\ln\lambda_M - 1/4 \ln L$ versus z. In contrast with the Ising case (Figure 2.4), strong oscillations with the parity of the intervals length ℓ are present and should be attributed to the finite-size of the chain. Indeed, similar scaling corrections are well known in the literature for the Rényi entropies [303, 305–307], and are due to the antiferromagnetic nature of the XXX interaction. Moreover, for $-\ln\lambda_M$ of ρ_A these corrections are known to decay logarithmically [196, 303, 308] with ℓ as $1/\ln\ell$. Since a similar behavior is expected for the largest eigenvalue of $\rho_A^{T_2}$, this explains the very weak dependence on L of the oscillations observed in Figure 2.5 (a). Still, the CFT result (2.2.40), which is shown as full line in Figure 2.5 (a), captures well the gross behavior of the DMRG data. Finally, in Figure 2.5 (b) we focus on λ_m, reporting $-\ln|\lambda_m| - 1/4 \ln L$ as a function of z, for the same chain sizes as in panel (a). Interestingly, the same oscillating corrections observed for λ_M are present. These oscillations prevent to understand the scaling with L of λ_m and so the data are even less conclusive than those for the Ising chain in Figure 2.4.

At this point, we do not have yet conclusive data to support the CFT scaling $\lambda_m = -\lambda_M$ for the negative edge of the negativity spectrum. We have strong evidence that the data in panels (b) of Figures 2.4 and 2.5 are affected by logarithmic corrections to the scaling. Consequently, in order to reveal the true asymptotic behavior, we would need to explore system sizes that are orders of magnitude larger than those already considered. This is clearly impossible with DMRG. For this reason we study the support of the negativity spectrum for the harmonic chain for which standard techniques for the diagonalization of bosonic quadratic Hamiltonians allowed us to investigate chains with 16000 sites with a minor numerical effort. The edges of the negativity spectrum for a tripartite harmonic chain (with $\ell_1 = \ell_2 = \ell$) are reported in Figure 2.6. Panel (a) focuses on the largest eigenvalue λ_M, reporting $\ln\lambda_M - 1/4 \ln L$ versus $z = \ell/L$ for chain up to $L = 16000$. The agreement between the CFT prediction (2.2.40) and the data is perfect (again the only fitting parameter is the additive constant). Notice, however, the vertical scale of Figure 2.6: we have a very large value, reflecting the fact that for the periodic harmonic chain the zero mode produces a large additive constant to the leading logarithmic behavior. On the other hand, in panel (b) we plot $\ln|\lambda_m| - 1/4 \ln L$ versus z. Strong scaling corrections are still visible at $L = 16000$. Specifically, while for $L \sim 100$ the data

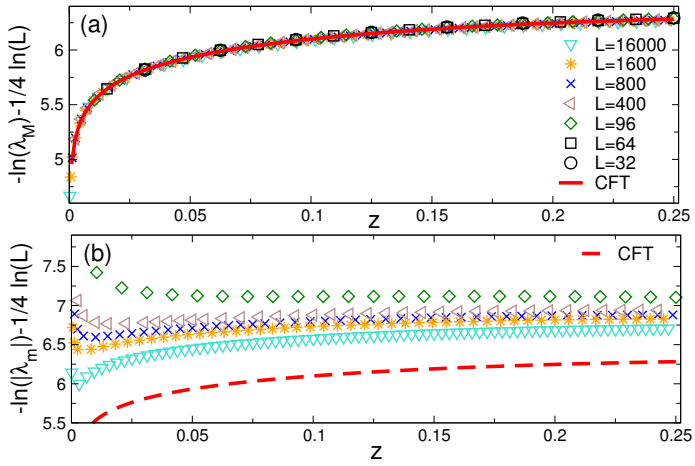

FIGURE 2.6: Largest and smallest negativity eigenvalues for two adjacent intervals in a mixed state: Same as in Figure 2.4 for the harmonic chain. Note in panel (b) the very large scaling corrections for λ_m. The dashed line is the same curve for $-\ln\lambda_M$ as in (a).

exhibit a "flat" behavior as a function of z which is reminiscent of what observed in Figure 2.4 (b) for the Ising chain, for larger chains the data become compatible with the CFT scaling (2.2.40): it is in fact clear that the curve for $L = 16000$ is just shifted compared to the asymptotic prediction $|\lambda_m| = \lambda_M$ (dashed line in the figure). However, from Figure 2.6 (b) it is clear that this can be true only for very large chain sizes (comparing the data with the dashed line). Once again this fact is fully compatible with the presence of the expected logarithmic corrections to the scaling.

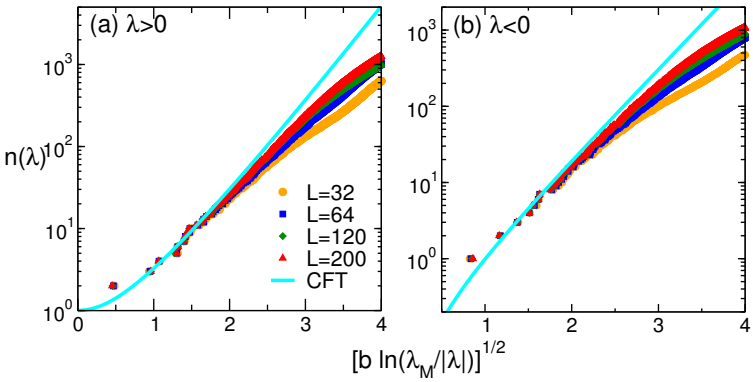

FIGURE 2.7: Negativity spectrum of two adjacent equal-length intervals in a mixed state: The number distribution function $n(\lambda)$ plotted as a function of $\xi \equiv [b\ln(\lambda_M/|\lambda|)]^{1/2}$, with $b \equiv -\ln\lambda_M$, and λ_M the largest positive eigenvalue of $\rho_A^{T_2}$. The symbols are DMRG results for the critical Ising chain for several chain sizes L. The subsystem size is always $\ell = L/4$. Panel (a) and (b) plot $n(\lambda)$ for positive and negative values of λ, respectively. In both panels the continuous line is the CFT prediction.

The negativity spectrum

We finally discuss the negativity spectrum of two adjacent intervals in a mixed state as in Figure 2.1 (b). The results for the critical Ising chain are reported in Figure 2.7. Panels (a) and (b) show the number distribution function $n(\lambda)$ plotted against $\xi \equiv \sqrt{b\ln(\lambda_M/|\lambda|)}$ for both $\lambda > 0$ and $\lambda < 0$. The symbols are DMRG data for $L = 32 - 200$. We consider two intervals of equal length $\ell = L/4$. Similarly to the pure case, in constructing the scaling variable ξ we used for λ_M the value from the DMRG simulation, so that the CFT prediction for large ℓ (2.2.36) is super-universal and does not have any free parameter. In the two panels the full lines are these super-universal CFT predictions (2.2.36). The agreement between the DMRG data and the CFT is fairly good. As usual in these plots (compare e.g. with Figure 2.3), some deviations are observed

for large ξ (small $|\lambda|$). As already explained these deviations are due to the finiteness of the Hilbert space of the interval and they are expected to disappear in the limit of large ℓ. Indeed, the observed trend of the data upon increasing L (and hence $\ell = L/4$) suggests that in the thermodynamic limit the CFT behavior should be recovered.

The analogous results for the XXX spin chain for the number distribution function are reported in Figure 2.8. The symbols are DMRG results now for $L = 32 - 96$. The theoretical CFT result is the same as for the Ising chain (2.2.36). For both positive and negative values of λ the DMRG data are in excellent agreement with the CFT prediction (full lines in the Figure). It is interesting to observe that at small ξ, the negativity spectrum exhibits some intriguing degeneracy structure, which is not captured by the CFT result. This is analogous to what observed also for the entanglement spectrum in systems with continuous symmetries [142, 301].

Concluding, the results in Figures 2.7 and 2.8 provide a quite strong evidence for the correctness of the CFT negativity spectrum prediction also for the case of two adjacent non-complementary intervals embedded in the ground state of model whose low energy features are captured by CFT. It is unfortunate that more stringent tests of the CFT prediction cannot be obtained from the study of the harmonic chain. Indeed, while for the harmonic chains methods allowing us to study systems of size 10^4 are available, as we have shown in Figure 2.6, the resulting value of λ_M is very large because of the presence of the zero mode. This implies that to get a stringent check of the CFT negativity spectrum, one would require to consider a really huge number of eigenvalues of $\rho_A^{T_2}$ which goes beyond our numerical possibilities.

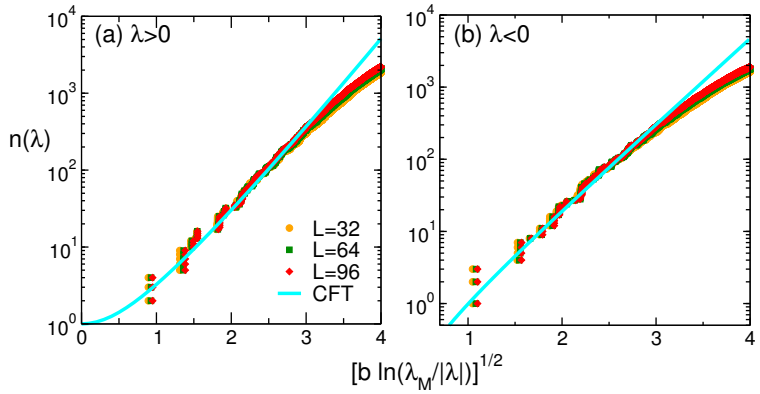

FIGURE 2.8: Negativity spectrum of two adjacent intervals in a mixed state: Same as in Figure 2.7, for the XXX chain. Note the degeneracy patterns at large $|\lambda|$.

2.4 Concluding remarks

In this Chapter we investigated the negativity spectrum in the ground state of $1d$ gapless systems described by a CFT. The main results have been already summarized at the beginning. Below we discuss some future research directions.

Clearly, it would be interesting to extend our analysis to the case of two *disjoint* intervals in a mixed state. It has been demonstrated in Ref. [94, 145] that the negativity of two disjoint intervals decays exponentially as a function of their distance. It would be interesting to clarify how this behavior is reflected in the negativity spectrum. Unfortunately, from the CFT side, this interesting problem is technically prohibitive because the moments $\mathrm{Tr}(\rho_A^{T_2})^n$ have a very complicated analytic structure [94, 145]. However, we are going to see that such analysis is possible at least for free fermions, as sketched in Chapter 3.

Here we focused only on the distribution of the negativity spectrum. It would be enlightening to investigate the fine structure of the spectrum, for instance, its degeneracy patterns and the eigenvalue spacing. This could potentially reveal deeper structures of the underlying CFT, similar to what happens for the entanglement spectrum [142, 288].

On the experimental side, there are recent proposals on how to measure the entanglement spectrum in cold-atom experiments [309] (see also Ref. [243]). It should be possible to extend these ideas to measure the negativity spectrum. Finally, our results could be useful to device simpler measures of the entanglement in mixed states. One interesting direction would be to focus only on a small portion of the spectrum, for instance exploring the region around the smallest negative eigenvalue.

Chapter 3

Twisted and untwisted negativity spectrum of free fermions

Despite the great success of LN in characterizing bosonic many-body systems, generalizing the operation of PT to fermionic systems remained a technical challenge until recently when a more natural definition of PT for fermions that accounts for the Fermi statistics has been put forward. Here, we study the many-body spectrum of the RDM of two adjacent intervals for $1d$ free fermions after applying the fermionic PT. We show that in general there is a freedom in the definition of such operation which leads to two different definitions of PT: the resulting density matrix is Hermitian in one case, while it becomes pseudo-Hermitian in the other case. Using the path-integral formalism, we analytically compute the leading order term of the moments in both cases and derive the distribution of the corresponding eigenvalues over the complex plane. We further verify our analytical findings by checking them against numerical lattice calculations. This Chapter is based on Ref. [310].

3.1 Introduction

It is well known that the whole set of eigenvalues of density matrices, i.e. the entanglement spectrum, contains more information than merely the entanglement entropies and this is why it has been studied extensively (see the introduction of Chapter 2 for references). Unlike the entanglement spectrum, however, less is known about the spectrum of PT density matrices in many-body systems, for which, as seen in the previous Chapter, a systematic study only started with Ref. [57].

In this Chapter, we reconsider the negativity spectrum, but now specialized to *fermionic* systems. The PT of fermionic density matrices, indeed, involves some subtleties due to the Fermi statistics (i.e., anti-commutation relation of fermion operators). Initially, a procedure for the PT of fermions based on the fermion-boson mapping (Jordan-Wigner transformation) was proposed [295] and was also used in the subsequent studies [92, 183, 296–299, 311]. However, this definition turned out to cause certain inconsistencies within fermionic theories such as violating the additivity property and missing some entanglement in topological superconductors, and gives rise to incorrect classification of time-reversal symmetric topological insulators and superconductors. Additionally, according to this definition, it is computationally hard to find the PT (and calculate the entanglement negativity) even for free fermions, since the PT of a fermionic Gaussian state is not Gaussian. This motivates us to use another way of implementing a fermionic PT which was proposed recently in the context of time-reversal symmetric SPT phases of fermions [312–314]. This definition does not suffer from the above issues and at the same time the associated entanglement quantity is an entanglement monotone [315]. From a practical standpoint, the latter definition has the merit that the PT Gaussian state remains Gaussian and hence can be computed efficiently for free fermions. A detailed survey of differences between the two definitions of PT from both perspectives of quantum information and condensed matter theory (specifically, topological phases of fermions) is discussed in Refs. [314, 315].

Before we get into details of the fermionic PT in the coming sections, let us finish this part with a summary of our main findings. To study the entanglement, we consider the usual setup, with a partition of a given system into three parts, with two of them being the subsystems of interest. To lighten the notation (in this Chapter only) we will refer to them as A and B (instead of A_1 and A_2) and, whenever clear, we will avoid the subscript of the subsystem to which the RDM is associated.

We consider the distribution of the many-body eigenvalues λ_i of the PT RDM, as defined in the previous Chapter, Eq. (2.1.1), for $1d$ free fermions. As a lattice realization, we consider the hopping Hamiltonian on a chain

$$\hat{H} = -\sum_j [t(f_{j+1}^\dagger f_j + \text{H.c.}) + \mu f_j^\dagger f_j], \tag{3.1.1}$$

where the fermion operators f_j and $f_j^\dagger$ obey the anti-commutation relation $\{f_i, {f_j}^\dagger\} = f_i {f_j}^\dagger + {f_j}^\dagger f_i = \delta_{ij}$ and $\{f_i, f_j\} = \{{f_i}^\dagger, {f_j}^\dagger\} = 0$.

Recall that using the regular (matrix) PT – we will refer to it as the *bosonic* PT –, which applies to generic systems where local operators commute, the obtained PT density matrix is a Hermitian operator and its eigenvalues are either negative or positive. However, it turned out that for fermions a consistent definition of PT involves a phase factor as we exchange indices in (1.2.3) and in general one can define two types of PT operation. As we will explain in detail, these two types correspond to the freedom of spacetime boundary conditions for fermions associated with the fermion-number parity symmetry. We reserve ρ^{T_A} and $\rho^{\widetilde{T}_A}$ to denote the fermionic PT which leads to anti-periodic (untwisted) and periodic (twisted) boundary conditions along fundamental cycles of the spacetime manifold, respectively. We should note that ρ^{T_A} is pseudo-Hermitian[1] and may contain complex eigenvalues, while $\rho^{\widetilde{T}_A}$ is Hermitian and its eigenvalues are real. We use the spacetime path integral formulation to analytically calculate the negativity spectrum. In the case of $\rho^{\widetilde{T}_A}$, we obtain results very similar to those of the previous CFT work [57], where the distribution of positive and negative eigenvalues are described by two universal functions. In the case of ρ^{T_A}, we observe that the eigenvalues are complex but they have a pattern and fall on six branches in the complex plane with a *quantized* complex phase of $\angle\lambda = 2\pi n/6$. We show that the spectrum is reflection symmetric with respect to the real axis and the eigenvalue distributions are described by four universal functions along $\angle\lambda = 0, \pm 2\pi/6, \pm 4\pi/6, \pi$ branches. We further verify our findings by checking them against numerical lattice simulations.

The rest of this Chapter is organized as follows: in Section 3.2 we provide a brief review of partial transpose for fermions, in Section 3.3 we discuss the spacetime path-integral formulation of the moments of PT density matrices. The spectrum of the twisted and untwisted partial transpose is analytically derived in Section 3.4 for different geometries, where numerical checks with free fermions on the lattice are also provided. The case of *disjoint* intervals is briefly discussed in Section 3.5. We close our discussion by some concluding remarks in Section 3.6.

3.2 Preliminary remarks

In this Section, we review some basic materials which we use in the next sections: the definition of PT for fermions, the moment problem introduced in Section 2.2.1 (here generalized to the moments of a generic observable), and some properties of PT Gaussian states.

3.2.1 Twisted and untwisted partial transpose for fermions

We consider a fermionic Fock space $\mathcal{H}$ generated by N local fermionic modes f_j, $j = 1, \cdots, N$. The Hilbert space is spanned by $|n_1, n_2, \cdots, n_N\rangle$ which is a string of occupation numbers $n_j = 0, 1$. We define the Majorana (real) fermion operators in terms of canonical operators as

$$c_{2j-1} = f_j^\dagger + f_j, \quad c_{2j} = i(f_j - f_j^\dagger), \quad j = 1, \ldots, N. \tag{3.2.1}$$

[1] A pseudo-Hermitian operator H is defined by $\eta H^\dagger \eta^{-1} = H$ with $\eta^2 = 1$ where η is a unitary Hermitian operator satisfying $\eta^\dagger \eta = \eta \eta^\dagger = 1$ and $\eta = \eta^\dagger$. Essentially, pseudo-Hermiticity is a generalization of Hermiticity, in that it implies Hermiticity when $\eta = 1$.

These operators satisfy the commutation relation $\{c_j, c_k\} = 2\delta_{jk}$ and generate a Clifford algebra. Any operator X acting on $\mathcal{H}$ can be expressed in terms of a polynomial of c_j's,

$$X = \sum_{k=1}^{2N} \sum_{p_1<p_2\cdots<p_k} X_{p_1\cdots p_k} c_{p_1}\cdots c_{p_k}, \tag{3.2.2}$$

where $X_{p_1\ldots p_k}$ are complex numbers and fully antisymmetric under permutations of $\{1,\ldots,k\}$. A density matrix has an extra constraint, i.e., it commutes with the total fermion-number parity operator, $[\rho,(-1)^F] = 0$ where $F = \sum_j f_j^\dagger f_j$. This constraint entails that the Majorana operator expansion of ρ only contains even number of Majorana operators, i.e., k in the above expression is even.

The Hilbert space associated with the region of interest admits a bipartition as $\mathcal{H}_A \otimes \mathcal{H}_B$ spanned by f_j with $j = 1,\cdots,N_A$ in subsystem A and $j = N_A+1,\cdots,N_A+N_B$ in subsystem B. Then, a generic density matrix on $\mathcal{H}_{A_1}\otimes\mathcal{H}_{A_2}$ can be expanded in Majorana operators as

$$\rho = \sum_{k_1,k_2}^{k_1+k_2=\text{even}} \rho_{p_1\cdots p_{k_1},q_1\cdots q_{k_2}} a_{p_1}\cdots a_{p_{k_1}} b_{q_1}\cdots b_{q_{k_2}}, \tag{3.2.3}$$

where $\{a_j\}$ and $\{b_j\}$ are Majorana operators acting on $\mathcal{H}^A$ and $\mathcal{H}^B$, respectively, and the even fermion-number parity condition is indicated by the condition $k_1+k_2 = \text{even}$. Our definition of the PT for fermions is given by [313, 314]

$$\rho^{T_A} \equiv \sum_{k_1,k_2}^{k_1+k_2=\text{even}} \rho_{p_1\cdots p_{k_1},q_1\cdots q_{k_2}} i^{k_1} a_{p_1}\cdots a_{p_{k_1}} b_{q_1}\cdots b_{q_{k_2}}, \tag{3.2.4}$$

and similarly for ρ^{T_B}. It is easy to see that the subsequent application of the PT with respect to the two subsystems leads to the full transpose $(\rho^{T_A})^{T_B} = \rho^T$, i.e. reversing the order of Majorana fermion operators. In addition, the definition (3.2.4) implies that

$$(\rho^{T_A})^\dagger = (-1)^{F_A}\rho^{T_A}(-1)^{F_A}, \tag{3.2.5}$$

$$(\rho^{T_A})^{T_A} = (-1)^{F_A}\rho(-1)^{F_A}, \tag{3.2.6}$$

where $(-1)^{F_A}$ is the fermion-number parity operator on H_A, i.e. $F_A = \sum_{j\in A} f_j^\dagger f_j$. The first identity, namely the pseudo-Hermiticity, can be understood as a consequence of the fact that $(\rho^{T_A})^\dagger$ is defined the same as (3.2.4) by replacing i^{k_1} with $(-i)^{k_1}$. The second identity reflects the fact that the fermionic PT is related to the action of time-reversal operator of spinless fermions in the Euclidean spacetime [313]. We should note that the matrix resulting from the PT is not necessarily Hermitian and may have complex eigenvalues, although $\text{Tr}\rho^{T_A} = 1$. The existence of complex eigenvalues is a crucial property which was used in the context of SPT invariants to show that the complex phase of $\text{Tr}(\rho\rho^{T_A})$, which represents a partition function on a non-orientable spacetime manifold, is a topological invariant. For instance, $\text{Tr}(\rho\rho^{T_A}) = e^{i2\pi\nu/8}$ for time-reversal symmetric topological superconductors (class BDI) which implies the Z_8 classification. (Here $\nu \in \mathrm{Z}_8$ is the topological invariant). Nevertheless, we may still use Eq. (1.2.5) to define an analog of entanglement negativity for fermions and calculate the trace norm in terms of square root of the eigenvalues of the composite operator $\rho_\times = [(\rho^{T_A})^\dagger\rho^{T_A}]$, which is a Hermitian operator with real positive eigenvalues. On the other hand, from Eq. (3.2.5) we realize that $\rho_\times = (\rho^{\widetilde{T}_A})^2$ where we introduce the *twisted* PT by

$$\rho^{\widetilde{T}_A} \equiv \rho^{T_A}(-1)^{F_A}. \tag{3.2.7}$$

It is easy to see from Eq. (3.2.5) that this operator is Hermitian and then similar to the bosonic PT always contains real eigenvalues. It is worth noting that

$$(\rho^{\widetilde{T}_A})^{\widetilde{T}_A} = \rho, \tag{3.2.8}$$

in contrast with the *untwisted* PT (3.2.6). As we will see shortly, this difference between ρ^{T_A} and $\rho^{\widetilde{T}_A}$ in the operator formalism will show up as anti-periodic and periodic boundary conditions across the fundamental cycles of spacetime manifold in the path-integral formalism.

3.2.2 The moment problem

In the replica approach to LN (1.2.5) and negativity spectrum, one first has to calculate the moments of PT, aka Rényi negativities (RNs),

$$\mathcal{N}_n^{(\mathrm{ns})}(\rho) = \ln \mathrm{Tr}[(\rho^{T_A})^n], \qquad \mathcal{N}_n^{(\mathrm{r})}(\rho) = \ln \mathrm{Tr}[(\rho^{\widetilde{T}_A})^n], \tag{3.2.9}$$

which are the (logarithmic) fermionic counterparts of the bosonic definition in Eq. (2.2.1). The superscripts (ns) and (r) stand for Neveu-Schwarz and Ramond respectively (the reason for this will be clear from the path integral representation of such quantities, see Section 3.3 below). Thus, the analog of analytic continuation (1.4.4) to obtain the LN is

$$\mathcal{E}(\rho) = \lim_{n\to 1/2} \mathcal{N}_{2n}^{(\mathrm{r})}(\rho). \tag{3.2.10}$$

The general framework to analytically obtain the distribution of eigenvalues of a density matrix (or its transpose) from the moments is reviewed in Section 2.2.1 of Chapter 2. For any given operator $\mathcal{O}$, the associated moments are of the form

$$R_n \equiv \mathrm{Tr}[\mathcal{O}^n]. \tag{3.2.11}$$

In terms of the eigenvalues of $\mathcal{O}$, $\{\lambda_j\}$, we have $R_n = \sum_j \lambda_j^n = \int P(\lambda)\lambda^n d\lambda$, where $P(\lambda)$ is the associated distribution function (see Eq. (2.1.1)). The essential idea is to compute the Stieltjes transform, Eq. (2.2.3). Then, assuming that the eigenvalues are *real*, the distribution function can be easily read off, Eq. (2.2.4), together with the complementary cumulative distribution function or simply the tail distribution, $n(\lambda) = \int_\lambda^{\lambda_{\max}} d\lambda P(\lambda)$.

For specific types of operators such as the density matrices and their PT in (1+1)d CFTs, the moments can be cast in the form,

$$R_n = r_n \exp\left(-bn + \frac{a}{n}\right), \qquad \forall n, \tag{3.2.12}$$

where $a, b \in \mathrm{R}$, $b > 0$ and r_n are non-universal constant. In such cases, the distribution function is found to be [95]

$$P(\lambda; a, b) = \begin{cases} \frac{a\,\theta(e^{-b}-\lambda)}{\lambda\sqrt{a\ln(e^{-b}/\lambda)}} I_1(2\sqrt{a\ln(e^{-b}/\lambda)}) + \delta(e^{-b}-\lambda), & a > 0, \\ \frac{-|a|\,\theta(e^{-b}-\lambda)}{\lambda\sqrt{|a|\ln(e^{-b}/\lambda)}} J_1(2\sqrt{|a|\ln(e^{-b}/\lambda)}) + \delta(e^{-b}-\lambda), & a < 0, \end{cases} \tag{3.2.13}$$

and the corresponding tail distribution is given by

$$n(\lambda; a, b) = \begin{cases} I_0(2\sqrt{a\ln(e^{-b}/\lambda)}), & a > 0, \\ J_0(2\sqrt{|a|\ln(e^{-b}/\lambda)}), & a < 0, \end{cases} \tag{3.2.14}$$

where $J_\alpha(x)$ and $I_\alpha(x)$ are the regular Bessel functions and modified Bessel functions of the first kind, respectively. Note again that (3.2.13) and (3.2.14) are derived by ignoring the presence of the constants r_n in (3.2.12).

3.2.3 Partial transpose of Gaussian states

Here, we discuss how to compute the spectrum of the PT of a Gaussian state from the corresponding covariance matrix. The idea is similar to that of the entanglement spectrum (based on the techniques of Section 1.4.3), while there are some differences as the covariance matrix associated with the PT density matrix may contain complex eigenvalues. Before we continue, let us summarize the structure of the many-body spectrum of ρ^{T_A} and $\rho^{\widetilde{T}_A}$ for free fermions,

$$\mathrm{Spec}[\rho^{T_A}]: \begin{cases} (\lambda_i, \lambda_i^*) & \mathrm{Im}[\lambda_i] \neq 0, \\ (\lambda_i, \lambda_i) & \mathrm{Im}[\lambda_i] = 0, \quad \lambda_i < 0, \\ \lambda_i & \mathrm{Im}[\lambda_i] = 0, \quad \lambda_i > 0, \end{cases} \tag{3.2.15}$$

$$\mathrm{Spec}[\rho^{\widetilde{T}_A}]: \begin{cases} (\lambda_i, \lambda_i) & \lambda_i < 0, \\ \lambda_i & \lambda_i > 0, \end{cases} \tag{3.2.16}$$

where repeating values mean two fold degeneracy. We should note that the pseudo-Hermiticity of ρ^{T_A} (3.2.5) ensures that the complex-valued subset of many-body eigenvalues of ρ^{T_A} appear in complex conjugate pairs. This property is general and applicable to any density matrix beyond free fermions. An immediate consequence of this property is that any moment of ρ^{T_A} is guaranteed to be real-valued.

A Gaussian density matrix in the Majorana fermion basis (3.2.1) is defined by

$$\rho_\Omega = \frac{1}{\mathcal{Z}(\Omega)} \exp\left(\frac{1}{4}\sum_{j,k=1}^{2N} \Omega_{jk} c_j c_k\right), \tag{3.2.17}$$

where Ω is a pure imaginary antisymmetric matrix and $\mathcal{Z}(\Omega) = \pm\sqrt{\det\left(2\cosh\frac{\Omega}{2}\right)}$ is the normalization constant. We should note that the spectrum of Ω is in the form of $\pm\omega_j$, $j = 1, \ldots, N$ and the $\pm$ sign ambiguity in $\mathcal{Z}(\Omega)$ is related to the square root of determinant where we need to choose one eigenvalue for every pair $\pm\omega_j$. The sign is fixed by the Pfaffian. This density matrix can be uniquely characterized by its covariance matrix,

$$\Gamma_{jk} = \frac{1}{2}\mathrm{Tr}(\rho_\Omega [c_j, c_k]), \tag{3.2.18}$$

which is a $2N \times 2N$ matrix. These two matrices are related by

$$\Gamma = \tanh\left(\frac{\Omega}{2}\right), \qquad e^{\Omega} = \frac{\mathbb{I} + \Gamma}{\mathbb{I} - \Gamma}. \tag{3.2.19}$$

Furthermore, one can consider a generic Gaussian operator which is also defined through Eq. (3.2.17), but without requiring that the spectrum is pure imaginary. An equivalent description in terms of the covariance matrix is also applicable for such operators. The only difference is that the eigenvalues do not need to be real. Let us recall how Rényi entropies (1.2.2) are computed for Gaussian states. The density matrix (3.2.17) can be brought into a diagonal form $\rho_\Omega = \mathcal{Z}^{-1}\exp\left(\frac{i}{2}\sum_n \omega_n d_{2n} d_{2n-1}\right)$, where ω_n is obtained from an orthogonal transformation of Ω. In terms of the eigenvalues of Γ, denoted by $\pm\nu_j$, we have $\rho_\Omega = \prod_n (1 + i\nu_n d_{2n} d_{2n-1})/2$, leading to

$$S_n(\rho_\Omega) = \frac{1}{1-n}\sum_{j=1}^{N} \ln\left[\left(\frac{1-\nu_j}{2}\right)^n + \left(\frac{1+\nu_j}{2}\right)^n\right]. \tag{3.2.20}$$

We consider a density matrix on a bipartite Hilbert space (3.2.3) where the covariance matrix takes a block matrix form as

$$\Gamma = \begin{pmatrix} \Gamma_{AA} & \Gamma_{AB} \\ \Gamma_{BA} & \Gamma_{BB} \end{pmatrix}. \tag{3.2.21}$$

Here, Γ_{AA} and Γ_{BB} denote the reduced covariance matrices of subsystems A and B, respectively; while $\Gamma_{AB} = \Gamma_{BA}^{\dagger}$ describes the correlations between them. We define the covariance matrix associated with a PT Gaussian state by

$$\Gamma_{\pm} = \begin{pmatrix} -\Gamma_{AA} & \pm i\Gamma_{AB} \\ \pm i\Gamma_{BA} & \Gamma_{BB} \end{pmatrix}, \tag{3.2.22}$$

where $[\Gamma_+]_{ij} = \frac{1}{2}\mathrm{Tr}(\rho^{T_A}[c_i, c_j])$ and $[\Gamma_-]_{ij} = \frac{1}{2}\mathrm{Tr}(\rho^{T_A\dagger}[c_i, c_j])$. We should note that Γ_+ and Γ_- have identical eigenvalues while they do not necessarily commute $[\Gamma_+, \Gamma_-] \neq 0$. In general, the eigenvalues of Γ_+ appear in quartets $(\pm\nu_k, \pm\nu_k^*)$ when $\mathrm{Re}[\nu_k] \neq 0$ and $\mathrm{Im}[\nu_k] \neq 0$ or doublet $\pm\nu_k$ when $\mathrm{Re}[\nu_k] = 0$ (i.e., pure imaginary) or $\mathrm{Im}[\nu_k] = 0$ (i.e., real) . $\pm$ is because of skew symmetry $\Gamma_{\pm}^T = -\Gamma_{\pm}$. In addition, the pseudo-Hermiticity of ρ^{T_A} (3.2.5) implies that

$$\Gamma_{\pm}^{\dagger} = U_1 \Gamma_{\pm} U_1, \tag{3.2.23}$$

where $U_1 = (-\mathbb{I}_A \oplus \mathbb{I}_B)$ is the matrix associated with the operator $(-1)^{F_A}$. This means that for every eigenvalue ν_k its complex conjugate ν_k^* is also an eigenvalue. As a result, the moments of PT can be written as

$$\mathcal{N}_n^{(\mathrm{ns})} = \sum_{j=1}^{N} \ln \left| \left(\frac{1-\nu_j}{2}\right)^n + \left(\frac{1+\nu_j}{2}\right)^n \right|. \tag{3.2.24}$$

Note that the sum is now over half of the eigenvalues (say in the upper half complex plane), due to the structure discussed above.

For $\rho^{\widetilde{T}_A}$ we use the multiplication rule for the Gaussian operators where the resulting Gaussian matrix is given by

$$e^{\widetilde{\Omega}_{\pm}} = \frac{\mathbb{I} + \Gamma_{\pm}}{\mathbb{I} - \Gamma_{\pm}} U_1, \tag{3.2.25}$$

which is manifestly Hermitian due to the identity (3.2.23). Using Eq. (3.2.17), the normalization factor is found to be $\mathcal{Z}_{\widetilde{T}_A} = \mathrm{Tr}(\rho^{\widetilde{T}_A}) = \mathrm{Tr}[\rho(-1)^{F_A}] = \sqrt{\det \Gamma_{AA}}$. From (3.2.19) we construct the covariance matrix $\widetilde{\Gamma}_{\pm} = \tanh(\widetilde{\Omega}/2)$ and compute the moments of $\rho^{\widetilde{T}_A}$ by

$$\mathcal{N}_n^{(\mathrm{r})} = \sum_{j=1}^{N} \ln \left| \left(\frac{1-\tilde{\nu}_j}{2}\right)^n + \left(\frac{1+\tilde{\nu}_j}{2}\right)^n \right| + n \ln \mathcal{Z}_{\widetilde{T}_A}, \tag{3.2.26}$$

where $\pm\tilde{\nu}_j$ are eigenvalues of $\widetilde{\Gamma}_{\pm}$ which are guaranteed to be real. Consequently, the LN (3.2.10) is given by

$$\mathcal{E} = \sum_{j=1}^{N} \ln \left[\left| \frac{1-\tilde{\nu}_j}{2} \right| + \left| \frac{1+\tilde{\nu}_j}{2} \right| \right] + \ln \mathcal{Z}_{\widetilde{T}_A}, \tag{3.2.27}$$

For particle-number conserving systems such as the lattice model in (3.1.1), the covariance matrix is simplified into the form $\Gamma = \sigma_2 \otimes \gamma$ where $\gamma = (\mathbb{I} - 2C)$ and $C_{ij} = \mathrm{Tr}(\rho f_i^{\dagger} f_j)$ is the correlation matrix and σ_2 is the second Pauli matrix acting on the even/odd indices of Majorana operators (c_{2j}, c_{2j-1}). In this

case, the transformed correlation matrix for ρ^{T_A} is given by

$$\gamma_{\pm} = \begin{pmatrix} -\gamma_{AA} & \pm i\gamma_{AB} \\ \pm i\gamma_{BA} & \gamma_{BB} \end{pmatrix}. \tag{3.2.28}$$

The eigenvalues can be divided to two categories: complex eigenvalues ν_k, $\mathrm{Im}[\nu_k] \neq 0$ and real eigenvalues u_k, $\mathrm{Im}[u_k] = 0$. The pseudo-Hermiticity property leads to the identity $\gamma_{\pm}^{\dagger} = U_1 \gamma_{\pm} U_1$ which implies that complex eigenvalues appear in pairs (ν_k, ν_k^*). Therefore, the many-body eigenvalues follow the form,

$$\lambda_{\sigma,\sigma'} = \prod_{\sigma_l} \frac{1+\sigma_l u_l}{2} \prod_{\sigma_k=\sigma_k'} \frac{1+|\nu_k|^2+2\sigma_k \mathrm{Re}[\nu_k]}{4} \prod_{\sigma_k=-\sigma_k'} \frac{1-|\nu_k|^2+2\sigma_k i\mathrm{Im}[\nu_k]}{4}, \tag{3.2.29}$$

where $\sigma = \{\sigma_k = \pm\}$ is a string of signs. Clearly, the many-body eigenvalues appear in two categories as well: complex conjugate pairs (λ_j, λ_j^*) and real eigenvalues which are not necessarily degenerate.

We can also derive a simple expression for the correlation matrix $\widetilde{C} = (\mathbb{I} - \widetilde{\gamma})/2$ associated with $\rho^{\widetilde{T}_A}$,

$$\widetilde{\gamma} = \begin{pmatrix} -\gamma_{AA}^{-1}(\mathbb{I}_A + \gamma_{AB}\gamma_{BA}) & i\gamma_{AA}^{-1}\gamma_{AB}\gamma_{BB} \\ i\gamma_{BA} & \gamma_{BB} \end{pmatrix}. \tag{3.2.30}$$

3.3 Spacetime picture for the moments of partial transpose

In the following two sections, we compute the moments of the PT density matrix and ultimately the LN. First, we develop a general method using the replica approach [94, 145, 299] and provide an equivalent spacetime picture of the Rényi negativity.

Before we proceed, let us briefly review the replica approach to find the entanglement entropy. Next, we make connections to our construction of PT. A generic density matrix can be represented in the fermionic coherent state as

$$\rho = \int d\alpha d\bar{\alpha}\, d\beta d\bar{\beta}\, \rho(\bar{\alpha}, \beta)\, |\alpha\rangle \langle\bar{\beta}|\, e^{-\bar{\alpha}\alpha - \bar{\beta}\beta}, \tag{3.3.1}$$

where α, $\bar{\alpha}$, β and $\bar{\beta}$ are independent Grassmann variables and we omit the real-space (and possibly other) indices for simplicity. The trace formula then reads

$$Z_{S_n} \equiv \mathrm{Tr}[\rho^n] = \int \prod_{i=1}^{n} d\psi_i d\bar{\psi}_i \prod_{i=1}^{n} [\rho(\bar{\psi}_i, \psi_i)]\, e^{\sum_{i,j} \bar{\psi}_i T_{ij} \psi_j}, \tag{3.3.2}$$

where the subscripts in ψ_i and $\bar{\psi}_i$ denote the replica indices and T is called the twist matrix,

$$T = \begin{pmatrix} 0 & -1 & 0 & \dots \\ 0 & 0 & -1 & 0 \\ \vdots & \vdots & \ddots & -1 \\ 1 & 0 & \cdots & 0 \end{pmatrix}. \tag{3.3.3}$$

The above expression can be viewed as a partition function on a n-sheet spacetime manifold where the n flavors (replicas) ψ_i are glued in order along the cuts. Alternatively, one can consider a multi-component field $\Psi = (\psi_1, \cdots, \psi_n)^T$ on a single-sheet spacetime. This way when we traverse a close path through the interval the field gets transformed as $\Psi \mapsto T\Psi$. Hence, each interval can be represented by two branch points $\mathcal{T}_n$ and $\mathcal{T}_n^{-1}$ (an equivalent way to denote $\bar{\mathcal{T}}_n$) –the so-called twist fields– and the REE of one interval

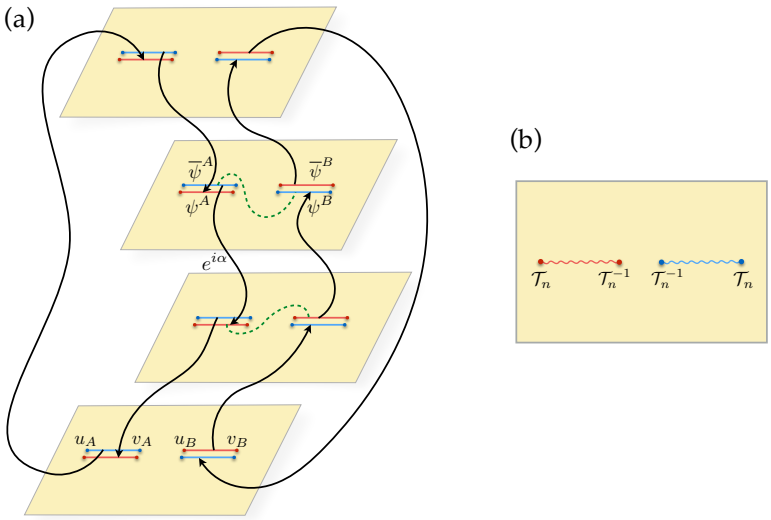

FIGURE 3.1: (a) Spacetime manifold associated with $Z_{\mathcal{N}_n}(\alpha)$, Eq. (3.3.11), for $n = 4$. The operator $e^{i\alpha F_A}$ twists the boundary condition of the cycles between two successive sheets, shown as the green path with dashed lines. (b) Equivalent picture in terms of twist field where we define a multi-component field on a single spacetime sheet.

can be written as a two-point correlator [316],

$$Z_{S_n} = \langle \mathcal{T}_n(u)\mathcal{T}_n^{-1}(v)\rangle\,, \tag{3.3.4}$$

where u and v denote the real space coordinates of the two ends of the interval defining the subsystem A.

Let us now derive analogous relations for the moments of PT density matrix. Using the definition of the PT in the coherent state basis [314]

$$(|\psi_A,\psi_B\rangle\langle\bar{\psi}_A,\bar{\psi}_B|)^{T_A} = |i\bar{\psi}_A,\psi_B\rangle\langle i\psi_A,\bar{\psi}_B|\,, \tag{3.3.5}$$

we write the general expression for the moments of ρ^{T_A} as

$$Z^{(\mathrm{ns})}_{\mathcal{N}_n} = \mathrm{Tr}[(\rho^{T_A})^n] = \int \prod_{i=1}^{n} d\psi_i d\bar{\psi}_i \prod_{i=1}^{n} [\rho(\bar{\psi}_i,\psi_i)]\, e^{\sum_{i,j}\bar{\psi}_{iA}[T^{-1}]_{ij}\psi_{jA}} e^{\sum_{i,j}\bar{\psi}_{iB}T_{ij}\psi_{jB}}, \tag{3.3.6}$$

where ψ_{js} and $\bar{\psi}_{js}$ refer to the field defined within the $s = A, B$ interval of j-th replica. Here, we are dealing with two intervals where the twist matrices are T and T^{-1} as shown in Fig. 3.1(a). Therefore, it can be written as a four-point correlator (3.1(b))

$$Z^{(\mathrm{ns})}_{\mathcal{N}_n} = \langle \mathcal{T}_n^{-1}(u_A)\mathcal{T}_n(v_A)\mathcal{T}_n(u_B)\mathcal{T}_n^{-1}(v_B)\rangle\,. \tag{3.3.7}$$

Note that the order of twist fields are reversed for the first interval.

From the coherent state representation, we can also write the moments of $\rho^{\widetilde{T}_A}$

$$Z^{(\mathrm{r})}_{\mathcal{N}_n} = \mathrm{Tr}[(\rho^{\widetilde{T}_A})^n] = \int \prod_{i=1}^{n} d\psi_i d\bar{\psi}_i \prod_{i=1}^{n} [\rho(\bar{\psi}_i,\psi_i)]\, e^{\sum_{i,j}\bar{\psi}^A_i\widetilde{T}_{ij}\psi^A_j} e^{\sum_{i,j}\bar{\psi}^B_i T_{ij}\psi^B_j}. \tag{3.3.8}$$

The twist matrix for interval A is modified to be

$$\widetilde{T} = \begin{pmatrix} 0 & \cdots & 0 & -1 \\ 1 & \ddots & \vdots & \vdots \\ 0 & 1 & 0 & 0 \\ \cdots & 0 & 1 & 0 \end{pmatrix}, \tag{3.3.9}$$

which can be viewed as a gauge transformed twist matrix T^{-1}. Analogously, Eq. (3.3.8) can be written in terms of a four-point correlator

$$Z^{(\mathrm{r})}_{\mathcal{N}_n} = \langle \widetilde{\mathcal{T}}_n^{-1}(u_A)\widetilde{\mathcal{T}}_n(v_A)\mathcal{T}_n(u_B)\mathcal{T}_n^{-1}(v_B)\rangle\,, \tag{3.3.10}$$

where $\widetilde{\mathcal{T}}_n$ and $\widetilde{\mathcal{T}}_n^{-1}$ are twist fields associated with $\widetilde{T}$.

For fermions with a global $U(1)$ gauge symmetry (i.e., particle-number conserving systems) there is a freedom to twist boundary condition along the fundamental cycles (e.g. the dashed-line path in Fig. 3.1(a)) of the spacetime manifold by a $U(1)$ phase (or holonomy). The boundary conditions are independent and in principle can be different for different pairs of sheets. If we assume a replica symmetry (i.e. uniform boundary conditions) $\psi_i \mapsto e^{i\alpha}\psi_i$, the expression for the PT moments in the operator formalism is given by

$$Z_{\mathcal{N}_n}(\alpha) = \mathrm{Tr}[(\rho^{T_A}e^{i\alpha F_A})^n]. \tag{3.3.11}$$

Let us mention that some related quantities such as $\mathrm{Tr}[(\rho\ e^{i\alpha F})^n]$ were previously introduced and dubbed charged entanglement entropies [317]. They were further used to determine symmetry resolved entanglement entropies which is the contribution from the density matrix to the entanglement entropies when projected onto a given particle-number sector [318, 319]: we will come back on this topic in Chapter 7.

From (3.3.11), we get a family of RN parametrized by α. However, for a generic fermionic system (including superconductors), the $U(1)$ symmetry is reduced to Z_2 fermion-parity symmetry. Hence, the two quantities of general interest would be

$$Z_{\mathcal{N}_n}(\alpha=\pi) = Z^{(\mathrm{r})}_{\mathcal{N}_n} = \mathrm{Tr}[(\rho^{\widetilde{T}_A})^n], \tag{3.3.12}$$

$$Z_{\mathcal{N}_n}(\alpha=0) = Z^{(\mathrm{ns})}_{\mathcal{N}_n} = \mathrm{Tr}[(\rho^{T_A})^n]. \tag{3.3.13}$$

We should reemphasize that either quantities are described by a partition function on the same spacetime manifold (Fig. 3.1) as in the case of bosonic systems [94], while they differ in the boundary conditions for fundamental cycles of the manifold. In other words, $Z^{(\mathrm{ns})}_{\mathcal{N}_n}$ and $Z^{(\mathrm{r})}_{\mathcal{N}_n}$ correspond to anti-periodic (i.e., Neveu-Schwarz in CFT language) and periodic (Ramond) boundary conditions, respectively. This can be readily seen by comparing T^{-1} and $\widetilde{T}$. These boundary conditions correspond to two replica-symmetric spin structures for the spacetime manifold. This is different from bosonic PT of fermionic systems [298, 299], where RN is given by sum over all possible spin structures. Essentially, the RNs associated with the two types of fermionic PT are identical to two terms in the expansion of bosonic PT in Ref. [298].

In what follows, we compute the two RNs for two partitioning schemes:

- Two **adjacent intervals** which is obtained by fusing the fields in v_A and u_B. Hence, the RNs are given in terms of three-point correlators

$$Z^{(\mathrm{ns})}_{\mathcal{N}_n} = \langle \mathcal{T}_n^{-1}(u_A)\mathcal{T}_n^{2}(v_A)\mathcal{T}_n^{-1}(v_B)\rangle\,, \tag{3.3.14}$$

  and

$$Z^{(\mathrm{r})}_{\mathcal{N}_n} = \langle \widetilde{\mathcal{T}}_n^{-1}(u_A)\mathcal{Q}_n^{2}(v_A)\mathcal{T}_n^{-1}(v_B)\rangle\,, \tag{3.3.15}$$

where we introduce the fusion of unlike twist fields,

$$\mathcal{Q}_n^2 \equiv \mathcal{T}_n \widetilde{\mathcal{T}}_n. \tag{3.3.16}$$

- **Bipartite geometry** where the two intervals together form the entire system which is in the ground state. This time the RNs are obtained by further fusing the fields in u_A and v_B and the final expressions are therefore given by the two-point correlators

$$Z_{\mathcal{N}_n}^{(\mathrm{ns})} = \langle \mathcal{T}_n^{-2}(u_A)\mathcal{T}_n^2(v_A)\rangle\,, \tag{3.3.17}$$

and

$$Z_{\mathcal{N}_n}^{(\mathrm{r})} = \langle \mathcal{Q}_n^{-2}(u_A)\mathcal{Q}_n^2(v_A)\rangle\,. \tag{3.3.18}$$

3.4 The spectrum of partial transpose

As mentioned, the first step to compute the tail distribution of the eigenvalues of PT density matrix is to find its moments. To this end, it is more convenient to work in a new basis where the twist matrices are diagonal and decompose the partition function of multi-component field Ψ to n decoupled partition functions. For REE, this leads to

$$Z_{S_n} = \prod_{k=-(n-1)/2}^{(n-1)/2} Z_{k,n}, \quad \text{where} \quad Z_{k,n} = \langle \mathcal{T}_{k,n}(u)\mathcal{T}_{k,n}^{-1}(v)\rangle\,. \tag{3.4.1}$$

The monodromy condition for the field around $\mathcal{T}_{k,n}$ and $\mathcal{T}_{k,n}^{-1}$ are given by $\psi_k \mapsto e^{\pm i2\pi k/n}\psi_k$. The calculation of the above partition function can be further simplified in terms of correlators of vertex operators using the bosonization technique in (1+1)d. For instance, in the case of REE, (3.4.1) can be evaluated by [316]

$$Z_{k,n} = \langle V_k(u)V_{-k}(v)\rangle\,, \tag{3.4.2}$$

where $V_k(x) = e^{-i\frac{k}{n}\phi(x)}$ is the vertex operator and the expectation values is understood on the ground state of the scalar-field theory $\mathcal{L}_\phi = \frac{1}{8\pi}\partial_\mu\phi\partial^\mu\phi$. The correlation function of the vertex operators is found by

$$\langle V_{e_1}(z_1)\cdots V_{e_N}(z_N)\rangle \propto \prod_{i<j} |z_j - z_i|^{2e_ie_j} \tag{3.4.3}$$

where $V_e(z) = e^{ie\phi(z)}$ is the vertex operator and $\sum_j e_j = 0$. Hence, we can write for the partition function

$$Z_{S_n} \propto |u-v|^{-2\sum_k \frac{k^2}{n^2}}\,, \tag{3.4.4}$$

leading to the familiar result (1.4.12) for the REE of 1d free fermions. In what follows, we apply the bosonization technique to evaluate $Z_{\mathcal{N}_n}^{(\mathrm{ns})}$ and $Z_{\mathcal{N}_n}^{(\mathrm{r})}$ similar to what we did for the REE. The scaling behavior of RNs in the lattice model is compared with the analytically predicted values of slopes (derived below) for various exponents $n = 1, \cdots, 7$ in Fig. 3.2, where the agreement is evident. We should note that the slope does not depend on the chemical potential μ in the Hamiltonian (3.1.1).

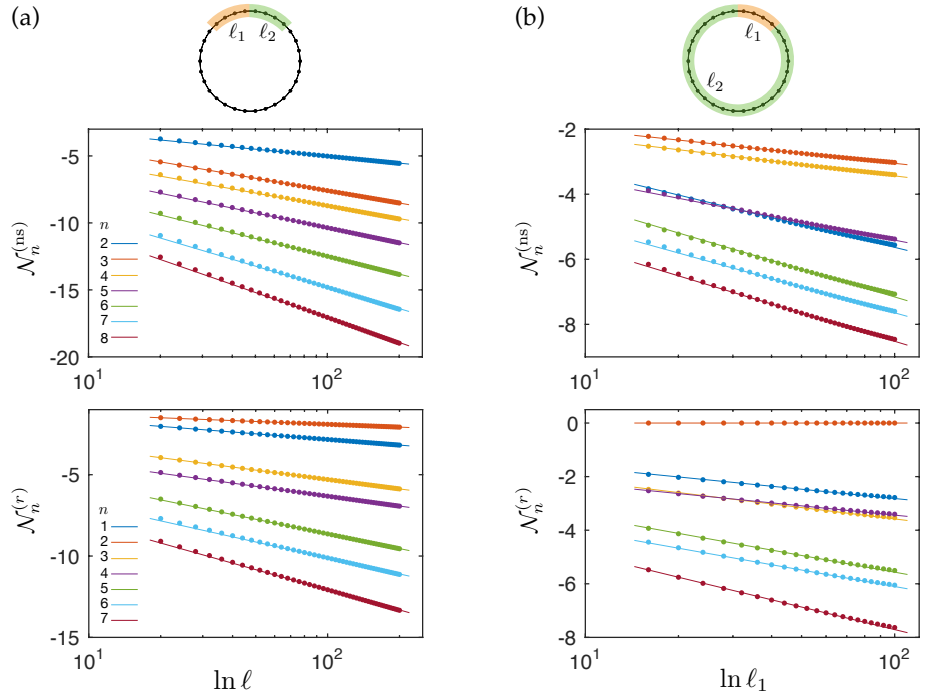

FIGURE 3.2: Comparison of numerical (dots) and analytical (solid lines) results for the scaling behavior of the moments of partial transpose (3.3.6) in the up row and (3.3.8) in the down row for two subsystem geometries: (a) two adjacent intervals, and (b) bipartite geometry. In (a), intervals have equal lengths $\ell_1 = \ell_2 = \ell$ and $20 \leq \ell \leq 200$ on an infinite chain. In (b), the total system size is $L = 400$ and $20 \leq \ell \leq 100$. Different colors correspond to different moments n.

3.4.1 Spectrum of ρ^{T_A}

In the case of RN (3.3.6), we can carry out a similar *momentum* decomposition as

$$Z_{\mathcal{N}_n}^{(\mathrm{ns})} = \prod_{k=-(n-1)/2}^{(n-1)/2} Z_{k,n}^{(\mathrm{ns})}, \tag{3.4.5}$$

where

$$Z_{k,n}^{(\mathrm{ns})} = \langle \mathcal{T}_{k,n}^{-1}(u_A)\mathcal{T}_{k,n}(v_A)\mathcal{T}_{k,n}(u_B)\mathcal{T}_{k,n}^{-1}(v_B)\rangle \tag{3.4.6}$$

is the partition function in the presence of four twist fields. We then use (3.4.3) to compute the above correlator for various subsystem geometries. We should note that the following results only include the leading order term in the scaling limit, $\ell_1, \ell_2 \to \infty$, where ℓ_1 and ℓ_2 are the length of A and B subsystems, respectively.

Adjacent intervals

Here, we consider adjacent intervals (c.f. upper panel of Fig. 3.2(a)). The final result is given by

$$Z_{k,n}^{(\mathrm{ns})} = \begin{cases} \ell_1^{-4\frac{k^2}{n^2}} \ell_2^{-4\frac{k^2}{n^2}} (\ell_1+\ell_2)^{2\frac{k^2}{n^2}} & |k/n| < 1/3 \\ f(\ell_1,\ell_2;|k/n|)\cdot(\ell_1+\ell_2)^{2|\frac{k}{n}|(|\frac{k}{n}|-1)} & |k/n| > 1/3 \end{cases} \tag{3.4.7}$$

where $f(x,y;q) = \frac{1}{2}\left[x^{2(q-1)(-2q+1)}y^{2q(-2q+1)} + x \leftrightarrow y\right]$. Notice that the exponents change discontinuously as a function of k. This can be understood as a consequence of the 2π ambiguity of the $U(1)$ phase

that the Fermi field acquires as it goes around the twist fields. Essentially, we need to find the dominant term with the lowest scaling dimension in the mode expansion (see Appendix 3.A for more details). Adding up the terms in the $Z^{(\mathrm{ns})}_{\mathcal{N}_n}$ expansion, the final expression in the limit of two equal-length intervals $\ell_1 = \ell_2$ is simplified into $\mathcal{N}^{(\mathrm{ns})}_n = c_n \ln \ell + \cdots$ where

$$c_n = \begin{cases} -\frac{1}{3}\left(n - \frac{3}{2n}\right) & n = 6N, \\ -\frac{1}{3}\left(n - \frac{1}{n}\right) & n = 6N+1, 6N+5, \\ -\frac{1}{3}\left(n + \frac{1}{2n}\right) & n = 6N+2, 6N+4, \\ -\frac{1}{3}\left(n + \frac{3}{n}\right) & n = 6N+3, \end{cases} \tag{3.4.8}$$

where N is a non-negative integer. It is worth recalling that for the bosonic systems, the spectrum of PT contains only positive and negative eigenvalues. As a result, we see even/odd effect for the moments. Here, however, the moments $Z^{(\mathrm{ns})}_n$ have a cyclic behavior with a periodicity of six, which signals the possibility for the eigenvalues to appear with a multiple of $2\pi/6$ complex phase. As we will see below, this is indeed the case in our numerical calculations. We should also note that the above result can be obtained from the adjacent limit $v_A \to u_B$ of two disjoint intervals (3.4.6) as explained in Section 3.5.

We now discuss the spectrum of ρ^{T_A} for two adjacent intervals. It is instructive to look at the many-body eigenvalues as obtained in (3.2.29) from the single-body eigenvalues of the covariance matrix (3.2.28). From the numerical observation that $\mathrm{Im}(\nu_k) \neq 0$, we may drop the u_l factor in (3.2.29). Hence, the many-body spectrum simplifies to

$$\lambda_{\sigma,\sigma'} = \prod_{\sigma_k = \sigma'_k} \omega_{R\sigma_k} \prod_{\sigma_k = -\sigma'_k} \omega_{I\sigma'_k}, \tag{3.4.9}$$

where

$$\omega_{R\sigma_k} = \frac{1 + |\nu_k|^2 + 2\sigma_k \mathrm{Re}[\nu_k]}{4}, \tag{3.4.10a}$$

$$\omega_{I\sigma_k} = \frac{1 - |\nu_k|^2 + 2\sigma_k i\mathrm{Im}[\nu_k]}{4}, \tag{3.4.10b}$$

and $\sigma_k = \pm$ is a sign factor. We should note that the complex and negative real eigenvalues come from product of $\omega_{I\sigma_k}$. This fact immediately implies that for every complex eigenvalue λ_j, λ_j^* is also in the spectrum, since $\omega_{I-\sigma_k} = \omega^*_{I\sigma_k}$. Moreover, the negative eigenvalues are at least two-fold degenerate.

In the case of free fermions, we numerically observe that $\omega_{I\pm} \to |\omega_{I\pm}| e^{\pm i \frac{2\pi}{6}}$ as we go towards the thermodynamic limit $N_A = N_B \to \infty$. As a result, the many-body eigenvalues are divided into two groups: first, real positive eigenvalues, and second, the complex or negative eigenvalues which take a regular form $\lambda_j \approx |\lambda_j| e^{\pm i \frac{\pi}{3} s_j}$ where $s_j = 1, 2, 3$. Figure 3.3(a) shows the numerical spectrum of ρ^{T_A}. To explicitly demonstrate the quantization of the complex phase of eigenvalues, we plot a histogram of the complex phase in Fig. 3.3(b) where sharp peaks at integer multiples of $\pi/3$ are evident. Due to this special structure of the eigenvalues, the moments of ρ^{T_A} can be written as

$$\begin{aligned} Z^{(\mathrm{ns})}_{\mathcal{N}_n} &= \sum_k |\lambda_k|^n e^{\frac{i\pi n s_k}{3}} \\ &= \sum_j \lambda_{0j}^n + 2\cos\left(\frac{\pi n}{3}\right) \sum_j |\lambda_{1j}|^n + 2\cos\left(\frac{2\pi n}{3}\right) \sum_j |\lambda_{2j}|^n + \cos(n\pi) \sum_j |\lambda_{3j}|^n, \end{aligned} \tag{3.4.11}$$

where $\{\lambda_{\alpha j}\}, \alpha = 0, 1, 2, 3$ denote the eigenvalues along $\angle\lambda = \alpha\pi/3$ branches. Note that $\{\lambda_{0j}\}, \{\lambda_{3j}\}$, i.e., positive and negative real eigenvalues, are treated separately, while $\{\lambda_{1j}\}$ and $\{\lambda_{2j}\}$ represent the eigenvalues for both $\angle\lambda = \pm\pi/3$ and $\angle\lambda = \pm 2\pi/3$ branches. A consequence of Eq. (3.4.11) is that there are four linearly independent combinations of the eigenvalues in $Z^{(\mathrm{ns})}_{\mathcal{N}_n}$. This exactly matches the four

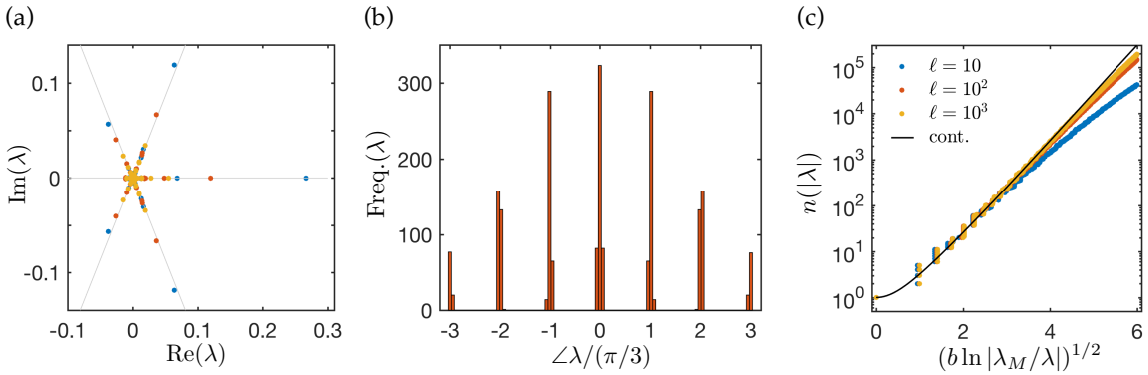

FIGURE 3.3: Spectral properties of ρ^{T_A} for two adjacent intervals with length ℓ on an infinite chain. (a) Many-body eigenvalues are plotted over the complex plane. The solid gray lines are guides for the eyes and a hint for the phase quantization. (b) Histogram of complex phases of eigenvalues which indicates nearly quantized phases in units of $\pi/3$. (c) Tail distribution function of modulus of eigenvalues. The solid line is the analytical result (3.4.12b). To compute the many-body spectrum, we truncate the single-particle spectrum with the first 28 largest (in euclidean distance from ± 1 on the complex plane) eigenvalues.

possible scaling behaviors of $Z^{(\mathrm{ns})}_{\mathcal{N}_n}$ from our continuum field theory calculations (3.4.8).

As a first characterization of the negativity spectrum, we compute the distribution of modulus of eigenvalues. To this end, it is sufficient to consider $Z^{(\mathrm{ns})}_{\mathcal{N}_n}$ for multiples of $n = 6N$ which is $Z^{(\mathrm{ns})}_{\mathcal{N}_n} = \sum_k |\lambda_k|^n$. Substituting (3.4.8) for b and a in (3.2.13) and (3.2.14), we get

$$P(|\lambda|) = \delta(\lambda_M - |\lambda|) + \sqrt{\frac{3}{2}}\frac{b\theta(\lambda_M - |\lambda|)}{|\lambda|\xi} I_1(\sqrt{6}\xi), \tag{3.4.12a}$$

$$n(|\lambda|) = I_0(\sqrt{6}\xi), \tag{3.4.12b}$$

where

$$\xi = \sqrt{b \ln |\lambda_M/\lambda|}, \tag{3.4.13}$$

and λ_M is the largest eigenvalue given by

$$b = -\ln \lambda_M = \lim_{n\to\infty} \frac{1}{n} \ln \mathrm{Tr}(\rho^{T_A})^n = \frac{1}{3}\ln \ell. \tag{3.4.14}$$

Figure 3.3(c) shows a good agreement between the analytical formula (3.4.12b) and the numerically obtained spectra for various subsystem sizes. We should note that there is no fitting parameter in (3.4.12b) and we only plug in λ_M from numerics.

We can further derive the distribution of eigenvalues along different branches in Fig. 3.3(a). The idea is to analytically continue $Z^{(\mathrm{ns})}_{\mathcal{N}_n}$ with $n = 6N + m$ to arbitrary n and solve the resulting four linearly independent equations generated by (3.4.11) to obtain the moments $\sum_j |\lambda_{s_j}|^n$ for each $s = 0, \cdots, 3$. This calculation relies on the assumption that $\lim_{n\to\infty} \frac{c_n}{n}$ does not depend on m, which is indeed the case in (3.4.8). Hence, we arrive at

$$P_\alpha(\lambda) = \delta(\lambda_M - \lambda)\delta_{\alpha 0} + \frac{b\theta(\lambda_M - |\lambda|)}{6|\lambda|\xi} \sum_{\beta=1}^{2} [M_{\alpha\beta} a_\beta I_1(2a_\beta\xi) - \widetilde{M}_{\alpha\beta}\tilde{a}_\beta J_1(2\tilde{a}_\beta\xi)], \tag{3.4.15a}$$

$$n_\alpha(\lambda) = \frac{1}{6}\left[\sum_{\beta=1}^{2} M_{\alpha\beta} I_0(2a_\beta\xi) + \widetilde{M}_{\alpha\beta} J_0(2\tilde{a}_\beta\xi)\right], \tag{3.4.15b}$$

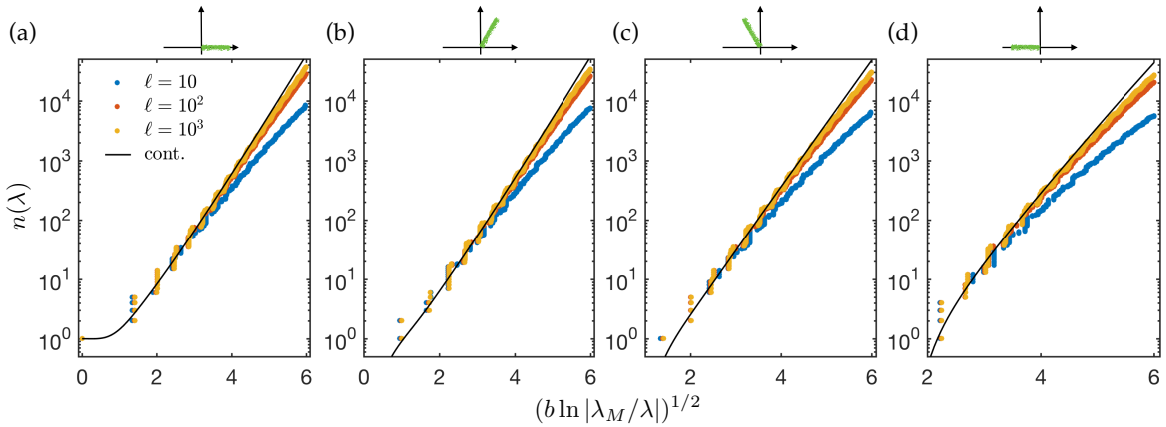

FIGURE 3.4: Spectrum of eigenvalues of ρ^{T_A} with a certain complex phase (c.f. Fig. 3.3(a)) for two equal intervals on an infinite chain. Solid lines are the prediction in Eq. (3.4.15b). Dots are numerics, with different colors corresponding to different subsystem sizes. We use the same numerical procedure as in Fig. 3.3 to obtain few thousand largest (in modulus) many-body eigenvalues from a truncated set of single particle eigenvalues.

where $P_\alpha(\lambda)$ and $n_\alpha(\lambda)$, $\alpha = 0, \cdots, 3$ describe the distribution of eigenvalues along the $\angle\lambda = \alpha\pi/3$ branch. Here, M and $\widetilde{M}$ encapsulate the coefficients

$$(M|\widetilde{M}) = \left(\begin{array}{cc|cc} 1 & 2 & 2 & 1 \\ 1 & 1 & -1 & -1 \\ 1 & -1 & -1 & 1 \\ 1 & -2 & 2 & -1 \end{array}\right), \tag{3.4.16}$$

$(a_1, a_2, \tilde{a}_1, \tilde{a}_2) = (\sqrt{\frac{3}{2}}, 1, \frac{1}{\sqrt{2}}, \sqrt{3})$, and ξ and b are defined in Eqs. (3.4.13) and (3.4.14), respectively. Several comments regarding the phase-resolved distributions (3.4.15a) and (3.4.15b) are in order. The largest eigenvalue $\lambda_M > 0$ is located on the real axis and hence only appears in $P_0(\lambda)$. The distribution of modulus is found by $(P_0 + 2P_1 + 2P_2 + P_3)$ which reproduces (3.4.12a). It is easy to check that the distribution is normalized and consistent with the identity $\mathrm{Tr}\rho^{T_A} = 1$,

$$\begin{aligned} \int \lambda P(\lambda) d\lambda &= \int \lambda [P_0(\lambda) + P_1(\lambda) - P_2(\lambda) - P_3(\lambda)] d\lambda \\ &= \int_0^{\lambda_M} \lambda [\delta(\lambda_M - \lambda) + \frac{a_2}{\lambda \xi_2} I_1(2\xi_2)] d\lambda = 1. \end{aligned} \tag{3.4.17}$$

It is also possible to study the scaling of the maximum eigenvalue (in modulus) $|\lambda_M|$ along each branch. For the bosonic negativity, there are only two branches (positive and negative real axis) and it was found that the scaling of the maxima is the same in the thermodynamic limit [57]. In our case, for a given branch (labeled by α) the maximum $|\lambda_M^\alpha|$ (with $|\lambda_M^0| \equiv \lambda_M$) can be extracted as

$$\ln|\lambda_M^{(\alpha)}| = \lim_{n\to\infty} \frac{1}{n} \ln \sum_j |\lambda_j^{(\alpha)}|^n = -b \tag{3.4.18}$$

where the result is independent of α. This again implies the same scaling along each branch, up to a possible unknown constant due to non-universal coefficient that we are dropping in the above formulas (see Eq. (3.2.12)).

We compare the analytical results with the numerical simulations for each branch in Fig. 3.4. As expected, the numerical spectra reach the continuum field theory calculations as we make the system larger. We should point out that in contrast with the bosonic negativity spectrum and the entanglement spectrum

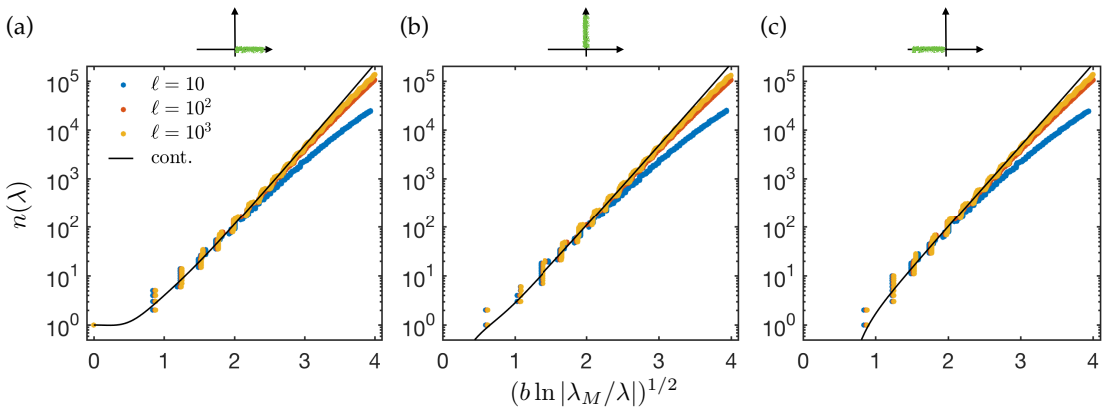

FIGURE 3.5: Spectrum of modulus of eigenvalues of ρ^{T_A} for bipartite geometry along the real and imaginary axes. The total system size is $L = 2\ell$ for each ℓ. Solid lines are the prediction in Eq. (3.4.24b). Dots are numerics, with different colors corresponding to different subsystem sizes. A numerical procedure similar to that of Fig. 3.3 is used to obtain few thousand largest (in modulus) many-body eigenvalues from a truncated set of single particle eigenvalues.

which are given solely in terms of $I_\alpha(x)$, the modified Bessel function of the first kind, here the fermionic negativity spectrum contains the Bessel functions $J_\alpha(x)$ as well. Recall that unlike $I_\alpha(x)$ which is strictly positive for $x > 0$, $J_\alpha(x)$ does oscillate between positive and negative values. Nevertheless, there is no issue in $P_\alpha(\lambda)$ which has to be non-negative, as the linear combinations of I_α and J_α in (3.4.15b) are such that they are strictly positive over their range of applicability within each branch.

Bipartite geometry

Here, we consider two intervals which make up the entire system as shown in the upper panel of Fig. 3.2(b). In this case, the branch points are identified pairwise as $u_A = v_B$ and $v_A = u_B$, where $\ell_1 = v_A - u_A$. The partition functions in momentum space are found to be

$$Z^{(\mathrm{ns})}_{k,n} = \begin{cases} \ell_1^{-8\frac{k^2}{n^2}} & |k/n| < 1/4, \\ \ell_1^{-2(2|\frac{k}{n}|-1)^2} & |k/n| > 1/4. \end{cases} \tag{3.4.19}$$

Similar to the adjacent intervals, the discontinuity in the k-dependence comes from the 2π ambiguity of the $U(1)$ monodromy (Appendix 3.A). As a result, we have $\mathcal{N}^{(\mathrm{ns})}_n = c_n \ln(\ell_1) + \cdots$ where

$$c_n = \begin{cases} -\frac{1}{6}\left(n - \frac{4}{n}\right) & n = 4N, \\ -\frac{1}{6}\left(n - \frac{1}{n}\right) & n = 2N+1, \\ -\frac{1}{6}\left(n + \frac{8}{n}\right) & n = 4N+2. \end{cases} \tag{3.4.20}$$

A benchmark of these expressions against the scaling of RN in numerical simulations is shown in Fig. 3.5(c). Because of the cyclic analyticity of the $\mathcal{N}^{(\mathrm{ns})}_n$ modulo four, we expect to have the many-body eigenvalues along the real and imaginary axes. In other words, the complex phase of eigenvalues are multiples of $2\pi/4$.

We now derive the complex phase structure of many-body eigenvalues from the single particle spectrum. In the current case, the density matrix is pure leading to the identity $\gamma^2 = \mathbb{I}$ for the covariance matrix. This property implies that the spectrum of the transformed covariance matrix (3.2.28) can be fully determined by the covariance matrix associated to the subsystem A, i.e., γ_{AA} in Eq. (3.2.28). Hence, the single particle eigenvalues are given by

$$\nu_k = \mu_k + i\sqrt{1-\mu_k^2}, \tag{3.4.21}$$

and its Hermitian conjugate for v_k^*, where μ_k's ($k = 0, \cdots, N_A$) denote the eigenvalues of γ_{AA} [295]. Using (3.2.29), the many-body eigenvalues can be written as

$$\lambda_{\sigma,\sigma'} = \prod_{\sigma_k=\sigma'_k} \frac{1+\sigma_k\mu_k}{2} \prod_{\sigma_k=-\sigma'_k} \frac{\sigma_k i\sqrt{1-\mu_k^2}}{2}. \tag{3.4.22}$$

This decomposition has two types of factors: real positive and pure imaginary. Therefore, the many-body eigenvalues manifestly lie on the real and imaginary axes. Moreover, the many-body spectrum contains pairs of pure imaginary eigenvalues $\pm i\lambda_j$. The real negative eigenvalues are also two-fold degenerate since they are obtained from the product of even number of pure imaginary factors. In contrast, the real positive eigenvalues are not necessarily degenerate. As a result, the moments of ρ^{T_A} take now the following form

$$Z_{\mathcal{N}_n}^{(\mathrm{ns})} = \sum_j \lambda_{0j}^n + 2\cos\left(\frac{\pi n}{2}\right) \sum_j |\lambda_{1j}|^n + \cos(n\pi) \sum_j |\lambda_{2j}|^n, \tag{3.4.23}$$

where $\{\lambda_{\alpha j}\}, \alpha = 0,1,2$ denote the eigenvalues along $\angle\lambda = \alpha\pi/2$. This expression in turn implies that there are three types of combinations of different branches for all n, which is again consistent with (3.4.20). By analytically continuing the three cases, we derive the moment $\sum_j |\lambda_{\alpha j}|^n$ for each branch. The resulting distributions are found to be

$$P_\alpha(\lambda) = \delta(\lambda_M - \lambda)\delta_{\alpha 0} + \frac{b\theta(\lambda_M - |\lambda|)}{4|\lambda|\xi} \left[\sum_{\beta=1}^{2} M_{\alpha\beta} a_\beta I_1(2a_\beta\xi) - \widetilde{M}_\alpha \tilde{a} J_1(2\tilde{a}\xi)\right], \tag{3.4.24a}$$

$$n_\alpha(\lambda) = \frac{1}{4}\left[\sum_{\beta=1}^{2} M_{\alpha\beta} I_0(2a_\beta\xi) + \widetilde{M}_\alpha J_0(2\tilde{a}\xi)\right], \tag{3.4.24b}$$

where M and $\widetilde{M}$ encode the coefficients

$$(M|\widetilde{M}) = \left(\begin{array}{cc|c} 1 & 2 & 1 \\ 1 & 0 & -1 \\ 1 & -2 & 1 \end{array}\right), \tag{3.4.25}$$

$(a_1, a_2, \tilde{a}) = (2, 1, 2\sqrt{2})$ and ξ is defined in (3.4.13) with $b = -\ln\lambda_M = \frac{1}{6}\ln\ell$. As shown in Fig. 3.5, the above formulas are in decent agreement with numerical results.

Also in this case the maximum (in modulus) $|\lambda_M^\alpha|$ along the different branches can be evaluated through Eq. (3.4.18), giving (up to an unknown non-universal constant) $\ln|\lambda_M^\alpha| = -b$ independent of α. Finally, also for the bipartite geometry, a consistency check is obtained from $\mathrm{Tr}\rho^{T_A} = 1$, which simply follows from a calculation analogous to Eq. (3.4.17).

3.4.2 Spectrum of $\rho^{\widetilde{T}_A}$

Again, the first step to find the moments is the momentum decomposition of (3.3.8), yielding

$$Z_{\mathcal{N}_n}^{(\mathrm{r})} = \prod_{k=-(n-1)/2}^{(n-1)/2} Z_{k,n}^{(\mathrm{r})}, \tag{3.4.26}$$

where the partition function

$$Z_{k,n}^{(\mathrm{r})} = \langle \widetilde{\mathcal{T}}_{k,n}^{-1}(u_A)\widetilde{\mathcal{T}}_{k,n}(v_A)\mathcal{T}_{k,n}(u_B)\mathcal{T}_{k,n}^{-1}(v_B)\rangle\,. \tag{3.4.27}$$

is subject to modified monodromy conditions for the $\widetilde{\mathcal{T}}_{k,n}$ and $\widetilde{\mathcal{T}}_{k,n}^{-1}$, which are $\psi_k \mapsto e^{\pm i(2\pi k/n-\pi)}\psi_k$.

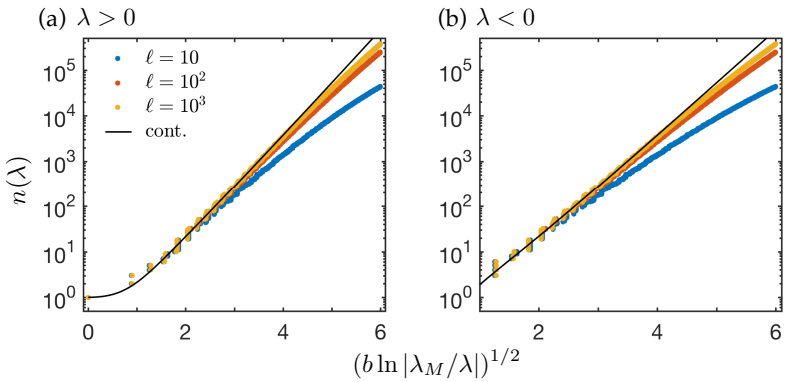

FIGURE 3.6: Tail distribution function for the spectrum of $\rho^{\widetilde{T}_A}$ of two equal adjacent intervals on an infinite chain. Solid lines are the analytical distributions from Eq. (3.4.34b). Dots are numerics, with different colors corresponding to different subsystem sizes. We use the same numerical procedure as in Fig. 3.3 to obtain few thousand largest (in modulus) many-body eigenvalues from a truncated set of single particle eigenvalues.

Adjacent intervals

In this case, we find that

$$Z^{(\mathrm{r})}_{k,n} \propto \ell_1^{-2(|\frac{k}{n}|-\frac{1}{2})(|\frac{2k}{n}|-\frac{1}{2})} \cdot \ell_2^{-2|\frac{k}{n}|(|\frac{2k}{n}|-\frac{1}{2})} \cdot (\ell_1+\ell_2)^{2|\frac{k}{n}|(|\frac{k}{n}|-\frac{1}{2})}. \tag{3.4.28}$$

It is important to note that for $k<0$, we modified the flux at u_1 and v_1 by inserting additional 2π and -2π fluxes, respectively, where the scaling exponent takes its minimum value (c.f. Appendix 3.A). Summing up $Z^{(\mathrm{r})}_{k,n}$ terms, we get

$$\mathcal{N}^{(\mathrm{r})}_n = c^{(1)}_n \ln(\ell_1) + c^{(2)}_n \ln(\ell_2) + c^{(3)}_n \ln(\ell_1+\ell_2) + \cdots \tag{3.4.29}$$

where

$$c^{(1)}_{n_o} = -\frac{1}{12}\left(n_o + \frac{5}{n_o}\right), \quad c^{(2)}_{n_o} = c^{(3)}_{n_o} = -\frac{1}{12}\left(n_o - \frac{1}{n_o}\right), \tag{3.4.30}$$

for odd $n = n_o$, and

$$c^{(1)}_{n_e} = c^{(2)}_{n_e} = -\frac{1}{6}\left(\frac{n_e}{2} - \frac{2}{n_e}\right), \quad c^{(3)}_{n_e} = -\frac{1}{6}\left(\frac{n_e}{2} + \frac{1}{n_e}\right), \tag{3.4.31}$$

for even $n = n_e$. As a consistency check, we show in Section 3.5 that the above formulae can be derived from two disjoints intervals as the distance between the intervals is taken to be zero. Notice that the even n case is identical to the general CFT results [94]. Also, from (3.2.10) we arrive at the familiar result for the LN,

$$\mathcal{E} = \frac{1}{4}\ln\left(\frac{\ell_1\ell_2}{\ell_1+\ell_2}\right) + \cdots \tag{3.4.32}$$

For equal length intervals, we may write $\mathcal{N}^{(\mathrm{r})}_n = c_n \ln \ell + \cdots$ where

$$c_n = \begin{cases} -\frac{1}{4}\left(n_o + \frac{1}{n_o}\right) & n = n_o \quad \text{odd}, \\ -\frac{1}{2}\left(\frac{n_e}{2} - \frac{1}{n_e}\right) & n = n_e \quad \text{even}. \end{cases} \tag{3.4.33}$$

As expected for Hermitian operator $\rho^{\widetilde{T}_A}$, here the moments $\mathcal{N}^{(\mathrm{r})}_n$ only depend on parity of n, i.e., whether

n is odd or even. This means that the eigenvalues are real positive or negative. We can also see this from the fact that the single particle spectrum is real. The many-body eigenvalues follow the form $\lambda_\sigma = \prod_{\sigma_k=\pm}(1+\sigma_k\nu_k)/2$, where ν_k are single-particle eigenvalues of the covariance matrix (3.2.30). As discussed in the previous Section, we carry out the same procedure to derive the distribution from analytic continuation of moments (in this case there are only two branches). The final result reads

$$P(\lambda) = \delta(\lambda_M - \lambda) + \frac{b\theta(\lambda_M - |\lambda|)}{2|\lambda|\xi}[-J_1(2\xi)\mathrm{sgn}(\lambda) + \sqrt{2}I_1(2\sqrt{2}\xi)], \tag{3.4.34a}$$

$$n(\lambda) = \frac{1}{2}[J_0(2\xi)\mathrm{sgn}(\lambda) + I_0(2\sqrt{2}\xi)], \tag{3.4.34b}$$

where ξ obeys the same form as Eq. (3.4.13) with a slight difference that $b = -\ln\lambda_M = \frac{1}{4}\ln\ell$. We present a comparison of the above expression with numerical spectrum of free fermions on the lattice of different lengths in Fig 3.6. There is a good agreement between analytical and numerical results.

We further find that, as it was the case for the bosonic negativity, the scaling of the minimum and maximum eigenvalue is the same. Finally, we confirm that the distribution probability is properly normalized such that $\int \lambda P(\lambda)d\lambda = \mathrm{Tr}[\rho(-1)^{F_A}]$ and it is consistent with $\mathcal{E} = \frac{1}{4}\ln\ell$, Eq. (3.2.10), which follows from

$$\mathcal{E} = \ln\int d\lambda\,|\lambda|P(\lambda) = \ln\left[\lambda_M + \int_0^{\lambda_M} d\lambda\,\frac{b\sqrt{2}}{\xi}I_1(2\sqrt{2}\xi)\right] = \frac{1}{4}\ln\ell. \tag{3.4.35}$$

Bipartite geometry

In this case, we start by computing the correlator

$$Z^{(\mathrm{r})}_{k,n} = \langle \mathcal{Q}^{-2}_{k,n}(u_A)\mathcal{Q}^{2}_{k,n}(v_A)\rangle \propto \ell_1^{-2(|\frac{2k}{n}|-\frac{1}{2})^2}. \tag{3.4.36}$$

Here again, we have to minimize the scaling exponent for $k<0$ by inserting additional 2π fluxes (c.f. Appendix 3.A). The RN is then found to be $\mathcal{N}^{(\mathrm{r})}_n = c_n\ln(\ell_1)+\cdots$ where

$$c_n = \begin{cases} -\frac{1}{6}\left(n_o + \frac{2}{n_o}\right) & n = n_o \quad \text{odd}, \\ -\frac{1}{3}\left(\frac{n_e}{2} - \frac{2}{n_e}\right) & n = n_e \quad \text{even}. \end{cases} \tag{3.4.37}$$

From this, we derive the distribution of many-body eigenvalues to be

$$P(\lambda) = \delta(\lambda_M - \lambda) + \frac{b\theta(\lambda_M - |\lambda|)}{2|\lambda|\xi}[-\sqrt{2}J_1(2\sqrt{2}\xi)\mathrm{sgn}(\lambda) + 2I_1(4\xi)], \tag{3.4.38a}$$

$$n(\lambda) = \frac{1}{2}[J_0(2\sqrt{2}\xi)\mathrm{sgn}(\lambda) + I_0(4\xi)], \tag{3.4.38b}$$

where ξ is given in (3.4.13) and $b = -\ln\lambda_M = \frac{1}{6}\ln\ell$.

We finish this part by a remark about the covariance matrix. Using the fact that $\gamma^2 = \mathbb{I}$ for pure states, the covariance matrix (3.2.30) can be further simplified into

$$\widetilde{\gamma} = \begin{pmatrix} \gamma_{AA} - 2\gamma_{AA}^{-1} & -i\gamma_{AB} \\ i\gamma_{BA} & \gamma_{BB} \end{pmatrix}. \tag{3.4.39}$$

Similar to the adjacent intervals, we can calculate the many-body spectrum out of eigenvalues of the above covariance matrix. We confirm that the numerical results and analytical expressions match. However, we avoid showing the plots here as they look quite similar to Fig. 3.6.

3.5 Rényi negativity for disjoint intervals

In this Section, we derive the RN associated with ρ^{T_A} and $\rho^{\widetilde{T}_A}$ for two disjoint intervals. The analysis to derive the spectrum is the same as for adjacent intervals and therefore we do not include it. Instead it is more interesting to show that upon taking the distance between the intervals to zero, we recover the results for two adjacent intervals as discussed in the main text. Taking this limit is a bit tricky and was previously overlooked in Ref. [299], where it was incorrectly deduced that $Z^{(\mathrm{ns})}_{\mathcal{N}_n} = 0$ for two adjacent intervals.

Moments of ρ^{T_A}

This geometry is characterized by $v_A - u_A = \ell_1$, $u_B - v_A = d$, and $v_B - u_B = \ell_2$ (c.f. Fig. 3.7(a)). The leading order term of the momentum decomposed partition function in the case of disjoint intervals is given by

$$Z^{(\mathrm{ns})}_{k,n} = c_{k0}\left(\frac{x}{\ell_1\ell_2}\right)^{2k^2/n^2} + \cdots \tag{3.5.1}$$

where

$$x = \frac{(\ell_1+\ell_2+d)d}{(\ell_1+d)(\ell_2+d)}. \tag{3.5.2}$$

Consequently, the RN is found to be

$$\mathcal{N}^{(\mathrm{ns})}_n = \left(\frac{n^2-1}{6n}\right)\ln\left(\frac{x}{\ell_1\ell_2}\right) + \cdots \tag{3.5.3}$$

We compare the above formula with the scaling behavior of the numerical results in Fig. 3.7(b), where we find that they match.

As a consistency check, we show that the RN between adjacent intervals can be derived as a limiting behavior of the disjoint intervals. However, we realize from (3.5.1) that $\lim_{d\to 0} Z^{(\mathrm{ns})}_{k,n} = 0$ (as is done also in Ref. [299]). A more careful treatment goes by considering higher order terms coming from different representations in (3.A.10)

$$Z^{(\mathrm{ns})}_{k,n} = c_{k0}\left(\frac{x}{\ell_1\ell_2}\right)^{2\frac{k^2}{n^2}} + c_{k1}\left(\frac{x}{\ell_1\ell_2}\right)^{2|\frac{k}{n}|(|\frac{k}{n}|-1)}[g(\ell_1,\ell_2;k/n)+g(\ell_1+d,\ell_2+d;k/n)] + \cdots \tag{3.5.4}$$

where $g(x,y;q) = x^{-2}(x/y)^{2|q|} + x \leftrightarrow y$ and c_{ki} are coefficients dependent on the microscopic details. Next, we obtain the leading order term in the coincident limit $d = \varepsilon$, where $\varepsilon \ll \ell_1, \ell_2$. To this end, we rewrite the above expansion (3.5.4) as

$$Z^{(\mathrm{ns})}_{k,n} = \varepsilon^{2k^2/n^2} Z^{(0)}_{k,n} + \varepsilon^{2|k/n|(|k/n|-1)} Z^{(1)}_{k,n} + \cdots \tag{3.5.5}$$

where the scaling dimensions are

$$[Z^{(0)}_{k,n}] \sim L^{-6N^2/n^2}, \tag{3.5.6a}$$

$$[Z^{(1)}_{k,n}] \sim L^{-2(3k^2/n^2 - 3|k/n|+1)}. \tag{3.5.6b}$$

As we see, for $|k/n| > 1/3$, the second term is dominant. This immediately implies that upon taking $(\ell_i + d) \sim \ell_i$, we recover the original result (3.4.7).

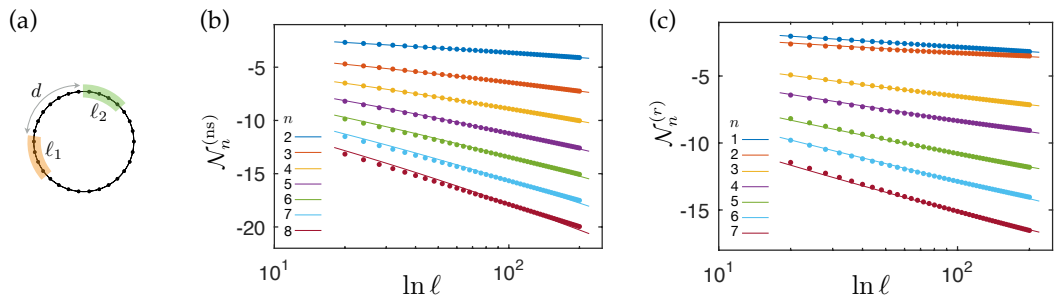

FIGURE 3.7: Comparison of numerical (dots) and analytical (solid lines) results for the scaling behavior of the moments of partial transpose (3.3.6) and (3.3.8) for two disjoint intervals (the geometry is shown in panel (a)). Here, $d = 40$ and intervals have equal lengths $\ell_1 = \ell_2 = \ell$ where $20 \leq \ell \leq 200$ on an infinite chain. The analytical results are given by Eq. (3.5.1) in panel (b) and Eq. (3.5.7) in panel(c). Different colors correspond to different moments n.

Moments of $\rho^{\widetilde{T}_A}$

Similarly, we find the k-th contribution to the n-th moment of $\rho^{\widetilde{T}_A}$ to be

$$Z^{(\mathrm{r})}_{k,n} = x^{2|k/n|(|k/n|-1/2)} \frac{1}{\ell_1^{2(|k/n|-1/2)^2} \ell_2^{2k^2/n^2}} + \cdots \tag{3.5.7}$$

which gives rise to the following form for the RN,

$$\mathcal{N}^{(\mathrm{r})}_n = c^{(1)}_n \ln(\ell_1) + c^{(2)}_n \ln(\ell_2) + c^{(3)}_n \ln(x) + \cdots \tag{3.5.8}$$

where

$$c^{(1)}_n = \begin{cases} -\frac{1}{6}\left(n_o + \frac{2}{n_o}\right) & n = n_o \quad \text{odd}, \\ -\frac{1}{6}\left(n_e - \frac{1}{n_e}\right) & n = n_e \quad \text{even}, \end{cases} \tag{3.5.9}$$

$$c^{(2)}_n = -\left(\frac{n^2-1}{6n}\right), \tag{3.5.10}$$

$$c^{(3)}_n = \begin{cases} -\frac{1}{12}\left(n_o - \frac{1}{n_o}\right) & n = n_o \quad \text{odd}, \\ -\frac{1}{6}\left(\frac{n_e}{2} + \frac{1}{n_e}\right) & n = n_e \quad \text{even}. \end{cases} \tag{3.5.11}$$

We compare the scaling behaviors of analytical expressions and numerical results in Fig. 3.7(c). As we see, they are in good agreement.

It is easy to verify that taking the adjacent limit $d = \varepsilon$ of two disjoint intervals in Eq. (3.5.8) leads to Eq. (3.4.29).

3.6 Concluding remarks

In this Chapter we studied the distribution of the eigenvalues of PT density matrices, aka the negativity spectrum, in free fermion chains. We presented analytical and numerical results for the negativity spectra using both types of the fermionic partial transpose. In the case of $\rho^{\widetilde{T}_A}$, we find that the negativity spectra share a lot of similarities with those found in the previous CFT work [57]. However, in the case of ρ^{T_A}, we realize that the eigenvalues form a special pattern on the complex plane and fall on six branches with a quantized phase of $2\pi n/6$. The spectrum in the latter case is mirror-symmetric with respect to the real axis, and there are four universal functions that describe the distributions along the six branches. The sixfold distribution of eigenvalues is not specific to complex fermion chain (described by the Dirac Hamiltonian)

with $c = 1$ and also appears in the critical Majorana chain with $c = 1/2$. We further confirmed that our analytical expressions are applicable to the Majorana chain upon modifying the central charge c.

Given our free fermion results in one dimension, there are several avenues to pursue for future research. A natural extension is to explore possible structures in the negativity spectrum of free fermions in higher dimensions. It would also be interesting to understand the effect of disorder and spin-orbit coupling on this distribution. In particular, the random singlet phase (RSP) introduced in Section 1.4.4 is characterized by logarithmic entanglement [86, 95, 320, 321] that is a hallmark of $(1+1)d$ critical theories. An interesting question is how the negativity spectrum of critical RSP differs from the clean limit which was studied here (this is work in progress [322]). Another direction could be studying strongly correlated fermion systems and specially interacting systems which have a description in terms of projected free fermions such as the Haldane-Shastry spin chain [323, 324]. Furthermore, it is worth investigating how thermal fluctuations affect the negativity spectrum in finite-temperature states. Finally, the negativity spectrum may be useful in studying the quench dynamics and shed light on thermalization.

3.A Twist fields, bosonization, etc.

The REEs of a RDM ρ are defined in Eq. (1.2.2). For non-interacting systems with conserved $U(1)$ charge, we can transform the trace formulas into a product of n decoupled partition functions: see Eq. (3.4.1) where $Z_{k,n}$ is the partition function containing an interval with the twisting phase $2\pi k/n$. We reformulate the partition function in the presence of phase twisting intervals in terms of a theory subject to an external gauge field which is a pure gauge everywhere (except at the points u_i and v_i where it is vortex-like). This is obtained by a singular gauge transformation

$$\psi_k(x) \to e^{i\int_{x_0}^{x} dx'^{\mu} A_{\mu}^{k}(x')} \psi_k(x)\,, \tag{3.A.1}$$

where x_0 is an arbitrary fixed point. Hence, for a subsystem made of p intervals, $A = \bigcup_{i=1}^{p}[u_i, v_i]$, we can absorb the boundary conditions across the intervals into an external gauge field and the resulting Lagrangian density becomes

$$\mathcal{L}_k = \bar{\psi}_k \gamma^{\mu} \left(\partial_{\mu} + i\, A_{\mu}^{k}\right) \psi_k. \tag{3.A.2}$$

where the $U(1)$ flux is given by

$$\epsilon^{\mu\nu}\partial_{\nu} A_{\mu}^{k}(x) = 2\pi \frac{k}{n} \sum_{i=1}^{p} \left[\delta(x-u_i) - \delta(x-v_i)\right]. \tag{3.A.3}$$

Note that there is an ambiguity in the flux strength, namely, $2\pi m$ (integer m) fluxes may be added to the right hand side of the above expression, while the monodromy for the fermion fields does not change. To preserve this symmetry (or redundancy), Z_k must be written as a sum over all representations [195, 196, 201, 325]. The asymptotic behavior of each term in this expansion is a power law $\ell^{-\alpha_m}$ in thermodynamic limit (large (sub-)system size). Here, we are interested in the leading order term which corresponds to the smallest exponent α_m.

As we will see, in the case of entanglement negativity we need to consider $m \neq 0$ for some values of k. Let us first discuss this expansion for a generic case. Let $\mathcal{Z}_n$ be a partition function on a multi-sheet geometry (for either Rényi entropy or negativity). As mentioned, after diagonalizing the twist matrices, $\mathcal{Z}_n$ can be decomposed as $\mathcal{Z}_n = \prod_k Z_k$, where Z_k is the partition function in the presence of $2p$ flux vortices at the two ends of p intervals between u_{2i-1} and u_{2i}, that is

$$Z_k = \left\langle e^{i\int A_{k,\mu} j_k^{\mu} d^2x} \right\rangle, \tag{3.A.4}$$

in which

$$\epsilon^{\mu\nu}\partial_\nu A_{k,\mu}(x) = 2\pi \sum_{i=1}^{2p} \nu_{k,i}\delta(x-u_i)\,, \tag{3.A.5}$$

and $2\pi\nu_{k,i}$ is vorticity of gauge flux determined by the eigenvalues of the twist matrix. The total vorticity satisfies the neutrality condition $\sum_i \nu_{k,i} = 0$ for a given k. In order to obtain the asymptotic behavior, one needs to take the sum over all the representations of Z_k (i.e., flux vorticities mod 2π),

$$Z_k = \sum_{\{m_i\}} Z_k^{(m)} \tag{3.A.6}$$

where $\{m_i\}$ is a set of integers and

$$Z_k^{(m)} = \left\langle e^{i\int A_{k,\mu}^{(m)} j_k^\mu d^2x} \right\rangle\,, \tag{3.A.7}$$

is the partition function for the following fluxes,

$$\epsilon^{\mu\nu}\partial_\nu A_\mu^{(m),k}(x) = 2\pi \sum_{i=1}^{2p} \widetilde{\nu}_{k,i}\delta(x-u_i), \tag{3.A.8}$$

with $\widetilde{\nu}_{k,i} = \nu_{k,i} + m_i$ being shifted flux vorticities. The neutrality condition requires $\sum_i m_i = 0$. Using the bosonization technique [326], we obtain

$$Z_k^{(m)} = C_{\{m_i\}} \prod_{i<j} |u_i - u_j|^{2\widetilde{\nu}_{k,i}\widetilde{\nu}_{k,j}}, \tag{3.A.9}$$

where $C_{\{m_i\}}$ is a constant depending on cutoff and microscopic details. We make use of the neutrality condition $-2\sum_{i<j}\widetilde{\nu}_{k,i}\widetilde{\nu}_{k,j} = \sum_i \widetilde{\nu}_{k,i}^2$ and rewrite

$$Z_k \sim \sum_{\{m_i\}} C_{\{m_i\}}\, \ell^{2\sum_{i<j}\widetilde{\nu}_{k,i}\widetilde{\nu}_{k,j}} = \sum_{\{m_i\}} C_{\{m_i\}}\, \ell^{-\sum_i \widetilde{\nu}_{k,i}^2} \tag{3.A.10}$$

where ℓ is a length scale. From this expansion, the leading order term in the limit $\ell \to \infty$ is clearly the one(s) which minimizes the quantity $\sum_i \widetilde{\nu}_{k,i}^2$. This is identical to the condition derived from the generalized Fisher-Hartwig conjecture [193,194]. A careful determination of the leading order term for REE by a similar approach was previously discussed in Ref. [196, 325, 327].

We now carry out this process for $Z_{\mathcal{N}_n}^{(\mathrm{ns})}$ in Eq. (3.4.6) for two adjacent intervals. Here, we need to minimize the quantity

$$f_{m_1m_2m_3}(\nu) = (\nu+m_1)^2 + (\nu+m_3)^2 + (-2\nu+m_2)^2 \tag{3.A.11}$$

for a given $\nu = k/n = -(n-1)/2n, \cdots, (n-1)/2n$ by finding the integers (m_1, m_2, m_3) constrained by $\sum_i m_i = 0$. For instance, by comparing $(0,0,0)$ with $(-1,1,0)$, we find $f_{000}(\nu) = 6\nu^2$ and $f_{-110}(\nu) = 6\nu^2 - 6\nu + 2$. So, we have $f_{000}(\nu) > f_{-110}(\nu)$ for $\nu > \frac{1}{3}$. Similarly, we find that $f_{000}(\nu) > f_{1-10}(\nu)$ for $\nu < -\frac{1}{3}$. In summary, we resolve the flux ambiguity by adding the triplet (m_1, m_2, m_3) as follows

$$\begin{cases} (0,0,0) & |\nu| \le 1/3 \\ (-1,1,0), (0,1,-1) & \nu > 1/3 \\ (1,-1,0), (0,-1,1) & \nu < -1/3. \end{cases} \tag{3.A.12}$$

This leads us to write Eq. (3.4.7). Finally, similar derivation can be carried out to arrive at Eqs. (3.4.19), (3.4.28) and (3.4.36).

Chapter 4

Relative entropy in CFT

The necessity to characterize the properties of extended subsystems rather than of the entire system should be clear at this point. At the same time, the information that entanglement measures provide about a given subsystem may not be enough for some applications. Specifically, it can be equally important to develop tools enabling to distinguish between subsystems in different states, i.e. to distinguish RDMs. Here we study the relative entanglement entropies of one interval between excited states of a $(1+1)d$ CFT, between excited states generated by primary fields of a free massless bosonic field. These predictions are tested against exact numerical calculations in the XX spin-chain finding perfect agreement, thus providing the first check of the recently proposed associated replica trick. This Chapter is based on Ref. [328].

4.1 Introduction

The relative entropy (ReE) attracted only recently the interests of the field theory community, but it is already taking a central role given the number of papers devoted to it, see e.g. [116, 143, 144, 329–340]. One of its advantages is that, contrarily to the EE which in a QFT framework suffers from the problem of ultraviolet divergences [cf. (1.3.1)], the ReE is finite and therefore well defined also in field theory. Moreover, it is related to the entanglement (or modular) Hamiltonian, or better to its variation between two quantum states. Indeed, given two RDMs, ρ_1 and ρ_0, from the definition (1.2.6), it straightforwardly holds

$$S(\rho_1||\rho_0) = \Delta\langle\mathcal{H}_0\rangle - \Delta S\,, \tag{4.1.1}$$

where $\Delta S \equiv S(\rho_1) - S(\rho_0)$ is the difference of von Neumann entropies $S(\rho) \equiv -\mathrm{Tr}\rho\log\rho$ and $\Delta\langle\mathcal{H}_0\rangle$ is the variation of the modular Hamiltonian $\mathcal{H}_0$ (implicitly defined as $\rho_0 = e^{-\mathcal{H}_0}/\mathrm{Tr}e^{-\mathcal{H}_0}$) relative to ρ_0, i.e.,

$$\Delta\langle\mathcal{H}_0\rangle \quad = \quad \mathrm{Tr}[(\rho_1-\rho_0)\mathcal{H}_0]. \tag{4.1.2}$$

This relation between ReE and modular Hamiltonian is the starting point of the recent (alternative) proofs of the Zamolodchikov's c-theorem [105] in Ref. [329] and of the boundary g-theorem [82] in Ref. [116].

The ReE may give useful insights also in the study of condensed matter systems. For example singularities in other measures of distinguishability among quantum states (as it is the case for the quantum fidelity [347, 348]) have already been proposed as a signature of a quantum phase transition. It has also been considered in connection to the laws of black hole thermodynamics [330, 331] and the Bekenstein bound [332], which can both be shown to follow from the properties of positivity and monotonicity of the ReE. Its holographic version has been discussed as well [333, 334].

In a QFT, the ReE can be obtained by a variation of the replica trick for the EE which has been introduced by Lashkari [143] and later refined by the same author [144]. The main idea is stated in the Introduction (see Eq. (1.4.2)). The method is completely general and permits (at least in principle) the computation of the ReE in a generic QFT. However, up to now, only a few direct calculations of ReE have been performed in 1+1 dimensional CFT [143, 144, 335, 337] and only very recently some results for arbitrary dimensions appeared [336].

In analogy to the REEs, we can define *Rényi relative entropies* (RReEs) as

$$S_n(\rho_1\|\rho_0) \equiv \frac{1}{1-n}\log\frac{\mathrm{Tr}(\rho_1\rho_0^{n-1})}{\mathrm{Tr}(\rho_1^n)}\,. \tag{4.1.3}$$

While it is still unknown whether these quantities have a quantum information interpretation, they surely have two interesting features: i) when ρ_0 equals the identity $S_n(\rho_1\|\rho_0)$ reduces to minus the Rényi entropy of ρ_1, i.e. $S_n(\rho_1\|\rho_0=\mathbb{I})=-S_n(\rho_1)$, alike $S(\rho_1\|\rho_0=\mathbb{I})=-S(\rho_1)$; (ii) its limit for $n\to 1$ is $S(\rho_1\|\rho_0)$. The main drawback of $S_n(\rho_1\|\rho_0)$ is that, contrarily to $S(\rho_1\|\rho_0)$, is not always a positive function (as we shall see in the following). This is similar to standard Rényi entropies that satisfy strong subadditivity [52,53] only for $n=1$.

Here, we report on a systematic study of the relative entanglement entropy and its Rényi counterpart between excited states associated to primary operators in the free massless bosonic field theory in 1+1 dimensions, generalizing the analysis of previous works [143,144,335,337] and providing the first explicit checks of the CFT results in concrete lattice models.

The Chapter is organized as follows. In Section 4.2 we recall the CFT approach to the RReE presented in the Introduction specialized to the case of two excited states associated with primary fields. In Section 4.3 we present explicit calculations of ReE in the massless bosonic theory and in particular for vertex and derivative operator $i\partial\phi$. These CFT results are tested in Section 4.4 against exact numerical calculations in the XX spin-chain, whose continuum limit is a free massless boson. Finally, we conclude in Section 4.5.

4.2 CFT approach to the relative entropy between excited states

We consider a one-dimensional system and a bipartition into two complementary regions A and $\bar{A}$. Given two generic states $|\psi_1\rangle,|\psi_0\rangle\in\mathcal{H}$, the RDMs of the subsystem A are denoted respectively by $\rho_1=\mathrm{Tr}_{\bar{A}}|\psi_1\rangle\langle\psi_1|$ and $\rho_0=\mathrm{Tr}_{\bar{A}}|\psi_0\rangle\langle\psi_0|$. The goal is to compute the ReE between two eigenstates of the CFT $|\psi_1\rangle$ and $|\psi_0\rangle$ using the replica approach explained in Section 1.4.2.

We will be interested only in excited states of the CFT which are obtained by acting on the ground state with a generic primary operator Y (i.e. $|\mathrm{Y}\rangle\equiv\mathrm{Y}(-i\infty)|0\rangle$), whose corresponding density matrix generalizes the one in Eq. (1.4.6) as

$$\langle\phi|\rho_{\mathrm{Y}}|\phi'\rangle=\langle\phi|\mathrm{Y}\rangle\langle\mathrm{Y}|\phi'\rangle=\frac{1}{Z}\int_{\varphi(-i\infty)=\phi}^{\varphi(i\infty)=\phi'}\mathcal{D}\varphi\;\mathrm{Y}(i\infty)\mathrm{Y}^\dagger(-i\infty)e^{-S(\varphi)}. \tag{4.2.1}$$

Following the usual procedure, we end up in a n-sheeted Riemann surface $\mathcal{R}_n$ but now with fields insertions as in

$$\mathrm{Tr}\rho_{\mathrm{Y}}^n(A)\propto Z_n(A)\langle\prod_{k=1}^n\mathrm{Y}(w_k)\mathrm{Y}_k^\dagger(w_k')\rangle_{\mathcal{R}_n}, \tag{4.2.2}$$

where the expectation value $\langle\cdots\rangle_{\mathcal{R}_n}$ is on the Riemann surface $\mathcal{R}_n$, $Z_n(A)\equiv\langle\mathbb{I}\rangle_{\mathcal{R}_n}$ (i.e. the n-th moment of the RDM of the ground state) and $w_k=i\infty, w_k'=-i\infty$ are points where the operators are inserted in the k-th copy. Taking properly into account the normalization, this is

$$\mathrm{Tr}\rho_{\mathrm{Y}}^n(A)=\frac{Z_n(A)}{Z_1^n}\frac{\langle\prod_{k=1}^n\mathrm{Y}(w_k)\mathrm{Y}_k^\dagger(w_k')\rangle_{\mathcal{R}_n}}{\langle\mathrm{Y}(w_1)\mathrm{Y}^\dagger(w_1')\rangle_{\mathcal{R}_1}^n}. \tag{4.2.3}$$

Finally, it is convenient to consider the universal ratio between the moment of the RDM in the excited state Y and the one of the ground state, i.e.

$$F_{\mathrm{Y}}^{(n)}(A)\equiv\frac{\mathrm{Tr}\rho_{\mathrm{Y}}^n}{\mathrm{Tr}\rho_{\mathbb{I}}^n}=\frac{\langle\prod_{k=1}^n\mathrm{Y}(w_k)\mathrm{Y}_k^\dagger(w_k')\rangle_{\mathcal{R}_n}}{\langle\mathrm{Y}(w_1)\mathrm{Y}^\dagger(w_1')\rangle_{\mathcal{R}_1}^n}, \tag{4.2.4}$$

in which the factors coming from the partition functions cancel out.

In order to calculate the correlators appearing in (4.2.4) in the case of A being a single interval $A=\{x\in(u,v)\}$, one considers the following sequence of conformal maps

$$w=x+it\to\zeta=\frac{\sin[\pi(w-u)/L]}{\sin[\pi(w-v)/L]}\to z=\zeta^{1/n}, \tag{4.2.5}$$

where $\zeta(w)$ brings $(u,v) \to (-\infty,0)$ and $z(\zeta)$ is a *uniformizing mapping* which maps the n-sheeted Riemann surface into the complex plane. According to these maps

$$\begin{cases} w_k = i\infty \to z_{k,n} = e^{i\frac{\pi}{n}(x+2(k-1))} \\ w'_k = -i\infty \to z_{k,n} = e^{i\frac{\pi}{n}(-x+2(k-1))} \end{cases} \qquad k = 1,\cdots,n, \quad x = \frac{v-u}{L} \equiv \frac{\ell}{L}. \tag{4.2.6}$$

We shall use the transformation properties of the primary fields under conformal maps

$$\mathrm{Y}(w,\bar{w}) = \left(\frac{dz}{dw}\right)^h \left(\frac{d\bar{z}}{d\bar{w}}\right)^{\bar{h}} \mathrm{Y}(z,\bar{z}), \tag{4.2.7}$$

being $(h,\bar{h})$ the scaling dimensions of Y. In our case this becomes [349]

$$\mathrm{Y}(w_k,\bar{w}_k) = \left(\frac{z_{k,n}}{n}\Lambda\right)^h \left(\frac{\bar{z}_{k,n}}{n}\bar{\Lambda}\right)^{\bar{h}} \mathrm{Y}(z_{k,n},\bar{z}_{k,n}), \tag{4.2.8}$$

with

$$\Lambda = \frac{4\pi}{L}\sin(\pi x) e^{-2\pi|w|/L} e^{i\pi(u+v)/L}. \tag{4.2.9}$$

Finally the complex plane can be mapped to a cylinder of circumference 2π by $t = -i\ln z$ which implies

$$\mathrm{Y}(t,\bar{t}) = e^{i\pi(h-\bar{h})} z^h \bar{z}^{\bar{h}} \mathrm{Y}(z,\bar{z}). \tag{4.2.10}$$

Combining all the above transformations, for our geometry of an interval A of length ℓ embedded in a finite system of length L, we end up in [349]

$$F_{\mathrm{Y}}^{(n)}(x) = n^{-2n(h+\bar{h})} \frac{\langle \prod_{k=1}^n \mathrm{Y}(t_{k,n})\mathrm{Y}^\dagger(t'_{k,n})\rangle_{\mathrm{cyl}}}{\langle \mathrm{Y}(t_{1,1})\mathrm{Y}(t'_{1,1})\rangle_{\mathrm{cyl}}^n}, \tag{4.2.11}$$

where we recall $x = \ell/L$ and

$$t_{k,n} = \frac{\pi}{n}(x+2(k-1)), \quad t'_{k,n} = \frac{\pi}{n}(-x+2(k-1)), \quad k = 1,\dots,n. \tag{4.2.12}$$

The above result has been generalized in the literature to many other circumstances such as generic states generated also by descendant fields [350, 351], boundary theories [352, 353], and systems with disorder [354].

We now turn to the path integral representation of $\mathrm{Tr}\,(\rho_1^m\rho_0^n)$, which is a simple generalization of $\mathrm{Tr}\rho^n$ discussed above. In this case, in fact, instead of n copies of the RDM ρ_0 only, one considers further m copies of ρ_1 and joins them cyclically as before. Considering two CFT excited states of the form (4.2.1) obtained from the action of two primaries Y_0 and Y_1 , the final result is a path integral on a Riemann surface with $(m+n)$ sheets with the insertion of $\mathrm{Y}_1, \mathrm{Y}_1^\dagger$ on m sheets and $\mathrm{Y}_0, \mathrm{Y}_0^\dagger$ on the remaining n sheets, i.e. [144]

$$\mathrm{Tr}\,(\rho_1^m\rho_0^n) \propto Z_n(A)\Big\langle \prod_{k=1}^m \mathrm{Y}_1(w_k)\mathrm{Y}_1^\dagger(w'_k) \prod_{i=1+m}^{n+m} \mathrm{Y}_0(w_i)\mathrm{Y}_0^\dagger(w_i)\Big\rangle_{\mathcal{R}_n}. \tag{4.2.13}$$

Keeping track of the normalization we get

$$\mathrm{Tr}\,(\rho_1^m\rho_0^n) = \frac{Z_n(A)}{Z_1^{m+n}} \frac{\langle \prod_{k=1}^m \mathrm{Y}_1(w_k)\mathrm{Y}_1^\dagger(w'_k) \prod_{i=1+m}^{n+m} \mathrm{Y}_0(w_i)\mathrm{Y}_0^\dagger(w'_i)\rangle_{\mathcal{R}_n}}{\langle \mathrm{Y}_1(w_1)\mathrm{Y}_1^\dagger(w'_1)\rangle_{\mathcal{R}_1}^m \langle \mathrm{Y}_0(w_1)\mathrm{Y}_0^\dagger(w'_1)\rangle_{\mathcal{R}_1}^n}. \tag{4.2.14}$$

In particular, for the RReE between ρ_1 and ρ_0, we compute the universal ratio

$$G^{(n)}(\rho_1\|\rho_0) \equiv \frac{\mathrm{Tr}\left(\rho_1\rho_0^{n-1}\right)}{\mathrm{Tr}\left(\rho_1^n\right)} = \frac{\langle \mathrm{Y}_1(w_1)\mathrm{Y}_1^\dagger(w_1')\prod_{i=2}^n \mathrm{Y}_0(w_i)\mathrm{Y}_0^\dagger(w_i')\rangle_{\mathcal{R}_n}\langle \mathrm{Y}_1(w_1)\mathrm{Y}_1^\dagger(w_1')\rangle_{\mathcal{R}_1}^{n-1}}{\langle\prod_{i=1}^n \mathrm{Y}_1(w_i)\mathrm{Y}_1^\dagger(w_i')\rangle_{\mathcal{R}_n}\langle \mathrm{Y}_0(w_1)\mathrm{Y}_0^\dagger(w_1')\rangle_{\mathcal{R}_1}^{n-1}}. \tag{4.2.15}$$

Also in this case, to compute (4.2.15), we use the conformal maps $w \to z \to t$ (4.2.5), which bring it to the final form

$$G^{(n)}(\rho_1\|\rho_0) = n^{2(n-1)((h_1+\bar{h}_1)-(h_0+\bar{h}_0))} \frac{\langle \mathrm{Y}_1(t_{1,n})\mathrm{Y}_1^\dagger(t_{1,n}')\prod_{i=2}^n \mathrm{Y}_0(t_{i,n})\mathrm{Y}_0^\dagger(t_{i,n}')\rangle_{\mathrm{cyl}}\langle \mathrm{Y}_1(t_{i,n})\mathrm{Y}_1^\dagger(t_{i,n}')\rangle_{\mathrm{cyl}}^{n-1}}{\langle\prod_{i=1}^n \mathrm{Y}_1(t_{i,n})\mathrm{Y}_1^\dagger(t_{i,n}')\rangle_{\mathrm{cyl}}\langle \mathrm{Y}_0(t_{i,n})\mathrm{Y}_0^\dagger(t_{i,n}')\rangle_{\mathrm{cyl}}^{n-1}}, \tag{4.2.16}$$

being h_1 and h_0 the scaling dimensions of Y_1 and Y_0 respectively. Note that $G^{(1)}(\rho_1\|\rho_0) = 1$ for any $\mathrm{Y}_{0,1}$, as it should.

As already mentioned, the ReE is not symmetric in ρ_1 and ρ_0. Therefore we are going to consider the two (generically different) quantities $S(\rho_1\|\rho_0)$ and $S(\rho_0\|\rho_1)$, obtained via replica limit from $G^{(n)}(\rho_1\|\rho_0)$ and $G^{(n)}(\rho_0\|\rho_1)$ respectively. Notice that the universal ratio $G^{(n)}(\rho_1\|\rho_0)$ gives the RReE (4.1.3) as

$$S_n(\rho_1\|\rho_0) = \frac{1}{1-n}\log G^{(n)}(\rho_1\|\rho_0)\,. \tag{4.2.17}$$

4.3 Relative entropy in free bosonic theory

In this Section we are going to apply the formalism reviewed above to work out some new results for the RReE between eigenstates of the massless free bosonic field theory, whose Euclidean action is

$$\mathcal{S}[\varphi] = \frac{1}{8\pi}\int dz d\bar{z}\;\partial_z\varphi\partial_{\bar{z}}\varphi\,, \tag{4.3.1}$$

which is a CFT with central charge $c = 1$. In the following we will denote with ϕ and $\bar{\phi}$ the chiral and antichiaral component of the bosonic field, i.e. $\varphi(z,\bar{z}) = \phi(z) + \bar{\phi}(\bar{z})$. We will only consider the case of A being one interval of length ℓ embedded in a finite system of total length L with periodic boundary conditions.

4.3.1 ReE between the ground state and the vertex operator: V_β/GS

The first case we study is the ReE between the ground state and the excited state generated by a vertex operator, which is a primary operator of the theory, defined as

$$V_{\alpha,\bar{\alpha}} \equiv :e^{i(\alpha\phi+\bar{\alpha}\bar{\phi})}: \,. \tag{4.3.2}$$

We will focus on its chiral component (i.e. $\bar{\alpha} = 0$), with conformal dimensions $(h,\bar{h}) = (\frac{\alpha^2}{2},0)$ and we will denote by $\rho_{V_\alpha} = \mathrm{Tr}_{\bar{A}}|V_\alpha\rangle\langle V_\alpha|$ the associated RDM. This ReE has already been considered in Ref. [144], but it is important to repeat the calculation here to set up the formalism and because we will need some informations from this calculation in the following.

The $2n$-point correlation function of vertex operators on the complex plane [83], after mapping to the variable t (cf. (4.2.12)) reads ($t_{ki} \equiv t_{k,n} - t_{i,n}$)

$$\langle\prod_k V_{\alpha_k}(t_k)\rangle = \prod_{k>i}[2\sin(t_{ki}/2)]^{\alpha_k\alpha_i}\,. \tag{4.3.3}$$

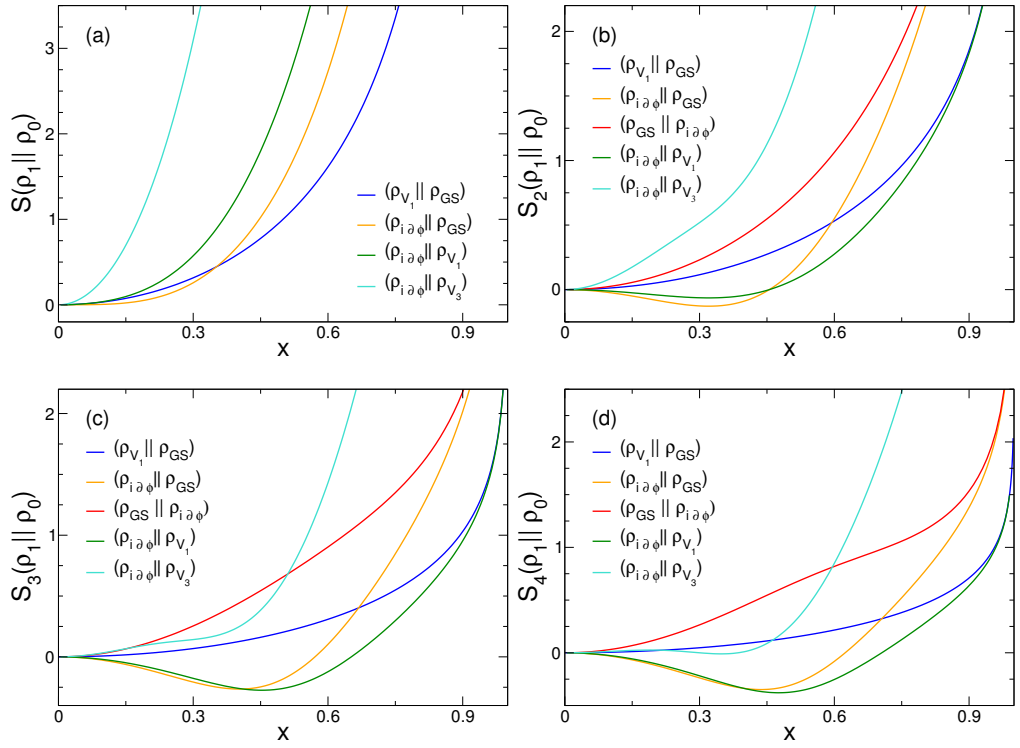

FIGURE 4.1: The CFT predictions for the Rényi relative entropies $S_n(\rho_1\|\rho_0)$ as a function of $x = \ell/N$ for different values of $n = 1,2,3,4$ in panels (a), (b), (c) and (d) respectively. In each panel (at fixed n) we report the various states that we have considered, in order to compare the various results. Notice the non-positivity and non-monotonicity of some $S_n(\rho_1\|\rho_0)$ for $n \neq 1$.

Plugging this expression in (4.2.16), we derive the following results for the replicated relative entropies

$$G^{(n)}(\rho_{GS}\|\rho_{V_\alpha}) = \left[n^{-(n-1)} \left(\frac{\sin(\pi x)}{\sin(\pi x/n)} \right)^{n-1} \prod_{m=1}^{n-2} \left(\frac{\sin^2(\pi m/n)}{\sin(\pi(x+m)/n)\sin(\pi(x-m)/n)} \right)^{n-1-m} \right]^{\alpha^2},$$

$$G^{(n)}(\rho_{V_\alpha}\|\rho_{GS}) = \left[n^{n-1} \left(\frac{\sin(\pi x)}{\sin(\pi x/n)} \right)^{1-n} \prod_{m=1}^{n-1} \left(\frac{\sin^2(\pi m/n)}{\sin(\pi(x+m)/n)\sin(\pi(x-m)/n)} \right)^{m-n} \right]^{\alpha^2},$$

which simplify to

$$G^{(n)}(\rho_{GS}\|\rho_{V_\alpha}) = G^{(n)}(\rho_{V_\alpha}\|\rho_{GS}) = \left(\frac{\sin(\pi x)}{n\sin(\pi x/n)} \right)^{\alpha^2}. \tag{4.3.4}$$

Thus, it turns out that, for these specific operators, the $G^{(n)}$ (and so the RReEs S_n) are symmetric under exchange of the two reduced density matrices $\rho_{V_\alpha} \leftrightarrow \rho_{GS}$, which, as already mentioned, is not true in general. Of course, by replica limit $n \to 1$, the same holds true also for the ReE which is

$$S(\rho_{V_\alpha}\|\rho_{GS}) = S(\rho_{GS}\|\rho_{V_\alpha}) = \alpha^2(1 - \pi x \cot(\pi x)). \tag{4.3.5}$$

In Figure 4.1 we plot the Rényi relative entropies $S_n(\rho_{V_\alpha}\|\rho_{GS})$ as function of x for $n = 1,2,3,4$. They are all monotonous and positive function of x.

More generally, in [144] it has been shown that Eq. (4.3.5) holds also for the ReE between two excited states of the form $V_\alpha|0\rangle$ with different charges α, β, but with the replacement $\alpha \to \alpha - \beta$, i.e.,

$$S(\rho_{V_\alpha}\|\rho_{V_\beta}) = S(\rho_{V_\beta}\|\rho_{V_\alpha}) = (\alpha - \beta)^2(1 - \pi x \cot(\pi x)). \tag{4.3.6}$$

4.3.2 ReE between the ground state and the derivative operator: $i\partial\phi$/GS

Here we consider a more complicated case, namely the ReE of the excited state generated by $i\partial\phi$ (which is a primary operator of the theory with conformal dimensions $(h,\bar{h}) = (1,0)$) again with respect to the ground state. We denote the RDM as $\rho_{i\partial\phi} = \mathrm{Tr}_{\bar{A}}|i\partial\phi\rangle\langle i\partial\phi|$.

The $2n$-point correlation function of $i\partial\phi$ in the complex plane is [83]

$$\langle\prod_{j=1}^{2n} i\partial\phi(z_j)\rangle_{\mathbb{C}} = \mathrm{Hf}\left[\frac{1}{z_{ij}^2}\right]_{i,j\in[1,2n]}, \tag{4.3.7}$$

where we denote with $z_{ij} \equiv z_i - z_j$ and we introduced the Hafnian (Hf) as

$$\mathrm{Hf}[A] \equiv \frac{1}{2^n n!}\sum_{p\in S_{2n}}\prod_{i=1}^{n} A_{p(2i-1),p(2i)}\,, \tag{4.3.8}$$

with the sum being over all cyclic permutations. This Hafnian can be expressed as a determinant using the following standard linear algebra identity

$$\mathrm{Hf}\Big[\frac{1}{z_{ij}^2}\Big] = \det\Big[\frac{1}{z_{ij}}\Big]. \tag{4.3.9}$$

For the case of our interest, after mapping to the cylinder of length 2π in the variable t (cf. (4.2.12)), we have

$$\langle\prod_{j=1}^{2n} i\partial\phi(t_{j,n})\rangle_{\mathrm{cyl}} = \frac{1}{4^n}\det\left[\frac{1}{\sin(t_{ij}/2)}\right]_{i,j\in[1,2n]}. \tag{4.3.10}$$

Plugging this result into (4.2.16), we get

$$G^{(n)}(\rho_{GS}\|\rho_{i\partial\phi}) = \left(\frac{\sin\pi x}{n}\right)^{2(n-1)}\det\left[\frac{1}{\sin(t_{ij}/2)}\right]_{i,j\in[1,2(n-1)]}, \tag{4.3.11}$$

$$G^{(n)}(\rho_{i\partial\phi}\|\rho_{GS}) = \left(\frac{\sin\pi x}{n}\right)^{2(1-n)}\left(\sin\frac{\pi x}{n}\right)^{-2}\left(\det\left[\frac{1}{\sin(t_{ij}/2)}\right]_{i,j\in[1,2n]}\right)^{-1}. \tag{4.3.12}$$

While the above functions are sufficient to determine the RReE of integer order, the relative entropies $S(\rho_{GS}\|\rho_{i\partial\phi})$ and $S(\rho_{i\partial\phi}\|\rho_{GS})$ are obtained from the analytic continuation of (4.3.11) and (4.3.12) and taking the replica limit $n\to 1$. Such analytic continuations are however very difficult since the integer n appear as the dimension of a matrix. Fortunately, for the determinant in (4.3.12) the analytic continuation has been already worked out [355] and it is given by

$$\det\left[\frac{1}{\sin(t_{ij}/2)}\right]_{i,j\in[1,2n]} = 4^n\frac{\Gamma^2\left(\frac{1+n+n\csc\pi x}{2}\right)}{\Gamma^2\left(\frac{1-n+n\csc\pi x}{2}\right)}. \tag{4.3.13}$$

Thus the ReE can be straightforwardly computed obtaining

$$S(\rho_{i\partial\phi}\|\rho_{GS}) = 2\left(\log(2\sin(\pi x)) + 1 - \pi x\cot(\pi x) + \psi_0\left(\frac{\csc(\pi x)}{2}\right) + \sin(\pi x)\right), \tag{4.3.14}$$

where $\psi_0(z)$ is the digamma function. The expansion of this ReE for small x agrees with the general result in [335].

Finding instead the analytic continuation of (4.3.11) is much more complicated. The technical difficulty stems from the matrix in (4.3.11) having dimension $n-1$ instead of n, an apparently innocuous change that alters completely the structure of the eigenvalues as it could be verified by a direct inspection for small n.

We mention that, in case one would be interested in an approximate estimate of this ReE, it is sufficient to employ a rational approximation for the analytic continuation as explained in Ref. [300].

In Figure 4.1 we plot the Rényi relative entropies $S_n(\rho_{GS}\|\rho_{i\partial\phi})$ and $S_n(\rho_{i\partial\phi}\|\rho_{GS})$ for $n = 1,2,3,4$. While $S_n(\rho_{GS}\|\rho_{i\partial\phi})$ for $n = 2,3,4$ is always positive and monotonous, this is not the case for $S_n(\rho_{i\partial\phi}\|\rho_{GS})$ which takes negative values and it is non monotonous for $n \neq 1$ (for $n = 1$ is always positive, as it should). Although $S_n(\rho_{GS}\|\rho_{i\partial\phi})$ is always positive and monotonous, its second derivative clearly changes sign as a difference compared to $S_n(\rho_{GS}\|\rho_{V_\alpha})$.

4.3.3 ReE between the vertex and the derivative operators: $i\partial\phi / V_\beta$

We finally consider the ReE between two different excited states, associated to $i\partial\phi$ and V_β respectively. In this case the replicated function is given by Eq. (4.2.16). This requires the calculation of the $2n$-point correlation function

$$\langle i\partial\phi(t_{1,n})i\partial\phi(t'_{1,n})\prod_{j=2}^{n-1}V_\beta(t_{j,n})V_{-\beta}(t'_{j,n})\rangle_{\text{cyl}}, \tag{4.3.15}$$

entering in $G^{(n)}(\rho_{i\partial\phi}\|\rho_{V_\beta})$, cf. (4.2.16). Noticing that $i\partial\phi(t) = \left(\frac{1}{\alpha}\frac{\partial}{\partial t}V_\alpha(t)\right)|_{\alpha=0}$, we can relate the desired correlation function to the derivative of the $2n$-point correlation function of vertex operators in the following way

$$\langle i\partial\phi(t_{1,n})i\partial\phi(t'_{1,n})\prod_{j=2}^{n}V_\beta(t_{j,n})V_{-\beta}(t'_{j,n})\rangle = \\ -\frac{1}{\alpha^2}\frac{\partial}{\partial t_{1,n}}\frac{\partial}{\partial t'_{1,n}}\langle V_\alpha(t_{1,n})V_{-\alpha}(t'_{1,n})\prod_{j=2}^{n}V_\beta(t_{j,n})V_{-\beta}(t'_{j,n})\rangle\Big|_{\alpha=0}. \tag{4.3.16}$$

At this point we only have to deal with the $2n$-point correlation function of vertex operators, which is given in (4.3.3). By simple algebra, we can rewrite

$$\langle i\partial\phi(t_{1,n})i\partial\phi(t'_{1,n})\prod_{j=2}^{n}V_\beta(t_{j,n})V_{-\beta}(t'_{j,n})\rangle = \frac{\tilde{C}_{\alpha,\beta}(n,x)}{4\sin^2\left(\frac{\pi x}{n}\right)}\langle\prod_{j=1}^{n-1}V_\beta(t_{j,n})V_{-\beta}(t'_{j,n})\rangle, \tag{4.3.17}$$

where we defined

$$\tilde{C}_{\alpha,\beta}(n,x) \equiv -\frac{4\sin^2\left(\frac{\pi x}{n}\right)}{\alpha^2}\partial_{t_{1,n}}\partial_{t'_{1,n}}C_{\alpha,\beta}(n,x), \tag{4.3.18}$$

and

$$C_{\alpha,\beta}(n,x) \equiv \langle V_\alpha(t_{1,n})V_{-\alpha}(t'_{1,n})\rangle\times \\ \times\prod_{m=1}^{n-1}\langle V_\beta(t_{m,n})V_\alpha(t_{1,n})\rangle\langle V_{-\beta}(t'_{m,n})V_{-\alpha}(t'_{1,n})\rangle\langle V_\beta(t_{m,n})V_{-\alpha}(t'_{1,n})\rangle\langle V_{-\beta}(t'_{m,n})V_\alpha(t_{1,n})\rangle. \tag{4.3.19}$$

The factor $4\sin^2\frac{\pi x}{n}$ has been introduced for later convenience. In $\tilde{C}_{\alpha,\beta}(n,x)$ the derivatives give rise to many different terms, but most of them vanish when considering the limit for $\alpha \to 0$. The explicit calculation is long but straightforward and the final result is

$$\tilde{C}_{\alpha=0,\beta}(n,x) = 1-\beta^2\sin^2\left(\frac{\pi x}{n}\right)\left(\sum_{k=1}^{n-1}\cot\frac{\pi}{n}(x+k)\right)\left(\sum_{l=1}^{n-1}\cot\frac{\pi}{n}(-x+l)\right). \tag{4.3.20}$$

We now have all the needed correlations for the RReE $S_n(\rho_{i\partial\phi}\|\rho_{V_\beta})$ (or its exponential $G^{(n)}(\rho_{i\partial\phi}\|\rho_{V_\beta})$). Plugging these correlations into (4.2.16), we have

$$G^{(n)}(\rho_{i\partial\phi}\|\rho_{V_\beta}) = n^{(\beta^2-2)(1-n)}\frac{\tilde{C}_{\alpha=0,\beta}(n,x)}{4\sin^2\left(\frac{\pi x}{n}\right)} \times \frac{\langle\prod_{k=1}^{n-1} V_\beta(t_{k,n})V_{-\beta}(t'_{k,n})\rangle_{\rm cyl}\langle i\partial\phi(t_{1,1})i\partial\phi(t'_{1,1})\rangle_{\rm cyl}^{n-1}}{\langle\prod_{k=0}^{n-1} i\partial\phi(t_{k,n})i\partial\phi(t_{k,n})\rangle_{\rm cyl}\langle V_\beta(t_{1,1})V_{-\beta}(t_{1,1})\rangle_{\rm cyl}^{n-1}}. \quad (4.3.21)$$

Finally, using the explicit expressions for all the correlation functions (which are known from previous cases), we get

$$G^{(n)}(\rho_{i\partial\phi}\|\rho_{V_\beta}) = \tilde{C}_{\alpha=0,\beta}(n,x)\left(\frac{\sin(\pi x)}{n\sin\left(\frac{\pi x}{n}\right)}\right)^{\beta^2}\left(\frac{\sin(\pi x)}{n}\right)^{2(1-n)}\frac{1}{4^n\sin^2\left(\frac{\pi x}{n}\right)}\frac{\Gamma^2\left(\frac{1-n+n\csc\pi x}{2}\right)}{\Gamma^2\left(\frac{1+n+n\csc\pi x}{2}\right)}. \quad (4.3.22)$$

This can be rewritten in the suggestive form

$$G^{(n)}(\rho_{i\partial\phi}\|\rho_{V_\beta}) = \tilde{C}_{\alpha=0,\beta}(n,x)G^{(n)}(\rho_{i\partial\phi}\|\rho_{GS})G^{(n)}(\rho_{GS}\|\rho_{V_\beta}), \quad (4.3.23)$$

which shows that $G^{(n)}(\rho_{i\partial\phi}\|\rho_{V_\beta})$ is the product of two $G^{(n)}$ of $\rho_{i\partial\phi}$ or ρ_{V_β} with respect to the ground state times an "interaction term" given by $\tilde{C}_{\alpha=0,\beta}(n,x)$.

Now in order to take the derivative with respect to n of (4.3.22) and take the replica limit for the ReE, we would need the analytic continuation to $n\in\mathbb{C}$ of the (finite) sum $\sum_{k=1}^{n-1}\cot\frac{\pi}{n}(z+k)$. This is easily done by using an integral representation of the cotangent an inverting the sum with the integral. However, this is not necessary because in the replica limit (1.4.2), these contributions are multiplied by a term vanishing for $n\to 1$. Therefore it is straightforward to derive an analytic expression for the ReE, which ultimately reads

$$S(\rho_{i\partial\phi}\|\rho_{V_\beta}) = (2+\beta^2)[1-\pi x\cot(\pi x)] + 2\log(2\sin(\pi x)) + 2\psi_0\left(\frac{\csc(\pi x)}{2}\right) + 2\sin(\pi x) = \\ = S(\rho_{i\partial\phi}\|\rho_{GS}) + S(\rho_{GS}\|\rho_{V_\beta}), \quad (4.3.24)$$

i.e. it is just the sum of the relative entropies of the two operators with respect to the ground state given that the "interaction term" $\tilde{C}_{\alpha=0,\beta}(n,x)$ vanishes in the replica limit.

The RReEs $S_n(\rho_{i\partial\phi}\|\rho_{V_\beta})$ for $n=1,2,3,4$ are reported for $\beta=1,3$ in the four panels of Figure 4.1. As it should, the ReE S_1 is always positive and also monotonous. For $n\neq 1$ we have instead a more complicated behavior. Indeed $S_n(\rho_{i\partial\phi}\|\rho_{V_\beta})$ can be either positive or negative and the range of negativity depends on the values of both n and β. It is easy to see numerically that for any integer n, it exists a critical value $\beta_c(n)$ such that for $\beta>\beta_c(n)$, $S_n(\rho_{i\partial\phi}\|\rho_{V_\beta})$ is always positive, but not always monotonous.

We mention that there are no conceptual difficulties for the calculation of $G^{(n)}(\rho_{V_\beta}\|\rho_{i\partial\phi})$ for finite integer n. However, the computation requires to take $2(n-1)$ derivatives and therefore it is rather involved, especially if one desires a closed form valid for arbitrary n.

4.4 The XX spin-chain as a test of the CFT predictions

The goal of this Section is to check the validity of the formulas presented in the previous Section in a lattice model, a fundamental test that has not yet been performed in the literature.

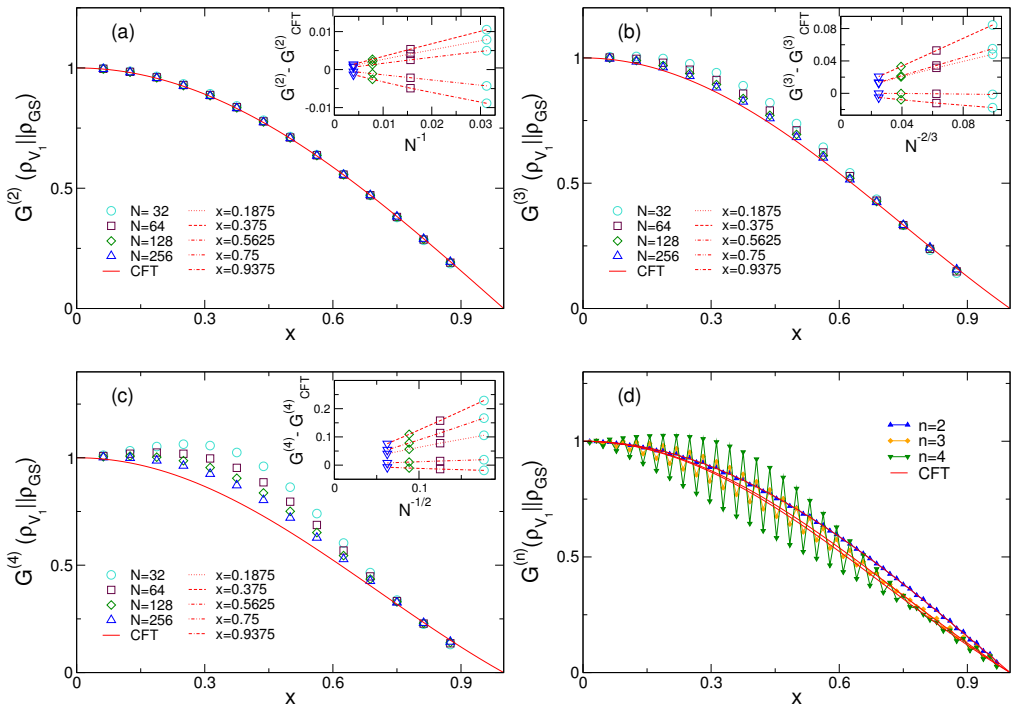

FIGURE 4.2: The quantity $G^{(n)}(\rho_{V_1}\|\rho_{GS})$ as a function of $x = \ell/N$ for different values of n ($= 2, 3, 4$ in panels (a), (b) and (c) respectively) plotted only for even values of ℓ. Different symbols correspond to different system sizes and the red curve is the CFT prediction. The insets show the difference between the data in the XX model and the CFT prediction, against the leading scaling corrections $N^{-2/n}$. Each line corresponds to a given value of x. Panel (d): highlight on the oscillations found with the parity of the block's length for a single chain of total length $N = 64$. Symbols of different colors correspond to different values of n and the red curves are the CFT predictions.

We consider the easiest model to study the entanglement properties, namely the XX spin-chain defined by the hamiltonian

$$H_{XX} = -\frac{1}{4}\sum_{m=1}^{N}\left[\sigma_m^x\sigma_{m+1}^x + \sigma_m^y\sigma_{m+1}^y - h\sigma_m^z\right], \tag{4.4.1}$$

where $\sigma_m^{x,y,z}$ are the Pauli matrices acting on the m-th spin and we assume periodic boundary condition. By a Jordan-Wigner transformation, the spin hamiltonian is mapped into

$$H_{XX} = -\frac{1}{2}\sum_{m=1}^{N}\left[c_m^\dagger c_{m+1} + c_{m+1}^\dagger c_m + 2h\left(c_m^\dagger c_m - \frac{1}{2}\right)\right]. \tag{4.4.2}$$

The ground-state is a partially filled Fermi sea with Fermi-momentum $k_F = \arccos|h|$ and the single-particle dispersion relation $\epsilon_k = |\cos k - h|$, which can be linearized close to the two Fermi points $k = \pm k_F$, ending up with the two chiral components of a massless Dirac fermion which describes the low energy physics of the model. Via bosonization this is nothing but the massless boson considered in the previous Section in CFT formalism.

The hamiltonian (4.4.2) is of the form (1.4.18), with $c_m^\dagger$ and c_m are creation and annihilation operators at the site m, and the discussion of Section 1.4.3 applies. Each eigenstate of the hamiltonian is in correspondence with a set of momenta K, with, e.g., the ground-state corresponding to K being the set of all momenta with absolute value smaller than k_F. Low-lying excited states are obtained by removing/adding some particles in momentum space close to the Fermi sea and are of the gaussian form (1.4.19). Moreover, in the continuum limit, they can be put in one to one correspondence with the action of CFT primary operators onto the vacuum. A detailed discussion on this correspondence between lattice and CFT excitations can be

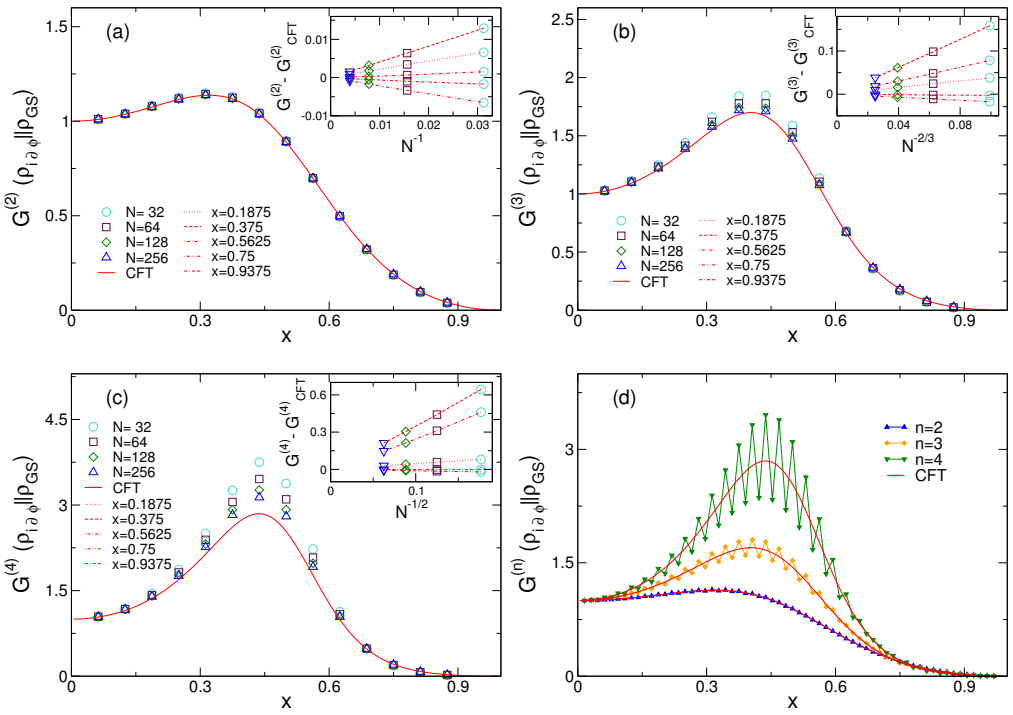

FIGURE 4.3: The quantity $G^{(n)}(\rho_{i\partial\phi}\|\rho_{GS})$ as a function of $x = \ell/N$ for different values of n. The description of the Figure is the same as in Fig. 4.2.

found in Ref. [147]. Here we just mention the two states of our interest. Considering a vanishing external field $h = 0$ which corresponds to a half-filled Fermi sea with $k_F = \pi/2$ and focusing on chains of length N multiples of 4, that at half-filling has $n_F = N/2$ fermions, the CFT state generated by a vertex operator $V_{\beta=1}|0\rangle$ corresponds in the XX chain to a hole-type, whereas the primary operator $(i\partial\phi)$ is associated to the particle-hole excitation.

We use the free fermionic techniques of Section 1.4.3 to test the CFT predictions for the quantities $G^{(n)}(\rho_1\|\rho_1)$, cf. (4.2.15), or equivalently the RREs of integer order $n \geq 2$. Consequently, they represent a very robust test on the validity of all the derivation presented in the previous Section. In particular, through Eq. (1.4.31), we numerically compute the ratio

$$\frac{\mathrm{Tr}\left(\rho_1\rho_0^{n-1}\right)}{\mathrm{Tr}\left(\rho_1^n\right)} \tag{4.4.3}$$

that in the limit $N \to \infty$ with $x = \ell/N$ kept constant should converge to the CFT predictions for $G^{(n)}(\rho_1\|\rho_0)$ in Eq. (4.2.15). We consider the reduced density matrices $\rho_{1,0}$ corresponding to all the states for which we calculated the CFT predictions using the identification between lattice and CFT eigenstates. The corresponding correlation matrices can be found in Ref. [328].

The numerical data for these $G^{(n)}$ between the chiral vertex operator V_1 and the ground state are shown in Figure 4.2 for different values of n and different system sizes. In the same figure we also report the CFT prediction $G^{(n)}(\rho_{V_1}\|\rho_{GS})$ (which we recall equals $G^{(n)}(\rho_{GS}\|\rho_{V_1})$). It is clear that the data converge to the CFT predictions by increasing the system size, but with a slower convergence for higher value of n.

It is very interesting to study quantitatively the convergence of the data to the CFT prediction when increasing N as shown in the insets of the Figure for various n. For the ground-state Rényi entropies $S_n(\ell)$ of free fermionic models, this convergence has been studied analytically in several works [196, 303, 308] and it has been found to be of the form $N^{-2/n}$. These corrections to the scaling found a CFT interpretation in Ref. [307] where it was understood that they originate from the local insertion of a relevant operator at the conical singularities defining the Riemann surface (alternatively can be thought as effects of the entangling

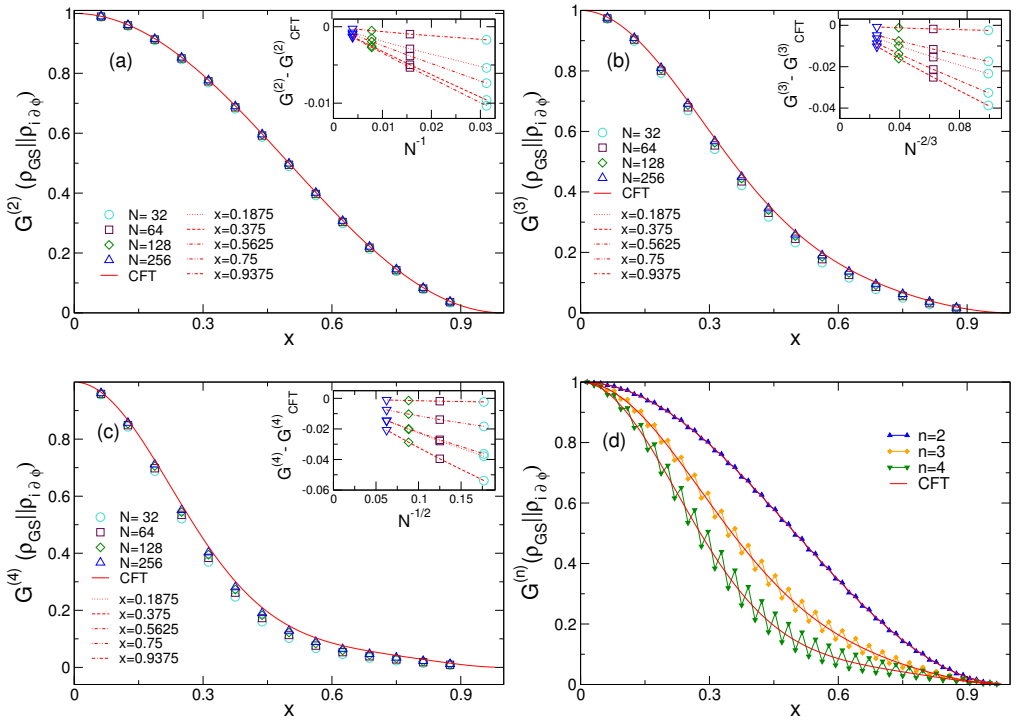

FIGURE 4.4: The quantity $G^{(n)}(\rho_{GS}\|\rho_{i\partial\phi})$ as a function of $x = \ell/N$ for different values of n. The description of the Figure is the same as in Fig. 4.2.

surface [155,156]). Generically, in an infinite system they scale as $\ell^{-2\Delta/n}$ where Δ is the scaling dimension of the operator at the conical singularity and ℓ being the subsystem size. In finite systems, at fixed $x = \ell/N$, one can just replace ℓ by N. For the XX model one finds $\Delta = 1$ [196, 303, 307]. The same corrections of the form $N^{-2/n}$ have also been found for excited states [349]. This is simply explained by the fact that the conical singularities are independent from the state, as studied in more details in [356].

Also in our study of the relative entropies, or more precisely of the quantities $G^{(n)}(\rho_1\|\rho_0)$, the structure of the Riemann surface is not altered by the presence of different fields generating the states. Thus one can safely conjecture that the leading corrections to the scaling must be once again of the form $N^{-2/n}$. For $G^{(n)}(\rho_{V_1}\|\rho_{GS})$, this is confirmed to a great level of accuracy by the insets of Figure 4.2.

In the last panel of Figure 4.2 we also study the effect of the parity of the subsystem size ℓ. In the ground state (as well as in excited states), it is well known that the leading corrections to the scaling are not smooth functions of $x = \ell/L$ but they behave as [303]

$$S_n(\ell) - S_n^{CFT}(\ell) \propto N^{-2/N} f_n(\ell/N)\cos(2k_F\ell). \tag{4.4.4}$$

This oscillating term reduces to $(-1)^\ell$ at half filling $k_F = \pi/2$ (i.e. for zero magnetic field). Again similar oscillations are expected also for $G^{(n)}(\rho_1\|\rho_0)$, as confirmed by the data in Figure 4.2 (d).

In Figures 4.3 and 4.4 we report the data for the replicated ReEs between the ground state and the particle-hole excitation (corresponding in the continuum limit to the state generated by $i\partial\phi$). The overall discussion is very similar to the one above for the state generated by V_β with the data approaching the CFT predictions $G^{(n)}(\rho_{i\partial\phi}\|\rho_{GS})$ and $G^{(n)}(\rho_{GS}\|\rho_{i\partial\phi})$ for large N as $N^{-2/n}$ (and also with pronounced parity effects in panels (d)). As in CFT, these functions are not symmetric under the exchange of the states in the ReE and in fact there is also a pronounced qualitative difference (already observed in CFT): while $G^{(n)}(\rho_{GS}\|\rho_{i\partial\phi})$ is a monotonous function of x (as $G^{(n)}(\rho_{GS}\|\rho_{V_1})$, $G^{(n)}(\rho_{i\partial\phi}\|\rho_{GS})$ grows as x increases from zero, has a maximum at a value depending on n and then decreases.

Finally in Figure 4.5 we report the data corresponding to $G^{(n)}(\rho_{i\partial\phi}\|\rho_{V_1})$. Once again the data approaches the CFT perditions as $N^{-2/n}$ and we find that this is not a monotonous function of x, in analogy

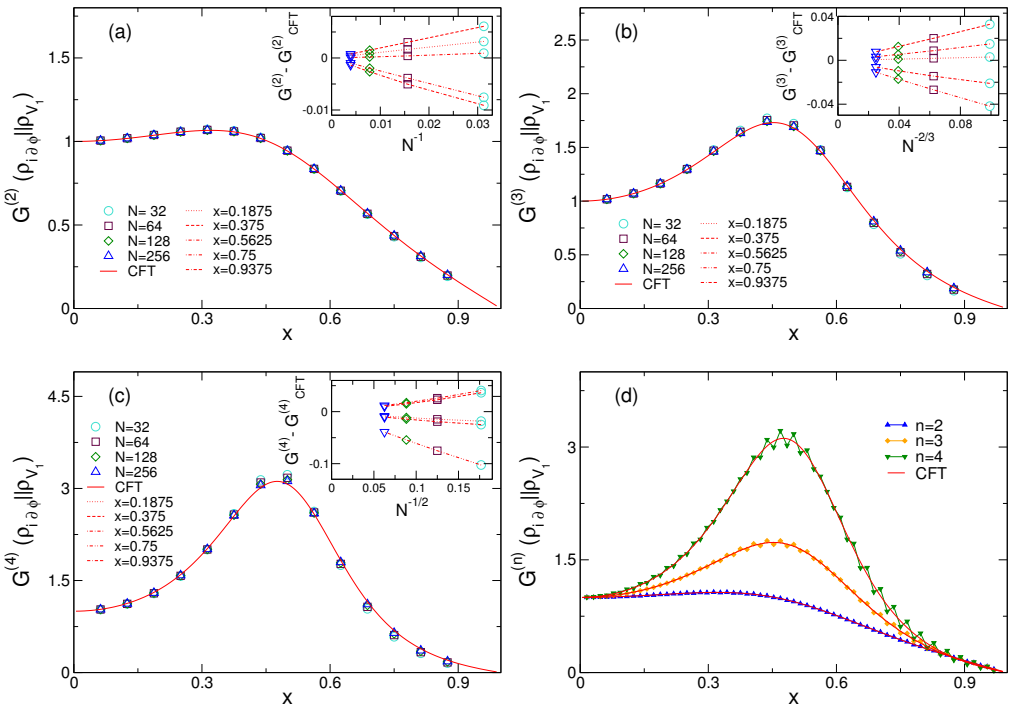

FIGURE 4.5: The quantity $G^{(n)}(\rho_{i\partial\phi}\|\rho_{V_1})$ as a function of $x = \ell/N$ for different values of n. The description of the Figure is the same as in Fig. 4.2.

to $G^{(n)}(\rho_{i\partial\phi}\|\rho_{GS})$.

4.5 Concluding remarks

In this Chapter we applied the replica method [144] to work out several explicit examples of ReE between primary fields of the free bosonic CFT, as well as the RReE (4.1.3). The CFT results have been carefully tested against exact lattice calculations for the XX spin-chain, finding perfect agreement, once corrections to the scaling are properly taken into account. We must mention that we did not manage to work out the analytic continuation in the replica index for all the states we considered. It is, indeed, well known that finding the analytic continuation is not always an easy task and in some cases, it is useful to resort to some approximations. For the ReE, a possible approximation is an expansion for small subsystem presented in Ref. [335] which has also been extended to the case of disjoint intervals [337], but its regime of validity is relatively small. A similar problem occurs also for the REEs of two disjoint intervals [248, 249]. In that case, among the many proposed approximations, an ingenious conformal block expansion has been considered [357, 358] which turned out to describe effectively numerical data although the expansion is not systematic (more on this topic in Chapter 6). It would be interesting to investigate whether some similar approach could be used also for the ReE.

Several generalizations could be worth investigating. For example, one can consider other CFTs (such as Ising or other minimal models) as well as one can study different lattice models both free and interacting. One could also deal with more general excitations, but when more complicated operators correspond to the excited states, the explicit calculations become very involved. For standard REEs, the extension of this kind of analysis to descendants operators is reported in Ref. [350] and in principle may be applied also to the ReE. However, the calculation appears to be very cumbersome and difficult to extend to arbitrary values of the replica index n.

Chapter 5

Trace distance in QFT

Despite the relative entropy provides an interesting quantity to look at to gain insights about two different quantum states, one of the main drawbacks is that it is not a proper distance (mathematically speaking). Among all the possible *metrics* we can borrow from quantum information, here we focus on the trace distance (TrD). In particular, we report on the replica approach to calculate the subsystem TrD for a generic QFT that we recently put forward in Ref. [146]. Restricting to CFT in $(1+1)d$, then, explicit results for the TrDs among the RDMs of several low lying states in $2d$ free massless boson and fermion theories are provided and further compared with numerical calculations in XX and Ising spin chains. This Chapter is based on the Letter [146] and the subsequent paper, Ref. [147].

5.1 Introduction

The problem of measuring the distance between density matrices has been intensively considered in quantum information theory, where several different measures have been introduced, see e.g. [9,59] as reviews. Given two normalized density matrices ρ and σ (i.e. with $\mathrm{Tr}\rho = \mathrm{Tr}\sigma = 1$), an important family of distances is given by (Schatten) n-distances $D_n(\rho,\sigma)$, defined in the Introduction, Eq. (1.2.7). Actually, as long as we are dealing with finite dimensional Hilbert spaces, all distances (including the D_n's) are equivalent, in the sense that they bound each other

$$c_{nm}\, D_n(\rho,\sigma) \leq D_m(\rho,\sigma) \leq c_{mn}\, D_n(\rho,\sigma), \tag{5.1.1}$$

for some constants c_{nm}. However this ceases to be the case for infinite dimensional Hilbert spaces, because the constants c_{nm} depend on the Hilbert space dimension. For this same reason, it is not obvious how to compare distances between RDMs associated with subsystems of different sizes, which is one of the main goals when dealing with the entanglement scaling behavior. Given this state of affairs, it is natural to wonder whether one distance is special compared to the others and, in this respect, it is well known that the TrD

$$D(\rho,\sigma) = \frac{1}{2}\|\rho-\sigma\|_1, \tag{5.1.2}$$

(i.e. Eq. (1.2.7) for $n=1$) has several properties that made it more effective than the others [9, 59, 360]. In particular, an important feature of such metric is that it provides an upper bound for the difference between the expectation values of observables in the two states ρ and σ, i.e.

$$|\mathrm{Tr}(\rho-\sigma)O| \leq \|\rho-\sigma\|_1 \|O\|_\infty = 2D(\rho,\sigma)\|O\|_\infty. \tag{5.1.3}$$

It is clear that the bound (5.1.3) does not depend on the Hilbert space dimension, while it would not be the case for $D_n(\rho\|\sigma)$ with $n \neq 1$. This means that if ρ and σ are "close", also the expectation values of an arbitrary observable O (of finite norm) are "close": we will provide important examples of how choosing the "wrong distance" could lead to misleading results.

In an extended quantum system, especially in a QFT, it is extremely difficult to evaluate the TD (5.1.2), as, for example, discussed in [360]. This is one of the reason why in the literature there has been an intensive

investigation of the relative entropy $S(\rho\|\sigma)$, which bounds the TrD according to the Pinsker's inequality [59]

$$D(\rho,\sigma) \leq \sqrt{\frac{1}{2}S(\rho\|\sigma)}. \tag{5.1.4}$$

In this Chapter, we review and apply the method to compute the TrD developed in Ref. [146], which is based on the path integral representation of the RDMs and an *ad hoc* replica trick, as anticipated in the Introduction, Eq. (1.4.5), and detailed in the following. The method can be applied to many different situations, but here we focus on $1d$ systems described by a $2d$ CFT, with the subsystem consisting of an interval of length ℓ embedded in a circle of length L. In such a setting, entanglement measures as the REEs and EE have been considered. In particular, using the *twist operators* [17, 18, 148] and their operator product expansion (OPE) [248, 357, 358, 361–365], a universal short interval expansion has been derived. This expansion also generalizes to subsystem TrDs between the low-lying excited states in $2d$ CFT.

The remaining part of this Chapter is arranged as follows. In Section 5.2, after presenting in details the replica trick for the TrD, we derive the universal formula of the leading order TrD of one interval in the short interval expansion and exact results for a special class of states. In Section 5.3 we consider the $2d$ free massless compact boson theory and calculate TrD and several n-distances. We test our analytic predictions against exact numerical calculations for the XX spin chain. The same quantities for the $2d$ free massless fermion theory are investigated in Section 5.4 and tested against exact numerical calculations in the critical Ising spin chain. We conclude with discussions in Section 5.5.

5.2 Subsystem trace distance in QFT

The problem in the calculations of the TrD (5.1.2) resides in the presence of the absolute value of the eigenvalues of $\rho_A - \sigma_A$. Because of this absolute value, the only way to directly get the desired quantity would be by explicitly diagonalising $\rho_A - \sigma_A$, a problem that is made even more complicated by the fact that the two RDMs generically do not commute. Absolute values of matrices can be anyhow tackled with a replica trick, an idea first introduced, to the best of our knowledge, by Kurchan [366] and later applied to many different situations [367–370], including to the entanglement negativity [94, 145]. This trick for the TrD, and more generically for all the n-distance for arbitrary real n, works as follows. Given two (Hermitian) density matrices ρ and σ, we have by definition

$$\|\rho-\sigma\|_n^n = \mathrm{Tr}|\rho-\sigma|^n = \sum_i |\lambda_i|^n, \tag{5.2.1}$$

with λ_i being the eigenvalues of $(\rho-\sigma)$. Note that, for n_e being an *even* integer, it holds

$$\mathrm{Tr}|\rho-\sigma|^{n_e} = \mathrm{Tr}(\rho-\sigma)^{n_e}. \tag{5.2.2}$$

Therefore, if we compute $\mathrm{Tr}(\rho-\sigma)^{n_e}$ for generic even integer $n_e = 2,4,\cdots$, we can then consider its analytical continuation to any real number. In case we manage to work out such an analytic continuation, the TrD is then simply obtained as

$$D(\rho_A,\sigma_A) = \frac{1}{2}\lim_{n_e\to 1}\mathrm{Tr}(\rho_A-\sigma_A)^{n_e}. \tag{5.2.3}$$

The calculation of $\mathrm{Tr}(\rho_A-\sigma_A)^n$ for general integer n is instead a relatively simple issue. Indeed, expanding the power of the difference, one just has to compute a sum of the traces of products of ρ_A's and σ_A's, Eq. (1.4.14). For example for $n=2$ we have $\mathrm{Tr}(\rho_A-\sigma_A)^2 = \mathrm{Tr}\rho_A^2 + \mathrm{Tr}\sigma_A^2 - 2\mathrm{Tr}(\rho_A\sigma_A)$ and so on for larger n (but keep in mind that ρ_A and σ_A do not commute). Incidentally, this simplicity is the main reason why in the literature the (Schatten) 2-distance has been largely studied in many applications, instead of the more physical trace norm. We stress that for odd $n = n_o$, $\mathrm{Tr}(\rho_A-\sigma_A)^{n_o}$ does *not* provide the

n_o-distance (because of the absence of the absolute value). Also, the limit $n_o \to 1$ gives the trivial result $\mathrm{Tr}(\rho_A - \sigma_A) = 0$ (in full analogy with what happens for the negativity [94, 145]).

Within QFT, the single objects within the sum (1.4.14) already appeared in the replica trick for the ReE [143, 144], and, in some cases, they have been explicitly computed [143, 144, 328, 335, 336]: this is done as explained in Section 1.4.2, Eq. (1.4.15) (see also Chapter (4)). Still, performing the whole sum and obtaining its analytic continuation is not an easy task. We remind that the method is very general in the sense it applies to generic situations for one-dimensional systems, even if in the following we just focus on eigenstates of CFTs.

5.2.1 The trace distance between primary states in CFT

In this Section, we specialize to the case when the RDMs ρ_A and σ_A correspond to low lying eigenstates of a $2d$ CFT; we focus on periodic systems of total length L and on a subsystem being an interval of length ℓ. Similarly to the discussion in Section 4.2, analytical results can be obtained by looking to a special class of states in a $2d$ CFT. We study the distance between RDMs of orthogonal eigenstates associated to primary operators; as we shall see, while the distance between the entire states is maximal, subsystems may be rather close and they distance has different functional form depending on the considered states.

For a general primary operator $\mathcal{X}$, let $(h_\mathcal{X}, \bar{h}_\mathcal{X})$ be its conformal weights and $\Delta_\mathcal{X} = h_\mathcal{X} + \bar{h}_\mathcal{X}$ and $s_\mathcal{X} = h_\mathcal{X} - \bar{h}_\mathcal{X}$ its scaling dimension and spin, respectively. We exploit Eq. (1.4.14) to compute $\mathrm{Tr}\,(\rho_\mathcal{X} - \rho_\mathcal{Y})^n$ for two RDMs associated to two primary operators $\mathcal{X}$ and $\mathcal{Y}$. For such states, as discussed in the previous Chapter, Section 4.2, each term of the sum corresponds to a correlation function with insertions of the fields $\mathcal{X}$ and $\mathcal{Y}$ on the Riemann surface [349, 371],

$$\mathrm{Tr}\,(\rho_\mathcal{Y}^m \rho_\mathcal{X}^n) = \frac{Z_{n+m}(A)}{Z_1^{m+n}} \frac{\langle \prod_{k=1}^m \mathcal{Y}(w_k)\mathcal{Y}^\dagger(w'_k) \prod_{i=1+m}^{n+m} \mathcal{X}(w_i)\mathcal{X}^\dagger(w'_i)\rangle_{\mathcal{R}_n}}{\langle \mathcal{Y}(w_1)\mathcal{Y}^\dagger(w'_1)\rangle_{\mathcal{R}_1}^m \langle \mathcal{X}(w_1)\mathcal{X}^\dagger(w'_1)\rangle_{\mathcal{R}_1}^n}. \tag{5.2.4}$$

In the case of A being a single interval, in order to calculate the correlators appearing in (5.2.4), one could either introduce twist fields or consider a conformal transformation mapping the Riemann surface to the complex plane, where the correlators themselves can be explicitly evaluated. While the representation in terms of twist field is a powerful tool to get the short-interval expansion, this second method allows in some cases to get the full analytic result for an interval of arbitrary length.

We first consider this second approach, in which case case, the mapping to the complex plane can be achieved, e.g., by

$$f(z) = \left(\frac{z - e^{2\pi \mathrm{i}\ell/L}}{z-1}\right)^{1/n}. \tag{5.2.5}$$

The final result for the entire sum in Eq. (1.4.14) can be then written as a sum of such correlation functions as follows

$$\begin{aligned}\mathrm{Tr}(\rho_\mathcal{X} - \rho_\mathcal{Y})^n = c_n \Big(\frac{L}{\pi\epsilon}\sin\frac{\pi\ell}{L}\Big)^{-4h_n} \\ \times \sum_{\mathcal{S}} \Big\{ (-)^{|\mathcal{S}|} \mathrm{i}^{2(|\bar{\mathcal{S}}|s_\mathcal{X} + |\mathcal{S}|s_\mathcal{Y})} \Big(\frac{2}{n}\sin\frac{\pi\ell}{L}\Big)^{2(|\bar{\mathcal{S}}|\Delta_\mathcal{X} + |\mathcal{S}|\Delta_\mathcal{Y})} \\ \times \Big\langle \Big[\prod_{j\in\bar{\mathcal{S}}} \Big(f_{j,\ell}^{h_\mathcal{X}} \bar{f}_{j,\ell}^{\bar{h}_\mathcal{X}} f_j^{h_\mathcal{X}} \bar{f}_j^{\bar{h}_\mathcal{X}} \mathcal{X}(f_{j,\ell}, \bar{f}_{j,\ell})\mathcal{X}^\dagger(f_j, \bar{f}_j)\Big)\Big] \\ \times \Big[\prod_{j\in\mathcal{S}} \Big(f_{j,\ell}^{h_\mathcal{Y}} \bar{f}_{j,\ell}^{\bar{h}_\mathcal{Y}} f_j^{h_\mathcal{Y}} \bar{f}_j^{\bar{h}_\mathcal{Y}} \mathcal{Y}(f_{j,\ell}, \bar{f}_{j,\ell})\mathcal{Y}^\dagger(f_j, \bar{f}_j)\Big)\Big]\Big\rangle_\mathbb{C}\Big\}. \end{aligned} \tag{5.2.6}$$

Here $\bar{\mathcal{S}} = \mathcal{S}_0/\mathcal{S}$, $f_j = \mathrm{e}^{\frac{2\pi\mathrm{i}j}{n}}$ and $f_{j,\ell} = \mathrm{e}^{\frac{2\pi\mathrm{i}}{n}(j+\frac{\ell}{L})}$. Eq. (5.2.6) relates the even (Schatten) n-distances between the RDM of two primary states $|\mathcal{X}\rangle$ and $|\mathcal{Y}\rangle$ to the $2n$-point correlation function of the corresponding primary fields on the complex plane. Such correlation functions may be calculated in some specific cases, as we shall see, but in general it is not possible to work them out in a closed form as function of n in

order to obtain the analytic continuation for the TrD. Anyway, even if too complicated to extract direct information, from Eq. (5.2.6) we can already draw one very important conclusion. Indeed, in the limit $n \to 1$ (independently of the parity of n) the dependence on the ultraviolet cutoff ϵ washes out. Importantly, this means that the TrD is a *universal, cutoff independent*, scale invariant function of ℓ/L (i.e., it does not separately depend on ℓ and L). This is another very important property that puts the TrD on a special foot compared to the other Schatten distances that instead are cutoff dependent and not scale invariant (but only scale covariant since they have non zero dimension). For this reason, as for other quantities discussed above (cfr. Eqs. (4.2.4), (4.2.15)), it is worth and useful to introduce a *scale-invariant* and *cutoff-independent* ratio for the n-distance as

$$\mathcal{D}_n(\rho_A, \sigma_A) = \frac{1}{2} \frac{\mathrm{Tr}|\rho_A - \sigma_A|^n}{\mathrm{Tr}\rho_0^n}, \tag{5.2.7}$$

in which ρ_0 is the RDM of the subsystem A in the CFT ground state. Within this normalisation by $\mathrm{Tr}\rho_0^n$, the function $\mathcal{D}_n$ in Eq. (5.2.7) has the simpler expression in CFT. When there is no ambiguity, we will also call $\mathcal{D}_n(\rho, \sigma)$ loosely as the n-distance, but the true n-distance is instead

$$D_n(\rho_A, \sigma_A) = [\mathcal{D}_n(\rho_A, \sigma_A)\, \mathrm{Tr}\rho_0^n]^{1/n}. \tag{5.2.8}$$

The replica limit (5.2.3) now takes the form

$$D(\rho_A, \sigma_A) = \lim_{n_e \to 1} \mathcal{D}_{n_e}(\rho_A, \sigma_A). \tag{5.2.9}$$

Eq. (5.2.8) also highlights one of the main reasons why the TrD is better than all other n-distances. In CFT $\mathcal{D}_n(\rho_A, \sigma_A)$ is always a smooth function of ℓ/L in the interval $[0, 1]$ and so it is its replica limit $D(\rho_A, \sigma_A)$. Conversely, since $\mathrm{Tr}\rho_0^n$ goes to zero as $L \to \infty$, irrespective of the value of ℓ/L, the n-distance always vanishes in the thermodynamic limit. Consequently, a study of n-distance may artificially signal the closeness of two RDMs that actually are very different.

5.2.2 Short interval expansion

The OPE of twist operators [248, 357, 361, 362] can be used to write down and asymptotic expansion of the multipoint correlation functions of the twist operators. For example, in terms of quasiprimary operators and their derivatives in the n-fold theory CFT^n (see Section 1.4.2), the OPE of twist operators takes the form [362]

$$\mathcal{T}(z, \bar{z})\bar{\mathcal{T}}(0, 0) = \frac{c_n \epsilon^{2(h_n + \bar{h}_n)}}{z^{2h_n} \bar{z}^{2\bar{h}_n}} \sum_K d_K \sum_{r,s \geq 0} \frac{a_K^r}{r!} \frac{\bar{a}_K^s}{s!} z^{h_K + r} \bar{z}^{\bar{h}_K + s} \partial^r \bar{\partial}^s \Phi_K(0, 0). \tag{5.2.10}$$

The summation K is over all the orthogonal quasiprimary operators Φ_K in CFT^n, with conformal weights $(h_K, \bar{h}_K)$, and they can be constructed from the orthogonal quasiprimary operators in the original one-fold CFT. In Eq. (5.2.10) the following constants have been defined

$$a_K^r \equiv \frac{C^r_{h_K + r - 1}}{C^r_{2h_K + r - 1}}, \qquad \bar{a}_K^s \equiv \frac{C^s_{\bar{h}_K + s - 1}}{C^s_{2\bar{h}_K + s - 1}}, \qquad \text{with} \quad C_x^y = \frac{\Gamma(x+1)}{\Gamma(y+1)\Gamma(x-y+1)}. \tag{5.2.11}$$

The OPE coefficients, moreover, can be calculated as [248]

$$d_K = \frac{1}{\alpha_K \ell^{h_K + \bar{h}_K}} \lim_{z \to \infty} z^{2h_K} \bar{z}^{2\bar{h}_K} \langle \Phi_K(z, \bar{z}) \rangle_{\mathcal{R}_n}, \tag{5.2.12}$$

with α_K being the normalisation of Φ_K and $\mathcal{R}_n$ being the n-fold Riemann surface for one interval $A = [0, \ell]$ on the complex plane. The expectation value on $\mathcal{R}_n$ is estimated by mapping to the complex plane.

For a general translationally invariant state ρ, in the OPE of twist operators we only need to consider CFT^n quasiprimary operators that are direct products of the quasiprimary operators $\{\mathcal{X}\}$ of the original

CFT [358, 364]

$$\Phi_K^{j_1,j_2,\cdots,j_k} = \mathcal{X}_1^{j_1}\cdots\mathcal{X}_k^{j_k}. \tag{5.2.13}$$

From the OPE coefficient of $\mathcal{X}_1^{j_1}\cdots\mathcal{X}_k^{j_k}$, which we denote by $d_{\mathcal{X}_1\cdots\mathcal{X}_k}^{j_1\cdots j_k}$, one can define the coefficient [364]

$$b_{\mathcal{X}_1\cdots\mathcal{X}_k} = \sum_{0\le j_1,\cdots,j_k\le n-1} d_{\mathcal{X}_1\cdots\mathcal{X}_k}^{j_1\cdots j_k}, \tag{5.2.14}$$

where the sum is constrained in order to avoid overcounting. For examples, for $\mathcal{X}_{j_1}\mathcal{X}_{j_2}$ one has $0\le j_1<j_2\le n-1$, and for $\mathcal{X}_{j_1}\mathcal{X}_{j_2}\mathcal{Y}_{j_3}$ with $\mathcal{X}\neq\mathcal{Y}$ one has $0\le j_1,j_2,j_3\le n-1$ with constraints $j_1<j_2$, $j_1\neq j_3$, $j_2\neq j_3$. For the RDM ρ_A of such states, one finds the following expansion [358, 363–365]

$$\mathrm{Tr}\rho_A^n = c_n\left(\frac{\ell}{\epsilon}\right)^{-4h_n}\Big[1+\sum_{k=1}^{n}\sum_{\{\mathcal{X}_1,\cdots,\mathcal{X}_k\}}\ell^{\Delta_{\mathcal{X}_1}+\cdots+\Delta_{\mathcal{X}_k}}b_{\mathcal{X}_1\cdots\mathcal{X}_k}\langle\mathcal{X}_1\rangle_\rho\cdots\langle\mathcal{X}_1\rangle_\rho\Big], \tag{5.2.15}$$

with the summation being over all the sets of orthogonal nonidentity quasiprimary operators $\{\mathcal{X}\}$. This allows to derive the short interval behaviour of the Rényi and entanglement entropies.

We then get to the TrD. Although Eq. (5.2.6) is model dependent and generically complicated to be worked out analytically, also in this case is indeed possible to use the OPE of twist fields to obtain a general result in the limit $\ell\ll L$.

Let ρ_A, σ_A be the RDMs of two CFT eigenstates ρ, σ, not only primary and quasiprimary states, but also descendents or even thermal states. The OPE of twist fields, Eq. (5.2.10), leads to

$$\mathrm{Tr}_A(\rho_A-\sigma_A)^n = c_n\left(\frac{\ell}{\epsilon}\right)^{-4h_n}\sum_{\{\mathcal{X}_1,\cdots,\mathcal{X}_n\}}\ell^{\Delta_{\mathcal{X}_1}+\cdots+\Delta_{\mathcal{X}_n}}b_{\mathcal{X}_1\cdots\mathcal{X}_n}\big(\langle\mathcal{X}_1\rangle_\rho-\langle\mathcal{X}_1\rangle_\sigma\big)\cdots\big(\langle\mathcal{X}_n\rangle_\rho-\langle\mathcal{X}_n\rangle_\sigma\big). \tag{5.2.16}$$

For two different states ρ, σ, quasiprimary operators ϕ such that

$$\langle\phi\rangle_\rho-\langle\phi\rangle_\sigma\neq 0, \tag{5.2.17}$$

should exist. Among these, we select the operator ϕ with the smallest scaling dimension $\Delta_\phi=h_\phi+\bar h_\phi$, and the spin is given by $s_\phi=h_\phi-\bar h_\phi$, where $(h_\phi,\bar h_\phi)$ denote the corresponding conformal weights. We choose ϕ to be Hermitian and so the normalisation factor is $\alpha_\phi>0$. Note that ϕ can only be bosonic, i.e. s_ϕ is an integer, otherwise $\langle\phi\rangle_\rho=\langle\phi\rangle_\sigma=0$. When s_ϕ is an even integer $\langle\phi\rangle_\rho$, $\langle\phi\rangle_\sigma$ are real, and when s_ϕ is an odd integer $\langle\phi\rangle_\rho$, $\langle\phi\rangle_\sigma$ are pure imaginary. Moreover, we only consider unitary CFTs, so that $h_\phi>0$, $\bar h_\phi>0$.

Here, for simplicity, we only consider the case when only one of such operators exists (non-degenerate case). For a general even integer n_e, we get

$$\mathrm{Tr}(\rho_A-\sigma_A)^{n_e} = c_{n_e}\left(\frac{\ell}{\epsilon}\right)^{-4h_{n_e}}\big[\ell^{n_e\Delta_\phi}b_{\phi^{n_e}}\big(\langle\phi\rangle_\rho-\langle\phi\rangle_\sigma\big)^{n_e}+o(\ell^{n_e\Delta_\phi})\big], \tag{5.2.18}$$

with ϕ^{n_e} denoting the direct product of n_e ϕ's. Note that $b_{\phi^{n_e}}=d_{\phi^{n_e}}^{0\cdots(n_e-1)}$. Then, we consider the analytical continuation in n_e and get $\mathrm{Tr}|\rho_A-\sigma_A|^{n_e}$ for a general real number. In particular, for $n_e\to 1$, this leads to the desired universal leading order term of the TrD in short interval expansion

$$D(\rho_A,\sigma_A) = \frac{x_\phi\ell^{\Delta_\phi}}{2}\left|\frac{\langle\phi\rangle_\rho-\langle\phi\rangle_\sigma}{\sqrt{\alpha_\phi}}\right|+o(\ell^{\Delta_\phi}). \tag{5.2.19}$$

Here α_ϕ is the normalisation of the field ϕ (in most of the cases $\alpha_\phi = 1$), and the to-be-determined coefficient x_ϕ is given by the replica limit ($n_e = 2p,\ p = 1, 2, \cdots$)

$$x_\phi = \lim_{p\to 1/2} \mathrm{i}^{2ps_\phi} \alpha_\phi^p d_{\phi^{2p}}^{0\cdots(2p-1)} = \lim_{p\to 1/2} \frac{\mathrm{i}^{2ps_\phi}}{\alpha_\phi^p (2p)^{2p\Delta_\phi}} \Big\langle \prod_{j=0}^{2p-1} \left[f_j^{h_\phi} \bar{f}_j^{\bar{h}_\phi} \phi(f_j, \bar{f}_j) \right] \Big\rangle_{\mathbb{C}}, \quad f_j = \mathrm{e}^{\frac{\pi \mathrm{i} j}{p}}. \tag{5.2.20}$$

Note that in (5.2.20), we did not keep track of the Schwarzian derivative part in the conformal transformation of the quasiprimary operator ϕ because it just cancels out in the limit $n_e \to 1$ (i.e. $p \to 1/2$), when using (5.2.12) to calculate the OPE coefficient $d_{\phi^{n_e}}^{0\cdots(n_e-1)}$.

We stress that Eq. (5.2.19) only applies to the case with no degeneracy at scaling dimension Δ_ϕ. We will see that one can relax this condition while applying to the specific case of the free boson. We also mention that, in a similar fashion, the universal leading order of the relative entropy in short interval expansion was derived [335, 336, 365]

$$S(\rho_A \| \sigma_A) = \frac{\sqrt{\pi}\Gamma(\Delta_\phi + 1)\ell^{2\Delta_\phi}}{2^{2(\Delta_\phi+1)}\Gamma(\Delta_\phi + \frac{3}{2})} \frac{(\langle\phi\rangle_\rho - \langle\phi\rangle_\sigma)^2}{\mathrm{i}^{2s_\phi}\alpha_\phi} + o(\ell^{2\Delta_\phi}). \tag{5.2.21}$$

with ϕ a quasiprimary operator with the smallest scaling dimension among the ones that satisfing Eq. (5.2.17). However, differently from the trace distance, this time in the degenerate case, we just need to sum all the quasiprimary operators ϕ satisfying the constraint (5.2.17).

From Eq. (5.2.20) and for an integer $p = 1, 2, \cdots$, the replica limit can be obtained using the function $F_\phi^{(p)}(\ell/L)$ defined in Eq. (4.2.4) and rewritten as

$$F_\phi^{(p)}\left(\frac{\ell}{L}\right) = \frac{\mathrm{i}^{2ps_\phi}}{\alpha_\phi^p}\left(\frac{2}{p}\sin\frac{\pi\ell}{L}\right)^{2p\Delta_\phi} \Big\langle \prod_{j=0}^{p-1} \left[f_{j,\ell}^{h_\phi} \bar{f}_{j,\ell}^{\bar{h}_\phi} f_j^{h_\phi} \bar{f}_j^{\bar{h}_\phi} \phi(f_{j,\ell}, \bar{f}_{j,\ell}) \phi^\dagger(f_j, \bar{f}_j) \right] \Big\rangle_{\mathbb{C}},$$

where $f_{j,\ell} = \mathrm{e}^{\frac{2\pi\mathrm{i}}{p}(j+\frac{\ell}{L})}, f_j = \mathrm{e}^{\frac{2\pi\mathrm{i}j}{p}}$. In fact, when ϕ is Hermitian we have $\phi^\dagger = \phi$ and so

$$x_\phi = \frac{F_\phi^{(1/2)}(1/2)}{2^{2\Delta_\phi}}. \tag{5.2.22}$$

Furthermore, if ϕ is a primary operator, $F_\phi^{(p)}(\ell/L)$ is related to the p-th order Rényi entropy $S_{A,\phi}^{(p)}(\ell)$ for $A = [0, \ell]$ in the state $|\phi\rangle$

$$F_\phi^{(p)}(\ell/L) = \mathrm{e}^{-(p-1)[S_{A,\phi}^{(p)}(\ell) - S_{A,0}^{(p)}(\ell)]}. \tag{5.2.23}$$

In Refs. [349, 371], Eq. (5.2.23) has been explicitly evaluated for several operators and in some cases also the analytic continuation is available [355]. Note that (5.2.23) only applies to the case that ϕ is a primary operator, while (5.2.22) also applies to the case that ϕ is a quasiprimary operator.

Finally we mention that from the inequality (5.1.4) and from the universal leading order of the relative entropy (5.2.21), one can get a universal upper bound to the coefficient x_ϕ, solely depending on the scaling dimension

$$x_\phi \le x_{\max}(\Delta_\phi) = \sqrt{\frac{\sqrt{\pi}\Gamma(\Delta_\phi + 1)}{2^{2\Delta_\phi+1}\Gamma(\Delta_\phi + \frac{3}{2})}}. \tag{5.2.24}$$

We will check such bound for various examples in the boson and fermion theories.

5.2.3 Exact general result for the 2-distance from the ground state

We mention that the second (Schatten) norm can be straightforwardly obtained between ground state ρ_0 and a primary state ρ_ϕ. Indeed, we have

$$\mathcal{D}_2(\rho_0,\rho_\phi) = \frac{1}{2}\frac{\mathrm{Tr}(\rho_0-\rho_\phi)^2}{\mathrm{Tr}\rho_0^2} = \frac{1}{2}\Big(1+\frac{\mathrm{Tr}\rho_\phi^2}{\mathrm{Tr}\rho_0^2}-\frac{2\mathrm{Tr}\rho_0\rho_\phi}{\mathrm{Tr}\rho_0^2}\Big), \tag{5.2.25}$$

on which the second term is just the universal function $F_\phi^{(2)}(\ell/L)$ in (5.2.22), while the last term is just a two point function in a two-sheeted surface given by

$$\frac{\mathrm{Tr}(\rho_\phi\rho_0)}{\mathrm{Tr}\rho_0^2} = \Big(\frac{\sin\frac{\pi\ell}{L}}{2\sin\frac{\pi\ell}{2L}}\Big)^{2\Delta_\phi}, \tag{5.2.26}$$

where Δ_ϕ is scaling dimension of ϕ. Hence, we finally have

$$\mathcal{D}_2(\rho_0,\rho_\phi) = \frac{1+F_\phi^{(2)}(\ell/L)}{2} - \Big(\cos\frac{\pi\ell}{2L}\Big)^{2\Delta_\phi}. \tag{5.2.27}$$

If in (5.2.25) we replace ρ_0 with a primary state, the only difference is that $\mathrm{Tr}\rho_{\phi_1}\rho_{\phi_2}$ is a four-point function in the 2-sheeted Riemann surface. The latter can be easily calculated on a case by case basis, but it has not a simple expression as (5.2.27). Notice that the property $F_\phi^{(2)}(\ell/L)\geq 1$ [349] ensures that the rhs of (5.2.27) is non negative, as it should.

5.3 Free massless compact boson

In this Section, we consider the $2d$ free massless compact boson theory (i.e. with the target space being a circle of finite radius) defined on an infinite cylinder of circumference L, usually denoted as a Luttinger liquid in condensed matter. The model has been introduced in Section 4.3 and further details can be found in [83]. We recall that the boson field has diffeomorphic ϕ and anti-diffeomorphic part $\bar\phi$. The states in which we are interested are those generated by the action of the following operators: the identity operator $\mathbb{I}$, with conformal weights $(0,0)$, and its descendent at the second level, the stress tensors T and $\bar T$ with conformal weights $(2,0)$, $(0,2)$; the currents $J = \mathrm{i}\partial\phi$, $\bar J = \mathrm{i}\bar\partial\bar\phi$ and $J\bar J$ whose conformal weights are given by $(1,0)$, $(0,1)$ and $(1,1)$, respectively; the vertex operators $V_{\alpha,\bar\alpha} = \exp(\mathrm{i}\alpha\phi + \mathrm{i}\bar\alpha\bar\phi)$ with conformal weights $(\alpha^2/2, \bar\alpha^2/2)$. While T and $\bar T$ are quasiprimary operators, all the others are primary operators. We denote the ground state as $|0\rangle$, and the low energy excited states are constructed by acting on it with a primary operator, obtaining the following set of states: $|V_{\alpha,\bar\alpha}\rangle$, $|J\rangle$, $|\bar J\rangle$, $|J\bar J\rangle$. We denote the RDMs of A in these states, respectively, as $\rho_{\alpha,\bar\alpha}$, ρ_J, $\rho_{\bar J}$, $\rho_{J\bar J}$ and ρ_0 for the ground state. Note that $\rho_{0,0} = \rho_0$.

5.3.1 Short interval results

In this subsection we report the explicit form of the short distance expansion for all the states we consider for the free boson. The general form is always given by Eq. (5.2.19) with x_ϕ in (5.2.20) or equivalently (5.2.22). Here we identify the leading operator ϕ contributing to each distance and explicitly provide the analytic continuation for x_ϕ.

Vertex-Vertex distance: non-degenerate case. We first consider the distance between two states generated by the a vertex operators, namely $|V_{\alpha,\bar\alpha}\rangle$ and $|V_{\alpha',\bar\alpha'}\rangle$. The leading operators entering in the OPE are the primaries J and $\bar J$ with expectation values

$$\langle J\rangle_{\alpha,\bar\alpha} = \frac{2\pi\mathrm{i}\alpha}{L}, \qquad \langle\bar J\rangle_{\alpha,\bar\alpha} = -\frac{2\pi\mathrm{i}\bar\alpha}{L}. \tag{5.3.1}$$

They are both operators with minimal dimension $\Delta_J = \Delta_{\bar{J}} = 1$ and we use the normalisation $\alpha_J = 1$. The CFT formula (5.2.19) only applies to the case with no degeneracies in the sense of Eq. (5.2.17): this implies for the vertex operator that either $\alpha = \alpha'$ or $\bar{\alpha} = \bar{\alpha}'$, else both J and $\bar{J}$ would contribute. At this point, for the non-degenerate case, the only missing factor is x_J (or $x_{\bar{J}}$). This can be read off Eqs. (5.2.22) and (5.2.23). Indeed the REEs in the current state have been derived in the form of a determinant in [349, 371] and analytically continued in [355]. The final result reads [355]

$$F_J^{(p)}(\ell/L) = F_{\bar{J}}^{(p)}(\ell/L) = \Big(\frac{2}{p}\sin\frac{\pi\ell}{L}\Big)^{2p}\frac{\Gamma^2\big(\frac{1+p+p\csc\frac{\pi\ell}{L}}{2}\big)}{\Gamma^2\big(\frac{1-p+p\csc\frac{\pi\ell}{L}}{2}\big)}. \tag{5.3.2}$$

Using such result and plugging $F_J^{(1/2)}(1/2)$ in Eq. (5.2.22), we get

$$x_J = x_{\bar{J}} = \frac{1}{\pi}. \tag{5.3.3}$$

Notice that they satisfy the bound (5.2.24) with $x_{\max}(1) = 1/\sqrt{6}$. Finally, putting all pieces together in Eq. (5.2.19) we get the leading orders of the TrDs:

$$D(\rho_{\alpha,\bar{\alpha}},\rho_{\alpha',\bar{\alpha}}) = \frac{|\alpha-\alpha'|\ell}{L} + o\Big(\frac{\ell}{L}\Big), \qquad D(\rho_{\alpha,\bar{\alpha}},\rho_{\alpha,\bar{\alpha}'}) = \frac{|\bar{\alpha}-\bar{\alpha}'|\ell}{L} + o\Big(\frac{\ell}{L}\Big). \tag{5.3.4}$$

Vertex-Current distance: non-degenerate case. Then we consider the TrD between a vertex state $|V_{\alpha,\bar{\alpha}}\rangle$ and one of the three current states $|J\rangle$, $|\bar{J}\rangle$, $|J\bar{J}\rangle$. The OPE is again dominated by the current operator, so to apply Eq. (5.2.19) we need the expectation value of the current in the vertex state, as in Eq. (5.3.1), and also the expectation values of $J, \bar{J}$ in the current states $|J\rangle$, $|\bar{J}\rangle$, $|J\bar{J}\rangle$. They are simply given by

$$\langle J\rangle_J = \langle J\rangle_{\bar{J}} = \langle J\rangle_{J\bar{J}} = \langle\bar{J}\rangle_J = \langle\bar{J}\rangle_{\bar{J}} = \langle\bar{J}\rangle_{J\bar{J}} = 0. \tag{5.3.5}$$

In this case, to apply Eq. (5.2.19), the non degeneracy condition implies either $\alpha = 0$ or $\bar{\alpha} = 0$, for which we simply get (using also Eq. (5.3.3))

$$\begin{aligned} &D(\rho_J,\rho_{\alpha,0}) = D(\rho_{\bar{J}},\rho_{0,\alpha}) = \frac{|\alpha|\ell}{L} + o\Big(\frac{\ell}{L}\Big), \qquad D(\rho_J,\rho_{0,\bar{\alpha}}) = D(\rho_{\bar{J}},\rho_{\bar{\alpha},0}) = \frac{|\bar{\alpha}|\ell}{L} + o\Big(\frac{\ell}{L}\Big), \\ &D(\rho_{J\bar{J}},\rho_{\alpha,0}) = D(\rho_{J\bar{J}},\rho_{0,\alpha}) = \frac{|\alpha|\ell}{L} + o\Big(\frac{\ell}{L}\Big). \end{aligned} \tag{5.3.6}$$

When both α and $\bar{\alpha}$ are non zero, we are in the degenerate case which will be considered in the following.

Instead, if $\alpha = \bar{\alpha} = 0$ (i.e. for the distance between the current and the ground state), the leading term vanishes and we have to go to the next operator in the OPE which is the stress energy tensor. This can be obtained as follows. The expectation values of the stress tensors in a general primary state $|\mathcal{X}\rangle$ with conformal weights $(h_{\mathcal{X}},\bar{h}_{\mathcal{X}})$ are given by

$$\langle T\rangle_{\mathcal{X}} = \frac{\pi^2 c}{6L^2} - \frac{4\pi^2 h_{\mathcal{X}}}{L^2}, \quad \langle\bar{T}\rangle_{\mathcal{X}} = \frac{\pi^2 c}{6L^2} - \frac{4\pi^2\bar{h}_{\mathcal{X}}}{L^2}. \tag{5.3.7}$$

This result together with Eq. (5.2.19), with the minimal dimension quasiprimary being one of the stress tensors, eventually leads to

$$D(\rho_0,\rho_J) = D(\rho_0,\rho_{\bar{J}}) = x_T\frac{2\sqrt{2}\pi^2\ell^2}{L^2} + o\Big(\frac{\ell^2}{L^2}\Big), \tag{5.3.8}$$

In this case, obtaining an analytic result for the coefficient x_T is much more complicated because T is not primary and Eq. (5.2.23) does not apply. The general expression for x_T may be written as

$$x_T = \lim_{p\to 1/2} \left(\frac{2}{c}\right)^p \left\langle \prod_{j=0}^{2p-1} [f_j^2 T(f_j)] \right\rangle_{\mathrm{C}'} \qquad f_j = \mathrm{e}^{\frac{\pi i j}{p}}. \tag{5.3.9}$$

This result may seem, at first, quite surprising because in the mapping from the Riemann surface to the complex plane anomalous terms are present since T is not primary. This is indeed the case for the OPE coefficient for $n \neq 1$. However, since for $n = 1$ the transformation from the n-sheeted surface to the plane is in $SL(2,\mathrm{C})$, then the Schwarzian derivative vanishes, and so all the anomaly terms are at least of order $(n-1)$ [372, 373]. Thus they cancel in the $n \to 1$ limit, i.e. in the $p \to 1/2$ limit. Anyhow, getting a general closed form for Eq. (5.3.9) is rather difficult and hence, an approximate value for this unknown coefficients x_T will be extracted from the numerical results in the XX spin chain later on.

Finally let us notice that from the decoupling of the holomorphic and anti-holomorphic sectors we simply have

$$\frac{\mathrm{Tr}(\rho_J - \rho_{J\bar{J}})^n}{\mathrm{Tr}\rho_0^n} = \frac{\mathrm{Tr}\rho_J^n}{\mathrm{Tr}\rho_0^n} \frac{\mathrm{Tr}(\rho_0 - \rho_{\bar{J}})^n}{\mathrm{Tr}\rho_0^n}. \tag{5.3.10}$$

In the limit $n \to 1$, this decoupling leads to

$$D(\rho_J, \rho_{J\bar{J}}) = D(\rho_0, \rho_{\bar{J}}), \tag{5.3.11}$$

and, using also Eq. (5.3.8), we get the OPE

$$D(\rho_{\bar{J}}, \rho_{J\bar{J}}) = D(\rho_J, \rho_{J\bar{J}}) = x_T \frac{2\sqrt{2}\pi^2\ell^2}{L^2} + o\Big(\frac{\ell^2}{L^2}\Big). \tag{5.3.12}$$

Vertex-Vertex and Vertex-Current distances: degenerate case. In the $2d$ free massless boson theory, we can actually generalize formula (5.2.19) to the degenerate case. Here we just report the results, for technical details about the derivation see Ref. [147]. The TrD between two generic vertex operators reads

$$D(\rho_{\alpha,\bar{\alpha}}, \rho_{\alpha',\bar{\alpha}'}) = \sqrt{(\alpha-\alpha')^2 + (\bar{\alpha}-\bar{\alpha}')^2}\,\frac{\ell}{L} + o\Big(\frac{\ell}{L}\Big), \tag{5.3.13}$$

generalising (5.3.4) to the degenerate cases. Similarly, the distance between the generic current and generic vertex states is given as

$$\begin{aligned} D(\rho_J, \rho_{\alpha,\bar{\alpha}}) &= D(\rho_{\bar{J}}, \rho_{\bar{\alpha},\alpha}) = \sqrt{\alpha^2+\bar{\alpha}^2}\,\frac{\ell}{L} + o\Big(\frac{\ell}{L}\Big), \\ D(\rho_{J\bar{J}}, \rho_{\alpha,\bar{\alpha}}) &= \sqrt{\alpha^2+\bar{\alpha}^2}\,\frac{\ell}{L} + o\Big(\frac{\ell}{L}\Big), \end{aligned} \tag{5.3.14}$$

which are the generalisations of (5.3.6) to the degenerate cases.

Numerical results in the XX spin chain

In this subsection we test the results for the short length expansion of the TrD against exact numerical calculations in the XX spin chain at half filling.

Before starting this discussion, we introduce the model in a more general form, meaning the XY model with transverse field. This is defined by the Hamiltonian

$$H = -\sum_{l=1}^{L} \Big(\frac{1+\gamma}{4}\sigma_l^x\sigma_{l+1}^x + \frac{1-\gamma}{4}\sigma_l^y\sigma_{l+1}^y + \frac{\lambda}{2}\sigma_l^z\Big), \tag{5.3.15}$$

with $\sigma_l^{x,y,z}$ denoting the Pauli matrices and L the total number of sites in the spin chain. One can impose either periodic boundary conditions (PBC) as $\sigma_{L+1}^{x,y,z} = \sigma_1^{x,y,z}$, or anti-periodic boundary conditions (APBC) as $\sigma_{L+1}^{x,y} = -\sigma_1^{x,y}$, $\sigma_{L+1}^{z} = \sigma_1^{z}$. When $\gamma = 0$ it defines the XX spin chain (which is the focus here), while for $\gamma = 1$ the Ising spin chain which is critical for $\lambda = 1$ (that will be used for numerical checks in Section 5.4). By Jordan-Wigner transformation [166], the Hamiltonian (5.3.15) is mapped to free fermions, where different boundary conditions can be imposed as well. In particular APBC on the fermions correspond to the Neveu-Schwarz (NS) sector in CFT, and PBC give rise instead to the Ramond (R) sector. At the end, one has totally four sectors (the parity of L is also to be taken into account, see Ref. [147]). In Fourier transform, for each sector one can write the Hamiltonian as

$$H = \sum_k \Big[(\lambda - \cos\varphi_k)\Big(b_k^\dagger b_k - \frac{1}{2}\Big) + \frac{\mathrm{i}\gamma}{2}(b_k^\dagger b_{-k}^\dagger + b_k b_{-k}) \Big]. \tag{5.3.16}$$

where b_k are fermionic operators and the states are selected according to the parity. Moreover, to diagonalise (5.3.16), a further Bogoliubov transformation to new fermionic operators, $\{c_k, c_k^\dagger\}$, is needed. Note that for $\gamma = 0$, the Hamiltonian (5.3.16) is already diagonal and the Bogoliubov transformation is not needed.

In the NS (R) sector of the spin chain, one can define an empty state $|\emptyset, \mathrm{NS}\rangle$ ($|\emptyset, \mathrm{R}\rangle$) that is annihilated by all the half integers (integers) modes c_k. Other energy eigenstates are obtained by applying a set of the modes $c_k^\dagger$ that are excited above them. The identification of the low-lying energy eigenstates in the spin chain with the corresponding ones in CFT can be found in Ref. [147].

We focus onto this model because it can be mapped in a free fermionic model, in which case again the approach of Section 1.4.3 holds. The construction of the correlation matrix of the excited states is discussed for example in Ref. [328]. Clearly this approach cannot be used for the TrD because this requires the diagonalisation of the difference $\rho_A - \sigma_A$ and, usually, the two RDMs do not commute. For this reason, we rely on a brute-force approach that consists in explicitly constructing ρ_A and σ_A as $2^\ell \times 2^\ell$ matrices as a Gaussian matrix (see Ref. [147] for details). Since RDMs are exponentially large in ℓ we can only access relatively small subsystem sizes (up to $\ell \sim 7$). Anyhow, compared to exact diagonalisation methods, we can consider arbitrarily large systems sizes L.

We will also consider the (Schatten) n-distances. When n is even, this amounts just to consider products of RDM that can be instad manipulated with standard correlation matrix techniques (cf. Eq. (1.4.31)). Consequently, in this case we can very easily access subsystem of very large lengths. We stress that this methods cannot be applied to the (Schatten) n-distances with n odd.

In the remaining of this Section we present our results for the TrDs among the RDMs of several low-lying excited states and discuss their behaviour for $\ell \ll L$, comparing with the universal CFT prediction just obtained. Our results for several representative states are reported in Figure 5.1. The various numerical data for the XX chain (symbols in the figure) perfectly match the leading order CFT results obtained above (and full lines in the figure) for $\ell \ll L$. Such agreement is highlighted in the fourth panel where the data are reported in log-log plots to make more evident the power law behaviour at small ℓ. Notice that in some (few) cases the first term in the short length expansion are equal, but the numerics surely rule out the possibility that the entire scaling functions are the same. This for example happens for the distances $D(\rho_{J\bar{J}}, \rho_{1,0})$ and $D(\rho_J, \rho_{1,0})$.

The numerical data reported in Figure 5.1 can be used to complement the analytic CFT results obtained above. Indeed for a few distances we have not been able to perform the analytic continuation to calculate exactly the amplitude x_ϕ appearing in the short length expansion (5.2.19). In such cases, matching Eq. (5.2.19) with the numerical results, we get approximately

$$\begin{aligned}
&D(\rho_0, \rho_J) = D(\rho_0, \rho_{\bar{J}}) = D(\rho_J, \rho_{J\bar{J}}) = D(\rho_{\bar{J}}, \rho_{J\bar{J}}) \approx 0.107 \frac{2\sqrt{2}\pi^2\ell^2}{L^2} + o\Big(\frac{\ell^2}{L^2}\Big), \\
&D(\rho_0, \rho_{J\bar{J}}) \approx 0.166 \frac{2\sqrt{2}\pi^2\ell^2}{L^2} + o\Big(\frac{\ell^2}{L^2}\Big), \\
&D(\rho_J, \rho_{\bar{J}}) \approx 0.141 \frac{2\sqrt{2}\pi^2\ell^2}{L^2} + o\Big(\frac{\ell^2}{L^2}\Big).
\end{aligned} \tag{5.3.17}$$

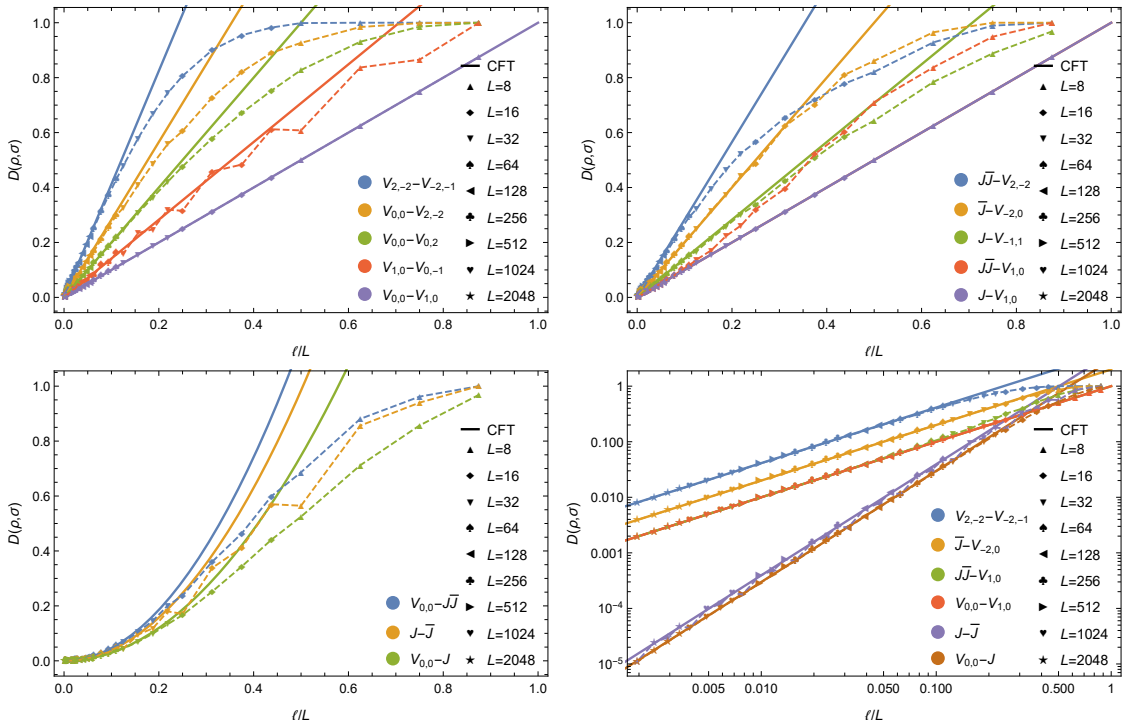

FIGURE 5.1: TD $D(\rho,\sigma)$ between the RDMs in several low-lying states as a function of the ratio between the subsystem ℓ and the system size L in the XX spin chain. The solid lines denote the leading order CFT prediction in the limit of short interval, Eqs. (5.3.13), (5.3.14) and (5.3.17). The symbols joined by dashed lines represent numerical data, obtained with the method in Section 1.4.3. Different symbols correspond to different L and different colours correspond to different pairs of states.

Some of these results are also shown in Figure 5.1. Comparison with (5.3.8) leads to $x_T \approx 0.107$ (which satisfies the bound (5.2.24) with $x_{\max}(2) = 1/\sqrt{30} \approx 0.183$).

5.3.2 n-distances for arbitrary subsystem size and analytic continuation

In this subsection, we consider the calculation of the n-distances for arbitrary n and for arbitrary values of the ratio ℓ/L, specialising the general approach in Section 5.2.1 to a few primary operators in the $2d$ free massless boson theory. In a specific case we have also been able to obtain the analytic continuation in n and find the exact expression of the TrD for an interval of arbitrary length.

Distances between vertex states

We first consider the distances between two states generated by vertex operators for which we can obtain many analytical results. Specialising Eq. (5.2.6) to vertex operators and using the explicit form of the multipoint correlation functions of the vertices, we straightforwardly obtain the general form for the n-distance with n even

$$\mathcal{D}_n[\Delta\alpha] \equiv \mathcal{D}_n(\rho_{\alpha,\bar\alpha},\rho_{\alpha',\bar\alpha'}) = \frac{1}{2}\sum_{k=0}^{n}(-)^k \sum_{0\le j_1<\cdots<j_k\le n-1} h_n(\{j_1,\cdots,j_k\})^{\Delta\alpha}, \tag{5.3.18}$$

where we defined $\Delta\alpha \equiv (\alpha-\alpha')^2+(\bar\alpha-\bar\alpha')^2$, and the function $h_n(\{j_1,\cdots,j_k\})$ of the set $\{j_1,\cdots,j_k\}$ as

$$h_n(\mathcal{S}) = \Big(\frac{\sin\frac{\pi\ell}{L}}{n\sin\frac{\pi\ell}{nL}}\Big)^{|\mathcal{S}|}\prod_{j_1,j_2\in\mathcal{S}}^{j_1<j_2}\frac{\sin^2\frac{\pi(j_1-j_2)}{n}}{\sin\frac{\pi(j_1-j_2+\ell/L)}{n}\sin\frac{\pi(j_1-j_2-\ell/L)}{n}}. \tag{5.3.19}$$

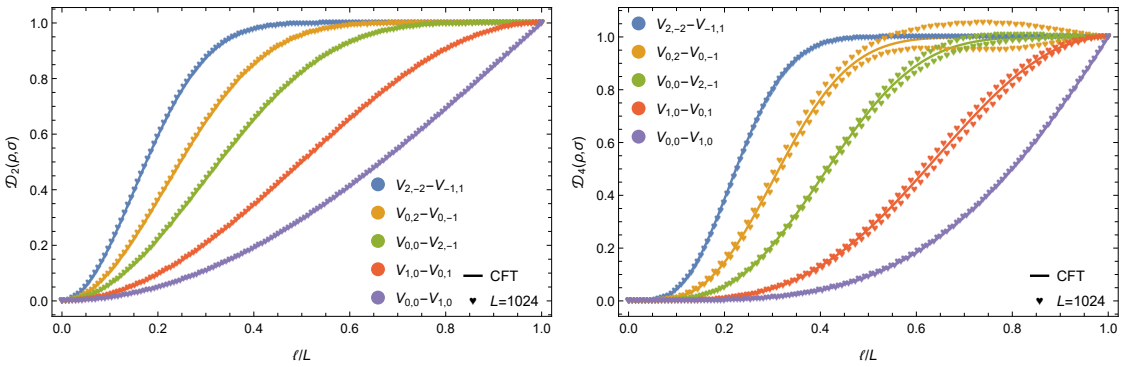

FIGURE 5.2: Even n-distance $\mathcal{D}_n[\Delta\alpha]$ for $n = 2, 4$ as a function of the ratio between the subsystem ℓ and the system size L in the free compact boson theory. The solid lines are the exact CFT predictions in (5.3.20). The symbols are the numerical data for a system of size $L = 1024$ and arbitrary ℓ. Different colours correspond to different pairs of vertex states ρ and σ (several values of $\Delta\alpha$ are considered).

We stress that for an odd integer, $n = n_o$, Eq. (5.3.18) does not provide the n_o-distance. Indeed, when $n = n_o$ is an odd integer, the RHS of Eq. (5.3.18) vanishes identically. For even integer $n = n_e$, (5.3.18) is the (Schatten) n_e-distance $\mathcal{D}_{n_e}$. Anyhow, the expression (5.3.18) as a sum of products of terms is not in the right form to be manipulated for the analytic continuation, but it can be considerably simplified for the smallest even integers, leading to the compact expressions

$$\begin{aligned}\mathcal{D}_2[\Delta\alpha] &= 1-\Big(\cos\frac{\pi\ell}{2L}\Big)^{\Delta\alpha},\\ \mathcal{D}_4[\Delta\alpha] &= 1+\Big(\cos^2\frac{\pi\ell}{2L}\Big)^{\Delta\alpha}+2\Big(\cos^2\frac{\pi\ell}{4L}\cos\frac{\pi\ell}{2L}\Big)^{\Delta\alpha},\end{aligned} \tag{5.3.20}$$

which can be shown to be consistent with the leading order results in short interval expansion. The numerical checks, as obtained via the approach of Section 1.4.3, are reported in Fig. 5.2: the agreement is excellent, although some oscillating subleading corrections to the scaling affect the data, but the presence of such deviations is not unexpected since their presence is well known for entanglement related quantities [173, 196, 303, 307, 308]. We checked carefully, by considering several values of L and performing extrapolations, that indeed such pronounced oscillations go to zero in the thermodynamic limit.

The (Schatten) n-distance $\mathcal{D}_n[\Delta\alpha]$ for general n (also odd or non-integer) is obtained from the analytic continuation of $\mathcal{D}_{n_e}[\Delta\alpha]$ from $n_e \in 2\mathbb{N}$ to an arbitrary real number. To obtain this analytic continuation, we need to rewrite (5.3.18) in such a way to remove the sum over the permutations. We managed to do this only for the special case $\Delta\alpha = 1$. Indeed, for $\Delta\alpha = 1$, the scaling function (5.3.18) for an even integer n_e may be rewritten (after some work) as

$$\mathcal{D}_{n_e}[1] = 2^{n_e-1}\prod_{j=1}^{n_e/2}\Big[\sin\frac{\pi(2j-1)x}{2n_e}\Big]^2, \tag{5.3.21}$$

where $x = \ell/L$. This product formula is of the right form to obtain the analytic continuation. Indeed, using the identity

$$\log\sin(\pi s) = \log\pi - \int_0^\infty dt\frac{e^{-t}}{t}\Big[\frac{e^{st}+e^{(1-s)t}-2}{1-e^{-t}}-1\Big], \tag{5.3.22}$$

we get the analytic continuation to arbitrary n

$$\log 2\mathcal{D}_n[1] = n\log(2\pi) - 2\int_0^\infty dt\frac{e^{-t}}{t}\Big\{\frac{1}{1-e^{-t}}\Big[\frac{(e^{\frac{tx}{2}}-1)\big[e^{\frac{tx}{2n}}+e^{\left(1-\frac{(n-1)x}{2n}\right)t}\big]}{e^{\frac{tx}{n}}-1}-n\Big]-\frac{n}{2}\Big\}. \tag{5.3.23}$$

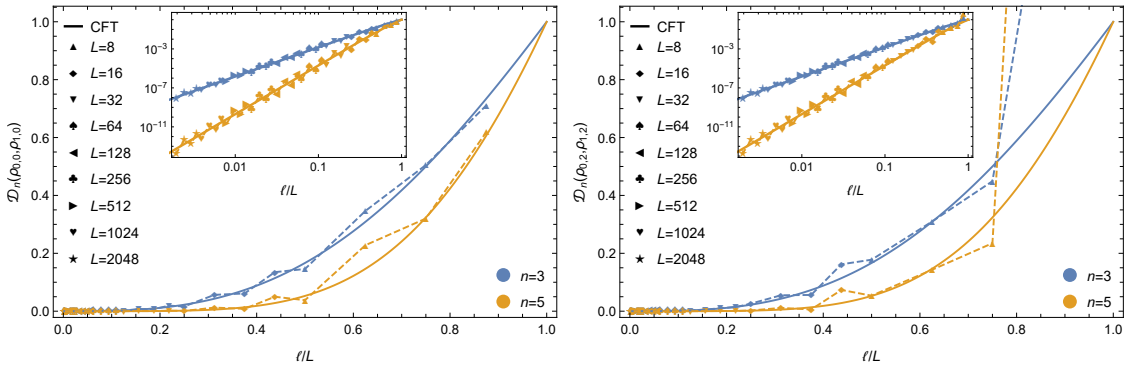

FIGURE 5.3: Odd n-distance $\mathcal{D}_n(\rho,\sigma)$ for $n = 3$ (blue) and $n = 5$ (yellow) as a function of the ratio between the subsystem ℓ and the system size L in the free compact boson theory. The solid lines are the analytic continuation (5.3.23) of the CFT prediction. The symbols (joined by dashed lines) are numerical data, with different symbols corresponding to different L. The two panels show two different pairs of vertex states ρ and σ, but both with $\Delta\alpha = 1$. Insets: Zoom in log-log scale of the region $\ell \ll L$.

In particular, for $n = 1$, Eq. (5.3.23) simplifies dramatically to

$$D[\Delta\alpha = 1] = \frac{\ell}{L}. \tag{5.3.24}$$

Such simple expression tells us that the TrD in this case is entirely determined by the leading OPE in Eq. (5.3.4). Then all the contributions from operators different from J have OPEs with amplitudes that must vanish in the limit $n_e \to 1$. It is rather natural to wonder whether there is a deeper and general explanation of this fact and if there are other non trivial implications of this property (not only for TrDs, but also for other quantities determined by the same OPE coefficients). Other OPE amplitudes in fact vanish in the limit $n \to 1$ [248] and this has important consequences, e.g., for the entanglement negativity [94, 145]. Finally notice that the data for the TrD $D[\Delta\alpha = 1]$ in Fig. 5.1 are perfectly compatible with the simple linear behaviour of Eq. (5.3.24).

The analytic continuation (5.3.23) provides also non-trivial predictions for the n-distance $\mathcal{D}_n[1]$, for arbitrary n. We can test this prediction against the XX results which we obtained from the full RDMs (see Ref. [147] for details). In Figure 5.3, we report the results we obtained for $n = 3, 5$. The spin chain calculations and the analytic continuation (5.3.23) match rather well, in spite of the presence of the oscillating correction to the scaling [173, 196, 303, 307, 308]. They can appear larger than those reported for even n in Fig. 5.2, but this is only due to the smaller values of ℓ we can access from the diagonalisation of the entire density matrix, compared to the correlation matrix technique used for even n.

When $\Delta\alpha \neq 1$, we are not able to simplify the general expression (5.3.18) to a form useful for the analytic continuation without the sum over the permutation. We only obtained few specific formulas [147].

Distances involving current states

The replicated distances involving current states have a much more complicated structure compared to the vertex states. For this reason, we briefly focus here on the distance $D(\rho_J, \rho_{1,0})$ because the numerical data in Figure 5.1 strongly suggest that this distance is exactly equal to ℓ/L, as the distance between vertex operator with $\Delta\alpha = 1$.

Using the correlation functions between current and vertex states, after long but straightforward algebra one arrives to

$$\frac{\mathrm{Tr}(\rho_J-\rho_{1,0})^n}{\mathrm{Tr}\rho_0^n}=\sum_{\mathcal{S}\subseteq\mathcal{S}_0}\sum_{\mathcal{R}\subseteq\bar{\mathcal{S}}}\Big[(-)^{|\bar{\mathcal{S}}|}\frac{(\frac{1}{n}\sin\frac{\pi\ell}{L})^{2n-|\bar{\mathcal{S}}|}}{(\sin\frac{\pi\ell}{nL})^{|\bar{\mathcal{S}}|-|\bar{\mathcal{R}}|}}\Big(\underset{r_1,r_2\in\mathcal{R}}{\tilde{\det}}\frac{1}{\sin\frac{\pi(r_1-r_2)}{n}}\Big)$$
$$\times\Big(\prod_{\bar{s}_1,\bar{s}_2\in\bar{\mathcal{S}}}^{\bar{s}_1<\bar{s}_2}\frac{\sin^2\frac{\pi(\bar{s}_1-\bar{s}_2)}{n}}{\sin\frac{\pi(\bar{s}_1-\bar{s}_2+\ell/L)}{n}\sin\frac{\pi(\bar{s}_1-\bar{s}_2-\ell/L)}{n}}\Big)$$
$$\times\Big(\prod_{\bar{r}\in\bar{\mathcal{R}}}\sum_{\bar{s}\in\bar{\mathcal{S}}}\frac{1}{\sin\frac{\pi(\bar{r}-\bar{s})}{n}\sin\frac{\pi(\bar{r}-\bar{s}-\ell/L)}{n}}\Big)\Big]. \tag{5.3.25}$$

Note that the sum of the set $\mathcal{S}$ is over all the subsets of $\mathcal{S}_0=\{0,1,\cdots,n-1\}$, and the complement set is $\bar{\mathcal{S}}=\mathcal{S}_0/\mathcal{S}$. The sum of $\mathcal{R}$ is over all the subsets of $\tilde{\mathcal{S}}=\mathcal{S}\cup(\mathcal{S}+\frac{\ell}{L})$, and the complement set is $\bar{\mathcal{R}}=\tilde{\mathcal{S}}/\mathcal{R}$. The determinant $\tilde{\det}$ is for the matrix whose diagonal entries are vanishing.

Unfortunately, further simplifications appear very difficult. Nonetheless, this general form is enough to rule out that the Schatten n-distances $\mathcal{D}_n(\rho_J,\rho_{1,0})$ and $\mathcal{D}_n(\rho_0,\rho_{1,0})$ are equal: it is enough to calculate the two distances for some even integer n. For example, for $n_e=2$ we have ($x=\ell/L$)

$$\mathcal{D}_2[J,V_{1,0}]=\frac{1}{2}\left(1-\sin^3\left(\frac{\pi x}{2}\right)\sin(\pi x)-2\cos^3\left(\frac{\pi x}{2}\right)+\frac{1}{64}(\cos(2\pi x)+7)^2\right), \tag{5.3.26}$$

which is different from (5.3.20) with $\Delta\alpha=1$. However, the differences between these distances are rather small and of higher order in x (e.g. $\mathcal{D}_2[J,V_{1,0}]-\mathcal{D}_2[V_{0,0},V_{1,0}]=O(x^6)$). The same seems true for higher n. Thus we are not able to distinguish whether $D(\rho_J,\rho_{1,0})$ is equal to ℓ/L or just very close to it.

5.4 Free massless fermion

In this Section, we consider the $2d$ free massless fermion theory. It is a $c=\frac{1}{2}$ CFT and the continuous limit of the critical Ising spin chain (which is another special case of the XY spin chain with transverse field defined in Eq. (5.3.15)). We will calculate various TrDs in the fermion theory and Ising spin chain. The calculations in the $2d$ free massless fermion theory and Ising spin chain parallel those in the $2d$ free massless boson theory and XX spin chain. Therefore, our discussion will be very brief.

In the $2d$ free massless fermion theory, besides the ground state $|0\rangle$, we consider the excited states generated by the primary operators σ, μ with conformal weights $(\frac{1}{16},\frac{1}{16})$, ψ and $\bar{\psi}$ with conformal weights $(\frac{1}{2},0)$ and $(0,\frac{1}{2})$, respectively, and ε whose conformal weights are instead given by $(\frac{1}{2},\frac{1}{2})$. We work in units such that all the primary operators are normalised to 1.

5.4.1 Short interval results

Here we first focus on the short interval expansion. Using the known scaling function for the Rényi entropies in the state σ and μ $F_\sigma^{(p)}(\ell)=F_\mu^{(p)}(\ell)=1$ [349], and exploiting Eq. (5.2.22), we immediately get

$$x_\sigma=x_\mu=\frac{1}{2^{1/4}}\approx 0.841. \tag{5.4.1}$$

For the ε state, we instead have [355]

$$F_\varepsilon^{(p)}(\ell)=\Big(\frac{2}{p}\sin\frac{\pi\ell}{L}\Big)^{2p}\frac{\Gamma^2(\frac{1+p+p\csc\frac{\pi\ell}{L}}{2})}{\Gamma^2(\frac{1-p+p\csc\frac{\pi\ell}{L}}{2})}, \tag{5.4.2}$$

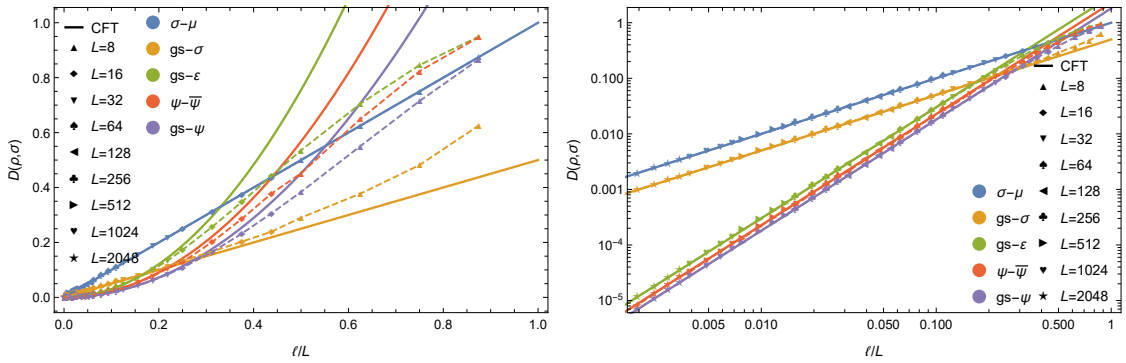

FIGURE 5.4: TrD $D(\rho,\sigma)$ among the RDMs in different low-lying states as a function of the ratio between the subsystem ℓ and the system size L in the free fermion theory. The solid lines denote the leading order CFT prediction in the limit of short interval, Eqs. (5.4.7) and (5.4.8). The symbols joined by dashed lines represent numerical data, with different symbols corresponding to different L. Different colours correspond to different pairs of states with "gs" denoting the ground state.

which, using (5.2.22), leads to

$$x_\varepsilon = \frac{1}{\pi} \approx 0.318. \tag{5.4.3}$$

As a consistency check, the bound (5.2.24) is satisfied with

$$x_{\max}(1/8) = \frac{\pi^{1/4}}{2^{5/8}}\sqrt{\frac{\Gamma(9/8)}{\Gamma(13/8)}} \approx 0.885, \tag{5.4.4}$$

for x_σ, x_μ, and

$$x_{\max}(1) = \frac{1}{\sqrt{6}} \approx 0.408\ldots, \tag{5.4.5}$$

for x_ε.

Plugging the coefficient (5.4.3) and the expectation values

$$\langle\varepsilon\rangle_0 = \langle\varepsilon\rangle_\psi = \langle\varepsilon\rangle_{\bar\psi} = \langle\varepsilon\rangle_\varepsilon = 0, \quad \langle\varepsilon\rangle_\sigma = -\langle\varepsilon\rangle_\mu = \frac{\pi}{L}, \tag{5.4.6}$$

into the general formula (5.2.19), we obtain the leading order behaviour of the following TrDs

$$\begin{aligned} &D(\rho_0,\rho_\sigma) = D(\rho_0,\rho_\mu) = \frac{\ell}{2L} + o\Big(\frac{\ell}{L}\Big), \\ &D(\rho_\sigma,\rho_\psi) = D(\rho_\sigma,\rho_{\bar\psi}) = D(\rho_\mu,\rho_\psi) = D(\rho_\mu,\rho_{\bar\psi}) = \frac{\ell}{2L} + o\Big(\frac{\ell}{L}\Big), \\ &D(\rho_\sigma,\rho_\varepsilon) = D(\rho_\mu,\rho_\varepsilon) = \frac{\ell}{2L} + o\Big(\frac{\ell}{L}\Big), \end{aligned} \tag{5.4.7}$$

and

$$D(\rho_\sigma,\rho_\mu) = \frac{\ell}{L} + o\Big(\frac{\ell}{L}\Big). \tag{5.4.8}$$

Moreover, still from Eq. (5.2.19) and from the expectation values (5.4.6), (5.3.7), we also get

$$D(\rho_0,\rho_\psi) = D(\rho_0,\rho_{\bar\psi}) = D(\rho_\psi,\rho_\varepsilon) = D(\rho_{\bar\psi},\rho_\varepsilon) = x_T\frac{2\pi^2\ell^2}{L^2} + o\Big(\frac{\ell^2}{L^2}\Big), \tag{5.4.9}$$

with the unknown coefficients $x_T = x_{\bar T}$.

We checked several of the CFT results (5.4.7) and (5.4.8) against Ising spin chain numerics in Figure 5.4. From numerical spin chain results, we also get approximately (see again Figure 5.4)

$$D(\rho_0,\rho_\psi) = D(\rho_0,\rho_{\bar\psi}) = D(\rho_\psi,\rho_\varepsilon) = D(\rho_{\bar\psi},\rho_\varepsilon) \approx 0.0916\frac{2\pi^2\ell^2}{L^2} + o\Big(\frac{\ell^2}{L^2}\Big),$$
$$D(\rho_0,\rho_\varepsilon) \approx 0.153\frac{2\pi^2\ell^2}{L^2} + o\Big(\frac{\ell^2}{L^2}\Big),\ \ D(\rho_\psi,\rho_{\bar\psi}) \approx 0.115\frac{2\pi^2\ell^2}{L^2} + o\Big(\frac{\ell^2}{L^2}\Big). \tag{5.4.10}$$

Comparison with (5.4.9) leads to $x_T = x_{\bar T} \approx 0.0916$, which satisfies the bound (5.2.24) with $x_{\max}(2) = 1/\sqrt{30} = 0.183\ldots$.

5.4.2 An exact result

The data in Figure 5.4 strongly suggest that the distance $D(\rho_\sigma,\rho_\mu)$ is exactly ℓ/L, i.e. completely fixed by the first term in the OPE expansion. It is natural to wonder whether we can show this. By replica trick, the stating point is always $\mathrm{Tr}(\rho_\sigma-\rho_\mu)^n$ that for free massless fermion theory can be computed by bosonisation (see e.g. [83, 326]). Using standard bosonisation rules ($\sigma^2 = \sqrt{2}\cos(\varphi/2)$ and $\mu^2 = \sqrt{2}(\sin\varphi/2)$) and then the known correlation functions of the vertex operators in the bosonic theory, after some long but easy algebra we get

$$\begin{aligned}\frac{\mathrm{Tr}(\rho_\sigma-\rho_\mu)^n}{\mathrm{Tr}\rho_0^n} = \Big(\frac{1}{4n}\sin\frac{\pi\ell}{L}\Big)^{n/4} \sum_{\mathcal{S}\subseteq\mathcal{S}_0}\Big\{(-)^{|\mathcal{S}|}\Big\{(-)^{|\mathcal{S}|}\sum_{\{r_i=\pm1,s_j=\pm1\}}^{\sum_i r_i+\sum_j s_j=0}\Big[\Big(\prod_{j\in\tilde{\mathcal{S}}}s_j\Big)\\ \times\Big(\prod_{i,i'\in\tilde{\mathcal{S}}}^{i<i'}\Big|\sin\frac{\pi(i-i')}{n}\Big|^{r_ir_{i'}/2}\Big)\Big(\prod_{j,j'\in\tilde{\mathcal{S}}}^{j<j'}\Big|\sin\frac{\pi(j-j')}{n}\Big|^{s_js_{j'}/2}\Big)\\ \times\Big(\prod_{i\in\tilde{\mathcal{S}},j\in\mathcal{S}}\Big|\sin\frac{\pi(i-j)}{n}\Big|^{r_is_j/2}\Big)\Big]\Big\}^{1/2}\Big\}.\end{aligned} \tag{5.4.11}$$

Note that the sum of the set $\mathcal{S}$ is over all the subsets of $\mathcal{S}_0 = \{0,1,\cdots,n-1\}$, and the complement set is $\bar{\mathcal{S}} = \mathcal{S}_0/\mathcal{S}$. We also have $\tilde{\mathcal{S}} = \mathcal{S}\cup(\mathcal{S}+\frac{\ell}{L})$, $\tilde{\bar{\mathcal{S}}} = \bar{\mathcal{S}}\cup(\bar{\mathcal{S}}+\frac{\ell}{L})$.

Further simplifications of this formula appear very difficult. However it is straightforward to check numerically even for a quite large even integer n that

$$\frac{\mathrm{Tr}(\rho_\sigma-\rho_\mu)^{n_e}}{\mathrm{Tr}\rho_0^{n_e}} = 2^{n_e}\prod_{j=1}^{n_e/2}\Big[\sin\frac{\pi(2j-1)\ell/L}{2n_e}\Big]^2. \tag{5.4.12}$$

This is exactly the same as the quantity in free massless boson theory in Eq. (5.3.21). Then, using the result for the analytic continuation in the previous Section, we get the exact TrD

$$D(\rho_\sigma,\rho_\mu) = \frac{\ell}{L}, \tag{5.4.13}$$

which in fact is exactly what the data in Fig. 5.4 were suggesting.

5.5 Concluding remarks

We developed a systematic approach based on a replica trick to calculate the subsystem TrD in one-dimensional quantum systems and in particular $2d$ QFT. The method has been applied to the analytic computation of TrDs between the RDMs of one interval embedded in various low-lying energy eigenstates of a CFT, especially for free massless boson and fermion theories, where we were able to obtain a full analytic result for the analytic continuation for arbitrary values of ℓ/L only in one case for the free bosonic theory

and another for the fermionic one. For all other pairs of states, instead, we have an analytic prediction only for the first term in the expansion in ℓ/L.

There is at least one aspect of our specific computations that can have important consequences also for different applications. In fact, we have seen that there are pairs of RDMs of CFT eigenstates that have finite TrDs (and so local operators are not guaranteed to have the same expectation value in the two states), but their (Schatten) n-distances, instead, vanish in the thermodynamic limit for all $n > 1$. In CFT, by means of scaling arguments, we are able to build from the n-norms some indicators that remain finite in the thermodynamic limit (see e.g. Eq. (5.2.7)), but in a more general case (e.g. in the absence of scale invariance) it is not clear whether this is possible. It is then natural to wonder whether some of the conclusions based on the analysis of other distances (as e.g. in Refs. [360, 374]) could change if one uses a more appropriate indicator such as the TrD.

There are several possible generalizations to the results presented in this Chapter. First of all one can consider other states in CFT: open systems [352, 353], disjoint intervals [337], finite temperature, inhomogeneous systems [159, 375], etc. Secondly, one can consider subsystem TrDs in $2d$ massive theories [148]. Another interesting application is related to the study of lattice entanglement Hamiltonians and their relation to the Bisognano-Wichmann ones [341, 342, 374, 376–381]. Besides, one can consider higher-dimensional boson and fermion theories, trying to adapt the techniques of Refs. [382–385], at least in the small subsystem limit.

Chapter 6

Entanglement of disjoint intervals via the Zamolodchikov's recursion formula

The hardest step of all the replica tricks discussed in the previous Chapters is doubtless the analytic continuation from quantities defined only as functions of an integer parameter n to functions of a complex variable. While in many cases the exact solution of this problem remains out of reach, different viable ways to approximately tackle it exist. In this Chapter, based on Ref. [358], we reconsider the computation of the EE of two disjoint intervals in a $(1+1)$ dimensional CFT by conformal block expansion of the four-point correlation function of twist fields, as first introduced in [357]. We show that accurate results may be obtained by taking into account several terms in the OPE of twist fields and by iterating the Zamolodchikov recursion formula for each conformal block. We perform a detailed analysis for the Ising CFT and the free compactified boson. Each term in the conformal block expansion can be easily analytically continued and so this approach provides a good approximation for the von Neumann entropy.

6.1 Introduction

Twist fields have been presented in the Introduction as special fields allowing to simplify the calculations of partition functions on complicated geometries. They proved particularly useful in the context of $(1+1)d$ CFT, where they transform under conformal transformations as primary fields with scaling dimension $\Delta_n \equiv \Delta_{\mathcal{T}_n} = \Delta_{\tilde{\mathcal{T}}_n} = c/24(n-1/n)$ [17, 18]. In fact, we have seen in Section 1.4.2 that in the case of a single interval embedded in the infinite line, the determination of the ground state moments $\mathrm{Tr}\rho_A^n$ is equivalent to a 2-point function of such fields, whose form is fixed by global conformal invariance, Eq. (1.4.10).

The calculations are however much more complicated in the case of more disjoint intervals, Eq. (1.4.13). Indeed, global conformal invariance does not fix completely the twist fields correlation functions for N intervals with $N \geq 2$. For example, for $N = 2$ the required 4-point correlation function can be written as

$$\mathrm{Tr}\rho_A^n = c_n^2 \left(\frac{(u_2-u_1)(v_2-v_1)}{(v_1-u_1)(v_2-u_2)(v_2-u_1)(v_1-u_2)} \right)^{\frac{c}{6}(n-1/n)} \mathcal{F}_n(x), \tag{6.1.1}$$

where $\mathcal{F}_n(x)$ is a model dependent *universal* function of the cross ratio

$$x \equiv \frac{(u_1-v_1)(u_2-v_2)}{(u_1-u_2)(v_1-v_2)}. \tag{6.1.2}$$

A large literature has been devoted to the analytical and numerical determination of the functions $\mathcal{F}_n(x)$ [17, 158, 167–169, 173, 174, 198, 203, 204, 247–250, 298, 316, 318, 357, 361, 362, 372, 386–394], but exact results are known only for few models. However, even in those few cases when $\mathcal{F}_n(x)$ is analytically known for arbitrary integer n, the analytic continuation of the parameter n from integers to complex values, needed to get the EE, is a very hard unsolved problem. This is due to the fact that the n dependence of the function $\mathcal{F}_n(x)$ is extremely complicated (two examples will be reported in the following). Some results are also known for disconnected regions in higher dimensions [382, 387, 395–398], also in holographic settings [100, 101, 189, 190, 399–401].

A viable and practical way to overcome the difficulties in the analytic continuation has been proposed in Refs. [300, 402] and consists of performing the continuation numerically by proper rational interpolations

for several values of n. While this technique may provide rather accurate results in some instances [300], it is definitively not satisfactory from a theoretical point of view and we would prefer to have an analytic handle on the analytic continuation. To this aim, an alternative is to consider an expansion of the function $\mathcal{F}_n(x)$ in which each term shows a manageable dependence on n, with a feasible analytic continuation. This has been considered e.g. in [249], where a general expression for the expansion in powers of the parameter x has been worked out. Unfortunately, this expansion generically converges slowly, so that it is very difficult, if not impossible, to get a reliable approximation of the EE for all values of $x \in [0,1]$. In [357] the authors suggested that the expansion in powers of the elliptic variable $q(x)$ (see below for a definition) provides an accurate approximation of the EE already at the lowest order. The main idea was to use the fusion algebra of twist fields (already introduced in [249]) and consider a conformal blocks' expansion [83, 403], as usually done to deal with 4-point functions. Each conformal block is obtained from the recursion formula originally proposed by Al. B. Zamolodchikov [404], which is an expansion in $q(x)$ and provides an extremely rapid convergence for the conformal block itself. We must mention that other systematic expansions have also been considered, but focusing on the semiclassical limit of conformal blocks (i.e. in the limit of large central charge) and its relation to the holographic result [405–407]. Furthermore, the Zamolodchikov recursion formula has been used in Ref. [408] to study the time evolution of the entanglement entropy starting from locally excited states for large central charge.

Here we reconsider the technique introduced in [357] and we show how the results obtained there may be improved by including more *fusion channels*, i.e., further conformal families in the OPE of twist fields, and, when possible, by considering a better approximation of each conformal block through the iteration of the Zamolodchikov recursion formula.

The Chapter is organized as follows. In Section 6.2, we start by recalling the main steps needed for the expansion in conformal blocks of a generic 4-point function of a CFT, and we then generalize to the case of twist fields. In Section 6.3 we introduce the Zamolodchikov recursion relation, stressing some of its properties and discussing the approximations that we are going to use. In Section 6.4 we summarise some known results about the 4-point twist-field correlations which we need as a reference to test the truncations of conformal block expansion. In Section 6.5 and 6.6 we apply this technique to the computation of $\mathrm{Tr}\rho_A^n$ for the Ising CFT and for the compactified boson respectively, and consider their analytic continuation. The resulting predictions for the EE reasonably match available numerical results. In Section 6.7 we critically discuss our findings and stress some unsolved issues deserving further investigation.

6.2 Conformal blocks expansion of twist fields correlation functions

Standard conformal blocks expansion: main steps for the derivation

In a generic CFT, global conformal invariance fully fixes the dependence on the positions of the operators in the 2-point and 3-point functions, but the 4-point correlation is only fixed up to a function of the cross ratios

$$x \equiv \frac{z_{12}z_{34}}{z_{13}z_{24}}, \qquad \bar{x} \equiv \frac{\bar{z}_{12}\bar{z}_{34}}{\bar{z}_{13}\bar{z}_{24}}. \tag{6.2.1}$$

with $z_{ij} = z_i - z_j$. In fact, making use of a Moebius transformation, which maps four generic points as $(z_1, z_2, z_3, z_4) \to (\infty, 1, x, 0)$, the correlation of four generic scaling (quasi-primary) fields

$$\langle \phi_1(z_1,\bar{z}_1)\phi_2(z_2,\bar{z}_2)\phi_3(z_3,\bar{z}_3)\phi_4(z_4,\bar{z}_4)\rangle, \tag{6.2.2}$$

can be related to the function

$$\begin{aligned} \tilde{\mathcal{F}}(x,\bar{x}) &\equiv \lim_{w,\bar{w}\to\infty} w^{2\Delta_1}\bar{w}^{2\bar{\Delta}_1}\langle \phi_1(w,\bar{w})\phi_2(1,1)\phi_3(x,\bar{x})\phi_4(0,0)\rangle \\ &= \langle \Delta_1,\bar{\Delta}_1|\phi_2(1,1)\phi_3(x,\bar{x})|\Delta_4,\bar{\Delta}_4\rangle, \end{aligned} \tag{6.2.3}$$

which is not fixed by global conformal invariance, but depends on the dynamical input specifying the theory, i.e. the structure constants C_{ij}^k or equivalently the OPE coefficients of primary fields. Furthermore, $\tilde{\mathcal{F}}(x,\bar{x})$

can be written as a sum of *conformal blocks* as [83, 403]

$$\tilde{\mathcal{F}}(x,\bar{x}) = \sum_p C_{12}^p C_{34}^p \tilde{F}(x,c,\Delta_p,\boldsymbol{\Delta}) \tilde{F}(\bar{x},c,\bar{\Delta}_p,\bar{\boldsymbol{\Delta}}), \tag{6.2.4}$$

where $\boldsymbol{\Delta} \equiv \{\Delta_1,\Delta_2,\Delta_3,\Delta_4\}$, the sum is over all the primary fields of the theory and $\tilde{F}(x,c,\Delta_p,\boldsymbol{\Delta})$ are the conformal blocks.

The crucial ingredient to prove (6.2.4) is the fact that the fields form an algebra, i.e. for any pair of fields we can write an operator product expansion

$$\phi_3(x,\bar{x})\phi_4(0,0) = \sum_p \frac{C_{34}^p}{x^{\Delta_p-\Delta_3-\Delta_4}\bar{x}^{\bar{\Delta}_p-\bar{\Delta}_3-\bar{\Delta}_4}} \phi_p(0,0), \tag{6.2.5}$$

where $\{\phi_k\}$ is a basis of scaling fields. Moreover, since the scaling fields can be collected in conformal families denoted as $[\phi_p]$ (i.e. the set formed by a primary field ϕ_p and all its descendants), Eq. (6.2.5) can be rewritten as

$$\phi_3(x,\bar{x})\phi_4(0,0) = \sum_p \frac{C_{34}^p}{x^{\Delta_p-\Delta_3-\Delta_4}\bar{x}^{\bar{\Delta}_p-\bar{\Delta}_3-\bar{\Delta}_4}} [\phi_p(0,0)], \tag{6.2.6}$$

where we used the proportionality between the OPE coefficients of a primary operator with its own descendants. Plugging this OPE into Eq. (6.2.3), we get

$$\tilde{\mathcal{F}}(x,\bar{x}) \quad = \quad \sum_p \frac{C_{34}^p}{x^{\Delta_p-\Delta_3-\Delta_4}\bar{x}^{\bar{\Delta}_p-\bar{\Delta}_3-\bar{\Delta}_4}} \langle \Delta_1,\bar{\Delta}_1|\phi_2(1,1)[\phi_p(0,0)]|0\rangle. \tag{6.2.7}$$

Exploiting the factorisation in holomorphic and antiholomorphic parts, the comparison of the above equation with Eq. (6.2.4) determines the conformal block

$$\tilde{F}(x,c,\Delta_p,\boldsymbol{\Delta}) \equiv [C_{12}^p]^{-1/2} \frac{\langle \Delta_1,\bar{\Delta}_1|\phi_2(1,1)[\phi_k(0,0)]|0\rangle|_{hol}}{x^{\Delta_p-\Delta_3-\Delta_4}}, \tag{6.2.8}$$

and analogously for the antiholomorphic term.

In Eq. (6.2.4), the sum over p is a sum over conformal families showing that the only independent OPE coefficients are the ones of the primary fields. In particular, the contribution of the descendants is encoded in the conformal block $\tilde{F}(x)$. If one knows all the proportionality constants relating the OPE coefficients of primaries and their descendants, the conformal block can be computed explicitly, but their computation is not generically feasible. As we shall show, it is instead convenient to exploit the property that the conformal blocks only depends on few variables $(\Delta_p,\boldsymbol{\Delta},c)$, which are the true dynamical inputs.

In the case we are interested in, the four fields have the same scaling dimension $\Delta_i = \bar{\Delta}_i = \Delta$ and the points z_i are real $z_i = \bar{z}_i$ (implying $x = \bar{x}$). Hence, we get the simplified expression for the 4-point correlation function

$$\langle \phi_1(z_1,\bar{z}_1)\phi_2(z_2,\bar{z}_2)\phi_3(z_3,\bar{z}_3)\phi_4(z_4,\bar{z}_4)\rangle = \left|\frac{z_{13}z_{24}}{z_{14}z_{23}z_{12}z_{34}}\right|^{4\Delta} \mathcal{F}(x), \tag{6.2.9}$$

where, using the freedom we have on the definition of the function of the cross ratio, and according to the convention used for the prefactor in [249] we define

$$\mathcal{F}(x) \equiv [x(1-x)]^{4\Delta/3}\tilde{\mathcal{F}}(x). \tag{6.2.10}$$

With this notation, the conformal blocks expansion from (6.2.4) and (6.2.10) we get

$$\mathcal{F}(x) = \sum_p C_{12}^p C_{34}^p F(x,c,\Delta_p,\boldsymbol{\Delta}) F(x,c,\bar{\Delta}_p,\bar{\boldsymbol{\Delta}}). \tag{6.2.11}$$

Fusion algebra of twist fields and generalised conformal block expansion

We are interested in the EE of two disjoint intervals which is a 4-point correlation function of twist fields (cf. Eq. (1.4.13)). Since under conformal transformations twist fields behave like primary fields, we expect that the conformal block expansion could be applied to such a correlation function. The key ingredient is the operator algebra of the twist fields which have an OPE with a generalised form derived in [249] and which reads

$$\mathcal{T}_n(z)\tilde{\mathcal{T}}_n(w) = \sum_{\{k_j\}} C_{k_j} \bigotimes_{j=1}^{n} \phi_{k_j}\left(\frac{z+w}{2}\right), \tag{6.2.12}$$

where the sum is over the scaling fields $\{\phi_{k_1} \otimes \cdots \otimes \phi_{k_n}\}$ of the n-copy Hilbert space $\mathcal{H}^{\text{tot}} \equiv \otimes_{j=1}^{n} \mathcal{H}_j$. Eq. (6.2.12) tells that the monodromy of the product $\mathcal{T}_n(z)\tilde{\mathcal{T}}_n(w)$ does not affect the state for distance much larger than $|z-w|$ and therefore it is possible to expand $\mathcal{T}_n(z)\tilde{\mathcal{T}}_n(w)$ in a basis of the fields of the n-copy theory (where we have n identical decoupled fields).

One could then classify the fields entering the OPE according to the global symmetries of the theory. In fact, the theory we are dealing with, defined by n copies of the *mother* CFT, of central charge c, is itself a CFT with central charge nc, being invariant under conformal transformations generated by the total stress-energy tensor $T = \sum_{i=1}^{n} T^i$ (the sum of the stress tensors of each replica); the associated Virasoro generators are the modes of T, i.e., $L_k^{\text{tot}} = \sum_{j=1}^{n} L_k^{(j)}$. Therefore, in the expansion in conformal blocks of any 4-point correlation function for this CFT, each block will include the contribution of a primary operator and its descendants with respect to this total Virasoro algebra. Thus, Eq. (6.2.12) can be recast in the form

$$\mathcal{T}_n(z)\tilde{\mathcal{T}}_n(w) = \sum_{\alpha} C_\alpha[\Phi_\alpha] + \cdots, \tag{6.2.13}$$

where Φ_α are primary fields with respect to the total Virasoro algebra, i.e., they are defined by the property

$$L_m^{\text{tot}}\Phi_\alpha = 0 \quad \forall m > 0, \tag{6.2.14}$$

and C_α are the associated OPE coefficients, that can be computed with a method introduced in [249] (i.e. through the computation of n-point correlation function of the primaries on the n-sheeted Riemann surface, see [249] for details), generalized in [362] to deal with general primaries of the theory. Note that the 'blocks' considered here are different from the ones in the previous Chapter, where an expansion in *quasiprimaries* instead of *primaries* was considered (compare Eq. (6.2.13) with Eq. (5.2.10)).

Moreover, for a generic number of intervals it holds $Z_n \equiv \langle \mathcal{T}_n\tilde{\mathcal{T}}_n \cdots \mathcal{T}_n\tilde{\mathcal{T}}_n\rangle$, thus the correlation functions of twist fields have the same symmetries of the partition function Z_n. For the case of one interval, $Z_n = \langle \mathcal{T}_n\tilde{\mathcal{T}}_n\rangle$ is symmetric under cyclic permutations generated by the group $\mathbb{Z}_n$, hence only $\mathbb{Z}_n$-symmetric combinations of fields can enter the OPE $\mathcal{T}_n\tilde{\mathcal{T}}_n$. In particular tensor products of primary fields of the single copy algebras (plus cyclic permutations) belong to this class of fields. But they are not the only ones: more primaries can be constructed from the linear combination of tensor products of primary and descendants fields in different copies (in the following sections we will give explicit examples in concrete models).

Note also that, generally speaking, in this enlarged CFT there exist degenerate fields, i.e., fields with the same scaling dimensions and this is not a condition under which Zamolodchikov formula (Section 6.3) is derived. The obvious example would be to consider multiplets charged under permutation symmetry. However, as a consequence of the symmetry considerations above, just a combination of them enter the OPE (6.2.13) and therefore the conformal blocks expansion, thus excluding the presence of this kind of degeneracies. Still, we cannot exclude the presence of other degeneracies at higher order. This possibility surely deserves more investigation. However, for our analysis this is not an issue, since the leading fusion channels we are going to consider do not show any degeneracy, so that the Zamolodchikov recursion formula holds.

The fusion algebra of twist fields (6.2.13) allows us to derive (following the exact same steps of Sec. 6.2) an expansion in conformal blocks. Making use of global conformal invariance, we can factorise the

4-point correlation function as (in the notations of [249])

$$\langle \mathcal{T}_n(u_1)\tilde{\mathcal{T}}_n(v_1)\mathcal{T}_n(u_2)\tilde{\mathcal{T}}_n(v_2)\rangle = \left(\frac{(u_2-u_1)(v_2-v_1)}{(v_1-u_1)(v_2-u_2)(v_2-u_1)(u_2-v_1)}\right)^{4\Delta_n} \mathcal{F}_n(x). \tag{6.2.15}$$

The function $\mathcal{F}_n(x)$ can thus be expanded as

$$\mathcal{F}_n(x) = \sum_\alpha \left(C^\alpha_{\mathcal{T}_n\tilde{\mathcal{T}}_n}\right)^2 F(x, nc, \Delta_\alpha, \mathbf{\Delta}_n) F(x, nc, \bar{\Delta}_\alpha, \bar{\mathbf{\Delta}}_n), \tag{6.2.16}$$

where $\mathbf{\Delta}_n \equiv \{\Delta_n, \Delta_n, \Delta_n, \Delta_n\}$ and the structure constants $C^\alpha_{\mathcal{T}_n\tilde{\mathcal{T}}_n}$ can be related to the coefficients of the small x expansion given in [249]. The first terms have also been already computed (see [249, 361]).

6.3 Zamolodchikov recursion formula

The computation of conformal blocks is an old problem in CFT. To this aim, one of the most powerful techniques is the Zamolodchikov recursion formula [404] which turns out to be very useful in our case, because it provides an expansion where each term can be analytically continued to $n = 1$.

The Zamolodchikov formula is an expansion in the elliptic variable

$$q(x) = e^{i\pi\tau(x)}, \quad \tau(x) = i\frac{K(1-x)}{K(x)}, \tag{6.3.1}$$

where $K(x)$ is the complete elliptic integral of first kind and x the usual four-point ratio (6.1.2). Clearly, small q corresponds to small x, and the small x expansion can be recast in terms of small q expansion. Anyhow, it turned out that the expansion in $q(x)$ converges for finite x much faster than the direct x expansion [357].

According to the Zamolodchikov formula (under the hypothesis of non-degenerate fields), the conformal block $F(x, \tilde{c}, \Delta_l, \mathbf{\Delta})$ satisfies the following recursion relation

$$F(x, \tilde{c}, \Delta_l, \mathbf{\Delta}) = (16q)^{\Delta_l - \frac{\tilde{c}-1}{24}} x^{\frac{\tilde{c}-1}{24}} (1-x)^{\frac{\tilde{c}-1}{24}} \theta_3(\tau)^{\frac{\tilde{c}-1}{2} - 4\sum_{i=1}^4 \Delta_i} H(\tilde{c}, \Delta_l, \mathbf{\Delta}, q), \tag{6.3.2}$$

$$H(\tilde{c}, \Delta_l, \mathbf{\Delta}, q) = 1 + \sum_{m,n} (16q)^{mn} \frac{R_{mn}(\tilde{c}, \mathbf{\Delta})}{\Delta_l - \Delta_{mn}(\tilde{c})} H(\tilde{c}, \Delta_{mn} + mn, \mathbf{\Delta}, q), \tag{6.3.3}$$

where

- $\Delta_{mn}(\tilde{c}) = \frac{\tilde{c}-1}{24} + \frac{(\beta_+ m + \beta_- n)^2}{4}$,
- $\beta_\pm = \frac{1}{\sqrt{24}}\left((1-\tilde{c})^{1/2} \pm (25-\tilde{c})^{1/2}\right)$,
- θ_3 is the Jacobi elliptic function,
- $R_{mn}(\tilde{c}, \mathbf{\Delta}) = -\frac{1}{2}\prod'_{ab} \frac{1}{\lambda_{ab}} \prod_{p,q} (\lambda_1 + \lambda_2 - \frac{\lambda_{pq}}{2})(-\lambda_1 + \lambda_2 - \frac{\lambda_{pq}}{2})(\lambda_3 + \lambda_4 - \frac{\lambda_{pq}}{2})(\lambda_3 - \lambda_4 - \frac{\lambda_{pq}}{2})$,
- $\lambda_{pq} = p\beta_+ - q\beta_-$,
- $\Delta_i = \frac{\tilde{c}-1}{24} + \lambda_i^2$,
- the range of the indices run over

$$\begin{aligned} p &= -m+1, m+3, \cdots, m-3, m-1, \\ q &= -n+1, -n+3, \cdots, n-3, n-1, \\ a &= -m+1, -m+2, \cdots, m-1, m, \\ b &= -n+1, -n+2, \cdots, n-1, n, \end{aligned}$$

- $\prod'_{ab}$ means $(a,b) \neq (0,0),(m,n)$.

The function H can be given as an expansion in power of $q(x)$

$$H(\tilde{c},\Delta_l,\boldsymbol{\Delta}) = 1 + \sum_{k=1} h_k(\tilde{c},\Delta_l,\boldsymbol{\Delta})(16q)^k. \tag{6.3.4}$$

The first orders can be explicitly written plugging (6.3.4) into (6.3.3). However, as shown in Ref. [358], for correlation functions of fields with the same conformal dimensions (as in the case we are interested in) only the even powers appear in Eq. (6.3.4), which therefore takes the form

$$H(\tilde{c},\Delta_l,\boldsymbol{\Delta}) = 1 + \sum_{k=1} h_{2k}(\tilde{c},\Delta_l,\boldsymbol{\Delta})(16q)^{2k}. \tag{6.3.5}$$

Note that in Eq. (6.3.3) the dimensions of the fusion channels appear in the denominator of Zamolodchikov formula so that singularities could be present for $\Delta_l = \Delta_{mn}(\tilde{c})$. In particular, when $\tilde{c} = 1$, the denominator vanishes also for the identity channel (since $\Delta_l = \Delta_{11}(\tilde{c} = 1) = 0$). Moreover, still in the case $\tilde{c} = 1$, all the factors R_{mn} with $(m \cdot n) \geq 2$ show null denominator and hence all $h_{k\geq 2}$ do the same. We encounter this problem in both the examples considered here: for the function $\mathcal{F}_2(x)$ in the Ising model ($\tilde{c} = nc = 1$, if $n = 2$) and in the limit $n \to 1$ for the compact boson ($\tilde{c} = nc = 1$ for $n = 1$). However, we will show that in these two cases the limit $\tilde{c} \to 1$ exists, so that there is no problematic issue.

Truncations of Zamolodchikov recursion formula

In the previous Section we discussed how the conformal block technique can be generalised in order to compute the function $\mathcal{F}_n(x)$ for the 4-point correlation function of twist fields, as already pointed out in [357]. Eq. (6.2.16) is in fact a rewriting of the entire correlation function in terms of conformal blocks as building blocks. However, it is still unknown and probably impossible to resum the entire series, even for the easiest models. In the practical world, we are just able to truncate this formula, but there are several levels of truncations that can play a role, as we are going to discuss in the following.

The first one is a truncation of the conformal block expansion, Eq. (6.2.16). In a general model, the sum over the fusion channels is actually a series. Moreover the expansion involves more and more channels as the replica label n increases (as it should be clear from the structure of the generalised OPE of twist fields, cf. Eq. (6.2.12)). Therefore, when interested to generic n, we must truncate this sum to the first leading terms, depending on the accuracy we wish to reach (in the following we will see how to order the contributions of the different channels from the most to the less relevant). In [357], for the Ising model, a truncation to the first two leading channels was considered, and it provided a good approximation of $\mathcal{F}_2$ and $\mathcal{F}_3$ only. In the following, we are going to keep more terms in this expansion discussing how the final result for the EE at $n = 1$ (which requires the knowledge of $\mathcal{F}_n$ as a function of n) may be improved.

The second truncation is in the order in the recursion formula, i.e. in Eq. (6.3.3) we must fix a $\bar{k} \in \mathbb{N}$ s.t.

$$H(\Delta_l,\boldsymbol{\Delta}) \sim 1 + \sum_{k=1}^{\bar{k}} h_{2k}(16q(x))^{2k}. \tag{6.3.6}$$

Also in this case, the most important issue is to understand whether the first few terms in this series are enough to get a good approximation. For example, for the Ising model, it turned out [357] that a good approximation is obtained already at the zeroth-order $H(\Delta_l,\boldsymbol{\Delta}) \sim 1$. Here we will show that by keeping more terms in (6.3.6) it is possible to practically get convergence of the function, so that this truncation is minimally affecting the final result.

6.4 Some exact results for the EE of two disjoint intervals in CFT

In the following sections we will apply the Zamolodchikov recursion formula to entanglement entropies of the critical Ising model (aka $\mathcal{M}_3$ minimal model) and of the massless compact boson, which are CFTs

with central charge equal to $1/2$ and 1 respectively. In this Section we report the known exact results for the moments of the reduced density matrices for these two models since we will repeatedly compare our truncated expressions with them.

For the free boson compactified on a circle of radius R, the scaling function $\mathcal{F}_n(x)$ for general integers has been calculated in Ref. [248] (generalising the result at $n = 2$ in [247]) and it reads

$$\mathcal{F}_n(x) = \frac{\Theta\big(0|\eta\Gamma\big)\,\Theta\big(0|\Gamma/\eta\big)}{[\Theta\big(0|\Gamma\big)]^2}\,, \tag{6.4.1}$$

where $\eta = 2R^2$, Γ is an $(n-1)\times(n-1)$ matrix with elements [248]

$$\Gamma_{rs} = \frac{2i}{n}\sum_{k=1}^{n-1}\sin\left(\pi\frac{k}{n}\right)\beta_{k/n}\cos\left[2\pi\frac{k}{n}(r-s)\right]\,, \tag{6.4.2}$$

$$\beta_y = \frac{{}_2F_1(y,1-y;1;1-x)}{{}_2F_1(y,1-y;1;x)}\,, \tag{6.4.3}$$

and Θ is the Riemann-Siegel theta function

$$\Theta(0|\Gamma) \equiv \sum_{m\in\mathbf{Z}^{n-1}}\exp\left[\,i\pi\, m^{\mathrm{t}}\cdot\Gamma\cdot m\right]. \tag{6.4.4}$$

For the Ising model, the scaling function $\mathcal{F}_n(x)$ is [249]

$$\mathcal{F}_n(x) = \frac{1}{2^{n-1}\Theta(\mathbf{0}|\Gamma)}\sum_{\varepsilon,\delta}\left|\Theta\left[\begin{array}{c}\varepsilon\\ \delta\end{array}\right](\mathbf{0}|\Gamma)\right|\,. \tag{6.4.5}$$

Here Θ is the Riemann theta function with characteristic defined as

$$\Theta\left[\begin{array}{c}\varepsilon\\ \delta\end{array}\right](\mathbf{z}|\Gamma) \equiv \sum_{\mathbf{m}\in\mathbf{Z}^{n-1}}\exp\left[i\pi(\mathbf{m}+\varepsilon)^{\mathrm{t}}\cdot\Gamma\cdot(\mathbf{m}+\varepsilon)+2\pi i\,(\mathbf{m}+\varepsilon)^{\mathrm{t}}\cdot(\mathbf{z}+\delta)\right], \tag{6.4.6}$$

where $\mathbf{z}\in\mathbf{C}^{n-1}$ and Γ is the same as in Eq. (6.4.2). ε,δ are vector with entries 0 and $1/2$. The sum in $(\boldsymbol{\varepsilon},\boldsymbol{\delta})$ in Eq. (6.4.5) is intended over all the 2^{n-1} vectors $\boldsymbol{\varepsilon}$ and $\boldsymbol{\delta}$ with these entries. This result generalises the one for $n = 2$ in [167].

Finally, the *universal scaling function* $F_{\mathrm{vN}}(x)$ for the Von Neumman is usually defined as

$$F_{\mathrm{vN}}(x) \equiv S_{A_1} + S_{A_2} - S_{A_1\cup A_2} - \frac{c}{3}\ln(1-x)\,, \tag{6.4.7}$$

where A_1 and A_2 are the two intervals we are focusing on. Notice that the combination of entropy in the RHS is nothing but the mutual information which indeed is scale invariant.

6.5 Ising model

In this Section we apply the machinery of the conformal blocks expansion and the Zamolodchikov recursion formula to the minimal model $\mathcal{M}_3$, corresponding to the CFT describing the critical Ising model.

OPE of twist fields

For the $\mathcal{M}_3$ CFT, the mother theory contains only a finite number of primary fields with natural working basis

$$\mathbb{I}, \sigma, \epsilon, \tag{6.5.1}$$

with $\mathbb{I}$ the identity, σ the spin operator, and ϵ the energy density operator with dimensions $\Delta_{\mathbb{I}} = 0$, $\Delta_\sigma = 1/16$, and $\Delta_\epsilon = 1/2$. However, since we now consider n decoupled copies of the theory, the associated central charge is $\tilde{c} = nc \geq 1$ (if $n \geq 2$), therefore, as argued in [409], the number of primaries fields is in principle infinite (even if it may be reduced when taking into account the $\mathbb{Z}_n$ symmetry due to the boundary conditions connecting the different copies).

The OPE of $\mathcal{T}_n\tilde{\mathcal{T}}_n$ takes the general form (6.2.13), which for the Ising case reduces to

$$\mathcal{T}_n\tilde{\mathcal{T}}_n = 1 + ([\sigma_i\sigma_j] + \ perm) + ([\epsilon_i\epsilon_j] + \ perm) + ([\sigma_i\sigma_j\epsilon_k] + \ perm) + \cdots \tag{6.5.2}$$

where *perm* stands for all possible permutations of the indices from 1 to n. In this notation, the insertion of an operator in the family of the identity is implicit each time a given sheet is not explicitly indicated (see explicit examples below).

Since as we increase the number of sheets, there are more and more choices of operators, the families that must be considered depend on n. For example, for the lowest values of n, we have

- $n = 2$:

$$\mathbb{I}_1\mathbb{I}_2,\ \sigma_1\sigma_2,\ \epsilon_1\epsilon_2. \tag{6.5.3}$$

  Terms with only a single copy of any fields (e.g. $(\sigma_1\mathbb{I}_2)$, $(\epsilon_1\mathbb{I}_2)$) are not present, as already stressed in [357]; also the term $(\sigma_1\epsilon_2)$ is not there by symmetry. In this case it has been shown [410] that these families complete the OPE.

- $n = 3$:

$$\mathbb{I}_1\mathbb{I}_2\mathbb{I}_3,\ \sigma_1\sigma_2\mathbb{I}_3,\ \epsilon_1\epsilon_2\mathbb{I}_3,\ \sigma_1\sigma_2\epsilon_3,\ (L_{-1}\sigma)_1\sigma_2\mathbb{I} - \sigma_1(L_{-1}\sigma)_2\mathbb{I}, \tag{6.5.4}$$

  and permutations. Terms like $\sigma_1\sigma_2\sigma_3$ and $\epsilon_1\epsilon_2\epsilon_3$ vanish (due to the vanishing structure constants $C^\sigma_{\sigma\sigma}$ and $C^\epsilon_{\epsilon\epsilon}$ [83]). Note that the last example in Eq. (6.5.4) is still a primary operator according to definition (6.2.14) but is not in the form of a tensor product: in principle the associated OPE coefficient could be computed using the generalised formula in [362] but the calculation is more involved, therefore we do not include it in what follows. Other primaries of this type may in principle occur. All the other terms in Eq. (6.5.4) will be included in our approximation.

In the following we are going to denote as

$$C_{k,l}(n), \tag{6.5.5}$$

the coefficient of the generic term

$$(\sigma_1\cdots\sigma_k\epsilon_{k+1}\cdots\epsilon_{k+l}\mathbb{I}_{l+1}\cdots\mathbb{I}_n + perm), \tag{6.5.6}$$

in the expansion in conformal blocks. It can be related to the coefficient $s_{k,l}(n)$ entering the small x expansion [249] as

$$\left(\frac{x}{4n^2}\right)^{2(k\Delta_\sigma + l\Delta_\epsilon)} s_{k,l}(n). \tag{6.5.7}$$

In particular, one can show that it holds

$$C_{k,l}(n)^2 = \left(\frac{1}{4n^2}\right)^{2(k\Delta_\sigma + l\Delta_\epsilon)} s_{k,l}(n). \tag{6.5.8}$$

Eq. (6.5.7) also provides a criterion to order the different fusion channels from the most to the less relevant ones, by looking to the order at which they enter in the 4-point correlation function in the small x expansion.

Explicit results from recursion formula and comparison with the exact ones

In this Section we explicitly build the universal function $\mathcal{F}_n(x)$ for the $\mathcal{M}_3$ minimal model for various n and at several different orders in the truncation of Zamolodchikov formula. We compare our results with the exact function $\mathcal{F}_n(x)$ for increasing values of n. We also analytically obtain a truncation for the Von

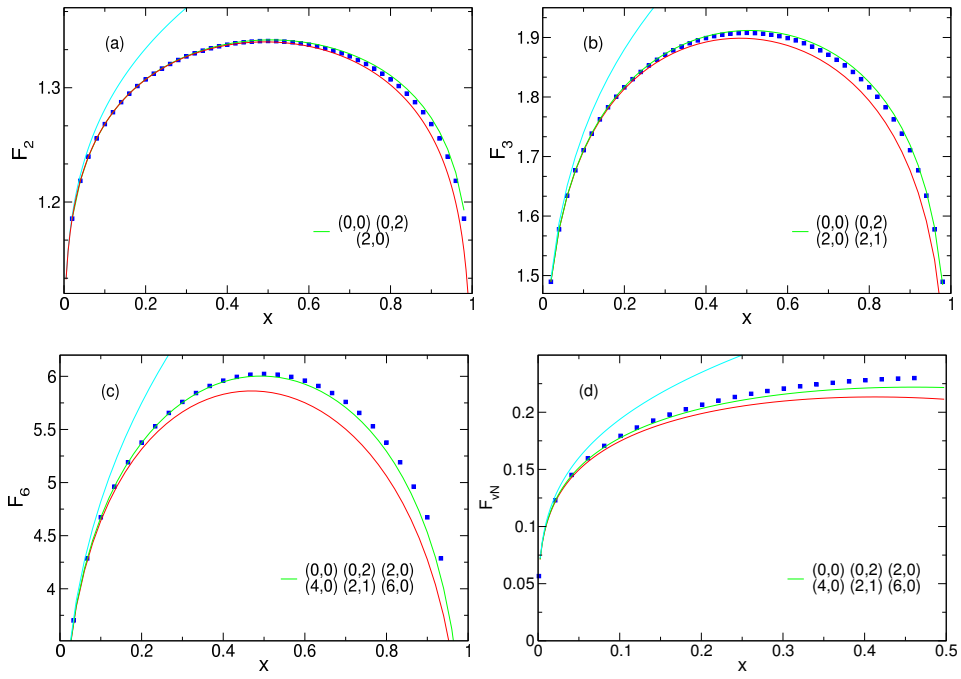

FIGURE 6.1: The best approximation we derived for $\mathcal{F}_n(x)$ ($n = 2,3,6$) and for the EE $F_{\rm vN}(x)$ in the Ising model, still at the 0-th order in the Zamolodchikov formula. The dots represent the exact functions. The red line is the curve derived with the approximation in [357]. The green curve is our approximation (the fusion channels included in the OPE of twist fields are listed with (k,l) denoting the inclusion of the fusion channel $[\sigma_1 \cdots \sigma_k \epsilon_1 \cdots \epsilon_l \mathbb{I}_{k+l+1} \cdots \mathbb{I}_n]$ and all its permutations). The cyan curve is the expansion in power of x derived in [249].

Neumann entropy scaling function $F_{\rm vN}(x)$ via replica trick and compare it with the very accurate results from numerical simulation in [167].

0-th order in the Zamolodchikov recursion formula. We start by truncating the Zamolodchikov recursion formula to the 0-th order (corresponding to $H \sim 1$ in [357]) and we proceed by including more and more terms in the OPE expansion of twist fields to reach a reasonable approximation of the function $\mathcal{F}_n(x)$, for a given n. As already stressed, the number of terms expected from the OPE is increasing quickly with n. Thus a good approximation requires more and more terms as n increases.

In Figure 6.1 (a), (b) and (c), we report the result for the zeroth order (green curves) for $n = 2,3,6$. We compare this zeroth order truncation (including several channels in the OPE) with the known exact results, with the truncation of [357] (which includes the first two channels only), and with the small x expansion of [249]. It is evident that including more channels in the OPE considerably improves the approximation which is extremely close to the exact result. In the figures we denoted by (k,l) the truncation with the inclusion of the fusion channel $[\sigma_1 \cdots \sigma_k \epsilon_1 \cdots \epsilon_l \mathbb{I}_{k+l+1} \cdots \mathbb{I}_n]$ (and all its permutations).

It is evident that for some values of x, our approximation gives a curve which is slightly larger than the exact result. We will see that the curve will be moved downward by the inclusion of higher terms in the recursion formula.

The von Neumann entropy can be obtained at a given order by analytic continuation. The first few terms leads to the truncation for the scaling function

$$F_{\rm vN}^{(\text{0-th})}(x) = \theta_3^{-\frac{1}{2}}(q) \left(\frac{x(1-x)}{16q}\right)^{-\frac{1}{24}} \times \\ \times \left[-\frac{5}{6}\ln\theta_3(q) + \frac{1}{24}\ln\left(\frac{x(1-x)}{16q}\right) + s'_{2,0}(1)(4q)^{\frac{1}{4}} + s'_{4,0}(1)(4q)^{\frac{1}{2}} + \cdots\right]. \quad (6.5.9)$$

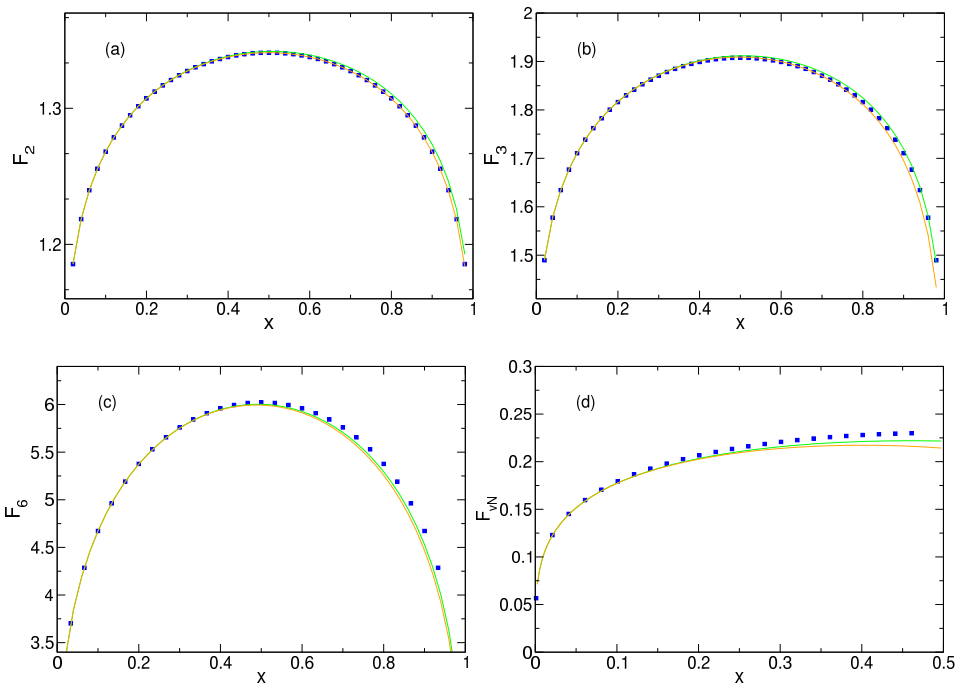

FIGURE 6.2: The best approximation we derived for $\mathcal{F}_n(x)$ ($n = 2,3,6$) and the von Neumann entropy $F_{\rm vN}(x)$ in the Ising model, by including further terms in the Zamolodchikov formula. The dots represent the exact functions. The green curve is our approximation at the 0-th order. The orange curve is the approximation at the 2-nd order. The fusion channels included in the OPE of twist fields are the same as in Figure 6.1.

The coefficients $s'_{k,l}(1)$ are calculated as explained in Ref. [358] by analytic continuation. All the other fusion channels give an additive contribution implicit in the dots above. Note that, even if a finite number of terms in the Zamolodchikov expansion may exactly reproduce $\mathcal{F}_n(x)$ for finite n, the same is not true for $F_{\rm vN}(x)$, since an infinite number of terms contributes to the analytic continuation.

In panel (d) of Figure 6.1 we report the von Neumann entropy scaling function $F_{\rm vN}(x)$ (6.5.9) and we compare it with the results from numerical simulations in [167] (we only report data for $x < 0.5$, the other half is better reproduced exploiting the symmetry $x \to 1-x$). We notice that the agreement of the truncation with the numerical data is reasonable, but not as good as those at finite n. In fact, although we included a number of terms reproducing well $\mathcal{F}_n(x)$ up to $n = 6$, the truncation for the EE deviate considerably from the exact numerical data, but it is still a much better approximation than the one considered in [357].

M-th order in the Zamolodchikov recursion formula. We now discuss how the approximation improves by taking into account more iterations in the Zamolodchikov recursion formula. It turns out that the Zamolodchikov series converges extremely fast for the functions $\mathcal{F}_n(x)$: the truncation to the first 2 orders in $q(x)$ (namely $H \sim 1 + h_2 q(x)^2$) is practically indistinguishable from the function we obtain by summing up numerically the whole series. The results of this improved truncation are shown in Figure 6.2 (a), (b) and (c) for $n = 2,3,6$ respectively. In the Figure, the results are compared to those computed at the 0-th order in the recursion formula and to the exact results. It is evident that the already very accurate truncation at zeroth order is further improved by the iteration of the recursion formula for $n = 2,3$. In particular for $n = 2$ the approximated result is indistinguishable from the exact one: this fact does not come unexpected because this is the only case where we know the OPE of twist fields to be complete (cf. Eq. (6.5.3)) and the recursion formula has converged. For $n = 6$ instead the agreement is imperceptibly worse.

We can also improve the truncation for the von Neumann entropy. The scaling function $F_{\rm vN}(x)$, as derived via replica trick, at the 2-nd order in the recursion formula takes the form

$$F_{\rm vN}^{(\text{2-nd})}(x) = \theta_3^{-\frac{1}{2}}(q)\left(\frac{x(1-x)}{16q}\right)^{-\frac{1}{24}} \times \\ \times\left[\left(-\frac{5}{6}\ln\theta_3(q)+\frac{1}{24}\ln\left(\frac{x(1-x)}{16q}\right)\right)(1+2h_2^{(0,0)}(1)(16q)^2)+\right. \\ +2h_2^{(0,0)\prime}(1)\,(16\,q)^2+s'_{2,0}(1)(4q)^{\frac{1}{4}}\left(1+2h_2^{(2,0)}(1)\,(16\,q)^2\right)+ \\ \left.+s'_{4,0}(1)(4q)^{\frac{1}{2}}\left(1+2h_2^{(4,0)}(1)\,(16\,q)^2\right)+\cdots\right], \quad (6.5.10)$$

where the coefficients $h_2^{(k,l)}(n)$ are a shortcut for the coefficients of the expansion in Eq. (6.3.4)

$$h_2^{(k,l)}(n) \equiv h_2(nc, \Delta_{(k,l)}, \mathbf{\Delta}_n), \quad (6.5.11)$$

for a given conformal family (identified by (k,l), with $\Delta_{(k,l)}$ its conformal dimension), which takes the simple form

$$h_2^{(k,l)}(n) = \frac{(-nc+(nc-32\Delta_n)^2+2\Delta_{(k,l)}(1+nc-32\Delta_n)(5+nc-32\Delta_n))}{(512(nc+2\Delta_{(k,l)}(-5+8\Delta_{(k,l)}+nc)))} \quad (6.5.12)$$

This higher order truncation is shown in panel (d) of Figure 6.2: we notice that it does not provide an improvement of the zeroth-order result of $F_{\rm vN}(x)$ for large values of x.

6.6 Compact boson

In this Section we apply the Zamolodchikov recursion formula to the truncation of the entanglement entropies in the CFT of a free massless boson compactified on a circle of radius R, which has central charge $c = 1$.

OPE of twist fields

As for the Ising model, the starting point of our analysis is the OPE of twist fields which is always of the form (6.2.13). The main difference with respect to the Ising model is that, while for the latter a basis of local field in the single copy theory is given by a set of three fields only $(\mathbb{I}, \sigma, \epsilon)$, for the compact boson we have an infinite set already in the mother theory.

The most relevant fields we consider are the derivative operators $\partial_z\varphi(z)$ and $\partial_{\bar z}\bar\varphi(\bar z)$, whose conformal weights are $(1,0)$ and $(0,1)$ respectively, and the *vertex operators*, uniquely identified by a pair of integers (m,n), $V_{(m,n)} \equiv :\exp(i\alpha_{m,n}\varphi(z)+i\bar\alpha_{m,n}\bar\varphi(\bar z)):$. Here $\alpha_{m,n}$ and $\bar\alpha_{m,n}$ are the holomorphic and antiholomorphic *charges*

$$\alpha_{m,n} = \left(\frac{m}{\sqrt{2\eta}}+n\sqrt{\frac{\eta}{2}}\right), \quad \bar\alpha_{m,n} = \left(\frac{m}{\sqrt{2\eta}}-n\sqrt{\frac{\eta}{2}}\right). \quad (6.6.1)$$

where $\eta = 2R^2$ is a function of the compactification radius R. They are associated to the vertex operators of conformal dimensions $h_{m,n} = \alpha_{m,n}^2/2, \bar h_{m,n} = \bar\alpha_{n,m}^2/2$.

Of course for the replicated theory, the primary fields with respect to the total Virasoro algebra are infinitely many. However, many of them do not appear in the fusion algebra of $\mathcal{T}_n\tilde{\mathcal{T}}_n$. For example, for

primaries constructed as tensor product of vertex operators on each copy, the structure constants are proportional to the correlator [249]

$$C_{\{m_j,n_j\}} \propto \langle \prod_j V_{(m_j,n_j)}(e^{2\pi i j/n}) \rangle_{\mathbb{C}}, \tag{6.6.2}$$

which due to the *neutrality condition* [83] vanishes unless $\sum_i \alpha_{m_i,n_i} = \sum_i \bar{\alpha}_{n_i,m_i} = 0$.

In our analysis we will not consider the contribution to $\mathcal{F}_n(x)$ from the two point function of the derivative operators because of their complicated analytic structure. Indeed, since the derivative operator has non zero conformal spin $s = 1$, as shown in [249], its contribution vanishes unless $4s/n \in \mathbb{Z}$. As a consequence, also the analytic continuation at $n = 1$ is highly non-trivial.

The non-vanishing primary terms that we consider are of the form

$$(\underbrace{V_{(m,0)} \cdots V_{(m,0)}}_{k} \underbrace{V_{(-m,0)} \cdots V_{(-m,0)}}_{k} + perm), \tag{6.6.3}$$

with $k \leq n/2$. At the leading order in the small x expansion of the conformal block, they contribute as $x^{km^2/2\eta}$, meaning that their contribution to the 4-point correlation function is of order $x^{km^2/\eta}$. Similarly, operators of the form

$$(\underbrace{V_{(0,n)} \cdots V_{(0,n)}}_{l} \underbrace{V_{(0,-n)} \cdots V_{(0,-n)}}_{l} + perm), \tag{6.6.4}$$

contribute in the 4-point correlation function as $x^{ln^2\eta}$. Consequently, the most general non vanishing combination of vertex operators in the small x expansion gives rise to terms of order

$$x^{k\frac{m^2}{\eta}+ln^2\eta}. \tag{6.6.5}$$

In the present case then, the relevance of the different contributions depend not only on the number of copies n, but also on the parameter η and consequently it is less obvious how to order them. The leading contribution either comes from the fusion channel

$$([V_{(1,0)}V_{(-1,0)}] + perm), \tag{6.6.6}$$

if $\eta < 1$, or from

$$([V_{(0,1)}V_{(0,-1)}] + perm), \tag{6.6.7}$$

if $\eta > 1$. Since there is a symmetry $\eta \to 1/\eta$ [83], we continue by discussing only $\eta < 1$, for which a next-to-leading term is

$$([V_{(1,0)}V_{(-1,0)}V_{(1,0)}V_{(-1,0)}] + perm). \tag{6.6.8}$$

For later convenience we define the coefficient of terms of the form

$$(\underbrace{V_{(p,0)} \cdots V_{(p,0)}}_{k} \underbrace{V_{(-p,0)} \cdots V_{(-p,0)}}_{k} \underbrace{V_{(0,q)} \cdots V_{(0,q)}}_{l} \underbrace{V_{(0,-q)} \cdots V_{(0,-q)}}_{l} + perm), \tag{6.6.9}$$

as

$$C_{k,l}^{(p,q)}(n), \tag{6.6.10}$$

which turns out to be related to the coefficients of the small x expansion $s_{2k,2l}^{(p,q)}(n)$ (introduced in analogy to the ones for the Ising model, cfr. Eq. (6.5.7) and Eq. (6.5.8))

$$C_{k,l}^{(p,q)}(n)^2 = \left(\frac{1}{4n^2}\right)^{\frac{k}{\eta}+l\eta} s_{2k,2l}^{(p,q)}(n). \tag{6.6.11}$$

The inclusion of such a fusion channel is denoted in the figures by $(p,q;k,l)$.

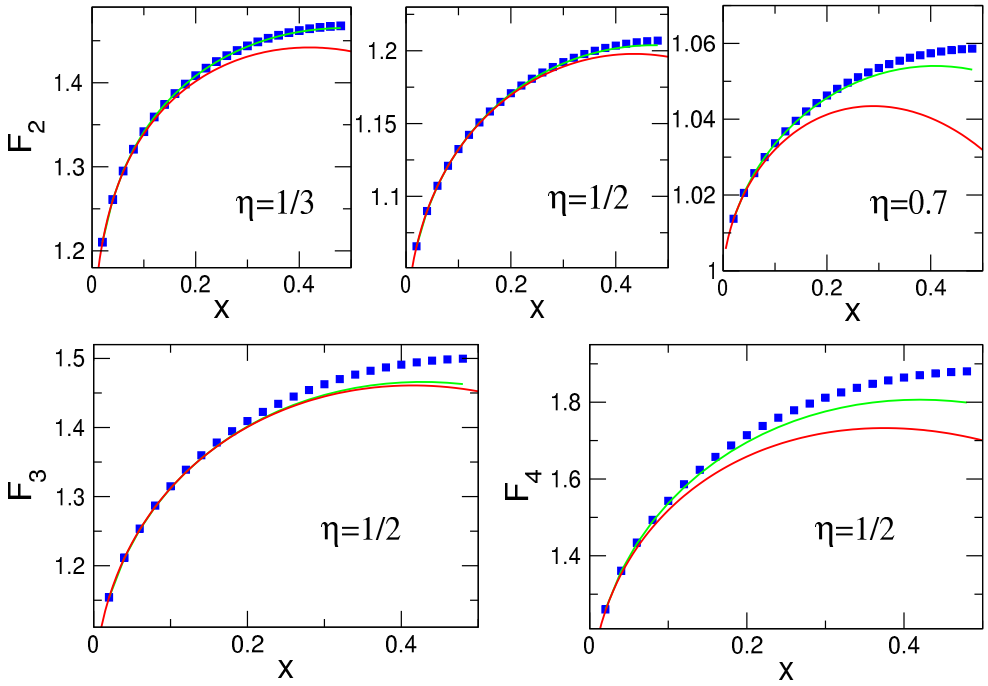

FIGURE 6.3: The function $\mathcal{F}_2(x)$ for different values of the compactification radius ($\eta = 1/3, 1/2, 0.7$) and the function $\mathcal{F}_3(x)$ and $\mathcal{F}_4(x)$ with $\eta = 1/2$ for a compactified boson. In all cases the truncation in the Zamolodchikov formula is at the 0-th order. Two different approximations in the OPE are considered: the fusion channels included are $(0,0;0,0),(1,0;1,0)$ for the red curves and $(0,0;0,0),(1,0;1,0),(1,0;2,0),(0,1;0,1),(2,0;1,0),(0,2;0,1)$ for the green curves (with $(p,q;k,l)$ denoting the inclusion of the term in Eq. (6.6.9)). The dots represent the exact functions.

Explicit results from recursion formula and comparison with the exact ones

As for the critical Ising model, in this Section we explicitly build the universal function $\mathcal{F}_n(x)$ for various n and at several different orders in the truncations of the Zamolodchikov formula. We compare our results with the exact function $\mathcal{F}_n(x)$ for increasing values of n. We also analytically obtain a truncation for the Von Neumann entropy scaling function $F_{\rm vN}(x)$ via replica trick and compare it with the simulations in [203].

We first consider the truncation of the Zamolodchikov formula to the first trivial order (i.e. $H \sim 1$ in [357]) and we include the contributions from the first leading conformal blocks. The results of this truncation are shown in Figure 6.3. In the figure the three panels in the top show $\mathcal{F}_2(x)$ for three values of η while the two panels in the bottom display $\mathcal{F}_3(x)$ and $\mathcal{F}_4(x)$ at fixed $\eta = 1/2$. The included families for each panel are listed in the caption of the figure. In all panels the truncated results are compared with the exact results from [248]. It is evident that the approximation improves upon increasing the number of the fusion channels in the OPE (red versus green curves). It is also to be notice that the quality of the approximation of the function $\mathcal{F}_n$ depends on the value of the parameter η. Moreover, like for the Ising model, as n increases a higher number of conformal blocks are required to well approximate $\mathcal{F}_n$.

We also considered the 2-nd order approximation in the recursion formula. However, in this case, the correction to the 0th-order is so small that the two curves are undistinguishable and therefore we do not show it here.

Finally, also for the compact boson, we derived the von Neumann entropy via analytic continuation. For $\eta < 1$, the best approximation we were able to derive is given by

$$F_{\rm vN}^{(0\text{-th})}(x) = -\frac{5}{3}\log\theta_3(q) + \frac{1}{12}\log\left(\frac{x(1-x)}{16q}\right) + s_{2,0}^{(1,0)'}(1)(4q)^{\eta} + s_{4,0}^{(1,0)'}(1)(4q)^{2\eta}. \qquad (6.6.12)$$

We report this truncation as function of x for several values of η in Figure 6.4. In the Figure, the truncation

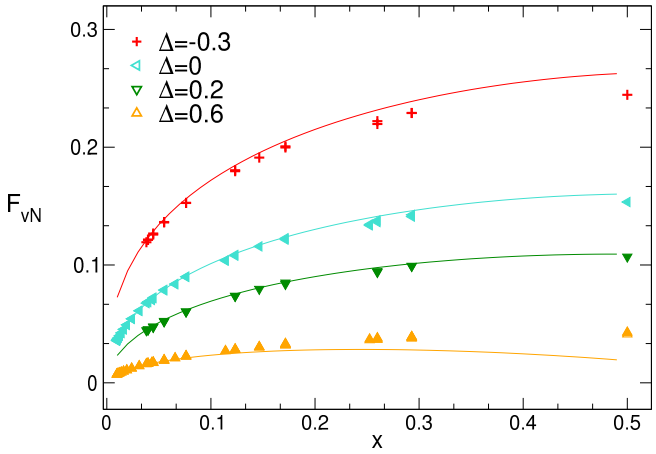

FIGURE 6.4: The continuous lines represent the approximation of the Von Neumann entropy $F_{\rm vN}(x)$ for a compactified boson in Eq. (6.6.12). The dots are the numerics of the XXZ chain in the gapless regime obtained via TTN techniques [203].

is compared with numerical simulations presented in Ref. [203]. These simulations have been obtained from tree tensor networks (TTN) techniques [203] of the XXZ spin chain with hamiltonian

$$H_{\rm XXZ}(\Delta) = \sum_j [\sigma_j^x \sigma_{j+1}^x + \sigma_j^y \sigma_{j+1}^y + \Delta\, \sigma_j^z \sigma_{j+1}^z]. \tag{6.6.13}$$

The model is critical for $\Delta \in [-1,1]$ and its scaling limit is described by the compact boson with radius $\eta = 2R^2 = \frac{\text{Arcos}(-\Delta)}{\pi}$. Also in this case the agreement for the various η is satisfactory. Furthermore, the sign of the difference clearly depends on η.

Surprisingly, for the Von Neumann entropy the introduction of further terms (both in the OPE of twist fields and in the recursion relation) seems to worsen the agreement. The origin of this behaviour is unclear and its understanding deserves further investigation, in particular in relation to the convergence of the Zamolodchikov series.

6.7 Concluding remarks

In this Chapter we reconsider the approach introduced in Ref. [357] for the calculation of the EE of two disjoint intervals by means of conformal blocks expansion and Zamolodchikov's recursion formula. We showed that the inclusion of further fusion channels in the OPE of twist fields in most cases improves the approximation for the scaling functions of the REEs $\mathcal{F}_n(x)$ and of the EE $F_{\rm vN}(x)$. Moreover, in those cases where the approximation is not good enough, we traced back the origin of the disagreement to the truncation of the OPE, rather than to the convergence in the Zamolodchikov's recursion formula for each block (which at the second-order appears already very stable). Interestingly, in the only case where the complete form of the OPE is known (i.e., $n = 2$ in the Ising model), our approximation perfectly reproduces the exact result [167]. In this respect, a complete classification of the fusion channel appearing in the OPE of twist fields, which is still missing in all the other cases, would be important.

As a future research direction, it would be interesting to investigate the possibility of using conformal blocks expansion and Zamolodchikov's recursion formula to obtain a feasible truncation of LN [55] (related, in the framework of CFT, to the same 4-point correlation function of twist fields, with points ordered in a different way [94, 145]). The latter is an entanglement measure in mixed states, that shows an essential singularity for small x [94, 145, 246]. Such singularity is not yet analytically understood and maybe conformal blocks expansion could shed some light on it.

Chapter 7

Symmetry resolved entanglement in free fermions

Recently, both from an experimental and a theoretical point of view, it has been understood the importance to understand the "internal symmetry structure" of the entanglement. While in the context of QFT a method to address this issue (again based on a replica trick) has been already considered, exact analytic results in free models were first given very recently in Ref. [197], on which this Chapter is based. In particular, we consider the symmetry resolved REEs in the $1d$ tight-binding model, equivalent to the spin-$1/2$ XX chain in a magnetic field. We exploit the generalized Fisher-Hartwig conjecture to obtain the asymptotic behavior of the REEs with a flux charge insertion at leading and subleading orders. We then use these results to extract the symmetry resolved entanglement, determining exactly all the non-universal constants and logarithmic corrections to the scaling that are not accessible to the field theory approach. Our results are also generalized to a one-dimensional free fermi gas.

7.1 Introduction

The recent experiment [37] in the context of disordered systems showed that the knowledge of entanglement content in a many-body system as a whole provides only partial information and it is instead also necessary to understand the different sources contributing to it. In particular, looking at systems possessing an internal global symmetry, entanglement turned out to have two different contributions, dubbed *configurational* and *number* or *fluctuation* entanglement [37]. These two contributions account for the entanglement within symmetry sectors and fluctuations thereof, respectively (see below for a precise definition).

At the same time, a new theoretical framework has been developed to address the problem of extracting the *symmetry resolved* contributions for different entanglement measures [318, 319, 411, 412]. Indeed, these contributions have been related to the moments of ρ_A where twisted boundary conditions are imposed along the cuts of the Riemann surface: we will refer to them as *charged* moments. As we are going to see more in detail, the twist can be implemented geometrically within field theory via threading an appropriate Aharonov-Bohm flux through the multisheeted Riemann surface [319]. The relation between twisted boundary conditions and flux insertion was actually previously explored, for example, in the context of free field theories [192, 316, 413, 414]. Moreover, similar quantities have also been introduced in the holographic setting [317, 415] and in the study of entanglement in mixed states [310, 314, 411].

If on one hand the field theory approach is very powerful and versatile in providing the scaling limit of both the charged and symmetry resolved entanglement entropies, on the other, it does not give access to non-universal model-dependent pieces which are also very important to accurately characterize critical systems. As we are going to see, for the special case of free fermions, we can go beyond the field theory results. In particular, we can rely on the *(generalized) Fisher-Hartwig conjecture* [193–196] to compute systematic expansions of these entropies which reproduce the field theory results and provide exact expressions for the non-universal terms. In fact, this method, which has already been explored for the standard entanglement and Rényi entropy [195, 196], can be simply generalized to the same quantities with a further flux insertion and therefore to their symmetry resolved analogue.

The rest of this Chapter is organized as follows. In Section 7.2 we carefully define all the quantities we will be dealing with and give an overview of the field theory results. Sections 7.3 and 7.4 are the core of this Chapter where we derive results for free fermions on a lattice for the charged and the symmetry resolved entanglement entropies, respectively. In Section 7.5 we show how all results derived for the lattice model can be directly adapted to a free Fermi gas. We conclude in Section 7.6 with some remarks and discussions.

7.2 Symmetry resolution and flux insertion

Let us consider a many body quantum system with an internal $U(1)$ symmetry. Let ρ be the density matrix in a given (pure) state and Q the operator generating such symmetry. If the system is in a given representation of the charge Q, i.e., in an eigenstate of Q corresponding to a definite eigenvalue, then $[\rho, Q] = 0$.

We will be interested in a bipartition of the total system into two complementary spatial subsystems A and B, with $\rho_A = \mathrm{Tr}_B \rho$ being the reduced density matrix of the subsystem A. Usually the operator Q splits in the sum $Q = Q_A + Q_B$, meaning that Q comes from local degrees of freedom within the two subsystems. Consequently, by taking the trace over B of $[\rho, Q] = 0$, we find that $[\rho_A, Q_A] = 0$. This implies that ρ_A acquires a block diagonal form, in which each block corresponds to a different charge sector with a definite eigenvalue q of Q_A, i.e.,

$$\rho_A = \oplus_q \Pi_q \rho_A = \oplus_q \left[p(q) \rho_A(q) \right], \tag{7.2.1}$$

where Π_q is the projector on eigenspace of fixed value of q in the spectrum of Q_A. In the last equality we factorised $p(q) = \mathrm{Tr}(\Pi_q \rho_A)$, the probability of finding q as the outcome of a measurement of Q_A. Note that in this way the density matrices $\rho_A(q)$ of different blocks are normalised as $\mathrm{Tr}\rho_A(q) = 1$.

Our goal is to understand how the entanglement is distributed in the different charge sectors. Focusing on the von Neumann EE as a prototypical example, Eq. (7.2.1) implies the following decomposition

$$S = \sum_q p(q) S(q) - \sum_q p(q) \ln p(q) \equiv S^c + S^f, \tag{7.2.2}$$

where we defined the *symmetry resolved entanglement entropy* as the one associated to $\rho_A(q)$ in (7.2.1)

$$S(q) \equiv -\mathrm{Tr} \left[\rho_A(q) \ln \rho_A(q) \right]. \tag{7.2.3}$$

The two different contributions in (7.2.2) are the *configurational* entanglement entropy, $S^c \equiv \sum_q p(q) S(q)$ [37, 416], measuring the total entropy due to each charge sector (weighted with their probability) and the *fluctuation* entanglement entropy $S^f = -\sum_q p(q) \ln p(q)$ [37], which instead takes into account the entropy due to the fluctuations of the value of the charge within the subsystem A.

Similarly, one defines also *symmetry resolved Rényi entropies* as

$$S_n(q) \equiv \frac{1}{1-n} \ln \mathrm{Tr} \left[\rho_A(q) \right]^n. \tag{7.2.4}$$

In general evaluating such symmetry resolved quantities is a highly non-trivial problem, mainly due to the non local nature of the projector Π_q. As mentioned in the introduction, recently, this problem has been understood from a different perspective in [318, 319]. This new approach works as follows. Let us first define the (unnormalised) quantity

$$\mathcal{Z}_n(q) \equiv \mathrm{Tr} \left(\Pi_q \rho_A^n \right), \tag{7.2.5}$$

which is related to the entanglement and Rényi entropies in (7.2.3) and (7.2.4) (respectively) through

$$S_n(q) = \frac{1}{1-n} \ln \left[\frac{\mathcal{Z}_n(q)}{\mathcal{Z}_1(q)^n} \right] \qquad S(q) = -\partial_n \left[\frac{\mathcal{Z}_n(q)}{\mathcal{Z}_1(q)^n} \right]_{n=1}. \tag{7.2.6}$$

Also the probability $p(q)$ is read off $\mathcal{Z}_n$ as

$$p(q) = \mathcal{Z}_1(q). \tag{7.2.7}$$

The key observation of Refs. [318, 319] is that (7.2.5) is given by the following Fourier transform

$$\mathcal{Z}_n(q) = \int_{-\pi}^{\pi} \frac{d\alpha}{2\pi} e^{-iq\alpha} Z_n(\alpha), \qquad Z_n(\alpha) \equiv \mathrm{Tr} \left(\rho_A^n e^{iQ_A \alpha} \right), \tag{7.2.8}$$

where $Z_n(\alpha)$ are the charged moments mentioned in the introduction. Note that $Z_n(0) = \mathrm{Tr}\rho_A^n$. Therefore,

we can access the symmetry resolved entanglement entropy by studying $Z_n(\alpha)$ (which, as explained below, are much easier to compute) and after Fourier transforming.

Replica method and results from QFT

In Ref. [319] a geometric approach in the framework of the replica trick has been introduced and it is applicable to generic (1+1)-dimensional QFT. The main idea is to insert an appropriate conjugate Aharonov-Bohm flux through a multi-sheeted Riemann surface $\mathcal{R}_n$, such that the total phase accumulated by the field upon going through the entire surface is α. The result is that $Z_n(\alpha)$ is the partition function on such modified surface.

In QFT language, the insertion of the flux corresponds to a twisted boundary condition, which, as usually done in this context, can be implemented by the action of a local operator, acting at the boundary of the subsystem A. This operator is a modified *twist field* $\mathcal{T}_{n,\alpha}$ whose action, in operator formalism, is defined by [319]

$$\mathcal{T}_{n,\alpha}(x,\tau)\phi_i(x',\tau) = \begin{cases} \phi_{i+1}(x',\tau)e^{i\alpha\delta_{i,j}}\mathcal{T}_{n,\alpha}(x,\tau) & (x<x'), \\ \phi_i(x',\tau)\mathcal{T}_{n,\alpha}(x,\tau) & \text{otherwise.} \end{cases} \tag{7.2.9}$$

In this way one can further reformulate the problem in terms of a correlation function of twist fields [148]. In the simplest case of the subsystem consisting of a single interval $A=[0,\ell]$

$$Z_n(\alpha) = \langle \mathcal{T}_{n,\alpha}(\ell,0)\tilde{\mathcal{T}}_{n,\alpha}(0,0)\rangle. \tag{7.2.10}$$

where $\tilde{\mathcal{T}}$ is the antitwist field. If we now specialise to (1+1) dimensional CFT, $\mathcal{T}_{n,\alpha}$ and $\tilde{\mathcal{T}}_{n,\alpha}$ behave as primary operators with conformal dimension given by [319]

$$h_{n,\alpha} = h_n + \frac{h_\alpha}{n}, \qquad h_n = \frac{c}{24}\left(n-\frac{1}{n}\right), \tag{7.2.11}$$

meaning that the phase shift is implemented by a composite twist field that can be written as $\mathcal{T}_{n,\alpha} = \mathcal{T}_n \cdot \mathcal{V}_\alpha$. This immediately implies

$$Z_n(\alpha) = c_{n,\alpha}\ell^{-\frac{c}{6}\left(n-\frac{1}{n}\right)-2\frac{h_\alpha+\bar{h}_\alpha}{n}}, \tag{7.2.12}$$

where c is the central charge of the CFT and $c_{n,\alpha}$ the unknown non-universal normalisation of the composite twist-field.

The focus of Ref. [319] was a free boson compactified on a circle of radius R, i.e., a Luttinger liquid with Luttinger parameter K. In this case the operator $\mathcal{V}_\alpha$ implementing the twisted boundary conditions is a vertex operator with (holomorphic and antiholomorphic) scaling dimensions

$$h_\alpha = \bar{h}_\alpha = \frac{1}{2}\left(\frac{\alpha}{2\pi}\right)^2 K. \tag{7.2.13}$$

From Eq. (7.2.12), the symmetry resolved moments are found by taking the Fourier transform as in Eq. (7.2.8). At leading order for large ℓ, this reads [319]

$$\mathcal{Z}_n(q) \simeq \ell^{-\frac{c}{6}\left(n-\frac{1}{n}\right)}\sqrt{\frac{n\pi}{2K\ln\ell}}e^{\frac{n\pi^2(q-\langle Q_A\rangle)^2}{2K\ln\ell}}. \tag{7.2.14}$$

Notice that we set a posteriori the average number of the charge in the subsystem $\langle Q_A\rangle$, since it is a non-universal quantity, not encoded in the CFT. For a given microscopical model, its origin can be easily traced back, e.g. as a phase shift in the bosonisation rule.

Through Eq. (7.2.6), this leads to the following result at leading order for the Rényi and the von Neumann entropy

$$S_n(q) = S_n - \frac{1}{2}\ln\left(\frac{2K}{\pi}\ln\ell\right) + O(\ell^0), \qquad S(q) = S - \frac{1}{2}\ln\left(\frac{2K}{\pi}\ln\ell\right) + O(\ell^0). \tag{7.2.15}$$

This result has been dubbed *equipartition of entanglement* [318]: at leading order the entanglement is the same in the different charge sectors, just the probability $p(q)$ of being in a given sector varies.

7.3 Free fermions on a lattice: flux insertion and charged entropies

Eq. (7.2.15) provides the leading symmetry resolved entanglement entropies of all microscopical models with a $U(1)$ symmetry, that, at low energy, are described by a CFT. Indeed the results in Eq. (7.2.15) have been tested numerically both for free fermions [318,319,417] and in interacting spin chains [302,318,418]. In this Section we are going to provide an analytic derivation for the special case of a chain of free fermions, whose scaling limit is indeed described by a free compact boson with $K = 1$. Our analysis will also provide the exact value of the non-universal constants, as well as the corrections to (7.2.15) for this specific model.

We consider the tight binding model in one dimension with hamiltonian

$$H = -\sum_{i=-\infty}^{\infty} \left[c_i^\dagger c_{i+1} + c_{i+1}^\dagger c_i - 2h \left(c_i^\dagger c_i - \frac{1}{2} \right) \right], \tag{7.3.1}$$

where c_i are free fermionic spinless degrees of freedom, satisfying the anticommutation relations $\{c_i, c_j^\dagger\} = \delta_{ij}$ and h is the chemical potential. H is diagonal in momentum space and its ground state is a Fermi sea with Fermi momentum $k_F = \arccos|h|$. As it is clear from (7.3.1), the particle number $Q = \sum_i c_i^\dagger c_i$ is a conserved $U(1)$ charge of the model. It is also local and $Q = Q_A + Q_B$ for any spatial bipartition of the chain. By Jordan Wigner transformation, Eq. (7.3.1) is mapped to the XX spin chain in a magnetic field h and the charge Q becomes the spin in the z direction.

In the following we will be interested in the bipartition where the subsystem A is given by ℓ contiguous lattice sites. We have seen that for this model the techniques in Section 1.4.3 to compute entanglement related quantities apply. It has been first noticed in Ref. [319] that the α-dependent moments $Z_n(\alpha)$, defined in (7.2.8), can be also easily written in terms of the eigenvalues $(1+\nu_k)/2$ (with $k \in [1,\ell]$) of the (reduced) correlation matrix, that for the ground-state of an infinite chain has elements

$$(C_A)_{i,j} = \frac{\sin k_F(i-j)}{\pi(i-j)}, \qquad i,j \in A. \tag{7.3.2}$$

With a simple modification of the formula for standard REEs (see Eqs. (1.4.22), (1.4.23)), in fact, one gets

$$Z_n(\alpha) = \prod_{i=1}^{\ell} \left[\left(\frac{1+\nu_i}{2} \right)^n e^{i\alpha} + \left(\frac{1-\nu_i}{2} \right)^n \right]. \tag{7.3.3}$$

The interpretation of this equation is straightforward: each particle carries a weight $e^{i\alpha}$ while the holes carry weight 1. Eq. (7.3.3) provides a very simple method for the numerical computation of $Z_n(\alpha)$. Not only: as we are going to discuss next, it is also the right starting point to get the asymptotic analytic expressions of $Z_n(\alpha)$.

Before embarking into the study of $Z_n(\alpha)$ a quick recap of its properties and limits is necessary, also to provide useful consistency checks for our calculations. First, for $n = 1$

$$Z_1(\alpha) \equiv \mathrm{tr}\rho_A e^{iQ_A\alpha} = \prod_{i=1}^{\ell} \left[\left(\frac{1+\nu_i}{2} \right) e^{i\alpha} + \left(\frac{1-\nu_i}{2} \right) \right], \tag{7.3.4}$$

is the moment-generating function of Q_A. This quantity has been already studied in the literature [171, 175, 218, 219, 419] also because of its relation with the entanglement entropy itself. The first moment is just the average number of particle in A, i.e., $\langle Q_A \rangle = \ell k_F/\pi$. Hence $Z_1(\alpha) = 1 + i\alpha\langle Q_A\rangle + O(\alpha^2)$. At half-filling $Z_1(\alpha)$ further simplifies as a consequence of the fact that, by particle-hole symmetry, for each ν_i

there is a ν_j such that $(1-\nu_i) = (1+\nu_j)$. Thus we have

$$Z_1(\alpha) = e^{i\alpha\ell/2}\prod_i \left[\left(\frac{1+\nu_i}{2}\right)e^{i\alpha/2} + \left(\frac{1-\nu_i}{2}\right)e^{-i\alpha/2}\right] = e^{i\alpha\ell/2}g(\alpha)\,, \tag{7.3.5}$$

with $g(\alpha)$ real and even. For general filling instead the odd cumulants are non-vanishing (the odd derivatives of $\ln Z_1(\alpha)$ are non zero) and $Z_1(\alpha)$ has no particular parity or reality properties. Indeed, Eq. (7.3.5) remains true for generic n

$$Z_n(\alpha) = e^{i\alpha\ell/2}\prod_i \left[\left(\frac{1+\nu_i}{2}\right)^n e^{i\alpha/2} + \left(\frac{1-\nu_i}{2}\right)^n e^{-i\alpha/2}\right] = e^{i\alpha\ell/2}g_n(\alpha)\,, \tag{7.3.6}$$

with $g_n(\alpha)$ real and even. This symmetry of $Z_n(\alpha)$ at half-filling represents a cross check of our numerical and analytic calculations. Again, away from half-filling, $\ln Z_n(\alpha)$ has all non-zero derivatives.

We notice that by Fourier transforming (7.3.3) one easily gets

$$\mathcal{Z}_n(q) = \sum_{\mathcal{S}_q}\prod_{i\in\mathcal{S}_q}\left(\frac{1+\nu_i}{2}\right)^n \prod_{j\in\bar{\mathcal{S}}_q}\left(\frac{1-\nu_j}{2}\right)^n, \tag{7.3.7}$$

where the sum is over all subset $\mathcal{S}_q$ of $\mathcal{S} = 1,\cdots,\ell$ of cardinality q and $\bar{\mathcal{S}}_q$ denotes the complementary subset. Unfortunately Eq. (7.3.7) is not a very convenient way to get $\mathcal{Z}_n(q)$, since one has to sum over $\ell!/((\ell-q)!q!)$ terms and this is impossible already for moderate values of ℓ. The most convenient way to extract $\mathcal{Z}_n(q)$ is by direct Fourier transform of $Z_n(\alpha)$.

7.3.1 Charged entropies via the generalised Fisher-Hartwig conjecture

The method that we employ takes advantage of the Toeplitz nature of the correlation matrix (7.3.2) that can be handled with the *(generalised) Fisher-Hartwig conjecture* providing the asymptotics of determinant of Toeplitz matrices. This technique has been used already in the context of entanglement in free lattice models to derive the leading term and the corrections to entanglement entropies [195, 196, 198, 199, 308, 359, 420–422]. We are going to show that the same technology applies also to the α-dependent moments $Z_n(\alpha)$ and therefore, as a consequence of the discussion above, to their symmetry resolved equivalent $\mathcal{Z}_n(q)$.

The starting point of our analysis is to rewrite the logarithm of Eq. (7.3.3)

$$\ln Z_n(\alpha) = \sum_{i=1}^{\ell} f_n(\nu_i,\alpha), \quad f_n(x,\alpha) = \ln\left[\left(\frac{1+x}{2}\right)^n e^{i\alpha} + \left(\frac{1-x}{2}\right)^n\right], \tag{7.3.8}$$

as a contour integral

$$\ln Z_n(\alpha) = \frac{1}{2\pi i}\oint d\lambda\, f_n(\lambda,\alpha)\frac{d\ln D_\ell(\lambda)}{d\lambda}, \tag{7.3.9}$$

where the contour of integration encircles the segment $[-1,1]$. Here we defined the characteristic polynomial of C_A as the determinant

$$D_\ell = \det\left[(\lambda+1)\mathbb{I}_A - 2C_A\right], \tag{7.3.10}$$

where $\mathbb{I}_A$ is the identity matrix restricted to A. In the basis that diagonalises C_A, such determinant simply becomes $D_\ell = \prod_i(\lambda-\nu_i)$ and therefore, by residue theorem, Eq. (7.3.9) is the same as (7.3.8).

In Refs. [195, 196] it has been exploited the fact that the matrix $(\lambda+1)\mathbb{I}_A - 2C_A$ has a Toeplitz form. Therefore the asymptotics for large ℓ of the determinant D_ℓ in (7.3.10) is obtained by means of the generalised Fisher-Hartwig conjecture. The derivation can be found in Ref. [196], here we just report the final result which is [196]

$$D_\ell(\lambda) \simeq (\lambda+1)^\ell\left(\frac{\lambda+1}{\lambda-1}\right)^{-\frac{k_F\ell}{\pi}} \sum_{m\in\mathbb{Z}} L_k^{-2(m+\beta_\lambda)^2} e^{-2ik_F m\ell}\left[G(m+1+\beta_\lambda)G(1-m-\beta_\lambda)\right]^2, \tag{7.3.11}$$

where $G(\cdot)$ is the Barnes G-function, $L_k = 2\ell|\sin k_F|$ and

$$\beta_\lambda = \frac{1}{2\pi i}\ln\left[\frac{\lambda+1}{\lambda-1}\right], \qquad \text{with} \quad \frac{d\beta_\lambda}{d\lambda} = \frac{1}{\pi i}\frac{1}{1-\lambda^2}. \tag{7.3.12}$$

For the moments $\mathrm{Tr}\rho_A^n$, i.e., $Z_n(\alpha=0)$ in (7.3.8), the leading term in the sum for D_ℓ in Eq. (7.3.11) is the one with $m=0$, first evaluated in [195]. The next to leading contributions come from the terms with $m=\pm1$ (at the same order) as shown in [196]. The situation for $\alpha\neq 0$ is slightly more complicated. For $-\pi<\alpha<\pi$ the leading term is always the one with $m=0$. Since $Z_n(\alpha)$ is periodic in α with period 2π we will restrict ourselves to $\alpha\in[-\pi,\pi]$, having in mind that, if required, the function can be extended outside of this interval by periodicity. Concerning the subleading contributions, the terms with $m=\pm1$ have different power laws, but one of them is always dominating, as we shall see. Anyhow, for values of α close to $\pm\pi$, also next-to-next leading terms should be taken into account in order to get reasonable results for moderately large values of ℓ. In the following we first compute the leading term and then we move to the calculations of the corrections.

Leading term $(m=0)$

For $\alpha\in[-\pi,\pi]$, the leading behaviour of Eq. (7.3.9) is given by term with $m=0$ in (7.3.11), i.e.,

$$D_\ell^{(0)}(\lambda) \equiv (\lambda+1)^\ell\left(\frac{\lambda+1}{\lambda-1}\right)^{-\frac{k_F\ell}{\pi}} L_k^{-2\beta_\lambda^2}\left[G(1+\beta_\lambda)G(1-\beta_\lambda)\right]^2, \tag{7.3.13}$$

so that the integral (7.3.9) is $\ln Z_n(\alpha) = \ln Z_n^{(0)}(\alpha) + o(\ell^0)$ with

$$\ln Z_n^{(0)}(\alpha) = \frac{1}{2\pi i}\oint d\lambda\, f_n(\lambda,\alpha)\frac{d\ln D_\ell^{(0)}(\lambda)}{d\lambda} = a_0\ell + a_1\ln L_k + a_2, \tag{7.3.14}$$

where

$$a_0 = \frac{1}{2\pi i}\oint d\lambda f_n(\lambda,\alpha)\left(\frac{1-k_F/\pi}{1+\lambda} - \frac{k_F/\pi}{1-\lambda}\right), \tag{7.3.15}$$

$$a_1 = \frac{1}{2\pi i}\oint d\lambda f_n(\lambda,\alpha)\frac{d(-2\beta_\lambda^2)}{d\lambda} = \frac{2}{\pi^2}\oint d\lambda f_n(\lambda,\alpha)\frac{\beta_\lambda}{1-\lambda^2}, \tag{7.3.16}$$

$$a_2 = \frac{1}{\pi i}\oint d\lambda f_n(\lambda,\alpha)\frac{d\ln[G(1+\beta_\lambda)G(1-\beta_\lambda)]}{d\lambda}, \tag{7.3.17}$$

are respectively the linear, the logarithmic and the constant term (in ℓ) coming from $\ln D_\ell^{(0)}$ in Eq. (7.3.13). These three integrals are explicitly calculated in Ref. [197] with final result

$$\ln Z_n^{(0)}(\alpha) = i\alpha\frac{k_F\ell}{\pi} - \left[\frac{1}{6}\left(n-\frac{1}{n}\right) + \frac{2}{n}\left(\frac{\alpha}{2\pi}\right)^2\right]\ln L_k + \Upsilon(n,\alpha), \tag{7.3.18}$$

where

$$\Upsilon(n,\alpha) = ni\int_{-\infty}^{\infty} dw[\tanh(\pi w) - \tanh(\pi n w + i\alpha/2)]\ln\frac{\Gamma(\frac{1}{2}+iw)}{\Gamma(\frac{1}{2}-iw)}, \tag{7.3.19}$$

in analogy with the definition $\Upsilon(n)$ in [195], which is recovered when $\alpha=0$. We stress that $\Upsilon(n,\alpha)$ is real for α real, even if not apparent from the formula. For future reference it is useful to write $\Upsilon(n,\alpha)$ as

$$\Upsilon(n,\alpha) = \Upsilon(n) + \gamma_2(n)\alpha^2 + \epsilon(n,\alpha), \qquad \epsilon(n,\alpha) = O(\alpha^4), \tag{7.3.20}$$

Eq. (3.18) contains several pieces of information. The linear term is just the mean number of particles in A, $\langle Q_A\rangle = k_F\ell/\pi$, as expected. Anyhow, this is the only term with an imaginary part up to order

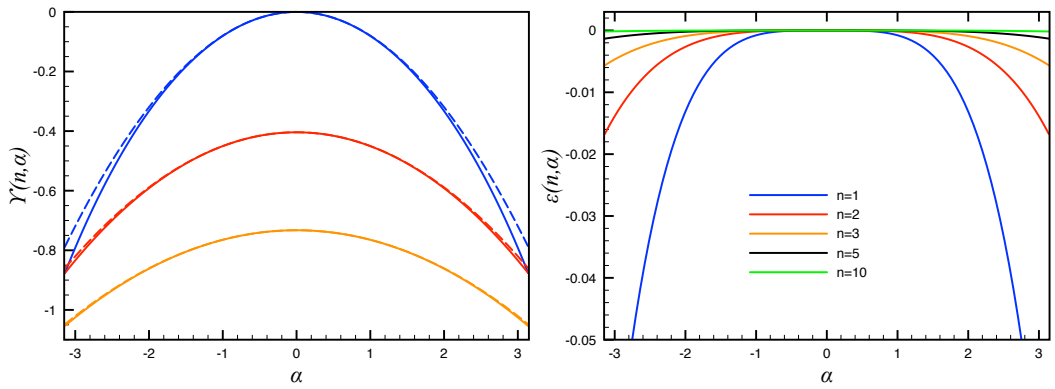

FIGURE 7.1: $\Upsilon(n,\alpha)$ in Eq. (7.3.19) as a function of α for $n = 1,2,3$ (top to bottom in the left panel). The exact forms (full lines) are compared with the quadratic approximation $\Upsilon(n) + \gamma_2(n)\alpha^2$ (dashed lines) showing that, although very close, they are definitively different. To highlight this similarity we plot in the right panel the difference $\epsilon(n,\alpha)$, cf. Eq (7.3.20) which is tiny, but non zero.

$O(1)$. We know that this is *exactly* true at half-filling ($k_F = \pi/2$), cf. Eq. (7.3.6). For generic filling, it is not true in general and we will observe in numerics tiny deviations at small ℓ in the imaginary part of $\ln Z_n(\alpha)$. The term $\propto \ln L_k$ provides the dimension of the modified twist field which comes out from the field theory calculation: the result agrees with the one found by CFT methods in (7.2.12) when specialised to a compact boson with $K = 1$. Indeed, this result, that was already checked numerically in [319], has been also analytically calculated by means of Widom conjecture in [417]. The constant term in Eq. (7.3.18) is probably the most interesting one, first because it is a result that was not known by other means (being non-universal cannot be fixed by field theory), and second because it provides few physical consequences. It is real and even in α, a property that was guaranteed only at half filling. It is independent from k_F, as its limit for $\alpha = 0$ [195]. Finally, it is very close to a parabola, but all the even terms in the series expansion are non zero, although $\epsilon(n,\alpha)$, cf. Eq. (7.3.20), is very small. In Figure 7.1 we report $\Upsilon(n,\alpha)$ as function of α for some n and compare it with the quadratic approximation $\Upsilon(n) + \gamma_2(n)\alpha^2$. The closeness of the two curves shows that the quadratic approximation will be enough for most of the applications, as we shall explicitly show. The accuracy of the quadratic approximation is also evident from the plot of $\epsilon(n,\alpha)$ in the right panel of Figure 7.1. On passing, this precision of the quadratic approximation of $\Upsilon(n,\alpha)$ explains, a posteriori, the quality of the symmetry resolved spectrum obtained in Ref. [319] exploiting the method of Stieltjes transform [142] which implicitly assumes this approximation.

In Figure 7.2 we report the numerical data for REEs with the insertion of a flux α for several values of n and α and with fillings $k_F = \pi/2$ (left) and $k_F = \pi/3$ (right). The theoretical prediction for the leading scaling in Eq. (7.3.18) is also reported for comparison. It is evident that the analytical result correctly describes the asymptotic data, but large and oscillating corrections to the scaling are present. The amplitude of these oscillations increase with n and with α. This peculiar n dependence was already known at $\alpha = 0$ [155, 196, 303, 307, 423]. In the following subsection we will explicitly consider these oscillations and work out their analytical description.

Leading corrections ($m = \pm 1$)

The leading correction to the determinant $D_\ell(\lambda)$ comes from the terms with $m = \pm 1$ in (7.3.11) and is given by [196]

$$D_\ell(\lambda) \simeq D_\ell^{(0)}(\lambda)[1 + \Psi_\ell(\lambda)],$$
$$\Psi_\ell(\lambda) = e^{-2ik_F\ell} L_k^{-2(1+2\beta_\lambda)} \frac{\Gamma^2(1+\beta_\lambda)}{\Gamma^2(-\beta_\lambda)} + e^{2ik_F\ell} L_k^{-2(1-2\beta_\lambda)} \frac{\Gamma^2(1-\beta_\lambda)}{\Gamma^2(\beta_\lambda)}. \quad (7.3.21)$$

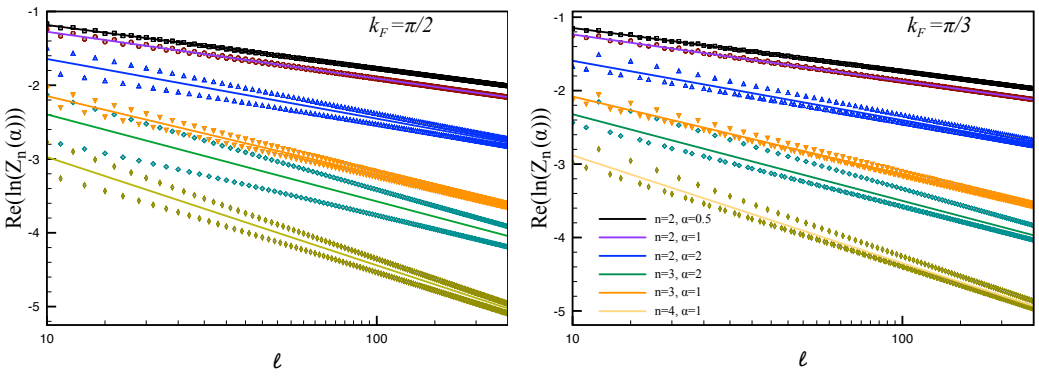

FIGURE 7.2: Leading scaling behaviour of the charged Rényi entropies with the insertion of a flux α. The numerical results (symbols) for several values of α and n are reported as function of ℓ for the filling $k_F = \pi/2$ (left) and $k_F = \pi/3$ (right). The numerical data match well the Fisher-Hartwig prediction (cf. Eq. (7.3.18)) although large oscillating corrections to the scaling are present.

We define the difference

$$d_n(\alpha) \equiv \ln Z_n(\alpha) - \ln Z_n^{(0)}(\alpha), \tag{7.3.22}$$

that for large L_κ is

$$d_n(\alpha) \simeq \frac{1}{2\pi i}\oint d\lambda\, f_n(\lambda,\alpha)\frac{d\ln\left[1+\Psi_\ell(\lambda)\right]}{d\lambda} = \frac{1}{2\pi i}\oint d\lambda\, f_n(\lambda,\alpha)\frac{d\Psi_\ell(\lambda)}{d\lambda} + \cdots . \tag{7.3.23}$$

Changing variable to $\lambda = \tanh(\pi w)$, in the final integral we only need the discontinuities across the branch cut that for the two cases are

$$\begin{aligned}
\left[L_\kappa^{-2-4\beta}\frac{\Gamma^2(1+\beta)}{\Gamma^2(-\beta)}\right]_{\beta=-iw-\frac{1}{2}} - \left[L_\kappa^{-2-4\beta}\frac{\Gamma^2(1+\beta)}{\Gamma^2(-\beta)}\right]_{\beta=-iw+\frac{1}{2}} &\simeq L_\kappa^{4iw}\gamma^2(w), \\
\left[L_\kappa^{-2+4\beta}\frac{\Gamma^2(1-\beta)}{\Gamma^2(\beta)}\right]_{\beta=-iw-\frac{1}{2}} - \left[L_\kappa^{-2+4\beta}\frac{\Gamma^2(1-\beta)}{\Gamma^2(\beta)}\right]_{\beta=-iw+\frac{1}{2}} &\simeq -L_\kappa^{-4iw}\gamma^2(-w),
\end{aligned}$$

where we have dropped terms of order $O(L_k^{-4})$ compared to the leading ones and we have defined

$$\gamma(w) = \frac{\Gamma(\frac{1}{2}-iw)}{\Gamma(\frac{1}{2}+iw)}. \tag{7.3.24}$$

Integrating by parts, we finally get

$$\begin{aligned}
d_n(\alpha) \simeq \frac{in}{2}\int_{-\infty}^{\infty} \mathrm{d}w\, &\left(\tanh(\pi w) - \tanh(\pi n w + i\alpha/2)\right) \\
&\times \left[e^{-2ik_F\ell}L_k^{4iw}\gamma^2(w) - e^{2ik_F\ell}L_k^{-4iw}\gamma^2(-w)\right].
\end{aligned} \tag{7.3.25}$$

This integral can be evaluated on the complex plane by residue theorem. For the first piece of the integral in square bracket, we should close the contour in the upper half plane, while for the second piece in the lower half plane. In principle we should sum over all residues inside the integration contour, but if we are interested in the limit of large L_k, we can limit ourself to consider the singularities closest to the real axis. For the first integral this is at $w = i/(2n)(1-\alpha/\pi)$ while for the second one it is at $w = -i/(2n)(1+\alpha/\pi)$.

Summing up the two contributions we finally have

$$d_n(\alpha) = e^{-2ik_F\ell} L_k^{-\frac{2}{n}\left(1-\frac{\alpha}{\pi}\right)} \left[\frac{\Gamma\left(\frac{1}{2}+\frac{1}{2n}-\frac{\alpha}{2\pi n}\right)}{\Gamma\left(\frac{1}{2}-\frac{1}{2n}+\frac{\alpha}{2\pi n}\right)}\right]^2 + e^{2ik_F\ell} L_k^{-\frac{2}{n}\left(1+\frac{\alpha}{\pi}\right)} \left[\frac{\Gamma\left(\frac{1}{2}+\frac{1}{2n}+\frac{\alpha}{2\pi n}\right)}{\Gamma\left(\frac{1}{2}-\frac{1}{2n}-\frac{\alpha}{2\pi n}\right)}\right]^2 . \quad (7.3.26)$$

Let us comment this result. First, it is obvious that the formula is valid only for $-\pi < \alpha < \pi$, else one

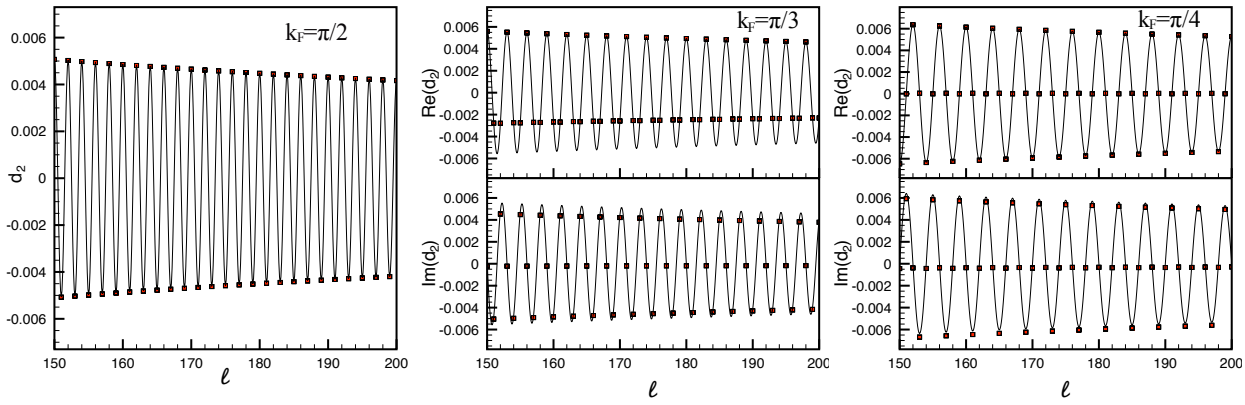

FIGURE 7.3: Behaviour of the leading corrections to the scaling. The difference $d_2(\ell) \equiv \ln Z_2(\alpha) - \ln Z_2^{(0)}(\alpha)$ is reported for $\alpha = 1$ and $k_F = \pi/2$ (left), $k_F = \pi/3$ (middle), $k_F = \pi/4$ (right) as a function of ℓ. The numerical data (symbols) perfectly match the calculated leading correction to the scaling from generalised Fisher-Hartwig conjecture in Eq. (7.3.26) both for real and imaginary part.

of the power laws would blow up as a consequence of the fact that one of the terms for $m = \pm 1$ becomes the leading ones. Then we see that this correction is real only for $\alpha = 0$ and at half-filling (when it should be real at all orders, cf. Eq. (7.3.6)). Away from half filling, there is generically a non-zero imaginary part. The two contributions have a different power-law decays (for $\alpha \neq 0$) and so only one of them is the leading correction depending on the sign of α. However, for α close to zero, the two powers are too close in magnitude and they should be both taken into account in order to have an accurate description of the data for moderately large values of ℓ. When α gets closer and closer to $\pm\pi$, Eq. (7.3.26) becomes accurate only for very large ℓ because the term with $m = 0$ is about of the same order of magnitude as the one with $m = \pm 1$ (depending on the sign of α). A better description of the asymptotic behaviour may be achieved using Eq. (7.3.11) without expanding as in Eq. (7.3.21). Finally, let us notice that, while in the absence of flux ($\alpha = 0$) the oscillating corrections to the scaling vanish in the limit $n \to 1$ [196], for $\alpha \neq 0$ also the von Neumann entropy presents leading oscillating corrections described by Eq. (7.3.26).

In Figures 7.3 and 7.4 we report the difference $d_2(\alpha)$ as calculated numerically for $k_F = \pi/2, \pi/3, \pi/4$ and for $\alpha = 1$ and $\alpha = 2$ as function of ℓ. The numerical data are compared with the leading prediction in Eq. (7.3.26) and the agreement is extremely good. We actually observe that this prediction works slightly worst for $\alpha = 2$ (cf. Fig. 7.4) than for $\alpha = 1$ (cf. Fig. 7.3). We indeed checked that the match becomes worst and worst when α moves close to π, when the leading term in the generalised Fisher-Hartwig changes. In principle it is possible to systematically analyse further corrections to $\ln Z_n(\alpha)$ by taking into account the known expansion of $D_\ell(\lambda)$ in powers of ℓ [196], but this is very cumbersome and far beyond the scope of this paper.

7.4 Free fermions on a lattice: symmetry resolved entropies

In this Section we finally move to the symmetry resolved entropies and to their analysis.

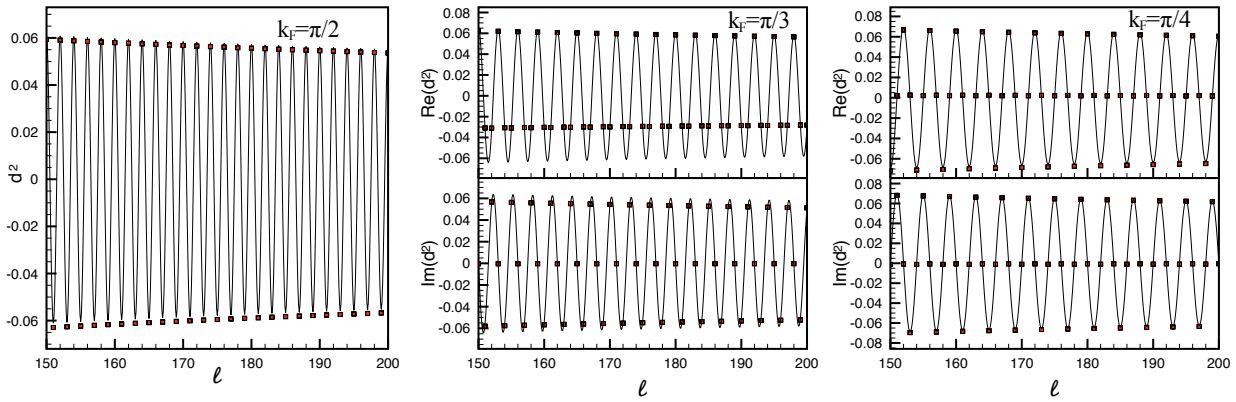

FIGURE 7.4: Behaviour of the leading corrections to the scaling. The difference $d_2(\ell) \equiv \ln Z_2(\alpha) - \ln Z_2^{(0)}(\alpha)$ is reported for $\alpha = 2$ and $k_F = \pi/2$ (left), $k_F = \pi/3$ (middle), $k_F = \pi/4$ (right) as a function of ℓ. The numerical data (symbols) perfectly match the calculated leading correction to the scaling from generalised Fisher-Hartwig conjecture in Eq. (7.3.26) both for real and imaginary part. We notice that here Eq. (7.3.26) works slightly worst compared to the case $\alpha = 1$ in Fig. 7.3.

7.4.1 Q_A-resolved moments via Fourier trasform

The first step toward the symmetry resolved entropies is to calculate $\mathcal{Z}_n(q)$, the Fourier transform of $Z_n(\alpha)$ as defined in Eq. (7.2.8). We will show that we may obtain a very accurate prediction by keeping only the $m = 0$ term in (7.3.11), but with all non-universal pieces. Within this approximation the Fourier transform $\mathcal{Z}_n(q)$ is

$$\mathcal{Z}_n(q) \simeq \int_{-\pi}^{\pi} \frac{d\alpha}{2\pi} e^{-iq\alpha} Z_n^{(0)}(\alpha) = L_k^{-\frac{1}{6}\left(n-\frac{1}{n}\right)} \int_{-\pi}^{\pi} \frac{d\alpha}{2\pi}\, e^{-i\left(q-\frac{k_F}{\pi}\ell\right)\alpha - b_n\alpha^2} e^{\Upsilon(n,\alpha)}, \tag{7.4.1}$$

where we defined the "bare variance"

$$b_n = \frac{2}{n}\frac{1}{4\pi^2}\log L_k. \tag{7.4.2}$$

We start by using Eq. (7.3.20) to rewrite $\mathcal{Z}_n(q)$ as

$$\begin{aligned}\mathcal{Z}_n(q) &\simeq e^{\Upsilon(n)} L_k^{-\frac{1}{6}\left(n-\frac{1}{n}\right)} \int_{-\pi}^{\pi} \frac{d\alpha}{2\pi}\, e^{-i\left(q-\frac{k_F}{\pi}\ell\right)\alpha - (b_n-\gamma_2(n))\alpha^2} e^{\epsilon(n,\alpha)} \\ &= Z_n^{(0)}(0) \int_{-\pi}^{\pi} \frac{d\alpha}{2\pi}\, e^{-i\left(q-\frac{k_F}{\pi}\ell\right)\alpha - b_n^R\alpha^2} g_n(\alpha),\end{aligned} \tag{7.4.3}$$

where $Z_n^{(0)}(0) = Z_n^{(0)}(\alpha = 0) = e^{\Upsilon(n)} L_k^{-\frac{1}{6}\left(n-\frac{1}{n}\right)}$, we defined the "renormalised variance"

$$b_n^R \equiv b_n - \gamma_2(n)\,, \tag{7.4.4}$$

and $g_n(\alpha) \equiv e^{\epsilon(n,\alpha)}$. Up to this point, we only rewrote the starting expression (7.4.1). We now proceed by treating the integral, for large subsystem size ℓ, by means of the saddle point approximation. When $\ell \gg 1$, the large parameter in (7.4.3) is b_n. Furthermore, we assume that $g_n(\alpha) = 1$, because we have shown in the previous Section that the function $\epsilon(n,\alpha) \ll 1$, cf. Fig. 7.1. Within this approximation we finally get

$$\begin{aligned}\mathcal{Z}_n(q) \simeq Z_n^{(0)}(0) \int_{-\infty}^{\infty} \frac{d\alpha}{2\pi}\, e^{-i\left(q-\frac{k_F}{\pi}\ell\right)\alpha - b_n^R\alpha^2} &= Z_n(0) e^{-\frac{(q-\bar{q})^2}{4b_n^R}} \sqrt{\frac{1}{4\pi b_n^R}} = \\ Z_n(0)\sqrt{\frac{n\pi}{2(\ln L_k - 2\pi^2 n\gamma_2(n))}}\, e^{-\frac{n\pi^2(q-\bar{q})^2}{2(\ln L_k - 2\pi^2 n\gamma_2(n))}}&,\end{aligned} \tag{7.4.5}$$

where we defined $\bar{q} \equiv \langle Q_A \rangle = \ell k_F/\pi$.

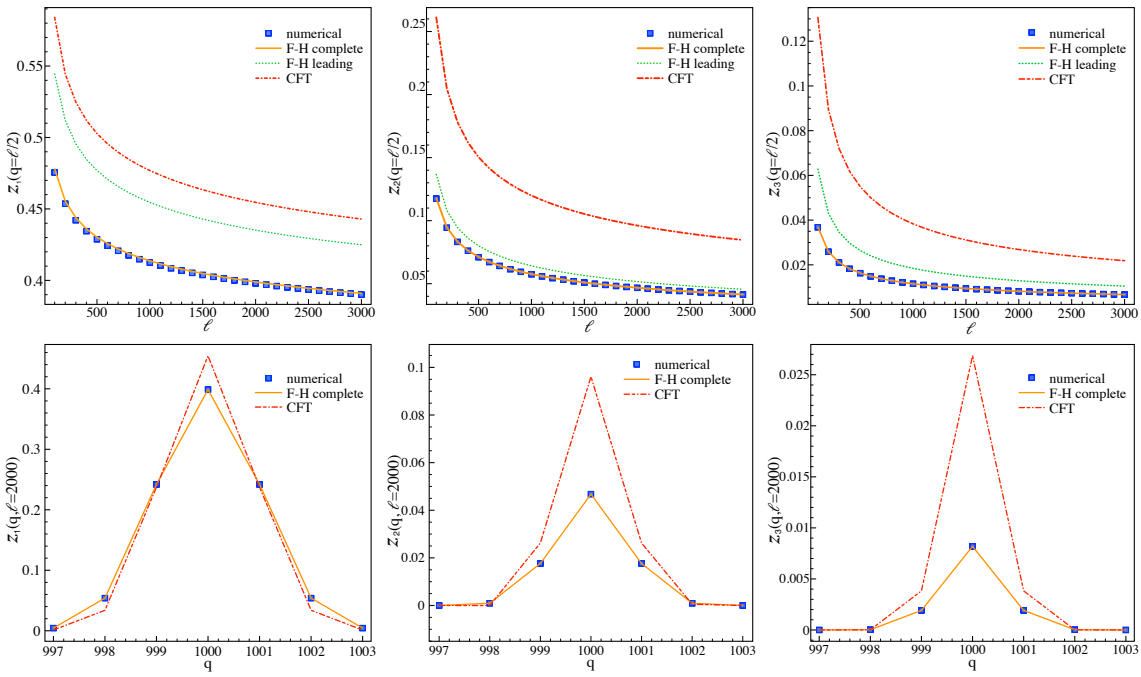

FIGURE 7.5: Symmetry resolved partition sums $\mathcal{Z}_n(q)$. Top: $\mathcal{Z}_n(q=\ell/2)$ at half filling as a function of ℓ. The numerical data for $n=1,2,3$ (left to right) are compared with: i) the CFT prediction without fixing the non universal constant (dot-dashed line); ii) the leading Fisher-Hartwig prediction at $O(1)$, i.e., Eq. (7.4.5) with $\gamma_2(n)=0$ (dotted line); iii) the complete Fisher-Hartwig result, Eq. (7.4.5) (full line). Clearly only the latter accurately describes the data, although the qualitative behaviour is the same for all curves. Bottom: $\mathcal{Z}_n(q)$ at half filling for $\ell=2000$ as function of q. The numerical data for $n=1,2,3$ (left to right) are compared with: i) the CFT prediction without fixing the non universal constant (dot-dashed line); ii) the complete Fisher-Hartwig result, Eq. (7.4.5) (full line).

Eq. (7.4.5) is one of the main results of this paper. Let us discuss its features. First, in the limit $\ell\to\infty$, we recover the CFT result (7.2.14) for $K=1$, but with the correct normalisation of $Z_n(0)$. Although this normalisation was not previously known rigorously (at least to the best of our knowledge), it could have been easily guessed from the results in the absence of flux (i.e., $\alpha=0$ of Ref. [195]). The mean of the gaussian term is $\bar{q}$ and it is not changed compared to the result (7.2.14). Consequently, the main new insight from Eq. (7.4.5) is the prediction for the constant term to add to $\ln L_k$ (or equivalently, the multiplicative scale for L_k as in [318]). Although this non-universal constant is a correction to the leading behaviour (expanding for large L_k, it gives a term going like $(\ln L_k)^{-1}$), it is very important: the $(\ln L_k)^{-1}$ decay is so slow that it must be taken into account even for very large L_k in order to quantitatively describe the data, as we shall see.

Given the importance that the quantity $\gamma_2(n)$ has in this analysis, we report its analytic expression

$$\gamma_2(n)=\frac{ni}{4}\int_{-\infty}^{\infty}dw[\tanh^3(\pi n w)-\tanh(\pi n w)]\ln\frac{\Gamma(\frac{1}{2}+iw)}{\Gamma(\frac{1}{2}-iw)}, \tag{7.4.6}$$

as well as its explicit numerical value for some n: $\gamma_2(1)=-0.0799027$, $\gamma_2(2)=-0.0462208\ldots$, and $\gamma_2(3)=-0.0319926\ldots$ (in particular $\gamma_2(1)=-(1+\gamma_E)/(2\pi^2)$ with γ_E the Euler constant, as anticipated in [318]). The importance of this constant in the description of the numerical data, was understood already in [318], where the authors define $g_n=2e^{-2\pi^2 n\gamma_2(n)}$ and provide the analytic results for $n=1$, as well as a numerical estimate for $n=2$, i.e., $g_2\sim 12.39$ which is very close to the exact value that we have found $g_2=12.4022\ldots$.

Let us briefly discuss the terms that have been neglected in the derivation of Eq. (7.4.5). The most relevant one comes from having approximated $g_n(\alpha)$ with 1. By expanding this function in powers of α, it is immediate to realise that the series coefficient α^{2k} (with $k\geq 2$) provides a correction to the leading

term of the order $(\ln L_k)^{-k}$. Anyhow, these factors influence little the final result because the amplitude of the various terms is very small. Another correction comes from the extremes of integration that we pushed to $\pm\infty$ instead of $\pm\pi$. Although their effect can be taken into account as done in Ref. [318], they provide corrections which decay as $e^{-\pi^2 b_n^R}/b_n^R$, i.e., algebraically in L_k, and so negligible at this level. Also the corrections due to the terms with $m \neq 0$ in (7.3.11) decay as power laws in L_k and can be safely neglected at this stage.

In Figure 7.5 we report the numerically calculated symmetry resolved partition sums $\mathcal{Z}_n(q)$. We compare the numerical data for $n = 1, 2, 3$ with the CFT prediction without fixing the non universal constant as in Eq. (7.2.14). The qualitative agreement is reasonable, but quantitatively far. We also report the prediction for $\mathcal{Z}_n(q)$ at order $O(\ell^0)$: the curves moves closer to the numerical data, but the match is still not perfect. Only when we use the complete Fisher-Hartwig prediction (7.4.5) (with the correct value of $\gamma_2(n)$), the data are perfectly reproduced. As anticipated, including the logarithmic corrections is fundamental to have an accurate description of the data. Also the q-dependence of $\mathcal{Z}_n(q)$ is perfectly captured by (7.4.5) as shown in the lower panels of Figure 7.5.

7.4.2 Symmetry resolved Rényi and entanglement entropy

We now use Eq. (7.4.5) to calculate the symmetry resolved Rènyi and the Von Neumann entropies. Let us start from the former. Eq. (7.2.6) implies

$$S_n(q) = \frac{1}{1-n}\ln\left[\frac{\mathcal{Z}_n(q)}{\mathcal{Z}_1(q)^n}\right] \simeq \frac{1}{1-n}\ln\frac{Z_n(0)}{(Z_1(0))^n}\frac{e^{-\frac{(q-\bar{q})^2}{4b_n^R}}}{e^{-\frac{n(q-\bar{q})^2}{4b_1^R}}}\frac{(4\pi b_n^R)^{-1/2}}{(4\pi b_1^R)^{-n/2}}. \tag{7.4.7}$$

The first ratio in (7.4.7) just gives the total Rényi entropy of order n, with the right additive constant (and indeed this is true at all orders). The other q-independent term is

$$\begin{aligned}\frac{1}{1-n}\ln\frac{(4\pi b_n^R)^{-1/2}}{(4\pi b_1^R)^{-n/2}} &= -\frac{1}{2}\ln\frac{2}{\pi} + \frac{\ln n}{2(1-n)} + \frac{1}{1-n}\ln\frac{(\ln L_k - 2\pi^2\gamma_2(1))^{n/2}}{(\ln L_k - 2\pi^2 n\gamma_2(n))^{1/2}} \\ &= -\frac{1}{2}\ln\left(\frac{2}{\pi}\ln\delta_n L_k\right) + \frac{\ln n}{2(1-n)} + \cdots. \end{aligned} \tag{7.4.8}$$

The constant δ_n has been introduced to resum partially the subleading corrections to the scaling and it is given by

$$\ln\delta_n = -\frac{2\pi^2 n(\gamma_2(n)-\gamma_2(1))}{1-n}. \tag{7.4.9}$$

The last term is the ratio of the two Gaussian factors which is the only one depending on q. For this last contribution we have

$$\frac{1}{1-n}\ln e^{\frac{n(q-\bar{q})^2}{4b_1^R}-\frac{(q-\bar{q})^2}{4b_n^R}} = (q-\bar{q})^2\pi^4\frac{n}{1-n}(\gamma_2(1)-n\gamma_2(n))\frac{1}{\ln^2\kappa_n L_k} + \dots, \tag{7.4.10}$$

where the constant

$$\ln\kappa_n = -\pi^2(\gamma_2(1)+n\gamma_2(n)), \tag{7.4.11}$$

has been introduced, again, to resum partially the subleading corrections.

Putting together the three pieces we have

$$S_n(q) = S_n - \frac{1}{2}\ln\left(\frac{2}{\pi}\ln\delta_n L_k\right) + \frac{\ln n}{2(1-n)} + (q-\bar{q})^2\pi^4\frac{n(\gamma_2(1)-n\gamma_2(n))}{1-n}\frac{1}{\ln^2\kappa_n L_k} + \cdots. \tag{7.4.12}$$

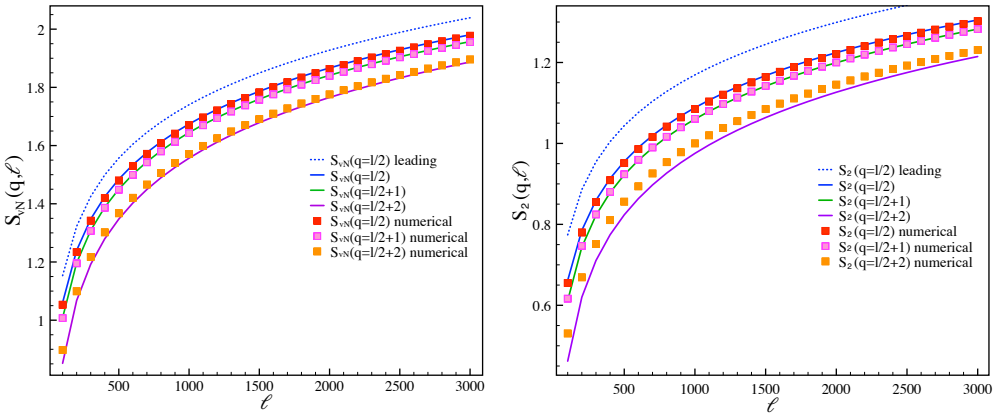

FIGURE 7.6: Von Neumann (left) and second Rényi (right) symmetry resolved entanglement entropies. The numerical data (symbols) for $q = \ell/2, \ell/2+1, \ell/2+2$ are compared with the theoretical predictions Eqs. (7.4.12) and (7.4.13). The figures also highlight the importance of the logarithmic corrections to the scaling which are fundamental in order to accurately describe the data for ℓ as large as 3000 and even larger. Increasing the values of $(q-\bar{q})^2$, the corrections to the scaling that we neglect become more important.

This equation not only predicts the leading diverging behaviour for large ℓ which was already known from CFT [318, 319] (cf. Eq. (7.2.15)), but also the non-universal additive constant, as well as the some subleading corrections in $\ln L_k$. The latter are not only important to correctly describe the data, but are also the leading q-dependent contributions. So while the leading and finite terms satisfy the equipartition of entanglement [318], within our approach we are able to identify the leading term that breaks this equipartition.

Taking now the limit for $n \to 1$, we get the von Neumann entropy

$$S(q) = S - \frac{1}{2}\ln\left(\frac{2}{\pi}\ln\delta_1 L_k\right) - \frac{1}{2} + (q-\bar{q})^2\,\pi^4\frac{(\gamma_2(1)+\gamma_2'(1))}{\ln^2\kappa_1 L_k} + \cdots, \tag{7.4.13}$$

with $\ln\delta_1 = 2\pi^2\gamma_2'(1)$ and $\gamma_2'(1) = 0.0545724$.

These Fisher-Hartwig calculations for the symmetry resolved entanglement are compared with the numerical data in Figure 7.6. It is evident in these figures that the results for different q are *not* on top of each other although we reported ℓ as large as 3000. Indeed their difference (that we know to go to zero as $(\ln\ell)^{-2}$) can be easily misinterpreted as a different additive constant if one would proceed with a fit of the numerical data. Only the exact knowledge of the asymptotic behaviour (7.4.12) and (7.4.13) allow us to correctly understand the data. In the figure we also report Eqs. (7.4.12) and (7.4.13) truncated at $o(1)$ (just for $q = \bar{q}$), showing that these leading curves are far from the data and that the distance between the two barely reduces. We stress that not only the prefactor of the logarithmic corrections are important, but also the precise values of the amplitudes (7.4.11) and (7.4.9), as it is easy to check. Finally we observe that increasing $(q-\bar{q})$ the corrections to the scaling that we neglected become more important.

We finish the Section commenting about the double log contribution in Eqs. (7.4.12) and (7.4.13). It may seem rather awkward that all the symmetry resolved contributions have a double log correction, while the total entanglement entropy does not. Indeed, when calculating the total entanglement this double log cancels when summing to the fluctuation entanglement S^f as in Eq. (7.2.2). Indeed, taking as a prototypical example the von Neumann entropy and using that the probability is $p(q) = \mathcal{Z}_1(q)$, we have

$$S^f = -\int_q \mathcal{Z}_1(q)\ln\mathcal{Z}_1(q) \simeq -\int dq \frac{e^{-\frac{(q-\bar{q})^2}{4b_1^R}}}{\sqrt{4\pi b_1^R}}\ln\frac{e^{-\frac{(q-\bar{q})^2}{4b_1^R}}}{\sqrt{4\pi b_1^R}} = \frac{1}{2}(1+\ln 4\pi b_1^R) =$$
$$= \frac{1}{2}\left(1+\ln\left(\frac{2}{\pi}\ln L_k - \gamma_2(1)\right)\right) = \frac{1}{2} + \frac{1}{2}\ln\left(\frac{2}{\pi}\ln L_k\right) + O(L_k^{-1}). \tag{7.4.14}$$

Note that both leading terms in S^f in the above equation cancel *exactly* with the corresponding ones in the symmetry resolved entanglement in Eq. (7.4.13). The same is true for all Rényi entropies of arbitrary order.

7.5 Charged and symmetry resolved entanglement for the Fermi gas

In this Section we derive the symmetry resolved entanglement entropy for a Fermi gas using the overlap matrix approach introduced in Section 1.4.3.

The system we are going to study consists of a gas of N free spinless non-relativistic fermions with some suitable boundary conditions in order to have a discrete energy spectrum. The many body wave functions $\Psi(x_1,...,x_N)$ is the Vandermonde determinant $\Psi(x_1,...,x_N) = \det[\phi_m(x_n)]/\sqrt{N!}$, built with the occupied single particle eigenstates with wave functions $\phi_m(x)$. The many body ground state is obtained by filling the N levels with lowest energies. Given that there is no lattice, the particle number N provides also the ultraviolet cutoff. In the case of a system with periodic boundary conditions in the interval $[0, L]$, the eigenfunctions are plane waves $\phi_k(x) = e^{2\pi i k x/L}/\sqrt{L}$ with integer wave-numbers k. When the subsystem is also an interval, say $A = [0, \ell]$, the overlap matrix [cf. Eq. (1.4.34)] is easily calculated and reads

$$\mathbb{A}_{nm} = \frac{\sin \pi(n-m)\ell/L}{\pi(n-m)}, \qquad n, m = 1, \cdots, N. \tag{7.5.1}$$

A crucial observation made in [173] is that such matrix is identical to the lattice correlation matrix, Eq. (7.3.2), upon identifying k_F/π with ℓ/L and N with ℓ. As a consequence, this simple replacement allows to translate all the results from the lattice to the continuous model. In particular all formulas derived for the tight binding model are valid also for the gas, where now L_k is not anymore $2\ell \sin k_F$, but

$$L_k = 2N \sin \pi \frac{\ell}{L}\,. \tag{7.5.2}$$

Thus, for the symmetry resolved entanglement we can straightforwardly make our predictions for the gas. The REEs in the presence of a flux are

$$\begin{aligned}\ln Z_n(\alpha) = i\alpha\frac{\ell N}{L} - \left[\frac{1}{6}\left(n-\frac{1}{n}\right)+\frac{2}{n}\left(\frac{\alpha}{2\pi}\right)^2\right]\ln\left[2N\sin\left(\pi\frac{\ell}{L}\right)\right] + \Upsilon(n,\alpha) + \\ e^{-\frac{2i\pi\ell N}{L}}\left[2N\sin\left(\pi\frac{\ell}{L}\right)\right]^{-\frac{2}{n}\left(1-\frac{\alpha}{\pi}\right)}\left[\frac{\Gamma\left(\frac{1}{2}+\frac{1}{2n}-\frac{\alpha}{2\pi n}\right)}{\Gamma\left(\frac{1}{2}-\frac{1}{2n}+\frac{\alpha}{2\pi n}\right)}\right]^2 + \\ + e^{\frac{2i\pi\ell N}{L}}\left[2N\sin\left(\pi\frac{\ell}{L}\right)\right]^{-\frac{2}{n}\left(1+\frac{\alpha}{\pi}\right)}\left[\frac{\Gamma\left(\frac{1}{2}+\frac{1}{2n}+\frac{\alpha}{2\pi n}\right)}{\Gamma\left(\frac{1}{2}-\frac{1}{2n}-\frac{\alpha}{2\pi n}\right)}\right]^2,\end{aligned} \tag{7.5.3}$$

where we only included the leading contributions at $m = 0, \pm 1$ in the generalised Fisher-Hartwig conjecture. We tested this result against exact numerical computations and, as for the lattice model, we found that it provides a very accurate description as long as α is not close to $\pm\pi$.

Similarly, for the symmetry resolved entropies the predictions for the gas are obtained simply by plugging Eq. (7.5.2) into Eqs. (7.4.12) and (7.4.13) for Rényi and von Neumann entropy respectively (with $\bar{q} = \frac{\ell N}{L}$).

7.6 Concluding remarks

In this Chapter, we derived exact formulas for the asymptotic behavior of the symmetry resolved entanglement entropies in free fermion systems. First, we obtained an exact expression for the charged entropies given by Eqs. (7.3.18) (asymptotic behaviour up to order $O(1)$) and (7.3.26) (leading corrections to the scaling). The leading logarithmic term in (7.3.18) perfectly matches the CFT prediction, but we also determined the non-universal $O(1)$ contribution. The $o(1)$ corrections present interesting oscillatory behavior

and a power-law decay with exponents that depend on the flux α. We then moved to the true symmetry resolved entropies given by the Fourier transform of the charged ones. The partition sums are given by Eq. (7.4.5), while Rényi and von Neumann entropy by Eqs. (7.4.12) and (7.4.13) respectively. These equations agree in the limit of large ℓ with the CFT results, but we also determine a number of non-universal constants as well as logarithmic corrections to the scaling which are fundamental for an accurate description of the numerical data. Our analysis also provides the first term in the expansion for large ℓ which depends on the symmetry sector, hence breaking the equipartition of entanglement [318]. We also related the double logarithmic correction to the fluctuation entanglement.

While we have considered the specific case of free fermions, many features we find are in fact universal. The CFT results [318, 319] (cf. Eq. (7.2.15)) shows how the leading term of the charged entropies get renormalised by the Luttinger liquid parameter K. A first natural question is how the exponent of the leading corrections to the scaling gets renormalized. It would be very interesting to adapt the field theoretical approach of Refs. [155, 307] to understand how this new universal exponent (equal to $2/n(1 \pm \alpha/\pi)$ for free fermions) can be obtained in CFT. For the symmetry resolved entanglement we showed the presence of very large logarithmic corrections to the scaling. The natural question here is whether they are universal and if they can be also understood within CFT. Furthermore, we find that many non-universal constants entering in these corrections are related to each other (e.g. Eqs. (7.4.9) and (7.4.11)): it is interesting to understand also the level of universality of these relations.

Finally, there are few possible generalizations of the present calculations that can be done following the same logic as here; for example the case of an open system can be analyzed exploiting the generalized Fisher-Hartwig results in [308], disjoint intervals using the approach in [199], and trapped gases can be studied by random matrix techniques [184, 419] to recover results from curved CFT [159].

Part II

QUANTUM CORRELATIONS IN INHOMOGENEOUS SETTINGS

Chapter 8

Entanglement and relative entropies in the trapped free fermi gas

CFTs in curved backgrounds have been used to describe inhomogeneous $1d$ systems, such as quantum gases in trapping potentials and non-equilibrium spin chains. This approach provided, in an elegant and simple fashion, non-trivial analytic predictions for quantities, such as the entanglement entropy, that are not accessible through other methods. Here, we generalize this approach to low-lying excited states, focusing on the entanglement and relative entropies in an inhomogeneous free-fermionic system. Our most important finding is that the universal scaling function characterizing these entanglement measurements is the same as the one for homogeneous systems, but expressed in terms of a different variable, being a non-trivial function of the subsystem length and system's inhomogeneity that is easily written in terms of the curved metric. This Chapter is based on Ref. [375].

8.1 Introduction

Universality is one of the most striking features of critical systems, clearly displayed in the ground state scaling of entanglement entropies and not only: it has been indeed pointed out that also low-energy eigenstates presents universal aspects [359, 371]. The REEs of these excitations, when corresponding to conformal primary fields, have been characterized in Refs. [349,371]. It has been shown that they are related to conformal properties of the operator defining the targeted excitation by a universal function, previously introduced in Eq. (4.2.4). Another important object capturing the universal features of low-lying excited states is the ReE, which in a replica approach is obtained as the limit of the universal ratio already found in Eq. (4.2.15). See Chapter 4 for further details.

Unfortunately, all these universal features seem to be completely lost, at least at first sight, in real experiments where different kinds of inhomogeneities are always present. For example, recent important advances in cold atoms have allowed to set up experiments to measure the many-body entanglement [34–37, 229,232,233,242,245]. However, these ultracold quantum gases are trapped by external (usually parabolic) potentials breaking translational invariance and therefore, *a fortiori*, conformal invariance. Nevertheless, it has been pointed out in Ref. [159] that, under certain assumptions, conformal invariance can be restored at the price of working in a curved background: it is still possible to have an underlying CFT description but in a spacetime that is not flat anymore. The key assumption for this approach is the *local density approximation* (LDA), i.e. the system has to exhibit separation of scales: more precisely, there must exist a mesoscopic scale ℓ at which the system is locally homogeneous (i.e. small compared to the scale at which inhomogeneity becomes important, of order $\rho|\partial_x\rho|$, with ρ the density of the system), but still contains a very large number of particles (i.e. large compared to the inter-particle distance, of order of the inverse of the local average density $\langle\rho(x)\rangle^{-1}$), that is the mesoscopic scale ℓ must satisfy $\langle\rho(x)\rangle^{-1} \ll \ell \ll \rho|\partial_x\rho|$, see Fig. 8.1.

This curved CFT approach has already been employed for many applications: the entanglement entropies [159], the entanglement hamiltonian [424], and some correlation functions [159,425,426] have been calculated for many different situations in inhomogeneous free-fermion models; the field theory description of the rainbow model was also unveiled [427], spin chains with gradients were studied [428], and the presence of curved lightcones has been investigated [429]. All these applications refer to free models, but some results for interacting systems are also available [430–433].

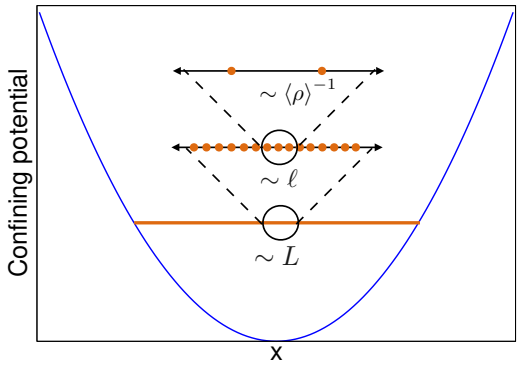

FIGURE 8.1: Illustration of the local density approximation (LDA). L is the typical macroscopic length of the system over which the density changes. The average local distance between particles is of the order of $\langle\rho(x)\rangle^{-1}$ ($\rho(x)$ being the density). The mesoscopic scale ℓ, where the approximation holds, must satisfy $L \ll \ell \ll \langle\rho\rangle^{-1}$.

Here we want to understand whether and in which form the universality features of the entanglement in low-lying excited states persist in inhomogeneous settings, as a consequence of the restored conformal invariance in curved spacetime. In particular, we are going to focus on the ratios defined by Eqs. (4.2.4) and (4.2.15) and their analytic continuations. As an explicit example, we are going to employ the curved metric approach for a free Fermi gas in a (harmonic) trapping potential. We will show that Eqs. (4.2.4) and (4.2.15) still display very universal features. Interestingly and surprisingly, they turn out to be the same functions as in the analogous homogeneous setting, but of a different variable, related to the subsystem size and to the curved metric.

This Chapter is organized as follows. In Section 8.2 we briefly review the curved CFT approach to the inhomogenous free Fermi gas and its bosonization. In Sections 8.3 and 8.4, after recalling how the calculations of REEs and ReEEs work in the homogeneous case, we adapt them to the inhomogeneous situation and derive the CFT predictions for different excited states. In Section 8.5 we benchmark our analytic results against exact numerical computations for a Fermi gas with a finite number N of particles, finding excellent agreement for large N. We finally conclude in Section 8.6.

8.2 Inhomogeneous systems, CFT in curved space, and bosonisation

Although our approach is very general and applies to many different inhomogeneous 1D free Fermi systems, for concreteness we will focus through the entire manuscript on a Fermi gas trapped by an external potential. According to Ref. [159], the long distance behaviour of this model is described by a massless Dirac fermion in a curved spacetime whose metric encodes the inhomogeneity parameters. We recall below the main steps to show this equivalence.

We start by considering the homogeneous free Fermi gas in 1D with hamiltonian

$$H = \int_{-\infty}^{+\infty} dx\, c^\dagger(x) \left[-\frac{\hbar^2}{2m}\partial_x^2 - \mu \right] c(x), \tag{8.2.1}$$

μ being the chemical potential. The ground-state propagator in imaginary time ($\tau = it$) is

$$\langle c^\dagger(x,\tau)c(0,0)\rangle = \int_{-k_F}^{k_F} \frac{dk}{2\pi} e^{-i[kx+\varepsilon(k)\frac{\tau}{\hbar}]}, \tag{8.2.2}$$

where $\varepsilon(k) = \hbar^2k^2/2m - \mu$ is the energy and $k_F = \frac{1}{\hbar}\sqrt{2m\mu}$ is the Fermi momentum. Linearising

the spectrum around the Fermi points $\pm k_F$, $\varepsilon(k) = \pm \frac{d\varepsilon}{dk}\Big|_{k=k_F}(k \mp k_F) = \pm v_F \hbar(k \mp k_F)$, in the limit $x, v_F\tau \gg 1/k_F$, it becomes

$$\langle c^\dagger(x,\tau)c(0,0)\rangle \simeq \frac{i}{2\pi}\left[\frac{e^{-ik_F x}}{x+iv_F\tau} - \frac{e^{ik_F x}}{x-iv_F\tau}\right]. \tag{8.2.3}$$

A crucial observation is that the two terms in (8.2.3) coincide with the two-point functions of the R/L-components ($\psi^\dagger_{R,L}(x,\tau)$) of a massless Dirac fermion in 2D euclidean spacetime, noting that

$$\langle \psi^\dagger_{R,L}(x,\tau)\psi_{R,L}(0,0)\rangle = \frac{1}{2}\frac{1}{x \pm iv_F\tau}, \qquad \langle \psi^\dagger_{R,L}(x,\tau)\psi_{L,R}(0,0)\rangle = 0. \tag{8.2.4}$$

We now add to the hamiltonian in Eq. (8.2.1) an external potential $V(x)$, that at first we consider harmonic $V(x) = m\omega^2 x^2/2$. In the TDL, the density profile of fermions follows the Wigner semicircle law [434]

$$\rho(x) = \frac{1}{\pi\hbar}\sqrt{2\mu m - m^2\omega^2 x^2}, \tag{8.2.5}$$

which is different from zero only in the interval $[-L, L]$ where $L = \frac{1}{\omega}\sqrt{\frac{2\mu}{m}}$. Hereafter we set $\hbar = m = \omega = 1$. The length L is related to the total number of particles as $L = \sqrt{2N}$ (given that $N = \int dx\, \rho(x) = \mu$) and it sets the macroscopic scale of the system. For the LDA to hold, it should exist an intermediate scale ℓ which is large compared to the microscopic scale but small compared to the scale on which physical quantities vary macroscopically, here measured by L. For large N and away from the edges, one has $N^{-1/2} \sim \langle\rho\rangle^{-1} \ll \ell \ll L \sim N^{1/2}$, and hence LDA applies. At this scale the system can be seen locally as homogeneous, with a Fermi momentum $k_F(x) = \pi\rho(x)$ and propagator of the same form as in (8.2.3)

$$\langle c^\dagger(x+\delta x, \tau+\delta\tau)c(x,\tau)\rangle \simeq \frac{i}{2\pi}\left[\frac{e^{-i(k_F(x)\delta x + iv_F(x)\delta\tau)}}{\delta x + iv_F(x)\delta\tau} - \frac{e^{i(k_F(x)\delta x - iv_F(x)\delta\tau)}}{\delta x - iv_F(x)\delta\tau}\right], \tag{8.2.6}$$

where $v_F(x) = \varepsilon'(k_F(x))$. The only consistent Dirac theory defined on the entire domain $(x,\tau) \in [-L, L] \times \mathbb{R}$ and locally having the propagator (8.2.6) is a massless Dirac action in which the metric (being the only available free parameter) varies with position. Thus, we end up in a field theory in curved spacetime, whose action in isothermal coordinates is

$$\mathcal{S} = \frac{1}{2\pi}\int dz\, d\bar{z}\sqrt{g}[\psi^\dagger_R \overleftrightarrow{\partial_{\bar{z}}}\psi_R + \psi^\dagger_L \overleftrightarrow{\partial_z}\psi_L], \tag{8.2.7}$$

where $g = -\det(g_{\mu\nu})$, $g_{\mu\nu}$ is the metric tensor and the line element is $d^2s = e^{2\sigma}\, dz\, d\bar{z}$, which is conformally flat. Indeed, the propagator associated to the action (8.2.6) is

$$\langle \psi^\dagger_R(z+\delta z)\psi_R(z)\rangle = \frac{1}{e^\sigma \delta z}, \tag{8.2.8}$$

and coincides with (8.2.6) upon choosing

$$z(x,\tau) = \arcsin\left(\frac{x}{L}\right) + i\tau, \tag{8.2.9}$$

which, as a complex coordinate, lives on the infinite strip $\left[-\frac{\pi}{2}, \frac{\pi}{2}\right] \times \mathbb{R}$.

This formalism may simply be adapted to deal with an arbitrary potential $V(x)$. In fact, even when we do not generally know the exact solution of the single-particle problem, in the TDL, the relevant single-particle states are the ones very high in the spectrum for which the semi-classical approximation becomes exact. We emphasise that, in order to obtain non-trivial results, we need to scale the potential with the

number N of particles, see [159] for details. For a generic potential, the local Fermi momentum is given by

$$k_F(x) = \sqrt{2(\mu - V(x))}, \tag{8.2.10}$$

and the underlying metric is given by $ds^2 = dx^2 + v_F(x)^2 d\tau^2$. Finally, Eq. (8.2.9) becomes

$$z(x,\tau) = \int \frac{dx'}{v_F(x')} + i\tau, \qquad e^{\sigma} = v_F(x), \tag{8.2.11}$$

where, we recall that $v_F(x) = \varepsilon'(k_F(x))$. The coordinate z is defined on a strip $[x_1, x_2] \times \mathbb{R}$, where x_1 and x_2 depend on $V(x)$ and μ.

Bosonisation of the Dirac fermion

By standard bosonisation techniques [83, 326], the action of the free Dirac fermion is mapped into a free bosonic CFT with the Euclidean action

$$\mathcal{S} = \frac{1}{8\pi} \int d\tau dx [(\partial_\tau \phi)^2 + (\partial_x \phi)^2], \tag{8.2.12}$$

where we set the speed of the sound $v = 1$. The bosonic field is *compact*, and the target space is a ring, i.e.

$$\phi(t, x + L) \equiv \phi(t, x) + 2\pi R m. \tag{8.2.13}$$

Here m is the winding number of the field configuration and R is the compactification radius, that in the case of the Dirac theory is $R = 1$.

In order to clarify the operator correspondence, we should also introduce the chiral vertex operator (for left and right movers) defined as

$$V_\alpha^{R,L} =: e^{i\alpha\phi_{R,L}(x)} :, \tag{8.2.14}$$

with conformal dimension given by $h_\alpha = \alpha^2/2$ ($\alpha \in \mathbb{R}$) and where $\phi_{L,R}(x)$ are the left and right components of the bosonic field.

By comparing the two point correlation function of vertex operators with that of left and right moving fermionic operators, the operator correspondence between these fields is

$$\psi_R(x) = \frac{\eta}{\sqrt{2}} V_1^R, \qquad \psi_L(x) = \frac{\overline{\eta}}{\sqrt{2}} V_1^L, \tag{8.2.15}$$

where the Klein factors η and $\overline{\eta}$ ensure the anticommutation relations between $\psi_L(x)$ and $\psi_R(x)$, being anticommuting variables themselves. This identity states that the chiral vertex operators, Eq. (8.2.14), correspond, in the fermionic language, to the annihilation/creation of a fermion.

The derivative operator $i\partial_x\phi = i\partial_x\phi_R + i\partial_x\phi_L$ can be written in fermionic language as

$$\psi_R^\dagger(x)\psi_R(x) = -\frac{1}{2} : i\partial_x\phi_R(x) : \quad \psi_L^\dagger(x)\psi_L(x) = -\frac{1}{2} : i\partial_x\phi_L(x) : . \tag{8.2.16}$$

The primary fields of the theory consists just of the vertex operator V_1 and the derivative field $i\partial_x\phi$ [83]. In fermionic language, via bosonisation they correspond to the creation of a particle and to a particle-hole excitation respectively.

We now discuss how the vanishing of the fermionic density at the edges of the interval $[-L, L]$ (cf. Eq. (8.2.5)) reflects on the boundary conditions (BCs) for the free compact boson (which also lies on the strip of length $2L$). Let us consider the fermion density operator $\rho(x) =: c^\dagger(x)c(x) :$ and linearise it around the

two Fermi points to get

$$\rho(x) \sim \Big[: \psi_R^\dagger(x)\psi_R(x) : + : \psi_L^\dagger(x)\psi_L(x) : + \\ : \psi_R^\dagger(x)\psi_L(x) : e^{-2ik_F x} + : \psi_L^\dagger(x)\psi_R(x) : e^{2ik_F x} \Big]. \quad (8.2.17)$$

Using that $\psi_R(x)$ and $\psi_L(x)$ vary very slowly on the system scale, we may drop the two terms involving the rapidly oscillating factors $e^{\pm 2ik_F x}$. Consequently, the vanishing of the fermion density $\rho(x)$ implies

$$\psi_R^\dagger(x)\psi_R(x) = -\psi_L^\dagger(x)\psi_L(x). \quad (8.2.18)$$

and, from Eq. (8.2.16), for the bosonic field

$$\partial_x \phi(x) = \partial_x \phi_R(x) + \partial_x \phi_L(x) = 0. \quad (8.2.19)$$

Then, in this boundary CFT, the operator content of theory is halved compared to the bulk (as for any CFT).

8.3 Entanglement and Rényi entropies of excited states of inhomogeneous systems

In this Section we apply the formalism reviewed in Section 8.2 to study EE and REEs for a special class of excited states in the presence of spatial inhomogeneities.

Homogeneous systems. The simplest class of excited states in a CFT are those generated by the action of a primary field Y, with scaling dimension Δ, on the CFT vacuum (cf. Section 4.2). A simple expression for the associated moments in terms of correlators of Y, given in Eq. (4.2.4), is reported here for completeness and denoted as

$$F_{\mathrm{Y},n}(A) = \frac{\langle \prod_{k=0}^{n-1} \mathrm{Y}(w_k^-)\mathrm{Y}^\dagger(w_k^+)\rangle_{\mathcal{R}_n}}{\langle \mathrm{Y}(w_0^-)\mathrm{Y}_1^\dagger(w_0^+)\rangle_{\mathcal{R}_1}^n}, \quad (8.3.1)$$

where the notation is the same as in Chapter 4. Eq. (8.3.1) holds for systems with both periodic (PBC) and open boundary conditions (OBC), but the worldsheet where the theory is defined, i.e., the Riemann surface $\mathcal{R}_n$ is different in the two cases. For PBC the single sheet geometry $\mathcal{R}_1$ is the cylinder (topologically equivalent to the complex plane), whereas for OBC $\mathcal{R}_1$ is an infinite strip [352].

For PBC, by conformal mappings, $F_{\mathrm{Y},n}(A)$ turns out to be a function of $\mathrm{x} = \ell/L$ only [349,371], where ℓ is the length of the interval A and L the total length of the system. The excess of the n-th REE of the excited state with respect to the ground state value is then given by

$$\hat{F}_{\mathrm{Y},n}(A) = \frac{1}{1-n} \log F_{\mathrm{Y},n}(A) = S_{\mathrm{Y}}^{(n)}(A) - S_{\mathrm{GS}}^{(n)}(A). \quad (8.3.2)$$

Since the $F_{\mathrm{Y},n}(A)$ is function only of x for all excitations, $\hat{F}_{\mathrm{Y},n}(A)$ is always of order 1 in L, showing that the universal logarithmic behaviour for the ground-state persists for all low-lying excited states in CFT.

For the case of OBC, which is of major interest here, we consider a systems of length $2L$, i.e. the segment $[-L, L]$ and a subsystem A starting from the left edge $A = [-L, \ell]$ (note that the length of A is $L + \ell$). Under these circumstances there are only minor differences compared to the calculation in the periodic case [352]. Again a series of conformal transformations maps can be used, but the resulting correlation functions are usually more complicated to be worked out [352]; the only special case being the one of interest for us, namely correlation functions of chiral operators in the compact boson with free boundary conditions (8.2.19). In this case, by use of image charges, we end up exactly in the same correlation function

as for the PBC case. The only difference is in the scaling variable x, which now is

$$\mathrm{x} = \frac{|x_1 - x_2|}{2L} = \frac{1}{2} + \frac{\ell}{2L}\,. \tag{8.3.3}$$

Inhomogeneous systems. We now apply the formalism of Section 8.2 to compute the entanglement entropy of the bipartition $A = [-L, \ell]$, $\bar{A} = [\ell, L]$. The coordinates of the associated field theory are $(z, \bar{z})$, defined for a generic trapping potential by (8.2.11) (that for the harmonic case simplified to (8.2.9)). Making use of such coordinates, the subsystem changes to $A' = [z_1, z_2]$, where $z_1 = z(-L)$ and $z_2 = z(\ell)$. In particular, for the harmonic case

$$z_1 = -\frac{\pi}{2}, \qquad z_2 = \arcsin\left(\frac{\ell}{L}\right). \tag{8.3.4}$$

In this coordinate system, the total length of the strip is $L' = \pi$.

As in Eq. (8.3.1), the ratio of moments of RDM is then

$$F^c_{\mathrm{Y},n}(A) = \frac{\langle \prod_{k=0}^{n-1} \mathrm{Y}(z_k^-)\mathrm{Y}^\dagger(z_k^+)\rangle_{\mathcal{R}_n,\mathrm{curved}}}{\langle \mathrm{Y}(z_0^-)\mathrm{Y}_1^\dagger(z_0^+)\rangle^n_{\mathcal{R}_1,\mathrm{curved}}}, \tag{8.3.5}$$

where $z_k^\pm = z(w_k^\pm) = \pm i\infty$, $\mathcal{R}_1$ is the strip $\mathcal{S} = [-\pi/2, \pi/2] \times \mathbb{R}$ and $\mathcal{R}_n$ the Riemann surface obtained by joining cyclically n copies of $\mathcal{R}_1$. We used the superscript "c" (for "curved") in order to avoid confusion with the same quantity for a homogeneous system: the difference with (8.3.1) is that the correlation functions are evaluated in a worldsheet where the metric is not flat ($d^2s = e^{2\sigma(z)} dz d\bar{z}$). Note that considering the universal ratio (4.2.4) presents also the advantage that we do not have to deal with the metric dependent cutoff $\epsilon = \epsilon(x)$, which, for non-uniform systems, depends on the position and is a non trivial function of the scales entering in the problem. In the case of the free Fermi gas, there is just one of such scales ($k_F(x)^{-1}$), thus fixing this dependence; in more complicated models, where different scales exist, finding such function is still an open problem.

It is now convenient to re-express the correlation in the numerator of Eq. (8.3.5) through twist fields as

$$\langle \prod_{k=0}^{n-1} \mathrm{Y}(z_k^-, \bar{z}_k^-)\mathrm{Y}^\dagger(z_k^+, \bar{z}_k^+)\rangle_{\mathcal{R}_n,\mathrm{curved}} = \frac{\langle \mathcal{T}_n(z_2)\tilde{\mathrm{Y}}\tilde{\mathrm{Y}}^\dagger\rangle_{\mathcal{R}_1,\mathrm{curved}}}{\langle \mathcal{T}_n(z_2)\rangle_{\mathcal{R}_1,\mathrm{curved}}}, \tag{8.3.6}$$

where $\tilde{\mathrm{Y}} = \mathrm{Y}^{\otimes n}$ corresponds to n replicas of the operator Y and we relied on the very definition of twist fields [18, 148]. A similar approach was considered in [158] in a different context. Thanks to this rewriting, Eq. (8.3.5) takes the form

$$F^c_{\mathrm{Y},n}(A) = \frac{\langle \mathcal{T}_n(z_2)\tilde{\mathrm{Y}}\tilde{\mathrm{Y}}^\dagger\rangle_{\mathcal{R}_1,\mathrm{curved}}}{\langle \mathcal{T}_n(z_2)\rangle_{\mathcal{R}_1,\mathrm{curved}}\langle \mathrm{Y}\mathrm{Y}^\dagger\rangle^n_{\mathcal{R}_1,\mathrm{curved}}}. \tag{8.3.7}$$

Since the inhomogeneity is encoded in the metric tensor, the idea is now to use a Weyl transformation to trace the calculation back to the one in flat space, as done for the entanglement entropy in the ground state in Ref. [159]. Under a Weyl transformation, which does not act on the coordinates, but on the metric tensor only

$$g_{\mu\nu}(z, \bar{z}) \to e^{-2\sigma(z,\bar{z})} g_{\mu\nu}(z, \bar{z}), \tag{8.3.8}$$

a primary field $\phi_\Delta(z, \bar{z})$ of conformal dimension Δ transforms as

$$\phi_\Delta(z, \bar{z}) \to e^{-\sigma(z,\bar{z})\Delta} \phi_\Delta(z, \bar{z}). \tag{8.3.9}$$

This transformation applies to all the fields in Eq. (8.3.7), therefore the prefactors due to the Weyl transformation cancel in the ratio, leading to

$$F^c_{\mathrm{Y},n}(A) = \frac{\langle \mathcal{T}_n(z_2)\tilde{\mathrm{Y}}\tilde{\mathrm{Y}}^\dagger\rangle_{\mathcal{R}_1}}{\langle \mathcal{T}_n(z_2)\rangle_{\mathcal{R}_1}\langle \mathrm{Y}\mathrm{Y}^\dagger\rangle^n_{\mathcal{R}_1}}, \tag{8.3.10}$$

where now the correlators are again evaluated on a flat space. Moreover, since, as already mentioned, also the position-dependent cutoff $\epsilon(x)$ simplifies, Eq. (8.3.10) coincide with Eq. (8.3.1) for a homogeneous system with OBC for a system of size $L' = \pi$ and subsystem $A' = [z_1, z_2]$, i.e.,

$$F^c_{\mathrm{Y},n}(A) = F_{\mathrm{Y},n}(A'). \tag{8.3.11}$$

The only *fundamental* difference between the homogeneous and the inhomogeneous system is that, while in the former case the function $F_{\mathrm{Y},n}(A)$ in Eq. (8.3.1) is a function of the variable $\mathrm{x} = 1/2 + \ell/(2L)$, in the latter $F^c_{\mathrm{Y},n}(A)$ is the same function but of the different variable

$$\mathrm{x}' = \frac{z_2 - z_1}{L'} = \frac{\arcsin(-1+2\mathrm{x})}{\pi} + \frac{1}{2}. \tag{8.3.12}$$

Thus we can make use of the results of Ref. [352, 371] for the function $F_{\mathrm{Y},n}(\mathrm{x})$ for a homogenous strip (Y being a primary of the compact boson CFT) to write explicit formulas for the functions $F^c_{\mathrm{Y},n}$ in the inhomogeneous case. For the harmonic trapping potential these read

$$F^c_{V_\alpha,n}(\mathrm{x}) = F_{V_\alpha,n}(\mathrm{x}'(\mathrm{x})) = 1, \tag{8.3.13a}$$

$$F^c_{i\partial\phi,n}(\mathrm{x}) = F_{i\partial\phi,n}(\mathrm{x}'(\mathrm{x})) = \left[\left(\frac{4\sqrt{\mathrm{x}(1-\mathrm{x})}}{n}\right)^n \frac{\Gamma\left(\frac{1+n}{2} + \frac{n}{4\sqrt{\mathrm{x}(1-\mathrm{x})}}\right)}{\Gamma\left(\frac{1-n}{2} + \frac{n}{4\sqrt{\mathrm{x}(1-\mathrm{x})}}\right)}\right]^2. \tag{8.3.13b}$$

By replica limit we get the EE in terms of the function (8.3.2)

$$\hat{F}^c_{V_\alpha,1}(\mathrm{x}) \equiv \lim_{n\to 1}\frac{1}{1-n}\log F^c_{V_\alpha,n}(\mathrm{x}) = 0, \tag{8.3.14a}$$

$$\begin{aligned}\hat{F}^c_{i\partial\phi,1}(\mathrm{x}) \equiv \lim_{n\to 1}\frac{1}{1-n}\log F^c_{i\partial\phi,n}(\mathrm{x}) &= 2\log|2\sin(\pi\mathrm{x}')| + 2\psi\left(\frac{1}{2\sin(\pi\mathrm{x}')}\right) + 2\sin(\pi\mathrm{x}') \\ &= 2\log(4\sqrt{\mathrm{x}(1-\mathrm{x})}) + 2\psi\left(\frac{1}{4\sqrt{\mathrm{x}(1-\mathrm{x})}}\right) + 4\sqrt{\mathrm{x}(1-\mathrm{x})},\end{aligned} \tag{8.3.14b}$$

where $\psi(z)$ is the digamma function. The analytic continuation leading to the last equation has been derived in [355, 435]. We stress that Eqs. (8.3.13) and (8.3.14) as function of x' are valid for an arbitrary external potential with $\mathrm{x}'(\mathrm{x})$ obtainable from (8.2.11). Only when using $\mathrm{x}'(\mathrm{x})$ in (8.3.12) we specialised to the harmonic case.

8.4 Relative entanglement entropies between inhomogeneous states

Here we generalise the results of the previous Section for the REE to the computation of the ReE between different pairs of low-lying excitations of the free Fermi gas, always using the bosonised CFT.

Homogeneous systems. For the relative entropy between ρ_1 and ρ_0 (associated to the primaries Y_1 and Y_0 respectively, again we can express the ratio in Eq. (4.2.15) in terms of correlation functions as [328]

$$G_{n,A}(\rho_1||\rho_0) = \frac{\langle \mathrm{Y}_1(w_0^-)\mathrm{Y}_1^\dagger(w_0^+)\prod_{k=1}^{n-1}\mathrm{Y}_0(w_k^-)\mathrm{Y}_0^\dagger(w_k^+)\rangle_{\mathcal{R}_n}\langle \mathrm{Y}_1(w_0^-)\mathrm{Y}_1^\dagger(w_0^+)\rangle_{\mathcal{R}_1}^{n-1}}{\langle\prod_{k=1}^{n-1}\mathrm{Y}_1(w_k^-)\mathrm{Y}_1^\dagger(w_k^+)\rangle_{\mathcal{R}_n}\langle \mathrm{Y}_0(w_0^-)\mathrm{Y}_0^\dagger(w_0^+)\rangle_{\mathcal{R}_1}^{n-1}}. \tag{8.4.1}$$

For a periodic system, the final expression is obtained after mapping the Riemann surface to the complex plane and finally to the cylinder. It is straightforward to show, that also $G_{n,A}(\rho_1\|\rho_0)$, for chiral excitations in a system with OBC has exactly the same expression.

Inhomogeneous systems. We now apply the formalism of Section 8.2 to compute the relative entropy of different couples of density matrices associated to the bipartition $A = [-L, \ell]$, $\bar{A} = [\ell, L]$. By the same reasoning of Section 8.3, the ratio we wish to compute is

$$G^c_{n,A}(\rho_1||\rho_0) = \frac{\langle \mathrm{Y}_1(w_0^-)\mathrm{Y}_1^\dagger(w_0^+)\prod_{k=1}^{n-1}\mathrm{Y}_0(w_k^-)\mathrm{Y}_0^\dagger(w_k^+)\rangle_{\mathcal{R}_n,\text{curved}}\langle \mathrm{Y}_1(w_0^-)\mathrm{Y}_1^\dagger(w_0^+)\rangle_{\mathcal{R}_1,\text{curved}}^{n-1}}{\langle\prod_{k=1}^{n-1}\mathrm{Y}_1(w_k^-)\mathrm{Y}_1^\dagger(w_k^+)\rangle_{\mathcal{R}_n,\text{curved}}\langle \mathrm{Y}_0(w_0^-)\mathrm{Y}_0^\dagger(w_0^+)\rangle_{\mathcal{R}_1,\text{curved}}^{n-1}}. \tag{8.4.2}$$

where, also in this case, we use the superscript "c" just to avoid confusion with the same quantity for a homogeneous system. The calculations proceed in complete analogy too, leading to

$$G^c_{n,A}(\rho_1\|\rho_0) = G_{n,A'}(\rho_1\|\rho_0). \tag{8.4.3}$$

Once again, the only difference between homogenous and inhomogeneous systems is that the scaling variable is not x but x′ as defined in (8.3.12).

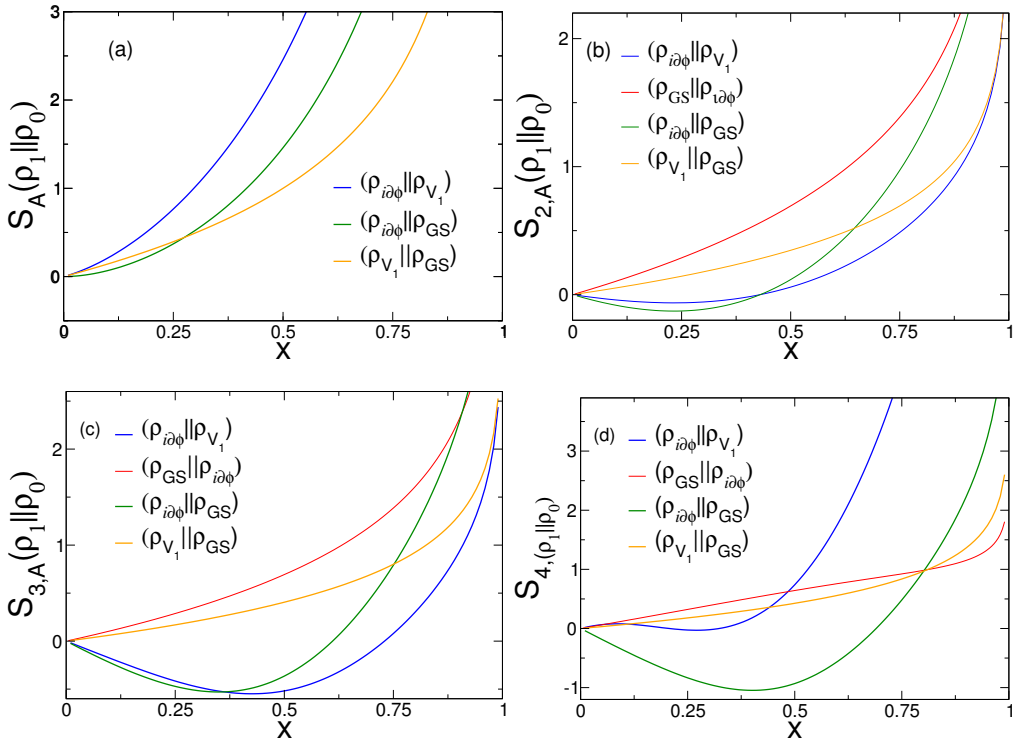

FIGURE 8.2: The CFT predictions for the Rényi relative entropies $S_{n,A}(\rho_1||\rho_0)$, as a function of the scaling variable $\mathrm{x} = 1/2 + \ell/(2L)$, for different values of $n = 1, 2, 3, 4$ in panels (a), (b), (c) and (d) respectively. In each panel (at fixed n) we report the couples of states considered.

Explicitly, we have [328]

$$G^c_{n,A}(\rho_{V_\alpha}\|\rho_{GS}) = G^c_{n,A}(\rho_{GS}\|\rho_{V_\alpha}) = \left(\frac{\sin(\pi x')}{n\sin(\pi x'/n)}\right)^{\alpha^2}, \tag{8.4.4a}$$

$$G^c_{n,A}(\rho_{i\partial\phi}\|\rho_{GS}) = \left(\frac{\sin\pi x'}{n}\right)^{2(1-n)} 4^{-n}\sin^2\left(\frac{\pi x'}{n}\right)\frac{\Gamma^2\left(\frac{1-n+n\csc(\pi x')}{2}\right)}{\Gamma^2\left(\frac{1+n+n\csc(\pi x')}{2}\right)}, \tag{8.4.4b}$$

$$G^c_{n,A}(\rho_{GS}\|\rho_{i\partial\phi}) = \left(\frac{\sin\pi x'}{n}\right)^{2(n-1)} \det\left[\frac{1}{\sin(t_{ij}(x')/2)}\right]_{i,j\in[1,2(n-1)]}, \tag{8.4.4c}$$

$$G^c_{n,A}(\rho_{i\partial\phi}\|\rho_{V_\beta}) = \tilde{C}_\beta(n,x')G^c_{n,A}(\rho_{i\partial\phi}\|\rho_{GS})G^c_{n,A}(\rho_{GS}\|\rho_{V_\beta}), \tag{8.4.4d}$$

where

$$\tilde{C}_\beta(n,x') = 1-\beta^2\sin^2\left(\frac{\pi x'}{n}\right)\left(\sum_{k=1}^{n-1}\cot\frac{\pi}{n}(x'+k)\right)\left(\sum_{l=1}^{n-1}\cot\frac{\pi}{n}(-x'+l)\right), \tag{8.4.5}$$

and, by replica trick,

$$S_A(\rho_{GS}||\rho_{V_\alpha}) = S_A(\rho_{V_\alpha}||\rho_{GS}) = \alpha^2(1-\cot(\pi x')), \tag{8.4.6a}$$

$$S_A(\rho_{i\partial\phi}||\rho_{GS}) = 2\left(\log(2\sin(\pi x')) + 1 - \pi x\cot(\pi x') + \psi\left(\csc(\pi x')/2\right) + \sin(\pi x')\right), \tag{8.4.6b}$$

$$S_A(\rho_{i\partial\phi}||\rho_{V_\beta}) = (2+\beta^2)[1-\pi x'\cot(\pi x')] + 2\log(2(\sin(\pi x'))) + \\ + 2\psi\left(\csc(\pi x')/2\right) + 2\sin(\pi x'). \tag{8.4.6c}$$

All these expressions may be easily rewritten in terms of x, but the final results are not very illuminating and we omit them. As stressed in Chapter 4 for the calculations in the homogeneous case, it is not yet possible to derive the analytic continuation of (8.4.4c).

In Figure 8.2 we plot the Rényi relative entropy $S_{n,A}(\rho_1||\rho_0)$ for different pairs of states. Note that, as already observed [328], while the relative entropy $S_A(\rho_1||\rho_0)$ is always positive and monotonous, this is not generally the case for $n \neq 1$. Moreover, we notice that $S_{n,A}(\rho_1\|\rho_0)$ as a function of x goes to zero faster than in the homogeneous case.

8.5 Numerical checks

We now compare the analytic formulas derived in the previous sections with the exact numerical data for the low-lying excited states of a Fermi gas trapped by a harmonic potential. The REEs in these excited states have been obtained by two different methods, i.e. by the *overlap matrix* technique (Section 1.4.3) and by *Gauss–Legendre discretisation* of the continuous correlation matrix (see Ref. [375]). Of course, they furnish identical results, providing a further test of the correctness of their implementation. For the calculation of the ReEEs the overlap matrix approach is not easily usable and therefore we only employ the Gauss–Legendre discretisation method for the correlation matrices and compute the trace of the product of the associated RDMs though Eq. (1.4.31).

We consider only two types of excited states. One is a particle-hole excitation in which the particle in the highest occupied single-particle level (i.e. the N-th one) is shifted up of one level (i.e. to the $(N+1)$-th one). In the CFT, this excitation corresponds to the state generated by the action of the primary operator $i\partial\phi$. The other corresponds to add a particle to the Fermi sea: this is a very trivial operation because the excited state is just the ground state in the canonical ensemble with one particle more. However, in the grand-canonical ensemble it is an excited state that in curved CFT corresponds to the action of the vertex operator with $\alpha = 1$, i.e. V_1 (which indeed, as already mentioned, acts as creation operator of a fermion).

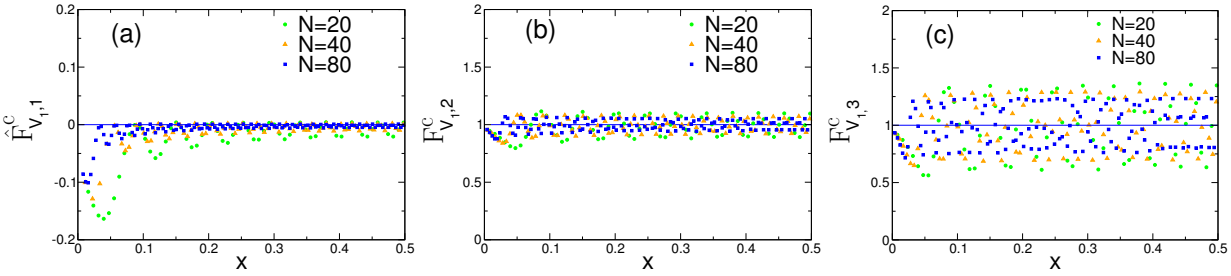

FIGURE 8.3: The universal scaling function for the Rényi entanglement entropy $\hat{F}^c_{V_1,n}(\mathrm{x})$ (cf. Eq. (8.3.2)), for the excited state given by an addition of a particle, which in CFT correspond to the vertex operator V_1. Data are shown as function of x (cf. (8.3.3)) for different values of n ($=1,2,3$ in panels (a), (b) and (c) respectively). Different colors correspond to different number of particles N. The continuous curve is the CFT prediction ($F^c_{V_1,n}(\mathrm{x})=1$), Eq. (8.3.13a). The data have been obtained with the method of the overlap matrix, Section 1.4.3.

8.5.1 Entanglement entropies in excited states

In Figures 8.3 and 8.4 we report the exact numerical data for the unversal scaling function $\hat{F}^c_{Y,n}(\mathrm{x})$ for the Rényi entanglement entropies of a Fermi gas of N particles trapped by a harmonic potential. In Fig. 8.3 we report the data for the excited state with one particle more (corresponding to the vertex operator, $Y=V_1$) and in Fig. 8.4 we report the data for a particle-hole excitation (corresponding to $Y=i\partial\phi$). In both cases, we consider the bipartition $A=[-\infty,\ell]$ and $\bar{A}=[\ell,\infty]$ (in the TDL it is irrelevant whether A starts from $-L$ or any point to its left, so we just fix to $-\infty$ which makes the numerical calculation easier). We plot the scaling function versus $\mathrm{x}=1/2+\ell/2L$ (cf. (8.3.3)) which is the natural variable one would have been using without knowing a priori the CFT solution in terms of x', cf. Eq. (8.3.12).

Let us now discuss these figures. For the excited state corresponding to the vertex operator (cf. Figure 8.3), the CFT prediction is $F_{V_1,n}(\mathrm{x}')=1$ as in Eq. (8.3.13a). It is evident that the data converge to the CFT predictions increasing the system size, as they should. This is a rather trivial result since the excited state is the ground state with one particle more; the analytic result for the ground-state entropies in the harmonic potential, cf. Refs. [159, 419], shows that the difference between the results at N and at $N+1$ is of order $o(1)$ for large N. However, in spite of this simplicity, we note the presence of oscillating deviations from the CFT prediction which clearly decrease with system size and hence are subleading corrections to the scaling. These corrections get larger for larger values of the Rényi index n. We are going to discuss and characterise them below.

Data for the particle-hole excited state are reported in Figure 8.4, for different values of the Rényi index n and number of particles N. We also show the highly non-trivial result for the CFT excited state generated by the action of the derivative operator, cf. Eq. (8.3.13b). The data at finite N are close to the CFT predictions for all n and the difference gets smaller as N increases. In particular for $n=1$ (von Neumann entropy), the data at finite N lie very close to the asymptotic prediction. The differences between numerical data and asymptotic predictions have to be attributed to subleading corrections that, in analogy with the case of the vertex operator, become larger as n increases.

Before addressing these corrections to the scaling, we wish to discuss qualitative and quantitative differences between the scaling functions in homogeneous and trapped systems. The data for $n=1$ and $n=3$ are reported once again in Fig. 8.5 together with the homogenous results for a system with open boundary conditions. The qualitative shapes of the two sets of curves are very different. In the homogenous case, the entropy excess starts off linearly at $\mathrm{x}=0$, while only quadratically in the trapped setting. Physically this behaviour may be understood as a consequence of the fact that the single-particle states at the edge have a lower density in the trapped case. Mathematically instead it just follows from the mapping (8.3.12) between x and x' which is quadratic close to $\mathrm{x}=0$. Furthermore, the linearity of the homogeneous scaling function for small x is a very general feature and the linear slope is proportional to the scaling dimension of the operator Y [371]. Hence, we conclude that for a general excited state $|\mathrm{Y}\rangle$ in this inhomogeneous setting,

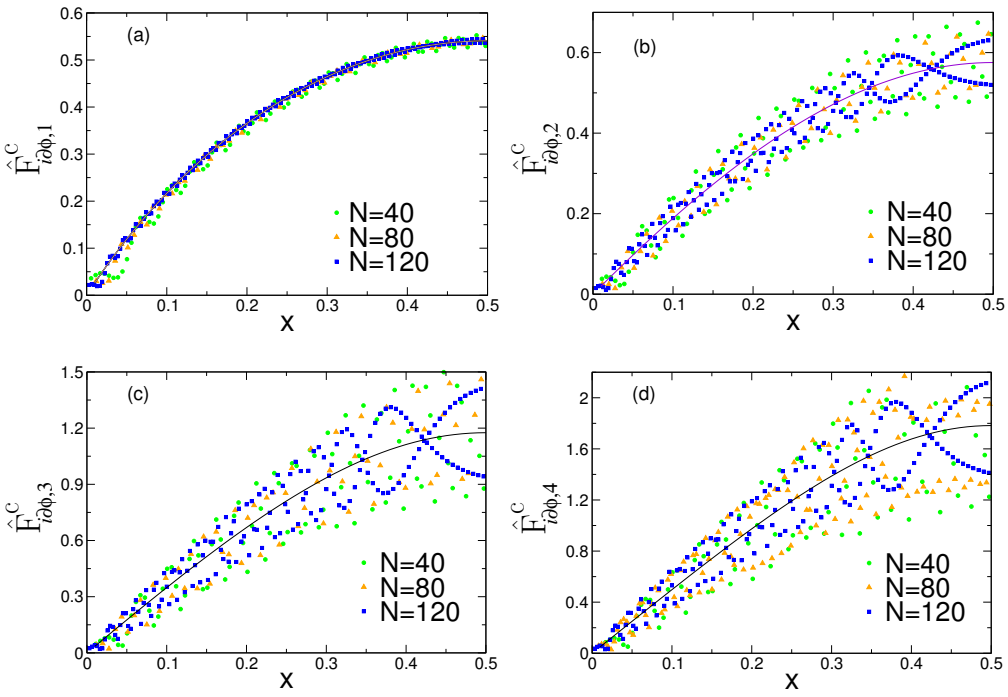

FIGURE 8.4: The universal scaling function for the Rényi entanglement entropy $\hat{F}^c_{i\partial\phi,n}(\mathrm{x})$, Eq. (8.3.2), for the particle-hole excitation, corresponding in CFT to the action of the derivative operator. Data are shown as function of x (cf. Eq. (8.3.3)) for different values on n ($= 1,2,3,4$ in panels (a), (b), (c) and (d) respectively). Different colours of the points correspond to different particle numbers N. The continuous curve is the CFT prediction, Eq. (8.3.13b). The data have been obtained with the Gauss–Legendre discretisation method [see Ref. [375]].

the function $\hat{F}^c(\mathrm{x})$ will start off quadratically with an amplitude proportional to the dimension of the operator Y. Another interesting observation is that while the two functions (homogenous and inhomogeneous ones) are very different, they have exactly the same value at $\mathrm{x} = 1/2$, i.e. in the center of the trap. Again, mathematically this just follows from the trivial observation that the point $\mathrm{x} = 1/2$ is a fixed point of the map between x and x′ (cf. Eq. (8.3.12)) and hence this result is valid for an arbitrary state. At first, this may seem surprising for the EE which depends on all the points to the left of the center (i.e. with $x < 0$) which are sensitive to the trapping potential. However, if we think of the entropy as a local one-point function of a twist field, the equivalence in the two geometries follows from the fact that at the center the gradient of the density vanishes in both cases and the system looks like homogenous and uniform.

We finally discuss the corrections to the scaling which strongly affect the data in Figures 8.3 and 8.4. Similar corrections have been found already for the ground state of the trapped gas [170, 419] and there is no quantitative understanding of them yet. The main reason for this lack of comprehension is that there are at least two different sources of corrections which are intertwined in the final result and disentangling them appears very complicated. First, also homogeneous systems in the ground state present oscillating deviations from the conformal asymptotic entanglement entropy which are called *unusual corrections*. These have been characterised both in CFT [155, 307], and in microscopic models [173, 174, 196, 303, 308, 423]. They are unusual in the sense that the exponent governing their decay depends on the order n of the Rényi entropy and it is not related to the leading irrelevant operator, like for standard corrections to the scaling. Indeed, it has been shown that these deviations decay as $\ell^{-\Delta/n}$ or $\ell^{-2\Delta/n}$, for open and periodic systems respectively, where Δ is the scaling dimension of a *relevant* operator located at the conical singularities of the Riemann surface $\mathcal{R}_n$ [155, 307]. Corrections with the same exponents have been found also for excited states of homogenous systems [356] (as expected since the structure of conical singularities does not depend on the state), but the amplitude depends in a very complicated and yet unknown manner on the state itself. These unusual corrections share many similarities with the ones observed in Figures 8.3 and 8.4, in particular they

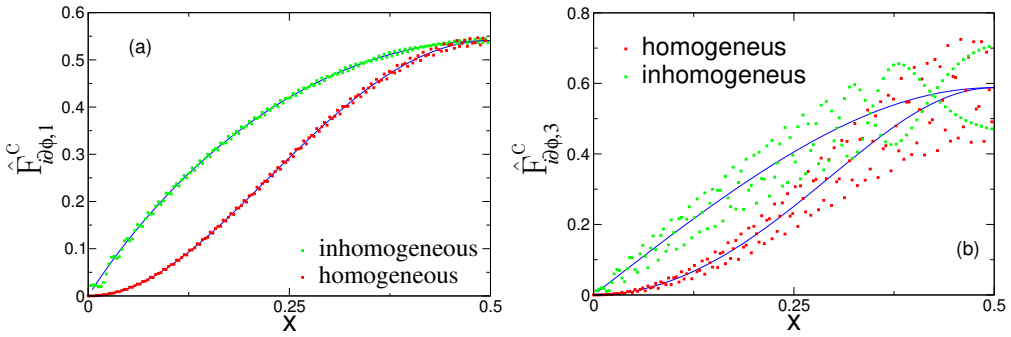

FIGURE 8.5: Comparison between the universal scaling functions $\hat{F}_{i\partial\phi,n}(\mathrm{x})$ (cf. Eq. (8.3.2)) for two Fermi gases: (i) with hard-wall boundary conditions (i.e. with vanishing density at the edges $\pm L$); (ii) trapped by a harmonic potential. The continuous curves are the two asymptotic CFT predictions versus $\mathrm{x} = 1/2 + \ell/(2L)$ (cf. (8.3.3)). The dots correspond to exact numerical data for gases with $N = 120$ particle.

are larger for larger n and very small at $n = 1$. However, in the trapped case, the period of the oscillations depends on the position (not surprisingly since the density does) in a yet unclear fashion. A first naive guess for these corrections deep in the bulk might be that they are the same as in the homogenous systems, but with the density (i.e. $k_F(x)$) replaced by the local one. If this would be true the data for $\hat{F}_{i\partial\phi,n}(\mathrm{x})$ and those for $\hat{F}^c_{i\partial\phi,n}(\mathrm{x})$ should be very similar when the former is written as a function of x and the latter of x′, because the mapping between the two makes the system homogenous. In Fig. 8.6, we explicitly perform this comparison, showing that deep in the bulk, while the amplitude of the oscillations is comparable, their periodicity has a different structure.

A second correction originates from the edges of the trapped system (at $\pm L$) and is strictly related to its inhomogeneities. Indeed, at finite N, near the edges, the fermion propagator deviates from thermodynamics form (8.2.6): in the proper subleading scaling variable, it can be expressed in terms of the Airy kernel, see e.g. [419, 436]. From the figures, in particular comparing with the results for the homogenous case in Figs. 8.5 and 8.6, it is evident that close to the edge at $\mathrm{x} = 0$, there are larger deviations than in the bulk and these are entirely due to the edge physics. These corrections right at the edge have been analytically worked out in [419, 436], but it is not known how they get modified when entering the bulk.

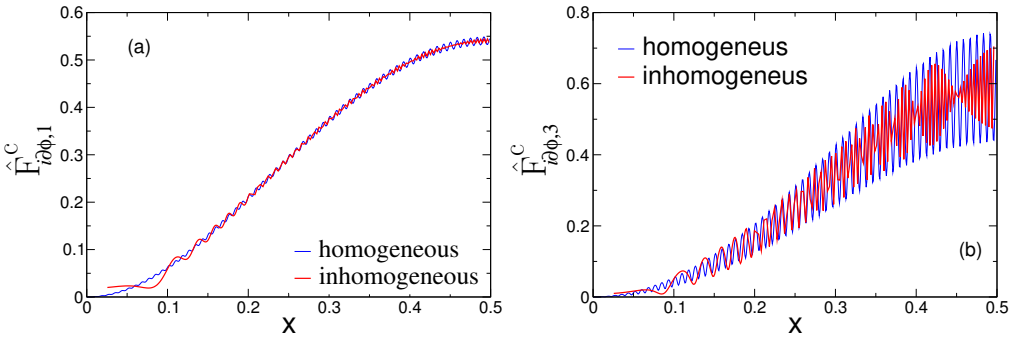

FIGURE 8.6: The same data as in Fig. 8.5, but using as scaling variable x for the homogeneous gas and x′ (cf. Eq. (8.3.12)) for the inhomogeneous one. The smooth parts of the two curves collapse on top of each other, as predicted by CFT. Conversely, the oscillations have very different features, in spite of the comparable amplitudes.

8.5.2 Relative entropies

In this subsection, we come to the Rényi relative entropies. Exploiting the same techniques, we numerically compute the ratio $G^c_{n,A}(\rho_1||\rho_0) = \mathrm{Tr}(\rho_1\rho_0^{n-1})/\mathrm{Tr}\rho_1^n$, for $n = 2, 3$ and with ρ_0 and ρ_1 corresponding to

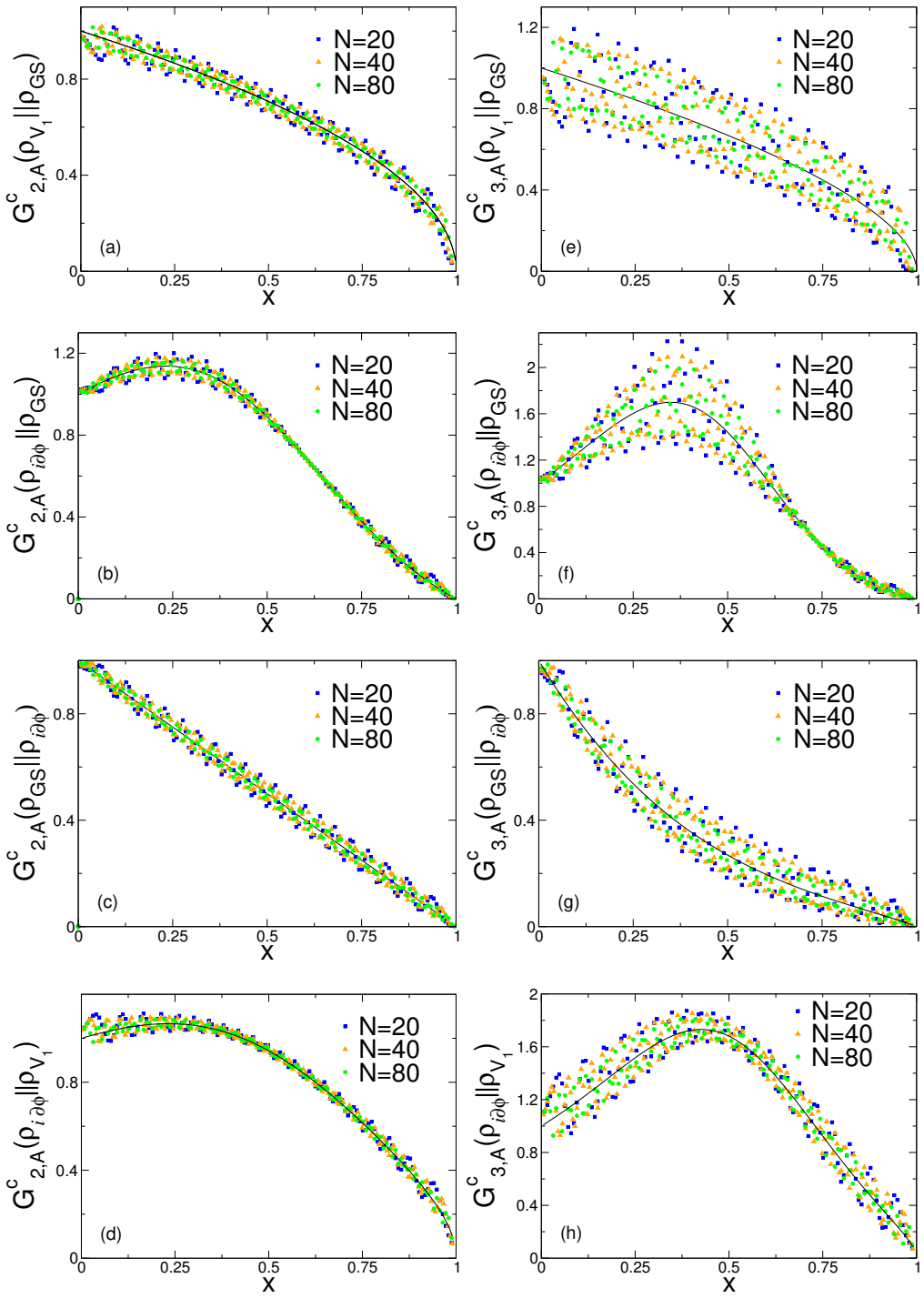

FIGURE 8.7: The ratio $G^c_{n,A}(\rho_1\|\rho_0)$, Eq. (8.4.2), as a function of x for $n = 2,3$, for different pairs of states. The considered states may be read off from the label of the vertical axis. The symbols are the exact numerical data at finite number of particles N. Different colours correspond to different N. The continuous curves are the CFT predictions in Eq. (8.4.4). The data have been obtained with the Gauss–Legendre discretisation method [see Ref. [375]]..

the possible pairs of states considered in the previous subsection, i.e. ground-state, particle-hole excitation, addition of a particle. In the TDL the numerical data are expected to converge to the CFT predictions for $G^c_{n,A}(\rho_1||\rho_0)$ in Eq. (8.4.4). The numerical results are shown in Figure 8.7 for different number of particles N and for all possible pairs of states.

It is evident from all data in Fig. 8.7 that increasing N the numerics converge toward the asymptotic

CFT predictions. Actually, the overall agreement is exceptionally good given the presence of oscillating corrections to the scaling (which, incidentally, appear to be larger than those in the homogeneous case, see [328]). Exactly like for the REEs in the previous subsection, these corrections have at least a twofold origin: i) the geometrical structure of the Riemann surface defining $G_{n,A}(\rho_1||\rho_0)$ is the same as the one for the Rényi entropies, in particular with the same conical singularities; hence the same kind of unusual corrections are expected; (ii) close to the edge, there are subleading corrections to the two-point function which affect both the density matrices ρ_0 and ρ_1 and hence the relative entropies. Unfortunately, as for the REEs, it is not possible to disentangle these effects and have a quantitative descriptions of these oscillating deviations from the asymptotic behaviour.

8.6 Concluding remarks

This Chapter is set within the context of the study of entanglement in inhomogeneous many-body quantum systems and its relation with conformal field theory. The core of this new line of research lies in the fact that the long-distance behavior of such systems may, under given assumptions, be described by CFT in a curved spacetime whose metric encodes the inhomogeneity parameters. In particular, here we provided new analytical predictions for the Rényi and relative entanglement entropies of low-energy excitations in the inhomogeneous one-dimensional free Fermi gas, for an interval adjacent to the physical edge (i.e. where the density of particles vanishes, $\rho(x) = 0$). Our main analytical results are given by equations (8.3.13), (8.3.14) for the universal ratio $F^c_{Y,n}(A)$ and by equations (8.4.4), (8.4.6) for $G^c_n(\rho_1\|\rho_0)$. These predictions have been tested against exact numerical data, which are fully consistent with them, up to subleading terms that are not captured by CFT.

Starting from these results, several directions would be worth investigating. First, we only considered excitations associated with primary fields. It would be interesting to generalize our findings to a generic excited state. For homogeneous systems, this generalization was considered in Refs. [351]. However, as soon as descendent fields are involved, the calculations become much more cumbersome. It is also quite natural to ask whether our formalism could be generalized to interacting problems, e.g., to some inhomogeneous version of the XXZ spin chain or Lieb-Liniger gas, as e.g. in [428]. The main problem is that for interacting systems the inhomogeneity affects two parameters: in addition to the metric, also the Luttinger parameter K, related to the couplings of the microscopic Hamiltonian [326], varies in space. Fixing these parameters is not an easy task, but, more importantly, this space-dependent parameter K turns out to break conformal invariance [431], so that we have to deal with a more complicated theory.

Chapter 9

Conformal field theory on top of the breathing Tonks-Girardeau gas

The techniques employed in the previous Chapter, providing access to large scale correlation functions of inhomogeneous critical $1d$ quantum systems, can be extended to dynamical situations. Here, in particular, we focus on a breathing gas of $1d$ hardcore bosons in a time-dependent harmonic trap. This model is well known to be exactly solvable, and can thus be used as a benchmark of our method. We give an extensive discussion of the approach and its relation with classical and quantum hydrodynamics in one dimension, and derive new formulas for correlation functions, not easily obtainable by other means. In particular, a remarkable formula for the large scale asymptotics of the bosonic n-particle function is obtained. This Chapter is based on Ref. [439].

9.1 Introduction

In the past two years, we have witnessed an important breakthrough in the physics of $1d$ quantum systems with the development of a "Generalized HydroDynamic" description [440, 441] of these systems (see also Refs. [442–456] for further developments) which, contrary to previously existing hydrodynamic approaches, is able to reproduce experimental observations of out-of-equilibrium isolated integrable quantum systems [457–459]. Although it applies to systems that are definitely made of quantum objects (cold atoms), the hydrodynamic approach leads to a classical description of the system.

At the moment an important open problem is to understand how to extend the new "Generalized HydroDynamic" approach to incorporate quantum effects, such as quantum correlations or interference effects. In fact, it is known that hydrodynamics accurately predicts one-point functions but fails instead to predict higher-point functions (more specifically, it simply predicts them to be zero). Here we are going to explain how it can be extended to obtain more generic quantum correlation functions. The idea is to use the classical hydrodynamics solution as the background on which one can build an effective action for the quantum fluctuations.

The problem we will treat is the one of a gas of hard-core bosons, also known as the Tonks-Girardeau gas, in a time-dependent harmonic potential $V(x,t)$. This model is well-known to be exactly solvable [460–462], and our goal is to use it to illustrate our approach, which extends recent works [159, 327, 375, 424–433, 463–465].

Bosons in $1d$ with delta repulsion in an external potential $V(x,t)$ are described by the following Hamiltonian

$$H(t) \;=\; \int dx \left(\frac{\hbar^2}{2m} (\partial_x \Psi^\dagger)(\partial_x \Psi) + V(x,t) \Psi^\dagger \Psi + g \Psi^{\dagger 2} \Psi^2 \right) \tag{9.1.1}$$

where $\Psi^\dagger(x)$, $\Psi(x)$ are operators that create/annihilate a boson at position x, which satisfy the canonical commutation rule $[\Psi(x), \Psi^\dagger(x')] = \delta(x-x')$. Here we focus exclusively on the hard-core limit (or Tonks-Girardeau limit), $g \to +\infty$, and on a harmonic trapping potential with a time-dependent frequency,

$$V(x,t) \;=\; \frac{1}{2} m\, \omega(t)^2 x^2. \tag{9.1.2}$$

At $t = 0$, the system is in the ground state $|\psi_0\rangle$ of H with an initial trap frequency ω_0 and a chemical potential μ. It is well-known that, in $1d$, hard-core bosons can be mapped to free fermions. Using this, the number of bosons N in the ground state is easily calculated: it is equal to (the integer part of) $\mu/(\hbar\omega_0)$. Importantly, this means that

$$\hbar N = \mathcal{O}(\mu/\omega_0), \tag{9.1.3}$$

so when we work in units where μ and ω_0 are both of order 1, taking N very large is equivalent to taking $\hbar$ very small. In that sense, for this problem, *the thermodynamic limit is a semiclassical limit*. To keep track of quantumness in the problem, we do not set $\hbar$ to one. Our goal is to learn how to calculate correlation functions of local observables

$$\langle O_1(x_1,t_1)O_2(x_2,t_2)\dots O_p(x_p,t_p)\rangle \tag{9.1.4}$$

in the limit $1/N \sim \hbar \to 0$. Throughout this Chapter, $\langle . \rangle$ is the expectation value in the initial state $|\psi_0\rangle$.

A number of results on this particular problem are available in the literature. These include exact finite-N results that exploit the mapping to fermions for correlation functions of some observables *at equal time* $t_1 = t_2 = \dots = t_p$ [460] (see also Refs. [178, 179, 466–471]); however to our knowledge, such results do not exist for correlations at different times. There are also results for observables that are not straightforwardly expressed in terms of the underlying free fermions and that have been derived in the thermodynamic/semiclassical limit above, for the *static case*. These include the one-particle density matrix [472] or the entanglement entropy [419]. We will see below that the approach we take here [159, 327, 424–433, 463–465] automatically reproduces the large-N asymptotics of these known results; moreover, it gives access to correlations at different times.

The rest of the Chapter is organized as follows. In Section 9.2 we present our approach, starting with the Wigner function of the free fermion problem, the reduction to a classical hydrodynamic description, and the reconstruction of quantum fluctuations and correlations on top of that classical description. In Section 9.3 we introduce a few notations and useful formulas that are specific to the problem of the time-dependent harmonic oscillator; those formulas follow naturally from a "holographic" picture [473] which we briefly review. In Section 9.4 we use that formalism to write the asymptotics of correlation functions of boson creation/annihilation operators, see formula (9.4.9). In particular, this yields a remarkably simple formula for the n-particle correlation function at equal time $\langle \Psi^\dagger(x_1,t)\dots\Psi^\dagger(x_n,t)\Psi(x'_1,t)\dots\Psi(x'_n,t)\rangle$, see formula (9.4.10). In Section 9.5 we focus on the fermionic two-point function. We evaluate its asymptotics using our approach —including low-energy contributions captured by the CFT, but also an important contribution that lies beyond CFT, which we properly take into account— and compare to a numerical evaluation of that two-point function at finite N. We find perfect agreement, thus validating the approach. We conclude in Section 9.6.

9.2 Strategy: reconstruction of quantum fluctuations on top of a classical hydrodynamic solution

In this Section we briefly sketch the most important ideas of the classical hydrodynamic description of the gas, and of its quantization. Concrete examples of calculations of correlation functions are given in the next sections. We stress that the reconstruction of quantum fluctuations on top of a classical hydrodynamic solution is an old problem in theoretical physics, dating back to Landau [474], with contributions by many authors motivated by different topics [475–477].

Generalized Hydrodynamics/Wigner function evolution

It is well known that hard core bosons in $1d$ are equivalent to free fermions. The mapping from bosons to fermions is done by inserting a Jordan-Wigner string,

$$\Psi_F^\dagger(x) = e^{i\pi\int_{y<x}\rho(y)dy}\,\Psi^\dagger(x), \tag{9.2.1}$$

where $\rho(y) = \Psi^\dagger(y)\Psi(y) = \Psi_F^\dagger(y)\Psi_F(y)$ is the density operator, such that the fermion creation/annihilation modes satisfy the canonical anti-commutation relations $\{\Psi_F(x), \Psi_F^\dagger(x')\} = \delta(x-x')$. In terms of the fermions, the Hamiltonian (9.1.1) in the hard core limit is quadratic,

$$H(t) = \int dx \left(\frac{\hbar^2}{2m} (\partial_x \Psi_F^\dagger)(\partial_x \Psi_F) + V(x,t) \Psi_F^\dagger \Psi_F \right). \tag{9.2.2}$$

To go towards a hydrodynamic description, it is useful to introduce the Wigner function of these free fermions,

$$n(x,k,t) = \int dy\, e^{iky} \left\langle \Psi_F^\dagger(x+y/2,t)\Psi_F(x-y/2,t) \right\rangle, \tag{9.2.3}$$

which has the semiclassical interpretation of being the probability to find a fermion at position (x,k) in phase space. The Wigner function satisfies the exact evolution equation

$$\partial_t n(x,k,t) + \frac{\hbar k}{m} \partial_x n(x,k,t) = \frac{1}{\hbar} (\partial_x V(x,t)) \partial_k n(x,k,t). \tag{9.2.4}$$

In our case this equation is exact because since we focus exclusively on harmonic potentials $V(x,t)$. For more general potentials, Eq. (9.2.4) would be the leading order term in an expansion in $\hbar$ and in higher order derivatives $\partial_x^p V$, $p \geq 2$ [478]. Eq. (9.2.4), which holds for free fermions, is the simplest possible occurence of the Generalized HydroDynamics equations (GHD) discovered in 2016 [440, 441].

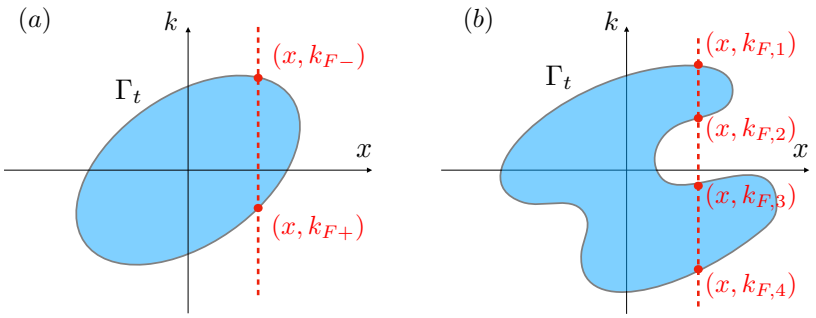

FIGURE 9.1: The curve Γ_t encircling the points (x,k) at which the Wigner function $n(x,k,t)$ is equal to one. Panel (a): the simple situation considered in this paper, where at any given position x there are only two Fermi points on the contour Γ, labeled as $k_{F\pm}$. Panel (b): the general situation with more than two Fermi points.

Reduction to classical hydrodynamics

We focus on the evolution from the ground state, which is a so-called *classical* or *zero-entropy* state. This class of states has been studied in several references [443, 479–481]. What is important is that in the thermodynamic/semiclassical limit $1/N \sim \hbar \to 0$, the Wigner function $n(x,k,t)$ of the ground state is just an indicatrix function, parametrized by a certain curve Γ_t in phase space:

$$n(x,k,t) = \begin{cases} 1 & \text{if } (x,k) \text{ is inside the contour } \Gamma_t \\ 0 & \text{if } (x,k) \text{ is outside } \Gamma_t. \end{cases} \tag{9.2.5}$$

The evolution equation (9.2.4) for the Wigner function can be viewed as an evolution equation for the Fermi contour Γ_t. One can parametrize Γ_t locally as $(x, k_{F,j}(x,t))$ where $k_{F,j}(x,t)$, $j = 1,2,\ldots$ are the Fermi points at position x, where the Wigner function jumps from 0 to 1 (see Fig. 9.1). Eq. (9.2.4) is then an evolution equation for the Fermi points which takes the form of a Burgers equation [327],

$$\hbar \partial_t k_{F,j}(x,t) + \frac{\hbar^2 k_{F,j}(x,t)}{m} \partial_x k_{F,j}(x,t) = -\partial_x V(x,t). \tag{9.2.6}$$

Importantly, here we will always be dealing with situations in which the number of position dependent Fermi points is at most two, as illustrated in Fig. 9.1(a). A situation like the one in Fig. 9.1(b) will never occur. When there are at most two Fermi points $k_{F,1}(x,t)$ and $k_{F,2}(x,t)$ at each position x—we label them as $k_{F-}(x,t)$ and $k_{F+}(x,t)$ in that case—, the gas in the small cell $[x, x+dx]$ is locally in a macrostate which is nothing but the ground state of the homogeneous gas up to a Galilean boost. This simple situation is then captured by the standard Euler hydrodynamic equations for the gas. The latter are expressed in terms of the local density and local velocity (defined as the particle current j divided by the density ρ),

$$\begin{aligned} \rho(x,t) &= \int \frac{dk}{2\pi} n(x,k,t) = \frac{k_{F-}(x,t) - k_{F+}(x,t)}{2\pi}, \\ u(x,t) &= \frac{j(x,t)}{\rho(x,t)} = \frac{1}{\rho(x,t)} \int \frac{dk}{2\pi} n(x,k,t) \frac{\hbar k}{m} = \frac{\hbar}{m} \frac{k_{F-}(x,t) + k_{F+}(x,t)}{2}, \end{aligned} \tag{9.2.7}$$

and are obtained straightforwardly from Eq. (9.2.6),

$$\begin{cases} \partial_t \rho + \partial_x(\rho u) &= 0 \\ \partial_t u + u \partial_x u &= -\frac{1}{m\rho} \partial_x P - \frac{1}{m} \partial_x V. \end{cases} \tag{9.2.8}$$

The first equation is the continuity equation for ρ which expresses conservation of mass. The second equation is the Euler equation, with a pressure given by $P(\rho) = \frac{\pi^2 \hbar^2 \rho^3}{3m}$, which is specific to hard core bosons in $1d$ at zero temperature.

We stress that the reduction to standard hydrodynamics is not specific to the free model we are considering: in fact, it has been shown [443] that for zero-entropy states GHD is equivalent to standard hydrodynamics as long as the number of Fermi points is two (i.e. before the appearance of *shocks* in the solution of the hydrodynamic equations (9.2.8)). In our case, this means that, for finite repulsion strength in the bosonic model (9.1.1), we would still get a system of the form (9.2.8), but with the appropriate pressure, i.e. the pressure of the Lieb-Liniger model at zero temperature.

Moreover in the initial state, $u = 0$, so the classical hydrodynamic equations (9.2.8) simplify to a *hydrostatic* equation: $\frac{1}{m\rho} \partial_x P = -\frac{1}{m} \partial_x V$. Using thermodynamic relations, this equation can be rewritten as $\partial_x [\mu + V(x)] = 0$. This is solved by tuning locally the chemical potential, $\mu \to \mu(x) = \mu - V(x)$, so it is equivalent to the Local Density Approximation (LDA).

At this point, we have reached an entirely classical description of the gas in terms of standard hydrodynamic equations (9.2.8). In that description, the "quantumness" resides exclusively in the equation of state—i.e. in the formula for the pressure—. In particular, at this level of description, the *connected parts of all correlation functions at equal time* —but different positions $x_i \neq x_j$ in Eq. (9.1.4)— *vanish*, because by construction all the fluid cells are independent. There are no correlations at equal time in classical hydrodynamics. Our goal is to learn how to reintroduce quantumness in that description, in order to reconstruct such quantum correlations.

Quantum fluctuations around the classical hydrodynamic solution

In order to re-quantize the problem, we start by writing an action for the density $\rho(x,t)$ and the associated current $j(x,t) = \rho(x,t) u(x,t)$,

$$\mathcal{S} = \int dx dt \left[m \frac{j^2}{2\rho} - \varepsilon(\rho) - \rho V \right] \tag{9.2.9}$$

where $\varepsilon(\rho) = \frac{\pi^2 \hbar^2 \rho^3}{6m}$ is the ground state energy density, and where the two functions $\rho(x,t)$ and $j(x,t)$ are constrained by the continuity equation $\partial_t \rho + \partial_x j = 0$. Let us check that, with that additional constraint, the action (9.2.9) is compatible with the Euler equation —the second equation in (9.2.8)—. One way to do that is to represent fluctuations around a given classical configuration $(\rho(x,t), j(x,t))$ which satisfies the

continuity equation by a height field $h(x,t)$,

$$\delta\rho(x,t) = \frac{1}{2\pi}\partial_x h(x,t), \qquad \delta j(x,t) = -\frac{1}{2\pi}\partial_t h(x,t), \tag{9.2.10}$$

such that $(\rho+\delta\rho, j+\delta j)$ also satisfies the continuity equation. Then it is easy to check that the Euler-Lagrange equation for the height field h yields the Euler equation. Indeed, varying the action to the first order in $\delta\rho, \delta j$ gives (substituting (9.2.10) and integrating by parts)

$$\begin{aligned}\delta\mathcal{S}^{(1^{\text{st}}\text{ order})} &= \int dxdt\left[m\frac{j\delta j}{\rho} - m\frac{j^2}{2\rho^2}\delta\rho - \delta\rho\partial_\rho\varepsilon - \delta\rho V\right] \\ &= \frac{m}{2\pi}\int dxdt\left[\partial_t\left(\frac{j}{\rho}\right) + \frac{1}{m}\partial_x\left(\frac{j^2}{2\rho^2}\right) + \partial_x(\partial_\rho\varepsilon + V)\right]h.\end{aligned}$$

The expression inside the bracket must vanish; using $u = j/\rho$ and the thermodynamic relation $\partial_x(\partial_\rho\varepsilon) = \frac{1}{\rho}\partial_x P$, this gives precisely the second equation in (9.2.8). So a classical configuration for the action (9.2.9) is indeed a solution of the classical hydrodynamic equations (9.2.8), as required.

Around such a classical configuration, one can then expand to second order to get

$$\begin{aligned}\mathcal{S}[h] &\equiv \delta\mathcal{S}^{(2^{\text{nd}}\text{ order})} \\ &= \frac{1}{8\pi}\int dxdt\left[\frac{m}{\pi\rho}(\partial_t h)^2 + 2\frac{mj}{\pi\rho^2}(\partial_x h)(\partial_t h) + (\frac{mj^2}{\pi\rho^3} - \frac{1}{\pi}\partial_\rho^2\varepsilon)(\partial_x h)^2\right].\end{aligned} \tag{9.2.11}$$

This gives an action for the quantum fluctuations around the classical hydrodynamic solution. Of course, there are also higher order terms, but these higher order terms are RG irrelevant in two spacetime dimensions, and we will omit them. Quantum fluctuations are thus captured by a quadratic action, a fact that is very well known from Luttinger liquid theory [326, 482].

CFT in emergent curved spacetime

The next step is to rewrite the quadratic action (9.2.11) in a more friendly form,

$$\mathcal{S}[h] = \frac{\hbar}{8\pi}\int g^{ab}(\partial_a h)(\partial_b h)\sqrt{-\det g}\, d^2\mathrm{x}, \tag{9.2.12}$$

with coordinates $\mathrm{x}^0 = t$ and $\mathrm{x}^1 = x$, and where g^{ab} are the components of the inverse of the 2×2 matrix

$$g = \begin{pmatrix} \frac{mj^2}{\pi\hbar\rho^3} - \frac{1}{\pi\hbar}\partial_\rho^2\varepsilon & -\frac{mj}{\pi\hbar\rho^2} \\ -\frac{mj}{\pi\hbar\rho^2} & \frac{m}{\pi\hbar\rho}\end{pmatrix}$$

that we want to interpret as a *metric tensor*. [Notice that, to arrive at Eq. (9.2.12), we use the explicit form of the internal energy $\varepsilon(\rho) = \frac{\pi^2\hbar^2\rho^3}{6m}$. This result is then specific to the hard core limit of $1d$ bosons, which map to free fermions. In contrast, when dealing with truly interacting $1d$ liquids, one would end up with a quadratic action of a slightly more general form than (9.2.12), with a position-dependent coupling constant, see Refs. [431, 432] for full details.]

The action (9.2.12) is invariant under diffeomorphisms, and also under Weyl transformations of the metric $g_{ab} \to e^{2\sigma}g_{ab}$. The metric can thus be rescaled and be put in the form

$$g \to \frac{\pi\hbar\rho}{m}g = \begin{pmatrix} u^2 - v_F^2 & -u \\ -u & 1\end{pmatrix},$$

where $v_F(x,t) = \frac{\pi\hbar}{m}\rho(x,t)$ is the Fermi velocity, so that

$$ds^2 = g_{ab}dx^a dx^b = -v_F(x,t)^2dt^2 + (dx - u(x,t)dt)^2. \tag{9.2.13}$$

Written in this way, the emergent spacetime metric (9.2.13) —fixed by the classical hydrodynamic background $\rho(x,t), u(x,t)$— possesses a clear interpretation. The gas consists of local fluid cells, which locally look like the ground state of the translation invariant Tonks-Girardeau gas, up to a Galilean boost. The velocity of sound waves, or of gapless excitations around the ground state at density ρ, is the Fermi velocity $v_F = \frac{\pi\hbar}{m}\rho$. In the ground state the metric that would encode the propagation of those excitations would be $ds^2 = -v_F^2dt^2 + dx^2$. But here the local macrostate of the gas is boosted, in order for the fluid to have a local mean velocity $u \neq 0$. Thus, locally, the sound waves are also boosted by the hydrodynamic velocity u, resulting in Eq. (9.2.13). Another way to say this is that such gapless excitations propagate along the null geodesics of the metric (9.2.13), and those satisfy the simple equation $\frac{d}{dt}x(t) = u(x(t),t) \pm v_F(x(t),t)$, where the $\pm$ sign corresponds to left or right moving trajectories.

What is important now is that we are in a CFT, so all local observables $O(x,t)$ can be decomposed into left $(+)$ and right $(-)$ moving components, of the form $O_+ \otimes O_-$ or as linear combinations thereof. Each chiral component just follows its own null geodesics, and, following these, every operator can be traced back to its original position at time $t = 0$. In particular, focusing on observables of the form $O = O_+ \otimes O_-$, correlation functions can be rewritten as

$$\begin{aligned}&\big\langle O_1(x_1,t_1)O_2(x_1,t_1)\dots O_p(x_p,t_p)\big\rangle \\ &\quad\propto \big\langle O_{1+}(x_+^0(x_1,t_1),0)O_{1-}(x_-^0(x_1,t_1),0)\dots O_{p+}(x_+^0(x_p,t_p),0)O_{p-}(x_-^0(x_p,t_p),0)\big\rangle\,,\end{aligned} \tag{9.2.14}$$

up to some Jacobian factors and where $x_\pm^0(x_i,t_i)$ is the position at initial time of the (right/left) null geodesics passing through x_i at time t_i. Note that in flat space $x_\pm^0(x_i,t_i)$ would simply be $x_i \mp t_i$, while here we have something more complicated because spacetime is curved. This is simplified by using isothermal coordinates, see below. Importantly, the r.h.s. of Eq. (9.2.14) is a correlation function in the initial state, so it is a correlation function at equilibrium.

Correlations in the initial state

Correlation functions in the initial state were studied in Refs. [159, 425, 429, 431], where the same trick of incorporating most effects of the inhomogeneity into the metric of the CFT was used. To get correlation functions at equilibrium in the ground state of the trapped gas, one works with a metric with Euclidean signature, $ds^2 = dx^2 + v_F^2(x)d\beta^2$, where β is now imaginary time, and $v_F(x) = \frac{\pi\hbar}{m}\rho_0(x)$ is the local Fermi velocity in the ground state. Moreover, there always exist *isothermal coordinates* such that the metric takes the form $ds^2 = e^{2\sigma_0}(d\xi^2 + d\beta^2)$. Then a Weyl transformation ($g_{ab}e^{2\sigma_0} \to g_{ab}$) brings the above metric back to the flat one, $ds^2 = d\xi^2 + d\beta^2$. Under that Weyl transformation, primary fields transform as $O \to e^{-\sigma_0\Delta}O$, where Δ is the conformal dimension of O. Therefore the (equilibrium) correlator in the r.h.s. of Eq. (9.2.14) becomes

$$\left(\prod_{a=1}^{p} e^{\Delta_p\sigma_0}\right)\big\langle O_1(\xi_1,0)O_2(\xi_2,0)\dots O_p(\xi_p,0)\big\rangle_{\text{flat}}\,, \tag{9.2.15}$$

where Δ_p is the scaling dimension of O_p and the correlation function is evaluated in the flat metric.

Isothermal coordinates

The procedure we just described is simplified by using isothermal coordinates directly for our emergent $2d$ spacetime. In these coordinates the metric is of the form

$$d^2s = e^{2\sigma}(-d\tau^2 + d\xi^2), \tag{9.2.16}$$

with a conformal factor $e^{2\sigma}$ given by the Jacobian of the transformation $(x,t) \mapsto (\xi,\tau)$. In particular, in these coordinates, doing the backward evolution is trivial (Fig. 9.2). For the particular case studied here the explicit coordinate system (ξ,τ) will be given in Sec. 9.3. Then Eq. (9.2.14) becomes

$$\begin{aligned}\big\langle O_1(x_1,t_1)O_2(x_1,t_1)\dots O_p(x_p,t_p)\big\rangle \\ = \left(\prod_{a=1}^{p} e^{\Delta_p \sigma(x_p,t_p)}\right)\big\langle O_1(\xi_1,\tau_1)O_2(\xi_2,\tau_2)\dots O_p(\xi_p,\tau_p)\big\rangle_{\text{flat}}\end{aligned} \tag{9.2.17}$$

and, in these coordinates, the dynamics is trivial

$$\begin{aligned}\big\langle O_1(\xi_1,\tau_1)O_2(\xi_2,\tau_2)\dots O_p(\xi_p,\tau_p)\big\rangle_{\text{flat}} \\ = \big\langle O_{1+}(\xi_1+\tau_1)O_{1-}(\xi_1-\tau_1)\dots O_{p+}(\xi_p+\tau_p)O_{p-}(\xi_p-\tau_p)\big\rangle_{\text{flat}}\,.\end{aligned} \tag{9.2.18}$$

Here each chiral component is just a function of one of the null coordinates $\xi_\pm = (\xi \pm \tau)$. Notice that, contrary to Eq. (9.2.14), there is no multiplication by Jacobian factors in Eq. (9.2.18), because the Jacobians of the transformation $(\xi,\tau) \mapsto (\xi-\tau,\xi+\tau)$ are trivial.

Again, we stress that the correlator in the r.h.s. of (9.2.18) is an equilibrium one. Moreover, it is further simplified by the fact that right and left moving components are related in a simple way at the edges of the system, as we now explain.

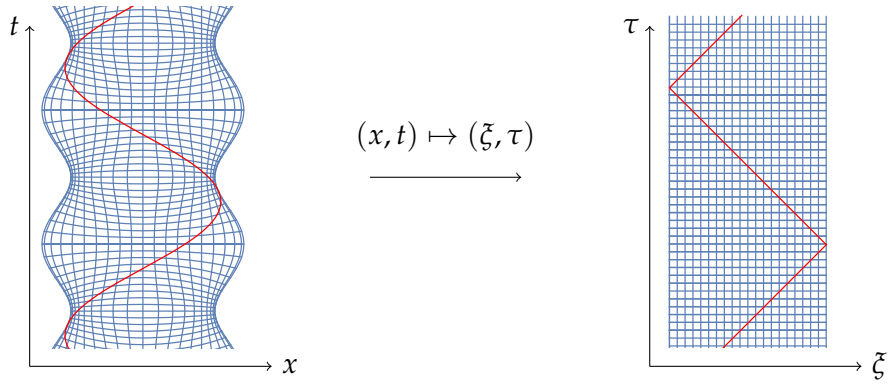

FIGURE 9.2: (Left) Spacetime trajectory of a gapless excitation on top of the breathing gas —drawn for the particular case $\omega(t) = \omega_0$ if $t \le 0$ and $\omega(t) = \omega_1$ if $t > 0$ here—. (Right) In isothermal coordinates (ξ,τ), the trajectory is simply given by $\xi \pm \tau = \text{const}$. Since we have a conformal boundary condition at the left and right edges, the excitations are simply reflected at the boundaries. This allows to easily trace back observables at position x at time t to their original position at $t = 0$.

Reflection against boundaries and "chiralization" of the CFT

At the edges of the cloud, when $1/N \sim \hbar \to 0$, the density vanishes. In this Section we argue that, in such limit, from the point of view of the CFT that describes low-energy fluctuations around the classical solution, the edges of the cloud become particularly simple: they are simply encoded as a Dirichlet boundary condition at the left and right edges $x_L(t)$ and $x_R(t)$,

$$h(x_L(t),t) = h(x_R(t),t) = 0. \tag{9.2.19}$$

This follows directly from the definition of the height field (9.2.10): since the velocity of the right interface is $\dot{x}_R(t) = u(x_R(t),t) = j(x_R(t),t)/\rho(x_R(t),t)$, one gets

$$\frac{1}{2\pi}\frac{d}{dt}h(x_R(t),t) = 0.$$

Thus $h(x_R(t),t)$ is a constant; the same conclusion holds for $h(x_L(t),t)$. To see that the two constants for the left and right edges are equal, one uses the definition (9.2.10) and the fact that the total number of particles N is a constant, so the fluctuations of the density $\delta\rho$ vanish when they are integrated over the whole system, leading to $h(x_L(t),t) = h(x_R(t),t) = \text{const.}$, and the value of the constant can be chosen arbitrarily; we chose to fix it to zero. We then arrive at the boundary condition (9.2.19) as claimed.

Now, since this is a conformal boundary condition, the low-energy excitations are simply reflected against the edge. Left moving operators and right moving ones are just the analytic continuations of one another, as usual in boundary CFT [483]. This is easier to explain this in coordinates (ξ,τ). We will see below that the coordinate system (ξ,τ) can be chosen such that the left and right boundary are at $\xi = -\pi$ and $\xi = 0$. Then it is convenient to think of the height field as being a sum of right- and left-moving components $h(\xi,\tau) = \varphi_-(\xi-\tau) + \varphi_+(\xi+\tau)$, where both components are constrained by the boundary condition (9.2.19). The constraint is implemented by imagining that one has a single right-moving chiral boson $\varphi(\xi-\tau)$ on a circle of circumference 2π, $\varphi(\xi-\tau) = \varphi(\xi-\tau+2\pi)$, and that

$$h(\xi,\tau) = \varphi(\xi-\tau) - \varphi(-\xi-\tau). \tag{9.2.20}$$

Thus h automatically vanishes at $\xi = -\pi$ and $\xi = 0 \pmod{2\pi}$.

This representation in terms of a single chiral boson is very useful because it allows to trace observables at time t back to the ones at time 0 in a straightforward way. Indeed, right-moving components of observables $O_-(\xi-\tau)$ will be expressible in terms of $\varphi(\xi-\tau)$ only, in some form which we write generically as $O_-[\varphi(\xi-\tau)]$. Similarly, the left-moving component $O_+(\xi-\tau)$ will be expressible as $O_+[\varphi(-\xi-\tau)]$. Then the correlation function (9.2.18) becomes a correlator that involves the chiral boson φ at different points on the circle $\mathbb{R}/(2\pi\mathbb{Z})$, i.e.,

$$\begin{aligned}&\big\langle O_1(\xi_1,\tau_1)O_2(\xi_2,\tau_2)\dots O_p(\xi_p,\tau_p)\big\rangle \\ &\qquad = \big\langle O_{1+}[\varphi(-\xi_1-\tau_1)]O_{1-}[\varphi(\xi_1-\tau_1)]\dots O_{p+}[\varphi(\xi_p+\tau_p)]O_{p-}[\varphi(\xi_p-\tau_p)]\big\rangle\,.\end{aligned} \tag{9.2.21}$$

The propagator of the chiral boson $\varphi(\xi)$ with $\xi \in \mathbb{R}/2\pi\mathbb{Z}$ in the r.h.s. of Eq. (9.2.21) is the one on an infinitely long cylinder (adding the imaginary time direction) with Euclidean metric:

$$\langle\varphi(\xi_1)\varphi(\xi_2)\rangle \;=\; -\log\left[2\,\sin\frac{\xi_1-\xi_2}{2}\right]. \tag{9.2.22}$$

Then all correlation functions of the form (9.2.21) can be evaluated by using Wick's theorem.

Summary

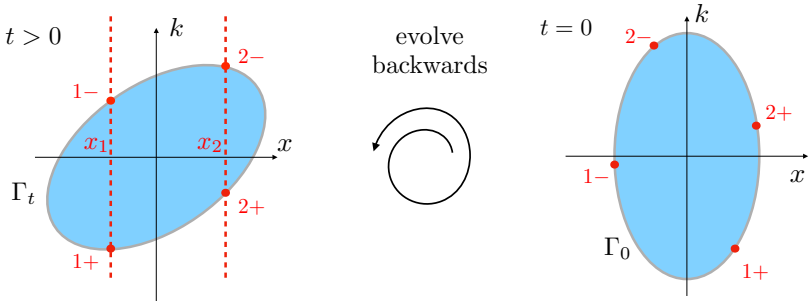

FIGURE 9.3: Summary of our approach. To calculate the correlation function $\langle O_1(x_1,t)O_2(x_2,t)\rangle$ at time t, we start by writing it in terms of chiral operators $\langle O_{1+}O_{1-}O_{2+}O_{2-}\rangle$ that generate low-energy excitations around the Fermi points $(x_1,k_{F-}(x_1,t))$, $(x_1,k_{F+}(x_1,t))$, $(x_2,k_{F-}(x_2,t))$, $(x_2,k_{F+}(x_2,t))$. Then we trace the Fermi points back to their original positions in phase space. The problem boils down to calculating a correlation function of observables along the initial Fermi contour Γ_0.

In the end, we have reached the following simple framework to compute a correlation function of the form (9.1.4). First of all, since we are in CFT, every operator O_i can be decomposed in chiral components acting on low-energy fluctuations around the Fermi points $(x_i, k_{F\pm}(x_i,t))$ for $i = 1, \cdots, p$. Those Fermi points are identified in phase space as the intersections of the vertical line passing through x_j and the Fermi contour Γ_t, see Figs. 9.1 and 9.3. Then we "play the movie backwards" in phase space, i.e. we trace the Fermi points back to their original positions in phase space. Actually, the whole contour Γ_t can be traced back to its initial configuration Γ_0 and the problem boils down to calculating a correlation function of chiral observables along the contour Γ_0 at time $t = 0$.

The general procedure, however, can be simplified if one is able to find a set of *isothermal* coordinates (ξ, τ) (Eq. (9.2.16)) and, in this case, the recipe to perform the calculation is as follows. For each (x_j, t_j) one first needs to identify the corresponding (ξ_j, τ_j). By performing the associated Weyl transformation, we are left with the same correlator but in the usual CFT in flat spacetime (Eq. (9.2.17)). Then one simply traces each chiral component of the observable sitting at (ξ_j, τ_j) back to its initial position at time zero, i.e., $(\xi_{j,\pm}, 0)$, with $\xi_{j,+} = \xi_j - \tau_j$ and $\xi_{j,-} = \xi_j + \tau_j$ for right and left movers respectively (Eq. (9.2.18)), ending up with the problem of computing a correlation function of (chiral) observables at equilbrium. Because of the simple Dirichlet boundary condition that we found at the edges of the system, left and right movers are simply reflected against the boundaries, and correlation functions can be expressed in terms of a single chiral bosonic field φ living on a circle of circumference 2π (Eq. (9.2.21)).

All those steps lead to a simple formula in the end,

$$\begin{aligned}&\big\langle O_1(x_1,t_1)O_2(x_1,t_1)\dots O_p(x_p,t_p)\big\rangle\\ &= \left(\prod_{a=1}^{p} e^{\Delta_p \sigma}\right)\big\langle O_{1+}[\varphi(-\xi_1-\tau_1)]O_{1-}[\varphi(\xi_1-\tau_1)]\dots O_{p+}[\varphi(\xi_p+\tau_p)]O_{p-}[\varphi(\xi_p-\tau_p)]\big\rangle\,,\end{aligned} \tag{9.2.23}$$

where the r.h.s. is understood as a correlator in the ground state of a CFT in Euclidean spacetime and can be evaluated using only the propagator of the bosonic field φ (Eq. (9.2.22)) and Wick's theorem.

9.3 Time-dependent harmonic trap: useful formulas

In this Section we provide the explicit formulas that solve the classical hydrodynamic equations (9.2.8) for the time-dependent harmonic trap, and give the corresponding isothermal coordinates (ξ, τ) that allow to propagate correlation functions at arbitrary times back to the ones in the initial state, see Eq. (9.2.18). This is greatly simplified by the existence of a "holographic" picture for the time-dependent harmonic potential [473], which we briefly describe.

A simple "holographic" model

Consider a classical rigid pendulum of length $\ell(t)$ attached to the origin in the two-dimensional plane (x, y), and rotating freely around it. The position of the endpoint of the pendulum is parametrized as

$$\begin{cases} x(t) = \ell(t)\cos\xi(t) \\ y(t) = \ell(t)\sin\xi(t), \end{cases} \tag{9.3.1}$$

where $\xi(t)$ is defined modulo 2π. At time $t = 0$, the length of the pendulum is ℓ_0 and its angular velocity is ω_0. The length $\ell(t)$ varies, so the energy of the pendulum is not conserved, but its angular momentum is. This implies

$$\frac{d\xi(t)}{dt} = \frac{\omega_0}{b(t)^2}, \tag{9.3.2}$$

where $b(t) = \ell(t)/\ell_0$. Now, we imagine that for some reason we are unaware of the two-dimensional nature of the problem, and that we have access only to the projection of the motion along the x-direction.

We observe the trajectory $x(t)$, and what we see is precisely the motion of a point-like particle *in a time-dependent harmonic potential* [473],

$$m\frac{d^2x}{dt^2} = -\partial_x V, \qquad \text{where} \qquad V(x,t) = \frac{1}{2}m\left(\frac{\omega_0^2}{b(t)^4} - \frac{\ddot{b}(t)}{b(t)}\right)x^2. \tag{9.3.3}$$

[This follows straightforwardly from plugging $x = \ell\cos\xi$ into Newton's equation, using conservation of angular momentum (9.3.2).] Thus, from now on, we assume that the function $b(t)$ is related to the time-dependent frequency of our trap (9.1.2) through the differential equation

$$\ddot{b}(t) + \omega(t)^2 b(t) = \frac{\omega_0^2}{b(t)^3}, \tag{9.3.4}$$

known as the *Ermakov equation* [484, 485], with the initial condition $b(0) = 1$ and $\dot{b}(0) = 0$. [The latter condition is imposed because in our problem we are assuming that we are initially at rest in a trap with frequency ω_0, so $\dot{b}(t) = 0$ for $t < 0$, and $\dot{b}(t)$ must be continuous in order to be a solution of (9.3.4).] From this higher-dimensional perspective, and assuming that the function $b(t)$ has been calculated for the given $\omega(t)$ defining our problem —see Ref. [485] for the solution to Eq. (9.3.4)—, it is straightforward to calculate the trajectory of the classical point-like particle in the time-dependent trap: it is simply given by $x(t) = \ell_0 b(t)\cos(\xi(0) + \tau(t))$ with

$$\tau(t) \equiv \int_0^t \frac{\omega_0\, ds}{b(s)^2}. \tag{9.3.5}$$

As we will see shortly, the trajectories $(x(t), t)$ are nothing but the null geodesics of the metric (9.2.13), and the coordinates (ξ, τ) are isothermal for that metric.

Formulas and parametrizations

This $2d$ picture of the $1d$ time-dependent harmonic oscillator leads to simple explicit formulas that are useful in the context of the formalism of Sec. 9.2. We start by writing the $1/N \sim \hbar \to 0$ limit of the Wigner function in the form (9.2.5). In the initial state, it is obtained by saying that all points (x,k) in phase space are occupied iff their total energy $E(x,k) = \frac{\hbar^2k^2}{2m} - \mu + \frac{m\omega_0^2x^2}{2}$ is negative. Thus, the curve $\Gamma_{t=0}$ that encloses all these points is an ellipse. Then, at $t > 0$, since the motion of each semi-classical particle is given by $x(t) = b(t)\cos(\xi(0) + \tau(t))$, its phase space position is $(x(t), k(t)) = (x(t), \frac{m}{\hbar}\frac{dx(t)}{dt})$. Hence, the curve Γ_t of Eq. (9.2.5) is the (rotated) ellipse

$$(x,k) \in \Gamma_t \quad \Leftrightarrow \quad \frac{b(t)^2(\hbar k - mx\dot{b}(t)/b(t))^2}{2m} - \mu + \frac{m\omega_0^2x^2}{2b(t)^2} = 0. \tag{9.3.6}$$

Classical hydrodynamic solution. Using Eqs. (9.2.7) one gets the following solution to the classical hydrodynamic equations (9.2.8),

$$\rho(x,t) = \frac{1}{b(t)} \times \frac{m\omega_0}{\pi\hbar}\sqrt{\frac{2\mu}{m\omega_0^2} - \frac{x^2}{b(t)^2}}, \qquad u(x,t) = x\,\frac{d\log b(t)}{dt}. \tag{9.3.7}$$

This explicit solution is well known in the literature and is usually referred to as a *scaling solution* [460–462, 486] since the density profile at time t is a simple rescaling of the one at time zero.

Isothermal coordinates (ξ, τ). Next, we turn to the metric (9.2.13). By construction, the null geodesics of that metric are the trajectories of low-energy excitations around the classical solution (9.3.7), or in other words of points in phase space that lie along the Fermi contour Γ_t. Thus the geodesics read simply $x(t) = b(t)\cos(\xi + \tau)$, and we see, as anticipated by our notations, that the coordinate system (ξ, τ) is indeed isothermal for the metric (9.2.13). To be more precise, for each $x \in [-b(t)\sqrt{\frac{2\mu}{m\omega_0^2}}, b(t)\sqrt{\frac{2\mu}{m\omega_0^2}}]$ there are

two possible ξ (mod 2π) such that $x/(b(t)\sqrt{\frac{2\mu}{m\omega_0^2}}) = \cos\xi$. We write these two solutions as

$$\begin{cases} \xi(x,t) \equiv -\arccos\left(\frac{x}{b(t)}/\sqrt{\frac{2\mu}{m\omega_0^2}}\right) \in [-\pi,0] \pmod{2\pi}, \\ 2\pi - \xi(x,t) \in [0,\pi] \pmod{2\pi}. \end{cases} \tag{9.3.8}$$

Then as in Sec. 9.2, observables that are sensitive only to left moving excitations will involve the chiral boson $\varphi(\xi-\tau)$ while the ones sensitive to right moving excitations will involve $\varphi(2\pi-\xi-\tau)$.

One can easily check that the metric (9.2.13) is given by $ds^2 = e^{2\sigma(x,t)}(-d\tau^2 + d\xi^2)$ with

$$e^{\sigma(x,t)} = \sqrt{\frac{2\mu}{m\omega_0^2}b(t)^2 - x^2}. \tag{9.3.9}$$

Phases. In the next sections we will be interested in correlation functions of observables which create/annihilate particles, i.e. observables that possess a non-zero U(1) charge. Thus we will have to be careful about phases. One phase that will appear is the WKB phase at the Fermi points $k_{F-}(x,t)$ and $k_{F+}(x,t)$. It is defined such that its differential is

$$d\phi_{\mathrm{WKB}\mp}(x,t) = k_{F\mp}(x,t)dx - \frac{1}{\hbar}\left(\frac{\hbar^2 k_{F\mp}^2(x,t)}{2m} + V(x,t)\right)dt. \tag{9.3.10}$$

This has the following interpetation: if one imagines that one creates a free fermion at position $(x, k_\mp(x,t))$ in phase space, then the single-particle wavefunction of that new fermion will behave as $\exp(-i\frac{1}{\hbar}(\frac{\hbar^2 k_{F\mp}^2}{2m} + V)\delta t + ik_{F\mp}\delta x)$ at small distance δx and small time δt; the latter phase then also multiplies the many-body wavefunction. Integrating Eq. (9.3.10), one gets (with $m = \omega_0 = \mu = 1$)

$$\phi_{\mathrm{WKB}\mp}(x,t) = \left(-\tau(t) + \frac{\dot b(t)}{b(t)}\frac{x^2}{2} \pm \left(\frac{x}{b(t)\sqrt{2}}\sqrt{1-\left(\frac{x}{b(t)\sqrt{2}}\right)^2} - \arccos\frac{x}{b(t)\sqrt{2}}\right)\right)N, \tag{9.3.11}$$

up to an unimportant additive constant independent of x and t.

Another phase that will show up is the combination of $\phi_{\mathrm{WKB}-}$ and $\phi_{\mathrm{WKB}+}$, corresponding to a local Galilean boost, such that $\partial_x\phi(x,t) = \frac{m}{\hbar}u(x,t)$. This is satisfied by

$$\phi(x,t) \equiv \frac{1}{2}[\phi_{\mathrm{WKB}-}(x,t) + \phi_{\mathrm{WKB}+}(x,t)] = \left(-\tau(t) + \frac{\dot b(t)}{b(t)}\frac{x^2}{2}\right)N. \tag{9.3.12}$$

9.4 Boson correlation functions

We now apply the above formalism to calculate the $2n$-point correlation function of boson creation/annihilation operators,

$$g_n((x_1,t_1),\dots,(x_n,t_n),(x_1',t_1'),\dots,(x_n',t_n')) \equiv \left\langle \Psi^\dagger(x_1,t_1)\dots\Psi^\dagger(x_n,t_n)\Psi(x_1',t_1')\dots\Psi(x_n',t_n')\right\rangle, \tag{9.4.1}$$

always in the limit $1/N \sim \hbar \to 0$. To the best of our knowledge, such results cannot be obtained by any other method. From the numerical side, there exist efficient algorithms to compute the one-particle density matrix $g_1((x,t),(x',t'))$ in the initial state ($t = t' = 0$) based on the lattice version of this problem [487, 488], which map to the continuum problem at low fillings [489]; the extension to the dynamical situation ($t, t' \neq 0$) after a generic evolution is non trivial. Analytically, on the other hand, we are aware only of one result by Forrester *et al.* [472] (see also Gangardt [490] and the related work [370] for the

extension to the anyonic case) which gives the one-particle density matrix $g_1(x,x')$ in the initial state in the same limit $1/N \sim \hbar \to 0$. The formula we obtain below naturally coincides with the known results in particular cases (see also Ref. [425], where this is explained in great detail). The methods of Refs. [472,490], however, do not seem to be easily generalizable to arbitrary times or to higher point correlations. The fact that the approach we take here leads to such results in a relatively simple way is a clear demonstration of its power and efficiency. In this Section we set $\omega_0 = \mu = m = 1$.

Identification of $\Psi^\dagger$, Ψ with CFT operators

In order to use the above formalism to calculate the correlation function (9.4.1), we need to be able to express correlations of $\Psi^\dagger$ and Ψ in the microscopic model —the inhomogeneous Tonks-Girardeau gas— as correlators of properly identified operators in the CFT. This was done in detail in Ref. [425], but we briefly recall the result. The guiding principle is that any local operator in the microscopic model can be expanded as a sum of operators in the low-energy theory, and the latter sum can be organized in increasing order of scaling dimension of the operators. The only restriction on terms in the sum is that they should have the same symmetries as the microscopic model. For $\Psi^\dagger$ and Ψ, the CFT operators appearing in the expansion should carry a U(1) charge ± 1, so the expansion should start as [425]

$$\begin{aligned} \Psi^\dagger(x,t) &\propto :e^{-\frac{i}{2}(\varphi_-(x,t)-\varphi_+(x,t))}: + \text{less relevant operators} \\ \Psi(x,t) &\propto :e^{\frac{i}{2}(\varphi_-(x,t)-\varphi_+(x,t))}: + \text{less relevant operators,} \end{aligned} \tag{9.4.2}$$

where φ_- and φ_+ are the right- and left-moving parts of the height field $h = \varphi_- + \varphi_+$. As we have seen in Sec. 9.2, the latter can also be written in terms of a single chiral boson $\varphi_-(\xi-\tau) = \varphi(\xi-\tau)$ and $\varphi_+(\xi+\tau) = -\varphi(2\pi-\xi-\tau)$.

Here we will keep only the leading order in Eq. (9.4.2), but in principle higher order could be taken into account as well, giving rise to subleading corrections in the limit $1/N \sim \hbar \to 0$ [431]. Importantly, we need to fix the prefactor of that leading term in Eq. (9.4.2). Since $\Psi^\dagger$ is homogeneous to a length to the power $-1/2$, while the vertex operator $:e^{-\frac{i}{2}(\varphi_- - \varphi_+)}:$ has scaling dimension $1/4$, we see by dimensional analysis that the prefactor must scale as $\rho(x,t)^{1/4}$, because the inverse density ρ^{-1} is the only local length scale in the problem. Additionally, because the operators carry a U(1) charge, they must be multiplied by the U(1) phase identified in Eq. (9.3.12). This gives

$$\begin{aligned} \Psi^\dagger(x,t) &= C\,\rho(x,t)^{\frac{1}{4}}\, e^{-i\phi(x,t)}\, :e^{-\frac{i}{2}(\varphi_-(x,t)-\varphi_+(x,t))}: \\ \Psi(x,t) &= C^*\,\rho(x,t)^{\frac{1}{4}}\, e^{i\phi(x,t)}\, :e^{\frac{i}{2}(\varphi_-(x,t)-\varphi_+(x,t))}:, \end{aligned} \tag{9.4.3}$$

where C is a complex dimensionless constant which depends neither on position nor on time. Because of the global U(1) invariance, the phase of C is arbitrary and does not affect the correlation function (9.4.1). The amplitude $|C|$ can be fixed from exact results for the homogeneous Tonks-Girardeau gas based on the analysis of Toeplitz determinants [491–493, 493], see also the discussion in Ref. [425],

$$|C|^2 = \frac{G^4(3/2)}{\sqrt{2\pi}} \simeq 0.521409, \tag{9.4.4}$$

where $G(.)$ is Barnes' G-function.

9.4.1 The one-particle density matrix

Now that the boson creation/annihilation operators are identified with CFT operators, the $2n$-point correlation function is straightforwardly computed by following the strategy of Section 9.2. We shall start with the simplest case $n = 1$ and work out all the details.

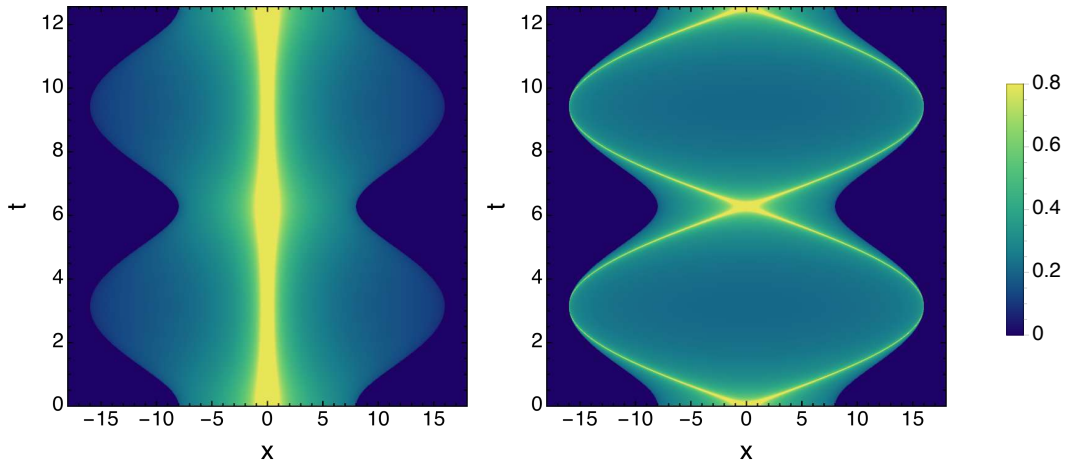

FIGURE 9.4: Absolute value of the one-particle density matrix at equal times, $|g_1(x,0;t)|$ (left) and at different times, $|g_1((x,t),(0,0))|$ (right), as a function of x and t. The parameters are chosen as follows: $\omega_0 = 1, \omega_1 = 0.5, N = 32$.

Injecting the identification (9.4.3), we get

$$\begin{aligned} g_1((x,t),(x',t')) &= \left\langle \Psi^\dagger(x,t)\Psi(x',t') \right\rangle \\ &= |C|^2 \left(e^{-i(\phi(x,t)-\phi(x',t'))} \right) \left(\rho(x,t)\rho(x',t') \right)^{\frac{1}{4}} \\ &\quad \times \left\langle : e^{-\frac{i}{2}(\varphi_-(x,t)-\varphi_+(x,t))} : : e^{\frac{i}{2}(\varphi_-(x',t')-\varphi_+(x',t'))} : \right\rangle . \end{aligned} \tag{9.4.5}$$

Next, as we have seen in Section 9.2 the correlator can be evaluated in the initial state by tracing back the isothermal coordinates to $t = 0$. This is done by using formula (9.2.21) which gives

$$\begin{aligned} g_1((x,t),(x',t')) &= |C|^2 \left(e^{-i(\phi(x,t)-\phi(x',t'))} \right) \left(\frac{\rho(x,t)\rho(x',t')}{e^{\sigma(x,t)} e^{\sigma(x',t')}} \right)^{\frac{1}{4}} \\ &\quad \times \left\langle : e^{-\frac{i}{2}(\varphi(\xi-\tau)+\varphi(2\pi-\xi-\tau))} : : e^{\frac{i}{2}(\varphi(\xi'-\tau')+\varphi(2\pi-\xi'-\tau'))} : \right\rangle , \end{aligned} \tag{9.4.6}$$

where we have traded the right- and left-moving parts of the height field for the single chiral boson $\varphi(\xi)$ as explained in Sec. 9.2. Then, the 2-point correlator is equivalent to a 4-point correlator that is easily computed using Wick's theorem and the propagator of the chiral boson (9.2.22). Using $\frac{e^{\sigma(x,t)}}{\rho(x,t)} = \hbar\pi b(t)^2$ to simplify the scaling factors and Eq. (9.3.12) for the phases $\phi(x,t)$ and $\phi(x',t')$, this gives

$$\begin{aligned} g_1((x,t),(x',t')) &= \frac{|C|^2}{\sqrt{2\pi\hbar}} \frac{e^{-i\left(\frac{\dot{b}(t)}{b(t)}\frac{(x^2-x'^2)}{2} - \frac{(\tau-\tau')}{4}\right)N}}{\sqrt{b(t)\, b(t')}} \\ &\quad \times \frac{(\sin\xi)^{\frac{1}{4}}}{\left(\sin\frac{(\xi-\xi')-(\tau-\tau')}{2}\right)^{\frac{1}{4}} \left(\sin\frac{(\xi-\xi')+(\tau-\tau')}{2}\right)^{\frac{1}{4}}} \\ &\quad \times \frac{(\sin\xi')^{\frac{1}{4}}}{\left(\sin\frac{(\xi+\xi')+(\tau-\tau')}{2}\right)^{\frac{1}{4}} \left(\sin\frac{(\xi+\xi')-(\tau-\tau')}{2}\right)^{\frac{1}{4}}}, \end{aligned} \tag{9.4.7}$$

The latter can be explictly written in terms of the physical coordinates (x,t) and (x',t') by plugging the expressions for the the isothermal coordinates (9.3.8) and the density (9.3.7) Remarkably, the result at equal

time $t = t'$ takes a nice and compact form,

$$g_1(x,x';t) \equiv g_1((x,t),(x',t)) = \frac{|C|^2}{\sqrt{2\pi\hbar}} \frac{e^{-i\left(\frac{\dot b(t)}{b(t)}\frac{(x^2-x'^2)}{2}\right)N}}{b(t)} \frac{(\sin\xi)^{\frac14}(\sin\xi')^{\frac14}}{\left(\sin\frac{(\xi-\xi')}{2}\right)^{\frac12}\left(\sin\frac{(\xi+\xi')}{2}\right)^{\frac12}}$$

where the correlator in the first line precisely coincides with the one derived in [425]. In the second line, we see that the result obtained with our approach automatically satisfies the same scaling relation as the one found by Minguzzi and Gangardt [460]. It is also clear that at $t = 0$ (using $b(0) = 1$) we recover the result of Forrester et al. [472],

$$g_1(x,x';0) = |C|^2 \frac{\rho(x,0)^{\frac14}\rho(x',0)^{\frac14}}{|x-x'|^{\frac12}}. \tag{9.4.8}$$

In Fig. 9.4, we plot $g_1((x,t),(x',t'))$ for the particular case of a sudden quench of the frequency: $\omega(t) = \omega_0$ for $t \le 0$ and $\omega(t) = \omega_1 \neq \omega_0$ for $t > 0$. We were not able to compare this result to a numerical evaluation in finite size, because we are not aware of a method that would allow to calculate that quantity at different times and for a large number of particles, even approximately. In contrast, the fact that our approach gives directly a closed analytic formula for the asymptotic behavior of that correlation function in the regime $1/N \sim \hbar \to 0$ shows that it is quite powerful.

9.4.2 The general $2n$-point function

The above derivation generalizes straightforwardly to the $2n$-point case

$$g_n((x_1,t_1),\dots,(x_n,t_n),(x'_1,t'_1),\dots,(x'_n,t'_n)) = |C|^{2n}\left(\prod_{j=1}^n e^{-i(\phi(x_j,t_j)-\phi(x'_j,t'_j))}\right)\left(\prod_{i=1}^n \frac{\rho(x_i,t_i)\rho(x'_i,t'_i)}{e^{\sigma(x_i,t_i)}e^{\sigma(x'_i,t'_i)}}\right)^{\frac14}$$
$$\times\left\langle \prod_{p=1}^n :e^{-\frac{i}{2}(\varphi_-(\xi_p-\tau_p)-\varphi_+(\xi_p+\tau_p))}: \prod_{q=1}^n :e^{\frac{i}{2}(\varphi_-(\xi'_q-\tau'_q)-\varphi_+(\xi'_q+\tau'_q))}: \right\rangle_{\text{flat}} \tag{9.4.9}$$

One can further use that $\frac{e^{\sigma(x,t)}}{\rho(x,t)} = \hbar\pi b(t)^2$ to simplify the scaling factors, and Wick's theorem and the propagator of the chiral boson (9.2.22) to evaluate the correlator in the third line, thus obtaining a rather complicated but fully explicit result (reported in Ref. [439]). We stress that it is obtained relatively easily with our approach, as it boils down to simple calculations in a free boson CFT. As emphasized above, we do not know any other method that would allow to go that far in the calculation of correlation function for the trapped Tonks-Girardeau gas.

The result (9.4.9) can be put in a nicer form if one takes all the points at equal time, $t_1 = \dots = t_n = t'_1 = \dots = t'_n = t$. Indeed, after some algebra one arrives at the more compact formula

$$g_n(x_1,\dots,x_n,x'_1,\dots,x'_n;t) = \left(\frac{|C|^2}{\sqrt{b(t)}}\right)^n e^{-i\sum_j(\phi(x_j,t)-\phi(x'_j,t))}\prod_i \rho(x_i,t)^{\frac14}\prod_j \rho(x'_j,t)^{\frac14}$$
$$\times \frac{\prod_{p_1<p_2}\left|\frac{x_{p_1}-x_{p_2}}{b(t)}\right|^{\frac12}\prod_{q_1<q_2}\left|\frac{x'_{q_1}-x'_{q_2}}{b(t)}\right|^{\frac12}}{\prod_{p,q}\left|\frac{x_p-x'_q}{b(t)}\right|^{\frac12}}, \tag{9.4.10}$$

which simplifies even further in the initial state with $b(0) = 1$,

$$g_n(x_1,\dots,x_n,x'_1,\dots,x'_n;0) = |C|^{2n}\prod_i \rho(x_i,0)^{\frac{1}{4}}\prod_j \rho(x'_j,0)^{\frac{1}{4}} \times \frac{\prod_{p_1<p_2}\left|x_{p_1}-x_{p_2}\right|^{\frac{1}{2}}\prod_{q_1<q_2}\left|x'_{q_1}-x'_{q_2}\right|^{\frac{1}{2}}}{\prod_{p,q}\left|x_p-x'_q\right|^{\frac{1}{2}}}. \quad (9.4.11)$$

To the best of our knowledge, this formula is new and it generalizes the formula for $n = 1$ of Forrester et al. [472]. Also, one clearly sees that, in general, the $2n$-point function at equal time (9.4.10) satisfies the same scaling relation as the one found by Minguzzi and Gangardt in the $n = 1$ case [460].

9.5 The fermion propagator: large-N asymptotics and numerical check

To further illustrate the strategy outlined in Section 9.2, we now compute the large-N asymptotics of the fermion propagator at different times,

$$c(x,t,x',t') \equiv \langle \Psi_{\rm F}^\dagger(x,t)\Psi_{\rm F}(x',t')\rangle, \quad (9.5.1)$$

where $\Psi_{\rm F}^\dagger$, $\Psi_{\rm F}$ is the fermion creation/annihilation operator related to the bosonic one by Eq. (9.2.1). The final result for this propagator is given by formula (9.5.12) below. There are two contributions. The leading one is due to fermion excitations lying deep inside the Fermi sea, and is therefore beyond the approach sketched in Section 9.2, strictly speaking. Nevertheless, we are able to obtain that term by elementary means. Then, the next leading contribution is due to low energy excitations and is the one in which we are truly interested, as it is the one which we can get from our approach. In this Section we set $\mu = m = 1$.

9.5.1 Lessons from the infinite homogeneous case

We start from the homogeneous, translation-invariant case, where the two contributions are also present. In that case the fermion propagator for an infinite system is

$$c(x,t,0,0) = \int_{-k_F}^{k_F}\frac{dk}{2\pi}e^{-ikx+i\hbar t\frac{k^2}{2}}, \quad (9.5.2)$$

where k_F is the Fermi momentum (in terms of the notations of Section 9.3, we have $k_{F-} = k_F$ and $k_{F+} = -k_F$). Of course, the integral could be evaluated exactly in terms of some error function. But instead, we are interested in evaluating its large x and t behavior by the stationary phase approximation. The approximation is valid in the limit of large t and fixed ratio x/t, and it holds everywhere except along the lightcone $x/t = \pm v_F$, where $v_F = \hbar k_F$. There are two regimes to be considered: outside and inside the lightcone.

Outside the lightcone ($|x| > v_F t$). The integrand in Eq. (9.5.2) does not have a stationary point in the interval $[-k_F, k_F]$, therefore the main contribution to the integral in the stationary phase approximation comes from the regions around the two Fermi points $k \sim \pm k_F$,

$$\begin{aligned} c(x,t,0,0) &\simeq \int_{-\infty}^{k_F}\frac{dk}{2\pi}e^{-ik_Fx+i\hbar t\frac{k_F^2}{2}-i(k-k_F)(x-v_Ft)} + \int_{-k_F}^{\infty}\frac{dk}{2\pi}e^{ik_Fx+i\hbar t\frac{k_F^2}{2}+i(k-k_F)(x+v_Ft)} \\ &= \frac{i}{2\pi}\left[\frac{e^{-ik_Fx+i\hbar t\frac{k_F^2}{2}}}{(x-v_Ft)} - \frac{e^{ik_Fx+i\hbar t\frac{k_F^2}{2}}}{(x+v_Ft)}\right]. \end{aligned} \quad (9.5.3)$$

Inside the lightcone ($|x| < v_F t$). There the phase of the integral (9.5.2) has a stationary point inside the region of integration (the point $\hbar k = x/t$). Therefore the main contribution comes from this stationary point,

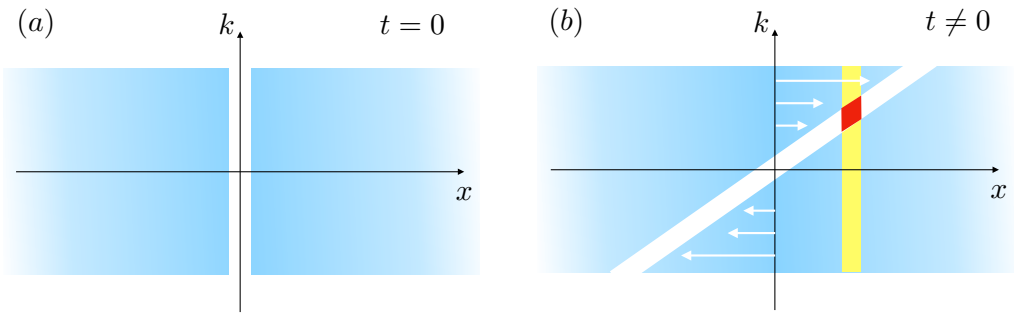

FIGURE 9.5: Wigner probability distribution for the homogeneous Fermi gas on an infinite line. Panel (a): we remove a particle at time $t = 0$ (white slice). Panel (b) The slice corresponding to the removed particle evolves. At time t we want to create a particle in x (yellow slice). The probability of doing it it proportional to the area shared by these two slides (red area).

whereas the contributions from the endpoints of the interval $[-k_F, k_F]$ give the next to leading correction. Explicitly, we have

$$c(x,t,0,0) \simeq \int_{-\infty}^{\infty} \frac{dk}{2\pi} e^{-i\frac{x^2}{2\hbar t}+i\hbar t\frac{(k-x/t)^2}{2}} e^{i\frac{\pi}{4}} \left(\frac{1}{2\pi\hbar t}\right)^{1/2} e^{-i\frac{x^2}{2\hbar t}} + \frac{i}{2\pi}\left[\frac{e^{-ik_F x+i\hbar t\frac{k_F^2}{2}}}{(x-v_F t)} - \frac{e^{ik_F x+i\hbar t\frac{k_F^2}{2}}}{(x+v_F t)}\right].$$

The leading term is thus associated with an excitation deep inside the Fermi sea, corresponding to a point inside the interval $[-k_F, k_F]$. The other two terms, however, clearly originate from the low-energy excitations around the Fermi points that are described by CFT.

We thus want to think of the fermion creation/annihilation operator as being a sum of three terms: an operator $d^\dagger/d$ exciting a state deep inside the Fermi sea, plus the right $(-)$ and left $(+)$ components of a Dirac field, or equivalently in terms of the chiral bosons φ_- and φ_+, as vertex operators $:e^{-i\varphi_-}:$ and $:e^{i\varphi_+}:$,

$$\begin{aligned}
\Psi_F^\dagger(x,t) &= d^\dagger(x,t) + \frac{e^{i\frac{\pi}{4}}}{\sqrt{2\pi}} e^{-ik_F x+i\frac{k_F^2}{2}t} :e^{-i\varphi_-(x-k_F t)}: - \frac{e^{-i\frac{\pi}{4}}}{\sqrt{2\pi}} e^{ik_F x+i\frac{k_F^2}{2}t} :e^{i\varphi_+(x+k_F t)}: \\
\Psi_F(x,t) &= d(x,t) + \frac{e^{i\frac{\pi}{4}}}{\sqrt{2\pi}} e^{ik_F x-i\frac{k_F^2}{2}t} :e^{i\varphi_-(x-k_F t)}: + \frac{e^{-i\frac{\pi}{4}}}{\sqrt{2\pi}} e^{-ik_F x-i\frac{k_F^2}{2}t} :e^{-i\varphi_+(x+k_F t)}:,
\end{aligned} \tag{9.5.4}$$

then the CFT terms in Eqs. (9.5.3)-(9.5.4) correspond to the two-point functions in the free boson CFT on the infinite line,

$$\left\langle :e^{-i\varphi_-(x-k_F t)}:: e^{i\varphi_-(0)}: \right\rangle = \frac{1}{x-k_F t}, \qquad \left\langle :e^{i\varphi_+(x+k_F t)}:: e^{-i\varphi_+(0)}: \right\rangle = \frac{1}{-x-k_F t}. \tag{9.5.5}$$

The mixed terms involving φ_- and φ_+ are zero on the infinite line, because there are no boundaries (there must be a boundary in order for left moving excitations to be reflected as right moving ones, thus inducing correlations between left and right sectors of the CFT). The term coming from the deeper excitation has propagator

$$\left\langle d^\dagger(x,t)d(0,0)\right\rangle = \begin{cases} e^{i\frac{\pi}{4}}\left(\frac{1}{2\pi\hbar t}\right)^{1/2} e^{-i\frac{x^2}{2\hbar t}} & \text{inside the lightcone} \\ 0 & \text{outside the lightcone} \end{cases}, \tag{9.5.6}$$

which has the following interpretation. The amplitude can be understood by looking at the Wigner function, which in this case is simply $n(x,k) = 1$ if $|k| < k_F$ and 0 otherwise. $d(0,0)$ destroys a particle at $x = 0$ and $t = 0$, corresponding in this language to removing a thin slice around $x = 0$, while $d^\dagger(x,t)$ creates a

new one at position x and time t. This is possible only inside the small area corresponding to the removed slice evolved up to time t (see the red area in Figure 9.5). From the picture, one sees that such a probability decreases as $1/t$ and thus the corresponding amplitude goes as $1/\sqrt{t}$. The phase $e^{-i\frac{x^2}{2\hbar t}}$ is nothing but the semiclassical phase accumulated along the classical trajectory of the particle, namely

$$e^{-\frac{i}{\hbar}\int_0^t ds\left[\frac{1}{2}\dot{x}^2(s)-V(x(s))\right]}, \tag{9.5.7}$$

here with $x(s)=s\,x/t$ and $V(x)=0$.

9.5.2 Fermion propagator in the time-dependent harmonic trap

Now let us come back to the breathing gas in the time-dependent harmonic trap. To the best of our knowledge, exact results exist in the literature only for equal-time correlators [178, 179, 460, 466]. Our method, instead, allows to obtain asymptotic results also at different times. Like in the uniform case, we write the creation/annihilation operators in the microscopic model as a sum of three field, the first one acting deep inside the Fermi sea, and the other two being fields that excite low-energy excitations close to the Fermi points,

$$\begin{aligned}
\Psi_{\rm F}^\dagger(x,t) &= d^\dagger(x,t) + \frac{e^{i\frac{\pi}{4}}}{\sqrt{2\pi}}e^{-i\phi_{\rm WKB-}(x,t)}:e^{-i\varphi_-(\xi-\tau)}: - \frac{e^{-i\frac{\pi}{4}}}{\sqrt{2\pi}}e^{-i\phi_{\rm WKB+}(x,t)}:e^{i\varphi_+(\xi+\tau)}: \\
\Psi_{\rm F}(x,t) &= d(x,t) + \frac{e^{i\frac{\pi}{4}}}{\sqrt{2\pi}}e^{i\phi_{\rm WKB-}(x,t)}:e^{i\varphi_-(\xi-\tau)}: + \frac{e^{-i\frac{\pi}{4}}}{\sqrt{2\pi}}e^{i\phi_{\rm WKB+}(x,t)}:e^{-i\varphi_+(\xi+\tau)}:.
\end{aligned} \tag{9.5.8}$$

The phases of the different terms are chosen in order to locally match the ones in the homogeneous case for small $|x-x'|$ and $|t-t'|$, see Eq. (9.5.4). The coordinate $\xi(x,t)$ is given by Eq. (9.3.8).

CFT contribution

We focus first on the contributions due to the vertex operators in (9.5.8), which is the one that is given by the approach outlined in Section 9.2. After evaluating the two-point functions of the vertex operators, we arrive at

$$\begin{aligned}
\frac{1}{2\pi}e^{-\frac{1}{2}\sigma(x,t)-\frac{1}{2}\sigma(x',t')}\Bigg[&\frac{e^{-i[\phi_{\rm WKB+}(x,t)-\phi_{\rm WKB+}(x',t')]}}{2i\sin\frac{(\xi-\xi')+(\tau-\tau')}{2}} - \frac{e^{-i[\phi_{\rm WKB-}(x,t)-\phi_{\rm WKB-}(x',t')]}}{2i\sin\frac{(\xi-\xi')-(\tau+\tau')}{2}} \\
&+\frac{e^{-i[\phi_{\rm WKB+}(x,t)-\phi_{\rm WKB-}(x',t')]}}{2\sin\frac{(\xi+\xi')+(\tau-\tau')}{2}} + \frac{e^{-i[\phi_{\rm WKB-}(x,t)-\phi_{\rm WKB+}(x',t')]}}{2\sin\frac{(\xi+\xi')-(\tau+\tau')}{2}}\Bigg]
\end{aligned} \tag{9.5.9}$$

The conformal factor $e^{\sigma(x,t)}$ is defined in Eq. (9.3.9).

Contribution from deep inside the Fermi sea

Like in the homogeneous case, there is a contribution coming from excitations deep inside the Fermi sea; we have learned that it consists of an amplitude which has a simple geometric interpretation, and of the semiclassical phase (9.5.7). We focus first on the amplitude.

The amplitude. It is proportional to the square root of the red area $A(t)$ shown in Figure 9.6. By virtue of the scaling approach, as time passes the evolution of the system can be viewed as a simple rescaling plus a rotation of phase space, encoded in the linear transformation sending a point $(x(0),k(0))$ to a point

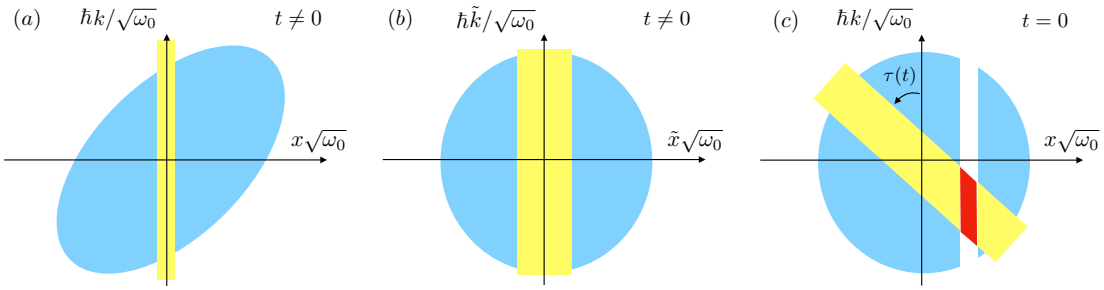

FIGURE 9.6: Wigner probability distribution in the harmonic trap after a generic harmonic protocol. Panel (a): The probability of having a particle at position $x = 0$ at $t \neq 0$ is proportional to the area of the yellow strip. Panel (b): Using the scaling approach, such strip gets a rescaled in the coordinates $\tilde{x} = x/b(t)$ and $\tilde{k} = (kb(t) + x\dot{b}(t))$. Note that in these variables the Wigner function is just a circle. Panel (c): In the original variables, the tilded coordinates just rotates, giving the rotated yellow strip. If at initial time we remove a particle at a given position $x \neq 0$, the probability of creating a new one at $x = 0$ at time t is proportional to the red area.

$(x(t), k(t))$ (see Sec. 9.3),

$$\begin{pmatrix} x(0)\sqrt{\omega_0} \\ \hbar k(0)/\sqrt{\omega_0} \end{pmatrix} \mapsto \begin{pmatrix} x(t)\sqrt{\omega_0} \\ \hbar k(t)/\sqrt{\omega_0} \end{pmatrix} = M(t) \begin{pmatrix} x(0)\sqrt{\omega_0} \\ \hbar k(0)/\sqrt{\omega_0} \end{pmatrix}$$

with

$$M(t) = \begin{pmatrix} b(t) & 0 \\ \dot{b}(t) & \frac{1}{b(t)} \end{pmatrix} \begin{pmatrix} \cos\tau(t) & \sin\tau(t) \\ -\sin\tau(t) & \cos\tau(t) \end{pmatrix}.$$

Then finding the area in red in Fig. 9.6 is an elementary geometric problem: for a white strip of initial width δx the result is $\frac{\det M(t)}{[M(t)]_{12}}\omega_0 \delta x^2$. Notice that when we go from t' to t we need to do that for $M(t)M(t')^{-1}$ instead of $M(t)$, so the area we are interested in is proportional to

$$A(t,t') = \frac{\omega_0 \det[M(t)M(t')^{-1}]}{[M(t)M(t')^{-1}]_{12}} = \frac{\omega_0}{b(t)b(t')\sin[\tau(t) - \tau(t')]}. \tag{9.5.10}$$

The phase. Like in the homogeneous case, the phase of $\langle d^\dagger(x,t)d(x',t')\rangle$ is given by the minimum of the Lagrangian of a single classical particle, see Eq. (9.5.7). The classical trajectory of the particle is (see Section 9.3) of the form $x(s) = \ell_0 b(s)\cos(\xi_0 + \tau(s))$ with ℓ_0 and ξ_0 chosen such that $x(t) = x$ and $x(t') = x'$. This gives

$$x(s) = b(s)\frac{\frac{x}{b(t)}\sin(\tau(s) - \tau(t')) - \frac{x'}{b(t')}\sin(\tau(s) - \tau(t))}{\sin(\tau(t) - \tau(t'))}.$$

After some algebra and putting phase and amplitude together, we arrive at the conclusion that the contribution from excitations deep inside the Fermi sea takes the form

$$\begin{aligned} \left\langle d^\dagger(x,t)d(x',t')\right\rangle = e^{\frac{i\pi}{4}} &\left(\frac{1}{2\pi\hbar}\frac{\omega_0}{b(t)b(t')\sin[\tau(t) - \tau(t')]}\right)^{\frac{1}{2}} \\ &\times \exp\left[-\frac{i}{2\hbar}\left(\frac{\omega_0}{\tan(\tau(t) - \tau(t'))}\left(\frac{x^2}{b(t)^2} + \frac{x'^2}{b(t')^2}\right) + \frac{x^2\dot{b}(t)}{b(t)}\right.\right. \\ &\left.\left. - \frac{x'^2\dot{b}(t')}{b(t')} - \frac{2\omega_0}{\sin(\tau(t) - \tau(t'))}\frac{x}{b(t)}\frac{x'}{b(t')}\right)\right]. \end{aligned} \tag{9.5.11}$$

Final result for $c(x,t,x',t')$ and comparison with numerics

We thus arrive at the following result for the asymptotics of the propagator, which is the sum of Eqs. (9.5.11) and (9.5.9). The asymptotics should be valid both inside and outside the lightcone (but not exactly along the lightcone, like in the infinite homogeneous case)

$$\begin{aligned} c(x,t,x',t') \;=\; & I(\xi,\xi',\tau-\tau')\, e^{\frac{i\pi}{4}} \left(\frac{A(t,t')}{2\pi}\right)^{\frac{1}{2}} \exp\left[-i\int_t^{t'}\left(\frac{1}{2}(\partial_s x(s))^2 - V(x(s))\right) ds\right] \\ & + \frac{1}{2\pi} e^{-\frac{1}{2}\sigma(x,t)-\frac{1}{2}\sigma(x',t')} \left[\frac{e^{-i[\phi_{\mathrm{WKB}+}(x,t)-\phi_{\mathrm{WKB}+}(x',t')]}}{2i\sin\frac{(\xi-\xi')+(\tau-\tau')}{2}} - \frac{e^{-i[\phi_{\mathrm{WKB}-}(x,t)-\phi_{\mathrm{WKB}-}(x',t')]}}{2i\sin\frac{(\xi-\xi')-(\tau+\tau')}{2}}\right. \\ & \left. + \frac{e^{-i[\phi_{\mathrm{WKB}+}(x,t)-\phi_{\mathrm{WKB}-}(x',t')]}}{2\sin\frac{(\xi+\xi')+(\tau-\tau')}{2}} + \frac{e^{-i[\phi_{\mathrm{WKB}-}(x,t)-\phi_{\mathrm{WKB}+}(x',t')]}}{2\sin\frac{(\xi+\xi')-(\tau+\tau')}{2}}\right]. \end{aligned} \tag{9.5.12}$$

Here $I(\xi,\xi',\tau)$ is the function which is one inside the lighcone and zero outside the lightcone, which is simple in the (ξ,τ) coordinates (see Figure 9.7): for $\tau \in [0,2\pi]$ it can be written in terms of the Heaviside function $\Theta(.)$ as

$$I(\xi,\xi',\tau) = \Theta(\tau - |\xi-\xi'|)\Theta(|\pi-\tau| - |\pi+\xi+\xi'|)\Theta(2\pi-\tau-|\xi-\xi'|) \tag{9.5.13}$$

and then it is extended to other values of τ by periodicity: $I(\xi,\xi',\tau\pm 2\pi) = I(\xi,\xi',\tau)$.

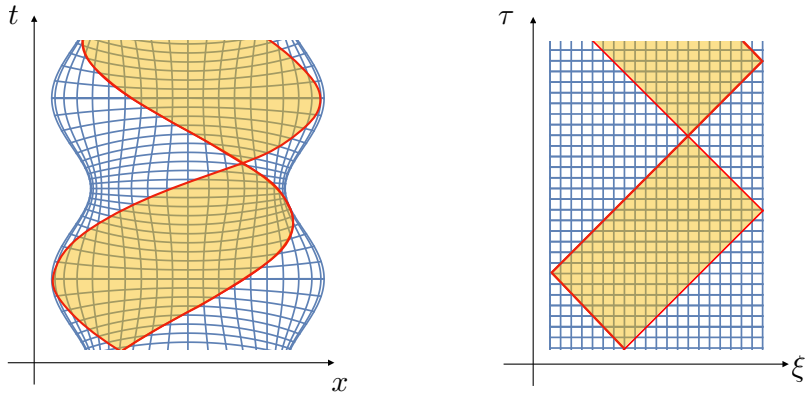

FIGURE 9.7: Left: Inside (yellow) and outside (white) lightcone regimes in the original (x,t) coordinates. The continuous red line represents the lightcone. Right: Same in the (ξ,τ) coordinates. The grid shows the boundary of the system.

Next, we compare those formulas to numerical evaluation of the propagator at finite N (see the Appendix), and to do this we specialize to the case of a sudden quench of the frequency: $\omega(t) = \omega_0$ if $t < 0$ and ω_1 if $t > 0$. The comparison between the asymptotic formula (9.5.12) and the exact propagator at finite N, Eq. (9.A.3), is shown in Figure 9.8. The agreement is perfect both inside and outside the lightcone. However, one clearly sees a small region along the lightcone where our approach is not expected to give the correct result. Note also that at the edges of the system, some corrections are expected to occur [419, 494].

9.6 Concluding remarks

In this Chapter, we have made one step forward in the calculation of correlation function of inhomogeneous one-dimensional critical systems by considering a truly dynamical situation: a breathing gas of hard core bosons at zero temperature. In particular, we have found new formulas for the $1/N \sim \hbar \to 0$ asymptotics of $2n$-point functions of boson creation/annihilation operators, and also for fermionic observables for which we provided numerical checks.

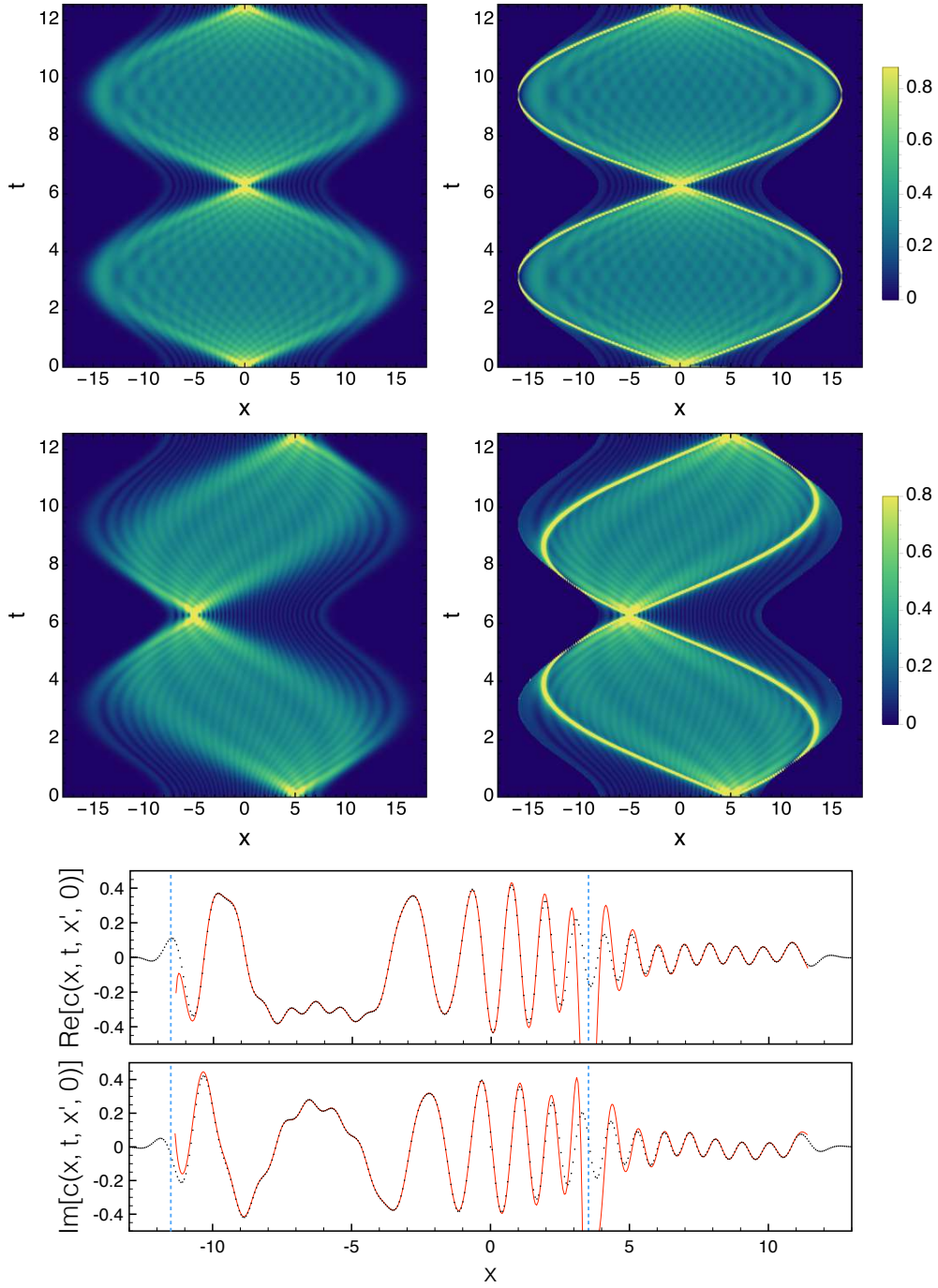

FIGURE 9.8: Fermionic propagator, $c(x,t,x',0)$, Eq.(9.5.1), as a function of x and t, for fixed values of x'. In the density plots the absolute value is shown. Upper row: $x'=0$. Lower row: $x'=5$. Left: Exact function from scaling approach, Eq. (9.A.3). Right: Our prediction, Eq. (9.5.12). The one dimensional plots below show the real and the imaginary part of $c(x,t,x',0)$ as a function of x, with $x'=5$ and fixed $t=5$. The black dots are the exact function from scaling approach, Eq. (9.A.3). The red line is our prediction, Eq. (9.5.12). The dashed vertical lines are the positions of the lightcone. The parameters are chosen as follows: $\omega_0=1, \omega_1=0.5, N=32$.

These results could be extended in several directions. First, it would be interesting to study a case with multiple Fermi points, as shown in Fig. 9.1(b). This could give rise to interesting interference effects (as discussed for instance in Ref. [481]) or interesting behavior of the entanglement entropy —because the entanglement entropy should be sensitive to the number of Fermi points—. This is work in progress [495]. Another very interesting direction would be to study the problem of the breathing Lieb-Liniger gas at finite repulsion strength g, extending the techniques of Ref. [431] for the static case to a dynamical situation. It is likely that such a study would be mostly numerical, since already the classical hydrodynamic equations (9.2.8) would not be analytically solvable in that case. Nevertheless, it should be possible to express large scale correlation functions in terms of the Green's function of a certain generalized Laplacian (as in Ref. [431]), which would then lead to an interesting efficient numerical method for the calculation of correlation functions in that case.

The most exciting direction would perhaps be to use the new formula (9.4.10) found in this paper to investigate correlations of the momentum distribution of particles in the gas. Correlations of the momentum distributions are in principle measurable, for instance by time-of-flight. This has been done in the weakly interacting regime of the gas [496,497], but, to our knowledge, not yet in the strongly interacting regime for which formula (9.4.10) would apply.

Finally, it would also be interesting to consider possible extension of our method to higher dimension, where even fewer results exist (see, for example, [498]).

9.A Fermion propagator from the scaling approach

In Sec. 9.5, the numerical checks were performed using the exact fermion propagator obtained from the scaling approach (see, e.g., [460]). Here, we simply summarize the main steps that lead to this exact result. Then, we will show that the equal-time asymptotics corresponds to the CFT contribution we computed with our approach. Below $\hbar = \omega_0 = m = 1$.

Exact propagator. Since we are dealing with a harmonic trap, the single particle wavefunctions at $t = 0$ are

$$\psi_n(x,0) = \sqrt{\frac{(1/\pi)^{1/2}}{2^n n!}} H_n(x) e^{-\frac{x^2}{2}}, \tag{9.A.1}$$

where H_n is the Hermite polynomial of order n. These are the eigenstates of the single-particle hamiltonian at $t = 0$ with energies $\varepsilon_n = n + \frac{1}{2}$. The scaling approach gives the time-evolved wavefunctions in terms of the scaling factor $b(t)$ which solves the Ermakov equation (9.3.4) and the function $\tau(t)$ defined in Eq. (9.3.5),

$$\psi_n(x,t) = \frac{1}{\sqrt{b(t)}} \psi_n\left(\frac{x}{b(t)}, 0\right) e^{i\frac{x^2}{2}\frac{\dot{b}(t)}{b(t)} - i\varepsilon_n \tau(t)}. \tag{9.A.2}$$

Then the propagator at different times is the many-body ground state with N particles is

$$\left\langle \Psi_{\mathrm{F}}^{\dagger}(x,t)\Psi_{\mathrm{F}}(x',t')\right\rangle = \sum_{n=0}^{N-1} \psi_n^*(x,t)\,\psi_n(x',t')\,. \tag{9.A.3}$$

This remarkably simple result follows from an elementary calculation (see Ref. [439]).

Equal-time asymptotics. At equal time $t' = t$, it is possible to evaluate the asymptotics of the propagator directly. In that case, the sum in (9.A.3) can be computed using the Christoffel-Darboux formula

$$\sum_{n=0}^{N-1} \frac{H_n(x)H_n(x')}{2^n n!} = \frac{H_{N-1}(x')H_N(x) - H_{N-1}(x)H_N(x')}{2^N\,(N-1)!\,(x-x')}.$$

If we let $N \to \infty$, we can inject the following asymptotics for the Hermite polynomials

$$e^{-\frac{x^2}{2}}\mathcal{H}_N(x) \sim \frac{2^{\frac{2N+1}{4}}\sqrt{N!}}{(\pi N)^{\frac{1}{4}}}\frac{1}{\sqrt{\sin(\alpha)}}\sin\left(\frac{2N+1}{4}\left(\sin(2\alpha)-2\alpha\right)+\frac{3\pi}{4}\right),$$

where $x = \sqrt{2N+1}\cos(\alpha)$, with $\epsilon \leq \alpha \leq \pi - \epsilon$ and $\epsilon \to 0$ when $N \to \infty$. Prior to the complete formulation of our approach, we observed that the result could be put in the nice form

$$\begin{aligned}\left\langle \Psi_{\rm F}^{\dagger}(x,t)\Psi_{\rm F}(x',t)\right\rangle &= \frac{1}{2\pi}\frac{e^{-i[\phi(x,t)-\phi(x',t)]}}{b(t)}\left[\left(2N-\frac{x^2}{b(t)^2}\right)\left(2N-\frac{x'^2}{b(t)^2}\right)\right]^{-\frac{1}{4}} \\ &\times\left[\frac{\sin\left(\phi^\star(x,t)-\phi^\star(x',t)\right)}{\sin\left(\frac{\xi(x,t)-\xi(x',t)}{2}\right)}+\frac{\cos\left(\phi^\star(x,t)+\phi^\star(x',t)\right)}{\sin\left(\frac{\xi(x,t)+\xi(x',t)}{2}\right)}\right] \end{aligned} \tag{9.A.4}$$

where

$$\phi^\star(x,t) \equiv \frac{1}{2}\left[\phi_{\rm WKB-}(x,t)-\phi_{\rm WKB+}(x,t)\right],$$

and $\xi(x,t)$, $\phi_{\rm WKB\mp}(x,t)$ and $\phi(x,t)$ are defined in Eqs. (9.3.8,9.3.11,9.3.12). What is remarkable here is that the resulting formula (9.A.4) corresponds exactly to the sum of the four terms given by the CFT contribution of Section 9.5.2.

Part III

ENTANGLEMENT & DISORDER

Chapter 10

Logarithmic negativity in the random singlet phase

The last part of this thesis is devoted to the study of the interplay between disorder and entanglement. In this Chapter, based on Ref. [95], we investigate the LN in strongly-disordered spin chains in the random-singlet phase. We show that for two arbitrary intervals the disorder-averaged LN and the mutual information are proportional to the number of singlets shared between the two intervals. Using the strong-disorder renormalization group (SDRG), the negativity of two adjacent intervals can be proved to grow logarithmically with the intervals' length. In particular, the scaling behavior is the same as in conformal field theory, but with a different prefactor. For two disjoint intervals, the negativity is given by a universal simple function of the cross-ratio, reflecting scale invariance. As a function of the distance of the two intervals, the negativity decays algebraically in contrast with the exponential behavior in clean models.

10.1 Introduction

The role of disorder in the entanglement scaling is an interesting question, which is widely studied in recent times and is nowadays a fruitful research area [68, 499]. For instance, in Ref. [86] it has been shown that, for disordered spin chains exhibiting the RSP, the scaling of the disorder-averaged EE is logarithmic with the subsystem size like in a CFT. This has been tested numerically in the random XX chain [320] (which is exactly solvable for each realization of the disorder), and in the random XXX chain [128] using DMRG. Furthermore, the moments of the RDM $\mathrm{Tr}\rho_A^\alpha$ have been also studied [321], as well as the spectrum [500], and the entanglement in low-lying excited states [501]. Other disordered spin models [502–514] have been also considered, obtaining similar results for the scaling of the EE. The EE in aperiodic spin chains has been investigated in Refs. [515, 516]. The non-equilibrium features of the entanglement in these random spin chains are also under intensive investigation [22, 23, 128, 517–521].

Here we investigate the disorder averaged LN in RSPs in the framework of the SDRG [85]. We focus on the spin-$1/2$ Heisenberg (XXX) chain with random antiferromagnetic couplings, and on the random XX chain. We consider both adjacent and disjoint intervals, A_1 and A_2, within a tripartition of a system as $B_2 \cup A_1 \cup B_1 \cup A_2 \cup B_2$ [as illustrated in Fig. 1.3 (a)]. We demonstrate that in a RSP the LN of two intervals is always proportional to the number of singlets shared between them. Surprisingly, due to the simple structure of the RSP, this is also the case for the mutual information, which is given as $\mathcal{I}_{A_1:A_2} = 2\mathcal{E}_{A_1:A_2}$. More quantitatively, the scaling for two adjacent and disjoint intervals was anticipated in Section 1.4.4, Eq. (1.4.49), and is further discussed in the following. In both cases, it is found to be similar to the known CFT scaling [94, 145], with nonetheless a more intricate dependence on the cross-ratio $x = \frac{\ell_1 \ell_2}{(\ell_1+r)(\ell_2+r)}$ (here ℓ_1, ℓ_2 and r are the lengths of the two subsystems and their distance respectively).

The rest of this Chapter is organized as follows. In Sec. 10.2 we provide the analytic expressions for the LN and the moments of the PT RDM in RSPs. The scaling of the LN is discussed in Sec. 10.3 for both adjacent and disjoint intervals. These results are verified in Sec. 10.4 using a numerical implementation of the SDRG method. In Sec. 10.5, we present DMRG results for the LN of two adjacent intervals in the random XX chain. Finally, we conclude in Sec. 10.6.

10.2 Logarithmic negativity in a single realization of the RSP

The model and the setting are the same as in Section 1.4.4. We just recall the hamiltonian of the random antiferromagnetic spin-$\frac{1}{2}$ XXZ chain, that for open boundary conditions (OBC) is given by

$$\mathcal{H} = \sum_{i=1}^{L-1} J_i (S_i^x S_{i+1}^x + S_i^y S_{i+1}^y + \Delta S_i^z S_{i+1}^z), \tag{10.2.1}$$

where $S_i^{x,y,z}$ are the spin components acting on site i, L is the length of the chain, Δ the anisotropy parameter, and $\{J_i\}_{i=1}^{L-1}$ are uncorrelated *positive* random variables, drawn from a distribution $P(J)$. For periodic boundary conditions (PBC) one has an extra term in (10.2.1) connecting site L with site 1. We will consider specifically the cases $\Delta = 1$ and 0, corresponding to the XXX and the XX random chains, respectively. For generic $\{J_i\}_{i=1}^{L-1}$, the latter can be treated analytically for each realization of the disorder, exploiting the mapping to free fermions [see Ref. [95]]. Here, we restrict ourselves to the family of distributions

$$P_\delta(J) \equiv \delta^{-1} J^{-1+1/\delta}, \tag{10.2.2}$$

with $J \in [0,1]$, and $0 \leq \delta < \infty$ a parameter tuning the disorder strength. For $\delta \to 0$ one recovers the clean, i.e., without disorder, XXZ chain, whereas $\delta \to \infty$ corresponds to the infinite-randomness fixed point (IRFP). The latter describes the low-energy physics of (10.2.1), irrespective of the chosen distribution $P(J)$. For $\delta = 1$, $P_\delta(J)$ becomes the flat distribution (box distribution) in the interval $[0,1]$.

For a generic realization of the disorder, assuming that the chain is in a RSP, the LN between two subsystems of the chain can be calculated analytically. Let us consider a partition of the chain as in Fig. 1.3 with $A \equiv A_1 \cup A_2$ the two intervals of interest and $B \equiv B_1 \cup B_2$ their complement. Given any two blocks X, Y in the chain, we denote as $n_{X:Y}$ the number of singlets shared between them.

Before considering the entire RSP, it is instructive to write the density matrix and its partial transpose for an isolated singlet. The density matrix ρ_{2S} of two spins forming a singlet is

$$\rho_{2S} = \frac{1}{2} \begin{pmatrix} 0 & 0 & 0 & 0 \\ 0 & 1 & -1 & 0 \\ 0 & -1 & 1 & 0 \\ 0 & 0 & 0 & 0 \end{pmatrix}, \tag{10.2.3}$$

in the basis $|\uparrow\uparrow\rangle$, $|\uparrow\downarrow\rangle$, $|\downarrow\uparrow\rangle$, and $|\downarrow\downarrow\rangle$. The RDM ρ_S for one of the spins is

$$\rho_S = \frac{1}{2} \begin{pmatrix} 1 & 0 \\ 0 & 1 \end{pmatrix}. \tag{10.2.4}$$

In order to calculate the LN, we need the partial transpose $\rho_{2S}^{T_2}$ that is

$$\rho_{2S}^{T_2} = \frac{1}{2} \begin{pmatrix} 0 & 0 & 0 & -1 \\ 0 & 1 & 0 & 0 \\ 0 & 0 & 1 & 0 \\ -1 & 0 & 0 & 0 \end{pmatrix}, \tag{10.2.5}$$

with eigenvalues $\{-1/2, 1/2, 1/2, 1/2\}$.

The density matrix ρ_{RSP} for a chain in a random singlet phase is the tensor product of the density matrices of its constituent singlets. Thus, for the partition in Fig. 1.3, one can write

$$\rho_{RSP} = \bigotimes_{i=1}^{n_{A:A}} \rho_{2S} \bigotimes_{i=1}^{n_{B:B}} \rho_{2S} \bigotimes_{i=1}^{n_{A:B}} \rho_{2S}. \tag{10.2.6}$$

The RDM ρ_A is obtained from (10.2.6) as

$$\rho_A = \bigotimes_{i=1}^{n_{A:A}} \rho_{2S} \bigotimes_{i=1}^{n_{A:B}} \rho_S, \tag{10.2.7}$$

and its partial transpose

$$\rho_A^{T_2} = \bigotimes_{i=1}^{n_{A:A}} \rho_{2S}^{T_2} \bigotimes_{i=1}^{n_{A:B}} \rho_S^{T_2}. \tag{10.2.8}$$

To compute $\mathcal{E}_{A_1:A_2}$ one can exploit the additivity of the LN on tensor products, leading to

$$\mathcal{E}_{A_1:A_2} = n_{A_1:A_2} \ln \mathrm{Tr}\big|\rho_{2S}^{T_2}(A_1 \cup A_2)\big| + \sum_{i=1,2} \Big[n_{A_i:A_i} \ln \mathrm{Tr}\big|\rho_{2S}^{T_2}(A_i)\big| + n_{A_i:B} \ln \mathrm{Tr}\big|\rho_S^{T_2}(A_i)\big| \Big]. \tag{10.2.9}$$

Interestingly, the terms in the square brackets vanish because for any A_i, $\rho_{2S}^{T_2}(A_i) = \rho_{2S}(A_i)$ and $\rho_S^{T_2}(A_i) = \rho_S(A_i)$. As a consequence, $\mathcal{E}_{A_1:A_2}$ *depends only on the number of singlets* $n_{A_1:A_2}$ *shared between* A_1 *and* A_2. Physically, this could have been expected because the LN is a measure of the *mutual* entanglement between A_1 and A_2. In conclusion, we have

$$\mathcal{E}_{A_1:A_2} = n_{A_1:A_2} \ln \mathrm{Tr}\big|\rho_{2S}^{T_2}(A_1 \cup A_2)\big|, \tag{10.2.10}$$

and using the explicit form of $\rho_{2S}^{T_2}$ (10.2.5)

$$\mathcal{E}_{A_1:A_2} = n_{A_1:A_2} \ln 2. \tag{10.2.11}$$

For a bipartition, i.e., for $A_2 \equiv \bar{A}_1$, with $\bar{A}_1$ the complement of A_1, Eq. (10.2.11) is equal to the EE of A_1 (see Ref. [86]). This is just a consequence of the fact that in the RSP the Rényi entropies S_α with varying α are all equal [321], while in the generic case the LN for a bipartition is always equal to $S_{1/2}$ [55, 145]. This is different from the *clean* bipartite system (which is conformal invariant) in which the Rényi entropies depend non trivially on the index α in a well-known fashion [17, 18].

Finally, it is interesting to compare (10.2.11) with the mutual information between two intervals $\mathcal{I}_{A_1:A_2} = S_{A_1} + S_{A_2} - S_{A_1 \cup A_2}$ which can be readily obtained using $S_X = n_{X:\bar{X}} \ln 2$. A straightforward calculation yields

$$\mathcal{I}_{A_1:A_2} = (n_{A_1:\bar{A}_1} + n_{A_2:\bar{A}_2} - n_{A_1 \cup A_2:B}) \ln 2 = 2 n_{A_1:A_2} \ln 2. \tag{10.2.12}$$

Interestingly, (10.2.12) coincides, apart from a factor 2, with $\mathcal{E}_{A_1:A_2}$ in (10.2.11).

10.2.1 The moments of the partially transposed reduced density matrix

It is instructive to consider the moments $M_\alpha^{T_2}$ of the PT density matrix

$$M_\alpha^{T_2} \equiv \mathrm{Tr}\big(\rho_A^{T_2}\big)^\alpha, \tag{10.2.13}$$

The LN can be obtained from (10.2.13) via the analytic continuation $\alpha \to 1$ restricted to the even α, as it is routinely done in CFT calculations [94, 145]. Although $M_\alpha^{T_2}$ are not entanglement measures, they encode universal information about critical systems and, as discussed in Chapters 2 and 3, are the crucial objects entering the calculations of the negativity spectrum [57].

The computation of the moments starts by rewriting (10.2.7) as

$$\rho_A = \Big\{ \prod_k \bigotimes_{i=1}^{n_{A_k:A_k}} \rho_{2S} \Big\} \bigotimes_{i=1}^{n_{A_1:A_2}} \rho_{2S} \Big\{ \prod_k \bigotimes_{i=1}^{n_{A_k:B}} \rho_S \Big\}. \tag{10.2.14}$$

Using that the partial transposition acts trivially on the terms in the curly brackets, one obtains

$$\rho_A^{T_2} = \Big\{ \prod_k \bigotimes_{i=1}^{n_{A_k:A_k}} \rho_{2S} \Big\} \bigotimes_{i=1}^{n_{A_1:A_2}} \rho_{2S}^{T_2} \Big\{ \prod_k \bigotimes_{i=1}^{n_{A_k:B}} \rho_S \Big\}. \tag{10.2.15}$$

The only two non-zero eigenvalues of $\rho_A^{T_2}$ are

$$\lambda_\pm = \pm 2^{-n_{A:B}-n_{A_1:A_2}}. \tag{10.2.16}$$

The corresponding degeneracies $d_\pm$ are

$$d_- = (2^{n_{A_1:A_2}} - 1) 2^{n_{A_1:A_2}-1}, \tag{10.2.17}$$

$$d_+ = 2^{n_{A:B}+2n_{A_1:A_2}} - d_-. \tag{10.2.18}$$

The moments $M_\alpha^{T_2}$ can be readily written down as

$$M_\alpha^{T_2} = 2^{(n_{A:B}+n_{A_1:A_2})(1-\alpha)} \begin{cases} 2^{n_{A_1:A_2}} & \alpha \text{ even} \\ 1 & \alpha \text{ odd.} \end{cases} \tag{10.2.19}$$

In Eq. (10.2.19) it is evident that for generic α, $M_\alpha^{T_2}$ cannot be measures of the entanglement between A_1 and A_2, since they depend on the number of singlets shared with B. By analytically continuing Eq. (10.2.19) from the even sequence we recover the negativity (10.2.11), i.e., denoting with n_e the even integers, we have

$$\mathcal{E} = \lim_{n_e \to 1} \ln M_{n_e}^{T_2}, \tag{10.2.20}$$

while the replica limit of the odd sequence gives the normalization $\mathrm{Tr}\rho_A^{T_2} = 1$.

10.3 Scaling of the disorder-averaged negativity in the RSP

In this Section, we derive the scaling properties of the LN between two intervals A_1 and A_2 in the random-singlet phase. From the previous Section, it is obvious that the only needed ingredient is the scaling of the average number of singlets $\langle n_{A_1:A_2} \rangle$ shared between A_1 and A_2 [cf. (10.2.11)]. Here, $\langle \cdots \rangle$ denotes the disorder average. Remarkably, $\langle n_{A_1:A_2} \rangle$ can be obtained from the result for a *single* interval [86]. Given an interval X of length ℓ_X embedded in the infinite line, the average number of shared singlets $\langle n_{X:\bar{X}} \rangle$ scales for large ℓ_X as [86]

$$\langle n_{X:\bar{X}} \rangle = \frac{1}{3} \ln \ell_X + k, \tag{10.3.1}$$

where k is a non-universal constant.

In order to derive $\langle n_{A_1:A_2} \rangle$, let us consider a generic multipartition of the chain into $2k$ blocks as $\cup_{Y \in \Omega_0} Y$, with $\Omega_0 = \{A_1, B_1, \cdots A_k, B_k\}$ [the case with $k = 2$ is in Fig. 1.3 (a)]. It is convenient to define the set Ω of all possible compact subintervals of the chain. For instance, for $\Omega_0 = \{A_1, B_1, A_2, B_2\}$ one has $\Omega = \{A_1, B_1, A_2, B_2, A_1 \cup B_1, B_1 \cup A_2\}$. For each $X \in \Omega$, one can decompose the number of singlets $n_{X:\bar{X}}$ as the sum of all the singlets emerging from an arbitrary block $Y \in X$ and ending in an arbitrary block $Z \in \bar{X}$, i.e., in formula

$$n_{X:\bar{X}} = \sum_{Y,Z \in \Omega_0} n_{(X \cap Y):(\bar{X} \cap Z)}. \tag{10.3.2}$$

After taking the disorder average, (10.3.2) gives

$$\frac{1}{3} \ln \ell_X + k = \sum_{Y,Z \in \Omega_0} \langle n_{(X \cap Y):(\bar{X} \cap Z)} \rangle, \tag{10.3.3}$$

where we used that (10.3.1) is valid for any $X \in \Omega$. One can obtain $\langle n_{X:Y} \rangle$ for any pair $X, Y \in \Omega_0$ by solving the linear system of equations in (10.3.3) generated by considering all $X \in \Omega$, as we are going to show in the following for two adjacent and disjoint intervals.

10.3.1 Two adjacent intervals

For two adjacent intervals we have $\Omega_0 = \Omega = \{A_1, A_2, B_2\}$, and so the system of equations (10.3.3) becomes

$$\begin{cases} \langle n_{A_1:A_2} \rangle + \langle n_{A_1:B_2} \rangle = \frac{1}{3} \ln(\ell_1) + k, \\ \langle n_{A_2:A_1} \rangle + \langle n_{A_2:B_2} \rangle = \frac{1}{3} \ln(\ell_2) + k, \\ \langle n_{B_2:A_1} \rangle + \langle n_{B_2:A_2} \rangle = \frac{1}{3} \ln(\ell_1 + \ell_2) + k. \end{cases} \tag{10.3.4}$$

This can be solved for $\langle n_{A_1:A_2} \rangle$ and, consequently [from (10.2.11)], one recovers the scaling of the LN in (1.4.49)

$$\mathcal{E}_{A_1:A_2} = \frac{\ln 2}{6} \ln \left(\frac{\ell_1 \ell_2}{\ell_1 + \ell_2} \right) + \tilde{k}, \tag{10.3.5}$$

with $\tilde{k} = \ln(k/2)$ a non universal constant.

10.3.2 Two disjoint intervals

Let us consider the case of two disjoint intervals [see Fig. 1.3 (a)] of lengths ℓ_1, ℓ_2, and at distance r, for which $\Omega = \{A_1, A_2, B_1, B_2, A_1 \cup B_1, B_1 \cup A_2\}$. From (10.3.3) one obtains a linear system of six equations to be solved for $\langle n_{A_1:A_2} \rangle$. In particular, from (10.3.6), the LN can be rewritten as

$$\mathcal{E}_{A_1:A_2} = \frac{1}{6} \ln \frac{(r + \ell_1)(r + \ell_2)}{r(\ell_1 + \ell_2 + r)} \ln 2. \tag{10.3.6}$$

which turns out to be a function of the cross-ratio x only [cf. Eq. (1.4.49)]. Interestingly, (10.3.6) does not depend on the non universal additive constant k indicating that the LN between two disjoint intervals is a *universal scale invariant quantity*, as in the clean case.

An intriguing consequence of (10.3.6) is that the entanglement between two disjoint intervals decays as $\propto r^{-2}$, i.e., with a power law of their mutual distance, in stark contrast with the CFT case where this decays is exponential [94]. The result for adjacent intervals is recovered from (10.3.6) by taking r of the order of the lattice spacing (fixed to 1 in all above formulas) and then considering $\ell_{1,2}$ much larger than that.

10.4 Numerical SDRG

In this Section, we present numerical evidence confirming the analytical results for the average number of singlets between two arbitrary intervals (adjacent and disjoint) and consequently for the LN and mutual information between them. In order to do so, we numerical implement the SDRG for finite-size spin chains which works according to the following steps: (a) for a given disorder realization, we apply the Dasgupta-Ma rule (1.4.41), i.e., we pair the spins interacting with the strongest bond to form a SU(2) singlet; (b) the two spins are then decimated, and the remaining couplings renormalized according to (1.4.40); (c) this SDRG step is iterated until all the spins are paired in singlets. At every RG step we monitor the distribution of the renormalized couplings, as well as the spin configurations. In this Section, we only consider a flat probability distribution of the coupling J between 0 and 1, presenting results only for the Heisenberg spin chain. However, we should mention that we performed the same analysis for the XX chain, which is expected to be in the same universality class of the XXX chain, finding perfect agreement with the analytic SDRG predictions.

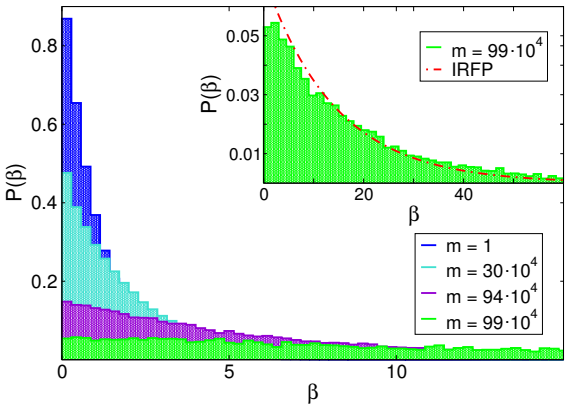

FIGURE 10.1: Numerical SDRG: flow of the couplings probability distribution $P(\beta^{(m)})$ as a function of the SDRG step m. Different histograms correspond to different m. Results are for the Heisenberg spin chain with $L = 10^6$ sites. The width of $P(\beta_i^{(m)})$ increases upon increasing m. Inset: $P(\beta^{(m)})$ for $m = 99 \times 10^4$, compared with the infinite-randomness fixed point (IRFP) result $P^*(\beta) = e^{-\beta/\Gamma}/\Gamma$, (dashed-dotted line) with $\Gamma^{(m)}$ given in (1.4.42).

SDRG flow of the renormalized couplings

As a preliminary check of the numerical SDRG, we study the flow of the couplings J_i in (10.2.1) as a function of the SDRG step m. The results are reported in Fig. 10.1, where we plot the probability distribution $P(\beta_i^{(m)})$, with $\beta_i^{(m)} \equiv \ln(J_M^{(m)}/J_i^{(m)})$ [cf. (1.4.42)], and $J_M^{(m)}$ the maximum coupling at step m. The data are for a finite chain with $L = 10^6$. The initial values of the couplings are drawn from the box distribution $[0,1]$.

Fig. 10.1 demonstrates the broadening of the couplings distribution upon increasing the SDRG step m, confirming that the SDRG procedure is asymptotically exact at large scale [188]. The convergence to the universal IRFP distribution $P^*(\beta)$ (1.4.44) is verified in the inset of Fig. 10.1.

Single-interval entanglement entropy

Another important check of the validity of the numerical SDRG is provided by the scaling of the single block EE. We consider the random XXX chain with both open and periodic boundary conditions. For OBC we expect different scalings depending on whether the block A is in the bulk of the chain or whether it touches the boundary. The EE, here denoted as S_A, is obtained by determining the number of singlets between A and its complement for each realization of the disorder and then by multiplying the average by $\ln 2$, Eq. (1.4.46). We report the variance of the distribution as an estimate of statistical error.

Numerical SDRG results for S_A are shown in Figs. 10.2 (a)–(d). In all panels, the data are for chains of length $L = 1000$ and 2000. The disorder average is over 73 000 disorder realizations. We start by considering in Fig. 10.2 (a) the block A in a periodic chain. For $\ell \lesssim L/2$, S_A increases logarithmically as function of the interval length ℓ (note the logarithmic scale on the x axis). Instead, for $\ell \gtrsim L/2$ finite-size effects are visible. The dashed-dotted line in the figure is a fit to the expected SDRG result [86]

$$S_A = \frac{\ln 2}{3} \ln \ell + K, \tag{10.4.1}$$

with K the only fitting parameter. For $\ell \lesssim L/2$ the data are in perfect agreement with (10.4.1).

As discussed in Ref. [321], finite-size effects can be taken into account by replacing in (10.4.5) the interval length ℓ with the *modified* chord length L_c as

$$\ell \to L_c \equiv \frac{L}{\pi} \Upsilon\Big(\frac{\pi \ell}{L}\Big). \tag{10.4.2}$$

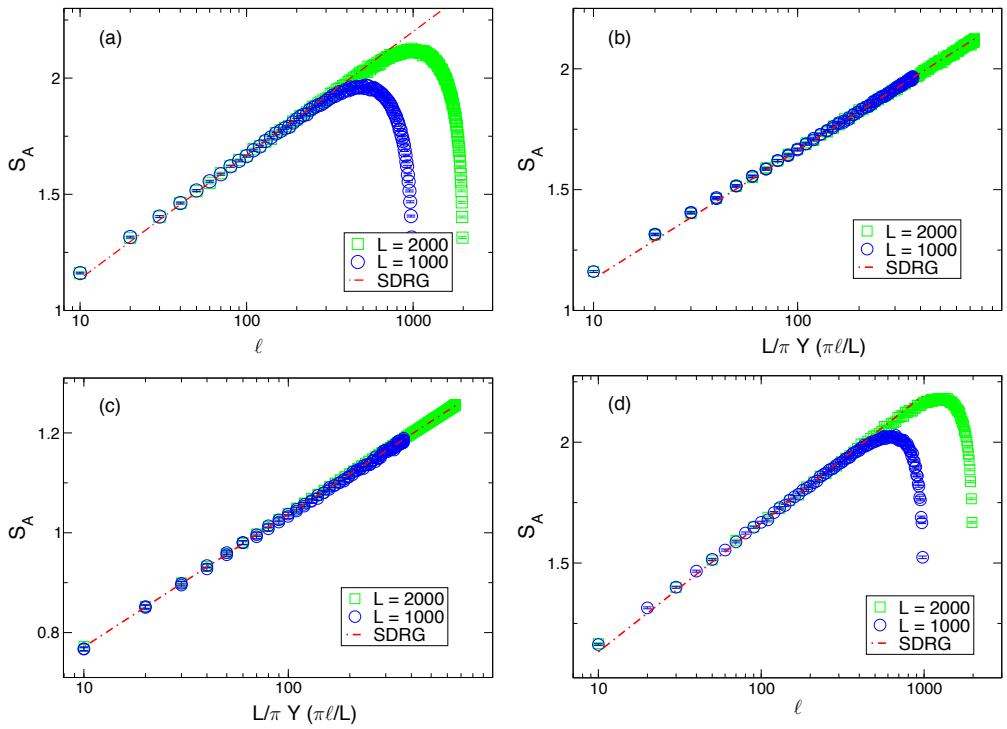

FIGURE 10.2: The single interval EE for the disordered Heisenberg spin chain. The data correspond to the average over 73 000 disorder realizations. Notice that (here and in the following figures) we report also the statistical errors, although the error bars are smaller than the symbol sizes. Different symbols correspond to different chain sizes L and dashed dotted lines are one-parameter fit to the analytic prediction from the SDRG. (a) A single interval in a periodic chain: S_A plotted versus the interval length ℓ. (b) Same data as in (a) plotted against the modified chord length (10.4.2). (c) A single interval starting from the boundary of a chain with OBC versus the modified chord length (10.4.2). (d) A single interval in the bulk of an open chain.

Here, $Y(x)$ is a symmetric function under $x \to \pi - x$, which ensures $S(\ell) = S(L-\ell)$. It has been found that for a single block in a periodic chain, $Y(x)$ is well approximated by [321]

$$Y(x) = \sin(x)\Big(1 + \frac{4}{3}k_1 \sin^2(x)\Big), \tag{10.4.3}$$

with $k_1 \sim 0.115$. Using (10.4.2) in (10.4.1) one obtains

$$S_A = \frac{\ln 2}{3}\ln(L_c) + K. \tag{10.4.4}$$

Figure 10.2 (b) reports the data for S_A versus L_c. The dashed-dotted line in Fig. 10.2 (b) is a fit to (10.4.4), and it is in perfect agreement with the SDRG data for all values of ℓ confirming the correctness of (10.4.4).

In Fig. 10.2 (c) we consider an open chain with the block A starting from the boundary. For a semi-infinite system, the EE is expected to be [86]

$$S_A = \frac{\ln 2}{6}\ln(\ell) + K', \tag{10.4.5}$$

where the prefactor of the logarithm takes into account that subsystem A shares only one edge with its complement. This formula indeed describes accurately the data for $\ell \lesssim L/2$. The finite-size and boundary effects can be taken into account again by replacing ℓ by a modified chord length (10.4.2). We find that the same function $Y(x)$ in Eq. (10.4.3) describes very accurately the data for OBC as shown in Fig. 10.2 (c). This is a non trivial result since there is no conformal invariance to guarantee the equality of the two finite-size scaling functions (i.e., open and periodic) as in the clean case.

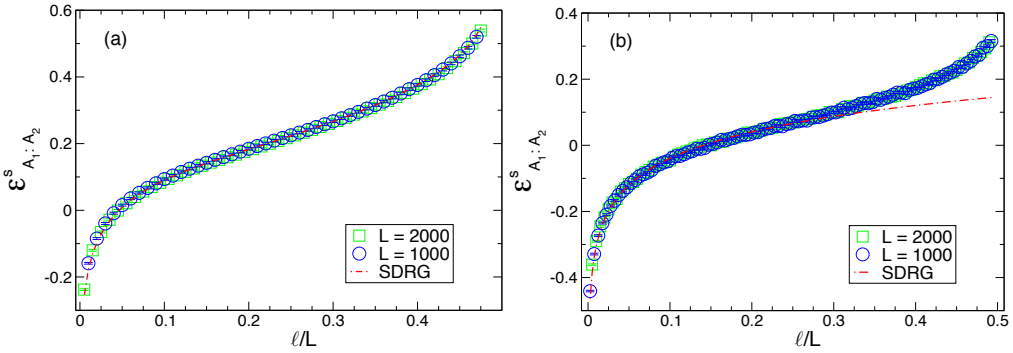

FIGURE 10.3: Shifted LN $\mathcal{E}^s_{A_1:A_2}$ (10.4.6) between two adjacent intervals of equal-length ℓ in the random Heisenberg chain. $\mathcal{E}^s_{A_1:A_2}$ is plotted against ℓ/L. The symbols correspond to the average over 73 000 disorder realizations. Different symbols correspond to different system sizes. (a): For a periodic chain the data are perfectly described by (10.4.7) with only one fitting parameter. (b): For an open chain, we can only use the prediction for the infinite chain which describes well the data as long as $\ell \ll L$.

Finally, in Fig. 10.2 (d) we consider a block of length ℓ in the center of an open chain. For $\ell \lesssim L/2$ we expect that the block A does not feel significantly the presence of the boundary and (10.4.1) should describe accurately the data, as evident from the figure. It is instead not obvious how to modify the prediction to take into account finite-size and boundary effects: we only mention that replacing ℓ with the modified chord length (10.4.3) does not work. This does not come unexpected since also in clean systems the results are more complicated [174].

Logarithmic negativity: Two adjacent intervals

Using the numerical SDRG method, we now study the scaling behavior of $\mathcal{E}_{A_1:A_2}$ between two adjacent intervals A_1 and A_2 in the random Heisenberg chain. Specifically, we provide robust numerical evidence for (10.3.5). The negativity is just obtained from the statistics of the singlets between A_1 and A_2 and multiplying the resulting average by $\ln 2$.

In Fig. 10.3, we report the SDRG data for two adjacent intervals of the same length ℓ. Figure 10.3 (a) shows the SDRG results for a periodic chain, while Fig. 10.3 (b) is for two intervals in the middle of an open chain. We plot the shifted negativity

$$\mathcal{E}^s_{A_1:A_2} = \mathcal{E}_{A_1:A_2} - \frac{\ln 2}{6} \ln L, \tag{10.4.6}$$

as a function of ℓ/L so that data for different chain lengths are expected to collapse on a single scaling curve. This clearly happens for both open and periodic chains. In both cases, $\mathcal{E}_{A_1:A_2}$ increases logarithmically for $\ell \lesssim L/4$, when finite-size effects kick in. Actually, for PBC one can take into account all the finite-size effects by replacing all lengths with modified chord lengths, obtaining

$$\mathcal{E}^s_{A_1:A_2} \simeq \frac{\ln 2}{6} \ln \frac{Y_c^2(\pi\ell/L)}{Y_c(2\pi\ell/L)} + k. \tag{10.4.7}$$

The SDRG are perfectly described by this prediction as clear from Fig. 10.3 (a) where the dashed line is a one-parameter fit to (10.4.7).

Conversely, for the OBC chain in Fig. 10.3 (b) there is not a simple modification of the result for infinite chain to take into account the boundary effects, as it was the case also for clean systems [256]. For this reason, in the figure we only report the one-parameter fit to the SDRG prediction for the infinite chain (10.3.5) valid for $\ell \ll L$.

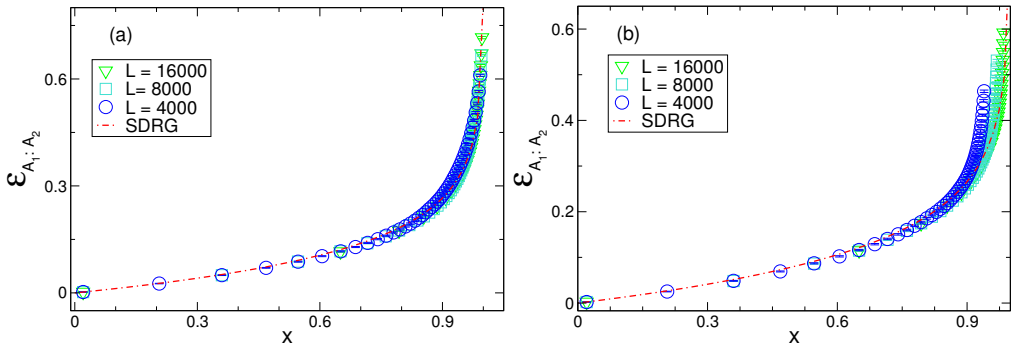

FIGURE 10.4: LN $\mathcal{E}_{A_1:A_2}$ between two disjoint intervals of equal length ℓ in the random Heisenberg spin chain plotted against the cross ratio x. The data are averaged over 73 000 disorder realizations. Different symbols correspond to different system sizes. (a): For a periodic chain, the crossr atio x is given by (10.4.8) and the dashed line is the analytic SDRG prediction (10.4.9). (b): For an open chain, we consider the infinite-volume definition of the cross ratio (8.3.3) and the dashed-dotted line is the SDRG prediction (10.4.9) to which the data tend for large chains.

Logarithmic negativity: Two disjoint intervals

We finally move to the most interesting case of the LN between two disjoint intervals of equal length ℓ at distance r. As usual in this Section, we compute the negativity from the statistics of the singlets between the two intervals. Our results are reported in Fig. 10.4 for both periodic and open chains.

In the case of a periodic chain, we plot $\mathcal{E}_{A_1:A_2}$ as a function of the cross ratio x (8.3.3) in which we have substituted all lengths by the corresponding modified chord lengths, i.e.,

$$x = \frac{Y_c^2(\pi\ell/L)}{Y_c^2[\pi(\ell+r)/L]}, \tag{10.4.8}$$

in order to take into account finite-size effects. The SDRG asymptotic prediction for the negativity is given by Eq. (10.3.6). which reads as

$$\mathcal{E}_{A_1:A_2} = -\frac{\ln 2}{6}\ln(1-x). \tag{10.4.9}$$

In Fig. 10.4 (a), the data correspond to a fixed choice of r, and ℓ is running up to $(L-r)/2$. It is clear from the figure that the prediction (10.4.9) describes incredibly well the numerical data, without any fitting parameter. Notice that x close to 0 corresponds to far away intervals and the decay of the negativity is algebraic, in contrast with the exponential behavior of clean systems [94, 145]. Oppositely, the limit $x \to 1$ corresponds to very close intervals and the logarithmic divergence is needed to reproduce the adjacent intervals results.

For the case of an open chain, we limit ourselves to consider two intervals centered around the middle of the chain, i.e., $A_1 = [-\ell - r/2, -r/2]$ and $A_2 = [r/2, \ell + r/2]$. We generate the data by fixing a value of r and letting ℓ run up to the boundary. In this case, we do not have a prediction which takes into account finite-size effects, so we expect Eq. (10.4.9) to describe correctly the data for $\ell, r \ll L$, i.e., when the effects of the boundary can be neglected. For this reason, in Fig. 10.4 (b) we report the negativity as function of the cross-ratio x given by the infinite volume formula $x = [\ell/(\ell+r)]^2$. It is evident from the figure that this prediction describes correctly the data for x far from 1, as it should. With increasing L, the effects of the boundaries becomes less and less relevant and the data get closer to the infinite-volume result, as expected.

10.5 Negativity in the random XX chain: DMRG results

Here, we discuss the LN of two adjacent intervals in the random XX chain. To this purpose we perform DMRG simulations, focusing on the disorder distribution $P_\delta(J) = \delta^{-1} J^{-1+1/\delta}$, with $\delta = 1/4, 1, 3/2$. Increasing values of δ correspond to increasing disorder strength. Our data for $\mathcal{E}_{A_1 \cup A_2}$ correspond typically

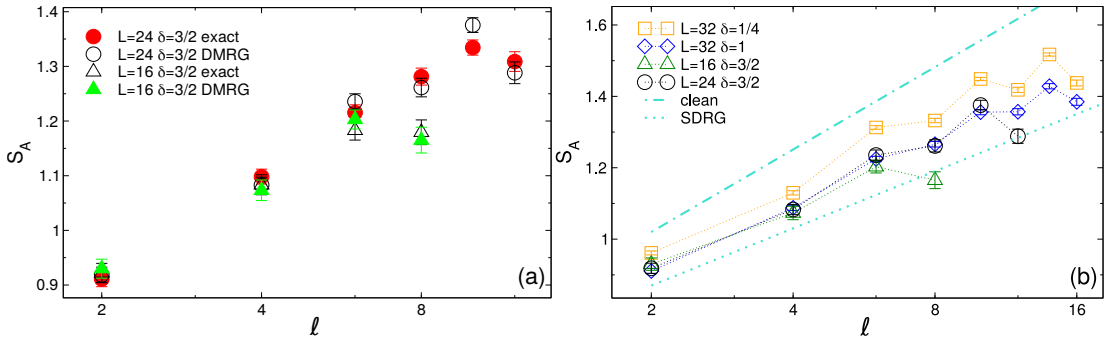

FIGURE 10.5: EE in the random XX spin chain. Panel (a): The von Neumann entropy S_A for a single interval at the center of an open chain plotted versus the interval length ℓ. The empty symbols denote DMRG results for chains with $L = 16, 24$ and disorder strength $\delta = 3/2$. The data are averaged over $\sim 10^3$ disorder realizations. The full symbols are exact results obtained using free-fermion techniques. Panel (b): Same geometry as in (a). The symbols are DMRG data for $L = 16, 24, 28, 32$ and $1/4 \leq \delta \leq 3/2$. Here $\delta = 0$ and $\delta \to \infty$ correspond to the clean case and the IRFP, respectively. The dash-dotted line is the CFT prediction for $\delta = 0$. The dotted line is the SDRG prediction in the TDL.

to an average over $\sim 10^3$ disorder realizations. Although exact results for the negativity are not yet available, many entanglement-related quantities, such as the EE, can be calculated for the random XX chain, via a mapping to free fermions [cf. Ref. [95] and Section 1.4.3]. Importantly, this provides a reliable way to check the accuracy of DMRG results.

Convergence of DMRG

For each disorder realization, a crucial aspect is the convergence of the DMRG method. This depends both on the chain sizes L and on the disorder strength δ. Specifically, we numerically observed that the convergence of DMRG becomes rapidly poor upon increasing L or δ. This is physically expected because the disorder gives rise to a "rough" energy landscape, which makes likely for DMRG to get trapped in a local minimum. This affects severely the convergence because typical DMRG update schemes are *local* [30]. This is also related to the exponential small gap [188] $\ln \Delta E \sim -L^{1/2}$ of the RSP.

To check the correctness of the DMRG results, for each disorder realization we compared the data for the half-chain von Neumann entropy with the exact one. We used as a DMRG convergence criterion the matching of the two results within a precision of 10^{-3}. We also defined the DMRG convergence rate R_c as the fraction of converged DMRG simulations. Only converged disorder configurations were included in the disorder averages. The fact that $R_c < 1$ results in a systematic error in the DMRG data. For instance, we observed that for $L = 63$ at $\delta = 1$ one has $R_c \approx 0.9$. Finally, to provide reliable error bars for our DMRG results, we always checked that the systematic error was negligible compared with the statistical error arising from the disorder average, providing the latter as our final error estimate.

Figure 10.5 (a) shows the comparison between the DMRG data for S_A (empty symbols in the figure) and the exact results (full symbols) obtained using free-fermion methods. Data are for $\delta = 3/2$, which is the most difficult value of δ to simulate, and $L = 16, 24$. The error bars are the statistical errors resulting from the disorder average. In all cases, the DMRG results are in agreement with the free-fermion result, within error bars. This suggests that, at least for the von Neumann entropy, the systematic error due to $R_c < 1$ is negligible compared to the statistical one.

DMRG results

Figure 10.5 (b) reports the von Neumann entropy S_A for the interval A at the center of the open chain. The symbols are DMRG data for different δ and L. The dashed-dotted line is the CFT result in the clean case

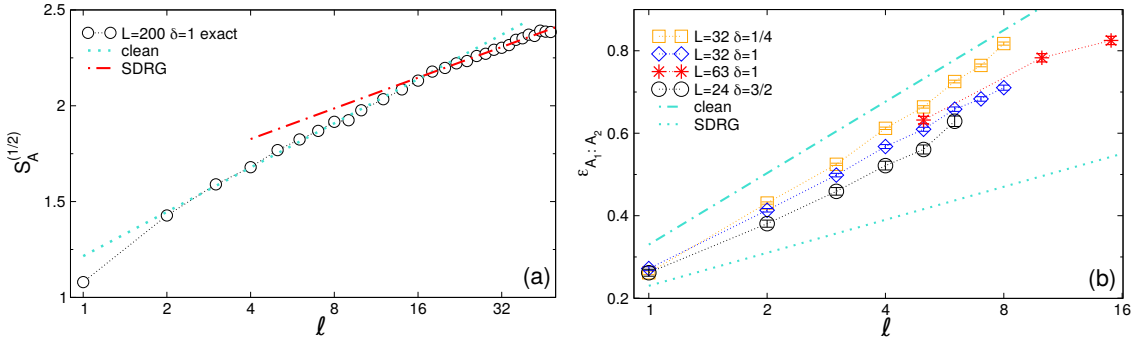

FIGURE 10.6: LN in the random XX spin chain. Panel (a): $S_A^{(1/2)}$ for a single interval at the center of an open chain plotted versus the interval length ℓ. The data (circles) are obtained by means of free-fermionic techniques which allow us to reach large systems sizes ($L = 200$). Note the crossover from the scaling of the clean model at short lengths (dotted line) to the SDRG one at large distances (dash-dotted line). Panel (b): $\mathcal{E}_{A_1:A_2}$ for two adjacent intervals of equal length ℓ (in the center of an open chain) plotted as a function of ℓ. The symbols denote DMRG results for chains with $L = 16, 24, 28, 32, 63$ and disorder strength $1/4 \leq \delta \leq 3/2$. The data are averaged over $\sim 10^3$ disorder realizations. The dash-dotted and dotted lines are the CFT prediction for $\delta = 0$, and the SDRG result, respectively.

$S_A \simeq 1/3 \ln \ell + c'$, whereas the dotted line is the SDRG result

$$S_A \simeq \frac{\ln 2}{3} \ln \ell + \text{const.} \tag{10.5.1}$$

We recall that the IRFP is expected to describe the numerical data for any disorder strength, but for asymptotically large ℓ and L. For finite interval and system lengths, we expect a complicated crossover between the clean and SDRG results, which is more severe for small disorder. In fact, from Fig. 10.5 (b) it is clear that for the smallest disorder strength ($\delta = 1/4$), the data are closer to the clean prediction than to the SDRG one. This does not come unexpected since the crossover between the two fixed points should be regulated by a δ-dependent crossover length ξ_δ. One should expect that $\xi_\delta \to \infty$ for $\delta \to 0$. At any δ, the IRFP results should be valid only for $\ell, L \gg \xi_\delta$. However, the data for $\delta = 1$ and $\delta = 3/2$ are almost indistinguishable, signaling that they should be both in the SDRG regime. Indeed, although oscillating corrections are present (as it is well known [321]), the data are in rough agreement with the SDRG prediction (10.5.1) (dotted line). A more quantitative analysis of the EE, with a proper robust determination of the prefactor to the logarithmic growth, requires the study of much longer chains as done by means of free fermionic methods [320, 321]. Unfortunately, simulating with DMRG chains of length of the order of hundreds sites and with sufficient statistics is beyond our current capability.

Although the data for the EE are asymptotically in rough agreement with the prediction of the SDRG already for $L = 32$ and $\delta \sim 1$, this does not imply that the same is true for the LN, because the crossover between the CFT (clean) and the IRFP fixed points in principle depends on the measured quantity. In order to understand the scaling of the LN, it is worth to consider the Rényi entropy

$$S_A^{(1/2)} \equiv 2\text{Tr}\rho_A^{1/2}, \tag{10.5.2}$$

for a single interval A of length ℓ at the center of an open chain. Indeed, the LN for pure states (e.g., for two adjacent intervals with $\ell_1 + \ell_2 = L$) coincides with $S_A^{(1/2)}$. Consequently, one could expect the scaling of the negativity to resemble that of $S_A^{(1/2)}$, rather than that of the von Neumann entropy S_A. In Fig. 10.6 (a), we report exact numerical data for $S_A^{(1/2)}$ at $\delta = 1$ obtained by means of free-fermionic techniques, which allow us to reach large systems sizes ($L = 200$). Interestingly, the data do not show strong parity effects (i.e., oscillations with the parity of the block size), in contrast with S_A [the same is true for the LN in Fig. 10.6 (b)]. Considering these large system sizes we can clearly see the crossover

from the scaling of the clean model at short lengths ($S_A^{(1/2)} \sim 1/2 \ln \ell$) to the SDRG one at large distances [$S_A^{(1/2)} \sim (\ln 2)/3 \ln \ell$]. The crossover starts around $\ell \sim 15$ and it is fully established around $\ell \sim 30$, implying that $L \approx 120 = 4 \times 30$ would be needed to fully confirm our results. This, however, is not possible with our current DMRG implementation.

Let us, however, consider $\mathcal{E}_{A_1:A_2}$ between the two adjacent intervals. The DMRG data are reported in Fig. 10.6 (b) for chain sizes up to $L = 63$ and for several disorder strengths. The dashed-dotted line is the CFT prediction for the clean model $\mathcal{E}_{A_1:A_2} \simeq 1/4 \ln(\ell) + c'$, while the dotted line is the SDRG result $\mathcal{E}_{A_1:A_2} \simeq (\ln 2)/6 \ln(\ell) + \text{const}$ (cf. (10.3.5)). For $\delta = 1/4$, $\mathcal{E}_{A_1 \cup A_2}$ grows with a slope similar to the clean case. This does not come unexpected since also the results for the EE in Fig. 10.5 (b) for $\delta = 1/4$ are affected by a strong crossover. Increasing the strength of the disorder, we observe that for the available subsystems' sizes the slopes of the LN appears to reduce, but, as a difference with the EE, there is no saturation with δ and also for $\delta = 3/2$ there are still strong crossover effects. This is in complete analogy with what observed for $S_A^{(1/2)}$ in Fig. 10.6 (a), where the crossover for $\delta = 1$ starts taking place around $\ell = 15$. Indeed, for $\delta = 1$, the last points for $L = 63$ with $\ell = 15$ seem to move in the right direction (we cannot access chains of this length for $\delta = 3/2$ because of the poor convergence of DMRG for this large disorder). However, these are only very encouraging signals for the correctness of our prediction: we can only conclude that for the system sizes and δ accessible to DRMG simulations, $\mathcal{E}_{A_1:A_2}$ exhibits deviations from the SDRG prediction (10.3.5), which are likely explained as crossover effects. Much larger chain sizes (of the order of $L \sim 120/130$ which are not accessible with our current DMRG implementation), would be needed for the asymptotic IRFP behavior to set in.

10.6 Concluding remarks

In this Chapter we studied the scaling behavior of the LN of disordered spin chains in the random-singlet phase. Our main results have been already summarized at the beginning, and for this reason here we only mention some new research directions. First, in the random XX chain it should be possible by generalizing the results for clean systems [295–297] to treat the moments of the PT density matrix exactly. By comparing with the analytic results of Sec. 10.2.1, this would allow providing a more robust check of some of our findings (as mentioned, this is work in progress [322]). Another intriguing direction would be to investigate to what extent the relation between the LN and the mutual information remains valid in more complicated disordered phases. In this respect, one possibility would be to focus on the spin-1 random Heisenberg chain [503]. Different physical behavior should also appear in the spin-$1/2$ Heisenberg chain in which, aside from antiferromagnetic couplings, ferromagnetic ones are allowed. Finally, it would be interesting to investigate the scaling of the LN in excited states of disordered spin models, also in connection with many-body localization.

Chapter 11

Unusual area law violation in inhomogeneous disordered models

A striking feature of local gapped quantum many-body systems is that the ground-state EE of a subsystem scales with the area of its boundary rather than with its volume. This is the essence of the famous *area law* for the entanglement [cf. Eq. (1.3.1)]. Even if an actual proof exists only in $1d$, there is a strong common belief that ground states of "physically reasonable local hamiltonians" fulfill the area law, and that violations are at most logarithmic. Here we provide an example of *unusual* area law violation in the ground state of a spin chain with random and inhomogeneous couplings. By employing the SDRG framework, we show that the EE exhibits a power-law growth with the subsystem size, with an exponent $1/2$ that can be related to the survival probability of certain random walks. We also investigate the role of interactions by considering the random inhomogeneous XXZ spin chain. Within the SDRG framework and in the strong inhomogeneous limit, we show that the above area-law violation takes place only at the free-fermion point of the phase diagram. This point divides two extended regions, which exhibit volume-law and area-law entanglement, respectively. This last Chapter is based on Ref. [91].

11.1 Introduction

Recently, devising local models that exhibit more dramatic area-law violations became an important research theme, the motivation being twofold. On the one hand, highly-entangled ground states are potentially useful for quantum computation technologies. On the other hand, from a condensed matter perspective, area-law violations could be witnesses of exotic features of quantum matter. As a matter of fact, examples of ground states non-trivially violating the area law start to be discovered (see, for instance, [88–90, 522–528]). These comprise inhomogeneous systems [87], translation invariant models with large spin [522], free-fermion hamiltonians [527] with a fractal Fermi surface, nonlocal QFTs [526], and supersymmetric models [525]. An interesting class of frustration-free, local, translational invariant models that exhibit area-law violations has been constructed by Movassagh and Shor in Ref. [88]. Their ground-state EE is $\propto \ell^{1/2}$, thus exhibiting a polynomial violation of the area law. Importantly, the exponent of the entanglement growth originates from universal properties of the random walk. This is due to the fact that the ground state of the model is written in terms of a special class of combinatorial objects, called Motzkin paths [529]. A similar result can be obtained [89, 528] using the Fredkin gates [530]. An interesting generalization of Ref. [88] obtained by deforming a colored version of the Motzkin paths has been presented in Ref. [90]. The ground-state phase diagram of the model exhibits two phases with area-law and volume-law entanglement, respectively.

In this Chapter, we show that unusual area-law violations can be obtained in a $1d$ inhomogeneous local system in the presence of disorder. Specifically, here we investigate the random inhomogeneous XX chain. In the clean limit, i.e., in the absence of disorder, our model reduces to the rainbow chain of Ref. [87], whose ground state, in the limit of strong inhomogeneity, is the rainbow state. In the rainbow state, long-range singlets are formed between spins across the chain center. An immediate striking consequence is that the half-chain EE is proportional to the subsystem volume (volume law). Here we show that upon including disorder the structure of the ground state changes dramatically. Indeed, in contrast with the clean case, the entropy exhibits an unusual square root growth, which represents a polynomial violation of the area law. We provide numerical evidence for this behavior by using the SDRG method [85]. We numerically verify that

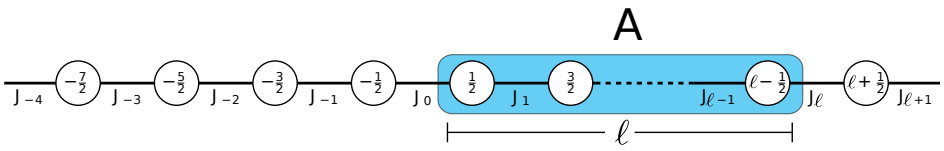

FIGURE 11.1: Setup used in this Chapter. (top) Definition of the random inhomogeneous XX chain. The chain couplings are denoted as $J_n = e^{-|n|h} K_n$, with n half integer numbers, h a real inhomogeneity parameter, and K_n independent random variables distributed with (11.2.3). We focus on the EE of a subregion A of length ℓ (shaded area in the Figure). Subsystem A starts from the chain center.

the unusual area law violation happens both in the strong inhomogeneous limit, as well as for weak inhomogeneity. Specifically, we numerically observe the square-root scaling for considerably weak inhomogeneity, although we do not have any proof that it persists for an arbitrarily small one. We provide robust numerical evidence of the unusual area-law violation in a microscopic model by calculating the EE of the random inhomogeneous XX chain, which is obtained by using the free-fermion solution of the model. Furthermore, we establish a mapping between the SDRG flow of the renormalized couplings and an alternating random walk. Interestingly, in the strong inhomogeneous limit the exponents of the entanglement scaling, and several ground-state features, can be quantitatively understood from certain survival probabilities of the random walk. Finally, we investigate the role of interactions by considering the random inhomogeneous spin-$1/2$ XXZ chain. Within the SDRG framework, we show that the unusual area-law violation does not survive in the presence of interactions. Interestingly, this marks the transition between two extended regions, where the EE exhibits area-law and volume-law scaling, respectively. This scenario is somewhat similar to the one presented in Ref. [90], although the models are substantially different.

The remaining is organized as follows. In Section 11.2 we introduce the random inhomogeneous XX chain, highlighting some of its peculiar properties. In Section 11.3 we present numerical SDRG results for the EE in the XX chain, providing a first understanding of the unusual area-law violation. Such violation is confirmed in the real model in Section 11.4, by exploiting the exact solvability of the random inhomogeneous XX chain. In Section 11.5 we address the strongly inhomogeneous limit of the model, by exploiting a mapping between the SDRG flow and the random walk. Section 11.6 is devoted to discussing the entanglement scaling in the XXZ chain. We conclude in Section 11.7.

11.2 The random inhomogeneous XX chain (randbow chain)

We consider a chain with $2L$ sites, described by the following inhomogeneous random hopping hamiltonian (see Figure 11.1)

$$H = -\frac{1}{2} \sum_{m=-L+1}^{L-1} J_m \, c^\dagger_{m-\frac{1}{2}} c_{m+\frac{1}{2}} + \text{h.c.}, \quad \text{with } m = 0, \pm 1, \pm 2, \cdots, \pm(L-1) \tag{11.2.1}$$

where $c_{m\pm\frac{1}{2}}$ ($c^\dagger_{m\pm\frac{1}{2}}$) denotes the annihilation (creation) operator of a spinless fermion at sites $m \pm \frac{1}{2}$, and $J_m > 0$ is the inhomogeneous random hopping parameter between the sites $m - \frac{1}{2}$ and $m + \frac{1}{2}$. In (11.2.1), the coupling J_0 is associated to the link $\left(-\frac{1}{2}, \frac{1}{2}\right)$ located at the center of the chain. The hopping parameters J_m are defined as

$$J_m \equiv K_m \times \begin{cases} e^{-h/2}, & m = 0\,, \\ e^{-h|m|}, & |m| > 0\,, \end{cases} \tag{11.2.2}$$

where $h > 0$ is a real parameter that measures the strength of the inhomogeneity. If $K_m = \mathcal{O}(1)$ are nonzero, for $h > 0$ the coupling strength decreases exponentially with the distance from the chain center. In (11.2.2), we choose K_m to be independent (from site to site) random variables distributed in the interval

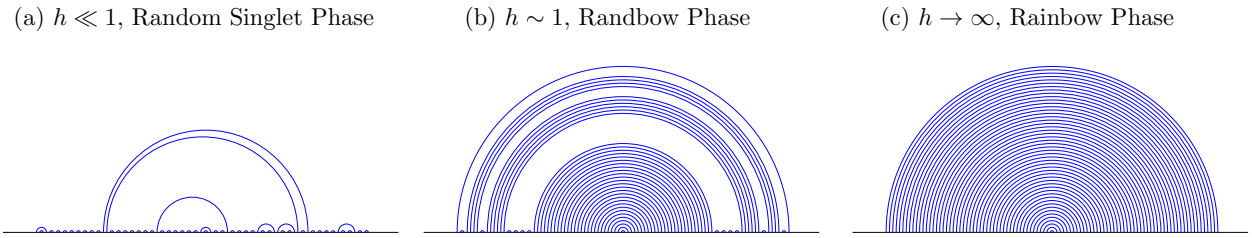

FIGURE 11.2: Summary of the phase diagram of the model, using open boundaries. Arcs in the Figure correspond to spins forming $SU(2)$ singlet bonds. Notice that for any $h \neq 0$ the coupling strength J_i decreases exponentially away from the center of the chain. (a) For $h \ll 1$ the model becomes the XX chain with random antiferromagnetic couplings. The ground state of the model is the RSP, where bonds of arbitrary length are present, but no symmetry with respect to the chain center is observed. RSPs exhibit logarithmic entanglement growth. (b) For intermediate values of h we observe some long distance bonds along with a proliferation of short ones, connecting neighboring sites (bubbles). The bond diagram presents left-right symmetry, and the entanglement is characterized by a subextensive (square root) entanglement growth. (c) For $h \to \infty$ the model approaches the standard rainbow chain, with all bonds symmetric with respect to the chain center and exhibiting volume-law entanglement.

$[0,1]$ according to

$$P(K) = \delta^{-1} K^{-1+\frac{1}{\delta}}, \tag{11.2.3}$$

with $\delta > 0$ parametrizing the noise strength, as in the previous Chapter.

After a Jordan-Wigner transformation, the random hopping model in (11.2.1) is mapped onto the spin-1/2 inhomogeneous XX chain defined by

$$H = \frac{1}{2} \sum_{m=-L+1}^{L-1} J_m \, S^+_{m-\frac{1}{2}} S^-_{m+\frac{1}{2}} + \text{h.c.}, \quad \text{with } m = 0, \pm 1, \pm 2, \cdots, \pm(L-1)\,. \tag{11.2.4}$$

with $S^\pm_m$ being spin-1/2 raising and lowering operators. In the following we investigate the ground-state EE of a subregion A that starts from the chain center. The precise bipartition that we consider is pictorially illustrated in Figure 11.1.

Clearly, the properties of the model (11.2.4) depend on two parameters, h and δ, giving rise to a two-dimensional ground-state phase diagram. The clean homogeneous XX chain is recovered for $\delta \to 0$ and $h = 0$. Its ground state is critical, and it is described by a CFT with central charge $c = 1$ which exhibits a logarithmic area-law violation of the EE [18]. Here, we focus on the entanglement properties of (11.2.4) at $\delta > 0$. In the limit $h \to 0$ and for any finite δ (cf. (11.2.2)), Eq. (11.2.4) defines the random antiferromagnetic XX chain. The ground state of the model has been extensively studied using SDRG [85, 188, 531], and it is described by the RSP, depicted in Figure 11.2 (a). See also Chapter 10, where the entanglement scaling (logarithmic in this case as well) is discussed extensively. For $\delta = 0$ and $h > 0$, the ground state of (11.2.4) is in the rainbow phase [87]. The structure of the ground state of (11.2.4) is illustrated in Figure 11.2 (c). The system exhibits a proliferation of long bonds connecting distant spins symmetrically across the chain center. In the language of fermions the *rainbow* state reads

$$|\text{RAINBOW}\rangle = \prod_{n=1/2}^{L-1/2} \left(c^\dagger_{-n} + (-1)^{n-1/2} c^\dagger_{+n} \right) |0\rangle. \tag{11.2.5}$$

In the spin representation, the state (11.2.5) corresponds to a product of singlets between the sites $(-n, +n)$ of the chain. An important feature of the rainbow state (11.2.5) is that the EE of a subsystem starting from the chain center grows linearly with its size ℓ (corresponding to a *volume* law) as [87, 427, 501, 514, 532, 533]

$$\lim_{h \to \infty} S(h, \ell) = \ell \ln 2, \tag{11.2.6}$$

where subleading $\mathcal{O}(1)$ terms have been neglected. Eq. (11.2.6) reflects that the entanglement is proportional to the number of singlets shared between A and its complement $\bar{A}$, i.e., connecting a site in A and the other in $\bar{A}$. Remarkably, the volume-law scaling (11.2.6) survives in the weak inhomogeneity limit $h \to 0$. One can take the continuum limit of (11.2.1), by sending the lattice spacing $a \to 0$ and by considering $h \to 0$ and $L \to \infty$ with h/a and aL fixed, to show that the half-chain EE is still linear with L, but with a different coefficient as [427]

$$S(h, L) \simeq \frac{1}{6} \ln \left(\frac{e^{hL} - 1}{h} \right) \to \frac{hL}{6}. \tag{11.2.7}$$

The last expression in (11.2.7) is obtained in the limit $hL \gg 1$, making use the techniques of *curved CFT* in Part II of this thesis.

We finally turn to the region of the phase diagram with finite nonzero δ and $0 < h < \infty$. In this regime the ground state of (11.2.4) is in a dramatically different phase. This is illustrated in Figure 11.2 (b). Its structure is easily understood in the limit $h \gg 1$. Similar to the rainbow phase, long bonds connecting spins on symmetric sites with respect to the center of the chain are present. However, now they are rare and do not form an extended phase. Precisely, the probability of forming a sequence of rainbow links ("rainbow" regions) decreases exponentially with its size, i.e., with the number of consecutive sites involved. On the other hand, the ground state of (11.2.4) exhibits a proliferation of short-range singlets between spins on nearest-neighbor sites. These form extended "bubble" regions (see Figure 11.2 (b)) of length ℓ_b, whose probability exhibits a power law decay as $\propto \ell_b^{-3/2}$. This has striking consequences for the scaling of the EE. First, only rainbow bonds can contribute to the entanglement between A and the rest, because short singlets connect mostly sites within A and $\bar{A}$, separately. On the other hand, the typical length scale over which the system is entangled is determined by the scaling of the regions with short-range singlets. Specifically, our main result is that for $0 < h < \infty$ and finite δ the EE exhibits a square-root scaling behavior as

$$S = C \cdot \ell^{1/2} + k'', \tag{11.2.8}$$

where C and k'' are non-universal constants. Notice that Eq. (11.2.8) represents a dramatic violation of the area-law.

11.2.1 Path invariance of the SDRG for the XX chain: A useful lemma

Away from the limits $h = \delta = 0$, the hamiltonian (11.2.4) can be studied using the SDRG technique, as reviewed in Section 1.4.4. Following the discussion there, it is useful to rewrite the SDRG procedure by introducing the logarithmic couplings, in this Chapter denoted as T_m

$$T_m \equiv -\ln J_m. \tag{11.2.9}$$

Notice that T_m takes into account both the random part of the coupling K_m (cf. (11.2.2)), as well as the inhomogeneity due to the presence of h, giving a non-random position-dependent shift in T_m. In the variables T_m the SDRG renormalization step becomes additive.

We choose K_m (see (11.2.2)) distributed according to (11.2.3). Writing this quantity as $K_m = \xi_m^{\delta}$, one can easily verify that ξ_m is a random variable uniformly distributed in the interval $[0, 1]$. This allows one to rewrite the couplings T_m as

$$T_m = \begin{cases} h\left(\frac{1}{2} - \frac{\delta}{h} \ln \xi_0\right), & m = 0\,, \\ \\ h\left(|m| - \frac{\delta}{h} \ln \xi_m\right), & |m| > 0\,. \end{cases} \tag{11.2.10}$$

An important consequence of (11.2.10) is that apart from the overall factor h, the couplings T_m are functions of the ratio δ/h only. Hence, the RSP, also known as valence bond state (VBS), obtained at the end of the SDRG, as well as the EE, only depends on δ/h.

Since in the following we mostly focus on the random XX chain, here we wish to discuss a crucial simplification that occurs when one applies the SDRG method to this model. We show that for the random XX

chain (cf. (11.2.4)) the renormalized coupling between two sites separated by an odd number of consecutive bonds is independent of the decimation pattern, and it has a simple form that we provide. To the best of our knowledge this interesting property has not been noticed before in the literature. Here we just report the result, that can be proven by induction. The proof can instead be found in Ref. [91]. The general expression for the renormalized coupling for a block $[i-\frac{1}{2}, i+n+\frac{1}{2}]$ with $n+1$ bonds is given by

$$T_{[i-\frac{1}{2},i+n+\frac{1}{2}]} = \sum_{j=0}^{n} (-1)^j \, T_{i+j}, \tag{11.2.11}$$

where n is the number of spins decimated, that must be an even number.

A few comments are in order to show the relevance of our result. First, Eq. (11.2.11) provides an exact mapping between the SDRG flow of the couplings T_i and an *alternating* random walk. This mapping holds true for any distribution of the initial couplings J_i. However, Eq. (11.2.11) does not contain any spatial information about the SDRG flow. This means that from (11.2.11) it is not straightforward to reconstruct the information about the place where the SDRG processes has occurred. This fact represents an obstacle to derive from Eq. (11.2.11) the scaling of correlation functions or of the EE. Still, we anticipate that this limitation can be overcome for the random inhomogeneous XX chain in the large h limit (strongly inhomogeneous limit). This happens because the presence of the inhomogeneity provides a simple relation between the SDRG step n and the distance from the chain center. More precisely, sites far away from the chain center are usually renormalized at later stages along the SDRG procedure.

Another important consequence of Eq. (11.2.11) is that, given a region containing n spins, Eq. (11.2.11) allows one to derive the distribution of the renormalized couplings after decimating all the spins. Using the random walk framework, one obtains that this is the distribution of the final position of the walker after n steps. It is straightforward to derive this distribution in the limit $n \to \infty$. Clearly, the sum of the even and odd sequences in Eq. (11.2.11) can be treated separately. Both are the sum of independent identically distributed exponential variables, that follow the gamma distribution. By using that for large n the gamma distribution is well approximated by a normal distribution, one has that the sum of the even and odd terms in Eq. (11.2.11) are distributed with $(\pi n)^{-1/2} \exp[(x-n/2)^2/n]$. The renormalized coupling after n SDRG steps is obtained as the difference between the sum of the odd and even sequences in Eq. (11.2.11). This is again a normal distribution with zero mean and variance n, i.e.,

$$P\left(T = T_{[i-\frac{1}{2},i+n+\frac{1}{2}]}\right) = \frac{1}{\sqrt{2\pi n}} e^{-T^2/(2n)}. \tag{11.2.12}$$

11.3 Area-law violation in the random inhomogeneous XX chain

Von Neumann entropy: numerical SDRG results

From the SDRG scheme, the entropy is obtained as $S = n_{A:\bar{A}} \ln 2$ [cf. Eq. (1.4.46)] . The disorder average $\langle S \rangle$ is then proportional to the average number of singlets $\langle n_{A:\bar{A}} \rangle$ shared between A and its complement $\bar{A}$. We now discuss the resulting scaling behavior of the ground-state EE in the random inhomogeneous XX chain.

In Figure 11.3 (left) we present numerical data for the EE S of a subsystem A placed at the center of the chain (see Figure 11.1). The results are obtained by implementing the SDRG method discussed in Section (1.4.4). The entropy S is plotted versus the subsystem size ℓ of A. The different symbols in the Figure correspond to different values of the inhomogeneity h. The disorder strength parameter δ (cf. (11.2.2)) is fixed to $\delta = 1$. For $h \to \infty$ the model reduces to the rainbow chain, and the volume law $S \propto \ell$ is expected. Oppositely, for $h \to 0$ the homogeneous random XX chain is recovered with logarithmic entanglement scaling. Surprisingly, for all the intermediate values of $0.5 < h < 10$, the entropy exhibits a power-law increase with ℓ (notice the logarithmic scale in both axes). A preliminary analysis suggests the

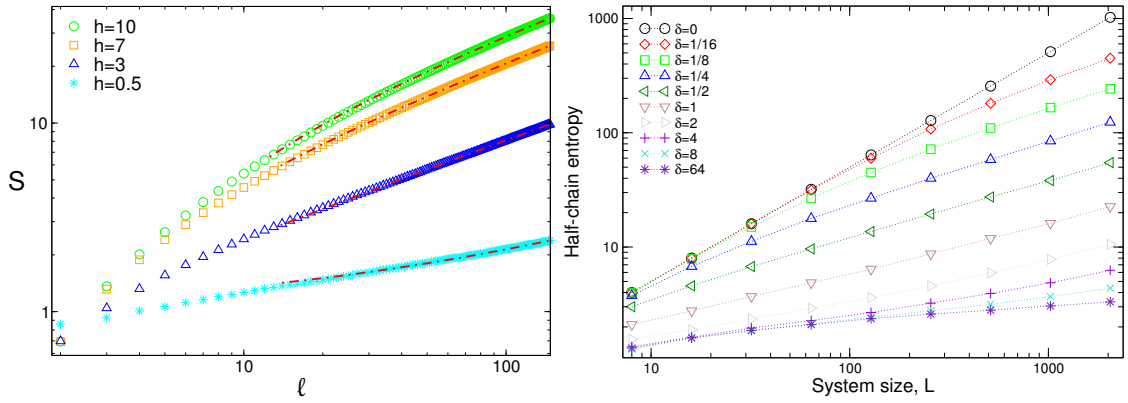

FIGURE 11.3: Unusual scaling of the EE in the randbow phase. Left: EE as a function of the subsystem length ℓ. The subsystem starts from the center of the chain (see Figure 11.1). The data are SDRG results for the random inhomogeneous XX chain. The different symbols are for different values of h and fixed value of $\delta = 1$. The dashed-dotted lines are fits to $a + b\ell^{1/2}$, with a, b fitting parameters. Right: EE as a function of the chain length L. The data are SDRG results for the random inhomogeneous XX chain. The different symbols are for different values of δ and $h = 1$. The data are averaged over 10^4 disorder realizations. Logarithmic scale is used on both axes.

behavior $S \propto \ell^{1/2}$. To perform a more careful finite-size analysis we fit the SDRG results to

$$S = a + b\ell^{1/2}, \tag{11.3.1}$$

where a and b are fitting parameters. The results of the fits are reported in Figure 11.3 (left) as dashed-dotted lines. Clearly, for small values of ℓ the data exhibit deviations from (11.3.1). This behavior has to be attributed to finite-size corrections, due to the small ℓ. Similar corrections are present for clean models, as well as for the random XX chain [320]. However, already for $\ell \gtrsim 10$ the data are in perfect agreement with (11.3.1) for all values of h considered.

Alternatively, in Figure 11.3 (right) we plot the half-chain entropy as a function of the chain length L. The data are now for a wide range of $0 \leq \delta \leq 64$. The data are for $h = 1$. For $\delta = 0$ the volume law behavior is visible, whereas the data for $\delta = 64$ are suggestive of the logarithmic behavior that is expected in the RSP. For all other values of δ the square root scaling is visible, confirming the results of Figure 11.3 (left).

It is interesting to investigate the combined effect of disorder and inhomogeneity on the scaling of S. This is discussed in Figure 11.4, by considering different values of δ and h. The Figure plots S as a function of ℓ for several values of h and δ (different symbols). All the data for different δ and h but with the same value of h/δ collapse on the same curve. This confirms that S is a function of h/δ only. The Figure shows SDRG results for $h/\delta = 7$ (empty symbols), $h/\delta = 4$ (filled symbols), and $h/\delta = 0.5$ (hatched symbols). This scaling behavior, however, is valid only within the SDRG method. We anticipate that for the random inhomogeneous XX chain the entanglement entropy can be calculated exactly (see Section 11.4) using free-fermion techniques, and it is a function of h/δ only for large h. For all values of h, δ considered in Figure 11.4 the EE exhibits the square-root scaling (11.3.1). The dashed-dotted lines in the Figures are fits to (11.3.1), and they are in good agreement with the SDRG results. We should also remark that for $h/\delta = 0.5$ the square root scaling of the EE is visible only for larger $\ell \gtrsim 100$, due to larger finite-size effects, as it is also clear also from Figure 11.3 (left).

Understanding the area-law violation: Bubble vs rainbow regions

The square-root entanglement scaling discussed above can be qualitatively derived from the distribution of the rainbow and bubble regions of the states. To this end we shall define ℓ_r as the number of consecutive concentric bonds that constitute a given rainbow region. For example, in the pure rainbow state we have

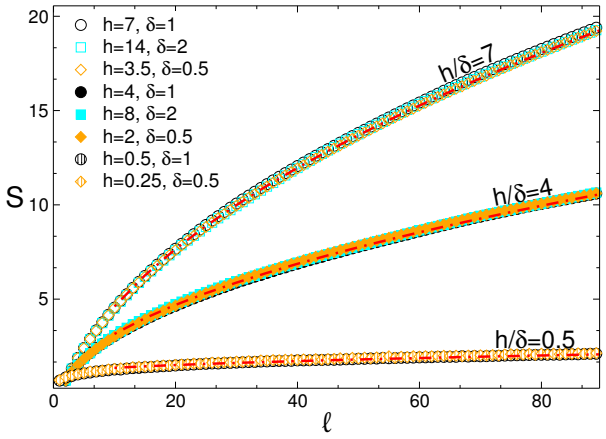

FIGURE 11.4: EE S plotted as a function of the subsystem size ℓ: SDRG results for the randbow XX chain. The symbols correspond to several values of δ and h. The data collapse shows that the EE is a function of the ratio h/δ.

$\ell_r = L$ bonds connecting the left and right halves of the chain. On the other hand, we define ℓ_b as the number of points that are connected by consecutive dimer bonds that constitute a bubble region (see Figure 11.2).

To compute the probability distribution of ℓ_r and ℓ_b we apply the SDRG method to decimate all the spins for a set of disorder realizations.

The distribution of the rainbow bonds $P_r(\ell_r)$ is obtained by constructing the histograms of the values of ℓ_r of the different rainbow regions. An average over different disorder realizations is performed. The resulting histograms for ℓ_r are shown in Figure 11.5 (left). The data are for the random inhomogeneous XX chain in the strongly inhomogeneous limit for $h \gg 1$. We use a logarithmic scale on the y-axis. The data show a clear exponential decay with ℓ_r. The exponential decay is smaller for greater values of h. This is an expected result because in the limit $h \to \infty$ the rainbow regions will start to proliferate.

A similar analysis can be performed for the distribution $P_b(\ell_b)$ of the extension ℓ_b of the bubble regions. The results are reported in Figure 11.5 (right). Interestingly, on the scale of the Figure the two histograms are not distinguishable, signalling that P_b does not depend significantly on h, at least for large h. In stark contrast with the rainbow regions, P_b exhibits a power-law decay with ℓ_b. A careful analysis suggests the behavior

$$P_b(\ell_b) \propto \ell_b^{-3/2}. \tag{11.3.2}$$

The dash-dotted line in Figure 11.5 (right) is a fit to the behavior (11.3.2), and it perfectly describes the numerical data.

The results of Figure 11.5 allow one to understand qualitatively the square-root behavior of the EE (11.2.8). First of all, since P_r is an exponential function, the average number of rainbow bonds $\langle \ell_r \rangle$ is a constant independent on L,

$$\langle \ell_r \rangle = \int_1^\infty dx\, x P_r(x)\,, \tag{11.3.3}$$

where we have replaced the upper limit of the integral, namely L (total number of bonds) by ∞, without changing essentially the final result. On the other hand, given a subsystem A of length ℓ, the average number of points of the bubble regions contained in A is given by

$$\langle \ell_b \rangle = \int_2^\ell dx\, x P_b(x) \propto \ell^{1/2}. \tag{11.3.4}$$

The short-range singlets forming the bubble phase do not contribute to the entanglement between A and the rest, because they mostly entangle spins within A. The entanglement between A and the rest is due to long range links forming the rainbow phase. However, the scaling of the entropy is determined by the distribution of ℓ_b, which determines the typical spatial separation between the different rainbow regions. A

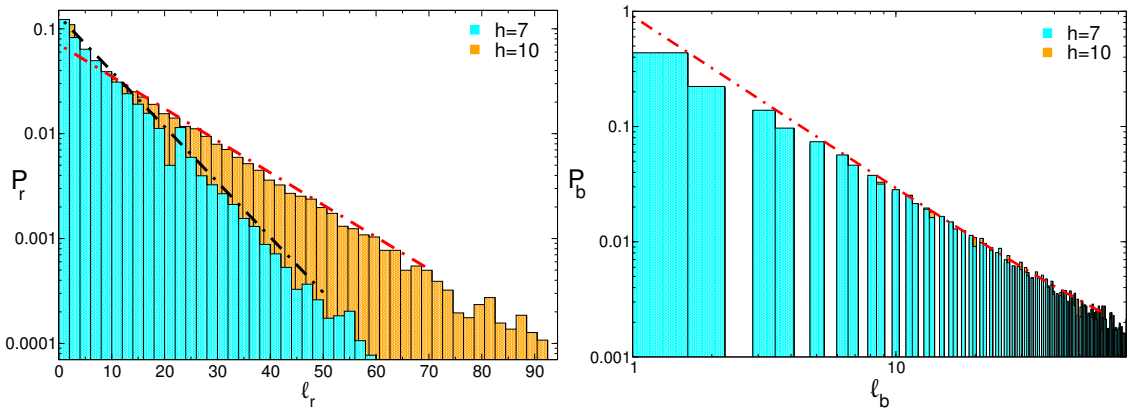

FIGURE 11.5: Left: Exponential decaying distribution of the rainbow bonds. The probability $P_r(\ell_r)$ of the number of bonds ℓ_r, of the rainbows. The Figure shows normalized histograms for the distribution of ℓ_r. Notice the logarithmic scale on the y-axis. The dashed-dotted lines are exponential fits. Right: Power law distribution of the size of the bubble regions. The Figure shows the probability $P_b(\ell_b)$ of the extension of the bubble regions. Notice the logarithmic scale on both axes. The data are renormalized histograms for the length of the bubble phase in the random inhomogeneous XX chain. The dashed-dotted line is a fit to $\sim x^{-3/2}$. In both panels the data are SDRG results for the random inhomogeneous XX chain. Each point is obtained by averaging over $\sim$ 1000 disorder realizations. The histograms correspond to the values $h = 7, 10$ and $\delta = 1$.

crude estimate of the entanglement entropy is obtained as follows. On average, there are $\langle \ell_r \rangle$ rainbow links every $\langle \ell_b \rangle$ sites. Hence a region A with ℓ sites can be divided roughly into $\ell / \langle \ell_b \rangle$ bubbles separated by $\langle \ell_r \rangle$ rainbow bonds. The EE can then be approximated as

$$S \propto \frac{\ell}{\langle \ell_b \rangle} \times \langle \ell_r \rangle \ln 2 \propto \ell^{1/2} \langle \ell_r \rangle \ln 2, \tag{11.3.5}$$

i.e., the square-root scaling in Eq. (11.2.8). Crucially, in (11.3.5) we have assumed that the average bubble size $\langle \ell_b \rangle$ and average number of rainbow bonds $\langle \ell_r \rangle$ do not depend on the position in the chain. This might be surprising at first look because the system is not homogeneous. However, as it will be clear in the following sections, due to the form of the coupling renormalization rule and the type of inhomogeneity, the condition that leads to the bubble formation does not depend on the precise SDRG step, and, consequently, on the position in the chain. Notice that this holds only for the XX model, and it breaks down for the interacting XXZ chain.

11.4 Numerical benchmarks using the exact solution of the XX chain

In this Section we provide exact results for the EE of the random inhomogeneous XX chain (11.2.4). The key observation is that for any disorder distribution, the XX chain is exactly solvable after mapping it to free fermions [full details are given in Ref. [95]].

Numerical results for the EE S are reported in Figure 11.6 versus the subsystem size ℓ. The Figure shows results for a chain with $2L = 100$ sites and several values of h and δ (different symbols in the Figure). We should mention that due to the exponential decay of the couplings J_i, the calculation of the eigenvalues of the correlation matrix [cf. Section 1.4.3] requires to use arbitrary precision routines. The results in Figure 11.6 were obtained requiring precision up to 10^{-80}. To highlight the power-law behavior of S, in the Figure we use a logarithmic scale on both axes. Clearly, for all values of h and δ, the data exhibit the behavior $S \propto \ell^{1/2}$. The dashed-dotted lines in the Figure are fits to (11.3.1). For small values of h the asymptotic scaling of S is already visible for $\ell \gtrsim 3$, whereas upon increasing h the asymptotic scaling sets in at larger values of ℓ, as expected. We should also mention that the finite-size effects due to L are negligible. This is expected because the subsystem is placed at the center of the chain. One should observe that all the data

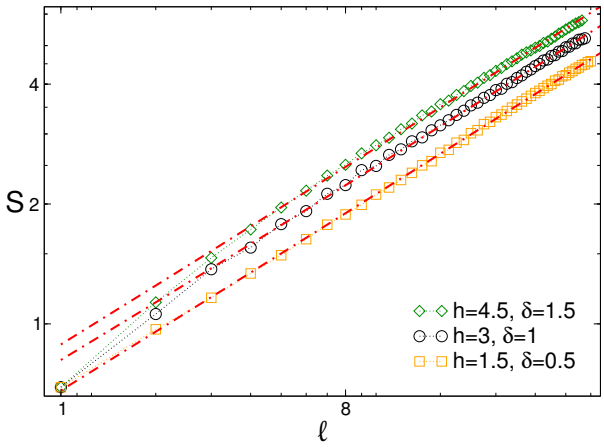

FIGURE 11.6: EE S in the random inhomogeneous XX chain: Exact results. The Figure shows S obtained using free-fermion techniques plotted versus the size ℓ of the subsystem. Note the logarithmic scale on both axes. The symbols are the data for a chain with $2L = 100$ sites and several values of h and δ. Each point is obtained by averaging S over 500 different disorder realizations. The dashed-dotted line is a fit to the expected behavior $S = a + b\ell^{1/2}$, with a, b fitting parameters. Notice that S is not a function of the ratio h/δ only.

shown in the Figure correspond to the same value of $h/\delta = 3$. Surprisingly, no data collapse is observed, suggesting that the entropy is not a function of the ratio h/δ only. This is in contrast with the SDRG data (see Figure 11.4), for which the scaling with h/δ holds.

11.5 A toy model for the strongly inhomogeneous limit

In this Section we discuss the strongly inhomogeneous limit of the random XX chain (cf. (11.2.4)), which is obtained for $h \to \infty$ in (11.2.2). In this limit, several analytical results can be obtained, for instance the scaling of the survival probabilities for the rainbow and the bubble regions presented in Figure 11.5. For $h \gg 1$, the ground state of (11.2.4) has the structure presented in Figure 11.2 (b). This consists of long links forming a "rainbow" phase connecting distant spins across the chain center, and of short links connecting spins on neighboring sites, forming a "bubble" phase. Importantly, for large h all the link configurations are symmetric with respect to the center of the chain. This is due to the fact that for large h, more bonds at the center of the chain are stronger and therefore get decimated first. This implies that SDRG decimations happen symmetrically with respect to the chain center. To further enforce this symmetry in the following we will restrict ourselves to symmetric couplings, i.e., $K_n = K_{-n}$ (cf. (11.2.2)). A crucial consequence of the large h limit is that the net effect of the SDRG procedure, at any step, is to renormalize the central coupling J_0 (see (11.2.1)). Moreover, the VBS state obtained at the end of the renormalization is constructed using only two types of diagrams that we term "rainbow diagrams" and "bubble diagrams". A typical singlet configuration is depicted in Figure 11.7 (a). The building blocks, i.e., rainbow and bubble diagrams, are better discussed in Figure 11.7 (b) and Figure 11.7 (c), respectively. In both (b) and (c) the coupling $J_0^{(n+1)}$, connecting sites $n+1$ and $-n-1$, is the renormalized coupling obtained after decimating the first $2n$ spins around the chain center (in this Section the position of the spins are labelled by integers: $\pm 1, \pm 2, \ldots, \pm L$). In the following we derive exact analytic expressions for $J_0^{(n+1)}$. Also, by using (11.2.11) we establish a relation between the survival probability of the rainbow and bubble diagrams with certain survival probabilities of an alternating random walk.

11.5.1 Rainbow diagrams: Random walk & survival probability

Here we discuss the renormalized coupling obtained from the rainbow configuration illustrated in Figure 11.7 (b). First, the initial coupling $J_0^{(n+1)}$ can result from both rainbow and bubble configurations. We

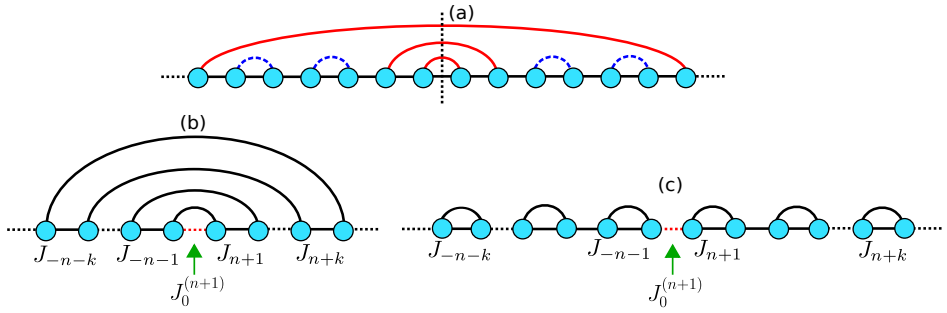

FIGURE 11.7: (a) Typical singlet configuration in the ground state of the random inhomogeneous chain in the limit $h \gg 1$. The continuous lines denote long-range singlets ("rainbow" configurations), whereas the dashed ones are short-range singlets connecting spins on nearest-neighbor sites and forming the "bubble" phase. Notice that only symmetric link configurations with respect to the center of the chain (marked by the vertical line) are allowed. (b) A rainbow diagram formed by long links connecting distant spins across the chain center. The renormalized central link $J_0^{(n+1)}$ results from link configurations as in (a). The length of the diagram is denoted as k. (c) Bubble diagram of length k formed by short singlets joining spins on nearest-neighbor sites. Notice in both (b) and (c) the symmetry with respect to the chain center. In the limit $h \to \infty$ typical bond configurations as in (a) are obtained by combining rainbow and bubble diagrams ((b) and (c)).

now consider the effect of a rainbow diagram of k links. This is obtained by decimating $k+1$ spin pairs around the chain center. Using the SDRG rule, the renormalized coupling $J_0^{(n+k+1)}$ that connects the spins at sites $n+k+1$ and $-n-k-1$ is given as

$$J_0^{(n+k+1)} = [J_0^{(n+1)}]^{(-1)^k} \left[\prod_{\alpha=0}^{k-1} \left(J_{n+\alpha+1} J_{-(n+\alpha+1)} \right)^{(-1)^\alpha} \right]^{(-1)^{k-1}}. \tag{11.5.1}$$

As in Eq. (11.2.11), it is useful to take the logarithm of (11.5.1) obtaining

$$-\ln J_0^{(n+k+1)} = (-1)^{k-1} \left[-X_0^{(n+1)} + \sum_{\alpha=0}^{k-1} (-1)^\alpha (X_{n+\alpha+1} + X_{-n-\alpha-1}) \right] + (n+k+1/2)h. \tag{11.5.2}$$

Here we defined $X_j \equiv -\ln K_j$. In (11.5.2), the term $(n+k+1/2)h$ is the contribution of the inhomogeneity (cf. (11.2.2)). Importantly, in (11.5.2), $X_0^{(n+1)}$ is obtained from $-\ln J_0^{(n+1)}$ by considering only the contributions of K_j (cf. (11.2.2)), i.e., it does not take into account the contribution of h, which is included in the last term in (11.5.2). Crucially, here we are using that the h-dependent term in (11.5.2) does not depend on the renormalization pattern leading to $J_0^{(n+1)}$. This is a simple consequence of (11.2.11). Specifically, we observe that the h-dependent term in $-\ln J_0^{(n)}$ is $(n-1/2)h$, from which the last term in (11.5.2) follows. This is easy to prove by induction. The proof is a simpler version of that for (11.2.11). One first assumes that after decimating all the spins between sites n and $-n$ the h-dependent contribution to the coupling is given by $(n+1/2)h$. Then one considers the two possible SDRG processes, which consist in adding a rainbow link between the spins at $(n+1)$ and $-(n+1)$, or two short links connecting spins $(n+1)$ and $(n+2)$ and the spins $-(n+1)$ and $-(n+2)$, respectively. It is trivial to verify that in both cases the formula holds.

It is important to observe in (11.5.2) the overall alternating term $(-1)^{k-1}$ and the alternating term $(-1)^\alpha$. We anticipate that the former is crucial to determine the survival probability of the rainbow diagrams. Here we are interested in the probability that the rainbow diagram survives k successive SDRG decimation steps. Crucially, while this survival probability could depend on the history of SDRG process, for the XX chain this is not the case, as we are going to show. Given a rainbow diagram of length k, we start by calculating the probability for the diagram to survive for an extra SDRG step. In terms of the couplings J_i

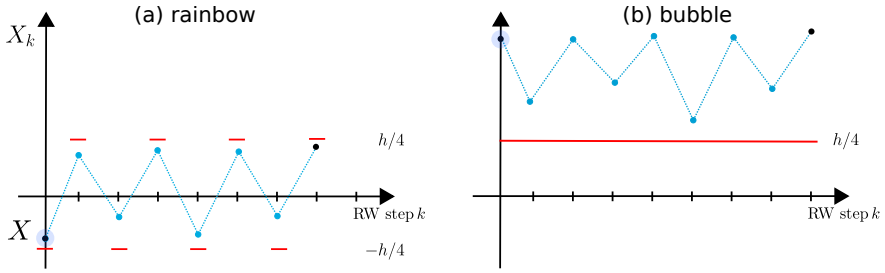

FIGURE 11.8: Random walk interpretation of the rainbow and bubble diagrams (see Figure 11.7 (b) and (c), respectively). (a) The probability for a rainbow diagram to survive k SDRG steps is mapped to the probability for an *alternating* random walk to be confined in the strip between $[-h/4, h/4]$ for k consecutive steps. (b) The probability for a bubble phase to survive k SDRG steps is the probability for the random walk to stay above the line $h/4$ for k consecutive steps. In both (a) and (b) the initial point of the walker x is related to the renormalized central bond J_0 in Figure 11.7 (b) and (c).

(cf. (11.2.2)), the survival condition is

$$J_0^{(n+k+1)} > J_{n+k+1}, \tag{11.5.3}$$

which ensures that an extra rainbow link is created by decimating the spins at positions $-n-k-1$ and $n+k+1$. Equivalently, in terms of the logarithmic variables X_k (cf. (11.5.2)) Eq. (11.5.3) reads

$$(-1)^{k-1}\left[X + \sum_{\alpha=0}^{k-1}(-1)^{\alpha} X_{n+\alpha+1}\right] < \frac{h}{4} + \frac{1}{2}X_{n+k+1}, \tag{11.5.4}$$

where we used that $X_\alpha = X_{-\alpha}$ and we defined $X = -X_0^{(n+1)}/2$ as the starting point of the random walk. The survival probability condition (11.5.4) does not depend on n and k. The linear term in $n+k$ in (11.5.2) cancels out with the h dependent term in J_{n+k+1}. We anticipate that this is not the case in presence of interactions, i.e., for the XXZ chain, and it will have striking consequences for the scaling of the EE (see Section 11.6). To further simplify the condition (11.5.4), in the following we shall neglect the term X_{n+k+1}. For large enough h this should be allowed because X_{n+k+1} is exponentially distributed in $[0,\infty]$. The condition in Eq. (11.5.4) has a simple interpretation in terms of random walks. Due to the factor $(-1)^{k-1}$ the rainbow survival probability is the probability of a walker to stay below $h/4$ if $(k-1)$ is even and above $-h/4$ if $(k-1)$ is odd, remaining confined in the alternating strip $[-h/4, h/4]$. This is illustrated pictorially in Figure 11.8 (a). Interestingly, the probability that the walker survives within the strip for n steps decays *exponentially* with n. The details of the calculation, based on standard techniques of random walks (see, for instance, Refs. [534, 535]), can be found in Ref. [91].

11.5.2 Bubble diagrams: Random walk & survival probability

We now discuss the survival probability for the bubble diagram. The typical bubble diagram is shown in Figure 11.7 (c), and it consists of a sequence of short-range singlets between nearest neighbor spins. Here we restrict ourselves to the situation in which the bubble diagrams appear in pairs (i.e., symmetrically) around the chain center, which is a consequence of the choice $J_m = J_{-m}$. Similar to the rainbow diagrams, the net effect of bubble diagrams is to renormalize the central coupling $J_0^{(n+1)}$. After a repeated application of the SDRG rule, the renormalized coupling $J_0^{(n+1+2k)}$ for the diagram in Figure 11.7 (c) is given as

$$J_0^{(n+1+2k)} = J_0^{(n+1)} \prod_{\alpha=0}^{2k-1} \left[J_{n+\alpha+1} J_{-n-\alpha-1}\right]^{(-1)^{\alpha+1}}. \tag{11.5.5}$$

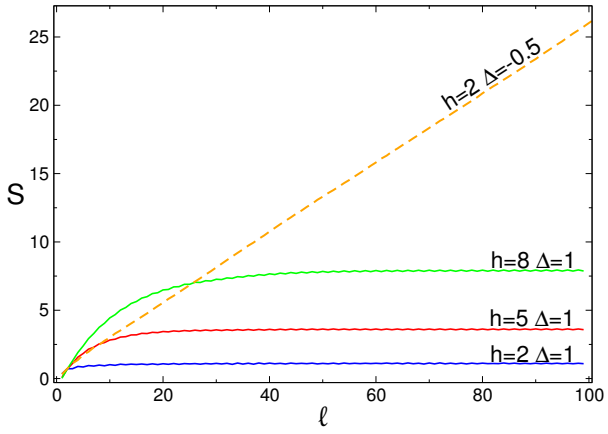

FIGURE 11.9: Scaling of the EE in an interacting inhomogeneous model. The Figure shows the EE S as a function of the subsystem size ℓ. The curves are SDRG results for the randbow XXZ chain for different values of h and Δ. In contrast with the XX chain, S exhibits a saturating behavior for $\Delta > 0$, whereas the volume-law behavior $S \propto \ell$ is observed for $\Delta < 0$. In particular, the dashed-dotted line is the SDRG result for $\Delta = -0.5$ and $h = 2$.

It is convenient to use logarithmic variables to obtain

$$-\ln J_0^{(n+1+2k)} = X_0^{(n+1)} + \sum_{\alpha=0}^{2k-1} (-1)^{\alpha-1} (X_{n+\alpha+1} + X_{-n-\alpha-1}) + (n+2k+1/2)h. \tag{11.5.6}$$

Again, the flow of the renormalized coupling in (11.5.6) can be interpreted as a random walk with starting point $X_0^{(n+1)}$. In contrast to the rainbow, there is no overall oscillating term $(-1)^{k-1}$, and the walker can only make an even number of steps, because bubbles are produced in pairs. The last term in (11.5.6) encodes the inhomogeneity contribution to the renormalized coupling, and it is independent on the renormalization pattern, as for the rainbow diagram. The condition for the bubble diagram to survive two SDRG steps is

$$J_0^{(n+1+2k)} < J_{n+1+2k}. \tag{11.5.7}$$

In the logarithmic variables one finds

$$X + \sum_{\alpha=0}^{2k-1} (-1)^{\alpha-1} X_{n+\alpha+1} > \frac{h}{4} + \frac{1}{2} X_{n+2k+1}. \tag{11.5.8}$$

where now the starting point of the random walk is defined as $X = X_0^{(n+1)}/2$. Similar to the rainbow, in the following we neglect the term X_{n+2k+1} in (11.5.8), because it does not affect the qualitative behavior of the results. In the random walk language, the condition (11.5.8) defines the probability that the walker stays above the line $h/4$, as depicted in Figure 11.8 (b). Importantly, the survival condition does not depend on the SDRG step, due to the cancellation of the linear term in n in (11.5.7). Now, the probability that the walker satisfies (11.5.8) for n steps decays as $n^{-3/2}$, in contrast with the rainbow survival probability, which decays exponentially. This is a standard calculation in the random walk literature. Details are again given in Ref. [91].

11.6 Entanglement entropy in the interacting case

Having established that in the random inhomogeneous XX chain the entanglement entropy exhibits an unusual area-law violation, it is natural to investigate whether this scenario survives in the presence of interactions. In this Section we show that the square-root scaling of the entropy (11.2.8) is very fragile, and it

does not survive if the model is interacting. To be specific, here we consider the inhomogeneous random Heisenberg XXZ chain. This is defined by the hamiltonian

$$H = \sum_{i=1}^{L-1} J_i \Big\{ \frac{1}{2} \Big[S_i^+ S_{i+1}^- + S_i^- S_{i+1}^+ \Big] + \Delta S_i^z S_{i+1}^z \Big\}. \tag{11.6.1}$$

Here Δ is an anisotropy parameter. and J_i are the same as in (11.2.2). For simplicity, we choose $J_i = J_{-i}$. The SDRG method for the Heisenberg chain is similar to that for the XX chain. The only difference is a factor $1+\Delta$ in the coupling renormalization [85]. Precisely, the SDRG rule for the renormalized coupling J' in the XXZ chain now reads [504]

$$J' = \frac{J_L J_R}{(1+\Delta) J_M}, \tag{11.6.2}$$

where, as usual, J_M is the largest coupling. In the random *homogeneous* XXZ chain (i.e., for $h = 0$) the factor $(1+\Delta)$ in (11.6.2) is irrelevant in the scaling limit of large systems. For instance, the SDRG fixed point describing the ground state is the same for both the XX and the XXX chain ($\Delta = 1$). This implies that universal properties are the same for both models. The EE exhibits logarithmic growth and the prefactor of the logarithm does not depend on Δ.

The goal of this Section is to show that in the presence of inhomogeneous couplings the factor $(1+\Delta)$ in (11.6.2) dramatically changes this picture, at least within the framework of the SDRG method. The results are discussed in Figure 11.9. The Figure shows SDRG data for the EE S of a subsystem at the center of the chain plotted as a function of the subsystem size ℓ. The continuous lines in the figure correspond to several values of the inhomogeneity parameter h and $\Delta = 1$. Surprisingly, for all values of h, S saturates in the limit $\ell \to \infty$. For $h = 8$ there is a large intermediate region where the square-root scaling behavior (11.2.8) holds. This signals the presence of an h dependent crossover length scale ξ_h separating the square-root behavior from the saturating behavior at $\ell \to \infty$. This behavior changes dramatically for $\Delta < 0$. For instance, the dashed line in Figure 11.9 denotes the SDRG data for $h = 2$ and $\Delta = -1/2$. Clearly, the EE exhibits the volume-law scaling $S \propto \ell$. We numerically observed that this volume-law scaling happens generically for $\Delta < 0$.

11.6.1 Random walk interpretation

We now discuss the origin of the behavior observed in Figure 11.9. Here we focus on the limit $h \gg 1$, where one can exploit the mapping between the SDRG flow and the alternating random walk. First, in the large h limit, similar to the non-interacting case, higher-energy degrees of freedom are nearer to the chain center, and are decimated first. This implies that the effect of the SDRG procedure is to renormalize the central coupling, similar to the XX chain. It is also natural to expect that for large h the most likely SDRG patterns are the rainbow and bubble patterns discussed in Figure 11.7 (b) and (c).

To proceed, we first discuss the renormalization of J_0 due to a rainbow diagram of length k (see Figure 11.7 (b)). A straightforward calculation gives

$$J_0^{(n+k+1)} = (1+\Delta)^{-k \bmod 2} (J_0^{(n+1)})^{(-1)^k} \Big[\prod_{\alpha=0}^{k-1} \Big(J_{n+\alpha+1} J_{-(n+\alpha+1)} \Big)^{(-1)^\alpha} \Big]^{(-1)^{k-1}}. \tag{11.6.3}$$

Notice that the renormalized coupling $J_0^{(n+k+1)}$ depends on the parity of k. The condition for the rainbow diagram to survive one SDRG step is still given by Eq. (11.5.3), and in the logarithmic variables X_i we have

$$(-1)^{k-1} \Big[X + \sum_{\alpha=0}^{k-1} (-1)^{\alpha-1} X_{n+\alpha+1} \Big] \lesssim \frac{h}{4} - \frac{\ln(1+\Delta)}{2} (k \bmod 2). \tag{11.6.4}$$

The condition (11.6.4) is the same as for the XX chain apart from the parity dependent term $\ln(1+\Delta)/2$. However, this extra term is not expected to change the qualitative behavior of the survival probability. Specifically, in the framework of the random walk (compare with Figure 11.8 (a)), one has that the walker

is now constrained to stay below $h/4 - \log(1+\Delta)/2$ if k is odd, and above $-h/4$ if k is even, i.e., in a strip that is not symmetric around zero (compare with Figure 11.8). It is natural to expect that the decay of the survival probability for the walker will remain exponential.

In stark contrast, the factor $(1+\Delta)$ in (11.6.2) has striking consequences for the survival probability of the bubble diagrams (see Figure 11.7 (c)). The renormalized coupling J_0 due to a bubble diagram of length $2k$ reads

$$J_0^{(n+1+2k)} = (1+\Delta)^{-2k} J_0^{(n+1)} \prod_{\alpha=0}^{2k-1} \left[J_{n+\alpha+1} J_{-n-\alpha-1} \right]^{(-1)^{\alpha+1}}. \tag{11.6.5}$$

Using Eq. (11.6.5), the condition Eq. (11.5.7) for the survival of the bubble phase can be rewritten as

$$X + \sum_{\alpha=0}^{2k-1} (-1)^{\alpha-1} X_{n+\alpha+1} \gtrsim \frac{h}{4} - k \ln(1+\Delta). \tag{11.6.6}$$

In contrast with the non-interacting case, the condition (11.6.6) depends on the step k of the walker. This means that for $\Delta > 0$ the survival condition (11.6.6) for the walker to be above the line $h/4 - k\ln(1+\Delta)$ is always satisfied for large k. Physically, this suggests that the bubble phase becomes more and more stable as its size increases. However, the short-range singlets in the bubble phase do not contribute to the EE, which explains the saturating behavior observed in Figure 11.9. On the other hand, for $\Delta < 0$ one has that for large k the condition (11.6.6) is never verified. This implies that the bubble phase is suppressed and the ground state of the model is in the rainbow phase, with volume-law entanglement.

11.7 Concluding remarks

In this Chapter, we have provided evidence of an unusual violation of the area law in a random inhomogeneous $1d$ model. Specifically, we showed that in a random inhomogeneous XX chain the ground-state entanglement entropy grows with the square root of the subsystem length. We derived this result by mapping the SDRG renormalization flow to an alternating random walk. The exponent $1/2$ of the entanglement growth can be understood via the mapping to an alternating random walk. We also investigated the effect of interactions, considering the random inhomogeneous XXZ chain. The unusual area law violation is very fragile, and it does not survive when interactions are present.

It is worth mentioning some research directions for future investigation. First, it would be interesting to further study the structure of the renormalization group flow in the light of the result (11.2.11). For instance, it natural to wonder whether (11.2.11) might be the starting point for an alternative derivation of the Refael and Moore result [86] for the entanglement entropy in the random XX chain. Another question concerns the fate of the unusual area-law violation in the limit of weak inhomogeneity. In the clean case, i.e., without disorder, using the approach of Ref. [159] it has been shown that the model can be mapped to a CFT in curved spacetime [424, 427], but what happens to this scenario in the presence of randomness is still unknown.

Going beyond the behavior of the XX spin-chain, it would be very useful to thoroughly investigate the phase diagram of the random inhomogeneous XXZ chain. For instance, while for strong inhomogeneity we observed that the EE has a volume-law scaling for $\Delta < 0$, the regime of weak inhomogeneity remains unexplored. The most relevant question would be to understand whether the volume-law behavior holds true at any value of the inhomogeneity. Another natural question is whether the mapping between the SDRG flow and the random walk allows one to obtain different exotic area-law violations, such as a power-law growth of the entanglement with an exponent $\alpha \neq 1/2$. A possibility would be to explore the effects of spatially-correlated disorder, that in the homogenous case are known to dramatically affect the critical behavior [85]. Moreover, the nature of the transition between the volume-law and the area-law entanglement in the random inhomogeneous XXZ chain has still to be clarified.

Finally, an independent, but very timely research direction would be to understand how the anomalous scaling of the ground-state entanglement can affect the out-of-equilibrium behavior of the random inhomogeneous XX chain after a (local or global) quantum quench, in particular for the entanglement evolution.

Bibliography

[1] E. Schrödinger, *Discussion of Probability Relations between Separated Systems*, *Math. Proc. Camb. Philos. Soc.* **31** (1935) 555–563.

[2] E. Schrödinger, *Probability relations between separated systems*, *Math. Proc. Camb. Philos. Soc.* **32** (1936) 446–452.

[3] A. Einstein, B. Podolsky and N. Rosen, *Can Quantum-Mechanical Description of Physical Reality Be Considered Complete?*, *Phys. Rev. E* **47** (1935) 777.

[4] M. Born, *The Born-Einstein Letters; Correspondence between Albert Einstein and Max and Hedwig Born from 1916 to 1955*. Walker, New York, 1971.

[5] E. H. Lieb and D. W. Robinson, *The finite group velocity of quantum spin systems*, *Commun. Math. Phys.* **28** (1972) 251.

[6] S. Wiesner, *Conjugate Coding*, *SIGACT News* **15** (1983) 78.

[7] C. H. Bennett, G. Brassard, C. Crépeau, R. Jozsa, A. Peres and W. K. Wootters, *Teleporting an unknown quantum state via dual classical and Einstein-Podolsky-Rosen channels*, *Phys. Rev. Lett.* **70** (1993) 1895.

[8] C. H. Bennett, D. P. Di Vincenzo, J. A. Smolin and W. K. Wootters, *Mixed-state entanglement and quantum error correction*, *Phys. Rev. A* **54** (1996) 3824.

[9] M. A. Nielsen and I. L. Chuang, *Quantum computation and quantum information*. Cambridge University Press, Cambridge (UK) 10th anniversary ed., 2010.

[10] L. Bombelli, R. K. Koul, J. Lee and R. D. Sorkin, *Quantum source of entropy for black holes*, *Phys. Rev. D* **34** (1986) 373.

[11] M. Srednicki, *Entropy and area*, *Phys. Rev. Lett.* **71** (1993) 666.

[12] C. Callan and F. Wilczek, *On geometric entropy*, *Phys. Lett. B* **333** (1994) 55 .

[13] J. D. Bekenstein, *Black Holes and Entropy*, *Phys. Rev. D* **7** (1973) 2333.

[14] S. W. Hawking, *Black hole explosions?*, *Nature* **248** (1974) 30.

[15] C. Holzhey, F. Larsen and F. Wilczek, *Geometric and renormalized entropy in conformal field theory*, *Nucl. Phys. B* **424** (1994) 443 .

[16] G. Vidal, J. I. Latorre, E. Rico and A. Kitaev, *Entanglement in Quantum Critical Phenomena*, *Phys. Rev. Lett.* **90** (2003) 227902.

[17] P. Calabrese and J. Cardy, *Entanglement entropy and quantum field theory*, *J. Stat. Mech.* **2004** (2004) P06002.

[18] P. Calabrese and J. Cardy, *Entanglement entropy and conformal field theory*, *J. Phys. A* **42** (2009) 504005.

[19] P. W. Anderson, *Absence of Diffusion in Certain Random Lattices*, *Phys. Rev. E* **109** (1958) 1492.

[20] L. Fleishman and P. W. Anderson, *Interactions and the Anderson transition*, *Phys. Rev. B* **21** (1980) 2366.

[21] B. L. Altshuler, Y. Gefen, A. Kamenev and L. S. Levitov, *Quasiparticle Lifetime in a Finite System: A Nonperturbative Approach*, *Phys. Rev. Lett.* **78** (1997) 2803.

[22] J. H. Bardarson, F. Pollmann and J. E. Moore, *Unbounded Growth of Entanglement in Models of Many-Body Localization*, *Phys. Rev. Lett.* **109** (2012) 017202.

[23] M. Serbyn, Z. Papić and D. A. Abanin, *Universal Slow Growth of Entanglement in Interacting Strongly Disordered Systems*, *Phys. Rev. Lett.* **110** (2013) 260601.

[24] M. Levin and X.-G. Wen, *Detecting Topological Order in a Ground State Wave Function*, *Phys. Rev. Lett.* **96** (2006) 110405.

[25] A. Kitaev and J. Preskill, *Topological Entanglement Entropy*, *Phys. Rev. Lett.* **96** (2006) 110404.

[26] Y. Zhang, T. Grover and A. Vishwanath, *Entanglement Entropy of Critical Spin Liquids*, *Phys. Rev. Lett.* **107** (2011) 067202.

[27] S. V. Isakov, M. B. Hastings and R. G. Melko, *Topological entanglement entropy of a Bose–Hubbard spin liquid*, *Nat. Phys.* **7** (2011) .

[28] S. Östlund and S. Rommer, *Thermodynamic Limit of Density Matrix Renormalization*, *Phys. Rev. Lett.* **75** (1995) 3537.

[29] S. Rommer and S. Östlund, *Class of ansatz wave functions for one-dimensional spin systems and their relation to the density matrix renormalization group*, *Phys. Rev. B* **55** (1997) 2164.

[30] U. Schollwöck, *The density-matrix renormalization group in the age of matrix product states*, *Ann. Phys.* **326** (2011) 96 .

[31] R. Orús, *A practical introduction to tensor networks: Matrix product states and projected entangled pair states*, *Ann. Phys.* **349** (2014) 117 .

[32] F. Verstraete, V. Murg and J. Cirac, *Matrix product states, projected entangled pair states, and variational renormalization group methods for quantum spin systems*, *Adv. Phys.* **57** (2008) 143.

[33] L. Tagliacozzo, T. R. de Oliveira, S. Iblisdir and J. I. Latorre, *Scaling of entanglement support for matrix product states*, *Phys. Rev. B* **78** (2008) 024410.

[34] R. Islam, R. Ma, P. M. Preiss, M. Eric Tai, A. Lukin, M. Rispoli et al., *Measuring entanglement entropy in a quantum many-body system*, *Nature* **528** (2015) .

[35] A. M. Kaufman, M. E. Tai, A. Lukin, M. Rispoli, R. Schittko, P. M. Preiss et al., *Quantum thermalization through entanglement in an isolated many-body system*, *Science* **353** (2016) 794.

[36] T. Brydges, A. Elben, P. Jurcevic, B. Vermersch, C. Maier, B. P. Lanyon et al., *Probing Rényi entanglement entropy via randomized measurements*, *Science* **364** (2019) 260.

[37] A. Lukin, M. Rispoli, R. Schittko, M. E. Tai, A. M. Kaufman, S. Choi et al., *Probing entanglement in a many-body–localized system*, *Science* **364** (2019) 256.

[38] E. Schmidt, *Zur Theorie der linearen und nichtlinearen Integralgleichungen*, *Mathematische Annalen* **63** (1907) 433.

[39] E. Chitambar, D. Leung, L. Mancinska, M. Ozols and A. Winter, *Everything You Always Wanted to Know About LOCC (But Were Afraid to Ask)*, *Commun. Math. Phys.* **328** (2014) 303.

[40] M. A. Nielsen, *Conditions for a Class of Entanglement Transformations*, *Phys. Rev. Lett.* **83** (1999) 436.

[41] K. Kraus, A. Bohm, J. D. Dollard and W. H. Wooters, *States, Effects and Operations – Fundamental Notions of Quantum Theory*, vol. Vol. 190 of *Lecture Notes in Physics*. Springer Berlin Heidelberg, 1983.

[42] C. H. Bennett, D. P. Di Vincenzo, C. A. Fuchs, T. Mor, E. Rains, P. W. Shor et al., *Quantum nonlocality without entanglement*, *Phys. Rev. A* **59** (1999) 1070.

[43] E. M. Rains, *Rigorous treatment of distillable entanglement*, *Phys. Rev. A* **60** (1999) 173.

[44] E. M. Rains, *A semidefinite program for distillable entanglement*, *IEEE Transactions on Information Theory* **47** (2001) 2921.

[45] A. Peres, *Separability Criterion for Density Matrices*, *Phys. Rev. Lett.* **77** (1996) 1413.

[46] C. H. Bennett, H. J. Bernstein, S. Popescu and B. Schumacher, *Concentrating partial entanglement by local operations*, *Phys. Rev. A* **53** (1996) 2046.

[47] V. Vedral, M. B. Plenio, M. A. Rippin and P. L. Knight, *Quantifying Entanglement*, *Phys. Rev. Lett.* **78** (1997) 2275.

[48] V. Vedral and M. B. Plenio, *Entanglement measures and purification procedures*, *Phys. Rev. A* **57** (1998) 1619.

[49] G. Vidal, *Entanglement monotones*, *J. Mod. Opt.* **47** (2000) 355.

[50] M. B. Plenio and S. Virmani, *An Introduction to Entanglement Measures*, *Quantum Info. Comput.* **7** (2007) 1.

[51] R. Horodecki, P. Horodecki, M. Horodecki and K. Horodecki, *Quantum entanglement*, *Rev. Mod. Phys.* **81** (2009) 865.

[52] E. H. Lieb and M. B. Ruskai, *A Fundamental Property of Quantum-Mechanical Entropy*, *Phys. Rev. Lett.* **30** (1973) 434.

[53] E. H. Lieb and M. B. Ruskai, *Proof of the strong subadditivity of quantum-mechanical entropy*, *J. Math. Phys.* **14** (1973) 1938.

[54] H. Li and F. D. M. Haldane, *Entanglement Spectrum as a Generalization of Entanglement Entropy: Identification of Topological Order in Non-Abelian Fractional Quantum Hall Effect States*, *Phys. Rev. Lett.* **101** (2008) 010504.

[55] G. Vidal and R. F. Werner, *Computable measure of entanglement*, *Phys. Rev. A* **65** (2002) 032314.

[56] M. B. Plenio, *Logarithmic Negativity: A Full Entanglement Monotone That is not Convex*, *Phys. Rev. Lett.* **95** (2005) 090503.

[57] P. Ruggiero, V. Alba and P. Calabrese, *Negativity spectrum of one-dimensional conformal field theories*, *Phys. Rev. B* **94** (2016) 195121.

[58] P. M. Hayden, M. Horodecki and B. M. Terhal, *The asymptotic entanglement cost of preparing a quantum state*, *J. Phys. A* **34** (2001) 6891.

[59] J. Watrous, *The Theory of Quantum Information*. Cambridge University Press, 2018, 10.1017/9781316848142.

[60] S. Kullback and R. A. Leibler, *On Information and Sufficiency*, *Ann. Math. Statist.* **22** (1951) 79.

[61] H. Araki, *Relative Entropy of States of Von Neumann Algebras*, *Publ. Res. Inst. Math. Sci. Kyoto* **1976** (1976) 809.

[62] M. Ohya and D. Petz, *Quantum entropy and its use*. Text and Monographs in Physics, Springer Study Edition, Springer, 2004.

[63] V. Vedral, *The role of relative entropy in quantum information theory*, *Rev. Mod. Phys.* **74** (2002) 197.

[64] K. M. R. Audenaert and J. Eisert, *Continuity bounds on the quantum relative entropy*, *J. Math. Phys.* **46** (2005) 102104.

[65] L. Amico, R. Fazio, A. Osterloh and V. Vedral, *Entanglement in many-body systems*, *Rev. Mod. Phys.* **80** (2008) 517.

[66] P. Calabrese, J. Cardy and B. Doyon, *Entanglement entropy in extended quantum systems*, *J. Phys. A* **42** (2009) 500301.

[67] J. Eisert, M. Cramer and M. B. Plenio, *Colloquium: Area laws for the entanglement entropy*, *Rev. Mod. Phys.* **82** (2010) 277.

[68] N. Laflorencie, *Quantum entanglement in condensed matter systems*, *Phys. Rep.* **646** (2016) 1 .

[69] M. B. Hastings, *An area law for one-dimensional quantum systems*, *J. Stat. Mech.* **2007** (2007) P08024.

[70] S. R. White, *Density matrix formulation for quantum renormalization groups*, *Phys. Rev. Lett.* **69** (1992) 2863.

[71] S. R. White, *Density-matrix algorithms for quantum renormalization groups*, *Phys. Rev. B* **48** (1993) 10345.

[72] U. Schollwöck, *The density-matrix renormalization group*, *Rev. Mod. Phys.* **77** (2005) 259.

[73] M. M. Wolf, *Violation of the Entropic Area Law for Fermions*, *Phys. Rev. Lett.* **96** (2006) 010404.

[74] D. Gioev and I. Klich, *Entanglement Entropy of Fermions in Any Dimension and the Widom Conjecture*, *Phys. Rev. Lett.* **96** (2006) 100503.

[75] P. Calabrese, M. Mintchev and E. Vicari, *Entanglement entropies in free-fermion gases for arbitrary dimension*, *EPL* **97** (2012) 20009.

[76] V. Popkov and M. Salerno, *Logarithmic divergence of the block entanglement entropy for the ferromagnetic Heisenberg model*, *Phys. Rev. A* **71** (2005) 012301.

[77] E. Ercolessi, S. Evangelisti, F. Franchini and F. Ravanini, *Essential singularity in the Renyi entanglement entropy of the one-dimensional XYZ spin-$1/2$ chain*, *Phys. Rev. B* **83** (2011) 012402.

[78] V. Alba, M. Haque and A. M. Läuchli, *Entanglement spectrum of the Heisenberg XXZ chain near the ferromagnetic point*, *J. Stat. Mech.* **2012** (2012) P08011.

[79] O. A. Castro-Alvaredo and B. Doyon, *Entanglement Entropy of Highly Degenerate States and Fractal Dimensions*, *Phys. Rev. Lett.* **108** (2012) 120401.

[80] K. G. Wilson, *Renormalization Group and Critical Phenomena. I. Renormalization Group and the Kadanoff Scaling Picture*, *Phys. Rev. B* **4** (1971) 3174.

[81] K. G. Wilson, *Renormalization Group and Critical Phenomena. II. Phase-Space Cell Analysis of Critical Behavior*, *Phys. Rev. B* **4** (1971) 3184.

[82] I. Affleck and A. W. W. Ludwig, *Universal noninteger "ground-state degeneracy" in critical quantum systems*, *Phys. Rev. Lett.* **67** (1991) 161.

[83] P. Di Francesco, P. Mathieu and D. Senechal, *Conformal Field Theory*. Springer, New York, USA, 1997.

[84] G. Mussardo, *Statistical Field Theory: An Introduction to Exactly Solved Models in Statistical Physics*, Oxford Graduate Texts. OUP Oxford, 2009.

[85] F. Iglói and C. Monthus, *Strong disorder RG approach of random systems*, *Phys. Rep.* **412** (2005) .

[86] G. Refael and J. E. Moore, *Entanglement Entropy of Random Quantum Critical Points in One Dimension*, *Phys. Rev. Lett.* **93** (2004) 260602.

[87] G. Vitagliano, A. Riera and J. I. Latorre, *Volume-law scaling for the entanglement entropy in spin-1/2 chains*, *New J. Phys.* **12** (2010) 113049.

[88] R. Movassagh and P. W. Shor, *Supercritical entanglement in local systems: Counterexample to the area law for quantum matter*, *PNAS* **113** (2016) 13278.

[89] O. Salberger and V. Korepin, *Fredkin spin chains*, [1605.03842].

[90] Z. Zhang, A. Ahmadain and I. Klich, *Novel quantum phase transition from bounded to extensive entanglement*, *PNAS* **114** (2017) 5142.

[91] V. Alba, S. N. Santalla, P. Ruggiero, J. Rodriguez-Laguna, P. Calabrese and G. Sierra, *Unusual area-law violation in random inhomogeneous systems*, *J. Stat. Mech.* **2019** (2019) 023105.

[92] V. Eisler and Z. Zimborás, *Entanglement negativity in two-dimensional free lattice models*, *Phys. Rev. B* **93** (2016) 115148.

[93] C. De Nobili, A. Coser and E. Tonni, *Entanglement negativity in a two dimensional harmonic lattice: area law and corner contributions*, *J. Stat. Mech.* **2016** (2016) 083102.

[94] P. Calabrese, J. Cardy and E. Tonni, *Entanglement Negativity in Quantum Field Theory*, *Phys. Rev. Lett.* **109** (2012) 130502.

[95] P. Ruggiero, V. Alba and P. Calabrese, *Entanglement negativity in random spin chains*, *Phys. Rev. B* **94** (2016) 035152.

[96] C. Castelnovo, *Negativity and topological order in the toric code*, *Phys. Rev. A* **88** (2013) 042319.

[97] Y. A. Lee and G. Vidal, *Entanglement negativity and topological order*, *Phys. Rev. A* **88** (2013) 042318.

[98] A. Kitaev, *Fault-tolerant quantum computation by anyons*, *Ann. Phys.* **303** (2003) 2 .

[99] R. B. Laughlin, *Anomalous Quantum Hall Effect: An Incompressible Quantum Fluid with Fractionally Charged Excitations*, *Phys. Rev. Lett.* **50** (1983) 1395.

[100] S. Ryu and T. Takayanagi, *Holographic Derivation of Entanglement Entropy from the anti–de Sitter Space/Conformal Field Theory Correspondence*, *Phys. Rev. Lett.* **96** (2006) 181602.

[101] S. Ryu and T. Takayanagi, *Aspects of holographic entanglement entropy*, *JHEP* **2006** (2006) 045.

[102] J. Maldacena, *The Large-N Limit of Superconformal Field Theories and Supergravity*, *Int. J. Theor. Phys.* **38** (1999) 1113.

[103] G. T. Hooft, *Dimensional Reduction in Quantum Gravity*, [9310026].

[104] L. Susskind, *The world as a hologram*, *J. Math. Phys.* **36** (1995) 6377.

[105] A. B. Zomolodchikov, *"Irreversibility" of the flux of the renormalization group in a 2D field theory*, *J. Exp. Theor. Phys.* **43** (1986) 730.

[106] H. Casini and M. Huerta, *A finite entanglement entropy and the c-theorem*, *Phys. Lett. B* **600** (2004) 142 .

[107] H. Casini and M. Huerta, *A c-theorem for entanglement entropy*, *J. Phys. A* **40** (2007) 7031.

[108] J. L. Cardy, *Is there a c-theorem in four dimensions?*, *Phys. Lett. B* **215** (1988) 749 .

[109] Z. Komargodski and A. Schwimmer, *On renormalization group flows in four dimensions*, *JHEP* **2011** (2011) 99.

[110] Z. Komargodski, *The constraints of conformal symmetry on RG flows*, *JHEP* **2012** (2012) 69.

[111] R. C. Myers and A. Sinha, *Seeing a c-theorem with holography*, *Phys. Rev. D* **82** (2010) 046006.

[112] R. C. Myers and A. Sinha, *Holographic c-theorems in arbitrary dimensions*, *JHEP* **2011** (2011) 125.

[113] I. R. Klebanov, S. S. Pufu and B. R. Safdi, *F-theorem without supersymmetry*, *JHEP* **2011** (2011) 38.

[114] D. L. Jafferis, I. R. Klebanov, S. S. Pufu and B. R. Safdi, *Towards the F-theorem: $\mathcal{N} = 2$ field theories on the three-sphere*, *JHEP* **2011** (2011) 102.

[115] H. Casini and M. Huerta, *Renormalization group running of the entanglement entropy of a circle*, *Phys. Rev. D* **85** (2012) 125016.

[116] H. Casini, I. S. Landea and G. Torroba, *The g-theorem and quantum information theory*, *JHEP* **2016** (2016) 140.

[117] A. Polkovnikov, K. Sengupta, A. Silva and M. Vengalattore, *Colloquium: Nonequilibrium dynamics of closed interacting quantum systems*, *Rev. Mod. Phys.* **83** (2011) 863.

[118] C. Gogolin and J. Eisert, *Equilibration, thermalisation, and the emergence of statistical mechanics in closed quantum systems*, *Rep. Prog. Phys.* **79** (2016) 056001.

[119] P. Calabrese, F. H. Essler and G. Mussardo, *Quantum Integrability in Out of Equilibrium Systems*, *J. Stat. Phys.* (2016) .

[120] P. Calabrese and J. Cardy, *Time dependence of correlation functions following a quantum quench*, *Phys. Rev. Lett.* **96** (2006) 136801.

[121] P. Calabrese and J. Cardy, *Quantum quenches in extended systems*, *J. Stat. Mech.* **06** (2007) .

[122] P. Calabrese and J. Cardy, *Quantum quenches in $1+1$ dimensional conformal field theories*, *J. Stat. Mech.* **2016** (2016) 064003.

[123] P. Calabrese and J. Cardy, *Entanglement and correlation functions following a local quench: a conformal field theory approach*, *J. Stat. Mech.* **11** (2007) .

[124] M. Fagotti and P. Calabrese, *Evolution of entanglement entropy following a quantum quench: Analytic results for the XY chain in a transverse magnetic field*, *Phys. Rev. A* **78** (2008) 010306.

[125] V. Alba and P. Calabrese, *Entanglement and thermodynamics after a quantum quench in integrable systems*, *PNAS* **114** (2017) 7947.

[126] V. Alba and P. Calabrese, *Entanglement dynamics after quantum quenches in generic integrable systems*, *SciPost Phys.* **4** (2018) 17.

[127] V. Alba and P. Calabrese, *Quantum information dynamics in multipartite integrable systems*, *EPL* **126** (2019) 60001.

[128] G. D. Chiara, S. Montangero, P. Calabrese and R. Fazio, *Entanglement entropy dynamics of Heisenberg chains*, *J. Stat. Mech.* **2006** (2006) P03001.

[129] A. M. Läuchli and C. Kollath, *Spreading of correlations and entanglement after a quench in the one-dimensional Bose-Hubbard model*, *J. Stat. Mech.* **2008** (2008) P05018.

[130] V. Balasubramanian, A. Bernamonti, N. Copland, B. Craps and F. Galli, *Thermalization of mutual and tripartite information in strongly coupled two dimensional conformal field theories*, *Phys. Rev. D* **84** (2011) 105017.

[131] H. Kim and D. A. Huse, *Ballistic Spreading of Entanglement in a Diffusive Nonintegrable System*, *Phys. Rev. Lett.* **111** (2013) 127205.

[132] H. Liu and S. J. Suh, *Entanglement growth during thermalization in holographic systems*, *Phys. Rev. D* **89** (2014) 066012.

[133] H. Liu and S. J. Suh, *Entanglement Tsunami: Universal Scaling in Holographic Thermalization*, *Phys. Rev. Lett.* **112** (2014) 011601.

[134] M. Mezei and D. Stanford, *On entanglement spreading in chaotic systems*, *JHEP* **05** (2017) 065.

[135] A. Nahum, J. Ruhman, S. Vijay and J. Haah, *Quantum Entanglement Growth under Random Unitary Dynamics*, *Phys. Rev. X* **7** (2017) 031016.

[136] T. Giamarchi and H. J. Schulz, *Localization and Interaction in One-Dimensional Quantum Fluids*, *EPL* **3** (1987) 1287.

[137] I. V. Gornyi, A. D. Mirlin and D. G. Polyakov, *Interacting Electrons in Disordered Wires: Anderson Localization and Low-T Transport*, *Phys. Rev. Lett.* **95** (2005) 206603.

[138] D. Basko, I. Aleiner and B. Altshuler, *Metal–insulator transition in a weakly interacting many-electron system with localized single-particle states*, *Ann. Phys.* **321** (2006) 1126 .

[139] X. Chen, T. Zhou, D. A. Huse and E. Fradkin, *Out-of-time-order correlations in many-body localized and thermal phases*, *Annalen der Physik* **529** (2017) 1600332.

[140] Y. Huang, Y.-L. Zhang and X. Chen, *Out-of-time-ordered correlators in many-body localized systems*, *Annalen der Physik* **529** (2017) 1600318.

[141] R. Fan, P. Zhang, H. Shen and H. Zhai, *Out-of-time-order correlation for many-body localization*, *Science Bulletin* **62** (2017) 707 .

[142] P. Calabrese and A. Lefevre, *Entanglement spectrum in one-dimensional systems*, *Phys. Rev. A* **78** (2008) 032329.

[143] N. Lashkari, *Relative Entropies in Conformal Field Theory*, *Phys. Rev. Lett.* **113** (2014) 051602.

[144] N. Lashkari, *Modular Hamiltonian for Excited States in Conformal Field Theory*, *Phys. Rev. Lett.* **117** (2016) 041601.

[145] P. Calabrese, J. Cardy and E. Tonni, *Entanglement negativity in extended systems: a field theoretical approach*, *J. Stat. Mech.* **2013** (2013) P02008.

[146] J. Zhang, P. Ruggiero and P. Calabrese, *Subsystem Trace Distance in Quantum Field Theory*, *Phys. Rev. Lett.* **122** (2019) 141602.

[147] J. Zhang, P. Ruggiero and P. Calabrese, *Subsystem trace distance in low-lying states of conformal field theories*, [1907.04332].

[148] J. Cardy, O. Castro-Alvaredo and B. Doyon, *Form Factors of Branch-Point Twist Fields in Quantum Integrable Models and Entanglement Entropy*, *J. Stat. Phys.* **130** (2008) 129.

[149] O. A. Castro-Alvaredo and B. Doyon, *Bi-partite entanglement entropy in massive $(1+1)$-dimensional quantum field theories*, *J. Phys. A* **42** (2009) 504006.

[150] O. Blondeau-Fournier, O. A. Castro-Alvaredo and B. Doyon, *Universal scaling of the logarithmic negativity in massive quantum field theory*, *J. Phys. A* **49** (2016) 125401.

[151] D. Bianchini and O. A. Castro-Alvaredo, *Branch point twist field correlators in the massive free Boson theory*, *Nucl. Phys. B* **913** (2016) 879 .

[152] O. A. Castro-Alvaredo and B. Doyon, *Bi-partite entanglement entropy in integrable models with backscattering*, *J. Phys. A* **41** (2008) 275203.

[153] O. A. Castro-Alvaredo and E. Levi, *Higher particle form factors of branch point twist fields in integrable quantum field theories*, *J. Phys. A* **44** (2011) 255401.

[154] D. Bianchini, O. A. Castro-Alvaredo and B. Doyon, *Entanglement entropy of non-unitary integrable quantum field theory*, *Nucl. Phys. B* **896** (2015) 835 .

[155] K. Ohmori and Y. Tachikawa, *Physics at the entangling surface*, *J. Stat. Mech.* **2015** (2015) P04010.

[156] J. Cardy and E. Tonni, *Entanglement Hamiltonians in two-dimensional conformal field theory*, *J. Stat. Mech.* **2016** (2016) 123103.

[157] V. Alba, P. Calabrese and E. Tonni, *Entanglement spectrum degeneracy and the Cardy formula in 1+1 dimensional conformal field theories*, *J. Phys. A* **51** (2017) 024001.

[158] T. Dupic, B. Estienne and Y. Ikhlef, *Entanglement entropies of minimal models from null-vectors*, *SciPost Phys.* **4** (2018) 031.

[159] J. Dubail, J.-M. Stéphan, J. Viti and P. Calabrese, *Conformal field theory for inhomogeneous one-dimensional quantum systems: the example of non-interacting Fermi gases*, *SciPost Phys.* **2** (2017) 002.

[160] I. Peschel and M.-C. Chung, *Density matrices for a chain of oscillators*, *J. Phys. A* **32** (1999) 8419.

[161] M.-C. Chung and I. Peschel, *Density-matrix spectra of solvable fermionic systems*, *Phys. Rev. B* **64** (2001) 064412.

[162] I. Peschel, *Calculation of reduced density matrices from correlation functions*, *J. Phys. A* **36** (2003) L205.

[163] M.-C. Chung and I. Peschel, *Density-matrix spectra for two-dimensional quantum systems*, *Phys. Rev. B* **62** (2000) 4191.

[164] I. Peschel and V. Eisler, *Reduced density matrices and entanglement entropy in free lattice models*, *J. Phys. A* **42** (2009) 504003.

[165] J. I. Latorre, E. Rico and G. Vidal, *Ground State Entanglement in Quantum Spin Chains*, *Quantum Info. Comput.* **4** (2004) 48.

[166] P. Jordan and E. Wigner, *Über das Paulische Äquivalenzverbot*, *Zeitschrift für Physik* **47** (1928) 631.

[167] V. Alba, L. Tagliacozzo and P. Calabrese, *Entanglement entropy of two disjoint blocks in critical Ising models*, *Phys. Rev. B* **81** (2010) 060411.

[168] F. Iglói and I. Peschel, *On reduced density matrices for disjoint subsystems*, *EPL* **89** (2010) 40001.

[169] M. Fagotti and P. Calabrese, *Entanglement entropy of two disjoint blocks in XY chains*, *J. Stat. Mech.* **2010** (2010) P04016.

[170] E. Vicari, *Entanglement and particle correlations of Fermi gases in harmonic traps*, *Phys. Rev. A* **85** (2012) 062104.

[171] P. Calabrese, M. Mintchev and E. Vicari, *Exact relations between particle fluctuations and entanglement in Fermi gases*, *EPL* **98** (2012) 20003.

[172] P. Calabrese, M. Mintchev and E. Vicari, *Entanglement entropy of quantum wire junctions*, *J. Phys. A* **45** (2012) 105206.

[173] P. Calabrese, M. Mintchev and E. Vicari, *Entanglement Entropy of One-Dimensional Gases*, *Phys. Rev. Lett.* **107** (2011) 020601.

[174] P. Calabrese, M. Mintchev and E. Vicari, *The entanglement entropy of one-dimensional systems in continuous and homogeneous space*, *J. Stat. Mech.* **2011** (2011) P09028.

[175] R. Süsstrunk and D. A. Ivanov, *Free fermions on a line: Asymptotics of the entanglement entropy and entanglement spectrum from full counting statistics*, *EPL* **100** (2012) 60009.

[176] V. Eisler and I. Peschel, *Free-fermion entanglement and spheroidal functions*, *J. Stat. Mech.* **2013** (2013) P04028.

[177] J. Nespolo and E. Vicari, *Equilibrium and nonequilibrium entanglement properties of two- and three-dimensional Fermi gases*, *Phys. Rev. A* **87** (2013) 032316.

[178] M. Collura, S. Sotiriadis and P. Calabrese, *Quench dynamics of a Tonks–Girardeau gas released from a harmonic trap*, *J. Stat. Mech.* **2013** (2013) P09025.

[179] E. Vicari, *Quantum dynamics and entanglement in one-dimensional Fermi gases released from a trap*, *Phys. Rev. A* **85** (2012) 062324.

[180] M. Collura, M. Kormos and P. Calabrese, *Stationary entanglement entropies following an interaction quench in 1D Bose gas*, *J. Stat. Mech.* **2014** (2014) P01009.

[181] A. Ossipov, *Entanglement Entropy in Fermi Gases and Anderson's Orthogonality Catastrophe*, *Phys. Rev. Lett.* **113** (2014) 130402.

[182] S. A. Hartnoll and E. A. Mazenc, *Entanglement Entropy in Two-Dimensional String Theory*, *Phys. Rev. Lett.* **115** (2015) 121602.

[183] P.-Y. Chang and X. Wen, *Entanglement negativity in free-fermion systems: An overlap matrix approach*, *Phys. Rev. B* **93** (2016) 195140.

[184] B. Lacroix-A-Chez-Toine, S. N. Majumdar and G. Schehr, *Rotating trapped fermions in two dimensions and the complex Ginibre ensemble: Exact results for the entanglement entropy and number variance*, *Phys. Rev. A* **99** (2019) 021602.

[185] I. Klich, *Lower entropy bounds and particle number fluctuations in a Fermi sea*, *J. Phys. A* **39** (2006) .

[186] F. Iglói, R. Juhász and H. Rieger, *Random antiferromagnetic quantum spin chains: Exact results from scaling of rare regions*, *Phys. Rev. B* **61** (2000) 11552.

[187] S.-k. Ma, C. Dasgupta and C.-k. Hu, *Random Antiferromagnetic Chain*, *Phys. Rev. Lett.* **43** (1979) 1434.

[188] D. S. Fisher, *Critical behavior of random transverse-field Ising spin chains*, *Phys. Rev. B* **51** (1995) 6411.

[189] M. Rangamani and T. Takayanagi, *Holographic Entanglement Entropy*. Springer, Cham, Switzerland, 2017, 10.1007/978-3-319-52573-0.

[190] T. Nishioka, S. Ryu and T. Takayanagi, *Holographic entanglement entropy: an overview*, *J. Phys. A* **42** (2009) 504008.

[191] T. Nishioka, *Entanglement entropy: Holography and renormalization group*, *Rev. Mod. Phys.* **90** (2018) 035007.

[192] H. Casini and M. Huerta, *Entanglement entropy in free quantum field theory*, *J. Phys. A* **42** (2009) 504007.

[193] E. L. Basor and C. A. Tracy, *The Fisher-Hartwig conjecture and generalizations*, *Physica A* **177** (1991) 167.

[194] E. L. Basor, *A Localization Theorem for Toeplitz Determinants*, *Indiana Math. J.* **28** (1979) 975.

[195] B.-Q. Jin and V. E. Korepin, *Quantum Spin Chain, Toeplitz Determinants and the Fisher-Hartwig Conjecture*, *J. Stat. Phys.* **116** (2004) 79.

[196] P. Calabrese and F. H. L. Essler, *Universal corrections to scaling for block entanglement in spin-1/2 XX chains*, *J. Stat. Mech.* **2010** (2010) P08029.

[197] R. Bonsignori, P. Ruggiero and P. Calabrese, *Symmetry resolved entanglement in free fermionic systems*, [1907.02084].

[198] F. Ares, J. G. Esteve, F. Falceto and E. Sánchez-Burillo, *Excited state entanglement in homogeneous fermionic chains*, *J. Phys. A* **47** (2014) 245301.

[199] F. Ares, J. G. Esteve and F. Falceto, *Entanglement of several blocks in fermionic chains*, *Phys. Rev. A* **90** (2014) 062321.

[200] A. G. Abanov and F. Franchini, *Emptiness formation probability for the anisotropic XY spin chain in a magnetic field*, *Phys. Lett. A* **316** (2003) 342 .

[201] F. Franchini and A. G. Abanov, *Asymptotics of Toeplitz determinants and the emptiness formation probability for the XY spin chain*, *J. Phys. A* **38** (2005) 5069.

[202] P. Buividovich and M. Polikarpov, *Numerical study of entanglement entropy in SU(2) lattice gauge theory*, *Nucl. Phys. B* **802** (2008) 458 .

[203] V. Alba, L. Tagliacozzo and P. Calabrese, *Entanglement entropy of two disjoint intervals in $c = 1$ theories*, *J. Stat. Mech.* **2011** (2011) P06012.

[204] M. Caraglio and F. Gliozzi, *Entanglement entropy and twist fields*, *JHEP* **2008** (2008) 076.

[205] F. Gliozzi and L. Tagliacozzo, *Entanglement entropy and the complex plane of replicas*, *J. Stat. Mech.* **2010** (2010) P01002.

[206] V. Alba, *Entanglement negativity and conformal field theory: a Monte Carlo study*, *J. Stat. Mech.* **2013** (2013) P05013.

[207] C.-M. Chung, V. Alba, L. Bonnes, P. Chen and A. M. Läuchli, *Entanglement negativity via the replica trick: A quantum Monte Carlo approach*, *Phys. Rev. B* **90** (2014) 064401.

[208] N. M. Tubman and D. C. Yang, *Calculating the entanglement spectrum in quantum Monte Carlo with application to ab initio Hamiltonians*, *Phys. Rev. B* **90** (2014) 081116.

[209] M. B. Hastings, I. González, A. B. Kallin and R. G. Melko, *Measuring Renyi Entanglement Entropy in Quantum Monte Carlo Simulations*, *Phys. Rev. Lett.* **104** (2010) 157201.

[210] R. G. Melko, A. B. Kallin and M. B. Hastings, *Finite-size scaling of mutual information in Monte Carlo simulations: Application to the spin-$\frac{1}{2}$ XXZ model*, *Phys. Rev. B* **82** (2010) 100409.

[211] R. R. P. Singh, M. B. Hastings, A. B. Kallin and R. G. Melko, *Finite-Temperature Critical Behavior of Mutual Information*, *Phys. Rev. Lett.* **106** (2011) 135701.

[212] S. Humeniuk and T. Roscilde, *Quantum Monte Carlo calculation of entanglement Rényi entropies for generic quantum systems*, *Phys. Rev. B* **86** (2012) 235116.

[213] G. Vidal, *Entanglement Renormalization*, *Phys. Rev. Lett.* **99** (2007) 220405.

[214] G. Vidal, *Class of Quantum Many-Body States That Can Be Efficiently Simulated*, *Phys. Rev. Lett.* **101** (2008) 110501.

[215] F. Verstraete and J. I. Cirac, *Renormalization algorithms for Quantum-Many Body Systems in two and higher dimensions*, [0407066].

[216] I. Klich, G. Refael and A. Silva, *Measuring entanglement entropies in many-body systems*, *Phys. Rev. A* **74** (2006) 032306.

[217] I. Klich and L. Levitov, *Quantum Noise as an Entanglement Meter*, *Phys. Rev. Lett.* **102** (2009) 100502.

[218] H. F. Song, C. Flindt, S. Rachel, I. Klich and K. Le Hur, *Entanglement entropy from charge statistics: Exact relations for noninteracting many-body systems*, *Phys. Rev. B* **83** (2011) 161408.

[219] H. F. Song, S. Rachel, C. Flindt, I. Klich, N. Laflorencie and K. Le Hur, *Bipartite fluctuations as a probe of many-body entanglement*, *Phys. Rev. B* **85** (2012) 035409.

[220] B. Hsu, E. Grosfeld and E. Fradkin, *Quantum noise and entanglement generated by a local quantum quench*, *Phys. Rev. B* **80** (2009) 235412.

[221] H. Häffner, W. Hänsel, C. F. Roos, J. Benhelm, D. Chek-al kar, M. Chwalla et al., *Scalable multiparticle entanglement of trapped ions*, *Nature* **438** (2005) 643.

[222] R. Blatt and D. Wineland, *Entangled states of trapped atomic ions*, *Nature* **453** (2008) .

[223] M. Steffen, M. Ansmann, R. C. Bialczak, N. Katz, E. Lucero, R. McDermott et al., *Measurement of the Entanglement of Two Superconducting Qubits via State Tomography*, *Science* **313** (2006) 1423.

[224] C. Song, K. Xu, W. Liu, C.-p. Yang, S.-B. Zheng, H. Deng et al., *10-Qubit Entanglement and Parallel Logic Operations with a Superconducting Circuit*, *Phys. Rev. Lett.* **119** (2017) 180511.

[225] A. K. Ekert, C. M. Alves, D. K. L. Oi, M. Horodecki, P. Horodecki and L. C. Kwek, *Direct Estimations of Linear and Nonlinear Functionals of a Quantum State*, *Phys. Rev. Lett.* **88** (2002) 217901.

[226] J. Cardy, *Measuring Entanglement Using Quantum Quenches*, *Phys. Rev. Lett.* **106** (2011) 150404.

[227] D. A. Abanin and E. Demler, *Measuring Entanglement Entropy of a Generic Many-Body System with a Quantum Switch*, *Phys. Rev. Lett.* **109** (2012) 020504.

[228] C. Moura Alves and D. Jaksch, *Multipartite Entanglement Detection in Bosons*, *Phys. Rev. Lett.* **93** (2004) 110501.

[229] A. J. Daley, H. Pichler, J. Schachenmayer and P. Zoller, *Measuring Entanglement Growth in Quench Dynamics of Bosons in an Optical Lattice*, *Phys. Rev. Lett.* **109** (2012) 020505.

[230] H. Pichler, L. Bonnes, A. J. Daley, A. M. Läuchli and P. Zoller, *Thermal versus entanglement entropy: a measurement protocol for fermionic atoms with a quantum gas microscope*, *New J. Phys.* **15** (2013) 063003.

[231] C. K. Hong, Z. Y. Ou and L. Mandel, *Measurement of subpicosecond time intervals between two photons by interference*, *Phys. Rev. Lett.* **59** (1987) 2044.

[232] J. Unmuth-Yockey, J. Zhang, P. M. Preiss, L.-P. Yang, S.-W. Tsai and Y. Meurice, *Probing the conformal Calabrese-Cardy scaling with cold atoms*, *Phys. Rev. A* **96** (2017) 023603.

[233] A. Elben, B. Vermersch, M. Dalmonte, J. I. Cirac and P. Zoller, *Rényi Entropies from Random Quenches in Atomic Hubbard and Spin Models*, *Phys. Rev. Lett.* **120** (2018) 050406.

[234] S. J. van Enk and C. W. J. Beenakker, *Measuring* $\mathrm{Tr}\rho^n$ *on Single Copies of* ρ *Using Random Measurements*, *Phys. Rev. Lett.* **108** (2012) 110503.

[235] W. S. Bakr, A. Peng, M. E. Tai, R. Ma, J. Simon, J. I. Gillen et al., *Probing the Superfluid–to–Mott Insulator Transition at the Single-Atom Level*, *Science* **329** (2010) 547.

[236] J. F. Sherson, C. Weitenberg, M. Endres, M. Cheneau, I. Bloch and S. Kuhr, *Single-atom-resolved fluorescence imaging of an atomic Mott insulator*, *Nature* **467** (2010) .

[237] T. D. Ladd, F. Jelezko, R. Laflamme, Y. Nakamura, C. Monroe and J. L. O'Brien, *Quantum computers*, *Nature* **464** (2010) .

[238] C. Monroe and J. Kim, *Scaling the Ion Trap Quantum Processor*, *Science* **339** (2013) 1164.

[239] M. H. Devoret and R. J. Schoelkopf, *Superconducting Circuits for Quantum Information: An Outlook*, *Science* **339** (2013) 1169.

[240] D. D. Awschalom, L. C. Bassett, A. S. Dzurak, E. L. Hu and J. R. Petta, *Quantum Spintronics: Engineering and Manipulating Atom-Like Spins in Semiconductors*, *Science* **339** (2013) 1174.

[241] H. Bernien, S. Schwartz, A. Keesling, H. Levine, A. Omran, H. Pichler et al., *Probing many-body dynamics on a 51-atom quantum simulator*, *Nature* **551** (2017) .

[242] J. Gray, L. Banchi, A. Bayat and S. Bose, *Machine-Learning-Assisted Many-Body Entanglement Measurement*, *Phys. Rev. Lett.* **121** (2018) 150503.

[243] H. A. Carteret, *Noiseless Quantum Circuits for the Peres Separability Criterion*, *Phys. Rev. Lett.* **94** (2005) 040502.

[244] H. Carteret, *Estimating the Entanglement Negativity from low-order moments of the partially transposed density matrix*, [1605.08751].

[245] E. Cornfeld, E. Sela and M. Goldstein, *Measuring fermionic entanglement: Entropy, negativity, and spin structure*, *Phys. Rev. A* **99** (2019) 062309.

[246] P. Calabrese, L. Tagliacozzo and E. Tonni, *Entanglement negativity in the critical Ising chain*, *J. Stat. Mech.* **2013** (2013) P05002.

[247] S. Furukawa, V. Pasquier and J. Shiraishi, *Mutual Information and Boson Radius in a $c = 1$ Critical System in One Dimension*, *Phys. Rev. Lett.* **102** (2009) 170602.

[248] P. Calabrese, J. Cardy and E. Tonni, *Entanglement entropy of two disjoint intervals in conformal field theory*, *J. Stat. Mech.* **2009** (2009) P11001.

[249] P. Calabrese, J. Cardy and E. Tonni, *Entanglement entropy of two disjoint intervals in conformal field theory: II*, *J. Stat. Mech.* **2011** (2011) P01021.

[250] A. Coser, L. Tagliacozzo and E. Tonni, *On Rényi entropies of disjoint intervals in conformal field theory*, *J. Stat. Mech.* **2014** (2014) P01008.

[251] H. Wichterich, J. Molina-Vilaplana and S. Bose, *Scaling of entanglement between separated blocks in spin chains at criticality*, *Phys. Rev. A* **80** (2009) 010304.

[252] S. Marcovitch, A. Retzker, M. B. Plenio and B. Reznik, *Critical and noncritical long-range entanglement in Klein-Gordon fields*, *Phys. Rev. A* **80** (2009) 012325.

[253] H. Wichterich, J. Vidal and S. Bose, *Universality of the negativity in the Lipkin-Meshkov-Glick model*, *Phys. Rev. A* **81** (2010) 032311.

[254] P. Calabrese, J. Cardy and E. Tonni, *Finite temperature entanglement negativity in conformal field theory*, *J. Phys. A* **48** (2015) 015006.

[255] M. Kulaxizi, A. Parnachev and G. Policastro, *Conformal blocks and negativity at large central charge*, *JHEP* **2014** (2014) 10.

[256] Coser, E. Tonni and P. Calabrese, *Entanglement negativity after a global quantum quench*, *J. Stat. Mech.* **2014** (2014) P12017.

[257] M. Hoogeveen and B. Doyon, *Entanglement negativity and entropy in non-equilibrium conformal field theory*, *Nucl. Phys. B* **898** (2015) 78 .

[258] V. Eisler and Z. Zimborás, *Entanglement negativity in the harmonic chain out of equilibrium*, *New J. Phys.* **16** (2014) 123020.

[259] X. Wen, P.-Y. Chang and S. Ryu, *Entanglement negativity after a local quantum quench in conformal field theories*, *Phys. Rev. B* **92** (2015) 075109.

[260] M. Rangamani and M. Rota, *Comments on entanglement negativity in holographic field theories*, *JHEP* **2014** (2014) 60.

[261] E. Perlmutter, M. Rangamani and M. Rota, *Central Charges and the Sign of Entanglement in 4D Conformal Field Theories*, *Phys. Rev. Lett.* **115** (2015) 171601.

[262] C. Castelnovo, *Distilling topological entropy from a single measurement of entanglement on projected systems*, *Phys. Rev. A* **89** (2014) 042333.

[263] A. Bayat, P. Sodano and S. Bose, *Negativity as the entanglement measure to probe the Kondo regime in the spin-chain Kondo model*, *Phys. Rev. B* **81** (2010) 064429.

[264] A. Bayat, H. Johannesson, S. Bose and P. Sodano, *An order parameter for impurity systems at quantum criticality*, *Nat. Commun.* **5** (2014) .

[265] B. Alkurtass, A. Bayat, I. Affleck, S. Bose, H. Johannesson, P. Sodano et al., *Entanglement structure of the two-channel Kondo model*, *Phys. Rev. B* **93** (2016) 081106.

[266] X. Wen, S. Matsuura and S. Ryu, *Edge theory approach to topological entanglement entropy, mutual information, and entanglement negativity in Chern-Simons theories*, *Phys. Rev. B* **93** (2016) 245140.

[267] X. Wen, P.-Y. Chang and S. Ryu, *Topological entanglement negativity in Chern-Simons theories*, *JHEP* **2016** (2016) 12.

[268] K. Audenaert, J. Eisert, M. B. Plenio and R. F. Werner, *Entanglement properties of the harmonic chain*, *Phys. Rev. A* **66** (2002) 042327.

[269] N. Regnault, B. A. Bernevig and F. D. M. Haldane, *Topological Entanglement and Clustering of Jain Hierarchy States*, *Phys. Rev. Lett.* **103** (2009) 016801.

[270] L. Fidkowski, *Entanglement Spectrum of Topological Insulators and Superconductors*, *Phys. Rev. Lett.* **104** (2010) 130502.

[271] A. M. Läuchli, E. J. Bergholtz, J. Suorsa and M. Haque, *Disentangling Entanglement Spectra of Fractional Quantum Hall States on Torus Geometries*, *Phys. Rev. Lett.* **104** (2010) 156404.

[272] R. Thomale, A. Sterdyniak, N. Regnault and B. A. Bernevig, *Entanglement Gap and a New Principle of Adiabatic Continuity*, *Phys. Rev. Lett.* **104** (2010) 180502.

[273] H. Yao and X.-L. Qi, *Entanglement Entropy and Entanglement Spectrum of the Kitaev Model*, *Phys. Rev. Lett.* **105** (2010) 080501.

[274] F. Pollmann, A. M. Turner, E. Berg and M. Oshikawa, *Entanglement spectrum of a topological phase in one dimension*, *Phys. Rev. B* **81** (2010) 064439.

[275] N. Regnault and B. A. Bernevig, *Fractional Chern Insulator*, *Phys. Rev. X* **1** (2011) 021014.

[276] J. Dubail and N. Read, *Entanglement Spectra of Complex Paired Superfluids*, *Phys. Rev. Lett.* **107** (2011) 157001.

[277] D. Poilblanc, N. Schuch, D. Pérez-García and J. I. Cirac, *Topological and entanglement properties of resonating valence bond wave functions*, *Phys. Rev. B* **86** (2012) 014404.

[278] L. Cincio and G. Vidal, *Characterizing Topological Order by Studying the Ground States on an Infinite Cylinder*, *Phys. Rev. Lett.* **110** (2013) 067208.

[279] S. Furukawa and M. Ueda, *Integer Quantum Hall State in Two-Component Bose Gases in a Synthetic Magnetic Field*, *Phys. Rev. Lett.* **111** (2013) 090401.

[280] B. Bauer, L. Cincio, B. P. Keller, M. Dolfi, G. Vidal, S. Trebst et al., *Chiral spin liquid and emergent anyons in a Kagome lattice Mott insulator*, *Nat. Commun.* **5** (2014) .

[281] M. A. Metlitski and T. Grover, *Entanglement Entropy of Systems with Spontaneously Broken Continuous Symmetry*, [1112.5166].

[282] V. Alba, M. Haque and A. M. Läuchli, *Entanglement Spectrum of the Two-Dimensional Bose-Hubbard Model*, *Phys. Rev. Lett.* **110** (2013) 260403.

[283] F. Kolley, S. Depenbrock, I. P. McCulloch, U. Schollwöck and V. Alba, *Entanglement spectroscopy of SU(2)-broken phases in two dimensions*, *Phys. Rev. B* **88** (2013) 144426.

[284] I. Frérot and T. Roscilde, *Entanglement Entropy across the Superfluid-Insulator Transition: A Signature of Bosonic Criticality*, *Phys. Rev. Lett.* **116** (2016) 190401.

[285] Z.-C. Yang, C. Chamon, A. Hamma and E. R. Mucciolo, *Two-Component Structure in the Entanglement Spectrum of Highly Excited States*, *Phys. Rev. Lett.* **115** (2015) 267206.

[286] S. D. Geraedts, R. Nandkishore and N. Regnault, *Many-body localization and thermalization: Insights from the entanglement spectrum*, *Phys. Rev. B* **93** (2016) 174202.

[287] M. Serbyn, A. A. Michailidis, D. A. Abanin and Z. Papic, *Power-Law Entanglement Spectrum in Many-Body Localized Phases*, *Phys. Rev. Lett.* **117** (2016) 160601.

[288] A. M. Läuchli, *Operator content of real-space entanglement spectra at conformal critical points*, [1303.0741].

[289] F. Pollmann, S. Mukerjee, A. M. Turner and J. E. Moore, *Theory of Finite-Entanglement Scaling at One-Dimensional Quantum Critical Points*, *Phys. Rev. Lett.* **102** (2009) 255701.

[290] B. Pirvu, G. Vidal, F. Verstraete and L. Tagliacozzo, *Matrix product states for critical spin chains: Finite-size versus finite-entanglement scaling*, *Phys. Rev. B* **86** (2012) 075117.

[291] A. Sanpera, R. Tarrach and G. Vidal, *Local description of quantum inseparability*, *Phys. Rev. A* **58** (1998) 826.

[292] S. Rana, *Negative eigenvalues of partial transposition of arbitrary bipartite states*, *Phys. Rev. A* **87** (2013) 054301.

[293] N. I. Akhiezer, *The Classical Moment Problem*. 1965.

[294] B. Simon, *The Classical Moment Problem as a Self-Adjoint Finite Difference Operator*, *Adv. Math.* **137** (1998) .

[295] V. Eisler and Z. Zimborás, *On the partial transpose of fermionic Gaussian states*, *New J. Phys.* **17** (2015) 053048.

[296] A. Coser, E. Tonni and P. Calabrese, *Partial transpose of two disjoint blocks in XY spin chains*, *J. Stat. Mech.* **2015** (2015) P08005.

[297] A. Coser, E. Tonni and P. Calabrese, *Towards the entanglement negativity of two disjoint intervals for a one dimensional free fermion*, *J. Stat. Mech.* **2016** (2016) 033116.

[298] A. Coser, E. Tonni and P. Calabrese, *Spin structures and entanglement of two disjoint intervals in conformal field theories*, *J. Stat. Mech.* **2016** (2016) 053109.

[299] C. P. Herzog and Y. Wang, *Estimation for entanglement negativity of free fermions*, *J. Stat. Mech.* **2016** (2016) 073102.

[300] C. De Nobili, A. Coser and E. Tonni, *Entanglement entropy and negativity of disjoint intervals in CFT: some numerical extrapolations*, *J. Stat. Mech.* **2015** (2015) P06021.

[301] F. Pollmann and J. E. Moore, *Entanglement spectra of critical and near-critical systems in one dimension*, *New J. Phys.* **12** (2010) 025006.

[302] N. Laflorencie and S. Rachel, *Spin-resolved entanglement spectroscopy of critical spin chains and Luttinger liquids*, *J. Stat. Mech.* **2014** (2014) P11013.

[303] P. Calabrese, M. Campostrini, F. Essler and B. Nienhuis, *Parity Effects in the Scaling of Block Entanglement in Gapless Spin Chains*, *Phys. Rev. Lett.* **104** (2010) 095701.

[304] I. Peschel and T. T. Truong, *Corner transfer matrices and conformal invariance*, *Zeitschrift für Physik B* **69** (1987) 385.

[305] N. Laflorencie, E. S. Sørensen, M.-S. Chang and I. Affleck, *Boundary Effects in the Critical Scaling of Entanglement Entropy in 1D Systems*, *Phys. Rev. Lett.* **96** (2006) 100603.

[306] I. Affleck, N. Laflorencie and E. S. Sørensen, *Entanglement entropy in quantum impurity systems and systems with boundaries*, *J. Phys. A* **42** (2009) 504009.

[307] J. Cardy and P. Calabrese, *Unusual corrections to scaling in entanglement entropy*, *J. Stat. Mech.* **2010** (2010) P04023.

[308] M. Fagotti and P. Calabrese, *Universal parity effects in the entanglement entropy ofXXchains with open boundary conditions*, *J. Stat. Mech.* **2011** (2011) P01017.

[309] H. Pichler, G. Zhu, A. Seif, P. Zoller and M. Hafezi, *Measurement Protocol for the Entanglement Spectrum of Cold Atoms*, *Phys. Rev. X* **6** (2016) 041033.

[310] H. Shapourian, P. Ruggiero, S. Ryu and P. Calabrese, *Twisted and untwisted negativity spectrum of free fermions*, [1906.04211].

[311] J. Eisert, V. Eisler and Z. Zimborás, *Entanglement negativity bounds for fermionic Gaussian states*, *Phys. Rev. B* **97** (2018) 165123.

[312] H. Shapourian, K. Shiozaki and S. Ryu, *Many-Body Topological Invariants for Fermionic Symmetry-Protected Topological Phases*, *Phys. Rev. Lett.* **118** (2017) 216402.

[313] K. Shiozaki, H. Shapourian, K. Gomi and S. Ryu, *Many-body topological invariants for fermionic short-range entangled topological phases protected by antiunitary symmetries*, *Phys. Rev. B* **98** (2018) 035151.

[314] H. Shapourian, K. Shiozaki and S. Ryu, *Partial time-reversal transformation and entanglement negativity in fermionic systems*, *Phys. Rev. B* **95** (2017) 165101.

[315] H. Shapourian and S. Ryu, *Entanglement negativity of fermions: Monotonicity, Separability criterion, and classification of few-mode states*, *Phys. Rev. A* **99** (2019) 022310.

[316] H. Casini, C. D. Fosco and M. Huerta, *Entanglement and alpha entropies for a massive Dirac field in two dimensions*, *J. Stat. Mech.* **2005** (2005) P07007.

[317] A. Belin, L.-Y. Hung, A. Maloney, S. Matsuura, R. C. Myers and T. Sierens, *Holographic charged Rényi entropies*, *JHEP* **2013** (2013) 59.

[318] J. C. Xavier, F. C. Alcaraz and G. Sierra, *Equipartition of the entanglement entropy*, *Phys. Rev. B* **98** (2018) 041106.

[319] M. Goldstein and E. Sela, *Symmetry-Resolved Entanglement in Many-Body Systems*, *Phys. Rev. Lett.* **120** (2018) 200602.

[320] N. Laflorencie, *Scaling of entanglement entropy in the random singlet phase*, *Phys. Rev. B* **72** (2005) 140408.

[321] M. Fagotti, P. Calabrese and J. E. Moore, *Entanglement spectrum of random-singlet quantum critical points*, *Phys. Rev. B* **83** (2011) 045110.

[322] X. Turkeshi and P. Ruggiero, *To appear* .

[323] F. D. M. Haldane, *Exact Jastrow-Gutzwiller resonating-valence-bond ground state of the spin-$\frac{1}{2}$ antiferromagnetic Heisenberg chain with $1/r^2$ exchange*, *Phys. Rev. Lett.* **60** (1988) 635.

[324] B. S. Shastry, *Exact solution of an S=1/2 Heisenberg antiferromagnetic chain with long-ranged interactions*, *Phys. Rev. Lett.* **60** (1988) 639.

[325] A. Ovchinnikov, *Fisher-Hartwig conjecture and the correlators in XY spin chain*, *Phys. Lett. A* **366** (2007) 357 .

[326] T. Giamarchi, *Quantum physics in one dimension*, vol. 121. Oxford university press, 2004, 10.1093/acprof:oso/9780198525004.001.0001.

[327] A. G. Abanov, *Hydrodynamics of correlated systems. Emptiness Formation Probability and Random Matrices*. Nato Science Series II: Mathematics, Physics and Chemistry, vol. 221 Springer, 2005, 10.1007/1 - 4020-4531 - X5.

[328] P. Ruggiero and P. Calabrese, *Relative entanglement entropies in 1 + 1-dimensional conformal field theories*, *JHEP* **2017** (2017) 39.

[329] H. Casini, E. Testé and G. Torroba, *Relative entropy and the RG flow*, *JHEP* **2017** (2017) 89.

[330] D. Song and E. Winstanley, *Information Erasure and the Generalized Second Law of Black Hole Thermodynamics*, *Int. J. Theor. Phys. Int. J. Theor. Phys.* **47** (2008) 1692.

[331] X.-K. Guo, *Black hole thermodynamics from decoherence*, [1512.05277].

[332] H. Casini, *Relative entropy and the Bekenstein bound*, *Class. Quantum Grav.* **25** (2008) 205021.

[333] D. D. Blanco, H. Casini, L.-Y. Hung and R. C. Myers, *Relative entropy and holography*, *JHEP* **2013** (2013) 60.

[334] D. L. Jafferis, A. Lewkowycz, J. Maldacena and S. J. Suh, *Relative entropy equals bulk relative entropy*, *JHEP* **2016** (2016) 4.

[335] G. Sárosi and T. Ugajin, *Relative entropy of excited states in two dimensional conformal field theories*, *JHEP* **2016** (2016) 114.

[336] G. Sárosi and T. Ugajin, *Relative entropy of excited states in conformal field theories of arbitrary dimensions*, *JHEP* **02** (2017) 060.

[337] T. Ugajin, *Mutual information of excited states and relative entropy of two disjoint subsystems in CFT*, *JHEP* **2017** (2017) 184.

[338] R. E. Arias, D. D. Blanco, H. Casini and M. Huerta, *Local temperatures and local terms in modular Hamiltonians*, *Phys. Rev. D* **95** (2017) 065005.

[339] V. Balasubramanian, J. J. Heckman and A. Maloney, *Relative entropy and proximity of quantum field theories*, *JHEP* **2015** (2015) 104.

[340] P. Caputa and M. M. Rams, *Quantum dimensions from local operator excitations in the Ising model*, *J. Phys. A* **50** (2017) 055002.

[341] J. J. Bisognano and E. H. Wichmann, *On the duality condition for quantum fields*, *J. Math. Phys.* **17** (1976) 303.

[342] J. J. Bisognano and E. H. Wichmann, *On the duality condition for a Hermitian scalar field*, *J. Math. Phys.* **16** (1975) 985.

[343] W. G. Unruh, *Notes on black-hole evaporation*, *Phys. Rev. D* **14** (1976) 870.

[344] P. D. Hislop and R. Longo, *Modular structure of the local algebras associated with the free massless scalar field theory*, *Commun. Math. Phys.* **84** (1982) 71.

[345] H. Casini, M. Huerta and R. C. Myers, *Towards a derivation of holographic entanglement entropy*, *JHEP* **2011** (2011) 36.

[346] G. Wong, I. Klich, L. A. P. Zayas and D. Vaman, *Entanglement temperature and entanglement entropy of excited states*, *JHEP* **2013** (2013) 20.

[347] H.-Q. Zhou, R. Orús and G. Vidal, *Ground State Fidelity from Tensor Network Representations*, *Phys. Rev. Lett.* **100** (2008) 080601.

[348] P. Zanardi and N. Paunkovic, *Ground state overlap and quantum phase transitions*, *Phys. Rev. E* **74** (2006) 031123.

[349] M. I. Berganza, F. C. Alcaraz and G. Sierra, *Entanglement of excited states in critical spin chains*, *J. Stat. Mech.* **2012** (2012) P01016.

[350] T. Pálmai, *Excited state entanglement in one-dimensional quantum critical systems: Extensivity and the role of microscopic details*, *Phys. Rev. B* **90** (2014) 161404.

[351] T. Palmai, *Entanglement entropy from the truncated conformal space*, *Phys. Lett. B* **759** (2016) 439 .

[352] L. Taddia, J. C. Xavier, F. C. Alcaraz and G. Sierra, *Entanglement entropies in conformal systems with boundaries*, *Phys. Rev. B* **88** (2013) 075112.

[353] L. Taddia, F. Ortolani and T. Pálmai, *Renyi entanglement entropies of descendant states in critical systems with boundaries: conformal field theory and spin chains*, *J. Stat. Mech.* **2016** (2016) 093104.

[354] G. Ramírez, J. Rodríguez-Laguna and G. Sierra, *Entanglement in low-energy states of the random-hopping model*, *J. Stat. Mech.* **2014** (2014) P07003.

[355] F. H. L. Essler, A. M. Läuchli and P. Calabrese, *Shell-Filling Effect in the Entanglement Entropies of Spinful Fermions*, *Phys. Rev. Lett.* **110** (2013) 115701.

[356] L. Cevolani, *Unusual Corrections to the Scaling of the Entanglement Entropy of the Excited states in Conformal Field Theory*, [1601.01709].

[357] M. A. Rajabpour and F. Gliozzi, *Entanglement entropy of two disjoint intervals from fusion algebra of twist fields*, *J. Stat. Mech.* **2012** (2012) P02016.

[358] P. Ruggiero, E. Tonni and P. Calabrese, *Entanglement entropy of two disjoint intervals and the recursion formula for conformal blocks*, *J. Stat. Mech.* **2018** (2018) 113101.

[359] V. Alba, M. Fagotti and P. Calabrese, *Entanglement entropy of excited states*, *J. Stat. Mech.* **2009** (2009) P10020.

[360] M. Fagotti and F. H. L. Essler, *Reduced density matrix after a quantum quench*, *Phys. Rev. B* **87** (2013) 245107.

[361] M. Headrick, *Entanglement Rényi entropies in holographic theories*, *Phys. Rev. D* **82** (2010) 126010.

[362] B. Chen and J. Zhang, *On short interval expansion of Rényi entropy*, *JHEP* **2013** (2013) 164.

[363] F.-L. Lin, H. Wang and J. Zhang, *Thermality and excited state Rényi entropy in two-dimensional CFT*, *JHEP* **2016** (2016) 116.

[364] B. Chen, J.-B. Wu and J. Zhang, *Short interval expansion of Rényi entropy on torus*, *JHEP* **2016** (2016) 130.

[365] S. He, F.-L. Lin and J. Zhang, *Subsystem eigenstate thermalization hypothesis for entanglement entropy in CFT*, *JHEP* **2017** (2017) 126.

[366] J. Kurchan, *Replica trick to calculate means of absolute values: applications to stochastic equations*, *J. Phys. A* **24** (1991) 4969.

[367] D. M. Gangardt and A. Kamenev, *Replica treatment of the Calogero–Sutherland model*, *Nucl. Phys. B* **610** (2001) 578 .

[368] S. M. Nishigaki, D. M. Gangardt and A. Kamenev, *Correlation functions of the BC Calogero Sutherland model*, *J. Phys. A* **36** (2003) 3137.

[369] P. Calabrese and R. Santachiara, *Off-diagonal correlations in one-dimensional anyonic models: a replica approach*, *J. Stat. Mech.* **2009** (2009) P03002.

[370] G. Marmorini, M. Pepe and P. Calabrese, *One-body reduced density matrix of trapped impenetrable anyons in one dimension*, *J. Stat. Mech.* **2016** (2016) 073106.

[371] F. C. Alcaraz, M. I. n. Berganza and G. Sierra, *Entanglement of Low-Energy Excitations in Conformal Field Theory*, *Phys. Rev. Lett.* **106** (2011) 201601.

[372] Z. Li and J. Zhang, *On one-loop entanglement entropy of two short intervals from OPE of twist operators*, *JHEP* **2016** (2016) 130.

[373] W.-z. Guo, F.-L. Lin and J. Zhang, *Note on ETH of descendant states in 2D CFT*, *JHEP* **2019** (2019) 152.

[374] T. Mendes-Santos, G. Giudici, M. Dalmonte and M. A. Rajabpour, *Entanglement Hamiltonian of quantum critical chains and conformal field theories*, [1906.00471].

[375] S. Murciano, P. Ruggiero and P. Calabrese, *Entanglement and relative entropies for low-lying excited states in inhomogeneous one-dimensional quantum systems*, *J. Stat. Mech.* **2019** (2019) 034001.

[376] M. Dalmonte, B. Vermersch and P. Zoller, *Quantum simulation and spectroscopy of entanglement Hamiltonians*, *Nat. Phys.* **14** (2018) 827.

[377] V. Eisler and I. Peschel, *Analytical results for the entanglement Hamiltonian of a free-fermion chain*, *J. Phys. A* **50** (2017) 284003.

[378] V. Eisler and I. Peschel, *Properties of the entanglement Hamiltonian for finite free-fermion chains*, *J. Stat. Mech.* **2018** (2018) 104001.

[379] V. Eisler, E. Tonni and I. Peschel, *On the continuum limit of the entanglement Hamiltonian*, *J. Stat. Mech.* **2019** (2019) 073101.

[380] F. Parisen Toldin and F. F. Assaad, *Entanglement Hamiltonian of Interacting Fermionic Models*, *Phys. Rev. Lett.* **121** (2018) 200602.

[381] G. Giudici, T. Mendes-Santos, P. Calabrese and M. Dalmonte, *Entanglement Hamiltonians of lattice models via the Bisognano-Wichmann theorem*, *Phys. Rev. B* **98** (2018) 134403.

[382] J. Cardy, *Some results on the mutual information of disjoint regions in higher dimensions*, *J. Phys. A* **46** (2013) 285402.

[383] B. Chen and J. Long, *Rényi mutual information for a free scalar field in even dimensions*, *Phys. Rev. D* **96** (2017) 045006.

[384] B. Chen, L. Chen, P.-x. Hao and J. Long, *On the mutual information in conformal field theory*, *JHEP* **2017** (2017) 96.

[385] B. Chen, Z.-Y. Fan, W.-M. Li and C.-Y. Zhang, *Holographic mutual information of two disjoint spheres*, *JHEP* **2018** (2018) 113.

[386] M. Headrick, A. Lawrence and M. Roberts, *Bose-Fermi duality and entanglement entropies*, *J. Stat. Mech.* **2013** (2013) P02022.

[387] H. Casini and M. Huerta, *Remarks on the entanglement entropy for disconnected regions*, *JHEP* **2009** (2009) 048.

[388] P. Facchi, G. Florio, G. Parisi and S. Pascazio, *Maximally multipartite entangled states*, *Phys. Rev. A* **77** (2008) 060304.

[389] P. Calabrese, *Entanglement entropy in conformal field theory: new results for disconnected regions*, *J. Stat. Mech.* **2010** (2010) P09013.

[390] M. Fagotti, *New insights into the entanglement of disjoint blocks*, *EPL* **97** (2012) 17007.

[391] B. Chen, J. Long and J. Zhang, *Holographic Rényi entropy for CFT with W symmetry*, *JHEP* **2014** (2014) 41.

[392] F. Liu and X. Liu, *Two intervals Rényi entanglement entropy of compact free boson on torus*, *JHEP* **2016** (2016) 58.

[393] A. Belin, C. A. Keller and I. G. Zadeh, *Genus two partition functions and Rényi entropies of large c conformal field theories*, *J. Phys. A* **50** (2017) 435401.

[394] S. Mukhi, S. Murthy and J.-Q. Wu, *Entanglement, replicas, and Thetas*, *JHEP* **2018** (2018) 5.

[395] H. Casini and M. Huerta, *Reduced density matrix and internal dynamics for multicomponent regions*, *Class. Quantum Grav.* **26** (2009) 185005.

[396] N. Shiba, *Entanglement entropy of two spheres*, *JHEP* **2012** (2012) 100.

[397] L.-Y. Hung, R. C. Myers and M. Smolkin, *Twist operators in higher dimensions*, *JHEP* **2014** (2014) 178.

[398] C. A. Agón, I. Cohen-Abbo and H. J. Schnitzer, *Large distance expansion of mutual information for disjoint disks in a free scalar theory*, *JHEP* **2016** (2016) 73.

[399] V. E. Hubeny and M. Rangamani, *Holographic entanglement entropy for disconnected regions*, *JHEP* **2008** (2008) 006.

[400] E. Tonni, *Holographic entanglement entropy: near horizon geometry and disconnected regions*, *JHEP* **2011** (2011) 4.

[401] P. Hayden, M. Headrick and A. Maloney, *Holographic mutual information is monogamous*, *Phys. Rev. D* **87** (2013) 046003.

[402] C. A. Agón, M. Headrick, D. L. Jafferis and S. Kasko, *Disk entanglement entropy for a Maxwell field*, *Phys. Rev. D* **89** (2014) 025018.

[403] A. Belavin, A. Polyakov and A. Zamolodchikov, *Infinite conformal symmetry in two-dimensional quantum field theory*, *Nucl. Phys. B* **241** (1984) 333 .

[404] A. B. Zamolodchikov, *Conformal symmetry in two-dimensional space: Recursion representation of conformal block*, *Theor. Math. Phys.* **73** (1987) 1088.

[405] T. Hartman, *Entanglement Entropy at Large Central Charge*, [1303.6955].

[406] P. Banerjee, S. Datta and R. Sinha, *Higher-point conformal blocks and entanglement entropy in heavy states*, *JHEP* **05** (2016) 127.

[407] B. Chen, J.-Q. Wu and J. Zhang, *Holographic Description of 2D Conformal Block in Semi-classical Limit*, *JHEP* **10** (2016) 110.

[408] Y. Kusuki and T. Takayanagi, *Renyi entropy for local quenches in 2D CFT from numerical conformal blocks*, *JHEP* **01** (2018) 115.

[409] J. L. Cardy, *Operator content of two-dimensional conformally invariant theories*, *Nucl. Phys. B* **270** (1986) 186 .

[410] C. Crnković, G. Sotkov and M. Stanishkov, *Genus-two partition functions for superconformal minimal models*, *Phys. Lett. B* **222** (1989) 217 .

[411] E. Cornfeld, M. Goldstein and E. Sela, *Imbalance entanglement: Symmetry decomposition of negativity*, *Phys. Rev. A* **98** (2018) 032302.

[412] N. Feldman and M. Goldstein, *Dynamics of Charge-Resolved Entanglement after a Local Quench*, [1905.10749].

[413] J. S. Dowker, *Conformal weights of charged Rényi entropy twist operators for free scalar fields in arbitrary dimensions*, *J. Phys. A* **49** (2016) 145401.

[414] J. S. Dowker, *Charged Renyi entropies for free scalar fields*, *J. Phys. A* **50** (2017) 165401.

[415] P. Caputa, M. Nozaki and T. Numasawa, *Charged entanglement entropy of local operators*, *Phys. Rev. D* **93** (2016) 105032.

[416] H. M. Wiseman and J. A. Vaccaro, *Entanglement of Indistinguishable Particles Shared between Two Parties*, *Phys. Rev. Lett.* **91** (2003) 097902.

[417] H. Barghathi, C. M. Herdman and A. Del Maestro, *Rényi Generalization of the Accessible Entanglement Entropy*, *Phys. Rev. Lett.* **121** (2018) 150501.

[418] H. Barghathi, E. Casiano-Diaz and A. D. Maestro, *Operationally accessible entanglement of one dimensional spinless fermions*, [1905.03312].

[419] P. Calabrese, P. Le Doussal and S. N. Majumdar, *Random matrices and entanglement entropy of trapped Fermi gases*, *Phys. Rev. A* **91** (2015) 012303.

[420] J. P. Keating and F. Mezzadri, *Entanglement in Quantum Spin Chains, Symmetry Classes of Random Matrices, and Conformal Field Theory*, *Phys. Rev. Lett.* **94** (2005) 050501.

[421] F. Ares, J. G. Esteve, F. Falceto and A. R. de Queiroz, *On the Möbius transformation in the entanglement entropy of fermionic chains*, *J. Stat. Mech.* **2016** (2016) 043106.

[422] F. Ares, J. G. Esteve, F. Falceto and A. R. de Queiroz, *Entanglement entropy and Möbius transformations for critical fermionic chains*, *J. Stat. Mech.* **2017** (2017) 063104.

[423] P. Calabrese, J. Cardy and I. Peschel, *Corrections to scaling for block entanglement in massive spin chains*, *J. Stat. Mech.* **2010** (2010) P09003.

[424] E. Tonni, J. Rodríguez-Laguna and G. Sierra, *Entanglement hamiltonian and entanglement contour in inhomogeneous 1D critical systems*, *J. Stat. Mech.* **2018** (2018) 043105.

[425] Y. Brun and J. Dubail, *One-particle density matrix of trapped one-dimensional impenetrable bosons from conformal invariance*, *SciPost Phys.* **2** (2017) 012.

[426] A. Colcelli, J. Viti, G. Mussardo and A. Trombettoni, *Universal off-diagonal long-range-order behavior for a trapped Tonks-Girardeau gas*, *Phys. Rev. A* **98** (2018) 063633.

[427] J. Rodríguez-Laguna, J. Dubail, G. Ramírez, P. Calabrese and G. Sierra, *More on the rainbow chain: entanglement, space-time geometry and thermal states*, *J. Phys. A* **50** (2017) 164001.

[428] V. Eisler and D. Bauernfeind, *Front dynamics and entanglement in the XXZ chain with a gradient*, *Phys. Rev. B* **96** (2017) 174301.

[429] J. Dubail, J.-M. Stéphan and P. Calabrese, *Emergence of curved light-cones in a class of inhomogeneous Luttinger liquids*, *SciPost Phys.* **3** (2017) 019.

[430] N. Allegra, J. Dubail, J.-M. Stéphan and J. Viti, *Inhomogeneous field theory inside the arctic circle*, *J. Stat. Mech.* **2016** (2016) 053108.

[431] Y. Brun and J. Dubail, *The Inhomogeneous Gaussian Free Field, with application to ground state correlations of trapped 1d Bose gases*, *SciPost Phys.* **4** (2018) 037.

[432] E. Granet, L. Budzynski, J. Dubail and J. L. Jacobsen, *Inhomogeneous Gaussian free field inside the interacting arctic curve*, *J. Stat. Mech.* **2019** (2019) 013102.

[433] E. Langmann and P. Moosavi, *Diffusive Heat Waves in Random Conformal Field Theory*, *Phys. Rev. Lett.* **122** (2019) 020201.

[434] G. Livan, M. Novaes and P. Vivo, *Introduction to Random Matrices–Theory and Practice*. Springer International Publishing, 2018.

[435] P. Calabrese, F. H. L. Essler and A. M. Läuchli, *Entanglement entropies of the quarter filled Hubbard model*, *J. Stat. Mech.* **2014** (2014) P09025.

[436] V. Eisler, *Universality in the Full Counting Statistics of Trapped Fermions*, *Phys. Rev. Lett.* **111** (2013) 080402.

[437] F. Bornemann, *On the Numerical Evaluation of Fredholm Determinants*, *Math. Comput.* **79** (2010) .

[438] F. Bornemann, *On the Numerical Evaluation of Distributions in Random Matrix Theory: A Review*, *Markov Process. Relat. Fields* **16** (2010) .

[439] P. Ruggiero, Y. Brun and J. Dubail, *Conformal field theory on top of a breathing one-dimensional gas of hard core bosons*, *SciPost Phys.* **6** (2019) 51.

[440] O. A. Castro-Alvaredo, B. Doyon and T. Yoshimura, *Emergent hydrodynamics in integrable quantum systems out of equilibrium*, *Phys. Rev. X* **6** (2016) 041065.

[441] B. Bertini, M. Collura, J. De Nardis and M. Fagotti, *Transport in Out-of-Equilibrium X X Z Chains: Exact Profiles of Charges and Currents*, *Phys. Rev. Lett.* **117** (2016) 207201.

[442] B. Doyon and T. Yoshimura, *A note on generalized hydrodynamics: inhomogeneous fields and other concepts*, *SciPost Phys.* **2** (2017) 014.

[443] B. Doyon, J. Dubail, R. Konik and T. Yoshimura, *Large-scale description of interacting one-dimensional Bose gases: generalized hydrodynamics supersedes conventional hydrodynamics*, *Phys. Rev. Lett.* **119** (2017) 195301.

[444] B. Doyon and H. Spohn, *Drude weight for the Lieb-Liniger Bose gas*, *SciPost Phys.* **3** (2017) 039.

[445] E. Ilievski and J. De Nardis, *Microscopic origin of ideal conductivity in integrable quantum models*, *Phys. Rev. Lett.* **119** (2017) 020602.

[446] L. Piroli, J. De Nardis, M. Collura, B. Bertini and M. Fagotti, *Transport in out-of-equilibrium XXZ chains: Nonballistic behavior and correlation functions*, *Phys. Rev. B* **96** (2017) 115124.

[447] M. Fagotti, *Higher-order generalized hydrodynamics in one dimension: The noninteracting test*, *Phys. Rev. B* **96** (2017) 220302.

[448] B. Doyon, T. Yoshimura and J.-S. Caux, *Soliton gases and generalized hydrodynamics*, *Phys. Rev. Lett.* **120** (2018) 045301.

[449] V. B. Bulchandani, R. Vasseur, C. Karrasch and J. E. Moore, *Bethe-Boltzmann hydrodynamics and spin transport in the XXZ chain*, *Phys. Rev. B* **97** (2018) 045407.

[450] M. Collura, A. De Luca and J. Viti, *Analytic solution of the domain-wall nonequilibrium stationary state*, *Phys. Rev. B* **97** (2018) 081111.

[451] J. De Nardis, D. Bernard and B. Doyon, *Hydrodynamic diffusion in integrable systems*, *Phys. Rev. Lett.* **121** (2018) 160603.

[452] B. Bertini, M. Fagotti, L. Piroli and P. Calabrese, *Entanglement evolution and generalised hydrodynamics: noninteracting systems*, *J. Phys. A* **51** (2018) 39LT01.

[453] D.-L. Vu and T. Yoshimura, *Equations of state in generalized hydrodynamics*, *SciPost Phys.* **6** (2019) 23.

[454] A. Bastianello, L. Piroli and P. Calabrese, *Exact Local Correlations and Full Counting Statistics for Arbitrary States of the One-Dimensional Interacting Bose Gas*, *Phys. Rev. Lett.* **120** (2018) 190601.

[455] A. Bastianello and L. Piroli, *From the sinh-Gordon field theory to the one-dimensional Bose gas: exact local correlations and full counting statistics*, *J. Stat. Mech.* **2018** (2018) 113104.

[456] V. Alba, *Towards a generalized hydrodynamics description of Rényi entropies in integrable systems*, *Phys. Rev. B* **99** (2019) 045150.

[457] T. Kinoshita, T. Wenger and D. S. Weiss, *A quantum Newton's cradle*, *Nature* **440** (2006) 900.

[458] J.-S. Caux, B. Doyon, J. Dubail, R. Konik and T. Yoshimura, *Hydrodynamics of the interacting Bose gas in the Quantum Newton Cradle setup*, *SciPost Phys.* **6** (2019) 70.

[459] M. Schemmer, I. Bouchoule, B. Doyon and J. Dubail, *Generalized Hydrodynamics on an Atom Chip*, *Phys. Rev. Lett.* **122** (2019) 090601.

[460] A. Minguzzi and D. Gangardt, *Exact coherent states of a harmonically confined Tonks-Girardeau gas*, *Phys. Rev. Lett.* **94** (2005) 240404.

[461] S. Scopa and D. Karevski, *One-dimensional Bose gas driven by a slow time-dependent harmonic trap*, *J. Phys. A* **50** (2017) 425301.

[462] S. Scopa, J. Unterberger and D. Karevski, *Exact dynamics of a one dimensional Bose gas in a periodic time-dependent harmonic trap*, *J. Phys. A* **51** (2018) 185001.

[463] X. Wen, S. Ryu and A. W. W. Ludwig, *Evolution operators in conformal field theories and conformal mappings: Entanglement Hamiltonian, the sine-square deformation, and others*, *Phys. Rev. B* **93** (2016) 235119.

[464] K. Gawedzki, E. Langmann and P. Moosavi, *Finite-time universality in nonequilibrium CFT*, *J. Stat. Phys.* (2017) 1.

[465] X. Wen and J.-Q. Wu, *Quantum dynamics in sine-square deformed conformal field theory: Quench from uniform to nonuniform conformal field theory*, *Phys. Rev. B* **97** (2018) 184309.

[466] M. Collura, S. Sotiriadis and P. Calabrese, *Equilibration of a Tonks-Girardeau Gas Following a Trap Release*, *Phys. Rev. Lett.* **110** (2013) 245301.

[467] J.-S. Caux and R. M. Konik, *Constructing the Generalized Gibbs Ensemble after a Quantum Quench*, *Phys. Rev. Lett.* **109** (2012) 175301.

[468] M. Collura and D. Karevski, *Critical Quench Dynamics in Confined Systems*, *Phys. Rev. Lett.* **104** (2010) 200601.

[469] M. A. Rajabpour and S. Sotiriadis, *Quantum quench of the trap frequency in the harmonic Calogero model*, *Phys. Rev. A* **89** (2014) 033620.

[470] A. S. Campbell, D. M. Gangardt and K. V. Kheruntsyan, *Sudden Expansion of a One-Dimensional Bose Gas from Power-Law Traps*, *Phys. Rev. Lett.* **114** (2015) 125302.

[471] R. Boumaza and K. Bencheikh, *Analytical results for the time-dependent current density distribution of expanding ultracold gases after a sudden change of the confining potential*, *J. Phys. A* **50** (2017) 505003.

[472] P. Forrester, N. Frankel, T. Garoni and N. Witte, *Finite one-dimensional impenetrable Bose systems: Occupation numbers*, *Phys. Rev. A* **67** (2003) 043607.

[473] C. Eliezer and A. Gray, *A note on the time-dependent harmonic oscillator*, *SIAM J. Appl. Math.* **30** (1976) 463.

[474] L. Landau, *Theory of superfluidity of helium-II*, *Zh. Eksp. Teor. Fiz.(Russ.)* **11** (1941) 592.

[475] H. Itô, *Variational principle in hydrodynamics*, *Prog. Theor. Phys.* **9** (1953) 117.

[476] L. P. Kadanoff and P. C. Martin, *Hydrodynamic equations and correlation functions*, *Ann. Phys.* **24** (1963) 419.

[477] M. Stone, *Bosonization*. World Scientific, 1994, 10.1142/2436.

[478] J. E. Moyal, *Quantum mechanics as a statistical theory*, in *Math. Proc. Camb. Philos. Soc.*, vol. 45, Cambridge University Press, 1949.

[479] E. Bettelheim, A. Abanov and P. Wiegmann, *Orthogonality catastrophe and shock waves in a nonequilibrium Fermi gas*, *Phys. Rev. Lett.* **97** (2006) 246402.

[480] E. Bettelheim and P. B. Wiegmann, *Universal Fermi distribution of semiclassical nonequilibrium Fermi states*, *Phys. Rev. B* **84** (2011) 085102.

[481] E. Bettelheim and L. Glazman, *Quantum ripples over a semiclassical shock*, *Phys. Rev. Lett.* **109** (2012) 260602.

[482] A. M. Tsvelik, *Quantum field theory in condensed matter physics*. Cambridge university press, 2007, 10.1007/978-3-662-03774-4.

[483] J. Cardy, *Conformal invariance and surface critical behavior*, *Nucl. Phys. B* **240** (1984) 514 .

[484] V. P. Ermakov, *Second-order differential equations: conditions of complete integrability*, *AADM* (2008) 123.

[485] E. Pinney, *The nonlinear differential equation* $y'' + p(x)y + cy^{-3} = 0$, *Proc. Am. Math. Soc.* **1** (1950) 681.

[486] V. Gritsev, P. Barmettler and E. Demler, *Scaling approach to quantum non-equilibrium dynamics of many-body systems*, *New J. Phys.* **12** (2010) 113005.

[487] M. Rigol and A. Muramatsu, *Universal properties of hard-core bosons confined on one-dimensional lattices*, *Phys. Rev. A* **70** (2004) 031603.

[488] M. Rigol and A. Muramatsu, *Ground-state properties of hard-core bosons confined on one-dimensional optical lattices*, *Phys. Rev. A* **72** (2005) 013604.

[489] W. Xu and M. Rigol, *Universal scaling of density and momentum distributions in Lieb-Liniger gases*, *Phys. Rev. A* **92** (2015) 063623.

[490] D. M. Gangardt, *Universal correlations of trapped one-dimensional impenetrable bosons*, *J. Phys. A* **37** (2004) 9335.

[491] A. Lenard, *Momentum Distribution in the Ground State of the One-Dimensional System of Impenetrable Bosons*, *J. Math. Phys.* **5** (1964) 930.

[492] A. Lenard, *One-Dimensional Impenetrable Bosons in Thermal Equilibrium*, *J. Math. Phys.* **7** (1966) 1268.

[493] H. G. Vaidya and C. A. Tracy, *One-Particle Reduced Density Matrix of Impenetrable Bosons in One Dimension at Zero Temperature*, *Phys. Rev. Lett.* **42** (1979) 3.

[494] J.-M. Stéphan, *Free fermions at the edge of interacting systems*, *SciPost Phys.* **6** (2019) 57.

[495] P. Calabrese, B. Doyon, J. Dubail and P. Ruggiero, *To appear* .

[496] T. Jacqmin, B. Fang, T. Berrada, T. Roscilde and I. Bouchoule, *Momentum distribution of one-dimensional Bose gases at the quasicondensation crossover: Theoretical and experimental investigation*, *Phys. Rev. A* **86** (2012) 043626.

[497] B. Fang, A. Johnson, T. Roscilde and I. Bouchoule, *Momentum-space correlations of a one-dimensional Bose gas*, *Phys. Rev. Lett.* **116** (2016) 050402.

[498] J. Nespolo and E. Vicari, *Equilibrium and nonequilibrium entanglement properties of two- and three-dimensional Fermi gases*, *Phys. Rev. A* **87** (2013) 032316.

[499] G. Refael and J. E. Moore, *Criticality and entanglement in random quantum systems*, *J. Phys. A* **42** (2009) 504010.

[500] M. Pouranvari and K. Yang, *Entanglement spectrum and entangled modes of random XX spin chains*, *Phys. Rev. B* **88** (2013) 075123.

[501] G. Ramírez, J. Rodríguez-Laguna and G. Sierra, *Entanglement in low-energy states of the random-hopping model*, *J. Stat. Mech.* **2014** (2014) P07003.

[502] R. Santachiara, *Increasing of entanglement entropy from pure to random quantum critical chains*, *J. Stat. Mech.* **2006** (2006) L06002.

[503] G. Refael and J. E. Moore, *Entanglement entropy of the random $s = 1$ Heisenberg chain*, *Phys. Rev. B* **76** (2007) 024419.

[504] J. A. Hoyos, A. P. Vieira, N. Laflorencie and E. Miranda, *Correlation amplitude and entanglement entropy in random spin chains*, *Phys. Rev. B* **76** (2007) 174425.

[505] Y.-C. Lin, F. Iglói and H. Rieger, *Entanglement Entropy at Infinite-Randomness Fixed Points in Higher Dimensions*, *Phys. Rev. Lett.* **99** (2007) 147202.

[506] N. E. Bonesteel and K. Yang, *Infinite-Randomness Fixed Points for Chains of Non-Abelian Quasiparticles*, *Phys. Rev. Lett.* **99** (2007) 140405.

[507] D. Binosi, G. De Chiara, S. Montangero and A. Recati, *Increasing entanglement through engineered disorder in the random Ising chain*, *Phys. Rev. B* **76** (2007) 140405.

[508] F. Iglói and Y.-C. Lin, *Finite-size scaling of the entanglement entropy of the quantum Ising chain with homogeneous, periodically modulated and random couplings*, *J. Stat. Mech.* **2008** (2008) P06004.

[509] L. M. Zhang, Z. Q. Li, D. N. Basov, M. M. Fogler, Z. Hao and M. C. Martin, *Determination of the electronic structure of bilayer graphene from infrared spectroscopy*, *Phys. Rev. B* **78** (2008) 235408.

[510] R. Yu, H. Saleur and S. Haas, *Entanglement entropy in the two-dimensional random transverse field Ising model*, *Phys. Rev. B* **77** (2008) 140402.

[511] J. A. Hoyos, N. Laflorencie, A. P. Vieira and T. Vojta, *Protecting clean critical points by local disorder correlations*, *EPL* **93** (2011) 30004.

[512] I. A. Kovács and F. Iglói, *Critical behavior and entanglement of the random transverse-field Ising model between one and two dimensions*, *Phys. Rev. B* **80** (2009) 214416.

[513] J. C. Getelina, F. C. Alcaraz and J. A. Hoyos, *Entanglement properties of correlated random spin chains and similarities with conformally invariant systems*, *Phys. Rev. B* **93** (2016) 045136.

[514] J. Rodríguez-Laguna, S. N. Santalla, G. Ramírez and G. Sierra, *Entanglement in correlated random spin chains, RNA folding and kinetic roughening*, *New J. Phys.* **18** (2016) 073025.

[515] R. Juhász and Z. Zimborás, *Entanglement entropy in aperiodic singlet phases*, *J. Stat. Mech.* **2007** (2007) P04004.

[516] F. Iglói, R. Juhász and Z. Zimborás, *Entanglement entropy of aperiodic quantum spin chains*, *EPL* **79** (2007) 37001.

[517] C. K. Burrell and T. J. Osborne, *Bounds on the Speed of Information Propagation in Disordered Quantum Spin Chains*, *Phys. Rev. Lett.* **99** (2007) 167201.

[518] F. Iglói, Z. Szatmári and Y.-C. Lin, *Entanglement entropy dynamics of disordered quantum spin chains*, *Phys. Rev. B* **85** (2012) 094417.

[519] R. Vosk and E. Altman, *Dynamical Quantum Phase Transitions in Random Spin Chains*, *Phys. Rev. Lett.* **112** (2014) 217204.

[520] D. Pekker, G. Refael, E. Altman, E. Demler and V. Oganesyan, *Hilbert-Glass Transition: New Universality of Temperature-Tuned Many-Body Dynamical Quantum Criticality*, *Phys. Rev. X* **4** (2014) 011052.

[521] R. Vasseur and J. E. Moore, *Multifractal orthogonality catastrophe in one-dimensional random quantum critical points*, *Phys. Rev. B* **92** (2015) 054203.

[522] I. Sandy, *Ground state entanglement in one-dimensional translationally invariant quantum systems*, *J. Math. Phys.* **51** (2010) 022101.

[523] D. Gottesman and M. B. Hastings, *Entanglement versus gap for one-dimensional spin systems*, *New J. Phys.* **12** (2010) 025002.

[524] S. Bravyi, L. Caha, R. Movassagh, D. Nagaj and P. W. Shor, *Criticality without Frustration for Quantum Spin-1 Chains*, *Phys. Rev. Lett.* **109** (2012) 207202.

[525] L. Huijse and B. Swingle, *Area law violations in a supersymmetric model*, *Phys. Rev. B* **87** (2013) 035108.

[526] N. Shiba and T. Takayanagi, *Volume law for the entanglement entropy in non-local QFTs*, *JHEP* **2014** (2014) 33.

[527] G. Gori, S. Paganelli, A. Sharma, P. Sodano and A. Trombettoni, *Explicit Hamiltonians inducing volume law for entanglement entropy in fermionic lattices*, *Phys. Rev. B* **91** (2015) 245138.

[528] L. Dell'Anna, O. Salberger, L. Barbiero, A. Trombettoni and V. E. Korepin, *Violation of cluster decomposition and absence of light cones in local integer and half-integer spin chains*, *Phys. Rev. B* **94** (2016) 155140.

[529] T. Motzkin, *Relations Between Hypersurface Cross Ratios, and a Combinatorial Formula for Partitions of a Polygon, for Permanent Preponderance, and for Nonassociative Products*, *Bull. Amer. Math. Soc.* **54** (1948) 352.

[530] E. Fredkin and T. Toffoli, *Conservative Logic*, *Int. J. Theor. Phys.* **21** (1982) .

[531] C. Dasgupta and S.-k. Ma, *Low-temperature properties of the random Heisenberg antiferromagnetic chain*, *Phys. Rev. B* **22** (1980) 1305.

[532] G. Ramírez, J. Rodríguez-Laguna and G. Sierra, *From conformal to volume law for the entanglement entropy in exponentially deformed critical spin 1/2 chains*, *J. Stat. Mech.* **2014** (2014) P10004.

[533] G. Ramírez, J. Rodríguez-Laguna and G. Sierra, *Entanglement over the rainbow*, *J. Stat. Mech.* **2015** (2015) P06002.

[534] S. N. Majumdar, *Universal first-passage properties of discrete-time random walks and Lévy flights on a line: Statistics of the global maximum and records*, *Physica A* **389** (2010) .

[535] A. Comtet and S. N. Majumdar, *Precise asymptotics for a random walker's maximum*, *J. Stat. Mech.* **2005** (2005) P06013.